

BULLETIN OF THE MINERAL RESEARCH AND EXPLORATION

Foreign Edition

2021

164

ISSN : 0026-4563

E-ISSN : 2651-3048



CONTENTS

Research Articles

Production of high purity thorium oxide from leach liquor of complex oresAyşe ERDEM, Haydar GÜNEŞ, Çiğdem KARA, Hasan AKÇAY, Akan GÜLMEZ and Zümrüt ALKAN	1
Petrographic characteristics of deep marine turbidite sandstones of the Upper Cretaceous Tanjero Formation, Northwestern Sulaimaniyah, Iraq: implications for provenance and tectonic settingHasan ÇELİK and Hemin Muhammad HAMA SALİH	11
Investigation of the paleodepositional environment of the middle Miocene aged organic matter rich rocks (Tavas/Denizli/SW Turkey) by using biomarker parameters and stable isotope compositions (¹³ C and ¹⁵ N)Demet Banu KORALAY	39
Organic geochemical characteristics, depositional environment and hydrocarbon potential of bituminous marls in Bozcahöyük (Seyitömer/Kütahya) BasinFatih BÜYÜK and Ali SARI	53
Discrimination of earthquakes and quarry blasts in Kula District (Manisa, Turkey) and its vicinity by using linear discriminate function method and artificial neural networksAylin TAN, Gündüz HORASAN, Doğan KALAFAT and Ali GÜLBAĞ	75
Clay Mineralogy and Paleoclimatic Properties of the Neogene Deposits in Sinanpaşa Basin (Afyon-Western Anatolia)Elif AKISKA and Zehra KARAKAŞ	93
Late Cretaceous-middle Eocene olistrostromal pelagic units in the Biga Peninsula (NW Anatolia); Balıkkaya formationSerdar AKGÜNDÜZ and İzver ÖZKAR ÖNGEN	119
Some criteria used in determining paleoshorelines, examples from Turkey and Rhodes IslandOkan TÜYSÜZ	147
Role of the Cretaceous normal faults on the formation of the Eocene (Pontide) fold-thrust belt structures in offshore Akcakoca-Amasra area, Western Black Sea basin, TurkeyÖzgür TÜRKMEN and İbrahim ÇEMEN	165
Systematics, biostratigraphy and paleoenvironmental investigation of early Ypresian Alveolina assemblages in the northern part of Isparta Angle (Keçiözü, Isparta, SW Turkey)Alper BOZKURT and Muhittin GÖRMÜŞ	183
Impact of solid waste on groundwater quality in selected dumpsites in Akwa Ibom State, Nigeria using resistivity and hydrochemical data Abraham Christopher UDOH, Augustine Ifeanyi CHINWUKO, Ajana Godwin ONWUEMESI, Emmanuel Kenechukwu ANAKWUBA, Augustine Oyunga OYONGA and Ayatu Ojonugwa USMAN	231
Optimization of leaching conditions for extraction of magnesium from a chromite beneficiation plant tailing predominantly containing lizarditeHakan ÇİFTÇİ, Bekir ARSLAN, Ayşegül BİLEN, Zeyni ARSOY and Bahri ERSOY	251
Geology of the Yeşilyurt gold deposit: an example of low-angle normal fault-related mineralization, Eastern Anatolia-TurkeyEsra YILDIRIM, Nail YILDIRIM, Cahit DÖNMEZ and Kurtuluş GÜNAY	261
Bulletin of the Mineral Research and Exploration Notes to the Authors.....	281

Phone : +90 (312) 201 10 00

Fax : +90 (312) 287 91 88

Adress : MTA 06530 - Ankara - TURKEY

www.mta.gov.tr

BULLETIN OF THE MINERAL RESEARCH AND EXPLORATION

Foreign Edition

2021

164

ISSN : 0026-4563
E-ISSN : 2651-3048

CONTENTS

Research Articles

- Production of high purity thorium oxide from leach liquor of complex ores
.....Ayşe ERDEM, Haydar GÜNEŞ, Çiğdem KARA, Hasan AKÇAY, Akan GÜLMEZ and Zümrüt ALKAN 1
- Petrographic characteristics of deep marine turbidite sandstones of the Upper Cretaceous Tanjero Formation, Northwestern Sulaimaniyah, Iraq: implications for provenance and tectonic setting
.....Hasan ÇELİK and Hemin Muhammad HAMA SALİH 11
- Investigation of the paleodepositional environment of the middle Miocene aged organic matter rich rocks (Tavas/Denizli/SW Turkey) by using biomarker parameters and stable isotope compositions (¹³C and ¹⁵N)
..... Demet Banu KORALAY 39
- Organic geochemical characteristics, depositional environment and hydrocarbon potential of bituminous marls in Bozcahöyük (Seyitömer/Kütahya) Basin
..... Fatih BÜYÜK and Ali SARI 53
- Discrimination of earthquakes and quarry blasts in Kula District (Manisa, Turkey) and its vicinity by using linear discriminate function method and artificial neural networks
..... Aylin TAN, Gündüz HORASAN, Doğan KALAFAT and Ali GÜLBAĞ 75
- Clay Mineralogy and Paleoclimatic Properties of the Neogene Deposits in Sinanpaşa Basin (Afyon-Western Anatolia)
..... Elif AKISKA and Zehra KARAKAŞ 93
- Late Cretaceous-middle Eocene olistrostromal pelagic units in the Biga Peninsula (NW Anatolia); Balıkkaya formation
.....Serdar AKGÜNDÜZ and İzver ÖZKAR ÖNGEN 119
- Some criteria used in determining paleoshorelines, examples from Turkey and Rhodes Island
..... Okan TÜYSÜZ 147
- Role of the Cretaceous normal faults on the formation of the Eocene (Pontide) fold-thrust belt structures in offshore Akcakoca-Amasra area, Western Black Sea basin, Turkey
..... Özgür TÜRKMEN and İbrahim ÇEMEN 165
- Systematics, biostratigraphy and paleoenvironmental investigation of early Ypresian Alveolina assemblages in the northern part of Isparta Angle (Keçiborlu, Isparta, SW Turkey)
..... Alper BOZKURT and Muhittin GÖRMÜŞ 183
- Impact of solid waste on groundwater quality in selected dumpsites in Akwa Ibom State, Nigeria using resistivity and hydrochemical data
Abraham Christopher UDOH, Augustine Ifeanyi CHINWUKO, Ajana Godwin ONWUEMESI, Emmanuel Kenechukwu
..... ANAKWUBA, Augustine Oyonga OYONGA and Ayatu Ojonugwa USMAN 231
- Optimization of leaching conditions for extraction of magnesium from a chromite beneficiation plant tailing predominantly containing lizardite
..... Hakan ÇİFTÇİ, Bekir ARSLAN, Ayşegül BİLEN, Zeyni ARSOY and Bahri ERSOY 251
- Geology of the Yeşilyurt gold deposit: an example of low-angle normal fault-related mineralization, Eastern Anatolia-Turkey
..... Esra YILDIRIM, Nail YILDIRIM, Cahit DÖNMEZ and Kurtuluş GÜNAY 261
- Bulletin of the Mineral Research and Exploration Notes to the Authors..... 281

OWNER ON BEHALF OF MTA GENERAL DIRECTORATE**GENERAL DIRECTOR**

Yasin ERDOĞAN

EXECUTIVE PUBLICATION EDITORIAL BOARD

Şule GÜRBOĞA (Chairman)

Oğuz ALTUN

Dilek Gülnur DEMİRAY

Huriye DEMİRCAN

Ash Zeynep YAVUZOĞLU

Füsün YİĞİT FETHİ

This issue was prepared for publication by the previous Executive Publication Editorial Board consisting of Erol TİMUR, Oğuz ALTUN, Dilek Gülnur DEMİRAY, Huriye DEMİRCAN, Füsün YİĞİT FETHİ, Şule GÜRBOĞA, Ash Zeynep YAVUZOĞLU.

EDITOR-IN-CHIEF

Halim MUTLU (Ankara-Turkey)

ASSOCIATED EDITORS

Orhan R. ABBASOV (Azerbaijan)

Sinan AKISKA (Ankara-Turkey)

Oğuz ALTUN (Ankara-Turkey)

Dilek Gülnur DEMİRAY (Ankara-Turkey)

Huriye DEMİRCAN (Ankara-Turkey)

Şule GÜRBOĞA (Ankara-Turkey)

Doğan KALAFAT (İstanbul-Turkey)

Sándor KELE (Hungary)

David LENTZ (Canada)

Robert MORITZ (Switzerland)

Neşe OYAL (Ankara-Turkey)

Eren PAMUK (Ankara-Turkey)

Ökmen SÜMER (İzmir-Turkey)

Pınar ŞEN (Ankara-Turkey)

Ash Zeynep YAVUZOĞLU (Ankara-Turkey)

Füsün YİĞİT FETHİ (Ankara-Turkey)

ADVISORY BOARD

Erdin BOZKURT (Ankara-Turkey)

Osman CANDAN (İzmir-Turkey)

Ahmet GÖKÇE (Sivas-Turkey)

M. Cemal GÖNCÜOĞLU (Ankara-Turkey)

Nilgün GÜLEÇ (Ankara-Turkey)

Cahit HELVACI (İzmir-Turkey)

Kamil KAYABALI (Ankara-Turkey)

Nuretdin KAYMAKÇI (Ankara-Turkey)

Aral İ. OKAY (İstanbul-Turkey)

Cengiz OKUYUCU (Konya-Turkey)

Osman PARLAK (Adana-Turkey)

Okan TÜYSÜZ (İstanbul-Turkey)

İbrahim UYSAL (Trabzon-Turkey)

Taner ÜNLÜ (Ankara-Turkey)

Yücel YILMAZ (İstanbul-Turkey)

EDITORIAL BOARD

Peyman AFZAL (İran)

Funda AKGÜN (İzmir-Turkey)

Mehmet ARSLAN (Trabzon-Turkey)

Serdar BAYARI (Ankara-Turkey)

Yavuz BEDİ (Ankara-Turkey)

Ömer BOZKAYA (Denizli-Turkey)

Emin CANDANSAYAR (Ankara-Turkey)

Ömer Faruk ÇELİK (Kocaeli-Turkey)

Emin ÇİFTÇİ (İstanbul-Turkey)

Atilla ÇİNER (İstanbul-Turkey)

Cengiz DEMİR (Trabzon-Turkey)

Harald DILL (Germany)

Mustafa Nuri DOLMAZ (İsparta-Turkey)

Bayram ERÇIKDI (Trabzon-Turkey)

Semih ERGİNTAV (İstanbul-Turkey)

Yalçın ERSOY (İzmir-Turkey)

Yener EYÜBOĞLU (Trabzon-Turkey)

Mustafa FENER (Ankara-Turkey)

Marie-Beatrice FOREL (France)

Yurdal GENÇ (Ankara-Turkey)

Klaus GESSNER (Germany)

Candan GÖKÇEOĞLU (Ankara-Turkey)

Muhittin GÖRMÜŞ (Ankara-Turkey)

Levent GÜLEN (Sakarya-Turkey)

Talip GÜNGÖR (İzmir-Turkey)

Zülfü GÜROCAK (Elazığ-Turkey)

Semih GÜRSU (Muğla-Turkey)

Nurullah HANILÇI (İstanbul-Turkey)

Murat HATİPOĞLU (İzmir-Turkey)

Zihni Mümtaz HİSARLI (İstanbul-Turkey)

James JACKSON (England)

Yusuf Kağan KADIOĞLU (Ankara-Turkey)

Selahattin KADİR (Eskişehir-Turkey)

Reyhan KARA GÜLBAY (Trabzon-Turkey)

Volkan KARABACAK (Eskişehir-Turkey)

Hüseyin KARAKUŞ (Kütahya-Turkey)

Ali İhsan KARAYİĞİT (Ankara-Turkey)

Nizamettin KAZANCI (Ankara-Turkey)

Gilbert KELLING (England)

Peter KÖNINGSHOF (Almanya)

İlkay KUŞÇU (Muğla-Turkey)

Atike NAZİK (Adana-Turkey)

Hakan NEFESLİOĞLU (Ankara-Turkey)

Roland OBERHÄNSLI (Almanya)

Bülent ORUÇ (Kocaeli-Turkey)

Vural OYAN (Van-Turkey)

Ercan ÖZCAN (İstanbul-Turkey)

Yılmaz ÖZÇELİK (Ankara-Turkey)

Sacit ÖZER (İzmir-Turkey)

Nazire ÖZGEN ERDEM (Sivas-Turkey)

Oya PAMUKÇU (İzmir-Turkey)

Dimitrios PAPANIKOLAU (Greece)

Franco PIRAJNO (Australia)

Alastair H.F. ROBERTSON (İngiltere)

Ioan SEGHEDI (Romania)

Gürol SEYİTOĞLU (Ankara-Turkey)

Carlos M. De SILVA (Portugal)

Hasan SÖZBİLİR (İzmir-Turkey)

Orhan TATAR (Sivas-Turkey)

Uğur Kağan TEKİN (Ankara-Turkey)

Erhan TERCAN (Ankara-Turkey)

Tamer TOPAL (Ankara-Turkey)

Selami TOPRAK (Ankara-Turkey)

Atiye TUĞRUL (İstanbul-Turkey)

Necati TÜYSÜZ (Trabzon-Turkey)

Katsumi UENO (Japan)

M. Emin ULUGERGERLİ (Çanakkale-Turkey)

Uğur ULUSOY (Sivas-Turkey)

Timur USTAÖMER (İstanbul-Turkey)

Alaaddin VURAL (Gümüşhane-Turkey)

John WINCHESTER (England)

Hüseyin YALÇIN (Sivas-Turkey)

Nurdan YAVUZ (Ankara-Turkey)

Özcan YİĞİT (Çanakkale-Turkey)

Erdiç YİĞİTBAŞ (Çanakkale-Turkey)

Halil YUSUFUĞLU (Ankara-Turkey)

MANAGING EDITOR

Banu Ebru BİNAL (Head of the Department of Scientific Documentation and Presentation), e-posta: banu.binal@mta.gov.tr

LOCATION OF MANAGEMENT

Redaksiyon Kurulu Başkanlığı

Maden Tetkik ve Arama Genel Müdürlüğü

Genel Müdürlük Binası (A Blok)

Dumlupınar Bulvarı No: 33/A 06530 Çankaya/ANKARA

e-posta: redaksiyon@mta.gov.tr

The translations of Erdem et al. Yıldırım et al. were made by Buğra ÇAVDAR. The translation of Çelik and Hama Salih was made by Mustafa Batuhan ERTEKİN. The translation of Büyük and Sarı was made by Catherine YİĞİT. The translation of Tan et al. was made by Esra AK. The translation of Tüysüz, Bozkurt and Görmüş were made by M.Kerem AVCI.

Bull. Min. Res. Exp. is indexed and abstracted in TR Dizin, Emerging Source Citation Index (ESCI), Scopus, The ICI Journals Master List (Copernicus), Directory of Open Access Journals (DOAJ), Open Academic Journals Index (OAJI), Georef, MIAR, EBSCO and Zoological Record.

The Bulletin of the Mineral Research and Exploration is published in three issues in a year. Each bulletin is printed in Turkish and English languages as two separate issues. The English and Turkish issues of the "Bulletin of the Mineral Research and Exploration" can be obtained from "BDT Department" free of charge, either directly or ordered by adding postage fee from the correspondence address. Typesetting and printing operations are carried out and followed by the Publication Service of the Scientific Documentation and Publicity Department. Typesetting and Print Review: Yaşar Özkan, Tuğba Uğur Aydın e-mail: bdt@mta.gov.tr

The section of "notes to the authors", format, copyright and other information can be obtained from www.mta.gov.tr as PDF files.

Printed Date:

Printing House: Kuban Matbaacılık - İvedik Organize Sanayi Matbaacılar Sitesi 1514. Sokak No: 20 • Phone: 0312 395 2070 • Fax: 0312 395 3723 • www.kubanmatbaa.com

Periodical

ISSN: 0026-4563

E-ISSN: 2651-3048

© All rights reserved. This journal and the individual contributions including in the issue are under copyright by the General Directorate of Mineral Research and Exploration (MTA), and may not be reproduced, resold, and used without permission and addressing the bulletin.



Bulletin of the Mineral Research and Exploration

<http://bulletin.mta.gov.tr>



Production of high purity thorium oxide from complex ores leach liquor

Ayşe ERDEM^{a*}, Haydar GÜNEŞ^a, Çiğdem KARA^a, Hasan AKÇAY^a, Akan GÜLMEZ^a and Zümrüt ALKAN^a

^aGeneral Directorate of Mineral Research and Exploration, Mineral Analysis and Technology Department, 06530, Ankara, Turkey

Research Article

Keywords:

Thorium, Solvent
Extraction, Leach Liquor.

ABSTRACT

This paper investigates a method for separation and purification of thorium from leach liquors containing rare-earth elements (REE). Iron, which causes problems in the stage of thorium extracting, was first removed by using Adogen 464 solvent. Thorium was extracted with 30% D2EHPA-in kerosene with 1/3 organic/aqueous ratio and stoichiometry of the thorium-D2EHPA complex was calculated as 1:2.6 from slope analysis. After the extraction, LREE and HREE were scrubbed from the extracted organic with 0.25 M H₂SO₄ and 6 M HCl, respectively. Thorium oxalate was precipitated by oxalic acid and calcined at 1,050 °C. It was, after calcination, determined that purity of thorium oxide is 99.23%, based on the ICP-OES analysis.

Received Date: 17.01.2020

Accepted Date: 25.03.2020

1. Introduction

Thorium is one of the radioactive elements that could be found within mineral structures in nature but cannot be directly used in nuclear reactors. Thorium can be converted to fissionable U²³³ isotope by several gradual neutron capture reactions (Kaya and Bozkurt, 2003). Thorium oxide, which has a high melting temperature of 3,300 °C, is also used in non-fuel areas. Aerospace industry, lighting, ceramic production, high quality lenses, petroleum distillation, sulfuric acid and nitric acid production can be exemplified as usage fields of that. Additionally, Th-Mg alloys, thanks to their lightness, high temperature resistance and creep resistance, are used in aircrafts (Yıldız, 2016). More than forty minerals containing significant amount of thorium have been discovered, but only three of them can be used in thorium production; thorianite (ThO₂), thorite (ThSiO₄), and monazite [(Ce, La, Nd, Th, Y)

PO₄] (Du et al., 1993; Zhang et al., 2012; Demol et al., 2018). Monazite, which contains mineable rate of REE, is the most widespread and most commercially used one among the minerals containing Th. In addition to monazite, bastnäsite and xenotime are also widespread REE minerals containing thorium (Ditz et al., 1990; Nasab et al., 2011).

In this study, Th-parisite was determined as the main mineral bearing thorium as a result of mineral liberation analysis of complex ore. Studies have shown that Th-parisite is the main mineral containing Th and REE in the ore. 99% of thorium element is in Th-parisite mineral.

Solvent extraction has become an important method for mineral processing studies after its usage during 1940's for uranium production. Thanks to this method, sufficient knowledge has been provided to be used in the production of various metals from

Citation Info: Erdem, A., Güneş, H., Kara, Ç., Akçay, H., Gülmez, A., Alkan, Z. 2021. Production of high purity thorium oxide from complex ores leach liquor. Bulletin of the Mineral Research and Exploration 164, 1-10.
<https://doi.org/10.19111/bulletinofmre.709316>

*Corresponding author: Ayşe ERDEM, ayse.erdem@mta.gov.tr

low grade ores, scraps, wastes and dilute aqueous solutions. It has facilitated, compared to old methods, the separation of chemically similar precious metals such as REE, Zr-Hf, Nb-Ta (Cox, 2004). The solvent extraction method takes place in three stages as loading the desired elements into the organic phase, scrubbing the co-added elements from the organic phase and stripping the desired elements from the organic phase (Ritcey and Ashbrook, 1979).

In recent years, cationic solvents have been used more for the production of REE, Th and U, but the main problem in cationic solvents has been stripping of the desired metal from extracted organic. The stripping problem encountered after extracting by D2EHPA was overcome with Cyanex 572. Wang et al. have studied the process of separation of Th and REE from radioactive waste with Cyanex 572. In these processes, since Fe as main impurity is extracted with Th, it prevents production of high purity Th. The purity of Th is up to 99% in Fe-free feed solution (Wang et al., 2017). To extract Fe, Mishra et al., 2011 have used tricaprylmethylammonium chloride (Aliquat 336), a quaternary amine, to extract Fe (III) from the chloride medium. It has been determined that extracting efficiencies increase as HCl and Aliquat 336 concentrations raise. As a result of the data obtained, Aliquat 336 makes it possible to extract the iron from the solution by extracting only the iron onto the organic phase (Mishra et al., 2011). In terms of this, Saji and Reddy investigated the synergic solvent extraction method to extract iron from chloride liquor obtained from wastes. They tried different ratios of tributyl phosphate (TBP) + methyl isobutyl ketone (MIBK) to produce high purity iron chloride and were able to achieve the highest synergic effect by using %70 TBP + %30 MIBK (Saji and Reddy, 2001). On the other hand, Sahu and Das investigated the synergistic solvent extraction of solutions containing iron over 100 g/L. They analyzed the synergistic effect of D2EHPA and TBP solvents in benzene and achieved the highest synergy coefficient with 40% TBP + 20% D2EHPA. Based on the information in this study, it was concluded that TBP additive facilitates stripping during the stripping phase (Sahu and Das, 1997).

The separation of Th and U from REE with 2-ethylhexyl phosphoric acid mono 2-ethylhexyl ester (PC-88A) has been studied by Dinkar et al., 2012. During extracting studies, Th was completely taken

into organic phase. Different chemicals have been used for stripping and carbonates have been identified as the best stripping chemicals (Dinkar et al., 2012). Bahri et al. (2018) have studied the extraction and purification of Malaysian monazite. Purification was carried out with chemical processes and solvent extraction. 98.85% purity of ThO₂ was produced from nitric acid medium (Bahri et al., 2018; Salehuddin et al., 2019). Th production from monazite was carried out by Ali et al., 2007 in eight stages with Aliquat 336 from nitric acid medium. The stripping experiments were performed in 5 steps with HCl and the Th recovery efficiency from leach liquor was calculated as 97% (Ali et al., 2007). Thorium and REE separations have also been worked in a sulfuric acid environment by Li et al., 2004 and it resulted with thorium extracting by using primary amine (N1923). Before extracting REE from the medium, MgO was used to extract Fe and REE were extracted with D2EHPA and stripped with HCl (Li et al., 2004).

After stripping, thorium with high efficiency can be precipitated with the help of oxalic acid. Different volumes of leach liquor and oxalic acid have been tested by Güneş et al. (2019) to selectively precipitate thorium. The precipitation of Th with the lowest level of REE content was achieved by amount of 12% oxalic acid by volume (Güneş et al., 2019). The kinetics of the thermal degradation required for the conversion of thorium oxalate to thorium oxide and the decomposition temperatures were investigated by Aybers (1998). At this stage, the conversion temperature of thorium oxalate to thorium oxide has been determined as 410 °C (Aybers, 1998). The effects of calcination temperature and temperature on crystal size were investigated by D'Eye and Sellman (1955). It was determined that thorium oxide calcined at temperatures lower than 400 °C is more hygroscopic than those calcined at higher temperatures (D'eye and Sellman, 1955).

In this study, high purity of ThO₂ production was achieved by using Th-parasite ore for the first time in the literature. Solvent extraction has been performed by using Adogen 464 to remove iron which is the element that causes problems with extracting and purity of Th. Thorium extracting with D2EHPA from the Fe-free solution was performed in 94% efficiency. The REE extracted to organic phase with Th were scrubbed first with dilute sulfuric acid and then with concentrated

hydrochloric acid. In the phase of obtaining ThO_2 , it was precipitated with oxalic acid and calcined.

2. Experimental Studies

2.1. Leach Liquor ve Chemicals

The ore, which is required to obtain the solution used in solvent extraction processes, was concentrated and extracted by General Directorate of Mineral Research and Exploration (MTA). The chemical composition of chlorinated leach liquor is presented in table 1. The LREE class referenced in table 1 consists of La, Ce, Pr, Nd, Sm and Eu elements, and the HREE class consists of Gd, Tb, Dy, Ho, Er, Tm, Yb, Lu and Y elements. The brand of di-2-ethylhexyl phosphoric acid (D2EHPA), methyltrialkyl C8-C10 ammonium chloride (Adogen 464), decyl alcohol (1-Decanol) and tributyl phosphate (TBP) is Merck. On the other hand, brand of bis 2,4,4-trimethylpenyl phosphinic acid (Cyanex 272), Cyanex 572 and trioctyl phosphine oxide (TOPO) is Cytec Inc. Kerosene was obtained from local sources. All solvents were used directly without any purification. All acids which were used are Merck brand. All chemicals used are analytically pure and are supplied by MTA.

2.2. Equipment

Metal concentrations in solution were determined with Agilent 725 Series Inductively Coupled Plasma Optic Emission Spectrometer (ICP - OES) device. Electron microscope images and EDS analyzes were

provided with the FEI Quanta 400 Scanning Electron Microscope (SEM-EDS) device.

2.3. Method

Cyanex 272, Cyanex 572 and D2EHPA solvents at different concentrations were tried to extract thorium directly from the leach liquor. With all three solvents, elements other than Fe, Th, REE, Cu, Ti, U and V did not exhibit extracting behavior. The separation factor between iron and thorium is low with D2EHPA solvent, where the highest thorium extracting efficiency is observed and also, it was determined that other elements do not exhibit remarkable extracting behavior. Therefore, Fe removal studies were performed by using Adogen 464 and TBP before thorium extracting. Determining the most favorable Adogen 464 concentration was based on the separation of Fe, Th, REE and impurities from each other.

Based on the information obtained from the preliminary experiments, thorium extracting was optimized with D2EHPA from the iron-extracted solution. It was also found that REE, Ti, Cu, V and U elements were extracted as impurities during the thorium extracting. The optimization at this stage was based on high thorium extracting efficiency and low impurity extracting efficiency. Experiments were carried out at the mixing speed at which the phases were completely mixed. Mixing time of 15 minutes was determined to ensure the chemical balance in all of the experiments. The pH value of the leach liquor without Fe was measured as -0.58 and there was no application to change the pH value. The organic/aqueous phase ratio was used as 1/1 unless otherwise specified.

D2EHPA concentration was varied from 10% (0.3 M) to 50% (1.5 M) by volume in kerosene. D2EHPA concentrations above 50% are not suitable due to gel formation and undesired cp-extractions. The organic/aqueous phase ratio was changed between 1/3 and 3/1 at a concentration of 30% D2EHPA. This ratio was found to be sufficient since a single stage extracting was achieved with a 94% efficiency.

Scrubbing processes were applied to reduce the effect of REE and other impurities extracted with thorium on the end product. Scrubbing was applied in varying concentrations of HCl, H_2SO_4 and HNO_3 to determine the acids and concentrations to be used

Table 1- Chemical composition of leach liquor.

Element	Concentration (mg/L)
Th	507.2
U	40.6
LREE	29,150
HREE	265
Fe _(total)	5,490
Al	3,000
Ca	4,300
Cu	12
Mg	425
Mn	1,570
Pb	112
Si	700
Ti	32
V	150
Zn	210

in this process. As a result, two separate acids were used for LREE and HREE. It was observed that only high concentration of sulfuric acid is effective for thorium stripping. After stripping from the organic phase, precipitation was carried out with oxalic acid. The solid product was dried in the oven at 105 °C and calcined in the oven at 1,050 °C. Purity of ThO₂ was determined in the ICP-OES device by the method of dissolving impurities.

2.4. Data Processing

Extracting efficiencies were taken into consideration to evaluate experimental data and the most suitable parameters for each step were determined according to the extracting efficiency values (E%) calculated with the mass balance presented in equation 1.

$$\%E = \frac{C_0 - C_e}{C_0} \times 100 \quad (1)$$

C₀ and C_e represent initial and equilibrium concentrations, respectively. Distribution ratio and separation factor are represented in equation 2 and equation 3, respectively.

$$D_A = \frac{(C_0 - C_e)V_a}{C_e V_o} \quad (2)$$

$$\beta_{A/B} = \frac{D_A}{D_B} \quad (3)$$

Aqueous and organic phase volumes, in equation 2, are respectively represented as V_a and V_o. D_A represents the distribution ratio of 'A' element. The distribution rate is the main measurement parameter for solvent extraction processes and is determined by mass balance. 'A' and 'B' are different elements and β_{A/B} represents the factor where 'A element' separates from 'B element'.

3. Experimental Results

3.1. Extraction of Iron

During iron extraction, TBP and Adogen 464 solvents were tried and the effect of concentration on separation of iron and other impurities from thorium was investigated. The effect of concentration on separation factors is presented in figures 1 and 2.

According to figures 1 and 2, the highest separation factors for Fe/Th and impurity/Th were obtained with

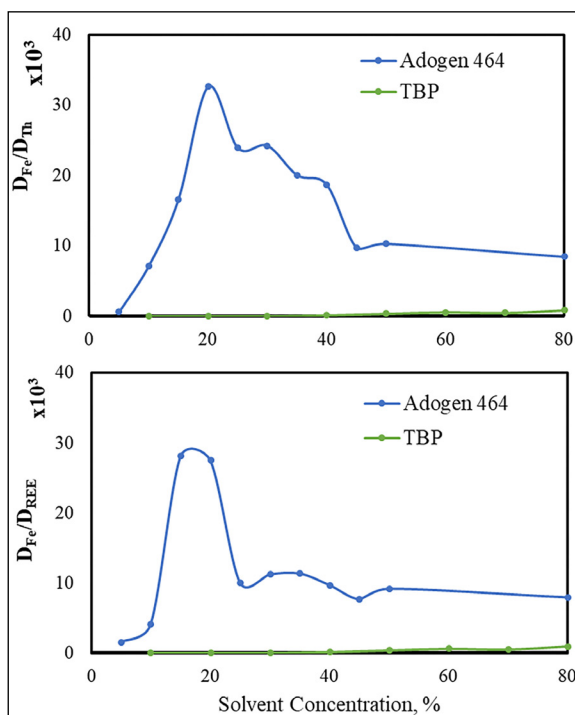


Figure 1- Separation factors of Fe/REE and Fe/Th according to different solvent concentrations.

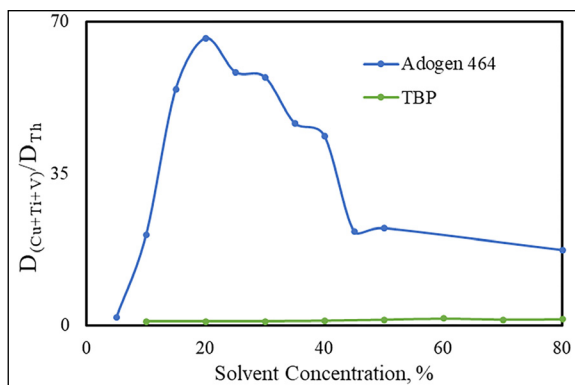


Figure 2- Separation factors of impurities (Cu+Ti+V)/Th according to different solvent concentrations.

20% Adogen in kerosene. Concentration of 20% Adogen 464 was preferred for further studies due to the highest level of separation factors between (Cu+Ti+V)-Th. In figure 3, the extracting efficiency of Fe, U and impurities versus Adogen are graphed and the effect of solvent concentration on extracting efficiency was examined.

Cu, Fe, Ti, U and V extracting efficiencies, which are other elements that will cause impurity during thorium production stage, are shown in figure 3. In addition, REE extracting rates remained below 1% in all concentrations. As a result of the experiments

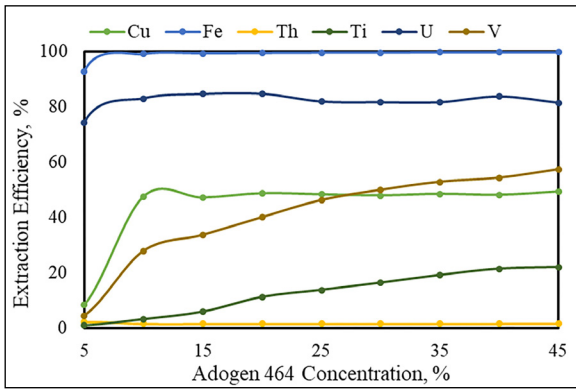


Figure 3- Effect of Adogen 464 concentration to the extraction efficiency.

performed, it was determined that all of the iron in solution can be removed with 20% Adogen 464 solvent dissolved in kerosene. The aqueous phase obtained as a result of the process was used in later stages for thorium extracting.

3.2. Extracting of Thorium

D2EHPA was used to transfer the thorium from aqueous phase to organic phase, and extracting efficiencies in proportion to the solvent concentration in kerosene are presented in figure 4. HREE, other than Dy, Er, Y and Yb, are not represented in the figures due to their low concentrations and low extracting efficiencies. The impurities having high extracting efficiencies and extracting efficiencies of Cu, Ti and U that might cause impurity in the final product in later stages are represented.

When figure 4 is examined, Th, Ti and U exhibit similar extracting behaviors and indicate a high

extracting efficiency even at low concentrations. Thorium extracting efficiency was determined as 95% at 30% D2EHPA usage rate. HREE were not extracted below 20% D2EHPA concentration. In general, it has been observed that the extracting efficiency of elements other than Cu increases with the concentration of D2EHPA. Distribution rates were calculated only for Th, Ti, Y and Yb. Distribution rates calculated according to the equation 2 are shown in figure 5.

Th, Y and Yb distribution rates increase logarithmically with D2EHPA concentration. This logarithmic relationship shows the first-order reaction between Th and D2EHPA. According to the slope analysis, stoichiometry of Th-D2EHPA was determined as 1:2.8. Stoichiometric ratios were calculated as 1:1.7, 1:1.5 and 1:2.5 for Ti, Y and Yb, respectively.

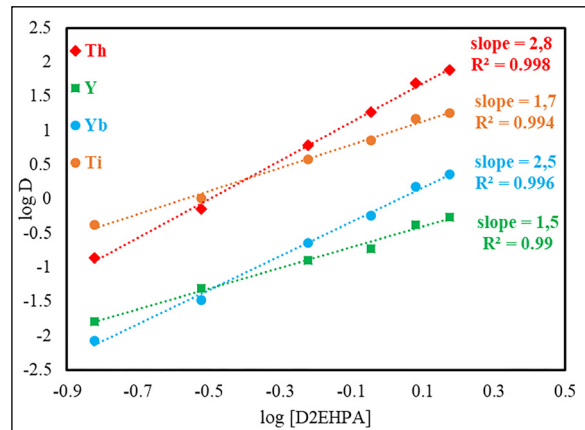


Figure 5- Logarithm of D2EHPA concentration vs logarithm of distribution ratios.

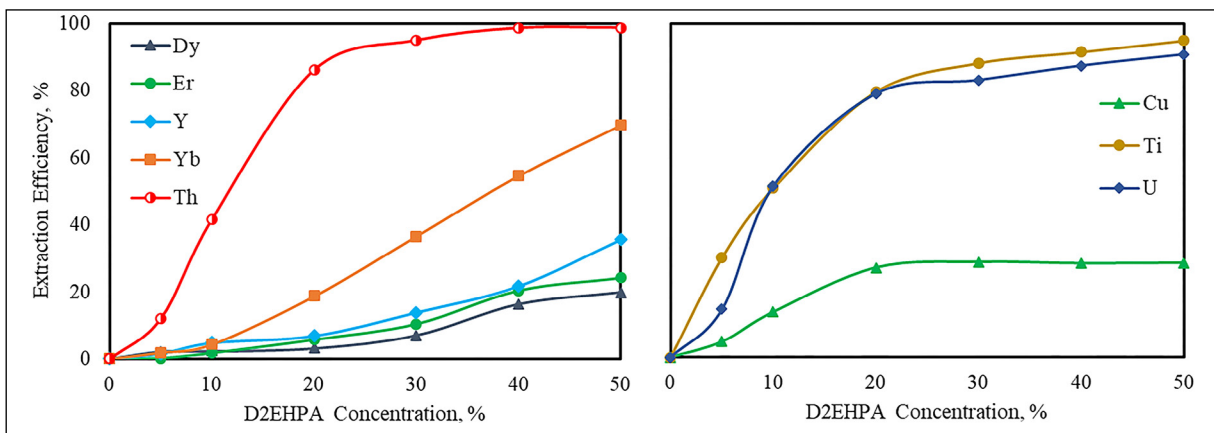


Figure 4- Effect of D2EHPA concentration to the extraction efficiencies of Th and HREEs.

The separation factors, which are the ratio of distribution coefficients obtained by equation 2, were calculated by equation 3 and the separation factors based on variable D2EHPA ratios are presented in figure 6.

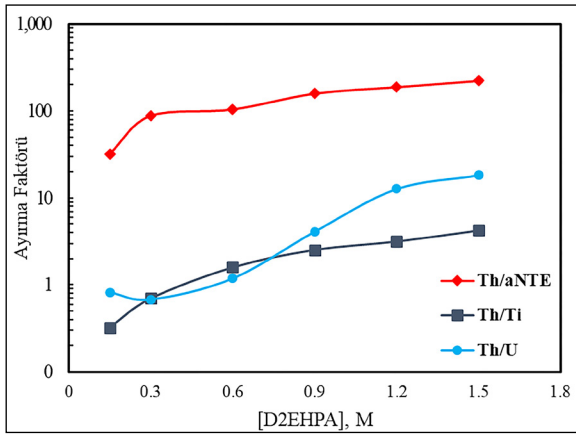


Figure 6- Separation factors between Th/Ti, Th/U and Th/HREEs.

Considering the separation factors, D2EHPA concentration of 0.9 M (30%) was determined as the most favorable parameter. For U element, the separation factor remained constant at first, but did not show a positive change afterwards. According to the results, concentration of 30% D2EHPA was used to determine the most favorable organic/aqueous phase ratio. The results of the experiments carried out at rates ranging between 1/3 and 3/1 by volume are presented in table 2.

Extracting efficiency increases directly proportional with the organic phase volume. Considering

Table 2- Extracting efficiencies of varying ratios of O/S.

O/S	Th, %	HREE, %	Ti, %	U, %	Cu, %
1/3	94	7	81	76	29
1/2	95	11	87	87	29
1	95	11	88	89	30
2	98	23	98	94	30
3	99	29	99	97	31

the extracting efficiency of thorium, HREE and impurities, 1/3 phase ratio has been determined as the most favorable ratio. In addition, as the organic phase volume decreases, it was observed that the elements that would create impurity are less extracted.

3.3. Scrubbing of Impurities

Scrubbing was applied during the removal of impurities loaded together to obtain purer thorium which is extracted in the organic phase. Scrubbing the impurities from the organic phase by using different acids and concentrations was examined and the relevant scrubbing efficiencies are presented in figure 7.

According to the results obtained, 0.25 M H₂SO₄ was used to scrub LREE with high efficiency. During the scrubbing experiments performed with 1/1 O/S ratio, concentration of scrubbing solution has been increased as scrubbing efficiency as LREE scrubbing efficiency has remained at 80% and a part of organic phase has been scrubbed by two part of acid so that, scrubbing efficiency has been raised to

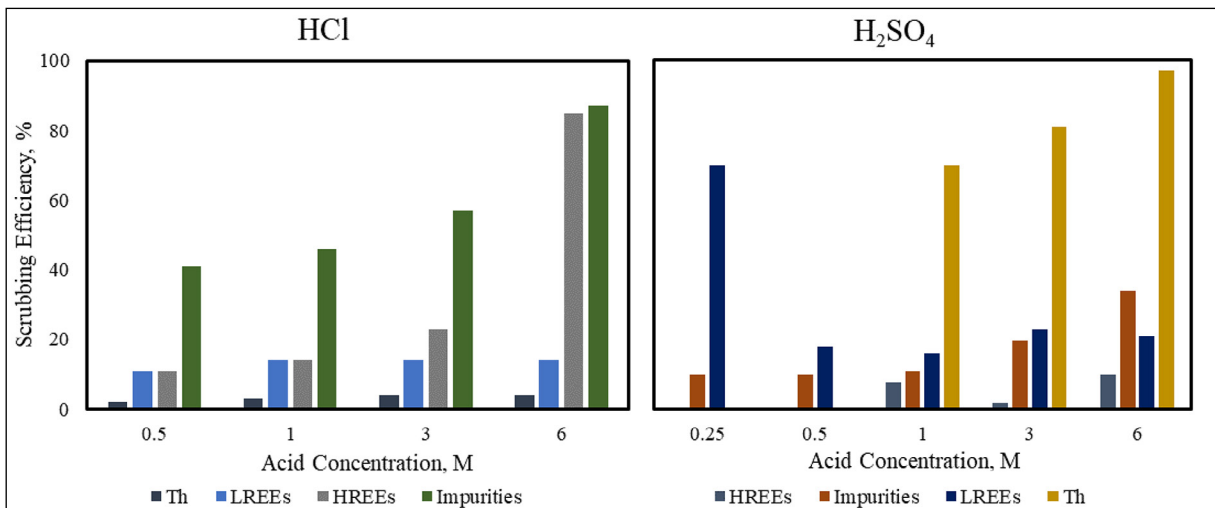


Figure 7- Scrubbing efficiency with varying acid concentrations.

95%. Scrubbing of HREE with high efficiency rates is possible with 6 M HCl. Organic phase was scrubbed with 0.25 M H_2SO_4 until LREE in organic phase disappear to increase the purity of HREE which are the side products to be produced. Afterwards, scrubbing process was continued until HREE in organic phase completely disappear. Concentrations and efficiencies of the solutions obtained are represented in table 3.

All of the elements causing impurity in scrubbed HREE were extracted by extracting 0.2 M TOPO and HREE were obtained by precipitation from the remaining aqueous phase.

3.4. Stripping of Thorium

Considering the preliminary experiments and literature studies, stripping the thorium from the organic phase is only possible with concentrated H_2SO_4 . It was observed that the phosphorus concentration in the aqueous phase increased with breaking down of organic phase due to increase in

the concentrations of acid solution by 9 M or above. For this reason, 6 M of H_2SO_4 was used for the thorium stripping stage. Obtained concentrations and calculated efficiencies are shown in table 4. According to the results from the stripping experiment performed with 6 M of H_2SO_4 , thorium stripping efficiency was found to be 90.4%.

3.5. Precipitation and Characterization

The stripped thorium from the solution was precipitated by using 30% by volume, 0.5 N oxalic acid and the precipitate was dried at 105 °C to obtain thorium oxalate dihydrate $[Th(C_2O_4)_2 \cdot 2H_2O]$. The dried solid product was calcined at 1,050 °C to obtain thorium oxide (ThO_2). Characterization of the final product was carried out with ICP-OES and the results are presented in table 5. SEM images of thorium oxalate and thorium oxide are presented in figure 8.

The proposed flow chart of the method is presented in figure 9.

Table 3- Chemical compositions and scrubbing efficiencies of scrubbing solutions.

Acid and Concentration		Th	LREE	HREE	Impurity*
0.25 M of H_2SO_4	Concentration, ppm	0	271.5	0.1	3.6
	Efficiency, %	0	95.1	0.3	10.1
6 M of HCl	Concentration, ppm	5.2	5.2	40.0	2.7
	Efficiency, %	0.3	1.9	77.8	9.2

*Cu, Ti, U, V

Table 4- Stripping efficiencies and chemical compositions obtained from stripping experiments.

Acid Concentration		Th	U	LREE	HREE	Impurity*
6 M H_2SO_4	Concentration, ppm	1,270.4	15.4	0.1	11.2	5.6
	Efficiency, %	90.4	63	0.05	21.9	48.7

*Cu, Ti, V

Table 5- ICP-OES results.

ICP – OES	
Oxide	Percentage
Al_2O_3	0,208
CeO_2	0,061
CuO	0,200
SiO_2	0,004
ThO_2	99,234
TiO_2	0,016
U_3O_8	0,180
Yb_2O_3	0,091

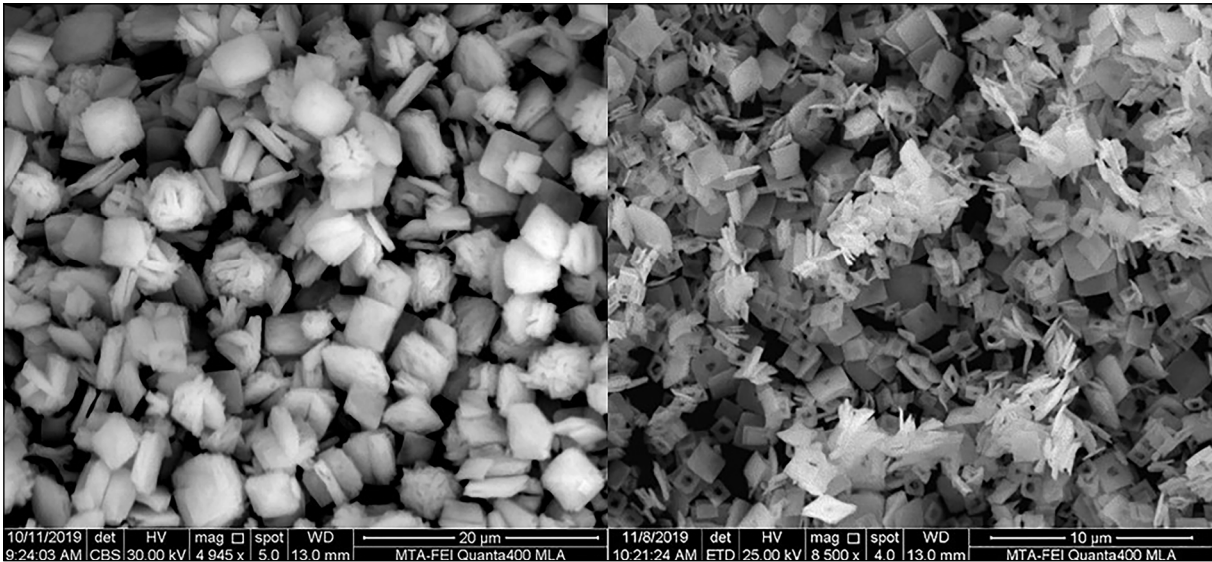


Figure 8- SEM image representing the thorium oxalate (left) and thorium oxide (right).

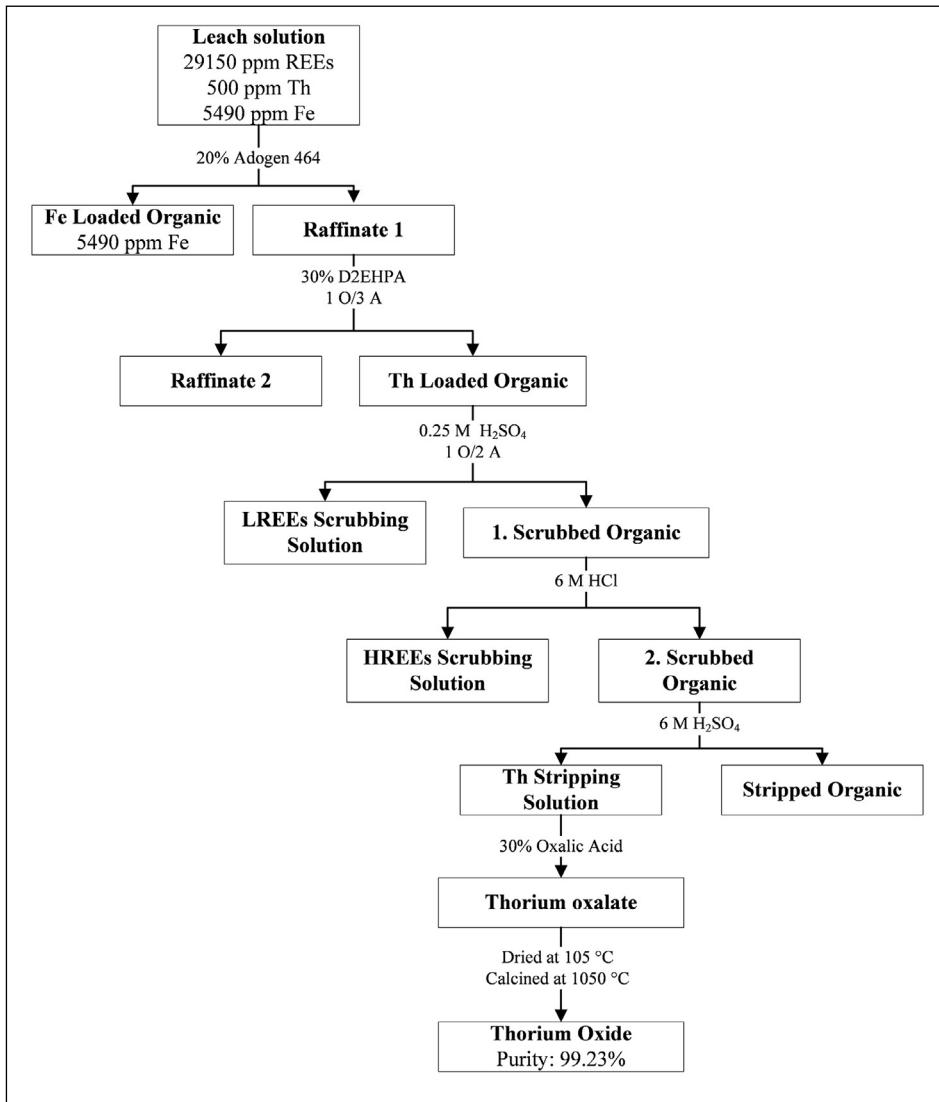


Figure 9- Flowchart of the process.

4. Discussions

As can be seen in the literature research and preliminary experiments, selective thorium solvent extraction is not possible from chlorinated solutions containing iron. When the effects of solvents tested for iron extraction on extracting process were examined, it was found that iron extracting with Adogen 464 was more effective than TBP at lower solvent concentrations. Also, when the separation factors between Fe-Th, Fe-REE and (Cu + Ti + V)-Th are examined, Adogen 464 is superior to TBP solvent in terms of Cu, Ti, V and U extracting which could be found as impurity in the final product. As a result, the concentration of 20% Adogen 464 (Cu + Ti + V) was preferred due to the highest levels of separation factors. Adogen 464, a quaternary amine, causes difficulties in application because of the third phase formation problem that is observed in other amine compounds as well. Therefore, experiments were carried out with 5% decanol additive and the formation of the third phase was prevented.

In experiments with varying D2EHPA ratios for thorium extracting from Fe-free solution, 30% of D2EHPA was determined as the most favorable concentration by considering the extracting of HREE and other impurities. Organic/Aqueous phase ratios were tested with 30% of D2EHPA and 1/3 O/S ratio with 94% thorium extracting efficiency was determined as the most favorable ratio. The use of low-volume organic phase enabled the thorium taken into organic phase to concentrate. A more concentrated organic phase was preferred because it reduces the amount of acid used during stripping phase and the amount of chemicals to be used for precipitation.

Direct thorium stripping was not preferred as it would cause impurities to pass into the aqueous phase with thorium. In addition, scrubbing experiments were carried out for HREE and LREE that emerged as by-products in the process. Since high acidity is needed to strip HREE forming more stable complex with D2EHPA, low concentration of H_2SO_4 has been used to scrub LREE and loss of HREE has been minimized. Then, HREE were stripped with high efficiency and low concentrations of thorium from the organic matter by using 6 M HCl. The impurities in the stripped HREE were extracted with TOPO and thus, HREE were recovered.

The thorium oxalate compound obtained as a result of the precipitation was first dried at 105 °C and $Th(C_2O_4)_2 \cdot 2H_2O$ was obtained. The dried solid product was calcined at 1,050 °C and the mass loss was calculated as 41.7%. This ratio is consistent with the theoretical mass loss in transition from thorium oxalate (444.107 g/mol) to thorium oxide (264.037 g/mol). The final product was subjected to ICP-OES analysis by dissolving it with four different acids and the exact values of the impurities were calculated.

5. Results

A process has been designed to produce high purity thorium oxide from leach liquors of complex ores. Adogen 464, which has the highest separation factors, is the most favorable among the solvents tested for iron extracting. 20% of Adogen 464 was chosen as the most suitable rate. In addition to iron, impurities such as Cu, Ti, V and U that may cause problems in further stages were also extracted at certain rates.

The most favorable parameters for the extracting phase were determined as 0.9 M (30%) D2EHPA and 1/3 organic/aqueous phase ratio. The separation factor between Th-HREE is around 200 for these parameters. Stoichiometry of Th-D2EHPA complex was found as 1:2.8 with slope calculation. Some of the HREE, Cu, Ti, V and U were extracted with thorium.

During the first scrubbing phase, LREE were scrubbed by using 0.25 M of H_2SO_4 . In the second stage, HREE were scrubbed with 6 M HCl. Thorium was stripped with 6 M H_2SO_4 from the scrubbed organic phase and then thorium was precipitated with oxalic acid. After drying and calcination processes, thorium oxide was characterized by ICP-OES and SEM-EDS. ThO_2 purity was measured as 99.23% by measuring with ICP-OES device.

This method can be used for the production of high purity ThO_2 from mineralization containing rare earth elements and is consistent with further studies that are going to be performed by using leach liquor.

Acknowledgement

This study was supported by the General Directorate of Mineral Research and Exploration within the scope of Scientific Research Projects. Authors would like to thank to Mehmet Ergin from

Cytec Inc. Turkey for his advices about the solvents and Ufuk Kibar, Nihal Görmüş and Gökçe Gürtekin from General Directorate of Mineral Research and Exploration for their contributions with SEM-EDS analyses and images.

References

- Ali, A.M.I., El-Nadi, Y.A., Daoud, J.A., Aly, H.F. 2007. Recovery of thorium (IV) from leached monazite solutions using counter-current extraction. *International Journal of Mineral Processing* 81, 217–223.
- Aybers, M.T. 1998. Kinetic study of the thermal decomposition of thorium oxalate dihydrate. *Journal of Nuclear Materials* 252, 28–33.
- Bahri, C.N.A.C.Z., Ismail, A.F., Majid, A.A., Ruf, M.I.F.M., Al-Areqi, W.M. 2018. Extraction and purification of thorium oxide (ThO₂) from monazite mineral. *Sains Malaysiana* 47, 1873–1882.
- Cox, M. 2004. Solvent Extraction in Hydrometallurgy, in: *Solvent Extraction Principles and Practice, Revised and Expanded*. CRC Press, 466–515.
- D'Eye, R.W.M., Sellman, P.G. 1955. The thermal decomposition of thorium oxalate. *Journal of Inorganic and Nuclear Chemistry* 1, 143–148.
- Demol, J., Ho, E., Senanayake, G. 2018. Sulfuric acid baking and leaching of rare earth elements, thorium and phosphate from a monazite concentrate: Effect of bake temperature from 200 to 800 °C. *Hydrometallurgy* 179, 254–267.
- Dinkar, A.K., Singh, S.K., Tripathi, S.C., Verma, R., Reddy, A.V.R. 2012. Studies on the Separation and Recovery of Thorium from Nitric Acid Medium using (2-ethyl hexyl) Phosphonic Acid, Mono (2-ethyl hexyl) Ester (PC88A)/N-Dodecane as Extractant System. *Separation Science and Technology* 47, 1748–1753.
- Ditz, R., Sarbas, B., Schubert, P., Töpper, W. 1990. Thorium, Natural Occurrence, Minerals (Excluding Silicates), 8th ed, *Gmelin Handbook of Inorganic Chemistry*. Springer Berlin Heidelberg, Berlin, Heidelberg.
- Du, H.S., Wood, D.J., Elshani, S., Wai, C.M. 1993. Separation of thorium from lanthanides by solvent extraction with ionizable crown ethers. *Talanta* 40, 173–177.
- Güneş, H., Obuz, H.E., Alkan, M. 2019. Selective Precipitation of Th and Rare-Earth Elements from HCl Leach Liquor, in: *Minerals, Metals and Materials Series*. Springer International Publishing, ss. 81–86.
- Kaya, M., Bozkurt, V. 2003. Thorium as A Nuclear Fuel, içinde: *18th International Mining Congress and Exhibition of Turkey*. ss. 572–578.
- Li, D., Zuo, Y., Meng, S. 2004. Separation of thorium(IV) and extracting rare earths from sulfuric and phosphoric acid solutions by solvent extraction method. *Journal of Alloys and Compounds* 374, 431–433.
- Mishra, R.K., Rout, P.C., Sarangi, K., Nathsarma, K.C. 2011. Solvent extraction of Fe(III) from the chloride leach liquor of low grade iron ore tailings using Aliquat 336. *Hydrometallurgy* 108, 93–99.
- Nasab, M.E., Sam, A., Milani, S.A. 2011. Determination of optimum process conditions for the separation of thorium and rare earth elements by solvent extraction. *Hydrometallurgy* 106, 141–147.
- Ritcey, G.M., Ashbrook, A.W. 1979. *Solvent extraction: principles and applications to process metallurgy*. Elsevier Scientific Pub. Co.
- Sahu, K.K., Das, R.P. 1997. Synergistic extraction of iron(III) at higher concentrations in D2EHPA-TBP mixed solvent systems. *Metallurgical and Materials Transactions B: Process Metallurgy and Materials Processing Science* 28, 181–189.
- Saji, J., Reddy, M.L.P. 2001. Liquid-liquid extraction separation of iron(III) from titania wastes using TBP-MIBK mixed solvent system. *Hydrometallurgy* 61, 81–87.
- Salehuddin, A.H.J.M., Aziman, E.S., Bahri, C.N.A.C.Z., Affendi, M.A.R.A., Idris, W.M.R., Ismail, A.F. 2019. Effectiveness study of thorium extraction from hydrochloric acid using di (2-Ethylhexyl) phosphoric acid (D 2 EHPA). *Sains Malaysiana* 48, 419–424.
- Wang, Y., Huang, C., Li, F., Dong, Y., Sun, X. 2017. Process for the separation of thorium and rare earth elements from radioactive waste residues using Cyanex® 572 as a new extractant. *Hydrometallurgy* 169, 158–164.
- Yıldız, N., 2017. *Uranyum Toryum*. Chamber of Mining Engineers of Turkey, Ankara.
- Zhang, Y., Xu, Y., Huang, X., Long, Z., Cui, D., Hu, F. 2012. Study on thorium recovery from bastnaesite treatment process. *Journal of Rare Earths* 30, 374–377.



Bulletin of the Mineral Research and Exploration

<http://bulletin.mta.gov.tr>



Petrographic characteristics of deep marine turbidite sandstones of the Upper Cretaceous Tanjero Formation, Northwestern Sulaimaniyah, Iraq: Implications for provenance and tectonic setting

Hasan ÇELİK^{a*} and Hemin Muhammad HAMA SALİH^b

^aFirat University, Engineering Faculty, Department of Geological Engineering, 23119, Elazığ, Turkey

^bMinistry of Higher Education and Scientific-Research, Sulaimaniyah, Iraq

Research Article

Keywords:

Sedimentary petrography, provenance, Tanjero Formation, Northwestern Sulaimaniyah, Iraq.

ABSTRACT

This study was carried out to determine the sedimentary provenance of Upper Cretaceous turbidites of Tanjero Formation. The sandstone portion of the unit has been examined based on field and laboratory studies. Seven sections were measured and described in detail on the perfectly cropped out part of the unit at the southern limb of the Sulaimaniyah Syncline. The thickness of the measured sections varies from 120 m to 192 m. The measured sections start from the top of the underlying Shiranish Formation to the syncline axis in the Tanjero Formation. For petrographic analysis sixty-nine representative rock samples were collected. Modal analysis and ternary diagrams point out that, the sandstones are calcilithite (litharenite), very fine to medium grained in size consisting of chert, siltstone, mudstone, radiolarian chert and radiolarian mudstone fragments, angular to subangular in shape, very poorly to moderately sorted, transported over short distances and represent submature stage. Grain contact types and high contact index (4.7) indicate moderate to tightly packing, moderate compaction. Transported broken neritic fossil shells, moderately rounded glauconite grains, and undefinable fossils in the altered carbonate rock fragments indicate that the tectonic provenance, lithic recycle category, composed of not only the clastics as interpreted in previous studies derived from Lower Cretaceous Qulqula (radiolarian) Formation which represents deep marine, but also it revealed that a sedimentary formation must also exist in the source area, which is the Lower Cretaceous Balambo Formation.

Received Date: 14.11.2019

Accepted Date: 19.09.2020

1. Introduction

Northern part of Iraq is an oil field area, there are many researches which are summarized in this part of the paper that majority of them were done on carbonate-sand some on clastic rocks excluding provenance analysis.

Provenance types contribute distinctive detritus preferentially to associate sedimentary rocks. For this

reason, clastic detrital components save valuable data on the provenance and pattern in which the sediments were transported, especially after modification of the original detritus by the interaction of physical and chemical processes such as weathering, erosion transportation and paleoclimate (Johnson, 1976; Dickinson, 1988). Turbidites also contain important information for interpreting both the compositional tectonic setting and evolution of the continental crust that can be linked to the depositional environment

Citation Info: Çelik, H., Hama Salih, H. M. 2021. Petrographic characteristics of deep marine turbidite sandstones of the Upper Cretaceous Tanjero Formation, Northwestern Sulaimaniyah, Iraq: Implications for provenance and tectonic setting. Bulletin of the Mineral Research and Exploration 164, 11-38.

<https://doi.org/10.19111/bulletinofmre.800132>

*Corresponding author: Hasan ÇELİK, hasancelik@firat.edu.tr

(Raymond, 1995; Cingolani et al., 2003). Petrographic studies show that clastic rocks can be used for classification the provenance (Dickinson et al., 1983; Bordy et al., 2004; Armas et al., 2014).

Studies of sedimentary petrography and palaeo flow direction for provenance analysis are important to refine depositional environment for assessing reservoir properties of the hydrocarbon reservoirs (Rieser et al., 2005; Mange and Morton 2007; Li et al., 2012; Ghosh et al., 2012).

So far the geological studies of the Tanjero Formation were carried out by Dunnington (1958), Bellen et al. (1959), Kassab (1975), Al-Mehaidi (1975), Abdel-Kireem (1986a, 1986b), Jaza (1992), Minas (1997), Karim (2004, 2007, 2010), Karim and Surdashy (2005a, 2005b), Sharbazheri (2007, 2010), Karim et al. (2012, 2014), Lawa et al. (2013, 2017) mainly in the manner of paleontology, lithostratigraphy, biostratigraphy, sequence stratigraphy, sedimentology, basin analysis, and lithofacies but despite these studies, mainly not published in international SCI journals, the petrography and mineralogical composition of the turbidites have not been studied seriously yet and still poorly understood.

Zagros Suture Zone is the one of the main tectonically active part of the area. In the recent decade

some tectonic and evolution studies of Neotethys were done by Alavi (2004, 2007), Karim and Taha (2009), Lawa et al. (2013), Sissakian (2013), Malekzade et al. (2016), Motaghi et al. (2017), Moradpour et al. (2017), Koshnaw et al. (2018, 2019).

The Tanjero Formation crops out in the northern Iraq province throughout Iran border (Figure 1 and 2) consisting of low density deep marine fan turbidites. Around Sulaimaniyah, the unit consisting of mainly sandstone, siltstone and shale were studied to interpret the provenance. Elsewhere in northern Iraq some researchers (e.g. Karim 2004, 2007, 2010; Karim et al., 2012; 2014) state that the unit comprises conglomerate and limestone indicating the shallow water rocks of the formation. However, the unit conformably overlies marly Shiranish Formation (lower Campanian-Maastrichtian) in general, but in some places an interfingering relations can be seen between these two formations (Figure 3). The Tanjero Formation is conformably covered by upper Maastrichtian-middle Paleocene Kolosh Formation (Karim, 2010).

A large-scale northwest-southeast trending anticline and syncline structures forming a zone are located in the northern Iraq parallel to the Iran border (Figure 2) including main thrust of the Zagros Mountain Belt. The formation is mainly crops out in this folded zone which is called as high folded zone.

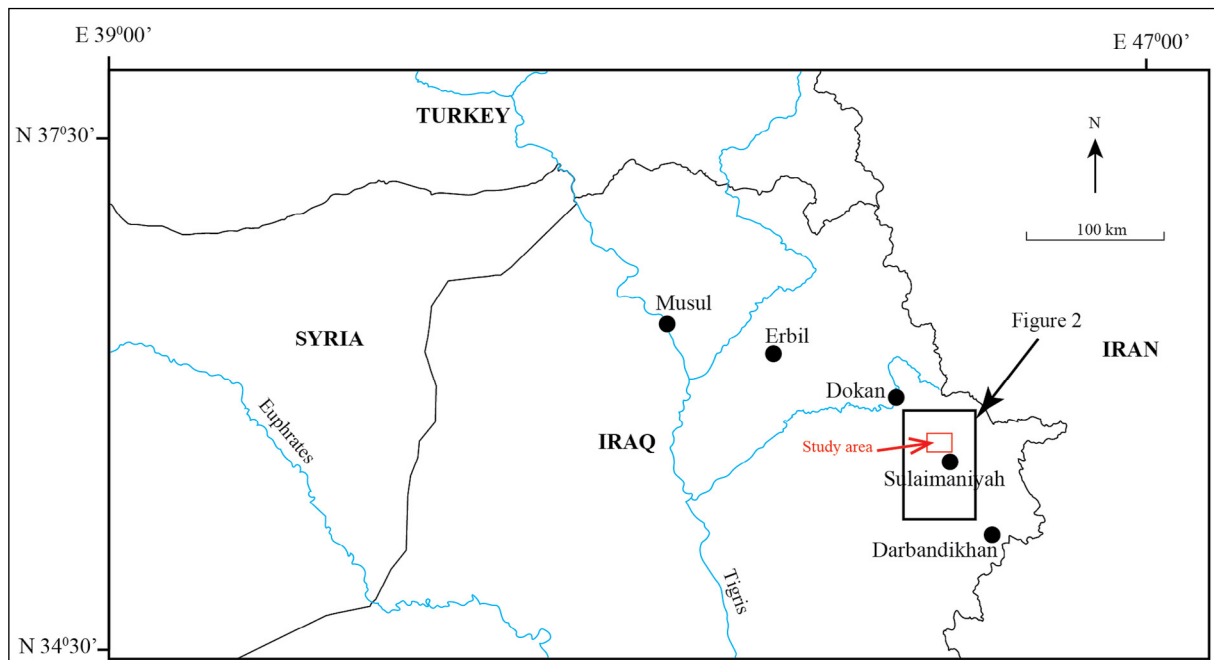


Figure 1- Location map showing study area. Northwestern Sulaimaniyah, northern Iraq.

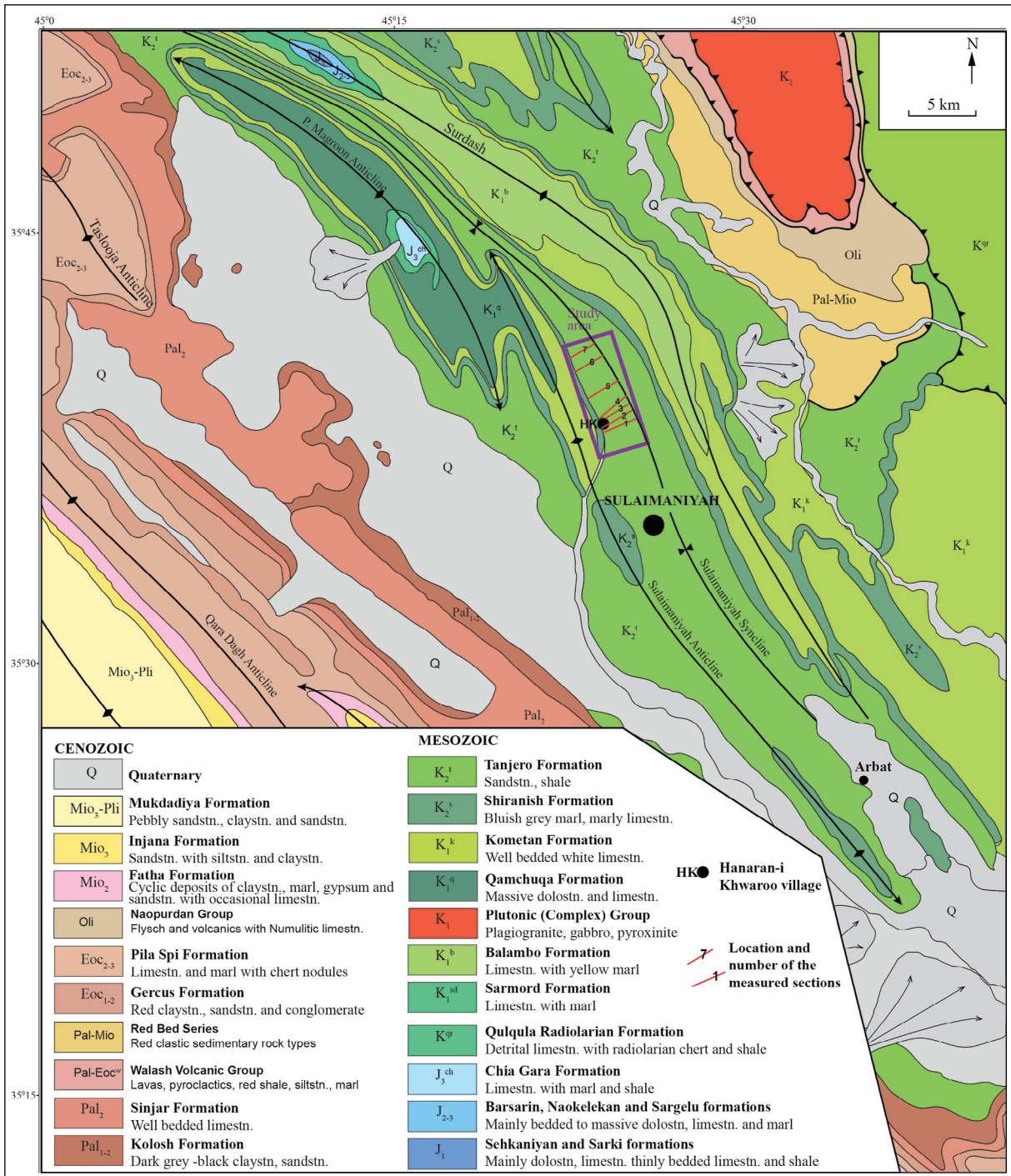


Figure 2- Detailed geological map of the northern Iraq including study area (modified and merged from Sissakian and Fouad, 2015).

The study area is located in the southern limb of the Sulaimaniyah Syncline (Figure 2).

The purpose of this paper is to describe the provenance of the low density turbidite sandstones of Upper Cretaceous Tanjero Formation exposed in the northwestern part of the Sulaimaniyah city, northern Iraq, using palaeoflow and modal analysis in

sedimentary petrography. These data are important to determine how the tectonics and geomorphology of the hinterland evolved during Cretaceous.

Modal analysis, and sandstone classification performed for provenance proposes is based on the genetically significant petrographic schemes by Folk (1966), Dickinson and Suczek (1979) and Dickinson

et al. (1983). In the first study (Çelik and Salih, 2018) on the petrographic characteristic and provenance of this formation, it was stated that Lower Cretaceous Balambo and Qamchuqa formations should be found in the feeding area of turbidite sandstones of the Tanjero Formation near Arbat province in northeastern Iraq. Presentpaper, which is a continuation of this study, was applied to the same turbidites cropped out in the northwest of Sulaimaniyah province. In this region, which has not been adequately studied in terms of petrography and therefore has led to incomplete palaeogeographic interpretations, large-scale exposures of this unit along the Iraqi-Iranian border in Darbandikhan (northeastern Iraq) and northwestern part of Sulaimaniyah has also opened a way for studies.

2. Geological Setting

The Tanjero Basin was being located in the northern portion of the Arabian Plate during Late Cretaceous and its deposits cover a wide area along the Iran border in the present day (Figure 2). The geological evolution of the basin was controlled by the Late Cretaceous northward subduction of the Arabian plate (Karim, 2004, 2007; Karim et al., 2012, 2014).

The studied area is located south of Zagros Thrust Belt, which is developed from the Neo-Tethys Oceanic basin fill and collision of Iranian and Arabian plates. Structurally the area partly located in the Imbricated and High Folded zones (Buday and Jassim, 1987) which is characterized by anticlines and synclines (Figure 2).

The formation is located at the both limbs of the Sulaimaniyah Syncline (Figure 2) only whereas their continuation along the axis and limb of the anticline is removed by erosion. The northern limit of the outcrop distribution of the unit nearly coincides with the boundary between thrust and imbricated zones.

The stratigraphic units cropped out of the Sulaimaniyah area were summarized in figure 3. In the studied area, Shiranish Formation conformably underlies Tanjero Formation gradationally. The contact is marked at the first appearance of gray sandstone or siltstone beds at the top of Shiranish Formation (bluish white marl and marly limestone) and starting of olive greenish-greyish lithology of Tanjero Formation (Figure 4).

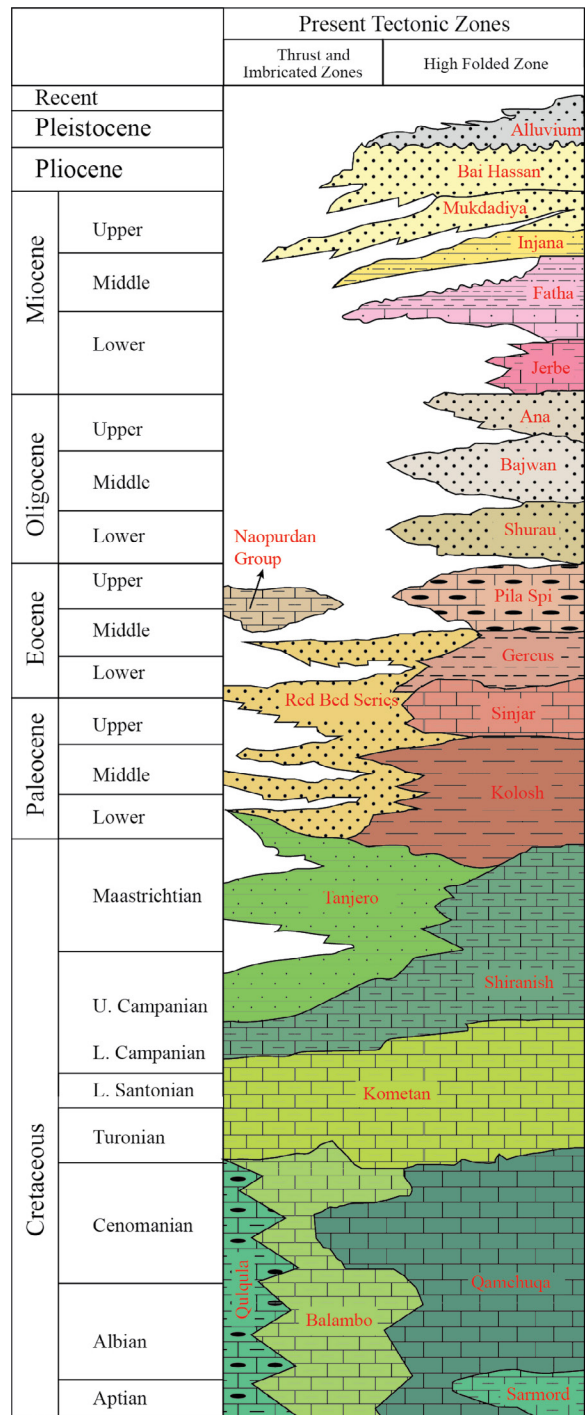


Figure 3- Stratigraphic columnar section of Sulaimaniyah area (no scale), (modified from Karim, 2010).

The unit is characterized by alternation of deep marine low density thin bedded and sheet turbidites (Figure 5 and 6) in the study area on the limbs of the fold and all other outcrops throughout the northern Iraq according to personal field works, despite of the

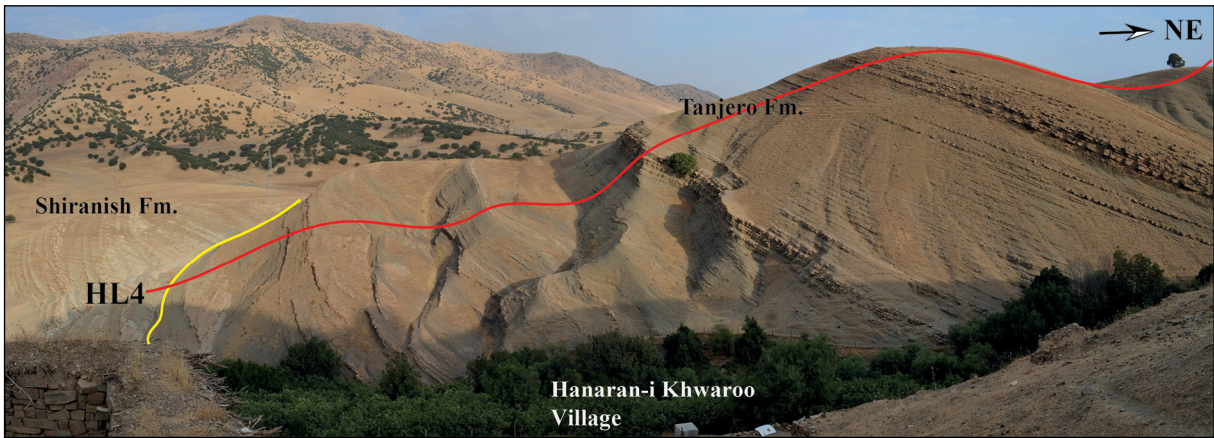


Figure 4- Conformable contact between Shiranish and Tanjero formations. Red line represents line of the measured section 4 (0-96 meters) labelled as HL4. Hanaran-i Khwaroo village, NE of Sulaimaniyah, view to the west (see also figure 2 and figure 8 for location of the village).



Figure 5- Lobe fringe to lobe distal fringe turbidites of the unit in the HL1 (60-65 meters) (A) and the Ta-b divisions including three mud chip levels (mch1-3) in the normal graded Ta with an erosional base on the underlying finer grained sandstone bed in the 20th meter of HL1 measured section (B). East of the Hanaran-i Khwaroo village, NE of Sulaimaniyah, view to the west.

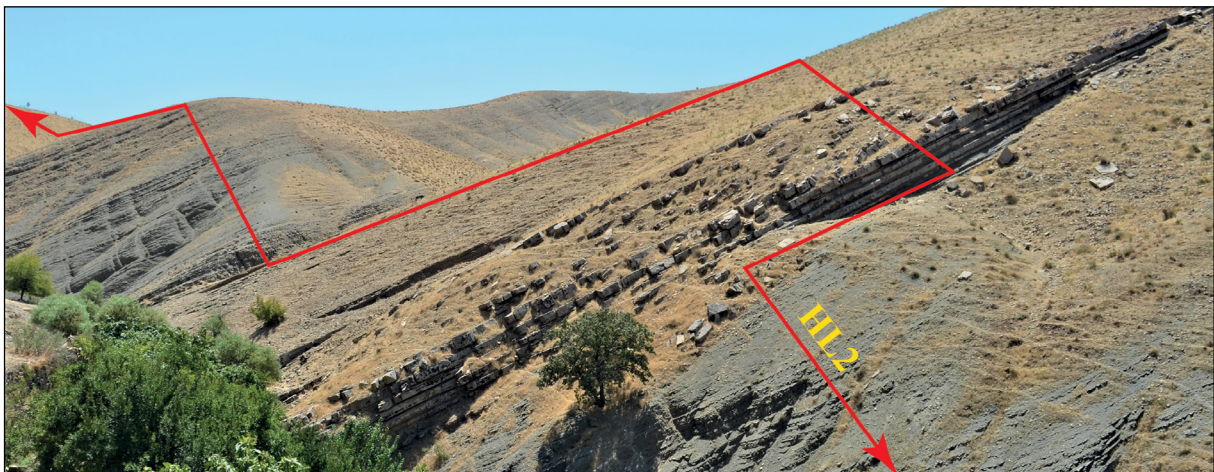


Figure 6- Thin bedded and sheet turbidites of the formation in HL2 (36-72 meters). East of the Hanaran-i Khwaroo village, NE of Sulaimaniyah, view to the east.

previous studies (e.g., Karim, 2004, 2007; Karim et al., 2012) stating conglomerate and limestone alternation outcrops somewhere.

The facies analysis, with the detail seven measured stratigraphic sections (Figure 7) framework including seven distinctive main lithofacies groups and forty-eight subfacies suggest middle part of outer fan and lobe fringe to lobe distal fringe sand rich depositional system in which the sandstone ratio is 18.14 % and shale ratio is 81.86 %. This sandstone/shale ratio (net to gross) is very low and represents distal turbidites.

3. Material and Method

Sixty-nine sandstone samples (labeled as HL1-1 as seen in the figure 7), were collected systematically from seven distinctive measured sections (Figure 8) from superbly exhumed deep marine turbidites of Tanjero Formation in the study area.

Thin section petrographic studies were carried out from 31 samples to identify the mineralogical composition and to apply modal analysis. Compositional analysis (Table 1) and classical point counting method were used to apply the quartz (Q), feldspars (F) and rock fragments (R) ternary diagram of Pettijohn et al. (1987). For each thin section 500 points were counted under a polarized light microscope, following the GD point-counting method (Gazzi, 1966; Dickinson, 1970) in the microscope lab of Geology Department in Firat University, Turkey.

Palaeoflow data were obtained by following the method of Tucker (2011), from micro-scaled unidirectional and bidirectional sedimentary structures such as flute mark, current ripple, oriented plant materials, parting lineation. These data were statistically processed with the rose diagrams in the software Geo Rose.

Folk's (1951) maturity type table, Folk (1966) Q-F-R ternary diagrams for the classification of the sandstone and Qm-F-Lt provenance ternary diagram of Dickinson et al. (1983) were used in order to differentiate maturity type and major provenance categories.

4. Petrography

A detailed table was formed for petrographic analysis (summarized in Table 1). which includes compositional ratios of Q, F and Rf, cement type, alteration/dissolution, fossils content, sedimentary structures, sorting, roundness, modal classification for Folk's (1966) ternary diagrams, the number of photo taken in each thin section and rock name depended on grain size. The turbidite sandstones are classified as calcilithite for the unit according to Folk's (1966) ternary diagrams (Figure 9).

The sandstones are very fine to medium grained (Table 1). Sandstone framework consist of subangular to subrounded rock fragments, very angular lithic cherts and quartz, reworked radiolaria fossils (Figure 10, 11, 12, 13, and 14) with sutured, concavo convex, long grain and little tangential grain contact types (Figure 15, 16, and 17). Poorly sorting (Figure 18) and high compaction ratio increases the grain contact index since the small grains fill the voids between the bigger lithic fragments.

These contact types reflecting the diagenetic events are implying that compaction degree is moderate. The effects of compaction are also manifested in the grain deformation. In the turbidite sandstone studied grains are not deformed, only exhibited evidences of fragile deformation in a few cases, mainly in the grains vertices or within internal grain cracks filled by mainly calcite and solid bitumen (Figure 19, 20 and 21).

Grain contact types and contact index (average number of contacts per grain) supply to researchers the packing character of the sandstone studied. The contact index of the sandstone is 4.7. The contact types of the sandstone in this study point out moderate to tightly packing.

The other grain contact type present in the sandstones of the unit is floating type, which is seen greywacke calcilithites since the cement ratio is more than %15, the grains can stay in the calcite cement without having contact with the other fragments in some parts of the thin sections.

Main cement is calcite filling the interstitial pores also replaces the grains, clay and matrix are secondary and in a very low ratio. Solid bitumen fillings are

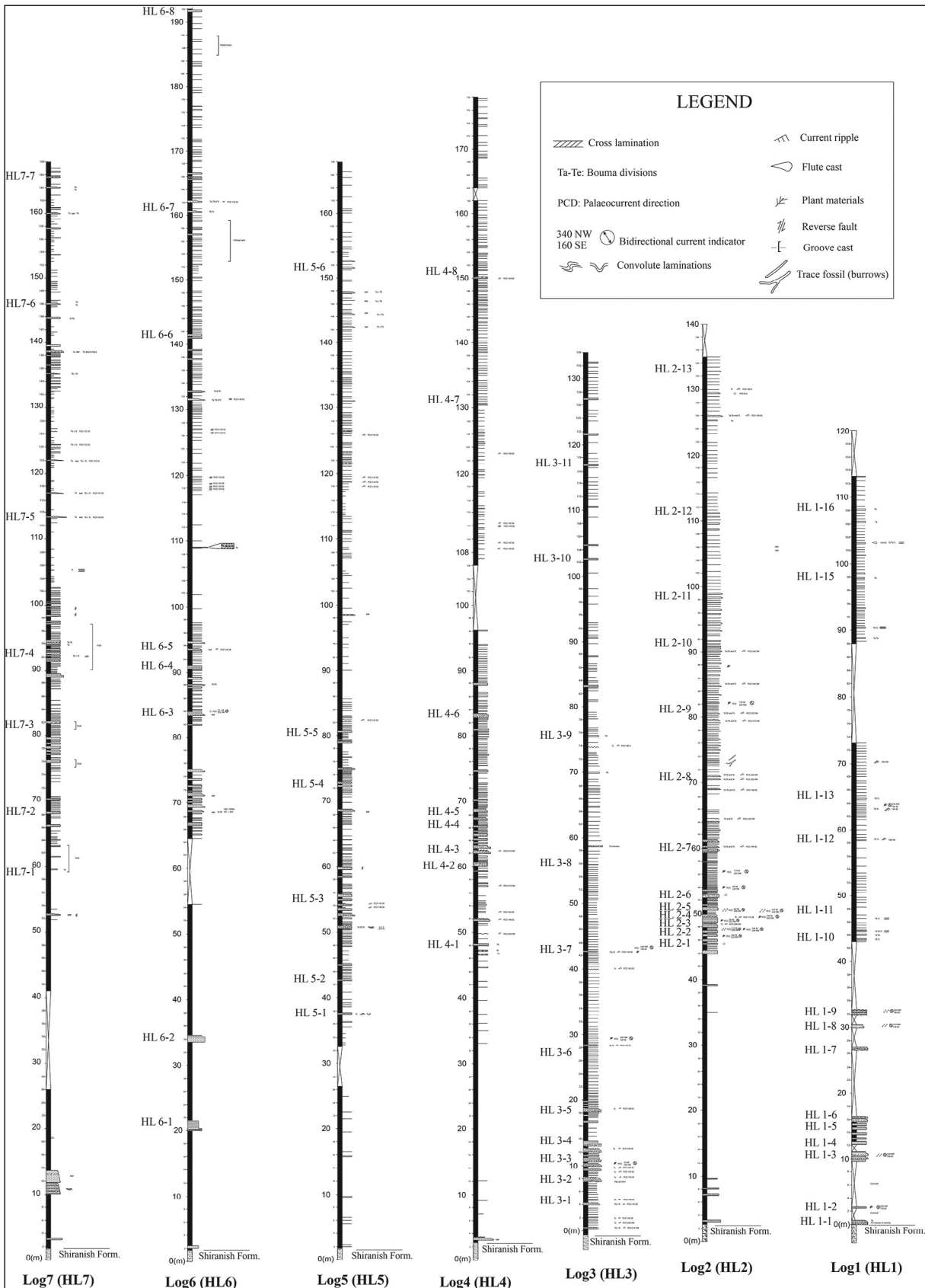


Figure 7- Measured sections logged in the study area. Coordinates of the measured sections (logs) are: HL1: N 35040'14.10" E 45022'38.39", HL2: N 35040'23.27" E 45022'35.79", HL3: N 35040'30.46" E 45022'38.18", HL4: N 35040'28.23" E 45022'30.06", HL5: N 35040'58.51" E 45022'11.78", HL6: N 35041'31.06" E 45021'36.80", HL7: N 35041'56.19" E 45021'19.54",

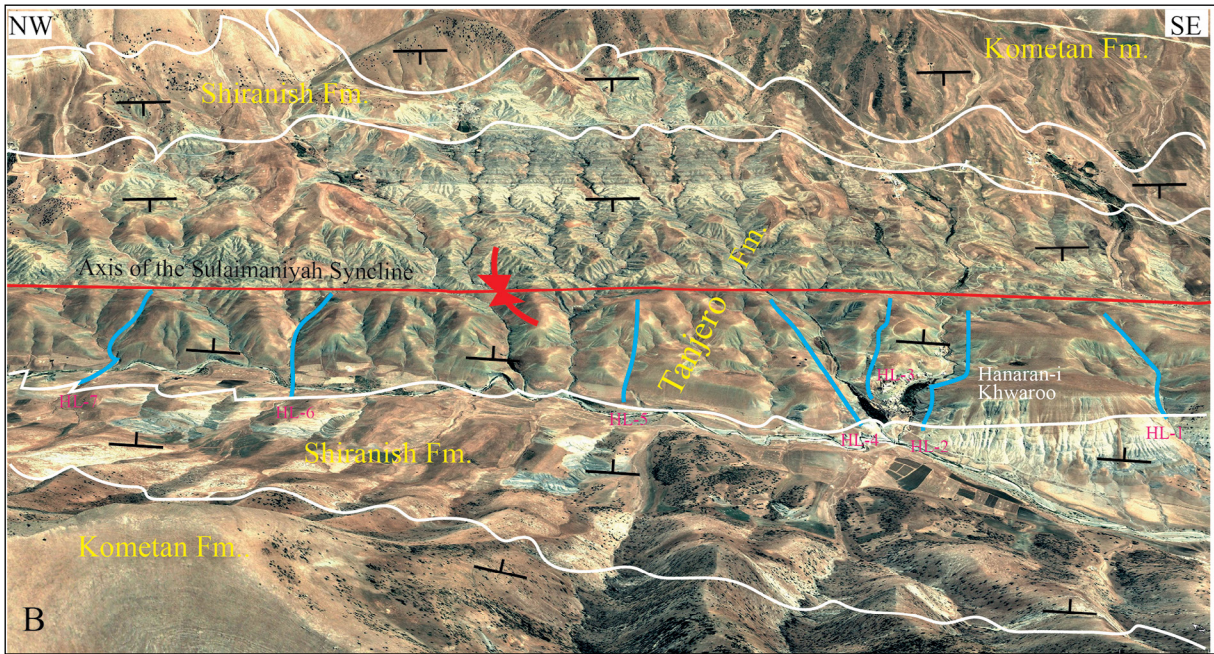


Figure 8- Google Earth image covering the study area around the Hanaran-i Khwaroo village located just where the HL-3 starts, northeast of Sulaimaniyah. Formations are repeating because of the Sulaimaniyah Syncline axis located approximately in NW-SE orientation where the logs end (see also Figure 2). For the scale, the thickness of HL1 is 120m. See Figure 7 for thickness of the other measured sections. View to the northeast.

seen in many thin section (Table 1, in the “other components” column) and it blocks pore spaces and stain the calcite cement to brownish – yellowish in colour which present in the all microphotographs except figure 15.

The only quartz type from the source area in the turbidite sandstone is monocrystalline, very angular to angular with straight fully extinction common quartz (see Figure 13, 14 and 15). The ratio of the quartz is 0.37% in average (Table 1) for the unit in this study.

Rare heavy mineral presence is notable with low concentration. Hematite and euhedral to subhedral black opaque minerals (were not differentiated in this study) are the most common. Feldspar ratio is 0,009% for the whole sandstone samples. It was seen with highly alteration in one sample (Table 1 with 0.3 percentages).

Carbonate rock fragments are the main lithoclasts constituent of the turbidite sandstone with 59.32 percentages. Chert without radiolaria has 16.65 percentages and the others are shale, silt, released-reworked radiolaria fossils, benthic fossil shell fragments, glauconite, radiolarian chert and radiolarian mudstone fragments with a ratio of 24.03% (Table 1).

No any metamorphic or magmatic rock clast was seen in the sandstone thin sections.

All the petrographic examines show that the turbidite sandstones of Upper Cretaceous Tanjero Formation, having less than 5 percentage clay, angular to subangular grains, poorly sorting, dominant tangential and point, a few sutured contact types, are submature (Figure 22).

Submature stage for the sandstones implies a short distance transportation of the lithic clasts into the deep marine environment of the Upper Cretaceous basin.

5. Provenance

Petrographic data obtained from the thin sections were applied to the Qm-F-Lt ternary diagram of Dickinson et al. (1983) to interpret the tectonic provenance of the sandstones. The modal classification indicates that the sedimentary rocks are included within the “lithic recycled” category (Figure 23). Also palaeoflow rose diagrams (Figure 24 and Figure 25) from the unidirectional and bidirectional sedimentary structures in the turbidites, indicate SE direction which useful to accurately establish the location of source area.

Table 1- Petrographic content of the thin sections (the numbers for Q, F and RF were rounded to the nearest whole numbers).

No	Thin Section No.	%Q	%F	%RF	Cement	Matrix	Other components	Alteration/ dissolution	Fossils	Sedimentary structures	Sorting	Roundness	Modal Classification	No. of photos	Rock name
1	HL 1-1	1	-	99 (chrt:8,Crbnt:65, Mudstone +released radiolaria:27)	Calcite	-	Bitumen fillings + euhedral to subhedral opaque minerals	Carbonate rock clasts to calcite	Fossil shell fragments+ reworked radiolaria	Slightly pebble orientation	Moderately	Subangular rock clasts, very angular cherts and quartz	Calcithite	6	Very fine grained sandstone
2	HL 1-2	1,6	-	98,4 (chrt:27,Crbnt:55, Mudstone +released radiolaria: 18)	Calcite	-	Bitumen fillings + euhedral to subhedral opaque minerals	Carbonate rock clasts to calcite	Fossil shell fragments+ reworked radiolaria	Slightly pebble orientation	Moderately	Subangular rock fragments, very angular cherts and quartz	Calcithite	6	Very fine grained sandstone
3	HL 1-7	0,4	-	99,6 (chrt:25,Crbnt:60, mudstone with and/ released radiolaria:15)	Calcite	-	Bitumen fillings + euhedral to subhedral opaque minerals+ carbonized plant materials	Carbonate rock clasts to calcite	Fossil shell fragments+ reworked radiolaria	Slightly pebble orientation	Moderately	Subangular-subrounded rock fragments, very angular cherts and quartz	Calcithite	6	Very fine grained sandstone
4	HL1-8	0,5	-	99,5 (chrt:27,Crbnt:53, mudstone with and/ released radiolaria:20)	Calcite	-	Bitumen fillings + euhedral to subhedral opaque minerals	Carbonate rock clasts to calcite	Fossil shell fragments+ reworked radiolaria	Slightly pebble orientation	Poorly	Subrounded rock fragments, very angular cherts and quartz	Calcithite	4	Very fine grained sandstone
5	HL1-9	0,3	-	99,7 (chrt: 19, Crbnt:58, Siltstone, mudstone with and/ released radiolaria and others:23)	Calcite	-	Glauconite+ bitumen fillings + euhedral to subhedral opaque minerals	Carbonate rock fragments to calcite	Rare benthic shell fragments+ plenty of reworked radiolaria	-	Very poorly	Subangular rock fragments, very angular cherts and quartz	Calcithite	14	Pebbly fine grained sandstone
6	HL1-14	1	-	99 (chrt: 10, Crbnt:50, Siltstone, mudstone with and/ released radiolaria and others:40)	Calcite	-	Bitumen fillings + carbonized plant materials	Carbonate rock fragments to calcite	Reworked radiolaria	-	Poorly	Subangular-subrounded rock fragments, very angular cherts	Calcithite	10	Pebbly fine grained sandstone

Table 1- (continue).

No	Thin Section No.	%Q	%F	%RF	Cement	Matrix	Other components	Alteration/ dissolution	Fossils	Sedimentary structures	Sorting	Roundness	Modal Classification	No. of photos	Rock name
7	HL 2-3	1	0.3	98,7 (chrt:10,Crbnt:55, Mudstone with and/ released radiolaria and others:35)	Calcite	-	Bitumen fillings + euhedral to subhedral opaque minerals	Feldspar to clay+ Carbonate rock fragments to calcite	Rare benthic shell fragments+ reworked radiolaria	Wavy deformed secondary calcite in fractures	Moderately	Subrounded rock fragments, very angular cherts and quartz	Calclithite greywacke	8	Pebbly fine grain sandstone
8	HL 2-4	0,3	-	99,7 (chrt:33, Crbnt:46, Siltstone, mudstone with and/ released radiolaria and others:21)	Calcite	-	Glauconite+ Bitumen fillings + euhedral to subhedral opaque minerals	Carbonate rock fragments to calcite	Globigerina +benthic shell fragments+ reworked radiolaria	Grain orientation throughout the section	Very poorly	Subangular rock fragments, very angular cherts and quartz	Calclithite	20	Medium grained sandstone
9	HL 2-7	-	-	100 (chrt:10,Crbnt:60, Siltstone, mudstone with and/ released radiolaria and others:30)	Calcite	-	Opaque angular heavy minerals 2%+ glauconite (0,2 %) +plant materials and pellets (0,3%)	Carbonate rock fragments to calcite	Reworked radiolaria	-	Poorly	Subangular- subrounded rock fragments, very angular cherts	Calclithite	2	Very fine grained sandstone
10	HL2- 10	-	-	100 (chrt:10,Crbnt:65, Siltstone, mudstone with and/ released radiolaria and others:25)	Calcite	-	Bitumen fillings	?	Rare benthic shell fragments+ reworked radiolaria	-	Poorly	Subangular- subrounded rock fragments, very angular cherts	Calclithite	6	Very fine grained sandstone
11	HL2- 13	0,5	-	99,5 (chrt:17,Crbnt:37, Siltstone, mudstone with and/ released radiolaria and others:46)	Calcite	+	Opaque angular heavy minerals 1%+ bitumen fillings	Carbonate rock fragments to calcite	Reworked radiolaria	-	Poorly		Calclithite	6	Fine grained sandstone
12	HL 3-2	-	-	100 (chrt:30 ,Crbnt:50, Siltstone, mudstone with and/ released radiolaria and others:20)	Calcite	-	Very well rounded glauconite + carbonized plant materials+ bitumen fillings	Carbonate rock fragments to calcite	Reworked radiolaria and fossil shell fragments	Compaction and contact types	Poorly	Subangular- subrounded rock fragments, very angular cherts	Calclithite	24	Pebbly fine grained sandstone

Table 1- (continue).

No	Thin Section No:	%Q	%F	%RF	Cement	Matrix	Other components	Alteration/dissolution	Fossils	Sedimentary structures	Sorting	Roundness	Modal Classification	No. of photos	Rock name
13	HL 3-4	-	-	100 (chrt:26, Crbnt:54, Siltstone, mudstone with and/ released radiolaria and others:20)	Calcite	-	Very well rounded glauconite + carbonized plant materials+ bitumen fillings	Carbonate rock fragments to calcite	Reworked radiolaria and fossil shell fragments	Compaction and contact types	Poorly	Subangular-subrounded rock fragments, very angular cherts	Calclithite	-	Pebbly fine grained sandstone
14	HL 3-6	-	-	100 (chrt:5,Crbnt:80, Mudstone with radiolaria+ released radiolaria:15)	Calcite	-	Bitumen fillings	Carbonate rock fragments to calcite	Reworked radiolaria + globigerina	grain orientation makes lineation in the section	Moderately	Subangular-subrounded rock fragments, angular cherts	Calclithite	2	Very fine grained sandstone
15	HL3-11	0,5	-	99,5 (chrt:5, Crbnt:75, Siltstone, mudstone with and/ released radiolaria and coal fragments:20)	Calcite	-	Opaque euhedral heavy minerals 1%+ glauconite+ bitumen fillings+ carbonized plant materials	Carbonate rock fragments to calcite	Fossil shell fragments+ reworked radiolaria	-	Poorly	Subangular-subrounded rock fragments and quartz very angular cherts	Calclithite	37	Fine grained sandstone
16	HL 4-1	1	-	99 (chrt:11, Crbnt:62, Siltstone, mudstone with and/ released radiolaria and others:27)	Calcite	-	Opaque euhedral heavy minerals 1,5%+ glauconite+ bitumen fillings+ carbonized plant materials	Carbonate rock fragments to calcite	Fossil shell fragments+ reworked radiolaria	grain orientation makes lineation in the section	Poorly	Subangular-subrounded rock fragments, very angular cherts and quartz	Calclithite	6	Very fine grained sandstone
17	HL 4-2	0,8	-	99,8 (chrt:32,Crbnt:40, Siltstone, mudstone with and/ released radiolaria and others:28)	Calcite	-	-	Carbonate rock fragments to calcite	Reworked radiolaria	-	Poorly	subrounded rock fragments, very angular cherts and quartz	Calclithite	8	Very fine grained sandstone
18	HL 4-3	-	-	100 (chrt:4,Crbnt:74, Siltstone, mudstone with and/ released radiolaria and others:22)	Calcite	-	-	Carbonate rock fragments to calcite	Reworked radiolaria	-	Moderately	subrounded rock fragments, very angular cherts	Calclithite	2	Very fine grained sandstone

Table 1- (continue).

No	Thin Section No:	%Q	%F	%RF	Cement	Matrix	Other components	Alteration/ dissolution	Fossils	Sedimentary structures	Sorting	Roundness	Modal Classification	No. of photos	Rock name
19	HL 4-5	0,2	-	99,8 (chrt:9, crbnt:77, siltstone, mudstone with and/ released radiolaria and others:14)	Calcite about %25	-	Opaque subhedral heavy minerals + glauconite + bright reddish hematite+ rare tiny bitumen fillings	Carbonate rock fragments to calcite	Rare benthic shell fragments+ reworked radiolaria + 2 globigerina	-	Moderately	Subangular- rock fragments, very angular cherts and quartz	Calcithite (greywacke)	7	Fine grained sandstone
20	HL 4-6	0,2	-	99,8 (chrt:14, crbnt:72, siltstone, mudstone with and/ released radiolaria and others:14)	Calcite about %25	-	Opaque subhedral heavy minerals + glauconite + bright reddish hematite+ tiny bitumen fillings	Carbonate rock fragments to calcite	Rare benthic shell fragments+ reworked radiolaria	-	Poorly	Subangular- rock fragments, very angular and needle shaped cherts and angular quartz	Calcithite (greywacke)	10	Fine grained sandstone
21	HL4-7	-	-	100 (chrt:27,Crbnt:55, Siltstone, mudstone with and/ released radiolaria and others:18)	Calcite	-	Opaque subhedral heavy minerals + plant materials+ glauconite + bright reddish hematite+ rare bitumen fillings	Carbonate rock fragments to calcite	Rare benthic shell fragments+ reworked radiolaria	-	Very poorly	Subangular- subrounded rock fragments, very angular cherts	Calcithite	8	Fine grained sandstone
22	HL4-8	-	-	100 (chrt:27,Crbnt:55, Siltstone, mudstone with and/ released radiolaria and others:18)	Calcite	-	Opaque subhedral heavy minerals+ bitumen fillings	Carbonate rock fragments to calcite	Rare benthic shell fragments+ reworked radiolaria	-	Very poorly	Subangular- subrounded rock fragments, very angular cherts	Calcithite	10	Very fine grained sandstone
23	HL 5-2	0,5	-	99,5 (chrt:20,Crbnt:45, Siltstone, mudstone with and/ released radiolaria and others:35)	Calcite	-	Subangular glauconite + black subhedral heavy minerals + bitumen fillings	Carbonate rock fragments to calcite	Rare benthic shell fragments+ reworked radiolaria	Slightly grain orientation	Very poorly	Subangular- subrounded rock fragments, very angular cherts	Calcithite	10	Very fine grained sandstone

Table 1- (continue).

No	Thin Section No:	%Q	%F	%RF	Cement	Matrix	Other components	Alteration/ dissolution	Fossils	Sedimentary structures	Sorting	Roundness	Modal Classification	No. of photos	Rock name
24	HL 5-3	0,4	-	99,6 (chrt:6,Crbnt:72, Siltstone, mudstone with and/ released radiolaria and others:22)	Calcite	-	Subangular glauconite + bitumen fillings	Carbonate rock fragments to calcite	Rare benthic shell fragments+ reworked radiolaria	Slightly grain orientation	Poorly	Subangular- subrounded rock fragments, very angular cherts and quartz	Calclithite	4	Very fine grained sandstone
25	HL 5-4	0,2	-	99,8 (chrt:23,Crbnt:47, Siltstone, mudstone with and/ released radiolaria and others:30)	Calcite	-	Rare bitumen fillings + glauconite	Carbonate rock fragments to calcite	Rare benthic shell fragments+ plenty of reworked radiolaria	-	Poorly	Subangular rock fragments, very angular cherts and quartz	Calclithite	10	Very fine grained sandstone
26	HL 6-3	0,5	-	99,5 (chrt:22,Crbnt:54, Siltstone, mudstone with and/ released radiolaria and others:34)	Calcite	-	Bitumen fillings	Carbonate rock fragments to calcite	Rare benthic shell fragments+ plenty of reworked radiolaria	Slightly grain orientation	Very poorly	Subangular- subrounded rock fragments, very angular cherts	Calclithite	4	Very fine grained sandstone
27	HL 6-5	-	-	100 (chrt:21,Crbnt:59, Siltstone, mudstone with and/ released radiolaria and others:20)	Calcite	-	Opaque subhedral heavy minerals +bitumen fillings	Carbonate rock fragments to calcite	Rare benthic shell fragments+ plenty of reworked radiolaria	Slightly grain orientation	Poorly	Subangular- subrounded rock fragments, very angular cherts	Calclithite	6	Fine grain siltstone
28	HL 6-7	0,2	-	99,8 (chrt:9, Crbnt:64, Siltstone, mudstone with and/ released radiolaria and others:27)	Calcite	-	Pretty much bitumen fillings+ glauconite	Carbonate rock fragments to calcite	Rare benthic shell fragments+ plenty of reworked radiolaria	Slightly grain orientation in some part of the section	Poorly	Subangular- subrounded rock fragments, very angular cherts and quartz	Calclithite	14	Fine grained sandstone

Table 1- (continue).

No	Thin Section No:	%Q	%F	%RF	Cement	Matrix	Other components	Alteration/dissolution	Fossils	Sedimentary structures	Sorting	Roundness	Modal Classification	No. of photos	Rock name
29	HL 7-3	0,4	-	99,6 (chrt:7, Crbnt:82, Siltstone, mudstone with and/ released radiolaria and others:11)	Calcite (%25)	-	Glauconite + hematite + rare bitumen fillings	Carbonate rock fragments to calcite	Rare benthic shell fragments+ plenty of reworked radiolaria	Slightly grain orientation and dark lithics form lamina like levels along the section	Moderately	Subangular-subrounded rock fragments, very angular cherts and quartz	Calclithite (greywacke)	7	Very fine grained sandstone
30	HL7-4	-	-	100 (chrt:17,Crbnt:56, Siltstone, mudstone with and/ released radiolaria and others:27)	Calcite	-	Subangular glauconite black subhedral heavy minerals + bitumen fillings	Carbonate rock fragments to calcite	Rare benthic shell fragments+ plenty of reworked radiolaria	Slightly grain orientation	Poorly	Subangular-subrounded rock fragments, very angular cherts	Calclithite	6	Very fine grained sandstone
31	HL7-7	-	-	100 (chrt:15,Crbnt:62, Siltstone, mudstone with and/ released radiolaria and others:23)	Calcite	+	?	Carbonate rock fragments to calcite	Rare benthic shell fragments (0,2%)+plenty of reworked radiolaria	-	Very poorly	Subangular-subrounded rock fragments, very angular cherts	Calclithite	20	Fine grained sandstone
Average		0,37	0,009	Lithic chert : 16,65 Carbonate rf : 59,32 Others :24,03	Calcite	-	Carbonized plant fragments, euhedral to subhedral opaque minerals, reddish brownish hematite, bright green subrounded glauconite, solid bitumen fillings (range between 1-15%) in pores	Carbonate rock fragments to calcite	Globigerina, reworked radiolaria, neritic fossil shell fragments	Slightly grain orientation (not representative for the all sections)	Very poorly to moderately	Subangular-subrounded rock fragments, very angular cherts and quartz	Calclithite	9,4333	Very fine to medium grained sandstone

Note: All the quartzs in the thin sections are monocrystalline with straight and fully extinction.

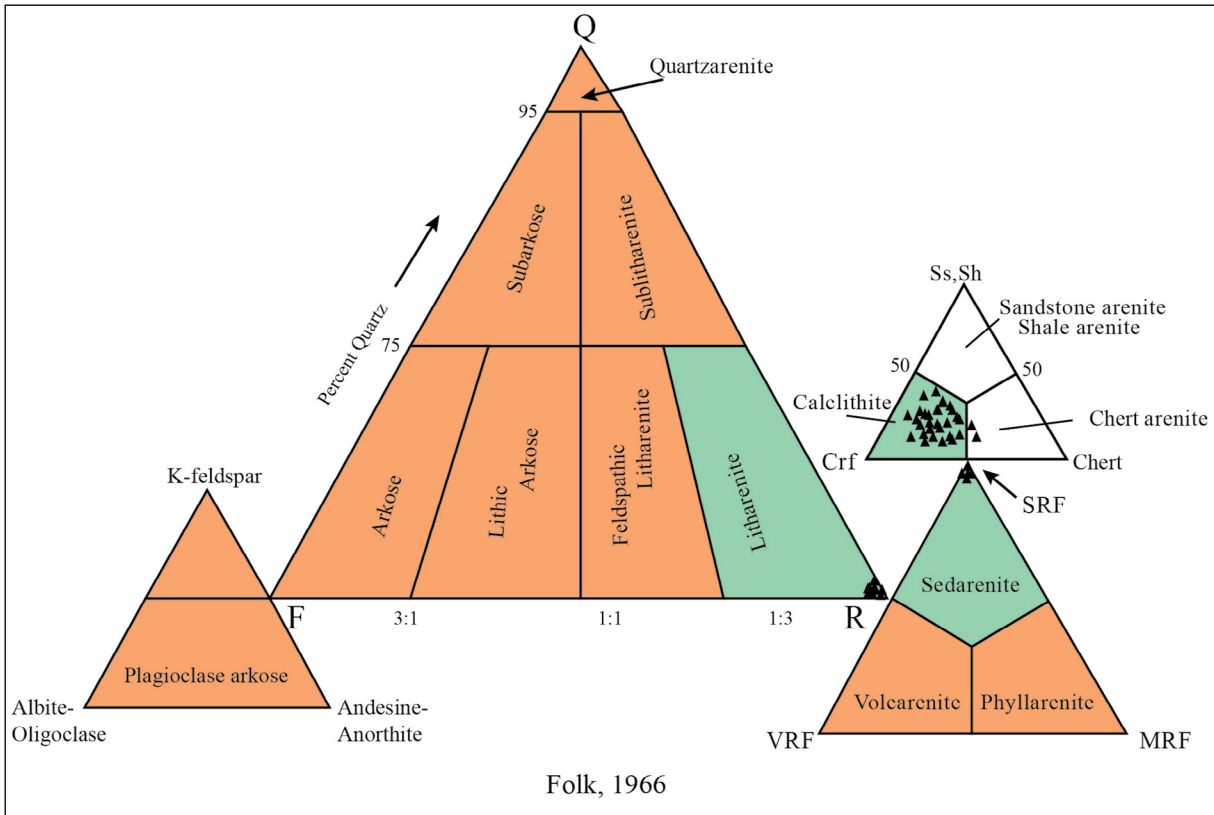


Figure 9- Q-F-R ternary diagrams (Folk, 1966) showing the classification of the turbidite sandstone studied. All the samples fall in the calcilithite corner.

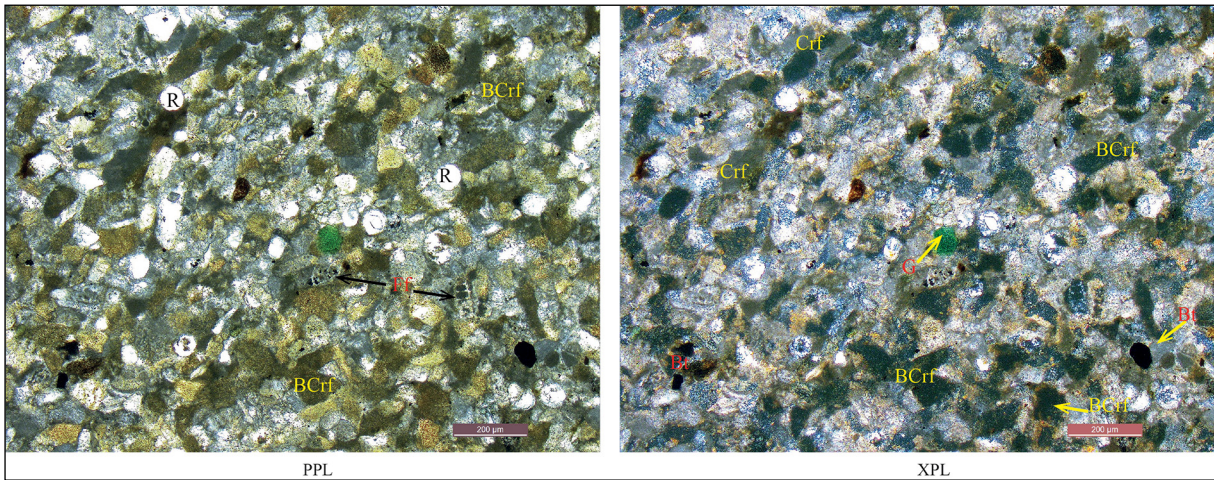


Figure 10- HL1-1. These two photomicrographs (4X-Magnification) represent general composition of the turbidites studied of Tanjero Formation. As the scale is very small it is not possible labelling all the clasts in the images. Dark dirty yellowish to brownish (PPL) angular to subangular clasts are BCrF as labeled some of them. Bluish angular fragments (XPL), angular white fragments (PPL) are lithic chert clasts. Solid bitumen (Bt) fillings are staining the calcite cement to yellowish- brownish in colour. White circles (PPL) are released-reworked radiolaria fossils. Rounded glauconite grain (G) is from shallow water environment. Two neritic fossil shell (Ef) clasts (reworked) are seen here which very rare in the all thin sections. More detail explanations will be in the following photo micrographs.

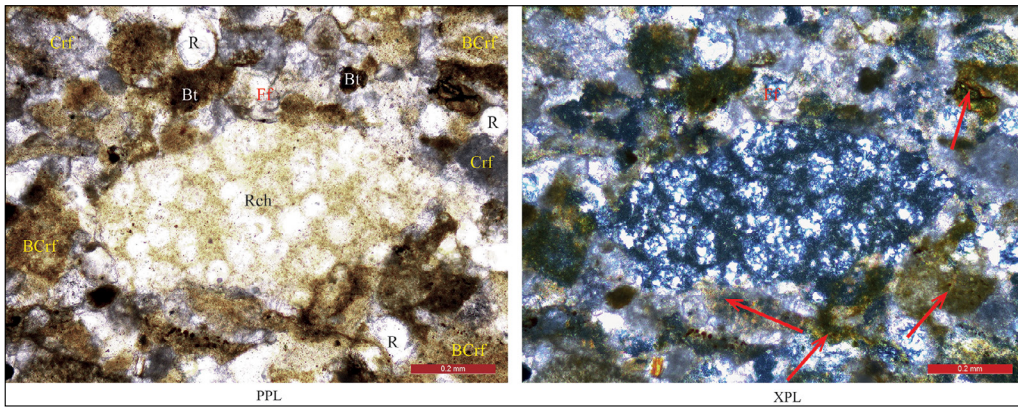


Figure 11- HL1-7. A big radiolaria fossils (white circular specks in Rch in PPL image) bearing angular radiolarian lithic chert clast (Rch). This is the host rock for released and reworked radiolaria fossils in the source area. The released fossils possibly left the host rock either during weathering or transportation. Red arrows point out the bitumen stained calcite cement. Very poorly sorted example for the sandstone studied.

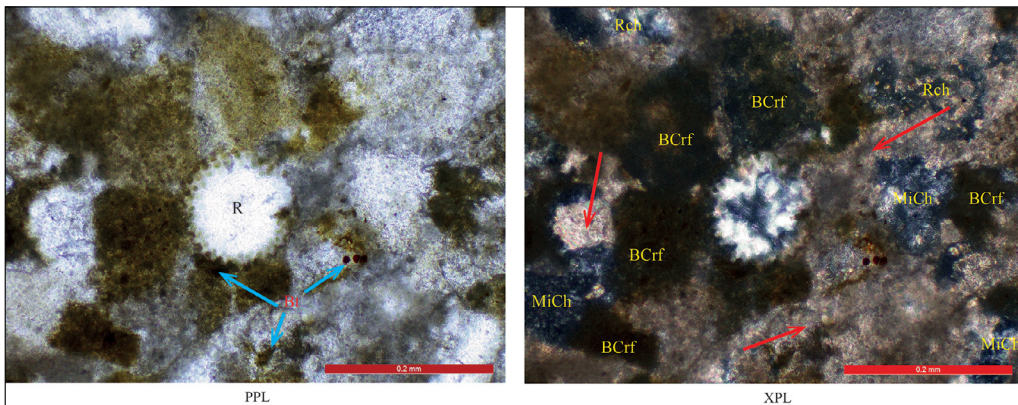


Figure 12- HL1-7. Released and reworked chalcedony filled (XPL view) radiolaria fossil in the center of the image. Although weathering and transportation, the forms of the fossil were nearly well sheltered. Note the concavo convex contact type (the best view PPL image) between the R and the surrounding BCrf fragments. Disseminated (black small circles) solid bitumen fillings are shown by the blue arrows directed to the right up hand side. Bitumen stained calcite cement is represented by red arrows in the XPL image. Mostly all the clasts (especially Rch) were replaced by calcite so the contact of the clast are not very clear in (XPL).

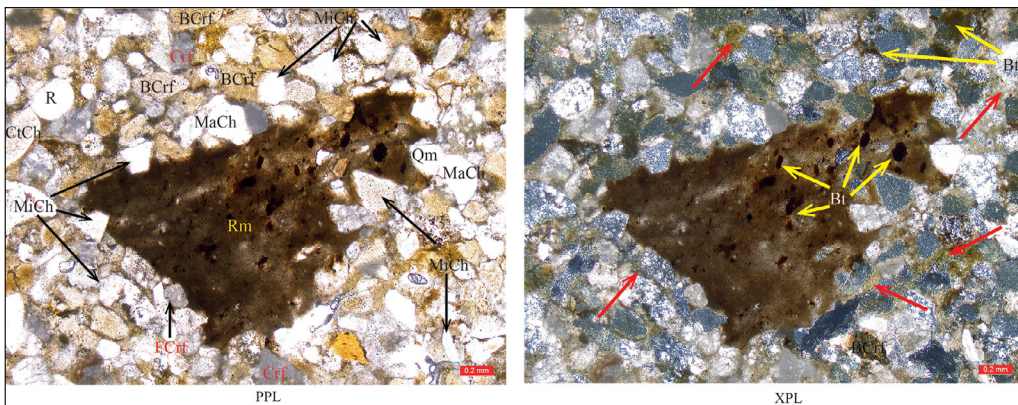


Figure 13- HL1-9. About 2 mm in size radiolarian mudstone clast including chert clasts and solid bitumen fillings. Good example for concavo convex grain contact type since the partly embedding of the all other lithic clasts into the mudstone along the contact. The Rm is most likely was a relatively softer mud intraclast during compaction than the other constituents transported from the source area. Tangential, point and long grain contact types are also present in the images (more visible in the PPL) Solid bitumen fillings in some pores caused the changing of the colour of calcite cement to greenish-yellowish. Very poorly sorted very angular cherts and subangular- subrounded carbonate rock fragments.

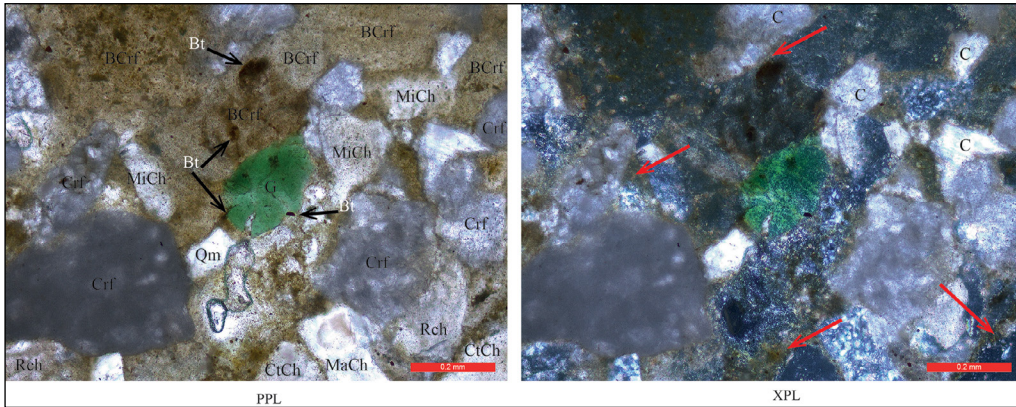


Figure 14- HL1-9. Well rounded reworked bright green glauconite has calcite and bitumen intrusion into the lower part through a small fracture occurred before settling. Two air bubbles as section fault below G. Crf clasts have undefined microfossils as white speckles. Sutured contact type visible between Rch and Crf above the scale bar (PPL), concavo convex contact type between G and two BCrf above G, point contact type between big Crf and the two clasts above (PPL). Calcite cement around the clasts was stained as dark brownish-greenish-yellowish in colour by bitumen fillings.

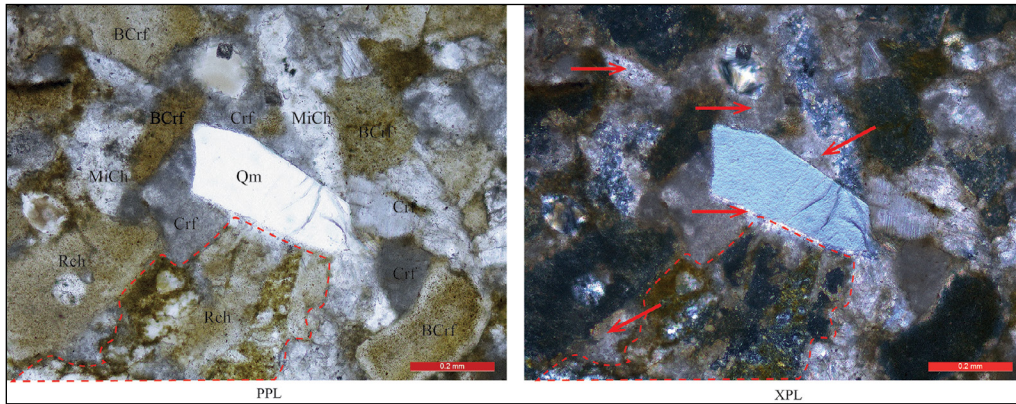


Figure 15- HL1-9. A superb example for very angular monocrystalline quartz (Qm) having straight full extinction in the center of the images. It has a very less ratio in the all thin sections. The Qm inserted into the Crf to the left hand side and split the Crf into two parts during compaction. Long grain contact between the majority of the lithic clasts indicate a tight packing and strong compaction. A big Rch grain located in the lower part of the photo mostly was replaced by calcite (bitumen stained, although Bt is not in this image but exist in the thin section HL1-9).

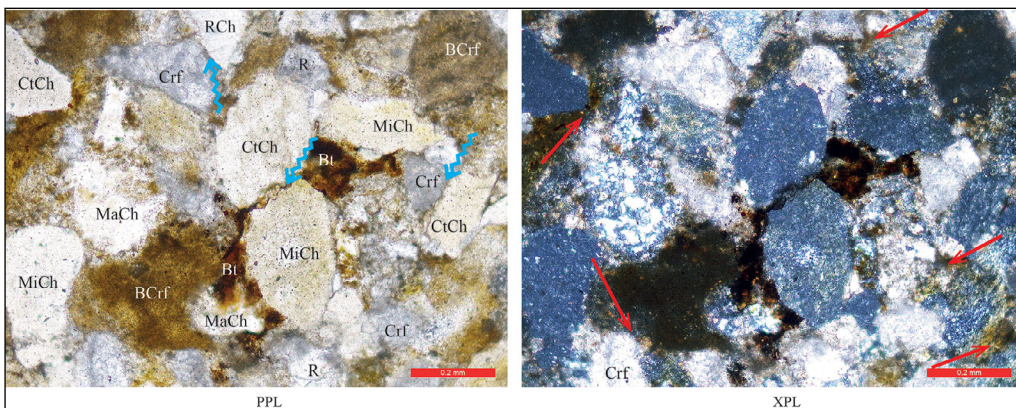


Figure 16- HL2-4. Concavo convex and sutured grain contact types are important for this section. Two Mach grains have concavo convex contact with the dark BCrf clast in the lower left part of the center of the image. Blue arrows indicate the sutured grain contacts. Solid bitumen filling which one of the most effective agents reducing porosity of the sandstones is blocking the intergranular pores and stains the calcite cement.

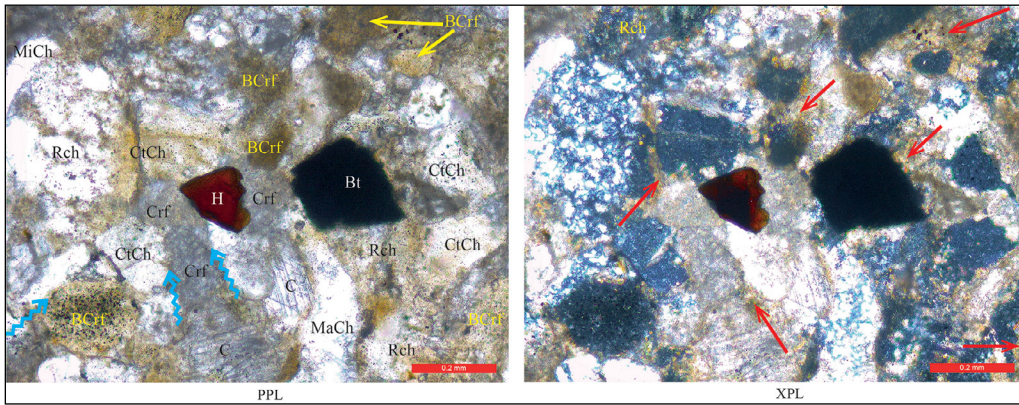


Figure 17- HL4-2. Solid bitumen filling in an intergranular pore and brownish red hematite in the middle part of the photomicrograph. Tightly compaction and sutured grain contact show the high compaction ratio. Rch clasts were mostly replaced by calcite.

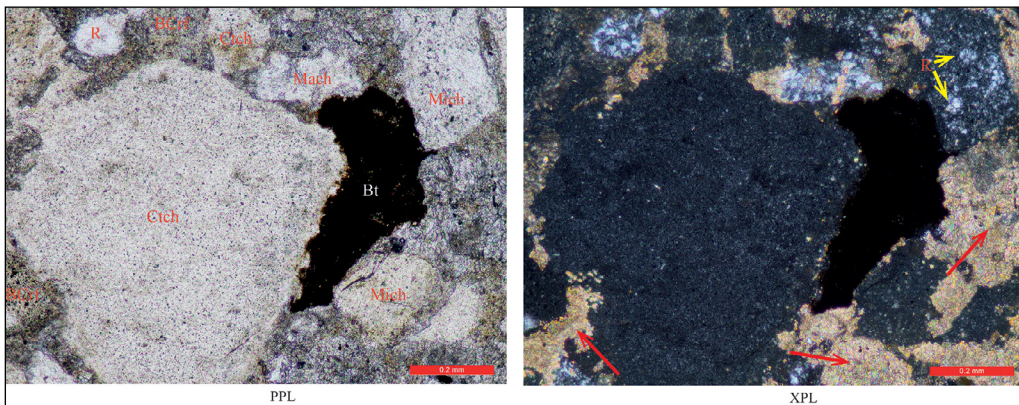


Figure 18- HL4-7. MacrocrySTALLINE microcrystalline and cyrcrocrystalline lithic chert clasts are seen together in one image. Red arrows represent slightly stained calcite cement. Solid bitumen visible in both images causes pale yellowish staining on the calcite cement. Note the point contact type between the big CtCh clast and two small lithic chert fragments above. Mich below bitumen filling has floating contact type as it is surrounded by fillings (Calcite cement and Bt).

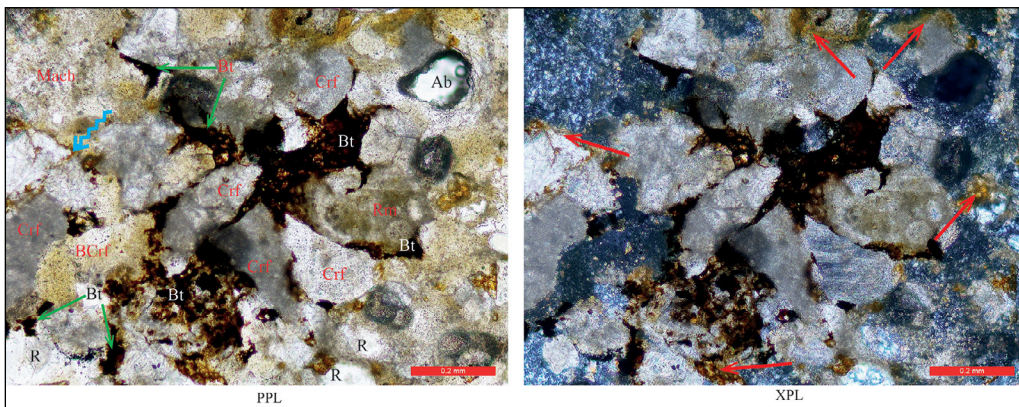


Figure 19- HL6-3. Mostly intergranular and little intragranular (lower left part of the center in this image) pores were blocked by bitumen fillings (Bt). Tangential, concavo convex and sutured grain contact types indicate tightly packing and high compaction. Note the moderately sorted and very angular to subangular grains.

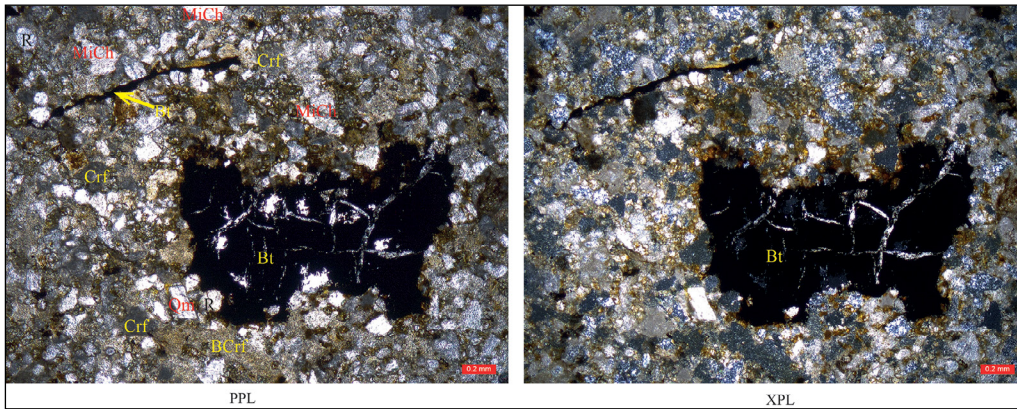


Figure 20- HL6-7. Microfractures in the solid bitumen were filled by calcite. Relative timing between the calcite fillings and bitumen shows that bitumen filled in pores before calcite, the fractures don't cut the section throughout, only limited in the bitumen filling. This relation indicates that the fractures occurred after bitumen became solid then the calcite filled into the fractures. Monocrystalline quarts with fully extinction to the left down of the bitumen. To the top left a microfracture is filled by bitumen. Subangular to subrounded Crf and very angular lithic chert fragments are the dominant constituents in this section.

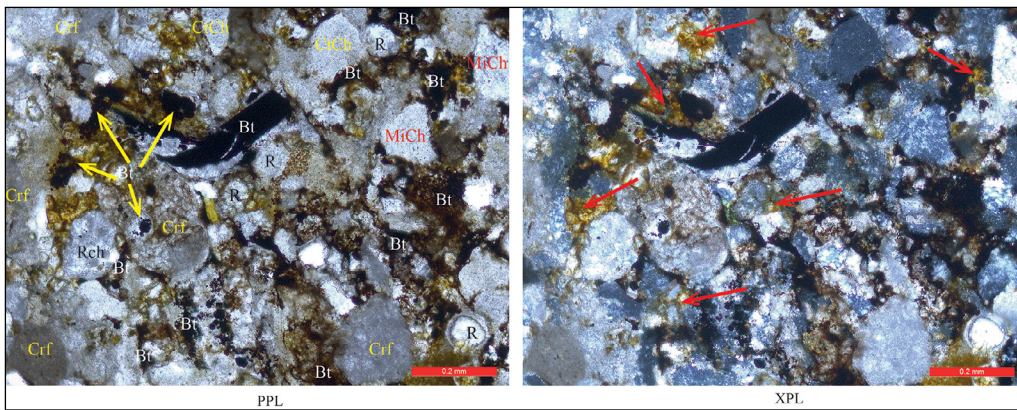


Figure 21- HL6-7. Majority of the intergranular and intragranular pore spaces filled by solid bitumen before or syn-calcite precipitation while the sandstone had pretty much pore spaces during early diagenesis. At that time the turbidite sandstones of Tanjero Formation had a good porosity which filled by solid bitumen since oil migration.

Both the provenance ternary diagram and the composition of the turbidite sandstones of Tanjero Formation in the studied area point out sedimentary rocks as source area. Taking together into account the petrographic and palaeoflow data (Table 1, and 2) (Figures 24 and 25) it is possible to consider only one source area composed of deep marine and shallow marine sedimentary rocks to the north as the main responsible for the composition of sandstones.

Lithic clast types in the petrographic composition of the sandstones represent the sedimentary rock types of the Lower Cretaceous Qulqula (radiolarian) Formation consisting of deep marine radiolarian sedimentary rocks and Balambo Formation composed of shallow marine limestone and shales supporting

the basin by such asneritic transported broken fossil shells, glauconite grains, and undefinable fossils in the altered carbonate rock clasts, located in the lowermost part of the stratigraphic column of the northern Iraq region.

The reason for the absence of ophiolite fragments in thin sections is in contrast to the palaeogeographic drawings in previous works (e.g. Ameen, 2008; Karim and Taha, 2009; Karim and Surdasy, 2005b). This suggests that in the source area feeding the turbidites in the study area, the ophiolites do not crop out.

All the data from provenance analysis and petrography in this study show that provenance is not changing during deposition of the sandstones for

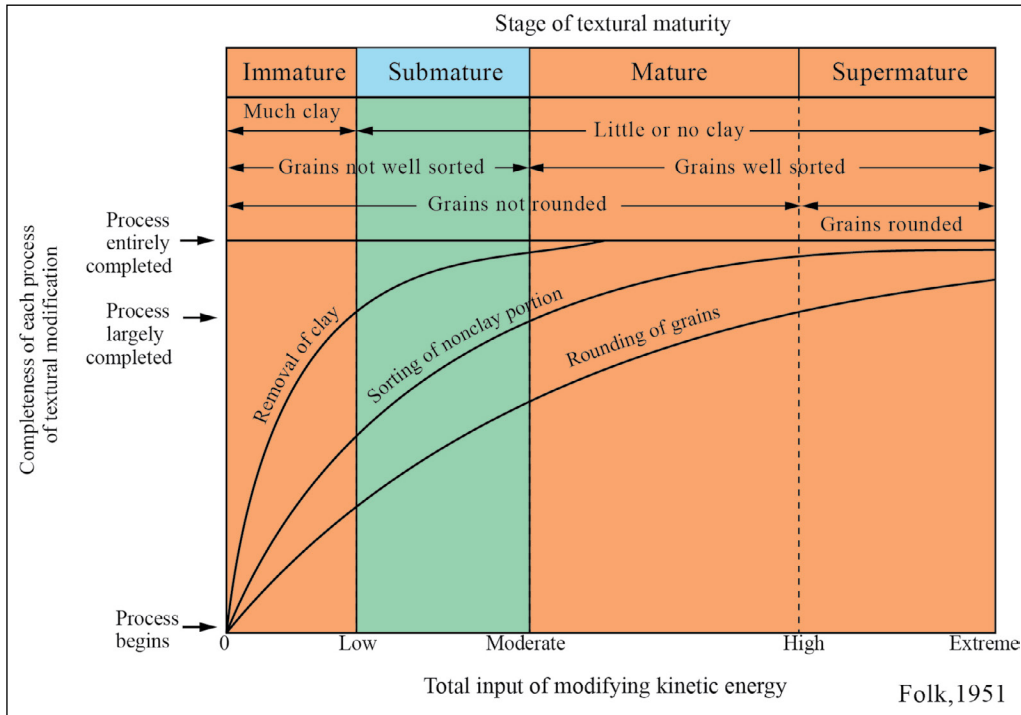


Figure 22- Turbidite sandstones of Tanjero Formation in the studied area indicate submature stage in the Folk's (1951) textural maturity table. Since as can be seen in table 1 and photomicrographs, there is no clay matrix in the sandstones, clay content of the turbidites is less than 5 %; poorly sorted; grains are not rounded.

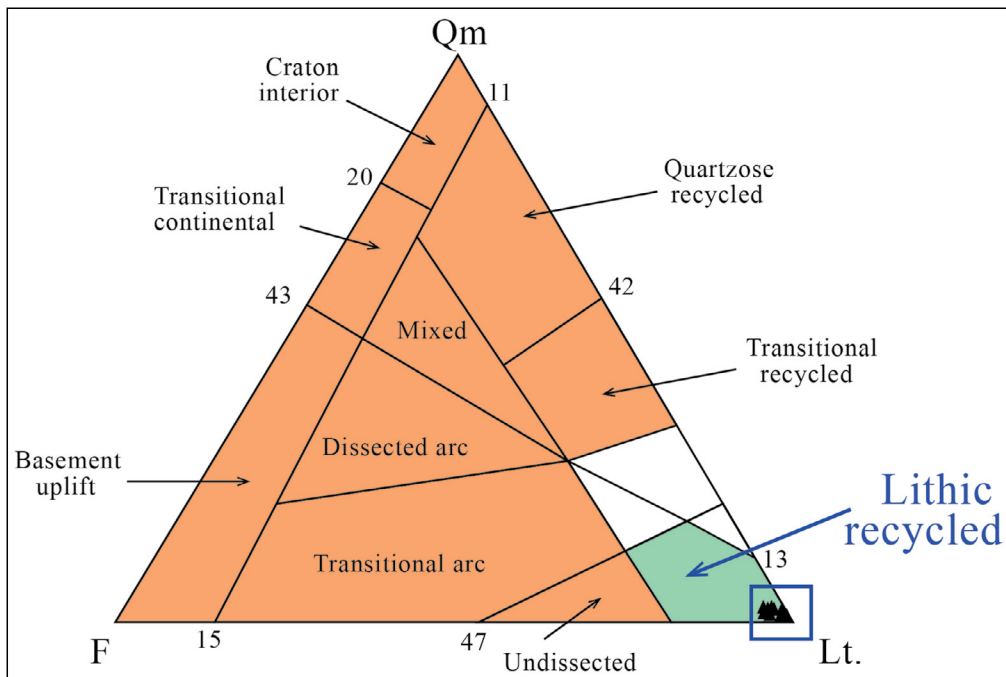


Figure 23- Qm-F-Lt ternary diagram showing tectonic provenance of the sandstones indicates "lithic recycled" category. Position of the samples in the Lt corner is exaggerated to make it visible (Dickinson et al., 1983).

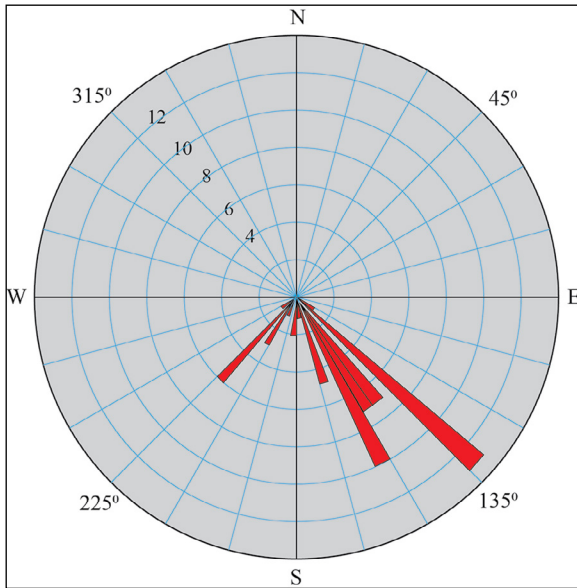


Figure 24- Rose diagram showing unidirectional palaeoflow of Tanjero Formation in the study area. Mean direction is toward south east.

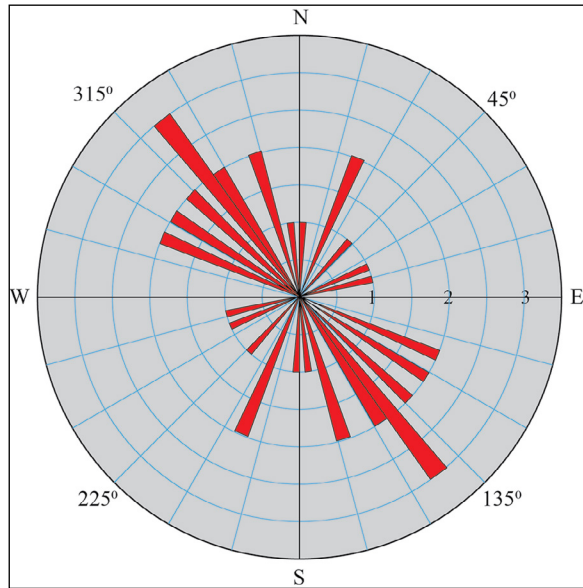


Figure 25- Rose diagram from bidirectional palaeoflow indicators shows Northwest – Southeast.

the studied area because of the average calcilithite sandstone composition is not varying along the measured sections.

The results for provenance analysis in this study show different source area than the interpretations in Karim’s studies in 2004, 2007 and 2010 as it is suggested that the source rock is only Qulqula Formation in his studies because of not sufficient petrographic analysis.

6. Palaeoflow Analysis

Previously two researchers, as in the following paragraphs, studied on palaeoflow direction of Tanjero Formation. They used many sedimentary structures, channel and incised valleys for indicating the direction in different places of northern Iraq.

Al-Rawi (1981) used flute casts, groove casts, ripple mark and cross bedding with N45°W and N85°W in Dokan area and N45°W in Sulaimaniyah area and concluded that the source area is in the East and the main direction of transport is toward northwest-west.

In Karim’s (2004) study palaeo flow direction from ripple mark, elongate fossil, cross bedding, oriented plant fragments, imbricated pebbles, the direction of channel and incised valleys is toward south-outhwest in Sulaimaniyah and Darbandikhan area.

In this study 83 sedimentary structures (Table 2) in both types of unidirectional and bidirectional have been used to determine the direction of palaeoflow for Tanjero Formation.

6.1. Unidirectional Sedimentary Structures

Sixty-three unidirectional palaeo flow measurements, obtained from three types of sedimentary structures such as ripple mark, cross bedding and flute cast, show moderately southeast orientation (Figure 24). According to Potter and Pettijohn (1977) and Tucker (2011) there is a limit for tilt correction and they revealed that tilt below 30 degrees needs no correction.

6.2. Bidirectional Sedimentary Structures

Twenty measurements from oriented plant material, parting lineation and groove cast were in the rose diagram (Figure 25). The mean direction shows NW-SE.

Petrographic and palaeoflow analysis in this study pointed out that the source area is located moderately in the north and consisting of Lower Cretaceous (radiolarian) Qulqula and Balambo formations. The turbidity currents feeding the Tanjero Formation are initiating from the north than diverted to the south-east possibly depending on the basin plain topography

Table 2- Palaeoflow measurements from the seven measured sections.

No	Palaeoflow direction	Sedimentary structure	Bedding attitude		
			Dip angle	Dip direction (Azimuth)	Strike
Measurements from unidirectional sedimentary structures					
1	186	Ripple mark	24	66	156
2	164	Ripple mark	24	66	156
3	186	Ripple mark	24	66	156
4	134	Flute cast	24	66	156
5	208	Ripple mark	25	68	158
6	116	Ripple mark	25	68	158
7	144	Ripple mark	25	68	158
8	220	Ripple mark	25	68	158
9	168	Ripple mark	25	68	158
10	220	Ripple mark	25	68	158
11	220	Ripple mark	25	68	158
12	210	Ripple mark	25	68	158
13	220	Ripple mark	25	68	158
14	236	Ripple mark	25	68	158
15	230	Ripple mark	25	68	158
16	140	Ripple mark	25	68	158
17	180	Ripple mark	25	68	158
18	216	Ripple mark	23	50	140
19	220	Ripple mark	23	50	140
20	140	Ripple mark	23	50	140
21	150	Ripple mark	23	50	140
22	150	Ripple mark	23	50	140
23	150	Ripple mark	23	50	140
24	150	Ripple mark	23	50	140
25	160	Ripple mark	23	50	140
26	160	Ripple mark	23	50	140
27	128	Ripple mark	23	50	140
28	146	Ripple mark	23	50	140
29	160	Ripple mark	23	50	140
30	150	Ripple mark	23	50	140
31	180	Ripple mark	23	50	140
32	220	Ripple mark	24	68	158
33	148	Ripple mark	24	68	158
34	160	Ripple mark	24	68	158
35	210	Ripple mark	24	68	158
36	210	Ripple mark	24	68	158
37	145	Ripple mark	24	68	158
38	147	Ripple mark	24	68	158
39	144	Cross bedding	24	68	158
40	145	Ripple mark	24	68	158
41	149	Ripple mark	24	68	158
42	144	Ripple mark	24	68	158

No	Palaeoflow direction	Sedimentary structure	Bedding attitude			
			Dip angle	Dip direction (Azimuth)	Strike	
43	148	Ripple mark	28	63	153	
44	142	Ripple mark	28	63	153	
45	134	Ripple mark	28	63	153	
46	138	Ripple mark	28	63	153	
47	134	Ripple mark	28	63	153	
48	134	Ripple mark	28	63	153	
49	140	Ripple mark	28	63	153	
50	134	Ripple mark	29	50	140	
51	134	Cross bedding	29	50	140	
52	134	Cross bedding	29	50	140	
53	134	Cross bedding	29	50	140	
54	134	Cross bedding	29	50	140	
55	134	Cross bedding	29	50	140	
56	134	Cross bedding	29	50	140	
57	134	Cross bedding	29	50	140	
58	134	Ripple mark	29	50	140	
59	150	Ripple mark	29	50	140	
60	152	Ripple mark	29	50	140	
61	152	Ripple mark	29	50	140	
62	152	Ripple mark	29	50	140	
63	152	Ripple mark	29	50	140	
Measurements from bidirectional sedimentary structures						
1	170-350	350	Plant material	24	66	156
2	148-328	328	Parting lineation	24	66	156
3	130-310	310	Parting lineation	24	66	156
4	140-320	320	Parting lineation	24	66	156
5	164-344	344	Plant material	24	66	156
6	146-326	326	Plant material	25	68	158
7	112-292	292	Parting lineation	25	68	158
8	140-320	320	Plant material	25	68	158
9	78-258	258	Plant material	25	68	158
10	120-300	300	Plant material	25	68	158
11	132-312	312	Parting lineation	25	68	158
12	68-248	248	Parting lineation	25	68	158
13	40-220	220	Plant material	25	68	158
14	114-294	294	Plant material	25	68	158
15	120-300	300	Plant material	25	68	158
16	0-180	180	Groove cast	25	68	158
17	20-200	200	Plant material	23	50	140
18	160-340	340	Plant material	23	50	140
19	140-320	320	Plant material	23	50	140
20	22-202	202	Groove cast	29	50	140

and NW-SE directed basin margins during Late Cretaceous. In the studied area dip angle of beds are less than 30 degrees (Table 2 and Figure 26), because of that no needs to correction.

7. Discussion

The northern Iraq region is one of the largest oil accumulation field so far discovered in Iraq including some 50% (De Vera et al., 2009) of over 100 bn barrels (Iraq Oil and Gas Report Q1, 2018) mainly within the carbonate formations. The discovery of this and since the basin is located on the northern

margin of the Arabian Plate, its tectonic evolution and collision with the Iranian Plate in along southern arm of the Neotethys ocean, led to vast amount of stratigraphic and tectonic national studies in the area mainly published in the national or regional journals that they are not international famous with little exception as given in the text and reference list in this paper. Additionally, the largest clastic turbidite unit on the geological map, Tanjero Formation, has not been petrographically studied yet as the main interest is on the carbonate units in the area for oil production. Also the political problems are the other important case that negatively affected sufficient international geological studies during the last decades.

For all that a consensus has not been reached yet on some of the subject such as the stratigraphic positions of many formations (etc. Red Bed Series, Qulqula Radiolarian Formation, Bekhme Formation), tectonic evolution and provenance for clastic rocks like Tanjero Formation since inadequate field and laboratory works. This study shows that these kind of controversial subjects like the gap on the provenance and related palaeogeographic evolution of the Tanjero Basin can be resolved successfully by a rigorous petrographic study which is open to international discussions and further studies in the other outcrops throughout on the unit.

Depositional history of the Cretaceous basin consisting of Tanjero Formation has been subjected to the following studies as illustrated in the figures 27, 28, 29 and 30. Qulqula Radiolarian Formation is the only

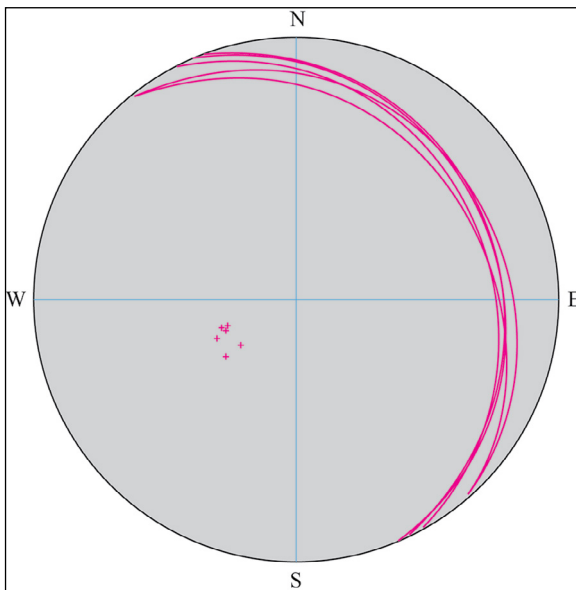


Figure 26- Stereonet showing bedding planes of sandstone in the studied area, dip angles are less than 30 degrees toward NE, plotted on the Geo Rose software.

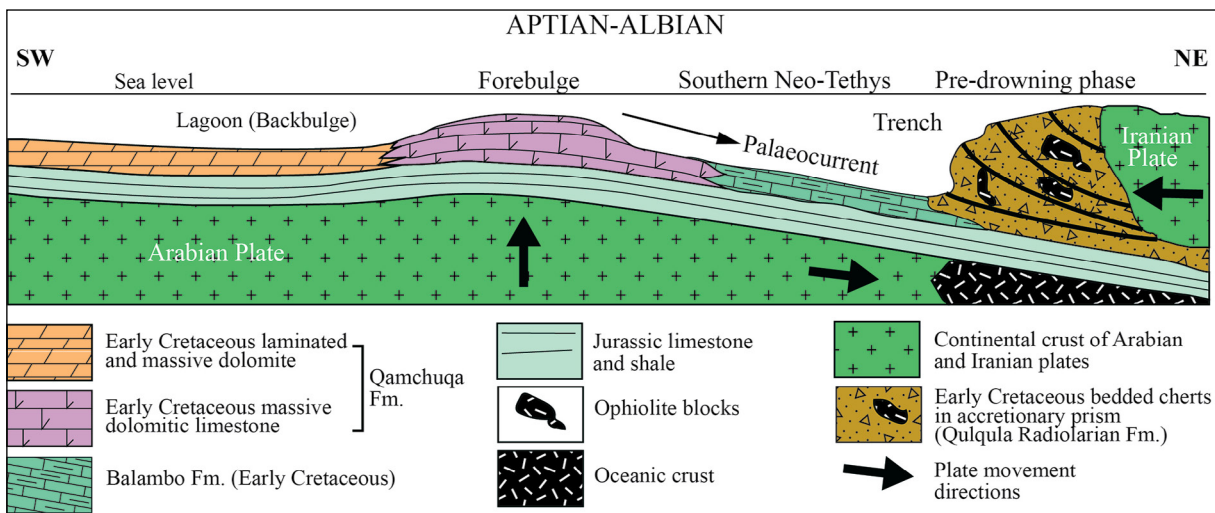


Figure 27- Depositional history of Early Cretaceous basin in which Qamchuqa and Balambo and Qulqula Radiolarite Formations are deposited (Ameen, 2008).

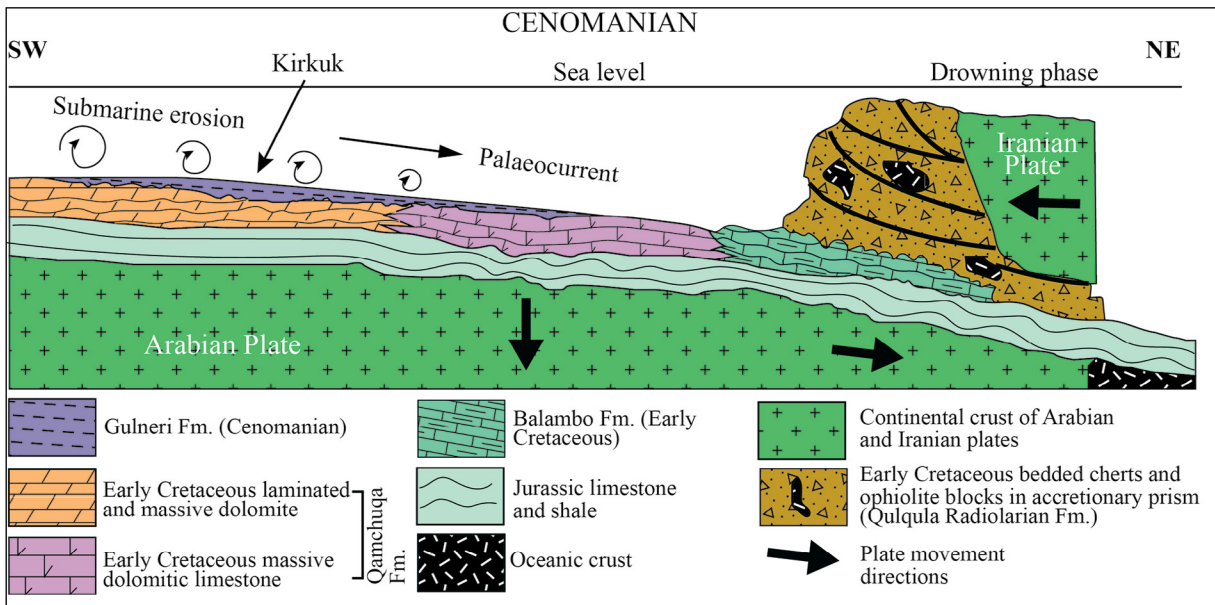


Figure 28- Tectonic and depositional model of the Late Cretaceous (Cenomanian) basin in which Kometan is deposited (Karim and Taha, 2009).

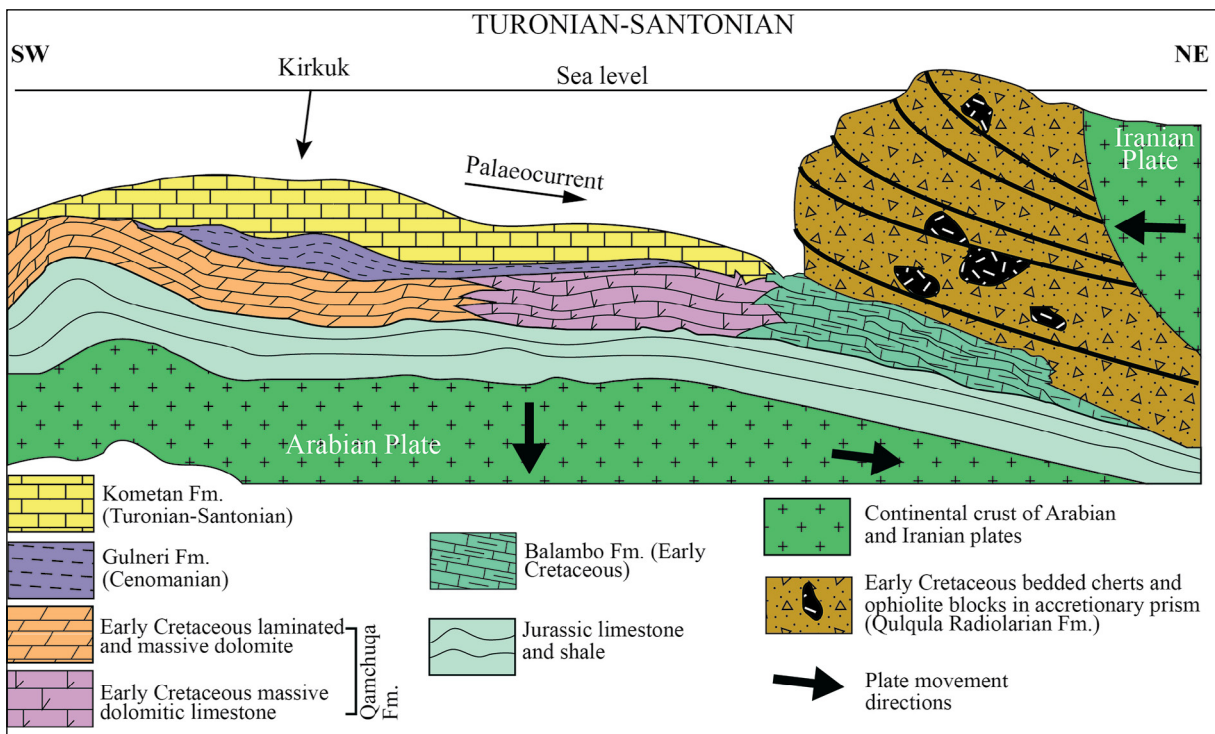


Figure 29- Tectonic and depositional model of the Late Cretaceous (Turonian-Campanian) basin in which Kometan and Bekhme Formation are deposited (Karim and Taha, 2009).

source rocks in these tectonic evolution models on the northern margin of the basin feeding Shiranish and Tanjero formations and the Red Bed Series. Balambo Formation is located under the accretionary prism and overthrust Qulqula Radiolarian Formation so it doesn't crop out anywhere to be a source for the basin.

During Early Cretaceous under the load of the trench materials, the Arabian plate is suffered from flexure which is formed fore bulge. On this palaeo high Qamchuqa Formation is deposited as reefal and lagoonal sediments (Figure 27) (Ameen, 2008). The Kometan Formation is deposited after drowning of

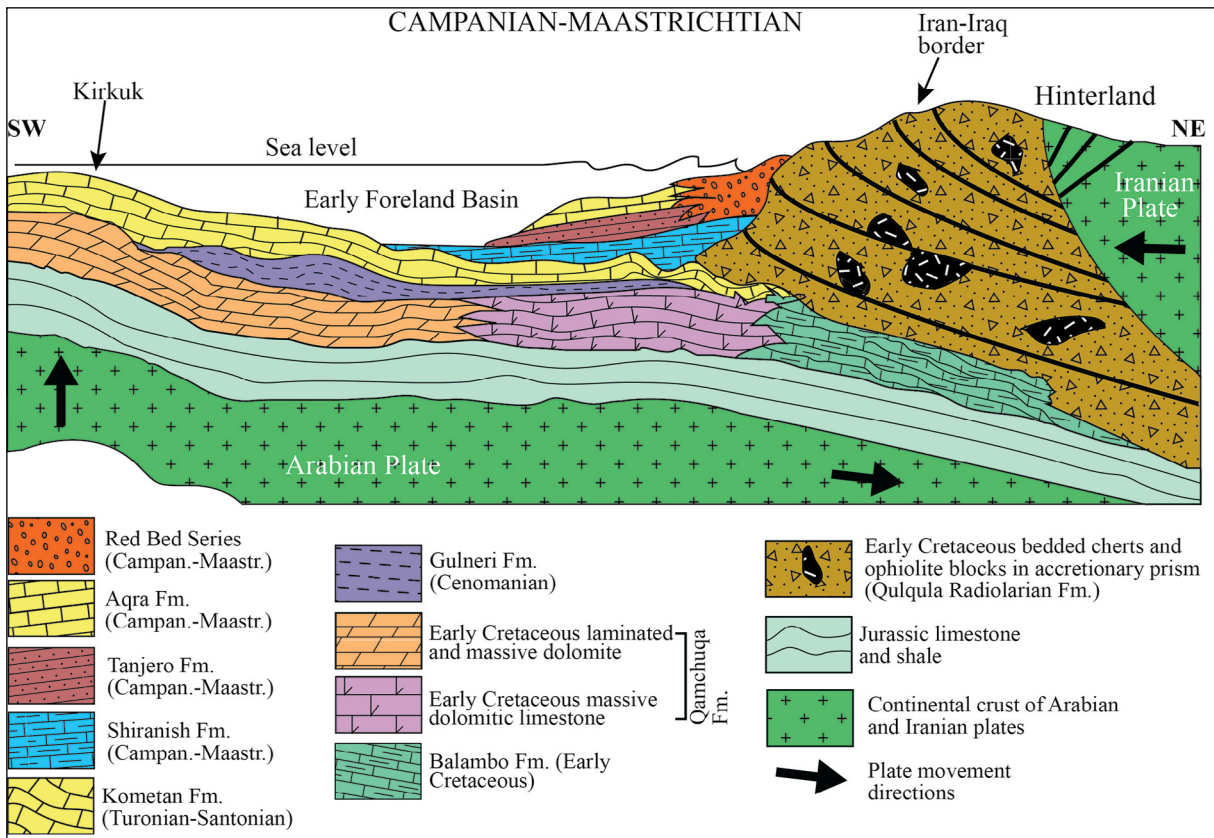


Figure 30- Combination of tectonic and depositional setting of Late Cretaceous basin in which Shiranish and Tanjero Formation are deposited (Karim and Surdasy, 2005b).

the Arabian Platform (Qamchuqa Formation) under the load of the trench material (accretionary prism materials) and Iranian plate in Cenomanian. The fore bulge is subsided and during subsiding Dokan and Gulneri formations are deposited as transitional facies, as sediments of intermediate depth between shallow (Qamchuqa) and deep (Kometan) during Turonian-Campanian (Figure 28) (Karim and Taha, 2009).

The Kometan Formation is deposited after drowning of the Arabian Platform Qamchuqa Formation under the load of the both accretionary prism materials and the Iranian plate, fore bulge subsided. The palaeocurrent was toward northeast. On this fore bulge, Qamchuqa Formation is deposited. Combination of tectonic and depositional setting of Late Cretaceous basin in which Kometan is deposited in Turonian-Campanian (Figure 29) (Karim and Taha, 2009).

During late Campanian the continental parts of the Iranian and Arabian plates are collided. The accretionary materials are pushed on to the Arabian

Platform. Due to this collision a terrestrial land had generated the palaeocurrent is reversed toward southwest. In addition to that a foreland basin is formed in front of the Iranian Plate in which Shiranish and Tanjero formations are deposited (Figure 29) (Karim and Taha, 2009).

Qulqula Radiolarian Formation is a radiolaria fossils bearing deep marine sedimentary unit as seen in the tectonic models above and in the text and figure 2 and 3. In this study, petrographic analysis (Table 1, and the photomicrographs) shows that the modal composition of the turbidite sandstone of Tanjero Formation consisting of 59.2 % carbonate rock clasts in average and has some neritic fossil shell fragments. This result requires at least one carbonate unit in the source area. Due to the alteration on the carbonate rock fragments in the thin sections it is difficult to identify the fossils on the clasts and the hosting source rocks. Qamchuqa Formation mainly consisting of dolomitic limestone but Tanjero Formation doesn't have any dolomitic clast representing Qamchuqa Formation (Figures 2 and 3). Balambo Formation is thought to

be the second source formation thrust by Qulqula Radiolarian Formation must be located together in the accretionary prism which is not exist in the previous studies like in figure 28, 29 and 30.

As a result, the palaeogeographic evolution models must include Balambo Formation too at the northern side of the Cretaceous depositional environment as source area which is not in the previous models. This result contributes a new finding for the palaeogeographic evolution of the northern Iraq region.

8. Conclusions

It was determined that the Tanjero Formation consists of low density turbidites containing different parts of the Bouma sequence and that high density turbidites identified by Lowe (1982), usually represented by conglomerates, are not seen in this area. The reason for this was thought to be due to the presence of distal fan sediments in the study area, according to facies and facies associations.

The compositional characteristics show the presence of only sedimentary rocks in the source areas. Petrographic modal analysis of the thin sections of the sandstone fall into the calcilithite area of litharenite division.

Very little amount of tangential, mainly long grain, concavo convex and sutured contact types and high contact index (4.7) represent moderate to tightly packing, moderate compaction. Less than 5 percentage clay, very fine to medium grained in size consisting of chert, siltstone, mudstone, radiolarian chert and radiolarian mudstone fragments, glauconite, neritic fossil shell fragments, fossil bearing carbonate rock clasts and angular to subangular in shape, very poorly to moderately sorted, transported over short distances are represented by submature stage.

Both the sandstone composition and the palaeoflow data indicating the flow towards the SE, measured from current ripples in Bouma Tc division and flute marks, and petrographic constituent of the sandstone point out a lithic recycle orogen category for the turbidite. This source area is the structural highs of the north of the Upper Cretaceous basin consisting of Lower Cretaceous (radiolarian) Qulqula and Balambo formations.

It was determined that the ophiolitic masses indicated in the previous studies as blocks within the accretionary prism did not constitute a source area for the turbidites of the Tanjero Formation widely exhumed around Sulaimaniyah.

Acknowledgements

The authors would like to thank to Professor Dr. Polla Azad Khanaqa head of the Institute for Strategic Studies and Scientific Research in Sulaimaniyah, Iraq, for his hospitality, valuable advices on security and the preparation of the thin sections in the laboratory of the institute. We also wish to thank two anonymous reviewers for the time spent on this manuscript; their comments and suggestions have made significant improvements to the work.

References

- Abdel Kireem, M. R. 1986a. Contribution to the Stratigraphy of the Upper Cretaceous and Lower Tertiary of the Sulaimaniyah - Dokan Region, Northeastern Iraq. *Neues Jahrbuch Für Geologie Und Paläontologie – Abhandlungen* 172 (1), 121-139.
- Abdel Kireem, M. R. 1986b. Planctonic Foraminifera and stratigraphy of the Tanjero Formation (Maastrichtian), northeastern Iraq. *Micropaleontology* 32, 215-231.
- Al Mehaiddi, H.M. 1975. Tertiary nappe in Mawat range, NE Iraq. *Geological Society of Iraq* 8, 31 - 44.
- Al Rawi, I. 1981. Sedimentology and Petrology of Tanjero Clastic Formation in north and northeastern Iraq. Unpublished Ph. D. Thesis, University of Baghdad, 295.
- Alavi, M. 2004. Regional stratigraphy of the Zagros fold-thrust belt of Iran and its proforeland evolution. *American Journal of Science* 304, 1-20.
- Alavi, M. 2007. Structures of the Zagros fold-thrust belt in Iran. *American Journal of Science* 307, 1067-1095.
- Ameen, B.M. 2008. Lithostratigraphy and Sedimentology of Qamchuqa Formation from, NE Iraq. Unpublished Ph. D. Thesis. University of Sulaimani 147p.
- Armas, P., Moreno, C., Sánchez, M.L., González, F. 2014. Sedimentary palaeoenvironment, petrography, provenance and diagenetic inference of the Anacleto Formation in the Neuquén Basin, Late Cretaceous, Argentina. *Journal of South American Earth Sciences* 53, 59-76.

- Bellen, R.C.V., Dunnington, H.V., Wetzel, R., Morton, D.M. 1959. *Lexique. Stratigraphique International, Asie Paris.*
- Bordy, E.M., Hancox, J.P., Rubidge, B.S. 2004. Provenance studies of the late Triassic-early Jurassic Elliot formation, main Karoo Basin, South Africa. *Geological Society of South Africa. South African Journal of Geology* 107, 587-602, 59-76.
- Buday, T., Jassim, S.Z. 1987. The Regional geology of Iraq: Tectonism Magmatism, and Metamorphism. In: M. J. Abbas and Jassim, S. Z (Ed.). *Geosurvey, Baghdad, Iraq*, 445.
- Cingolani, C.A., Manassero, M., Abre, P. 2003. Composition, provenance and tectonic setting of Ordovician siliciclastic rocks in the San Rafael block: southern extension of the Precordillera crustal fragment, Argentina. *Journal of South American Earth Science* 16, 91-106.
- Çelik, H, Salih, T.M.H. 2018. Provenance investigation from sedimentary petrography of the Upper Cretaceous deep marine low density turbidites of the Tanjero Formation around Arbat, northeastern Iraq. *Turkish Journal of Earth Sciences* 27 (6), 432-459.
- De Vera, J., Gines, J., Oehlers, M., McClay, K., Doski, J. 2009. Structure of The Zagros fold and thrust belt in the, northern Iraq. *Trabajos de Geología, Universidad de Oviedo* 29, 213-217.
- Dickinson, W.R. 1970. Interpreting detrital modes of greywacke and arkose. *Journal of Sedimentary Research* 40, 695-707.
- Dickinson, W.R. 1988. Provenance and sediment dispersal in relation to paleotectonics and paleogeography of sedimentary basins. In: Kleinspehn KL, Paola C, editors. *New Perspectives in Basin Analysis*. New York, NY, USA: Springer, pp. 3-25.
- Dickinson, W.R., Suczek, C. 1979. Plate tectonics and sandstone composition. *American Association of Petroleum Geologist Bulletin* 63, 2164-2194.
- Dickinson, W.R., Beard, S., Brakenbridge, F., Erjavec, J., Ferguson, R., Inman, K., Knepp, R., Linberg, P., Ryberg, P. 1983. Provenance of the North American Phanerozoic sandstones in relation to tectonic setting. *Geological Society of America Bulletin* 64, 222-235.
- Dunnington, H.V. 1958. Generation, Migration and Dissipation of Oil in northern Iraq. *Arabian Gulf, Geology and Productivity. American Association of Petroleum Geologist Foreign Reprint Series No. 2.*
- Folk, R.L. 1951. Stages of textural maturity in sedimentary rocks. *Journal of Sedimentary Petrology* 21,127-130.
- Folk, R.L. 1966. A review of grain-size parameters. *Sedimentology* 6, 73-93.
- Gazzi, P. 1966. Le arenarie del flysch sopracretaceo dell'Appennino modenese; correlazioni con il flysch di Monghidoro: *Mineralogische und Petrographische Acta* 12, p 69-97.
- Ghosh, S., Sarkar, S., Ghosh, P. 2012. Petrography and major element geochemistry of the Permo-Triassic sandstones, central India: implications for provenance in an intracratonic pull-apart basin. *Journal of Asian Earth Sciences* 43(1), 207-240.
- Iraq Oil and Gas Report Q1. 2018. Includes 10-Year Forecasts to 2026. BMI Research, A Fitch Group Company. <https://www.bmiresearch.com>.
- Jaza, I. 1992. Sedimentary facies analysis of the Tanjero Clastic Formation in Sulaimaniyah District, northeast Iraq. Unpublished MSc. Thesis, Salahaddin University, 121.
- Johnson. M.R. 1976. *Stratigraphy and Sedimentology of the Cape and Karoo Sequences in the Eastern Cape*. Ph.D. Thesis (Unpublished). Rhodes University, Grahams town, South Africa 1-267.
- Karim, K.H. 2004. Basin Analysis of Tanjero Formation in Sulaimaniyah Area, NE-Iraq. PhD. Thesis.
- Karim, K.H. 2007. Possible effect of storm on sediments of Upper Cretaceous Foreland Basin: a case study for tempestite in Tanjero Formation, Sulaimaniyah Area, NE-Iraq. *Iraqi Journal of Earth Science* 7, 1-10.
- Karim, K.H. 2010. Modification of the time-expanded stratigraphic column of North East Iraq during Cretaceous and Tertiary. Published in: *Petroleum Geology of Iraq (First Symposium, 21-22 April, Baghdad, Abstract book, 4.*
- Karim, K.H., Surdasy, A.M. 2005a. Palaeocurrent analysis of Upper Cretaceous Foreland basin a case study for Tanjero Formation in Sulaimaniyah area, NE-Iraq, 2005. *Iraqi Journal of Earth Science* 5, 30-44.
- Karim, K.H., Surdasy, A.M. 2005b. Tectonic and depositional history of Upper Cretaceous Tanjero Formation in Sulaimaniyah area, NE-Iraq. *Journal of Zankoi Sulaimani* 8, 47-62.
- Karim, K.H., Taha, Z.A. 2009. Tectonical history of Arabian platform during Late Cretaceous an example from NE Iraq. *Iranian Journal of Earth Sciences* 1, 1-14.
- Karim, K.H., Al-Hamadani, R.K., Ahmad, S.H. 2012. Relations between Deep and Shallow Stratigraphic Units of northern Iraq during Cretaceous. *Iranian Journal of Earth Sciences* 4, 95-103.

- Karim, K.H., Ismail, K.M., Bziany, M.M. 2014. Origin of Fossiliferous Limestone Beds inside the Upper Part of Tanjero Formation at the Northwest of Sulaimaniyah Area, NE Iraq. *Journal of Zankoi Sulaimaniyah* 17, 155-165.
- Kassab, I.I.M. 1975. Planktonic Foraminifera Range in the type Tanjero Formation Upper Campanian-Maastrichtian) of N. Iraq. *Geological Society of Iraq* 8, 73 - 86.
- Koshnaw, R.I., Stockli, D.F., Schlunegger, F. 2018. Timing of the Arabia-Eurasia continental collision—Evidence from detrital zircon U-Pb geochronology of the Red Bed Series strata of the northwest Zagros hinterland, K. region of Iraq. *Geology* 47: 47-50.
- Koshnaw, R.I., Horton, B.K., Stockli, D.F., Barber, D.E., Tamar-Agha, M.Y. 2019. Sediment routing in the Zagros foreland basin: Drainage reorganization and a shift from axial to transverse sediment dispersal in the northern Iraq Basin Research 00: 1-28.
- Lawa, F.A., Koyi, H., Ibrahim, A. 2013. Tectono-Stratigraphic Evolution of The NW Segment of the Zagros Fold-Thrust Belt, NE Iraq. *Journal of Petroleum Geology* 36 (1), 75-96.
- Lawa, F.A., Al-Karadakhi, A.I., Ismail, K.M. 2017. An interfingering of the Upper Cretaceous rocks from Chwarta-Mawat Region (NE-Iraq). *Iraqi Bulletin of Geology and Mining* 13 (1), 15-26.
- Li, G., Pe-Piper, G., Piper, D.J.W. 2012. The provenance of Middle Jurassic sandstones in the Scotian Basin: petrographic evidence of passive margin tectonics. *Canadian Journal of Earth Sciences* 49, 1463–1477.
- Lowe, D.R. 1982. Sediment gravity flows: II. Depositional models with special reference to the deposits of high-density turbidity currents. *Journal of Sedimentology* 52, 279-297.
- Malekzade, Z., Bellier, O., Abbassi, M.R., Shabanian, E., Authemayou, C. 2016. The effects of plate margin inhomogeneity on the deformation pattern within West-Central Zagros Fold-and-Thrust Belt. *Tectonophysics* 693, 304–326.
- Mange, M.A., Morton, A.C. 2007. Geochemistry of heavy minerals. In *Heavy Minerals in Use*. Edited by M. Mange, and D.K. Wright. *Developments in Sedimentology* 58, 345–391.
- Minas, H. 1997. Sequence stratigraphic analysis of the Upper Cretaceous succession of Central and northern Iraq. Unpublished PhD. Thesis, University of Baghdad. 188.
- Moradpour, A., Sahamieh, R.Z., Khalaji, A.A., Sarikhani, R. 2017. Textural records and geochemistry of the Kermanshah mantle peridotites (Iran): implications for the tectonic evolution of southern Neo-Tethys. *Journal of Geosciences* 62, 165–186.
- Motaghi, K., Shabanian, E., Tatar, M., Cuffaro, M., Doglioni, C. 2017. The south Zagros suture zone in tele seismic images. *Tectonophysics* 694, 292–301.
- Pettijohn, F.J., Potter, P.E., Siever, R. 1987. *Sand and Sandstone*. Second edition. Springer -Verlag. New York Inc. New York. 553.
- Potter, P.E., Pettijohn, F.J. 1977. *Palaeocurrent and Basin Analysis*, second ed., 413. Springer-Verlag, Berlin.
- Raymond, L.A. 1995. *The Study of Igneous, Sedimentary and Metamorphic Rocks*. Wm.C. Brown Communication Inc., United States of America, 264-388.
- Rieser, A.B., Neubauer, F., Liu, Y., Ge, X. 2005. Sandstone Provenance of north-western sectors of the intracontinental Cenozoic Qaidam basin, western China: Tectonic Vs Climatic control. *Journal of Sedimentary Geology* 177, 1–18.
- Sharbazheri, K.M. 2007. Aging of unconformity within Tanjero Formation in Chwarta Area Northeast of Iraq. *Iraqi Journal of Earth Science* 7, 37-54.
- Sharbazheri, K.M. 2010. Planktonic foraminiferal biostratigraphy of the upper Cretaceous reddish to pale brown transitional succession in Smaquli area, northeast Iraq. *Iraqi Bulletin of Geology and Mining* 6, 1-20.
- Sissakian, V.K. 2013. Geological evolution of the Iraqi Mesopotamia Foredeep, inner platform and near surroundings of the Arabian Plate. *Journal of Asian Earth Sciences* 72, 152–163.
- Sissakian, V.K., Fouad, S.F. 2015. Geological Map of Sulaimaniyah Quadrangle, at scale of 1: 250 000. *Journal of Zankoi Sulaimani Part-A- Pure and Applied Sciences*.
- Tucker, M.E. 2011. *Sedimentary rocks in the field: A practical guide*. 4th edn. A John Wiley and Sons Ltd. Publication, 276. ISBN: 978-0-470-68916-5.



Bulletin of the Mineral Research and Exploration

<http://bulletin.mta.gov.tr>



Investigation of the paleodepositional environment of the Middle Miocene aged organic matter rich rocks (Tavas/Denizli/SW Turkey) by using biomarker parameters and stable isotope compositions (^{13}C and ^{15}N)

Demet Banu KORALAY^{a*}

^aPamukkale University, Faculty of Engineering, Department of Geological Engineering, Denizli, Turkey

Research Article

Keywords:

Tavas (Denizli Basin),
Organic Geochemistry,
Biomarkers, Stable
Isotopes (^{13}C and
 ^{15}N), Depositional
Environment.

ABSTRACT

The study area is located 45 km south of Denizli. The purpose of this study is to identify the organic geochemical properties and paleo depositional environment of organic matter rich rocks from Tavas (Denizli/SW Turkey). For this purpose, total organic carbon (TOC, wt.%) and pyrolysis, n-alkane, isoprenoid, sterane, terpane and aromatic hydrocarbon parameters have been investigated of the studied samples. In addition, scanning electron microscopy (SEM) and stable isotope ($\delta^{13}\text{C}$ and $\delta^{15}\text{N}$) investigations were also carried out. Organic matter rich rocks which have type III kerogen have got 25.80 and 44.00 wt.% TOC content. Hydrogen index (HI, 73 and 120 mg HC/g TOC) and Oxygen index (OI, 34 and 59 mg $\text{CO}_2/\text{g TOC}$) values of samples are very low. The values of $\delta^{13}\text{C}$ and $\delta^{15}\text{N}$ show the terrestrial C3 ecosystem. The predominance of high molecular weight n-alkanes, degree of waxiness and less dibenzothiophene (DBT) concentrations indicate terrestrial organic matter. At the same time, biomarker and pyrolysis parameters indicate that the organic matter rich rocks (Tavas/Denizli) are in the immature stage. Pr/Ph, $\text{C}_{35}/\text{C}_{34}$ homohopane biomarker ratios and C_{35} homohopane index values point out oxic-suboxic paleo depositional environment.

Received Date: 05.12.2019

Accepted Date: 13.05.2020

1. Introduction

The study area is within the boundaries of the district Tavas, which is located in 43 km south of Denizli, in the neighborhood of Avdan (Figure 1). Neogene sedimentary rocks have a wide distribution in Western Anatolia. Among the terrestrial and / or lacustrine lithologies observed in the depression basin called Denizli Graben, there are coaly levels with low spread and thickness. Although Tavas coals are not used for the coal need of the whole city like other coals in the region, they meet the energy needs of small scale enterprises in the vicinity. The calories of the coal, which are operated by a local company in

the open pit method, are 2100-2400 Kcal / kg, and the reserve is 8-10 million tons. Moisture content is 45%, ash content is 15-20%, sulfur content is around 3%. To reduce the amount of moisture, a special drying oven is used in the coal mine. Before being offered for sale, the moisture content of the coals is reduced to 20% and the calorie is increased to 3000 calories. However, as a result of the drying process, 25% tonnage loss occurs in the coals. In the study area, starting from the bottom 90 cm, 1 m and 20 cm coal levels outcrop with intercalated claystones. Above this level, there is a cover unit consisting of sandstones approximately 4 m thick. The units below and above the Tavas clayey

Citation Info: Koralay, D. B. 2021. Investigation of the paleodepositional environment of the middle Miocene aged organic matter rich rocks (Tavas/Denizli/SW Turkey) by using biomarker parameters and stable isotope compositions (^{13}C and ^{15}N). Bulletin of the Mineral Research and Exploration 164, 39-52.
<https://doi.org/10.19111/bulletinofmre.742127>

*Corresponding author: Demet Banu KORALAY, dbkoralay@pau.edu.tr

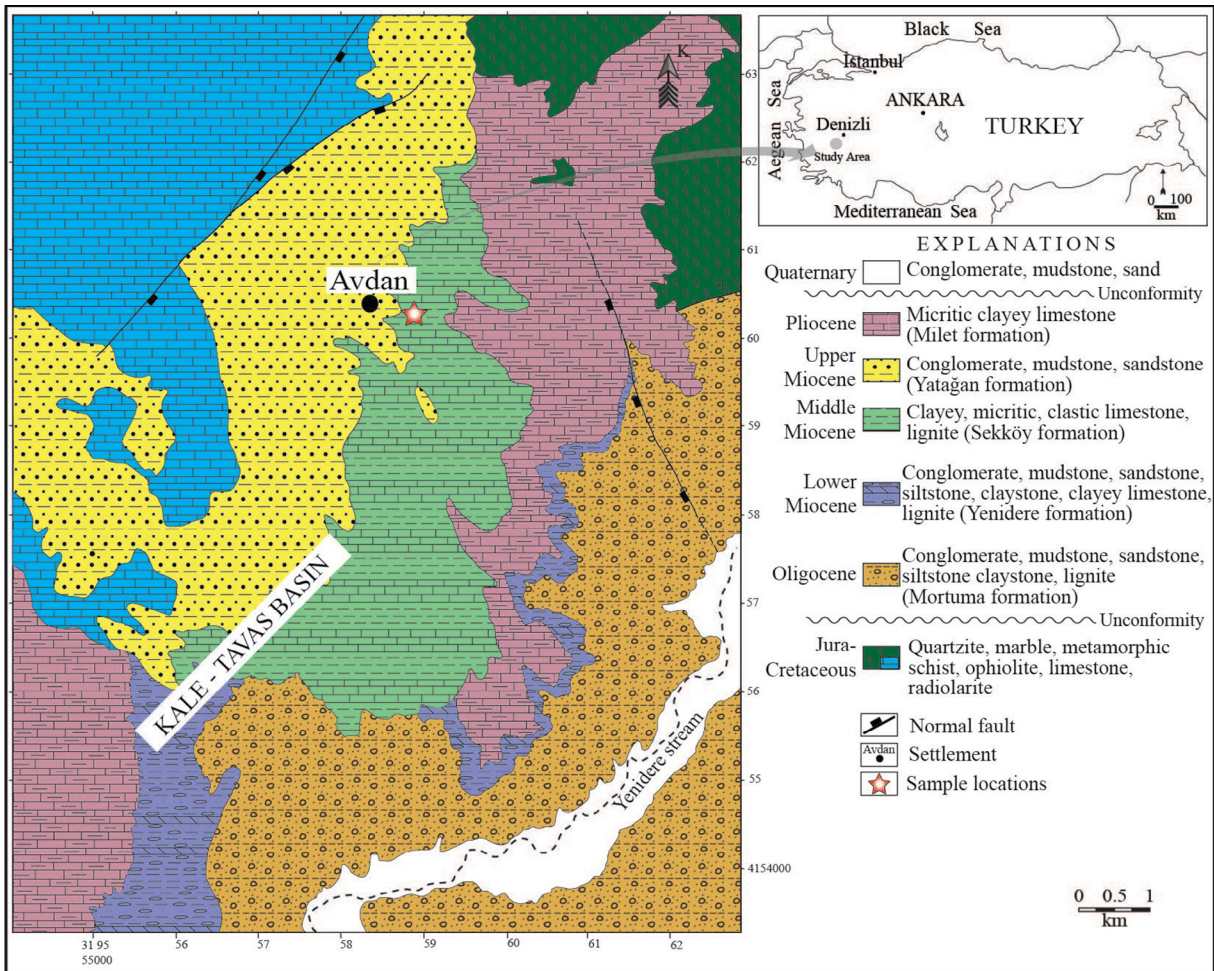


Figure 1- Geology and location map of the study area (Modified from Hakyemez, 1989).

coals belonging to the middle Miocene aged Sekköy formation is consisted of claystone, siltstone and marl lithologies.

Due to the increase in investments in the mining and energy sectors in recent years, coal research and production in our country has gained importance and brought along detailed research on Neogene aged lignites. In addition, a large part of the power generation from the thermal power plant comes from clayey, and lignites have gained importance due to the abundance of reserves. From this point of view, Tavas clayey coals reveal the difference of this study. Considering the thermal power plant project planned to be established in the region, in this study it is aimed to examine the organic geochemical properties and hydrocarbon (oil and / or gas) potential of the coals spreading in Tavas district of Denizli, Avdan neighborhood. In addition to the stable isotope and biomarker examinations performed in coals, (Rigby

and Batts, 1986; Dehmer, 1989; Whiticar, 1996; Fabiańska and Kruszewska, 2003; Bechtel et al., 2008; Xiao and Liu, 2011; Adedosu et al., 2012; Warwick and Ruppert, 2016; Ayinla et al., 2017) the literature gap in our country is considered to be closed by using these analysis techniques in Tavas clayey coals. There are some national and international researches on general geology, petrography, tectonism and prospecting in the study area and its surroundings (Hakyemez, 1989; Ercan et al., 1983; Okay, 1989; Gökaş et al., 1989; Akgün and Sözbilir, 2001; Gedik and Tunç, 2004; Büyükmeriç, 2017; Helvacı and Yağmurlu, 1995). Studies on Tertiary coals are quite limited (Özçelik and Altunsoy, 2005; Atalay and Karayığit, 2010; Kara-Gülbay, 2015; Koralay, 2018a, b, c, d; Koralay and Gedik Vural, 2018; Koralay and Koralay, 2018; 2019). For coals outcropping in Tavas, organic geochemical properties of clayey coals belonging to the middle Miocene Sekköy formation,

its hydrocarbon potential and paleoenvironment were determined by conducting total organic carbon and pyrolysis analysis, gas chromatography and gas chromatography mass spectrometry analysis, stable isotope (^{13}C and ^{15}N) scanning electron microscope studies.

2. Material and Methods

Clayey coals that make up the working materials were taken from the coal quarry where the production was made in 2018 by a private company located in Avdan neighborhood of Tavas district in the south of Denizli province (Figure 2a). Gas chromatography-

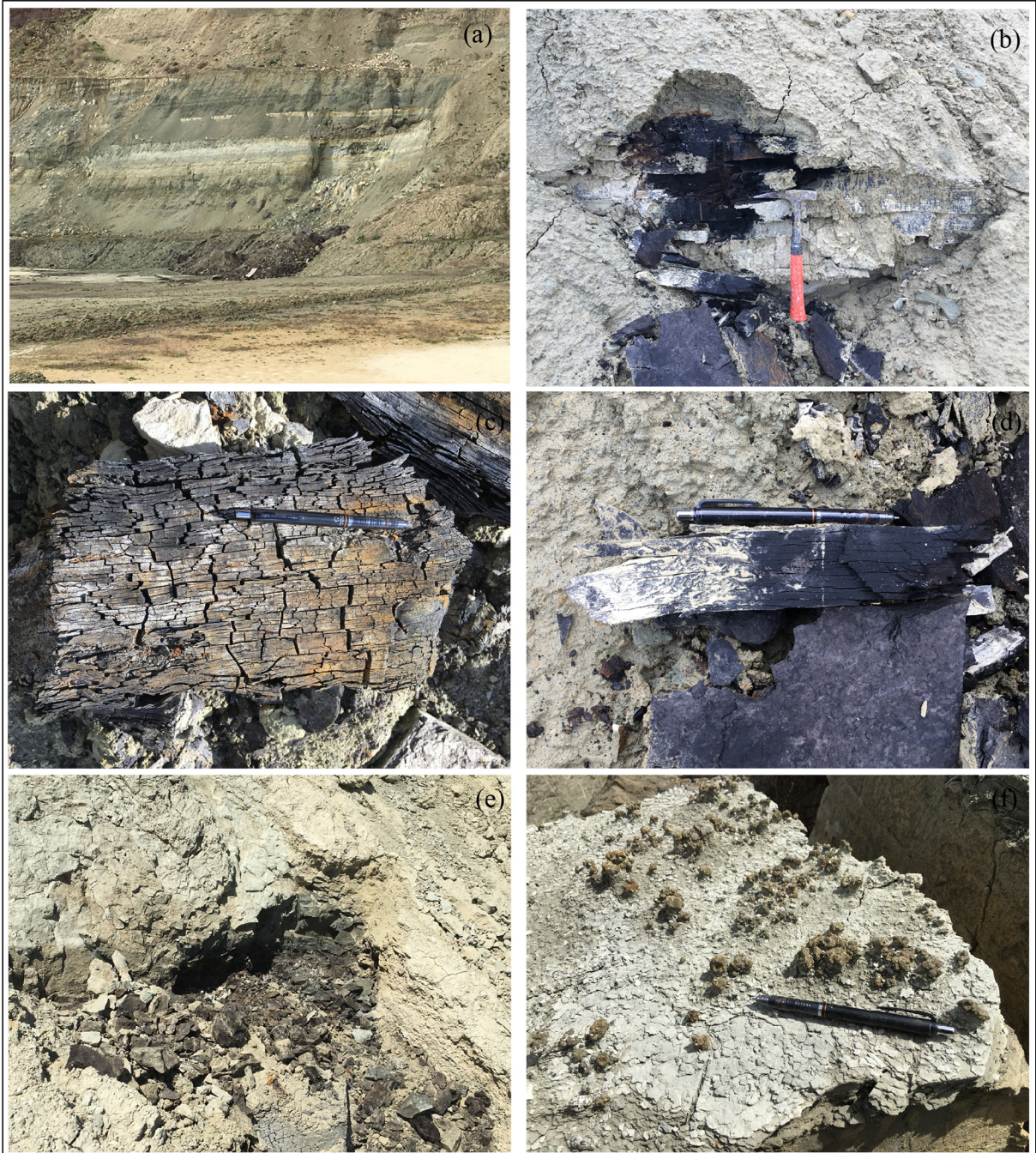


Figure 2- a) General view of open pit with organic matter-rich level, (b, c and d) Clayey coals and e) Organic matter-rich claystone, f) Pyrite crystals observed in clayey coals.

mass spectrometry (GC-MS) analysis of saturated and aromatic fractions of samples with total organic carbon (TOC, wt %), pyrolysis, gas chromatography (GC) analysis were performed in Applied Petroleum Technology Laboratories (Norway). GC and GC-MS analyzes are performed to see the general distribution of hydrocarbon compounds in extracts from coal samples and to determine the maturity level of organic matter. In addition to obtaining information about the type and maturation of organic matter by looking at the peak sizes and distributions in the chromatograms, the paleo deposition environment of the coals can be determined. Total organic carbon (TOC, wt%) and pyrolysis analyzes of three samples were performed on Leco and CS-632 Hawk devices, respectively. In order to remove carbonate in TOC measurement, diluted hydrochloric acid (HCl) was added to the sample, placed in the Leco furnace and the amount of carbon was measured with an IR detector. In pyrolysis analysis, measurements were checked according to NIGOGA standards (Espitalié et al., 1985). In the HP7890 A device, GC analysis was performed on two samples, and the analysis was performed using a 30 m long CP-Sil-5 CB-MS column, 0.25 µm film thickness and C20D42 internal standard. During the GC analysis, a temperature program was applied at 50 °C (1 min) - 4 °C / min - 320 °C (25 min). GC-MS analysis of saturated and aromatic hydrocarbons of two samples was performed on Thermo Scientific DFS device. The device is set to 3000 resolution and the data is taken in the selected ion recording (SIR) mode. The device has a 60 m CP-Sil-5 CB-MS column with a film thickness of 0.25 µm. The internal standards D4-27ααR were used to obtain the quantitative results of saturated compounds, and the internal standards D8-Naphthalene, D10-Biphenyl, D10-Phenanthrene and D12-Chrysene were used to obtain the quantitative results of aromatic compounds. During the GC-MS analysis, a temperature program of 50 °C (1 min) - 20 °C / min - 120 °C - 2 °C / min - 320 °C (20 min) was applied.

Carbon and nitrogen isotope ($\delta^{13}\text{C}$ and $\delta^{15}\text{N}$) analyzes of two samples were performed in Iso-Analytical Limited (UK) Laboratories, Elemental Analyzer - Isotope Ratio Mass Spectrometry (EA-IRMS) instrument. The standards used during ^{13}C and ^{15}N isotope analysis are $d^{13}\text{C}_{\text{V-PDB}} = \text{of } -26,43 \text{ ‰}$ and $d^{15}\text{N}_{\text{AIR}} = 2,55 \text{ ‰}$, respectively. Stable isotope compositions are used effectively together with

biomarkers to determine the type of organic matter and the depositional environment. It is possible to determine which ecosystem and plant species of the swamp environment where coals deposit, by using stable isotopes.

3. Geology of the Study Area

The study materials are clayey coals at the base of Sekköy formation in Kale-Tavas Basin (Figure 2b, c, d and e). Formations in the basin consist of shallow marine and terrestrial units from bottom to top. Basement rocks are arranged from bottom to top as follows Gneisses, schists and marbles, limestones at the top (Okay, 2001). Gneiss, schist and marble are the lithologies of the Menderes Massif. There are carbonate rocks called Lycian nappes, ranging from Permian to Paleocene on the schists and marbles. The marine sedimentary rocks covering the basement rocks unconformably are called Akçay Group at the bottom; It is defined as Karadere, Mortuma, Yenidere, Künar and Kale formations (Hakyemez, 1989; Yakupoğlu and Bayhan, 2017). Sekköy, Yatağan and Milet formations that overlie these units unconformably consist of terrestrial units and are called Muğla Group (Figure 3) (Göktaş et al., 1989). Tavas clayey coals which constitute the study material is placed in Miocene aged Sekköy formation. Sekköy formation overlies Kale formation unconformably and overlain conformably by Yatağan formation (Şafak, 2010; Yakupoğlu and Bayhan, 2017). The age of Sekköy formation was determined by *Zygodolophodon turicensis*, a taxon found in clayey coals and well-known in Eurasia in the early-late Miocene (Erten and Koralay, 2020, <https://doi.org/10.1007/s12549-020-00422-7>). Sekköy formation starts with coal levels at the bottom and continues with clayey, micritic, clastic limestone and siltstone levels. Medium-thick bedding and parallel lamination are common in the limestones of Sekköy formation.

4. Results

4.1. *n*-Alkanes and Isoprenoids

Gas chromatography (GC) examinations revealed that high molecular weight ($n\text{-C}_{20}$ +) *n*-alkanes were dominant in both samples. Long-chain *n*-alkanes, such as $n\text{-C}_{27}$, $n\text{-C}_{29}$, predominate peaks express the predominance of terrestrial tall plants (Figure 4)

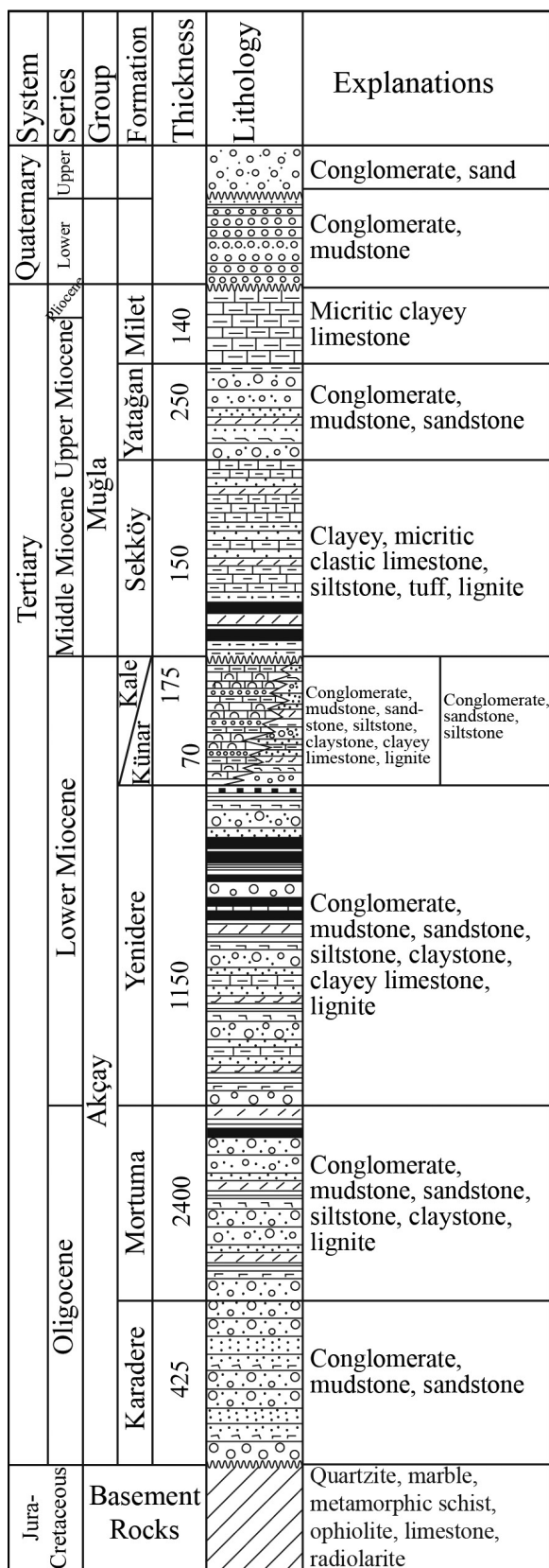


Figure 3- Generalized stratigraphic section of Kale-Tavas area (modified from Hakyemez, 1989).

(Meyers, 1997). The Pr / Ph ratio of Tavas clayey coals was calculated as 1.07 and 1.00, respectively. Its rank was determined as brown coal and subbituminous coal (Pr / Ph ratio between 1 and 3), and its paleo deposition condition was marshy environment are oxy-suboxic (Diessel, 1992).

In the ratio of $n-C_{17} / n-C_{31}$ (0.13 and 0.04), since the $n-C_{31}$ n -alkanes are more dominant, the samples examined contain organic matter originating from terrestrial plants (Hunt, 1996) (Table 1). Another way to determine the amount of terrestrial origin organic material is the degree of waxiness and is calculated by the ratio $\Sigma (n-C_{21}-n-C_{31}) / \Sigma (n-C_{15}-n-C_{20})$. The waxiness values in the TAV-3 and TAV-6 samples were calculated as 10.87 and 22.22 respectively, indicating the terrestrial input with mainly high plants in accordance with the above parameters (Hunt, 1996; Peters and Moldowan, 1993). High CPI (26-28) (4.63 and 4.76) and CPI (22-30) (4.25 and 4.80) values observed in TAV-3 and TAV-6 samples indicate that are deposited in relatively dry and cold paleo-climatic conditions, but it also points that terrestrial plants and low level of maturity depending on the high molecular weight n -alkane amount (Peters et al., 2005).

4.2. Steranes and Terpanes

Saturated and aromatic hydrocarbon biomarker ratios obtained from gas chromatography mass spectrometry (GC-MS) examinations in saturated hydrocarbon compounds were investigated. Ts / Tm ratio is the maturity parameter. Ts / Tm ratio of both samples is determined as 0.17 (Ts / Tm <1) (Table 2), Tavas clayey coals are immature phase according to Ts / Tm ratio (Seifert and Moldowan, 1986). Moretane / hopane ratio generally decreases with increasing thermal maturity (Kvenvolden and Simoneit, 1990). Moretane / hopane ratio decreases from 0.8 to 0.15-0.05 with increasing thermal maturity (Hoffmann et al., 1984). This ratio was calculated as 0.85 and 0.53, respectively, in TAV-3 and TAV-6 samples and indicates the early mature stage. C_{23} tricyclic terpane / (C_{23} tricyclic terpane + C_{30} hopane) ($C_{23} tt / (C_{23} tt + C_{30} H)$) ratio increases with maturity. Very low $C_{23} tt / (C_{23} tt + C_{30} H)$ ratios in TAV-3 (0.28) and TAV-6 (0.14) samples support low maturity (Aquino Neto et al., 1983). SC_{31} and SC_{32} homohopanes obtained by calculating 22S / 22S + 22R ratios increase from

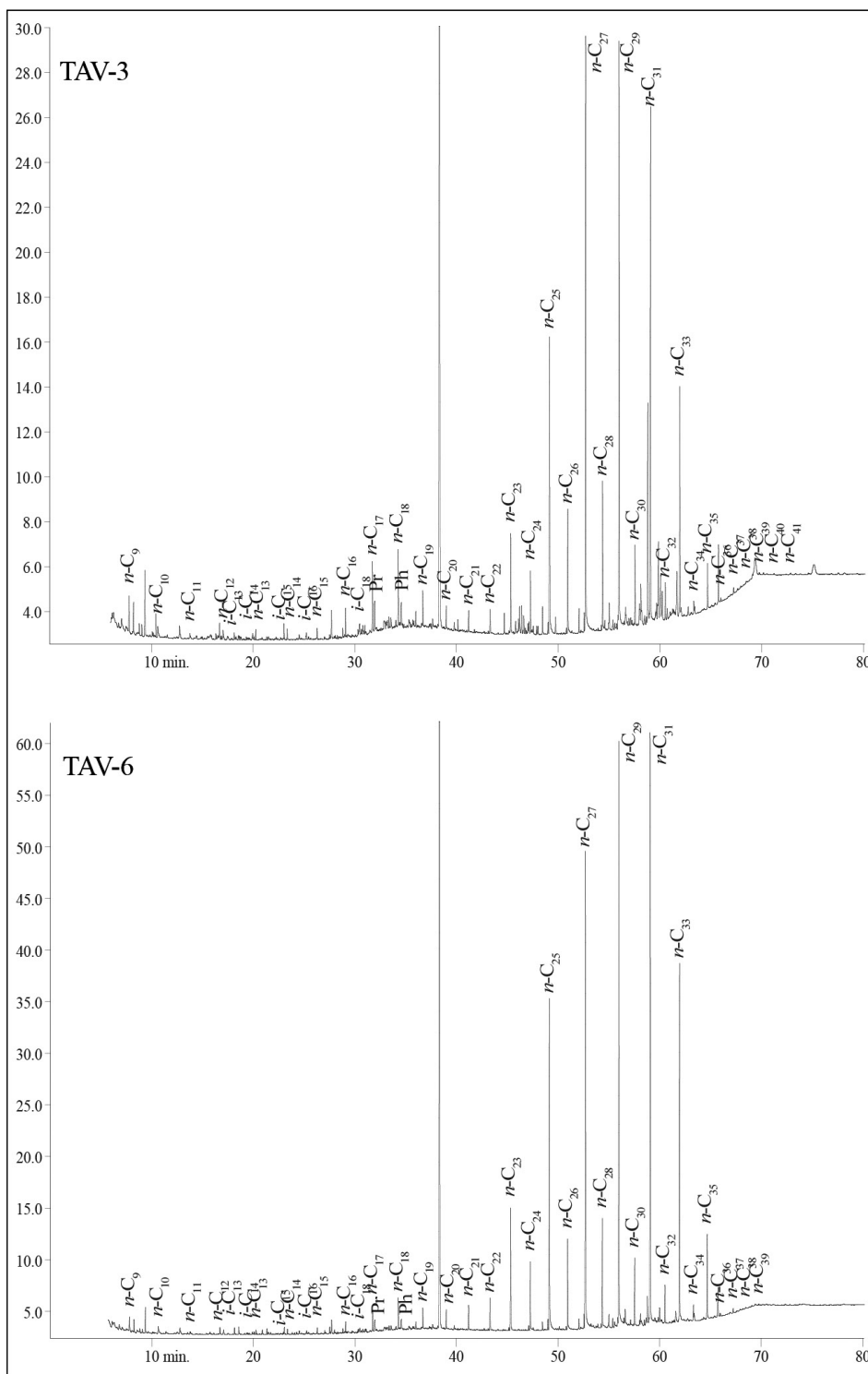


Figure 4- *n*-Alkane and isoprenoide distribution of the studied samples.

Table 1- Some parameters and general molecular composition (%) calculated from gas chromatograms of examined samples.

Sample No	Pr/Ph	$n-C_{17}/n-C_{31}$	$n-C_{23}/n-C_{29}$	$n-C_{23}/n-C_{25}$	$\Sigma(n-C_{21}-n-C_{31})/\Sigma(n-C_{15}-n-C_{20})$	$CPI_{(26-28)}$	$CPI_{(22-30)}$
TAV-3	1,07	0,13	0,17	0,32	10,87	4,63	4,25
TAV-6	1,00	0,04	0,20	0,36	22,22	4,76	4,80

Pr: Pristane, Ph: Phytane, $CPI_{(26-28)}: 2nC_{27}/(nC_{26}+nC_{28})$, $CPI_{(22-30)}: [2(nC_{23}+nC_{25}+nC_{27}+nC_{29})]/[nC_{22}+2(nC_{24}+nC_{26}+nC_{28})+nC_{30}]$.

0 to approximately 0.6 with maturity (Waples and Machihara, 1991). SC_{31} ($C_{31} 22S / 22S + 22R$; 0,12 and 0,21) and SC_{32} ($C_{32} 22S / 22S + 22R$; 0,27 and 0,44) values of TAV-3 and TAV-6 samples are immature-early mature states that it is in the stage (Figure 5a, Table 2). The C_{27} , C_{28} and C_{29} $\alpha\alpha\alpha$ 20R isomers from the steranes, respectively, in the TAV-3 sample; While 31%, 17% and 52%, respectively, in TAV-6; It was calculated as 26%, 6% and 68%. The abundance of C_{29} $\alpha\alpha\alpha$ R isomers in both examples ($C_{29} > C_{27} > C_{28}$); While referring to immature organic matter, Tavas shows that clayey coals have a terrestrial origin (Figure 5b, Table 2), (Czochanska et al., 1988). Dia / (Dia + Reg) steran [Diasteranes / (Diasteranes + Regular Steranes)] ratios of TAV-3 and TAV-6 samples were calculated as 17% and 29%, respectively (Table 2), the samples examined have immature organic matter (Peters and Moldowan, 1993). C_{29} $\alpha\alpha\alpha$ 20S / (20S + 20R) and $\beta\beta / (\beta\beta + \alpha\alpha) C_{29}$ steran ratios are used as an indicator of maturity at 0.52-0.55 and 0.67-0.71 balance values,

respectively (Seifert and Moldowan, 1986). Although the examined samples are below the equilibrium value, it can be said that when the $\beta\beta / (\beta\beta + \alpha\alpha) C_{29}$ steran (0,24) value in the TAV-6 sample is evaluated, the Tavas coals are in the immature-early mature stage (Table 2). Diasteranes / Hopane ratios are generally low in immature sediment extracts as in Tavas clayey coals (0.26 and 0.29) (Affouri et al., 2013).

As in TAV-3 (1.38) and TAV-6 (0.97) examples, the high $(C_{19} + C_{20}) / C_{23}$ tt ratio can be explained by the abundance of terrestrial organic matter input into the depositional environment of Tavas coals (Peters and Moldowan, 1993). As in TAV-3 and TAV-6 samples, lacustrine sediments and coals are characteristic with high C_{24} / C_{23} tt (1.42 and 0.51, respectively) and low C_{22} / C_{21} tt (0.30 and 0.36, respectively) (Peters et al., 2005). The C_{29} norhopane / C_{30} hopane ($C_{29} NH / C_{30} H$) ratio is used to distinguish between carbonate and clastic lithologies. The ratio of $C_{29} NH / C_{30} H$ less

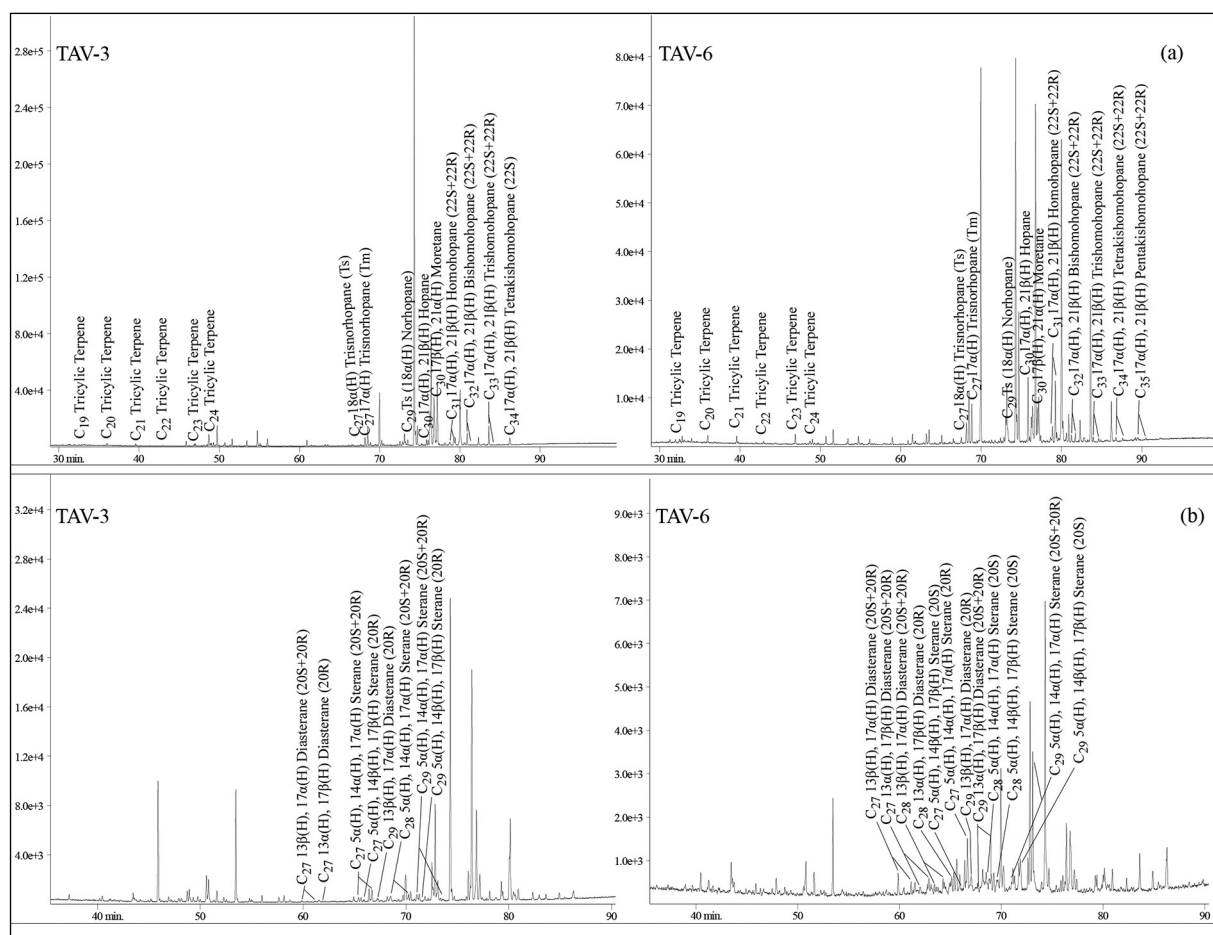


Figure 5- Distribution of the a) m/z 191 and b) m/z 217 molecules in the studied samples.

Table 2- Saturated and aromatic biomarkers ratios of Tavas (Denizli / SW Turkey) clayey coal m/z 191, 217, 178, 192, 184, 198, 231 and 253 determined from the mass chromatogram.

Saturated Hydrocarbon Molecules		TAV 3	TAV 6	Aromatic Saturated Hydrocarbon Molecules (ng/g)	TAV 3	TAV 6
m/z 191 Terpane	Ts/Tm	0,17	0,17	Dibenzothiophene (DBT)	362	166
	Moretane/Hopane	0,85	0,53	Phenanthrene (P)	2776	2139
	$C_{19} + C_{20}/C_{23}$ tt	1,38	0,97	DBT/P	0,13	0,08
	C_{23} tt/ C_{23} tt+ C_{30} H	0,28	0,14	C_{21} MA	34	46
	C_{24}/C_{23} tt	1,42	0,51	C_{22} MA	38	25
	C_{22}/C_{21} tt	0,30	0,36	C_{27} MA	32	83
	C_{29} NH/ C_{30} H	0,70	0,90	C_{28} MA	17	97
	C_{31} 22R/ C_{30} H	1,46	0,94	C_{29} MA	11	82
	SC_{31}	0,12	0,21	% MA(I)/MA(I+II)	0,55	0,21
	SC_{32}	0,27	0,44	1-MP	960	323
	$C_{35}/(C_{31}-C_{35})$ HH index	-	0,05	2-MP	711	403
	C_{35}/C_{34} HH	-	0,76	3-MP	588	332
	m/z 217 Sterane	% C_{27}	31	26	9-MP	1859
% C_{28}		17	6	MPI-3	0,46	0,79
% C_{29}		52	68			
% Dia/(Dia+Reg) Sterane		17	29			
20S/(20S+20R) (C_{29} $\alpha\alpha$)		0,13	0,13			
$\beta\beta/(\alpha\alpha+\beta\beta)$ (C_{29})		0,14	0,24			
Diasterane/Hopane		0,26	0,29			
Sterane/Hopane		0,33	0,12			

tt: Tricyclic Terpane, NH: Norhopane; H: Hopane; HH: Homohopane; SC_{31} (22S/22S+22R) HH; SC_{32} (22S/22S+22R) BHH; Dia/(Dia+Reg) Sterane: Diasteranes/(Diasteranes+Regular Steranes); MA: Monoaromatic Steroid; MA(I)/MA(I+II): $(C_{21}+C_{22})/(C_{21}+C_{22}+C_{27}+C_{28}+C_{29})$; DBT/P: Dibenzothiophene/Phenanthrene; MPI-3: Methyl-phenantrene Index (β/α MP) = $(2MP+3MP)/(1MP+9MP)$.

than 1 indicates the clastic origin rock (Waples and Machihara, 1991). In the TAV-3 and TAV-6 samples, this ratio is 0.70 and 0.90, respectively, confirming the fact that clayey coals deposition together with clastic lithologies such as claystone and siltstone (Figure 5a, Table 2). However, the C_{31} 22R / C_{30} Hopane ratio is the depositional environment parameter, which is calculated as 1.46 and 0.94 in TAV-3 and TAV-6 samples. According to the C_{31} 22R / C_{30} Hopane ratios less than 0.25, the samples analyzed show lacustrine origin rock characteristics (Table 2) (Peters et al., 2005). According to the C_{31} 22R / C_{30} Hopane ratios less than 5, the samples analyzed show a lacustrine origin rock feature (Table 2) (Peters et al., 2005). The C_{35} Homohopanes index $(C_{35} (S + R) / [C_{31} + C_{32} + C_{33} + C_{34} + C_{35} (S + R)])$ ratio determined only in TAV-6 sample is 0.05. This ratio shows that the length of the side chains in hydrocarbon molecules decreases with oxidation and suboxic paleo deposition conditions are predominant (Hunt, 1996). In addition, low sterane

/ hopane ratios (0.33 and 0.12) reflect the terrestrial and / or microbial reworked organic matter, as in the examples studied (Espitalié et al., 1985). The C_{35} / C_{34} homohopanes ratio was calculated as 0.76 in TAV-6 sample and points to suboxic depositional conditions in accordance with the homohopanes index and Pr / Ph ratio (Peters and Moldowan, 1993). In addition to the above findings to determine paleo depositional conditions; As a result of SEM studies, framboidal pyrites and fine grained pyrites were identified in Tavas coals (Figure 2f and figure 6). This indicates the presence of relatively reducing conditions (Rimstidt and Vaughan, 2003) in the deposition environment during peat formation, but also supports biomarker data.

4.3. Aromatic Hydrocarbons

As in the studied samples, terrestrial facies are generally dominant in the depositional environment

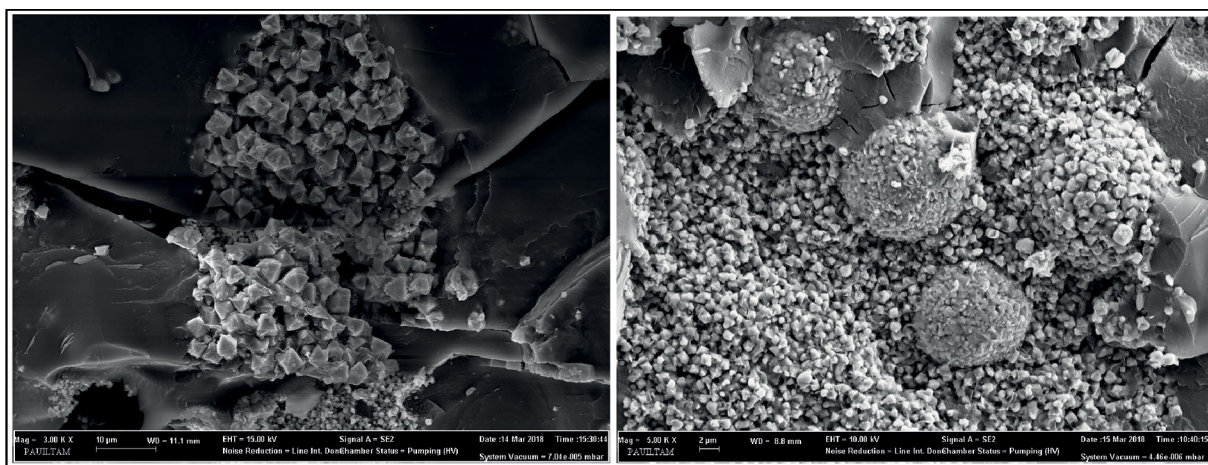


Figure 6- SEM images of framboidal pyrite in Tavas clayey coal samples.

due to low dibenzothiophene (DBT, 166 ng / g and 362 ng / g) concentrations (Radke et al., 1991). In coals, the dibenzothiophene / phenanthrene (DBT / P) ratio should generally be between 0.06 and 0.2 (Requejo, 1994). DBT / P ratio of Tavas coals was calculated as 0.08 and 0.13 (Table 2). Reten determined in TAV-6 sample; aromatic biomarker molecule derived from a typical gymnosperm (Figures 7a and b), (Izart et al., 2015).

Monromatic (I) (MA (I)) value increases with thermal maturity compared to monoaromatic (II) (MA (II)) (Hunt, 1996). The MA (I) / MA (I + II) ratio results in a complete conversion to MA (I) at the end of the extremely mature stage. In TAV-3 and TAV-6 samples, MA (I) / MA (I + II) ratios are calculated as 55% and 21%, and the TAV-3 sample indicates the early mature stage and the TAV-6 sample indicates

the immature stage (Peters and Moldowan, 1993). Methylphenanthrene index-3 (MPI-3) value; it is greater than 1 in mature organic matter and less than 0.8 in immature organic matter (Radke, 1987). MPI-3 values of the samples examined were calculated as 0.46 and 0.79, and it was determined that the organic matter was in the immature-early mature stage (Table 2).

4.4. Stable Isotope Analysis (^{13}C and ^{15}N)

In a total of three samples, ^{13}C and ^{15}N stable isotope analyzes were performed. $\delta^{13}\text{C}$ value ranges from ‰ -26,43 to ‰ -19,77, and ^{15}N value ranges from ‰ 3.71 to ‰ 6.87 (Table 3). The $\delta^{13}\text{C}$ contents of the studied samples are very similar to the $\delta^{13}\text{C}$ content of coal (Figure 8a). Also, figure 8b shows the compatibility of $\delta^{15}\text{N}$ contents of Tavas samples with $\delta^{15}\text{N}$ contents of

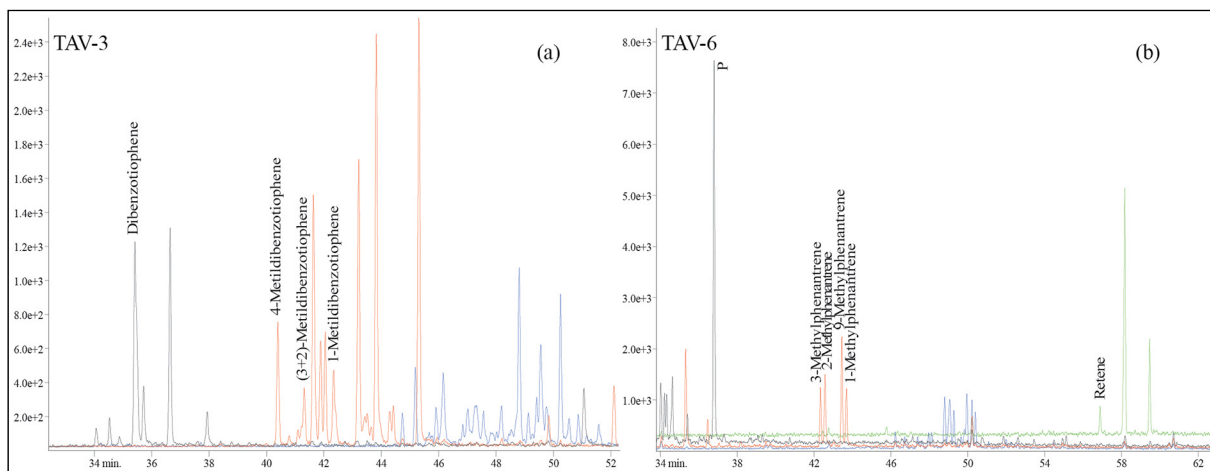


Figure 7- Mass fragmentograms of identifiable aromatic hydrocarbon molecules from the studied samples.

Table 3- C and N element (%) contents of ^{13}C (‰) and ^{15}N (‰) stable isotope of the samples examined.

Sample No	C (%)	$\delta^{13}\text{C}_{\text{V-PDB}}$ (‰)	N (%)	$\delta^{15}\text{N}_{\text{AIR}}$ (‰)	C/N
TAV-3	50,16	-26,43	1,55	3,71	32,36
TAV-4	3,50	-19,77	0,12	5,91	29,17
TAV-6	27,21	-25,90	1,03	6,87	26,42

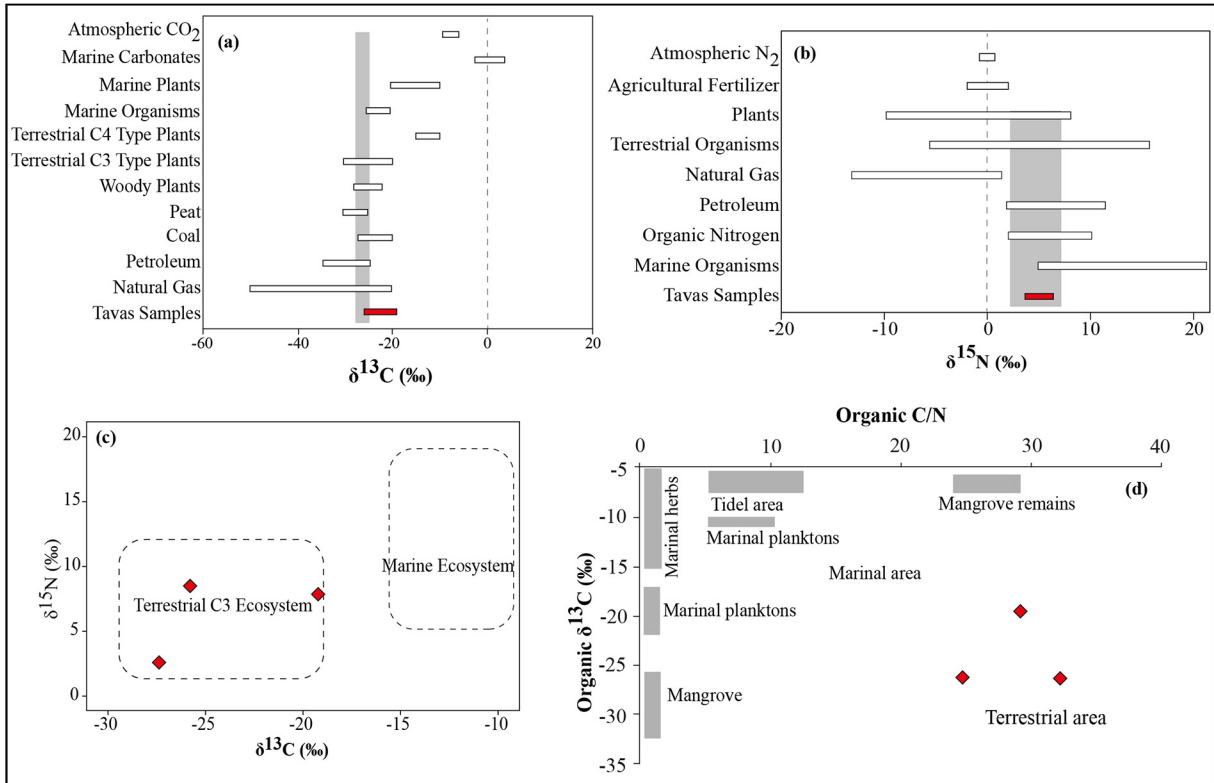


Figure 8- a) $\delta^{13}\text{C}$ and b) $\delta^{15}\text{N}$ concentrations according to some references c) $\delta^{15}\text{N}$ - $\delta^{13}\text{C}$ diagram of the studied samples (Coplen ve Shrestha, 2016) and d) Diagram of $\delta^{13}\text{C}$ values versus organic C/N ratio of the studied samples (Florentine, 2007).

some references such as terrestrial organisms, plants and organic nitrogen. As seen from the diagram $\delta^{13}\text{C}$ - $\delta^{15}\text{N}$ Tavas (Denizli / SW Turkey) clayey coal of paleo vegetation it is designated as C3 terrestrial ecosystem (Figure 8c) (Coplin and Shrestha, 2016). C / N ratios of samples (between 26.42 and 32.36) are greater than 10 and are characterized by high terrestrial plants (Table 3) (Inoue et al., 2012). When C / N and $\delta^{13}\text{C}$ are evaluated together, it can be said that Tavas coals have the same origin and originate from a terrestrial source (Figure 8d), (Florentine, 2007).

4.5. Total Organic Carbon and Pyrolysis Parameters Analysis

The total organic carbon amount (TOC) of Tavas clayey coals belonging to Sekköy formation varies

between 1,94-44,00%. Sample TAV-4 has very low S_2 (0.30 mg HC / g rock) and very high T_{max} (528 °C) (Table 4). T_{max} values determined by the device are not reliable when S_2 hydrocarbons are below 0.5 mg HC / g rock. In order not to cause misinterpretation, TAV-4 sample was excluded while evaluating pyrolysis parameters. TAV-3 and TAV-6 samples (Figure 9a), hydrogen index (HI, 120 and 73 mg HC / g TOC), T_{max} (414 °C and 413 °C) and S_2 / S_3 with very good source rock potential. According to the values (3,54 and 1,24), the gas contains type III kerogen suitable for hydrocarbon type (Figure 9b and c). Production index (PI) values, which are one of the maturation parameters, are 0,06 and 0,11. When T_{max} and PI are evaluated together, it is seen that the organic matter is in the immature stage (Peters and Cassa, 1994) (Figure 9d).

Table 4- TOC and pyrolysis analysis results of Tavas clayey coals.

Sample no	TOC (wt.%)	S ₁	S ₂	S ₃	Tmax (°C)	PY	PI	HI	OI	S ₂ /S ₃
TAV-3	44,00	3,29	52,83	14,94	414	56,12	0,06	120	34	3,54
TAV-4	1,94	0,05	0,30	2,61	528	0,35	0,14	15	135	0,11
TAV-6	25,80	2,45	18,92	15,29	413	21,37	0,11	73	59	1,24

S₁, S₂: mg HC/g rock, S₃: mg CO₂/g rock, PY(S₁+S₂): mg HC/g rock, PI: (S₁/(S₁+S₂)), HI(S₂/TOC): mg HC/g TOC, OI (S₃/TOC): mg CO₂/g TOC.

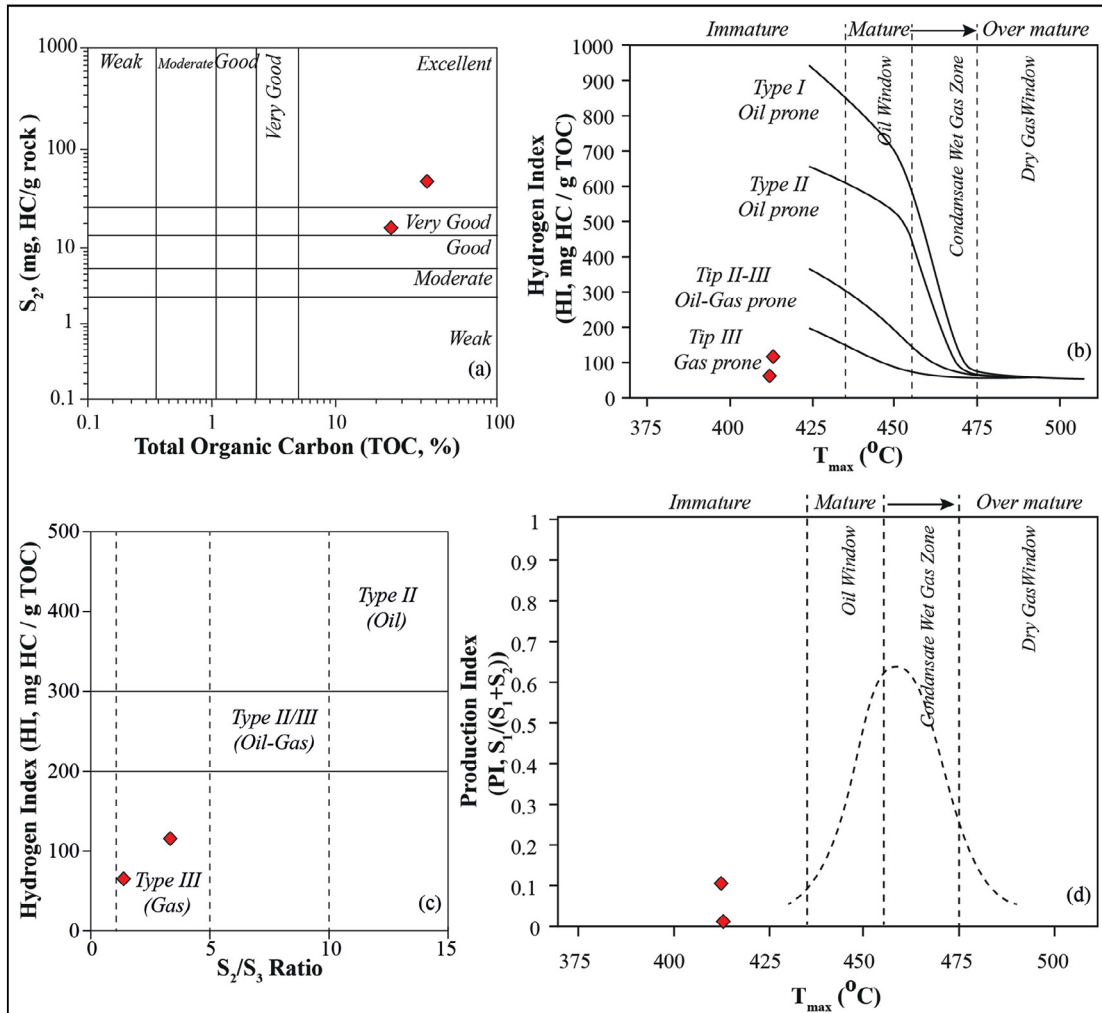


Figure 9- The positions of the data obtained as a result of pyrolysis analysis in a) S₂ – TOC, b) HI – T_{max}, c) HI – S₂/S₃ and d) PI – T_{max} diagrams.

4. Discussion

Tavas clay coals are located at the base of Sekköy Formation and the formation continues with clayey, micritic, clastic limestone and siltstone lithologies. As a result of organic geochemical investigations carried out within the scope of this study; Pr/Ph, C₃₅/C₃₄ homohopanes ratio and C₃₅ Homohopanes index values indicate oxic-suboxic depositional

conditions (Diessel, 1992; Peters and Moldowan, 1993; Hunt, 1996). In addition, the sterane/hopane ratio and framboidal pyrites referring to the reworked organic matter in the samples examined; it supports the oxic-suboxic depositional environment or the presence of relatively reducing conditions. While high molecular weight long chain *n*-alkanes indicate the presence of terrestrial plants, the concentration of dibenzothiophene from aromatic hydrocarbons

indicates that the terrestrial facies are predominant in the depositional environment. According to stable isotope studies ($\delta^{13}\text{C}$ and $\delta^{15}\text{N}$), paleo vegetation of coals is a terrestrial C3 ecosystem (Coplen and Shrestha, 2016). According to saturated and aromatic hydrocarbon molecules, which are observed to be compatible with isotope data; The predominance of high molecular weight *n*-alkanes, the degree of waxiness, $(\text{C}_{19}+\text{C}_{20})/\text{C}_{23}$ tt ratio and abundant C_{29} *aaa* R isomers indicate terrestrial source (Meyers, 1997; Hunt, 1996; Peters and Moldowan, 1993; Czochanska et al., 1988; Radke et al., 1991). In addition, the C_{29} NH/C_{30} H ratio supports paleo deposition in a clastic environment (Waples and Machihara, 1991). In addition to this information; the high $\text{C}_{24}/\text{C}_{23}$ tt and low $\text{C}_{22}/\text{C}_{21}$ tt rates and the C_{31} $22\text{R}/\text{C}_{30}$ Hopane ratio represent the lacustrine depositional environment (Peters et al., 2005). Coals containing type III kerogen suitable for gas hydrocarbon type are immature-early mature stage according to maturation parameters (Peters and Cassa, 1994).

5. Conclusion

According to all organic geochemical parameters and stable isotope data, terrestrial paleo vegetation, oxic-suboxic conditions and terrestrial facies predominate in the environment. As a result; in the light of site investigations, general geological information and organic geochemical investigations Tavass (Denizli / SW Turkey) clayey coals away from the marine influence of paleo-depositional environments, is thought to have marshes in the terrestrial environment in developing the lake shore facies.

Acknowledgement

The author would like to thank Prof. Dr. Tamer Koralay (Pamukkale University) for his contributions during the field works.

References

- Adedosu, T. A., Sonibare, O. O., Tuo, J., Ekundayo, O. 2012. Biomarkers, carbon isotopic composition and source rock potentials of Awgu coals, middle Benue trough, Nigeria. *Journal of African Earth Sciences* 66-67, 13-21.
- Affouri, H., Montacer, M., Disnar, J-R. 2013. Organic geochemistry of the Cenomanian-Turonian Bahloul Formation petroleum source rock, Central and Northern Tunisia. *Resource Geology* 63(3), 262-287.
- Akgün, F., Sözbilir, H. 2001. A palynostratigraphic approach to the SW Anatolian molasse basin: Kale-Tavas molasse and Denizli molasse. *Geodynamica Acta* 14(1-3), 71-93.
- Aquino, Neto F. R., Trendel, J. M., Connan, J., Albrecht, P. A. 1983. Occurrence and formation of tricyclic and tetracyclic terpanes in sediments and petroleum. Bjarøy, M., Albrecht, C., Cornford, C., et al., (Eds.). *Advances in Organic Geochemistry 1981*. John Wiley and Sons, London 659-667.
- Atalay, M., Karayığit, A. İ. 2010. Kale-Kurbalık (Denizli-Türkiye) kömürlerinin jeolojik konumu, mineralojisi ve petrografisi. 63. Türkiye Jeoloji Kurultayı, Ankara 266-267.
- Ayinla, H. A., Abdullah, W. H., Makeen, Y. M., Abubakar, M. B., Jauro, A., Yandoka, B. M. S., Mustapha, K. A., Abidin, N. S. Z. 2017. Source rock characteristics, depositional setting and hydrocarbon generation potential of Cretaceous coals and organic rich mudstones from Gombe Formation, Gongola Sub-basin, Northern Benue Trough, NE Nigeria. *International Journal of Coal Geology* 173, 212-226.
- Bechtel, A., Gratzner, R., Sachsenhofer, R. F., Gusterhuber, J., Lücke, A., Püttmann, W. 2008. Biomarker and carbon isotope variation in coal and fossil wood of Central Europe through the Cenozoic. *Palaeogeography, Palaeoclimatology, Palaeoecology* 262, 166-175.
- Büyükeriç, Y. 2017. Molluscan Biostratigraphy of Early Miocene Deposits of The Kale-Tavas and Acıpayam Basins (Denizli, SW Turkey). *Bulletin of the Mineral Research and Exploration* 155, 47-71.
- Coplen, T. B., Shrestha, Y. 2016. Isotope-abundance variations and atomic weights of selected elements: 2016 (IUPAC Technical Report). *Pure and Applied Chemistry* 88 (12), 1203-1224.
- Czochanska, Z., Gilbert, T. D., Philip, R. P., Shepard, C. M., Weston, R. J., Wood, T. A., Woolhouse, A. D. 1988. Geochemical application of sterane and triterpane biomarkers to a description of oils from the Taranaki Basin in New Zealand. *Organic Geochemistry* 12, 123-135.
- Dehmer, J., 1989. Petrographical and organic geochemical investigation of the Oberpfalz brown coal deposit, West Germany. *International Journal of Coal Geology* 11, 273-290.
- Diessel, C. F. K. 1992. *Coal-bearing Depositional Systems*. Springer-Verlag, 721p.

- Ercan, T., Güney, E., Baş, H. 1983. Denizli volkanitlerinin petrolojisi ve plaka tektoniği açısından bölgesel yorumu. Türkiye Jeoloji Kurumu Bülteni 26 (2), 153-159.
- Erten, H., Koralay, D.B. 2020. A Zygolophodon turicensis (Proboscidea, Mammalia) mandible fragment from the Kale-Tavas basin (Denizli, Turkey). Palaeobiodiversity and Palaeoenvironments <https://doi.org/10.1007/s12549-020-00422-7> 2 March 2020.
- Espitalié, J., Deroo, G., Marquis, F. 1985. Rock Eval pyrolysis and its applications. Institut Francais du Petrole 40, 563-784.
- Fabiańska, M. J., Kruszewska, K. K. J. 2003. Relationship between petrographic and geochemical characterisation of selected South African coals. International Journal of Coal Geology 54, 95-114.
- Florentine, C. 2007. Stable isotope analysis of sedimentary organic matter from bioluminescent Bays in Vieques, Puerto Rico, suggest a link between mangrove decay and bioluminescence. 20th Annual Keck Symposium, Wooster, Ohio, 143-148.
- Gedik, F., Tunç, M. 2004. Denizli yöresindeki denizel Oligosen çökellerinin bentik foraminiferleri ve onların biyostratigrafisi. 57. Türkiye Jeoloji Kurultayı, Maden Tetkik ve Arama Genel Müdürlüğü, Ankara, 217-218.
- Göktaş, F., Çakmakoğlu, A., Tari, E., Sütçü, Y. F., Sarıkaya, H. 1989. Çivril-Çardak arasının jeolojisi. Maden Tetkik ve Arama Genel Müdürlüğü Rapor No. 8701, Ankara (unpublished).
- Hakyemez, Y. 1989. Geology and stratigraphy of the Cenozoic sedimentary rocks in the Kale-Kurbalık area, Denizli, southwestern Turkey. Bulletin of the Mineral Research and Exploration 109, 1-14.
- Helvacı, C., Yağmurlu, F. 1995. Geological setting and economic potential of the lignite and evaporite-bearing Neogene basins of western Anatolia, Turkey. International Journal of Earth Science 44, 91-105.
- Hoffmann, C. F., Mackenzie, A. S., Lewis, C. A., Maxwell, J. R., Oudin, J. L., Durand, B., Vandenbroucke, M. 1984. A biological marker study of coals, shales and oils from the Mahakam Delta, Kalimantan, Indonesia. Chemical Geology 42, 1-23.
- Hunt, J. M. 1996. Petroleum Geochemistry and Geology, Second Edition. W. H. Freeman and Company, 743p.
- Inoue, T., Suzuki, N., Hasegawa, H., Saito, H. 2012. Differential transportation and deposition of terrestrial biomarkers in middle Eocene fluvial to estuarine environments, Hokkaido, Japan. International Journal of Coal Geology (96-97), 39-48.
- Izart, A., Suarez-Ruiz, I., Bailey, J. 2015. Paleoclimate reconstruction from petrography and biomarker geochemistry from Permian humic coals in Sydney Coal Basin (Australia). International Journal of Coal Geology 138, 145-157.
- Kara-Gülbay, R. 2015. Organic geochemical and petrographical characteristics of coal bearing Oligo-Miocene sequence in the Oltu-Narman Basin (Erzurum), NE Turkey. International Journal of Coal Geology 149, 93-107.
- Koralay, D.B. 2018a. Geç Miyosen yaşlı Honaz (Denizli) kömürlü birimlerinin organik jeokimyasal özellikleri ve çökeltme ortamı. Pamukkale Üniversitesi Mühendislik Bilimleri Dergisi 24(6). 1192-1199.
- Koralay, D.B. 2018b. Organic maturation and maceral associations of Oligocene sedimentary rocks from Eastern Denizli, Turkey. 18th International Multidisciplinary Scientific GeoConference SGEM 2018 Conference, Bulgaria, 18(1.1), 3-10.
- Koralay, D.B. 2018c. Denizli Güneydoğusundaki (GB Türkiye) kömürlerin hidrokarbon türetme potansiyeli ve biyomarker özellikleri. Kahramanmaraş Sütçü İmam Üniversitesi Mühendislik Bilimleri Dergisi 21(1), 20-42.
- Koralay, D.B. 2018d. A review of the elemental composition and redox conditions of Oligocene organic matter-rich deposits, Western Anatolia Turkey. Journal of Engineering Research and Applied Science 7(1), 711-721.
- Koralay, D. B., Gedik Vural, Z. 2018. Apreliminary evaluation of Buldan coals (Denizli/Western Turkey) using pyrolysis and organic petrographic investigations. 18th International Multidisciplinary Scientific GeoConference SGEM 2018 Conference, Bulgaria, 18(1.1), 379-386.
- Koralay, D.B., Koralay, T. 2018. Denizli güneydoğusundaki (Honaz/GB Türkiye) organik maddece zengin kayaların jeokimyası ve organik petrografik özelliklerinin incelenmesi. Türkiye Bilimsel ve Teknolojik Araştırma Kurumu Rapor No: 114Y668, 233 s. Ankara (unpublished).
- Koralay, D. B., Koralay, T. 2019. Geochemistry for the Pliocene carbonaceous rocks from southeastern Denizli: Provenance signature and tectonic setting. 19th International Multidisciplinary Scientific GeoConference SGEM 2018 Conference, Bulgaria 19(1.1), 211-219.

- Kvenvolden, K. A., Simoneit, B. R. T. 1990. Hydrothermally derived petroleum: Examples from Guaymas Basin, Gulf of California, and Escanaba Trough, Northeast Pasific Ocean (1). AAPG Bulletin 74(3), 223-237.
- Meyers, P. A. 1997. Organic geochemical proxies of paleoceanographic, paleolimnologic, and paleoclimatic processes. *Organic Geochemistry* 27, 213-50.
- Okay, A. İ. 1989. Geology of the Menderes Massif and the Lycian Nappes South of Denizli, Western Taurides. *Bulletin of the Mineral Research and Exploration* 109, 45-58.
- Okay, A. İ. 2001. Stratigraphic and metamorphic inversions in the central Menderes Massif: a new structural model. *International Journal of Earth Sciences* 89, 709-727
- Özçelik, O., Altunsoy, M. 2005. Organic geochemical characteristics of the Miocene bituminous units in the Beypazarı Basin, Central Anatolia, Turkey. *Arabian Journal Science and Engineering* 30, 181-194.
- Peters, K. E., Moldowan, J. M. 1993. *The Biomarker Guide: Interpreting, Molecular Fossils in Petroleum and Ancient Sediments*. Prentice-Hall, 363.
- Peters, K. E., Cassa, M. R. 1994. *Applied Source Rock Geochemistry*. AAPG Memoir 60, 93-120.
- Peters, K. E., Walters, C. C., Moldowan, J. M. 2005. *The Biomarker Guide, Volume 1*. Cambridge University Press, 1132 p.
- Radke, M. 1987. Organic geochemistry of aromatic hydrocarbons. Brooks, J., Welte, D. (Eds.). *Advances in Petroleum Geochemistry volume 2*. Academic Press, London 141-205.
- Radke, M., Welte, D. H., Willsch, H. 1991. Distribution of alkylated aromatic hydrocarbons and dibenzothiophenes in rock of the Upper Rhine Graben. *Chemical Geology* 93, 325-341.
- Requejo, A. G. 1994. Maturation of petroleum source rocks-II Quantitative changes in extractable hydrocarbon content and composition associated with hydrocarbon generation. *Organic Geochemistry* 21, 91-105.
- Rigby, D., Batts, B. D. 1986. The isotopic composition of nitrogen in Australian coals and oil shales. *Chemical Geology (Isotope Geoscience Section)* 58, 273-282.
- Rimstidt, J. D., Vaughan, D. J. 2003. Pyrite oxidation: A state-of-the-art assessment of the reaction mechanism. *Geochimica et Cosmochimica Acta* 67(5), 873-880.
- Seifert, W. K., Moldowan, J. M. 1986. Use of biological markers in petroleum exploration. *Methods in Geochemistry and Geophysics* 24, 61-290.
- Şafak, Ü. 2010. Güney-Buldan-Yenicekent-Babadağ-Kale (Denizli, GB Anadolu) çevresi Tersiyer çökellerinin ostrakod topluluğu ve ortamsal özellikleri. *Kahramanmaraş Sütçü İmam Üniversitesi Mühendislik Bilimleri Dergisi* 13(2), 44-62.
- Waples, D. W., Machihara, T. 1991. Biomarkers for geologists-a practical guide to the application of steranes and triterpanes in *Petroleum Geology*. AAPG Methods in Exploration Series No:9, Oklahoma, Tulsa, 85 p.
- Warwick, P. D., Ruppert, L. F. 2016. Carbon and oxygen isotopic composition of coal and carbon dioxide derived from laboratory coal combustion: A preliminary study. *International Journal of Coal Geology* 166, 128-135.
- Whiticar, M. J. 1996. Stable isotope geochemistry of coals, humic kerogens and related natural gases. *International Journal of Coal Geology* 32, 191-215.
- Xiao, H. Y., Liu, C. Q. 2011. The elemental and isotopic composition of sulfur and nitrogen in Chinese coals. *Organic Geochemistry* 42, 84-93.
- Yakupoğlu, T., Bayhan, E. 2017. Yatağan Havzasındaki (Muğla/GB Türkiye) Neojen yaşlı sedimanter kayaçların sedimentolojik ve petrografik özellikleri. *Yüzüncü Yıl Üniversitesi Fen Bilimleri Enstitüsü Dergisi* 22(2), 120-131.



Bulletin of the Mineral Research and Exploration

<http://bulletin.mta.gov.tr>



Organic geochemical characteristics, depositional environment and hydrocarbon potential of bituminous marls in Bozcahüyük (Seyitömer/Kütahya) Basin

Fatih BÜYÜK^{a*} and Ali SARI^b

^aAnkara University, Institute of Science Directorate, İrfan Baştuğ Caddesi, 06110 Dışkapı/Ankara, Turkey

^bAnkara University, Faculty of Engineering, Department of Geological Engineering, 06830 Gölbaşı, Ankara, Turkey

Research Article

Keywords:

Bituminous Marl, Organic Matter, Kerogen, GC, GC-MS, MFA, Synthetic Oil.

ABSTRACT

In this study, the geochemical properties, sedimentation conditions and hydrocarbon potential of the bituminous marls, having quite rich organic carbon content (average 9.27% TOC), composed of gray-green colored, dominant marl lithology with marl-claystone intercalation in the Bozcahüyük (Seyitömer/Kütahya) Basin has been evaluated. In this context, Rock-Eval pyrolysis, Gas Chromatography (GC), Gas Chromatography-Mass Spectrometry (GC-MS) and Modified Fischer Assay (MFA) analyses of the samples taken from the study area were performed and their organic facies have been evaluated. The marls have an excellent source rock characteristics, and include kerogen predominantly as Type I and rarely as Type II. The precipitation of organic matter took place under reducing anoxic redox conditions where oxygen was limited. Analysed samples contain terrestrial phytoclasts and palynomorphs as well as freshwater algae indicating Type-I kerogen such as *Botryococcus braunii*. Organic geochemical data show that the study area is deposited in the "AB" organic facies continental-marine transition zone. Carbon preference index (CPI), C_{27} , C_{28} and C_{29} sterane abundance distribution of the samples as well as presence of Gamsaran as a salty environment indicator indicates that the lake environment has been under marine environment influence from time to time and therefore the study area has lagoon character. The average of the T_{max} values of analysed samples is 432 °C and it was determined that the bituminous marls in the region could not produce conventional petroleum due to their immaturity. However, it has been evaluated that these marls have the potential to produce synthetic petroleum as the kerogen types are dominantly Type-I, TOC and HI contents are high, as well as the analyzed samples have an average of 12.60% (133 L / ton) MFA oil content.

Received Date: 06.12.2019

Accepted Date: 08.09.2020

1. Introduction

The study area is located 30 km from the center of Kütahya province in the Bozcahüyük locale linked to Seyitömer town and is found on İ23-c3 and c4 sheets of the 1/25,000 scale maps (Figure 1). In this study, the aim was to determine the organic geochemical features of grey-green colored bituminous marls outcropping in the Bozcahüyük (Seyitömer/Kütahya) Basin.

Within this framework, samples had organic matter amounts, types and maturity, source rock depositional environment and petroleum yield identified in an attempt to estimate the hydrocarbon potential of the study area.

In this region, much research has been performed about general and economic geology topics to date due to outcrops of lignite along with bituminous marls

Citation Info: Büyüç, F., Sari, A.2021. Organic geochemical characteristics, depositional environment and hydrocarbon potential of bituminous marls in Bozcahüyük (Seyitömer/Kütahya) Basin. Bulletin of the Mineral Research and Exploration 164, 53-73.
<https://doi.org/10.19111/bulletinofmre.792155>.

*Corresponding author: Fatih BÜYÜK, buyukfatih@hotmail.com

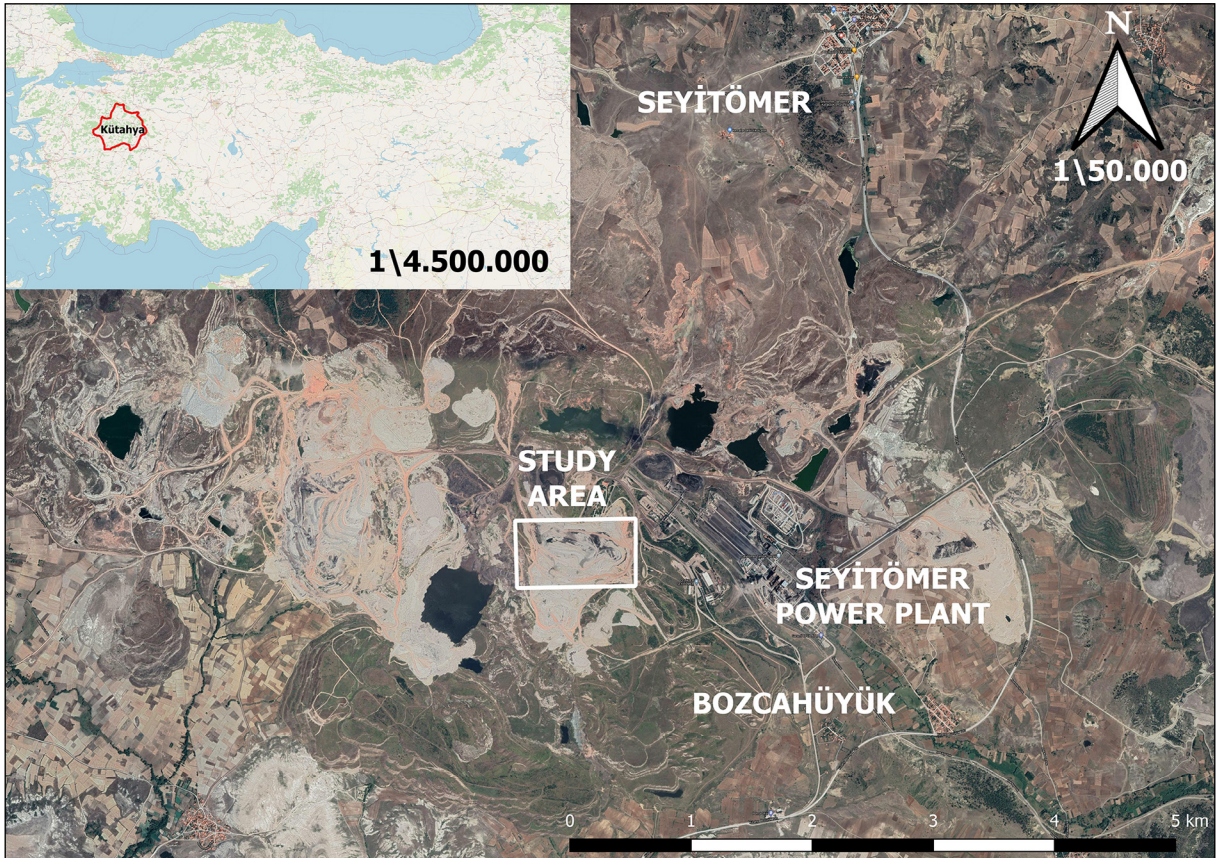


Figure 1- Satellite appearance of the study area on Google Earth and location map.

(Lebküchner, 1957, 1959; Nebert, 1960; Beseme, 1969; Ercan et al., 1978; Baş, 1986; Sarıyıldız, 1987; Şener et al., 1995; Şengüler et al., 1998; Şengüler, 1999; Kök et al., 2001; Çelik, 2003; Hepbaşlı, 2004; Kara Gülbay, 2004; Dikmen, 2005; Ekinci, 2006; Altun et al., 2006; Şengüler, 2007; Özburan, 2009; Murat, 2010; Kıratlı, 2019).

Organic matter-rich rocks which may be named bituminous shale, oil shale, bituminous schist, bituminous claystone and bituminous marl, generally have black, dark grey, grey, dark and light brown and dark green color and are mostly laminated, while some of the organic matter they contain comprises bitumen, which dissolves in organic solvents, and some comprises kerogen which cannot be dissolved with organic solvents (Dyini, 2003). These rocks are sedimentary units that may produce oil and gas with retorting and extraction processes and the residues provide ash which can be used in different sectors. Linked to technological developments, these rocks can be used for synthetic oil and gas production in addition to use as solid fuel with low-quality lignite in

thermal power plants, while some major, trace and rare elements may be used for active carbon production and by paper, pharmaceutical, paint, plastic, ceramic, cement and fertilizer industries.

Studies by the Turkish Geological Survey (MTA) and other researchers have identified nearly 10 billion tons of bituminous rock resources in Turkey. However, it is very important to include this resource, calculated mainly in the possible and probable reserve category in past years, is made proven reserves with geophysical and drilling studies. This is because the bituminous rock potential is in second place among our country's energy resources after the 17.5 billion tons lignite resource (Büyük, 2019).

There is a need for synthetic petroleum to be produced from bituminous rocks due to increasing energy demands, external dependence on 88% of fossil fuels, excessive fluctuations in oil prices and rising energy bills. With the aim of searching for alternative energy sources globally and increasing local resources, it is important to complete technological innovations

to meet these needs economically and to lower production costs.

2. Material and Method

Within the scope of organic geochemical investigations, analysis of a total of 23 samples taken from the study area were completed in Turkish Petroleum (TP) R and D Central Laboratories. All of these samples underwent Rock Eval pyrolysis analyses and Modified Fischer Assay (MFA) analysis was used for 6 samples chosen according to high TOC, S_2 and HI values on table 1. In order to make correlations with MFA analysis results, 3 samples chosen for MFA analysis according to variable TOC, S_2 and HI values in table 1 were assessed with gas chromatography (GC) and gas chromatography-mass spectrometry (GC-MS). Additionally, 5 samples chosen according to variable TOC, HI and OI values in table 1 and organic petrography (kerogen type identification) analyses were used for organic facies analysis.

Within this framework, with the aim of determining organic matter type, hydrocarbon potential and maturation status, pyrolysis analyses were performed using a Rock Eval VI device with IFP 160000 standard and samples had total organic carbon (%TOC), S_1 , S_2 , S_3 , S_4 , T_{max} , residual carbon (RC) and pyrolysable carbon (PC) values determined. Using this data, the following parameters were calculated: hydrogen index [$HI=(S_2/TOC) \times 100$], oxygen index [$OI=(S_3/TOC) \times 100$], production index [$PI=S_1/(S_1+S_2)$], hydrocarbon type index (S_2/S_1), genetic potential ($PY:S_1+S_2$) and bitumen/migration index (S_1/TOC).

In order to identify the oil, water and gas contents contained within the investigated bituminous marls with the retorting process in the laboratory environment, MFA analysis was performed according to the American Society for Testing and Materials (ASTM D) 3904 standard in order to determine the synthetic oil content as (%) and liter/ton that can be obtained from the bitumen (S_1) and kerogen within some samples (HB-8A, 10, 12, 14, 18 and 19A).

Dichloromethane was used as solvent to distil liquid hydrocarbon (bitumen) within the investigated samples (HB-7, 12 and 18) using an accelerated solvent extraction (ASE) 300 system for extraction analysis. The bitumen obtained from extraction of bituminous marls was used for GC and GC-MS analyses.

Certain samples (HB-8A, 10, 12, 19A, 20) had organic facies analysis performed. Samples had terrestrial amorphous organic matter (AOM), terrestrial palynomorphs (spores and pollen), freshwater algae and herbaceous and woody phytoclast content identified. Using diagenesis and geochemical features of organic matter, based on pyrolysis data and dominant organic matter type, the depositional environment in the region was interpreted within the scope of identifying 7 separate organic facies types of A, AB, B, BC, C, CD and D.

Samples (HB-7, 12 and 18) firstly were diluted with dichloromethane solvent to determine organic matter type, general distribution of HC compositions, thermal maturity, biological degradation and depositional environment of bituminous marls. These samples were analyzed with GC according to the ASTM D 5307-97 method with an Agilent 6850 GC device. Data obtained from GC analyses were used to calculate the Pr (pristane)/Ph (phytane) ratio, isoprenoid/n-alkane ratio, and carbon preference index (CPI) and additionally interpretations related to the depositional environment were made based on n-alkane distributions. In this study, the formula of Bray and Evans (1961) was used [$CPI_{(16-24)} = (nC_{15} + nC_{17} + nC_{19} + nC_{21} + nC_{23}) / (nC_{16} + nC_{18} + nC_{20} + nC_{22} + nC_{24})$].

Samples (HB-7, 12 and 18) investigated with the aim of revealing biological fossils (biomarkers), separating molecules geochemically and obtaining information about storage environment of source rocks, maturity and degree of biological degradation had GC using Norwegian Oil Standards and GC-MS analyses performed in an Agilent 5975C-four tip mass spectrometer device with automatic liquid sample intake. Ion fragmentograms from the chromatograms assessed the m/z 191 peaks for triterpenes and m/z 217 peaks for steranes.

3. General Geology

The Bozcakıyık (Seyitömer/Kütahya) Neogene Basin investigated within the scope of the study is included in the "İzmir-Ankara Ocean Zone" as defined by Brinkmann (1971). Basins began to form with N-S strike under an extensional regime with E-W orientation in the early Miocene. The Seyitömer Basin formed during this process. The metamorphics,

ophiolitic rocks and granitoids forming the basement of this basin before the Neogene are unconformably overlain by Miocene-Pliocene basin fill (Çelik, 2003). Sarıyıldız (1987) stated that the fill materials in the basin are generally ancient fluvial, lacustrine and modern fluvial sediments.

The Late Cretaceous Ayvalı formation (Ka) representing ophiolitic mélangé containing radiolarites, serpentinite and crystallized limestone forming the basement in the region was described by Ercan et al. (1978). Above the Ayvalı formation (Ka) over an angular unconformity, there are fluvial sediments comprising conglomerates, sandstone and claystone belonging to the early Miocene Elmacık formation (Ne) (Nebert, 1960). The lacustrine Seyitömer formation (Ns) containing lower and upper lignite beds was deposited conformably overlying the Elmacık formation (Ne) in the basin in the middle-late Miocene (Lebküchner, 1957 and 1959). The lower lignite bed in the Seyitömer Basin was called the “main vein” by Lebküchner (1959), Nebert (1960) and Beseme (1969). The thickness of the lower coal bed reaches up to 36.75 m in some drill holes with mean 15 m thickness (Gökmen et al., 1993). Additionally, the thickness of the upper lignite bed in the region reaches up to 10 meters (Şengüler, 1999). The Seyitömer formation (Ns) was divided into five members by Şengüler (1999) of the lacustrine green clay member (Nsa), the lower lignite member (Nsb), the bituminous marl member (Nsc), the upper lignite member (Nsd) containing the burnt series (Nsy) with upper levels outcropping around Arslanlı village and the yellow clay member (Nse) from older to younger, respectively.

In the Western Anatolian region, the late Miocene was a period when the N-S effective extensional tectonic regime began in the region which had thickened and risen in elevation under a N-S oriented compressional regime. After the deposition of the Seyitömer formation (Ns), a break was experienced in sedimentation in the region for a short duration in the late Miocene. In the Pliocene the lacustrine İshakçılar formation (Ni) comprising silicified limestone and tuff interlayers was deposited unconformably above the Seyitömer formation (Ns). The region was a large freshwater lacustrine and fluvial basin in the late Miocene (Özburan, 2009). With the neotectonic period, grabens began to develop with west-east strike from the

end of the Pliocene to the beginning of the Pleistocene with the effect of north-south oriented extension. Large clastics belonging to the Kocayataktepe formation (Nk) comprising reddish and cream colored, poorly consolidated conglomerate, sandstone and occasional tuffs and clays forming in a fluvial environment in the Pleistocene were unconformably deposited above the İshakçılar formation (Ni). The unit comprising large clastics reflecting the fluvial environment shows that lake waters regressed in the areas where it outcrops (Baş, 1986). In the present day, as the final stage in graben and deposition, alluvium (Qal) comprising unconsolidated pebbles, sand, clay and silt and alluvial fan deposits continue unconformably above all units (Figure 2).

There are uncommon local faults with N-S strike in the Seyitömer Basin (Figure 3). Tectonic deformation structures in Western Anatolia are not observed in the study area. The late Miocene bituminous marl member (Nsc) displays distribution east and west of ancient Seyitömer and partly to the north of Ayvalı village. According to Şener and Şengüler (1992), drilling by MTA in the region found the thickness

SYSTEM	SERIES	FORMATION	MEMBER	SYMBOL	THICKNESS (M)	LITHOLOGY	DESCRIPTION
QUATERNARY	HOLO CENE			Qal	20		Unconsolidated pebble, sand, silt and clay
	PLEISTO CENE	KOCAYA TAKIŞTEPE		Nk	50		Reddish and cream colour, poorly consolidated conglomerate, sandstone and occasional tuff and clay
NEOGENE	PLIOCENE	İSHAKÇILAR		Ni	150		Limestone in upper sections Marl in middle sections Tuff in lower sections
				Ns			
MIOCENE	MIDDLE-UPPER MIOCENE	SEYİTÖMER	YELLOW CLAY	Nse	25		Yellow clay, yellow, grey, greenish grey and cream marls and silicified limestone, lenses of tuff, diatomaceous marl interlayers
			UPPER LIGNITE	Nsd	10		Upper lignite: grey and light grey coloured marl interlayers
			BITUMINOUS MARL	Nsc	30		Bituminous: Marl: grey, greenish grey limestone, silicified limestone, marl, occasional chert interlayers
			LOWER LIGNITE	Nsb	20 - 40		Lower lignite: lignite, clayey lignite, sandstone, siltstone, claystone and marl interlayers
			GREEN CLAY	Nsa	50		Green plastic clay Grey claystone in upper sections Sandy claystone in lower sections
LOWER MIOCENE	ELMACIK		Ne	75 - 150		Pebblestones, sandstone and claystone interlayers, poorly sorted, large grain size, cross-bedding, finer grain towards upper levels, braided fluvial environment	
PRE-UPPER CRETACEOUS	AYVALI		Ca	>300		Ophiolitic melange: Serpentinite, radiolarite, limestone blocks	

Figure 2- Generalized stratigraphic section for Seyitömer (Kütahya) (Şengüler, 1999; Dikmen, 2005; Büyük, 2019).

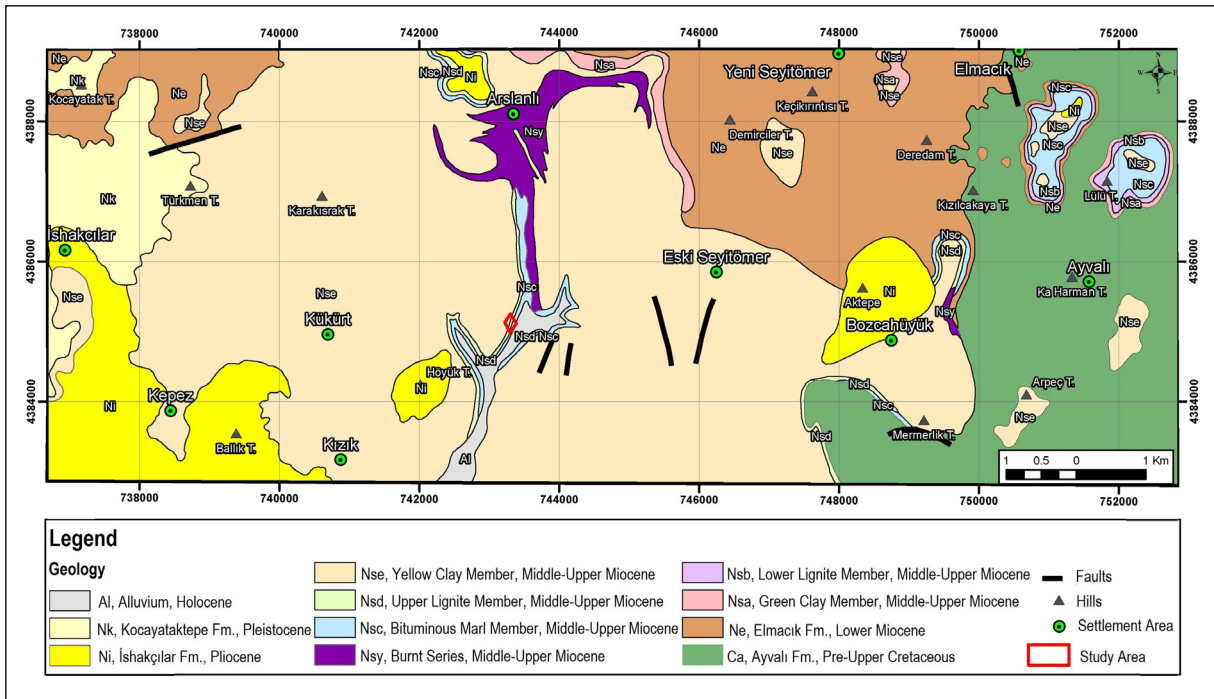


Figure 3- Geological map for Seyitömer (Kütahya) (Şengüler, 1999; Dikmen, 2005; Büyük, 2019).

of the bituminous marl member varied from 8.5-50.0 m and thickness increased from the edges of the basin toward the central sections. While coal and bituminous marl levels thicken toward the east of the basin, these units were not deposited in the west of the basin as the necessary depositional conditions did not exist. The Seyitömer Basin is stated to have nearly 110 million tons of economic bituminous rock resource. Mineralogical investigations revealed the bituminous marls, which should be dark colored normally due to high organic matter, have light colors due to high Mg/Ca ratio in the environment (montmorillonite in marls has Ca composition in dark-colored sections of the marls and Al, Fe and Mg composition in light-colored sections) and dense diatoms (Şengüler, 1999).

From the level of the “Höyük Pano” located in the study area, a measured stratigraphic section containing 37.25 meter sequence of only bituminous marls was taken and sampling was performed in this zone (Figures 4, 5).

4. Organic Geochemical Findings and Assessment

In this section, the organic geochemical analysis results from 23 bituminous rock samples taken from the study area are given and evaluated (Table 1).

Additionally, as seen in table 1, only sample number HB-20* contained organic material (HI:16 mg HC/g TOC and OI: 231 mg CO₂/g TOC) that was oxidized and reworked according to the classifications by Peters and Cassa (1994) and Jones (1987) (HI<50 and OI>200), and was excluded from the assessment due to having inertinitic organic matter transported outside the depositional environment and kerogen type IV.

4.1. Source Rock Potential

TOC values vary from 1.06-29.87% with mean value of 9.27%. According to this data, the investigated samples were understood to have rich source rock potential according to Tissot and Welte (1984) (TOC>2), adequate according to Jarvie (1991) (TOC>1) and perfect according to Peters and Cassa (1994) (TOC>4).

Mean S₁ and S₂ hydrocarbon values were 2.11 mg HC/g rock and 66.40 mg HC/g rock and according to Peters and Cassa (1994) samples are source rocks with between generally good (1<S₁<2) and perfect (4<S₁) oil potential for S₁ and are source rocks with perfect (20<S₂) oil potential for S₂. Additionally, in all samples S₂>S₁ which indicates there is no organic contamination of the source rocks.



Figure 4- Distant and close-up general appearance of bituminous marl layer from the measured stratigraphic section preparation area.

4.2. Organic Matter Type

The investigated samples had HI values varying from 290 to 769 mg HC/g TOC with mean value of 654.59 mg HC/g TOC. As can be seen from the HI-OI and HI- T_{max} diagrams and also based on variable (S_2/S_3) hydrocarbon type index having values from 3.01 to 31.26 (Peters and Cassa, 1994), assessment of kerogen type identified dominant Type I kerogen ($15 < S_2/S_3$) and rare Type II kerogen ($10 < S_2/S_3 < 15$) types (Figures 6, 7). Again, samples examined with the HI associated with S_2 -TOC diagram showed the samples had Type I-Type II kerogen types (Figure 8).

4.3. Thermal Maturity of Organic Matter

The investigated samples had T_{max} values varying from 426 °C to 441 °C with mean T_{max} of 432 °C. Accordingly the maturation parameters are in the immature-oil window ($430 < T_{max} (°C) < 435$) according to Espitalie et al. (1984) and in the immature stage ($T_{max} (°C) < 435$) according to Peters and Cass (1984). According to the T_{max} standards of Espitalie et al. (1985), degree of maturity of bituminous marl samples determined to have kerogen Type I is immature-early mature ($T_{max} (°C) < 440$); while samples HB-13 (Type II-III) and HB-18 (Type I) are in the oil window

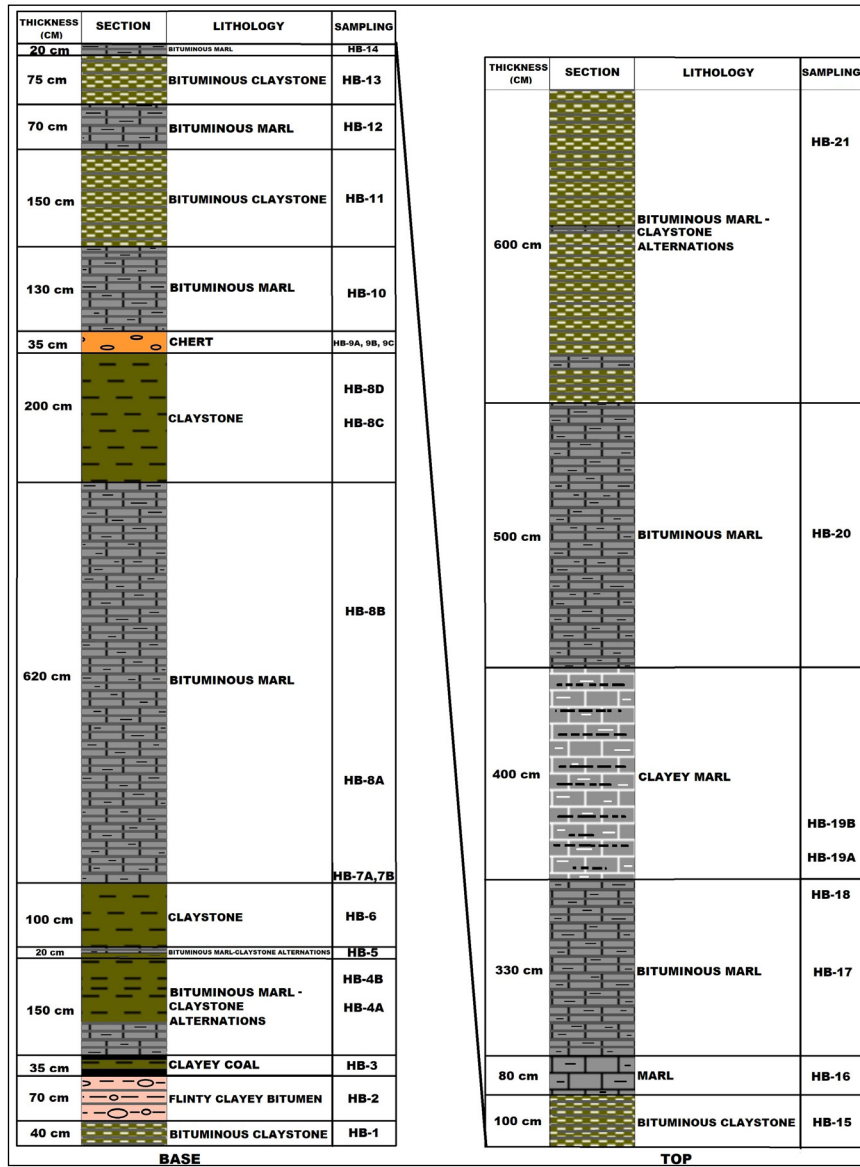


Figure 5- Measured stratigraphic section for bituminous marls in Höyük Pano in the Bozcahüyük (Seyitömer/Kütahya) Basin (Büyük, 2019).

($425 < T_{max} (°C) < 450$); and sample HB-20 (Type IV- T_{max} : $414°C$) is in the immature stage. The HI- T_{max} diagram in figure 7 shows that five (HB-4, 8B, 12, 14, 18) of the samples have $T_{max} > 435 °C$, and these are in the mature zone and have oil derivation potential. The other 18 samples have $T_{max} < 435 °C$ so these samples are immature and are not in a position to produce hydrocarbons.

Due to the investigated samples having PI values lower than 0.1, they are in the immature zone on figure 9 and it appears oil derivation cannot occur from these samples.

Using the triterpene and sterane peak heights on the ion fragmentograms from GC-MS chromatograms in figures 24-29 according to the peak identifications in table 2, the biomarker parameters related to maturity of organic matter in the investigated samples were assessed on table 3. Though the $20S/(20S+20R)$ and $\beta\beta/(\beta\beta+\alpha\alpha)$ sterane ratios on GC-MS m/z 217 chromatograms and $22S/(22S+22R)$ homohopane ratio and $Ts/(Ts+Tm)$ ratio values on GC-MS m/z 191 chromatograms are very low, the moretane/hopane ratio is high which shows that bituminous marls in the region are in the immature stage complying with the pyrolysis results.

Table 1-Rock-Eval pyrolysis analysis results for bituminous rock samples from the Bozcakühük (Seyitömer/Kütahya) Basin (Büyük, 2019).

#	Sample #	TOC (%)	S ₁ (mg HC/g rock)	S ₂ (mg HC/g rock)	S ₃ (mg CO ₂ /g rock)	T _{max} (°C)	HI (100xS ₂)/TOC	OI (100xS ₃)/TOC	PI S ₁ /(S ₁ +S ₂)	HC Type Index (S ₂ /S ₃)	PY S ₁ +S ₂ (ppm)	Bitumen Index S ₁ /TOC	RC (%)	PC (%)
1	HB-21	6.16	1.01	40.80	2.64	433	662.00	43.00	0.02	15.45	41.810	0.16	2.52	3.64
2	HB-20*	0.62	0.02	0.10	1.43	414	16.00	231.00	0.20	0.07	120	0.03	0.54	0.08
3	HB-19B	10.46	1.71	69.60	3.68	433	665.00	35.00	0.02	18.91	71.310	0.16	4.30	6.16
4	HB-19A	18.13	6.11	130.68	6.01	430	721.00	33.00	0.04	21.74	136.790	0.34	6.45	11.68
5	HB-18	29.87	3.52	229.56	10.05	441	769.00	34.00	0.02	22.84	233.080	0.12	9.99	19.88
6	HB-17	5.65	1.98	39.78	1.91	434	704.00	34.00	0.05	20.83	41.760	0.35	2.04	3.61
7	HB-16	8.21	1.94	57.38	3.15	432	699.00	38.00	0.03	18.22	59.320	0.24	3.09	5.12
8	HB-15	6.67	1.46	46.78	2.63	432	701.00	39.00	0.03	17.79	48.240	0.22	2.49	4.18
9	HB-14	11.35	5.34	86.40	3.61	438	761.00	32.00	0.06	23.93	91.740	0.47	3.53	7.82
10	HB-13	1.06	0.15	3.07	1.02	430	290.00	96.00	0.05	3.01	3.220	0.14	0.70	0.36
11	HB-12	27.56	5.05	203.60	9.81	436	739.00	36.00	0.02	20.75	208.650	0.18	9.70	17.86
12	HB-11	1.84	0.20	7.18	1.10	427	390.00	60.00	0.03	6.53	7.380	0.11	1.16	0.68
13	HB-10	11.53	3.62	78.04	4.19	430	677.00	36.00	0.04	18.63	81.660	0.31	4.52	7.01
14	HB-8D	6.80	1.14	50.96	2.17	435	749.00	32.00	0.02	23.48	52.100	0.17	2.32	4.48
15	HB-8C	9.71	2.02	71.46	2.61	432	736.00	27.00	0.03	27.38	73.480	0.21	3.43	6.28
16	HB-8B	8.00	2.70	60.88	2.69	436	761.00	34.00	0.04	22.63	63.580	0.34	2.54	5.46
17	HB-8A	19.92	4.23	151.46	6.08	434	760.00	31.00	0.03	24.91	155.690	0.21	6.64	13.28
18	HB-7	3.43	0.68	25.17	0.92	432	734.00	27.00	0.03	27.36	25.850	0.20	1.22	2.21
19	HB-6	4.81	0.69	29.23	1.60	429	608.00	33.00	0.02	18.27	29.920	0.14	2.20	2.61
20	HB-5	2.75	0.52	20.32	0.65	427	739.00	24.00	0.03	31.26	20.840	0.19	0.94	1.81
21	HB-4	5.89	2.06	40.49	1.98	436	687.00	34.00	0.05	20.45	42.550	0.35	2.23	3.66
22	HB-2	2.13	0.17	9.67	1.56	427	454.00	73.00	0.02	6.20	9.840	0.08	1.17	0.96
23	HB-1	2.08	0.15	8.22	1.32	426	395.00	63.00	0.02	6.23	8.370	0.07	1.24	0.84
	Mean	9.27	2.11	66.40	3.24	432.27	654.59	40.64	0.03	18.95	68.508	0.22	3.38	5.89

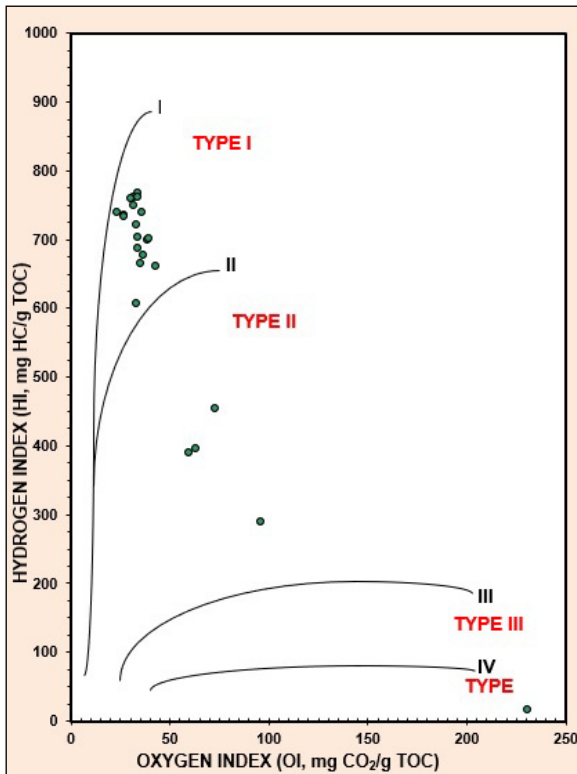


Figure 6- HI-OI diagram (Van Krevelen, 1993).

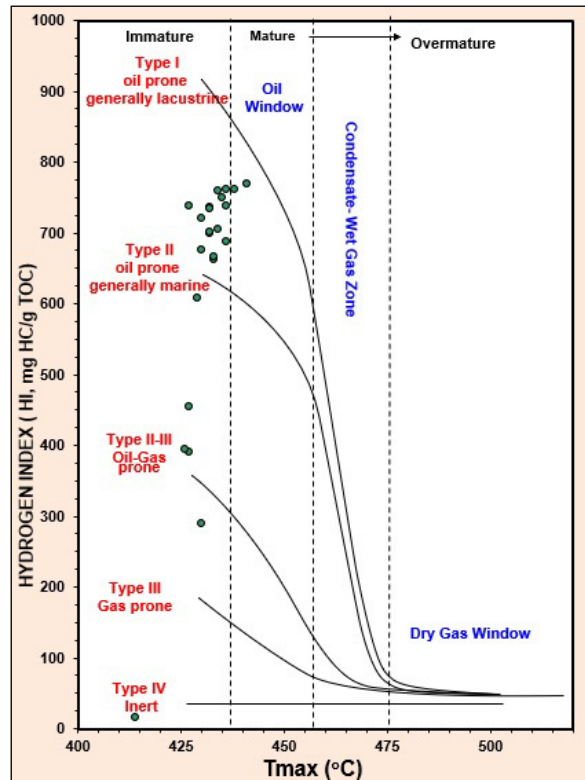


Figure 7- HI-T_{max} diagram (Hunt, 1995; Mukhopadhyay et al., 1995).

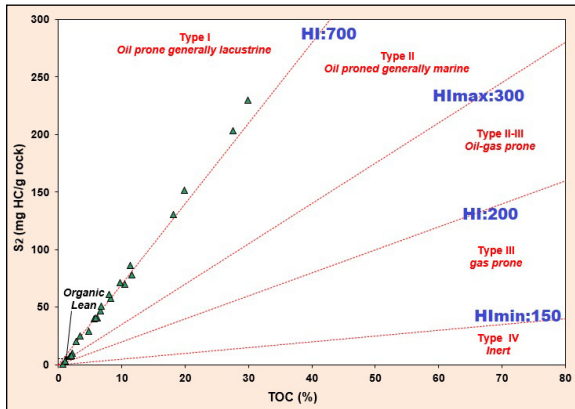


Figure 8- S₂-TOC, HI diagram (Langford and Blanc-Valleron, 1990).

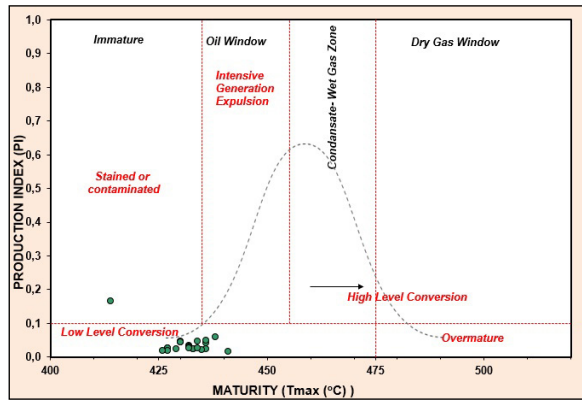


Figure 9- PI-Tmax maturation with kerogen maturation diagram (Peters, 1986).

Table 2- Identification of triterpene and sterane peaks on ion fragmentograms in a) m/z 191 and b) m/z 217 GC-MS chromatograms.

COMPONENT #	COMPONENT NAME	COMPONENT #	COMPONENT NAME
1	C ₁₉ Triterpene	1	C ₂₇ 13β (H)-17α (H)-Diasterane (20S)
2	C ₂₀ Triterpene	2	C ₂₇ 13β (H)-17α (H)-Diasterane (20R)
3	C ₂₁ Triterpene	3	C ₂₇ 13α (H)-17β (H)-Diasterane (20S)
4	C ₂₂ Triterpene	4	C ₂₇ 13α (H)-17β (H)-Diasterane (20R)
5	C ₂₃ Triterpene	5	C ₂₈ 13β (H)-17α (H)-Diasterane (20S)
6	C ₂₄ Triterpene	6	C ₂₈ 13β (H)-17α (H)-Diasterane (20R)
7	C ₂₅ (22S+22R) Triterpene	7	C ₂₈ 13α (H)-17β (H)-Diasterane (20S)
8	C ₂₄ Tetracyclic Hopane (SECO)	8	C ₂₇ 5α (H), 14α (H), 17α (H)-Sterane (20S)+ C ₂₈ 13α (H)-17β (H)-Diasterane (20S)
9	C ₂₆ 22 (S) Triterpene	9	C ₂₇ 5α (H), 14β (H), 17β (H)-Sterane (20R)+ C ₂₈ 13β (H)-17α (H)-Diasterane (20S)
10	C ₂₆ 22 (R) Triterpene	10	C ₂₇ 5α (H), 14β (H), 17β (H)-Sterane (20S)+ C ₂₈ 13α (H)-17β (H)-Diasterane (20R)
11R	C ₂₈ Triterpene (R)	11	C ₂₇ 5α (H), 14α (H), 17α (H)-Sterane (20R)
11S	C ₂₈ Triterpene (S)	12	C ₂₈ 13β (H)-17α (H)-Diasterane (20R)
12R	C ₂₉ Triterpene (R)	13	C ₂₈ 13α (H)-17β (H)-Diasterane (20S)
12S	C ₂₉ Triterpene (S)	14	C ₂₈ 5α (H), 14α (H), 17α (H)-Sterane (20S)
13	C ₂₇ 18α (H)-22, 29, 30-Trisnorhopane (Ts)	15	C ₂₈ 5α (H), 14β (H), 17β (H)-Sterane (20R)+ C ₂₉ 13α (H)-17β (H)-Diasterane (20R)
14	C ₂₇ 17α (H)-22, 29, 30-Trisnorhopane (Tm)	16	C ₂₈ 5α (H), 14β (H), 17β (H)-Sterane (20S)
15	17α (H)-28, 30-Bisnorhopane	17	C ₂₈ 5α (H), 14α (H), 17α (H)-Sterane (20R)
16	C ₃₀ Triterpene	18	C ₂₉ 5α (H), 14α (H), 17α (H)-Sterane (20S)
17	17α (H)-28, 30-Bisnorhopane	19	C ₂₉ 5α (H), 14β (H), 17β (H)-Sterane (20R)
18	C ₂₉ 17α (H)-21β (H)-30-Norhopane	20	C ₂₉ 5α (H), 14β (H), 17β (H)-Sterane (20S)
19	C ₂₉ TS (18α (H)-30-Norhopane)	21	C ₂₉ 5α (H), 14α (H), 17α (H)-Sterane (20R)
20	C ₃₀ (17α (H)-Diahopane)	22	C ₂₉ 5α (H), 14α (H), 17α (H)-Sterane (20S)
21	C ₂₉ 17β (H)-21α (H)-30-Normoretane	23	C ₂₉ 5α (H), 14β (H), 17β (H)-Sterane (20R)
22	Oleanane	24	C ₃₀ 5α (H), 14β (H), 17β (H)-Sterane (20S)
23	C ₃₀ 17α (H)-21β (H)-Hopane	25	C ₃₀ 5α (H), 14α (H), 17α (H)-Sterane (20R)
24	C ₃₀ 17β (H)-21α (H)-Moretane		
25	C ₃₁ 17α (H)-21β (H)-30-Homohopane (22S)		
26	C ₃₁ 17α (H)-21β (H)-30-Homohopane (22R)		
27	Gammacerane		
28	Homomoretane		
29	C ₃₂ 17α (H)-21β (H)-30, 31-Bishomohopane (22S)		
30	C ₃₂ 17α (H)-21β (H)-30, 31-Bishomohopane (22R)		
31	C ₃₃ 17α (H)-21β (H)-30, 31, 32-Trishomohopane (22S)		
32	C ₃₃ 17α (H)-21β (H)-30, 31, 32-Trishomohopane (22R)		
33	C ₃₄ 17α (H)-21β (H)-30, 31, 32, 33-Tetrakishomohopane (22S)		
34	C ₃₄ 17α (H)-21β (H)-30, 31, 32, 33-Tetrakishomohopane (22R)		
35	C ₃₅ 17α (H)-21β (H)-30, 31, 32, 33, 34-Pentakishomohopane (22S)		
36	C ₃₅ 17α (H)-21β (H)-30, 31, 32, 33, 34-Pentakishomohopane (22R)		

(a)

(b)

4.4. Hydrocarbon Generation Potential

Assessment of the “migration index” or “bitumen index” (S₁/TOC) used to identify the depth at which a source rock will begin to generate hydrocarbon, in other words expel oil, found that 10 of the samples were in the initial generation-migration step (0.1 < S₁/TOC < 0.2), while another 10 had too much generation-migration (0.2 < S₁/TOC) and the remaining 3 had no generation-migration (S₁/TOC < 0.1) (Smith, 1994; Hunt, 1995).

The S₂-TOC diagram in figure 10 shows the samples dominantly had perfect hydrocarbon potential. The mean hydrocarbon type index (S₂/S₃) value was 18.95 with samples identified to have oil derivative potential (5.0 < S₂/S₃) according to Clementz (1979) and Peters (1986). Additionally, the HI-TOC diagram in figure 11 to determine the hydrocarbon generation potential of samples shows they are good-perfect oil sources origin. The mean potential product/genetic potential PY (ppm /mg HC/g rock): (S₁+S₂) value of these samples is 68,508 ppm which indicates good

Table 3- Biomarker parameters calculated for maturity of organic matter in samples according to m/z 191 and m/z 217 GC-MS chromatograms.

	HB-7	HB-12	HB-18
20S/(20S+20R) Sterane Ratio (C₂₉) = [18/(18+21)] height of peaks (m/z 217 GC-MS) If this ratio is <0.5 it is immature (Hunt, 1995).	0.04 Immature	0.12 Immature	0.06 Immature
ββ/(ββ+αα) Sterane Ratio (C₂₉) = [(19+20)/(18+19+20+21)] height of peaks (m/z 217 GC-MS) This ratio is 0.72 in the oil formation zone of thermal maturation equilibrium (Peters et al., 2005).	0.23 Immature	Could not be identified	0.26 Immature
22S/(22S+22R) Homohopane Index (C₃₁) = [25/(25+26)] height of peaks (m/z 191 GC-MS) This ratio reaches 0.5 thermal equilibrium value in the oil formation zone (Peters et al., 2005).	0.02 Immature	0.10 Immature	0.05 Immature
Ts/(Ts+Tm) = [13/(13+14)] height of peaks (m/z 191 GC-MS) This ratio reaches 1.0 in the late mature oil formation field (Peters et al., 2005).	Could not be identified	0.11 Immature	Could not be identified
Moretane/Hopane Ratio (C₃₀) = (24/23) height of peaks (m/z 191 GC-MS) This ratio may fall from 0.8 to 0.15-0.05 with the increase in thermal maturation (Seifert and Moldowan, 1986).	0.95 Immature	5.52 Immature	0.87 Immature

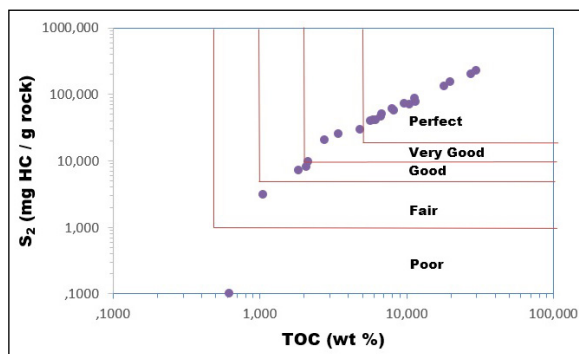


Figure 10- Hydrocarbon potential according to S₂ and TOC values (Ghori, 2000).

source rock potential (6,000 ppm < S₁+S₂) according to Tissot and Welte (1978). The samples are observed to dominantly plot in the perfect source rock potential area on the PY-TOC diagram (Figure 12). The S₁-TOC diagram used with the aim of differentiating migrated hydrocarbons from indigenous hydrocarbons shows the hydrocarbon in the samples is locally produced, with no mechanical or anthropogenic contamination from outside (Figure 13).

The investigated samples have %RC values from 0.70% to 9.99% which are not on the residue carbon line (TOC=RC) so they are observed to still have oil generation potential (Figure 14). The reason for

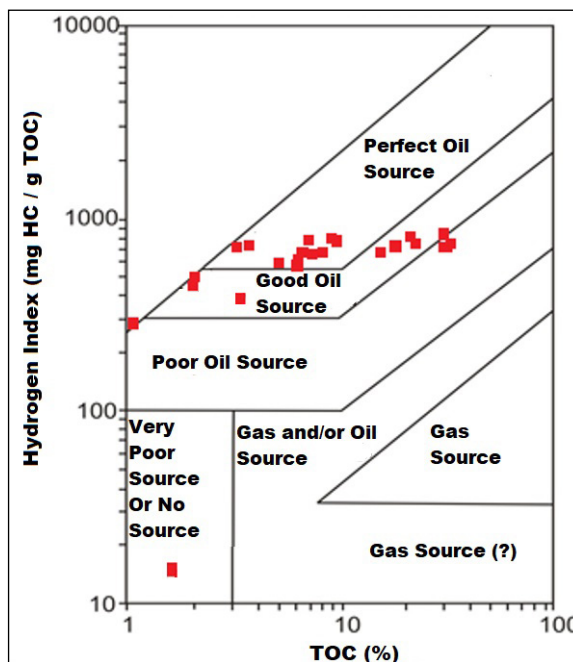


Figure 11- HI-TOC diagram (Jackson et al., 1985).

samples being more distant from the TOC=RC line on figure 14 is that samples still have excess amounts of S₁ and S₂ hydrocarbons that can be generated. The %PC values vary from 0.36% to 19.88% which is close to the pyrolysable carbon line (TOC=PC) on figure 15 showing that the kerogen type in samples is suitable

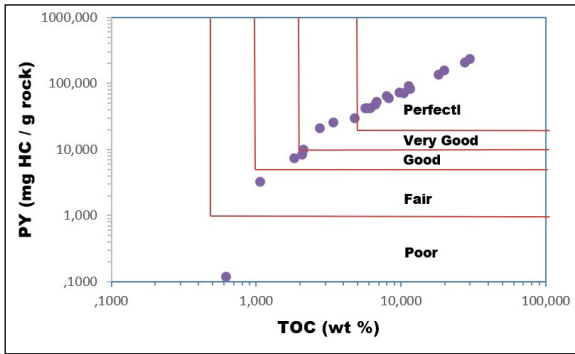


Figure 12- PY - TOC diagram (Ghori, 2002).

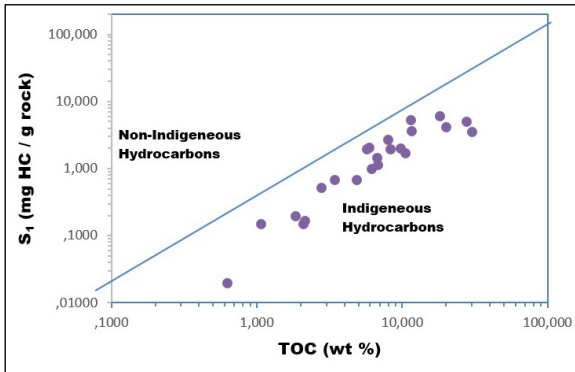


Figure 13- S_1 (mg HC/ g rock) - TOC (%) HC characterisation diagram (Hunt, 1995).

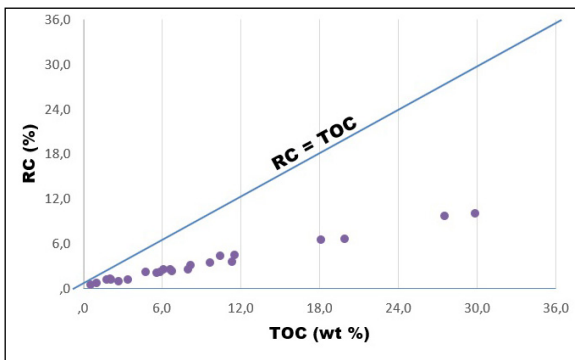


Figure 14- RC (%) - TOC (%) diagram (English et al., 2004).

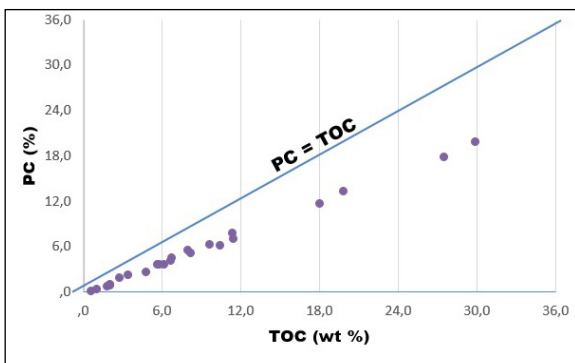


Figure 15- PC (%) - TOC (%) diagram (English et al., 2004).

for oil generation. During pyrolysis, as the amount of organic matter increases, the generation from S_1 and S_2 hydrocarbons increases; however, all samples are not on the TOC=PC line which indicates the presence of pyrolysable S_1 and S_2 hydrocarbons.

4.4.1. Modified Fischer Assay (MFA) Analysis and Synthetic Petroleum Production

Bituminous marl samples (HB-8A: 21.57%; HB-10: 3.22%; HB-12: 14.66%; HB-14: 5.38%; HB-18: 21.28%; HB-19A: 9.48%) analyzed with the MFA method had mean oil content of 12.6% (3.22%-21.57%). Economic assessment of synthetic petroleum that can be produced by these samples found potential was dominantly very highly economic according to Hou (1984), dominantly very economic according to Snape (1995) and has dominantly very good economic potential according to Committee Office of Mineral Resources in China (1987), Liu et al. (2006) and Tao et al. (2010) (Table 4).

When the correlations of the MFA yield of samples with TOC, S_1 and S_2 are assessed, these samples of perfect source rock were determined to be able to produce oil with very good economic potential (Tables 1 and 4, figures 16-18). Figures 16 and 18 show a strong positive correlation between MFA petrol content with %TOC ($r = 0.848$, $p = 0.033$) and with S_2 ($r = 0.875$, $p = 0.022$) and these are statistically significant. This indicates that with the increase in %TOC and S_2 values, the MFA yield increases. In other words, it appears the Type I kerogen features may produce oil at very good economic levels from these samples. However, statistical assessment did not find a correlation between MFA oil content with S_1 ($r = -0.285$, $P = 0.584$) and there did not appear to be a strong correlation with HI ($r = -0.735$, $P = 0.096$) (Tables 1 and 4, figures 17 and 19).

Generally, about 5-10% of the TOC value of a rock comprises S_1 hydrocarbons, while 90-95% comprises S_2 hydrocarbons derived from kerogen. As a result, while the S_1 values obtained from pyrolysis analyses are low, S_2 values are high. All conventionally produced oils comprise S_1 and S_2 hydrocarbons. Due to this, the relationships between MFA analysis results with S_1 and S_2 data should be assessed. While the samples show positive correlation for S_2 -MFA values on figure 18, the reason for the perception of

Table 4- Economic assessment criteria related to Fischer Assay yield (oil content) according to some researchers.

Hou (1984)		Snape (1995)		Hou (1984); Committee Office of Mineral Resources in China (1987); Liu et al. (2006); Tao et al. (2010)		
FISCHER ASSAY YIELD (%)	ECONOMIC ASSESSMENT	FISCHER ASSAY YIELD (%)	ECONOMIC ASSESSMENT	FISCHER ASSAY YIELD		ECONOMIC ASSESSMENT
				(%)	(L/ton)	
< 4.0%	Not economic	< 4.0%	Not economic	< 3.5%	< 35	Weak
4.0%-10.4%	Moderately economic	4.0%-13.8%	Moderately economic	3.5%-5.0%	35-50	Moderate
10.4%-13.8%	Highly economic	13.8%-23.6%	Highly economic	5.0%-10.0%	50-100	Good
> 13.8%	Very highly economic	> 23.6%	Very highly economic	> 10.0%	> 100	Very Good

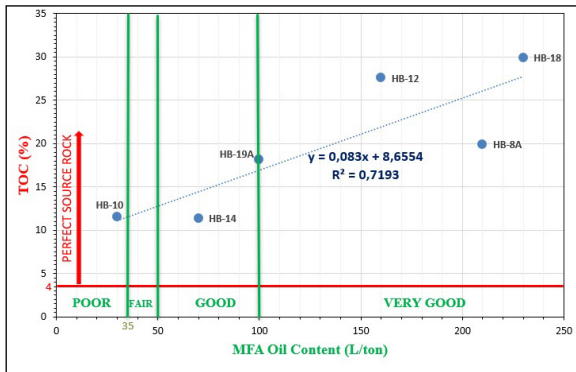


Figure 16- MFA oil content (L/ton)-TOC (%) diagram (Büyük, 2019).

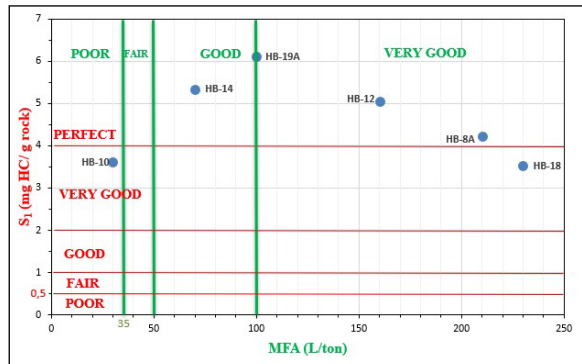


Figure 17- MFA oil content (L/ton)-S₁ (mg HC/ g rock) diagram (Büyük, 2019).

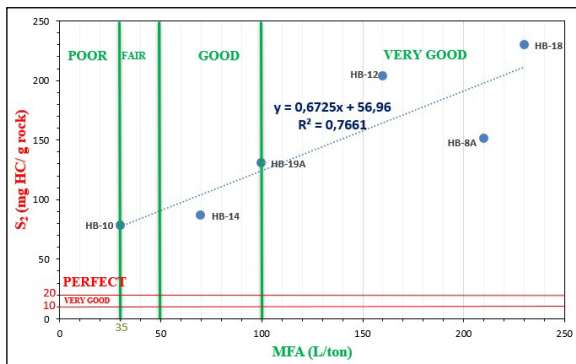


Figure 18- MFA oil content (L/ton)-S₂ (mg HC/ g rock) diagram (Büyük, 2019).

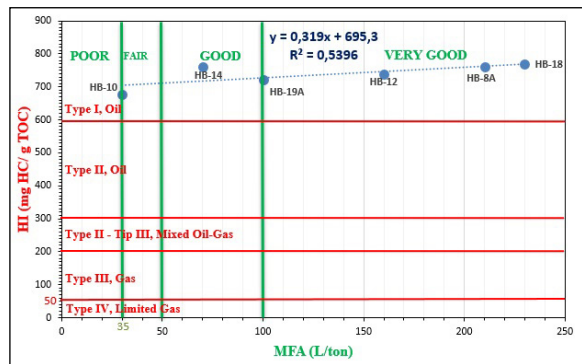


Figure 19- MFA oil content (L/ton)-HI (mg HC/ g TOC) diagram (Büyük, 2019).

a negative correlation between S₁ and MFA values on figure 17 is the oil and gas derived from a very small portion of 5-10% of organic matter comprising S₁ in the rock. In spite of this, according to MFA assessment of the S₁ hydrocarbon values on figure 17, most appear to be within very good economic boundaries.

In previous years, bituminous marls in the Seyitömer Basin were revealed to have oil content of 30-38 liters/ton according to Ünalın (1978), 5% oil content (54.3 L/ton) according to Şener et al. (1995), have 22 API gravity heavy oil equivalent of synthetic oil produced with density 0.92 g/mL according to Şengüler (1999), oil content of 4-5.9% (56 kg/ton)

according to Hepbaşlı (2004), and be able to produce 4.46 L/ton synthetic petroleum with the in-place pyrolysis method according to Kök et al. (2008). Additionally, Ekinci (2006) reviewed many studies related to the Seyitömer Basin and stated 2.41% oil, 1.51% gas and 88.67% residue could be obtained from bituminous shale according to Fischer assay (FA) analysis results. Though there was low oil content and high ash, after representative distillation from bituminous shale with Type I kerogen 14% naphtha, 21.5% kerosene, 14.5% mild gas-oil, 29% atmospheric gas-oil, 18% vacuum distillation and 2% residue could be obtained and pyrolysis of the bituminous shale had FA percentage 7 gpt (26.5 L/ton). In other words, the region had uneconomic potential in terms of synthetic oil production. Şengüler (1999) stated that the 5meter economic bituminous marl zone had thermal values of 800-1,000 kcal/kg and that there were levels suitable to obtain synthetic oil occasionally among levels with highest TOC values. However, as the lateral continuity of these levels was variable and there was general inadequacy of thickness in the region, synthetic oil production from bituminous marls was revealed not to be economic. Due to this, the recommendation was made to evaluate these units as solid fuel in thermal power plants using fluid-bed incineration systems with 20% bituminous marl and 80% lignite.

4.5. Biomarker Investigations

4.5.1. Gas Chromatography Analysis (GC)

n-Alkane Distributions: GC analyses were performed to make interpretations about the depositional environment, organic matter type, biological degradation and thermal maturity. Gas chromatograms belonging to samples investigated in figures 20-22 have a skewed n-alkane distribution toward the nC_{23} - nC_{30} array; in other words, as the long-chain C_{23} , C_{25} , C_{27} and C_{29} peaks are higher compared to others, the depositional environment reflects a terrestrial lacustrine environment containing high plants and non-marine phytoplankton algae (Tissot and Welte, 1984; Peters and Moldowan, 1993). This situation, along with the dominant Type I kerogen type on figures 6-8 and the observation of green freshwater algae, *Botryococcus branuii* on organic facies analyses, is compatible with indications of a freshwater lacustrine environment.

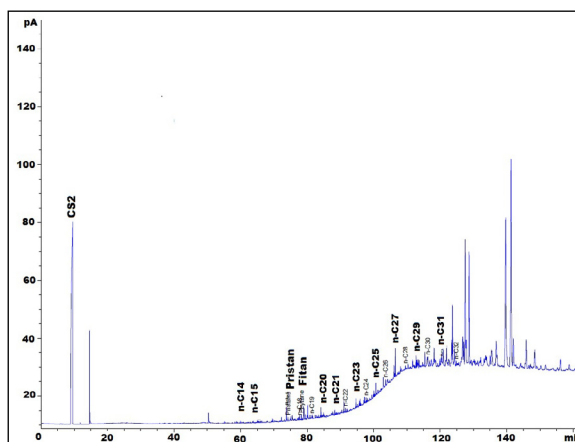


Figure 20- Gas chromatogram for sample no. HB-7.

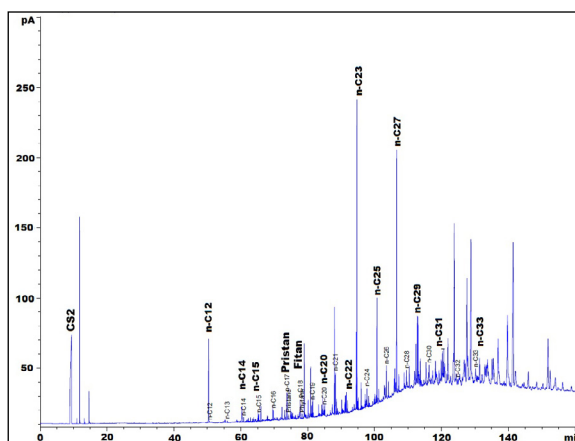


Figure 21- Gas chromatogram for sample no. HB-12.

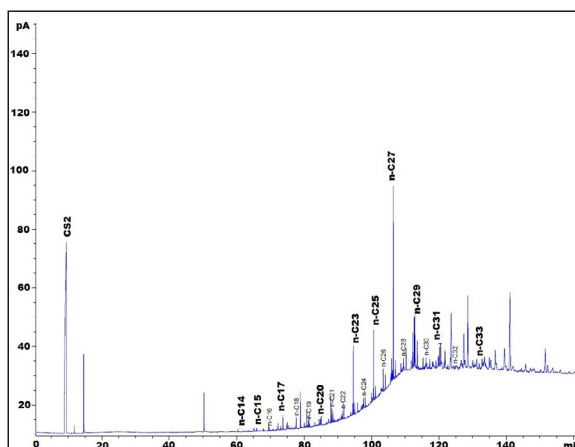


Figure 22- Gas chromatogram for sample no. HB-18.

It was observed that the investigated samples were deposited in the terrestrial-marine transition zone in the distribution of C_{27} , C_{28} and C_{29} sterane abundances in the triangular diagram in figure 23 (Huang and Meinschein, 1979).

As the $\sum(nC_{21}-nC_{31}) / \sum(nC_{15}-nC_{20})$ ratio is >1 (HB-7 7.38; HB-12 12.29; HB-18 14.99), it indicates the degree of waxiness increases; in other words, there was input of terrestrial organic material into the depositional environment (Bakr, 2009). Additionally, the n-alkane ratio (TAR) of the terrestrial environment source/aquatic environment source, or the ratio of the total of long-chain n-alkanes with odd carbon number ($C_{27}+C_{29}+C_{31}$) to the total of short-chain n-alkanes with odd carbon number ($C_{15}+C_{17}+C_{19}$) is larger than 1 (HB-7 6.7; HB-12 7.7; HB-18 13.5), the depositional environment reflects terrestrial environment source with high plant content (Rieley et al., 1991). Again, as the $(n-C_{17}/n-C_{31})$ ratio is smaller than 1 (HB-7 0.34; HB-12 0.62; HB-18 0.43), the depositional environment indicates terrestrial organic matter input (Koralay, 2018).

Pristane/Phytane Ratio (Pr/Ph): According to GC graph data in figures 20-22, the Pr/Ph ratios are smaller than 1 (HB-7 0.87 and HB-12 0.68) so the depositional environment was identified to have reducing/anoxic redox conditions (Tissot and Welte, 1984).

Carbon Preference Index (CPI): The CPI values of bituminous marl samples in the region were calculated according to the formula of Bray and Evans (1961) using the GC graph data in figures 20-22 and values of 1.18 for HB-7, 5.88 for HB-12 and 3.06 for HB-18 were found. This indicates a terrestrial/lacustrine environment with marine connection fed by marine plankton in sample HB-7 and fed by high terrestrial plants in samples HB-12 and HB-18. Additionally, $CPI > 1$ indicating dominant odd-number carbons and the high CPI values for samples HB-12 and HB-18 emphasize that the samples are in the immature field (Tran and Philippe, 1993).

Isoprenoid/n-Alkane Ratios: According to the GC graph data in figures 20-22, sample HB-12 had Pr/nC_{17} : 0.15 and Ph/nC_{18} : 1.00 and sample HB-7 had Pr/nC_{17} : 0.70 and Ph/nC_{18} : 1.82. According to Petersen et al. (2001), these samples were deposited in an anoxic reducing environment, while according to Chaula et al. (1987) this indicates an algal source for kerogen.

4.5.2. Gas Chromatography-Mass Spectrometry Analysis (GC-MS)

Using the triterpene and sterane distributions on m/z 191 and m/z 217 mass chromatograms belonging

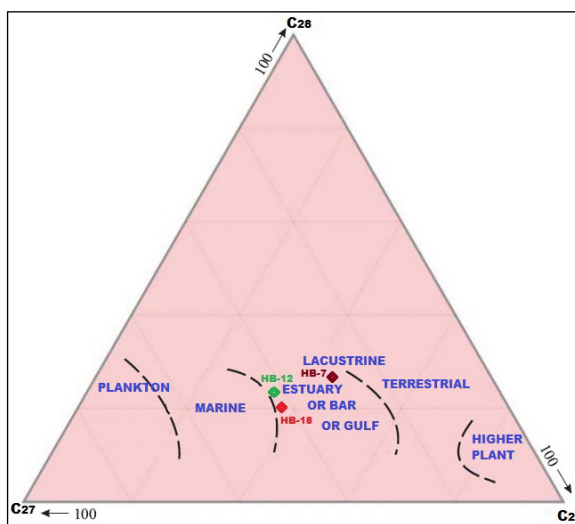


Figure 23- C_{27} , C_{28} and C_{29} sterane abundance and precipitation environment diagram for bituminous marls in the region (Huang and Meinschein, 1979).

to samples HB-7, 12 and 18, biomarker parameters were calculated and attempts were made to interpret the depositional environments for bituminous marls in the region (Figures 24-29 and table 2).

On the m/z 191 mass chromatograms, the presence of Gammacerane (0.25 and 0.13, respectively) in samples HB-12 and HB-18 indicates a saline and reducing environment under marine effect in the region (Peters and Moldowan, 1993). All three samples did not have Oleanane observed, indicating terrestrial environments; however, this situation does not mean that the depositional environment did not have terrestrial organic matter input (Peters and Moldowan, 1991; Hunt, 1995). The (C_{29}/C_{30}) hopane ratio was larger than 1 for sample HB-7 (1.16) due to marl source rock according to Peters and Moldowan (1993) and is smaller than 1 in samples HB-12 and HB-18 (0.55 and 0.96, respectively) reflecting source rock with high clay content according to Waples and Machihara (1991).

Again, on m/z 191 chromatograms, the $C_{31} 22R/C_{30}$ hopane ratios in samples (HB-7: 3.89; HB-12: 2.07; HB-18: 1.82) were larger than 0.25 reflecting marl source rock (Koralay, 2009). Additionally, a lacustrine depositional environment with high clay content was indicated due to the $[C_{29} Ts / (C_{29} Ts + C_{29} Norhopane)]$ ratio being smaller than 1 (HB-7: 0.06 and HB-12: 0.69) (Philip and Gilbert, 1986). The $[Ts / (Ts + Tm)]$ ratio was calculated as 0.11 for HB-12 assessed as reflecting an environment suitable for carbonate

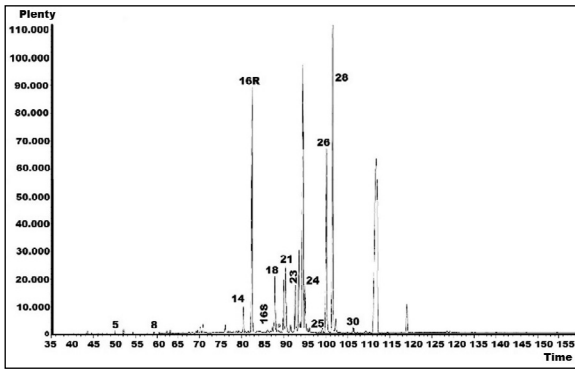


Figure 24- GC-MS m/z 191 chromatogram for HB-7 bituminous marl sample.

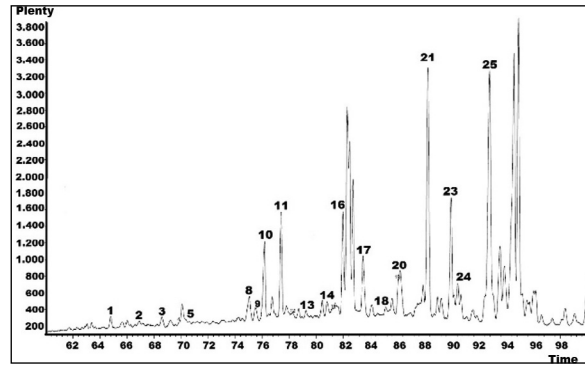


Figure 25- GC-MS m/z 217 chromatogram for HB-7 bituminous marl sample.

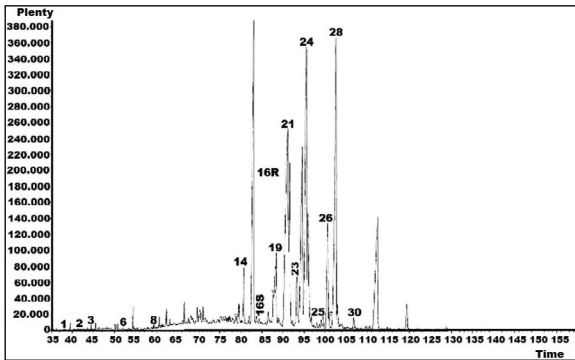


Figure 26- GC-MS m/z 191 chromatogram for HB-12 bituminous marl sample.

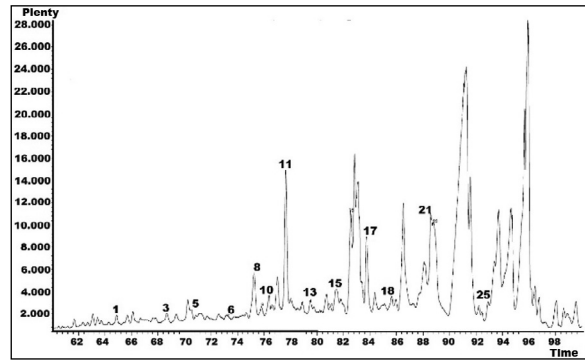


Figure 27- GC-MS m/z 217 chromatogram for HB-12 bituminous marl sample.

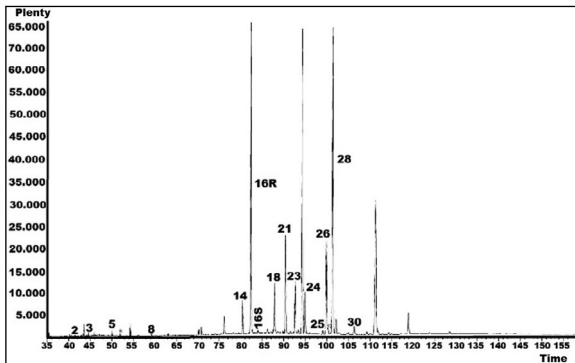


Figure 28- GC-MS m/z 191 chromatogram for HB-18 bituminous marl sample.

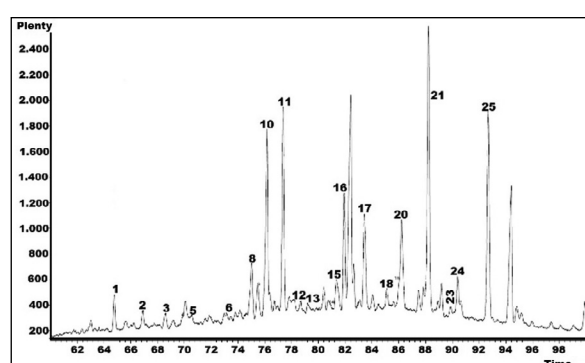


Figure 29- GC-MS m/z 217 chromatogram for HB-18 bituminous marl sample.

deposition in the region, while the environment was identified as anoxic as the (Ts/Tm) ratio was <1 for sample HB-12 (0.12) (Peters and Moldowan, 1993).

The abundance of C_{30} formethyl sterane on m/z 217 mass chromatogram for samples indicates lacustrine environment according to Koralay (2009). The high diasterane/sterane ratios (HB-7: 13.4; HB-12: 4.7; HB-18: 21.2) indicate the depositional environment included clastic sediments with high clay ratio

containing organic matter with algal source (Mello et al., 1988; Peters and Moldowan, 1993). However, it can be seen that the samples fall in the terrestrial-marine transition zone on the pyramid diagram in Figure 23 showing C_{27} , C_{28} and C_{29} sterane abundances and depositional environment.

Due to samples investigated on m/z 191 and m/z 217 GC-MS chromatograms having sterane/hopane ratios ≥ 1 (HB-7: 1.0; HB-12: 2.69; HB-18: 2.23),

samples were identified to have algal organic matter content (Peters and Moldowan, 1993). On the m/z 191 mass chromatogram, the reason for the high peak value for C₂₃ tricyclic terpene is the lacustrine source of the depositional environment and it is understood that it came from a source rock in the carbonate lithology containing diagenetic products of cell membranes from single-celled organisms (Hunt, 1995).

4.6. Organic Facies Investigations

Organic facies analysis was completed to determine the organic matter content of bituminous marls and in order to be able to evaluate the depositional environment (Figures 30-32). However, as sample HB-20 contained oxidized and inertinitic organic matter, this sample was excluded from the assessment. Organic palynofacies analysis linked to organic matter type (Figure 30) shows;

- Terrestrial amorphous organic matter (AOM) was observed at similar values (40%) in all samples. Palynomorph groups generally reflected terrestrial bisaccate pollens and flowering plant pollens (angiosperm) assemblages.
- *Botryococcus braunii* freshwater algae (25%) was observed to be present in all samples, but highest in sample HB-19A.
- Semi-quantitative analysis generally did not identify marine palynomorph findings, with the presence of terrestrial organic matter and terrestrial palynomorphs along with freshwater algae reflecting a freshwater lacustrine environment.

When the maceral group composition and HC generation potential of these samples are assessed on pyramid diagrams, 80% of samples appear to fall in the oil-generating algal and amorphous kerogen field (Figure 32). The HI values for samples from the region were 290-769 mg HC/g TOC (mean 654.59 mg HC/g TOC), OI values were 24-96 mg HC/g TOC (mean 40.64 mg HC/g TOC) and TOC values varied from 1.06%-29.87% (mean 9.27%) (Tables 1-5).

All samples were dominantly observed to have terrestrial amorphous organic matter input. According to Ebukanson and Kinghorn (1985), large particles like vitrinite and inertinite deposit close to the coast, while

fine-grained particles like spores, pollen and waxy organic matters deposit in deeper water environments. When samples are investigated from this aspect, terrestrial organic matter content comprising spores and pollen appears to comprise 25% of the total organic content (Figure 30). Linked to this, in addition to the HI, OI and TOC values, dominantly Type I with lower rates of Type II kerogen is observed in this facies and hence it was assessed that mostly oil with lower rates of gas may be observed according to maturity stage. However, as the source rock in the region is in the immature field, according to current depositional conditions of bituminous marls, conventional oil and gas generation was identified not to have occurred. Along with all this data, when figures 30-32 and table 5 are investigated, bituminous marls in the region were assessed to have deposited in the AB organic facies region. As this facies is included in the terrestrial-marine environment transition zone, it may be considered that the study area reflects a lacustrine environment with marine effects observed like occasional estuary-bay-tidal plane-lagoon settings.

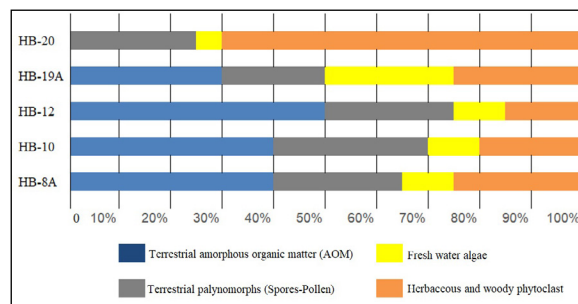


Figure 30- Organic facies analysis for 5 samples from bituminous marl in the region.

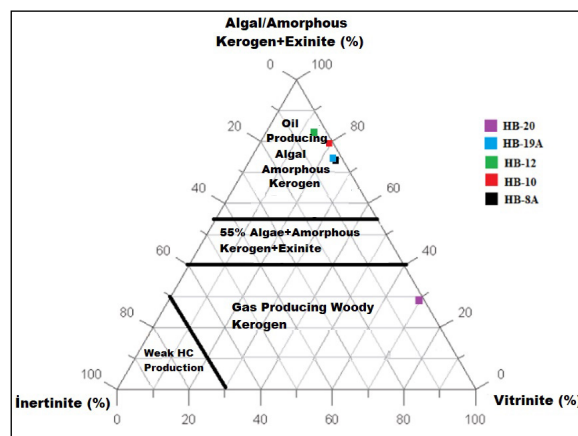


Figure 31- Schematic illustration of relationship between organic facies and precipitation environments (Altunsoy and Özçelik, 1993).

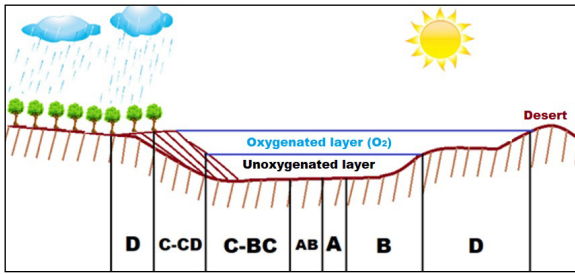


Figure 32- Pyramid diagram for maceral group composition and HC type potential (Stach, 1982).

Çelik (2003) stated that the lower lignite bed in the Seyitömer formation contained clay bands and that these clay bands formed in a freshwater lacustrine environment with relatively high water table during formation of fine clasts and peat. Şengüler (1999) interpreted the marls in Seyitömer Basin as having deposited in shallow and stagnant lacustrine environment due to the presence of abundant gastropods, lamellibranch, and ostracod fossils and fauna like coalified leaves and branches in the bituminous marls. Later studies by Şengüler (2007) proposed that the Seyitömer bituminous marls deposited in lake and lagoon environments connected with swamp environments. Again, Dikmen (2005) revealed the increase in Mg amount in the water mass in the lake environment reflected an alkali and saline environment and that the water mass in this region varied from freshwater to bitter-saline water and back to freshwater again in a study performed to determine the organic facies properties of the coal-bituminous marl transition around Aslanlı (Seyitömer/Kütahya).

5. Discussion and Conclusion

In this study, bituminous marls with mean 9.27% TOC in the Bozcahüyük (Seyitömer/Kütahya) Basin had perfect source rock properties, with dominant Type I and rare Type II kerogen type deposited in reducing anoxic redox conditions, and were understood to have lacustrine depositional environment due to containing terrestrial phytoclasts and palynomorphs along with freshwater algae like *Botryococcus braunii*. However, according to data from the investigated samples, the inclusion of the depositional environment in the “AB” terrestrial-marine organic facies transition zone, CPI data along with C_{27} , C_{28} and C_{29} sterane abundance distributions and presence of Gammacerane as saline environment indicator, the study area had lagoonal features and occasionally the lacustrine environment came under marine effect. Mean T_{max} value was $432^{\circ}C$ and based on assessment of other pyrolysis, GC and GC-MS data, it was determined the bituminous marls in the region had not produced conventional oil due to still being immature. According to the results of hydrocarbon generation potential assessment, bituminous marls in the region appear to have perfect petroleum generation potential.

Contrary to oil content (2.4-5.9%) of bituminous marls in the Seyitömer Basin in previous years and studies about synthetic oil production from these marls, MFA analysis of samples taken from bituminous marls from near Bozcahüyük locale within the scope of this study had mean oil content of 12.6% (3.22-21.57%) in addition to mean value of 133 L/ton (30 L/ton-230 L/ton). In addition to these values, considering

Table 5- Organic facies distribution in the region (Jones and Demaison 1982; Jones 1984,1987).

ORGANIC FACIES	PYROLYSIS DATA			DOMINANT ORGANIC MATTER	KEROGEN TYPE	SEDIMENTARY STRUCTURE
	HI, mg HC/g rock	OI, mg CO ₂ /g rock	TOC, wt %			
A	> 850	10 - 30	5(3) - 20+	Algal; amorphous	Tip I	Laminated
AB	650 - 850	20 - 50	3-10+	Amorphous; very little terrestrial	Tip I / Tip II	
B	400 - 650	30 - 80		Amorphous; widespread terrestrial	Tip II / Tip I	Good bedding - Laminated
BC	250 - 400	40 - 80	3(1) - 3+	Mixed; sometimes oxidised	Tip II / Tip III	Weak bedding
C	125 - 250	50 - 150	≤ 3	Terrestrial; sometimes oxidised	Tip III / Tip II	Very weak bedding - bioturbated
CD	50 - 125	40 - 150+	< 0.5	Oxidised; transported	Tip III / Tip IV	Massive; bioturbated
D	< 50	20 - 200+		Highly oxidised; transported	Tip IV	

the presence of dominant Type I kerogen and high TOC, S₂ and HI pyrolysis data, the bituminous marls in the study area have synthetic petroleum production potential as they abide by the required criteria accepted internationally for economic and technological use of bituminous rocks according to Hufnagel (1989) of minimum petrol content limit 4% and thermal value of 750 kcal/kg.

For production of Seyitömer lignites, the bituminous marls overlying the lignite are removed during mining activities as stripping material and piled in tallow/spoil heaps. As a result, acquiring these marls for the economy by use in a retorting facility for synthetic oil production from these bituminous marls; use with low-quality lignite as solid fuel; production of some major, trace and rare earth elements and use in cement, fertilizer and other industrial areas from residual ash after processing or pyrolysis of bituminous marls will make the region more advantageous without additional mining costs.

To date, only 20% of the bituminous rocks distributed in lignite fields in our country have had source potential determined. For the rapid, effective and continuous assessment of this hydrocarbon potential as alternative energy resource, exploration activities like in the Göynük (Bolu) region should be popularized through the country in general and it is necessary to create pilot retorting facilities in regions suitable for synthetic oil production. Within this scope, it is important to implement incentives for the sector like tax exemptions, and guaranteeing use of synthetic oil produced from bituminous rocks in energy production.

Acknowledgements

We are grateful to Ankara University Scientific Research Projects Unit for supporting this study within the scope of the project entitled “Investigation of Biogeochemical Properties and Hydrocarbon Potential of Miocene Organic Rocks between Tunçbilek-Seyitömer (Kütahya)” numbered 18B04430001.

References

- Altun, N.E., Hiçyılmaz, C., Hwang, J.Y., Suat Bağcı, A., Kök, M.V. 2006. Oil shales in the world and Turkey; reserves, current situation and future prospects: a review. *Oil Shale, Estonia* 23, 211-227.
- Altunsoy, M., Özçelik, O. 1993. Organik fasiyeler. *Cumhuriyet Üniv. Müh. Fak. Jeoloji Mühendisliği Dergisi* 34-43.
- Bakr, M.M.Y. 2009. Molecular organic geochemistry of crude oil from Shushan and Abu Gharadig Basins, Western Desert, Egypt. *Journal of King Abdulaziz University Earth Science* 20, 97-125.
- Baş, H. 1986. Domaniç-Tavşanlı-Kütahya-Gediz yöresinin Tersiyer jeolojisi. *Jeoloji Mühendisliği Dergisi* 27, 11-18.
- Beseme, P. 1969. Seyitömer (Tavşanlı-Kütahya) monoklinalinin genel jeolojik ve uygulamalı incelenmesi. *Maden Tetkik ve Arama Genel Müdürlüğü Rapor No: 4673, Ankara* (unpublished).
- Bray, E.E., Evans, E.D. 1961. Distribution of n-paraffins as a clue to recognition of source beds. *Geochimica et Cosmochimica Acta* 22, 2-15.
- Brinkmann, R. 1971. The geology of western Anatolia. *Geology and history of Turkey. The Petroleum exploration society of Libya*.
- Büyük, F. 2019. Bozcahüyük (Seyitömer/Kütahya) Havzası bitümlü şeyllerinin organik jeokimyasal değerlendirmesi ve hidrokarbon potansiyeli. *Yüksek Lisans Tezi, Ankara Üniversitesi, Fen. Bil.Ens., Jeoloji Mühendisliği Anabilim Dalı, Ankara*.
- Chaula, B.R., Chopra, A.K., Shukla, R.K. 1987. Geochemistry of sedimentary organics of Jurassic of India. In *Petroleum Geochemistry Exploration in the Afro-Asian Region, Balkema, Rotterdam*.
- Clementz, D.M. 1979. Effect of oil and bitumen saturation on source-rock pyrolysis. *AAPG Bulletin* 63, 2227-2232.
- Committee Office of Mineral Resources in China, 1987. Reference manual of mining industry demands. *Geology Publishing House, Beijing*, 312-315.
- Çelik, Y. 2003. Seyitömer (Kütahya) Neojen Havzası linyitlerinin petrografisi, jeokimyası ve depolanma ortamı. *İ.Ü. Mühendislik Fakültesi, Mühendislik Bilimleri Genç Araştırmacılar I. Kongresi, İstanbul*, 691-700.
- Dikmen, D. 2005. Seyitömer (Kütahya) yöresindeki kömür-bitümlü marn geçişinin organik fasiyeler özellikleri. *Yüksek Lisans Tezi, İstanbul Üniversitesi, Fen.*

- Bil. Ens., Jeoloji Mühendisliği Anabilim Dalı, İstanbul.
- Dyni, J. R. 2003. Geology and resources of some world oil-shale deposits. *Oil Shale* 20, 193-252.
- Ebukanson, E.J., Kinghorn, R.R.F. 1985. Kerogen facies in the major mudrock formations of Southern England and the implication on the depositional environments of their precursors. *Journal of the Petroleum Geology* 8, 435-462.
- Ekinci, E. 2006. Turkish oil shales potential for synthetic crude oil and carbon materials production. International Conference on Oil Shale, Recent Trends in Oil Shale, 7-9 November 2006, Amman, Jordan.
- English, J.M., Fowler, M., Johnston, S.T., Mihalynuk, M.G., Wight, K.L. 2004. The thermal maturity in the Central Whitehorse Trough, Northwest British Columbia. Resource Development and Geosciences Branch, British Columbia Ministry of Energy and Mines, 79-85.
- Ercan, T., Dinçel, A., Metin, S., Türkecan, A., Günay, E. 1978. Uşak yöresindeki Neojen Havzalarının jeolojisi. *Türkiye Jeoloji Kurumu Bülteni* 21, 97-106.
- Espitalie, J., Marquis, F., Barsony, I. 1984. Geochemical logging. In: Analytical pyrolysis: techniques and applications, Voorhees, London. Butterworth and Guildford, 276-304.
- Espitalie, J., Deroo, G., Marquis, F. 1985. La pyrolysis rock-eval applications, *Premiere Partie. Institut Français du Pétrole* 40, 563-579.
- Ghori, K.A.R. 2000. High-quality oil-prone source rocks within carbonates of the Silurian Dirk Hartog Group, Gascoyne Platform, Western Australia. *Geological Survey of Western Australia*, 58-62.
- Ghori, K.A.R. 2002. Modelling the hydrocarbon generative history of the Officer Basin, Western Australia. *PESA Journal* 29, 29-42.
- Gökmen, V., Memikoğlu, O., Dağlı, M., Öz, D., Tuncalı, E. 1993. Türkiye linyit envanteri. Maden Tetkik ve Arama Genel Müdürlüğü Yayını, Ankara, 356.
- Hepbaşlı, A. 2004. Oil shale as an alternative energy source. *Energy Sources* 26(2), 107-108.
- Hou, X.L. 1984. Shale oil industry of China. *Petroleum Industry Press*, 1-28.
- Huang, W.Y., Meinschein, W.G. 1979. Sterols as ecological indicators. *Geochimica et Cosmochimica Acta* 43, 739-745.
- Hufnagel, H. 1989. Investigation of oil shale deposits in Western Turkey. Bundesanstalt für Geowissenschaften und Rohstoffe, Project no.84.2127.3, Hannover, Germany (unpublished).
- Hunt, J.M. 1995. *Petroleum geochemistry and geology*. W. H. Freeman and Company, New York, 743 p.
- Jackson, K.S., Hawkins, P.L., Bennet, A.J.R. 1985. Regional facies and geochemical evaluation of southern Denison Trough. *APEA Journal* 20, 143-158.
- Jarvie, D.M. 1991. Factors affecting rock-eval derived kinetic parameters. *Chemical Geology* 93, 79-99.
- Jones, R.W. 1984. Comparison of carbonate and shale source rocks. In: Palacas, J. (Ed.), *Petroleum Geochemistry and Source Potential of Carbonate Rocks*. AAPG Studies in Geology 18 p.
- Jones, R.W. 1987. Organic facies, In: *Advances in petroleum geochemistry*. Brooks, J. and Welte, D. (eds), Academic Press, London, 2,1-91.
- Jones, R.W., Demaison, G.J. 1982. In proceedings of the second ASCOPE conference and exhibition, Manila, 51-68.
- Kara Gülbay, R. 2004. Kuzeybatı Anadolu'daki bitümlü şeyllerin organik jeokimyasal özellikleri, çökelme ortamları ve hidrokarbon potansiyeli. Doktora Tezi, Karadeniz Teknik Üniversitesi, Fen. Bil. Ens., Jeoloji Mühendisliği Anabilim Dalı, Trabzon.
- Kıratlı, U.Z. 2019. Aslanlı (Kütahya-Seyitömer) sahası Bitümlü şeyllerinin organik jeokimyasal yönden incelenmesi ve hidrokarbon potansiyellerinin belirlenmesi. Yüksek Lisans Tezi, Ankara Üniversitesi, Fen. Bil. Ens., Jeoloji Mühendisliği Anabilim Dalı, Ankara.
- Koralay, D.B. 2009. Bolu Havzası bitümlü şeyllerinin hidrokarbon potansiyeli ve iz element dağılımlarının belirlenmesi. Doktora Tezi, Ankara Üniversitesi, Fen. Bil. Ens., Jeoloji Mühendisliği Anabilim Dalı, Ankara.
- Koralay, D.B. 2018. Geç Miyosen yaşlı Honaz (Denizli) kömürlü birimlerinin organik jeokimyasal özellikleri ve çökelme ortamı. *Pamukkale Üniversitesi Mühendislik Bilimleri Dergisi* 24(6), 1192-1199.
- Kök, M.V., Şengüler, I., Hufnagel, H., Sonel, N. 2001. Thermal and geochemical investigation of Seyitömer oil shale. *Elsevier, Therochimica Acta* 37, 111-119.
- Kök, M.V., Güner, G., Bağcı, S. 2008. Application of EOR techniques for oil shale fields (In situ combustion approach). *Oil shale, Estonia* 25(2), 217-225.
- Langford, F.F., Blanc-Valleron, M.M. 1990. Interpreting rock-eval pyrolysis data using graphs of

- hydrocarbons vs. total organic carbon. AAPG Bulletin 74, 799-804.
- Lebküchner, R.F. 1957. Linyit bulunması muhtemel Ayvalı (Kütahya) sahasında yapılan jeolojik ve madencilikle ilgili etütlerin neticesi hakkında rapor. Maden Tetkik ve Arama Genel Müdürlüğü Rapor No: 2984, Ankara (unpublished).
- Lebküchner, R.F. 1959. Seyitömer (Kütahya) Neojen sahasında jeoloji ve linyit yatakları ile ilgili olarak yapılan etütler hakkında rapor. Maden Tetkik ve Arama Genel Müdürlüğü Rapor No: 2985, Ankara (unpublished).
- Liu, Z.J., Dong, Q.S., Ye, S.Q., Zhu, J.W., Guo, W., Li, D.C., Liu, R., Zhang, H.L., Du, J.F. 2006. The situation of oil shale resources in China. Journal of Jilin University: Earth Science Edition 36(6), 869–876.
- Mello, M.R., Telnaes, N., Gaglianone, P.C., Chicarelli, M.I., Brassell, S.C., Maxwell, J.R. 1988. Organic geochemical characterisation of depositional paleoenvironments of source rock and oils in Brazilian Marginal Basins. In, Advances in Organic Geochemistry 1987 (L. Mattavelli and L. Novelli, eds.), Oxford, Pergamon Press, 31-45.
- Mukhopadhyay, P.K., Wade, J.A., Kruger, M.A. 1995. Organic facies and maturation of Jurassic/Cretaceous rocks, and possible oil-source rock correlation based on pyrolysis of asphaltenes, Scotian Basin, Canada. Organic Geochemistry 22(1), 85-104.
- Murat, A. 2010. Ülkemizde yeni belirlenen petrolü şeyl, şeyl potansiyel rezervi ve yerinde şeyl petrolü üretiminin araştırılması. Maden Tetkik ve Arama Genel Müdürlüğü, Doğal Kaynaklar ve Ekonomi Bülteni 9, 1-7.
- Nebert, K. 1960. Tavşanlı'nın batı ve kuzeyindeki linyit ihtiva eden Neojen sahasının mukayeseli stratigrafisi ve tektoniği. Maden Tetkik ve Arama Genel Müdürlüğü Dergisi 54, 8-35.
- Özburan, M. 2009. Kütahya ve çevresinin Neotektonik incelemesi. Doktora tezi, Kocaeli Üniversitesi, Fen. Bil. Ens., Jeoloji Mühendisliği Anabilim Dalı, Trabzon.
- Peters, K.E. 1986. Guidelines for evaluating petroleum source rock using programmed pyrolysis. The American Association of Petroleum Geologists Bulletin 70(3),318-329.
- Peters, K.E., Cassa, M.R. 1994. Applied source rock geochemistry, in L.B. Magoon and W.G. Dow, eds., The petroleum system from source to trap. AAPG Memoir 60, 93-120.
- Peters, K.E. Moldowan, J.M. 1991. Effects of source, thermal maturity and biodegradation on the distribution and isomerization of homohopanes in petroleum. Organic Geochemistry 17(1), 47-61.
- Peters, K.E., Moldowan, J.M. 1993. The biomarker guide: Interpreting molecular fossils in petroleum and ancient sediments. Englewood Cliffs, N.J.: Prentice-Hall.
- Peters, K.E., Walters, C.C., Moldowan, J.M. 2005. The biomarker guide. Cambridge University Press, V. 1, 471, UK.
- Petersen, H.I., Andersen, C., Anh, P.H., Bojesen-Koefoed, J.A., Nielsen, L.H., Nytoft, H.P., Rosenberg, P., Thanh, L. 2001. Petroleum potential of Oligocene lacustrine mudstones and coals at Dong Ho, Vietnam an outcrop analogue to terrestrial source rocks in the greater Song Hong Basin. Journal of Asian Earth Sciences 19, 135–154.
- Philip R.P., Gilbert T.D. 1986. Biomarker distributions in oil predominantly derived from terrigenous source material. Advances in Organic Geochemistry, Oxford, United Kingdom, Pergamon Press, 73-84.
- Rielely, G., Collier, R.J., Jones, D.M., Eglinton, G. 1991. The biochemistry of Ellesmere Lake, UK I: Source correlation of leaf wax inputs to the sedimentary record. Organic Geochemistry 17, 901-912.
- Sarıyıldız, M. 1987. Seyitömer (Kütahya) kuzeybatısındaki kömürlü Neojen kayalarının jeolojisi. Yüksek Lisans Tezi, Dokuz Eylül Üniversitesi, Fen. Bil. Ens., Jeoloji Mühendisliği Anabilim Dalı, İzmir (unpublished).
- Seifert, W.T., Moldowan, J.M. 1986. Use of biological markers in petroleum exploration. In, Methods in Geochemistry and Geophysics (P. B. Johns, ed.) 24, 261-290.
- Smith, J.T. 1994. Petroleum system logic as an exploration tool in frontier setting, in L. P. Magoon, and W. G. Dow (eds.), The petroleum system from source to trap. AAPG Memoir 60, 25-49.
- Snape, C. 1995. Composition, geochemistry and convention of oil shales. Nato ASI Series, Series C. Mathematical and Physical Sciences, 455, 501 p.
- Stach, E., Mackowsky, M., Teichmüller, M., Taylor, G.H., Chandra, D., Teichmüller, R. 1982. Stach's Textbook of Coal Petrology. Gebrüder Borntraeger, Berlin, 535 p.
- Şener, M., Şengüler, İ. 1992. Seyitömer bitümlü marnların jeolojisi, kullanım olanakları ve akışkan yataкта yakma test sonuçları. Maden Tetkik ve Arama Genel Müdürlüğü Rapor No: 9441, Ankara (unpublished).

- Şener, M., Şengüler, İ., Kök, V. 1995. Geological consideration for the economic evaluation of oil shale deposits in Turkey. Butterworth Heinemann, Britain 74(7), 999-1003.
- Şengüler, İ. 1999. Seyitömer (Kütahya) Petrollü şeyllerin ekonomik kullanım olanaklarının araştırılması. Doktora Tezi, Ankara Üniversitesi, Fen. Bil. Ens., Jeoloji Mühendisliği Anabilimdalı, Ankara.
- Şengüler, İ. 2007. Asfaltit ve bitümlü şeylin Türkiye'deki potansiyeli ve enerji değeri. Türkiye VI. Enerji Kongresi, Ankara.
- Şengüler, İ., Sonel, N., Şener, M. 1998. Seyitömer (Kütahya) bitümlü marnların termik santralde linyit ile birlikte değerlendirilmesi. Türkiye 11. Kömür Kongresi Kitabı, Bartın-Amasra.
- Tao, S., Tang, D.Z., Li, J.J., Xu, H., Li, S., Chen, X.Z. 2010. Indexes in evaluating the grade of Bogda Mountain oil shale in China. Oil Shale 27(2), 179-189.
- Tissot, B.P., Welte, D.H. 1978. Petroleum formation and occurrence, Springer-Verlag, Berlin.
- Tissot, B.P., Welte, D.H. 1984. Petroleum formation and occurrence. Springer-Verlag, Berlin, 699 p.
- Tran, K.L., Philippe, B. 1993. Oil and rock extract analysis, in: Applied petroleum geochemistry (M.L., Bordenave, eds.), Paris.
- Ünalın, G. 1978. Bitümlü şeyllerden enerji hammaddesi olarak yararlanma yolları. Dünya Enerji Konferansı Tebliği, 35-38.
- Van Krevelen, D.W. 1993. Coal. 3rd Edition, Elsevier Science Publishers, Amsterdam.
- Waples, D.W., Machihara, T. 1991. Biomarkers for geologists-A practical guide to the application of steranes and triterpanes in petroleum geology. AAPG Bulletin, Methods in Exploration Series, No: 9.



Bulletin of the Mineral Research and Exploration

<http://bulletin.mta.gov.tr>



Discrimination of earthquakes and quarries in Kula District (Manisa, Turkey) and its vicinity by using linear discriminate function method and artificial neural networks

Aylin TAN^{a*}, Gündüz HORASAN^b, Doğan KALAFAT^c and Ali GÜLBAĞ^d

^aSakarya University, Geophysical Engineering EABD, Institute of Science, Sakarya, Turkey

^bSakarya University, Faculty of Engineering, The Department of Geophysical Engineering, Sakarya, Turkey

^cBoğaziçi University Kandilli Observatory and Earthquake Research Institute, , İstanbul, Turkey

^dSakarya University, Faculty of Computer and Information Sciences, The Department of Computer Engineering, Sakarya, Turkey

Research Article

Keywords:

Manisa, Earthquake, Quarry Blast, Linear Discriminant Function (LDF), Artificial Neural Networks (ANNs).

ABSTRACT

In this study, seismic events in Kula district (Manisa, Turkey) and its vicinity have been investigated and then natural and artificial seismic activities are discriminated. Total of 77 digital vertical component velocity seismograms of seismic activities with $M_L \leq 3.5$ magnitude from seismic activity catalogs between 2009 to 2014 recorded by Manisa Kula (KULA) broadband station operated by Bogazici University, Kandilli Observatory and Earthquake Research Institute Regional Earthquake-Tsunami Monitoring Center (RETMTC) were used in this study. The maximum S-wave and maximum P-wave amplitude ratio (Ratio) of vertical component velocity seismograms and power ratio for (1 and 12 sec.) (Complexity-C) and total signal duration (Duration) of the waveform were calculated. The earthquakes and the quarry blasts have been discriminated using linear discriminant function (LDF) and Back Propagation-Feed Forward Neural Networks (BPNNs) that is one of the learning algorithms at the artificial neural networks (ANNs) methods taking correlation between these parameters into consideration. 39 (51%) of the 77 seismic activities were identified as quarry blasts and 38 (49%) of them as earthquakes. LDF and ANNs methods have been applied together for the first time for Ratio-C, Ratio-logS and Ratio-duration parameter pairs with the data of Manisa and surroundings, and earthquakes and quarry blasts have been distinguished from each other. LDF and ANNs methods were compared for each pair of parameters. Both of two methods are successful but the ANNs method has higher accuracy percentage values than LDF method when there is sufficient number of data. The accuracy percentages are different for a pair of Ratio versus C, for a pair of Ratio versus logS and for a pair of Ratio versus duration, respectively.

Received Date: 20.12.2019

Accepted Date: 24.06.2020

1. Introduction

While seismic recorders record seismic events in a region, they also record artificially induced seismic activities such as mines and quarries along with earthquakes of natural origin. Taking these events together in earthquake catalogs may cause errors in

scientific studies. Therefore, problems may occur in the preparation of earthquake catalogs. In order to determine the real seismic activity in the study areas, earthquakes and quarry blasts should be distinguished from each other. For this differentiation process, it may not be sufficient to use the location, distance and time of occurrence parameters of the area where the blast

Citation Info: Tan, A., Horasan, G., Kalafat, D., Gülbağ, A. 2021. Discrimination of earthquakes and quarries in Kula District (Manisa, Turkey) and its vicinity by using linear discriminate function method and artificial neural networks. Bulletin of the Mineral Research and Exploration 164, 75-92.

<https://doi.org/10.19111/bulletinofmre.757701>

*Corresponding author: Aylin TAN, aylin.tan@ogr.sakarya.edu.tr

is made. In such a case, the waveform of the seismic event should also be examined (Horasan et al., 2006).

So far, about to be distinguished from each other by using different methods of earthquakes and quarry blasts in the world and in Turkey has been much scientific research. Baumgardt and Young (1990) studied the separation of earthquakes and blasts using the P_n / S_n and P_n / L_g ratio method in Western Norway. Dowla et al. (1990), similar to the LDF method, used the ANNs method to distinguish between natural earthquakes and underground nuclear blasts in the United States. Wüster (1993) distinguished earthquakes and explosions with L_g / P_g and L_g / R_g ratio methods in Vogland (Germany-Czechia) region. Horasan et al. (2006; 2009) distinguished earthquakes and explosions in İstanbul with the LDF method. Deniz (2010) in Bursa, Ögütçü et al. (2010) in Konya and Kartal (2010) in Trabzon made the separation analysis of earthquake and quarry blast with Linear Discrimination Method. Kalafat (2010) has distinguished earthquakes and quarry blast with extraction methods in the immediate vicinity of Turkey. Kekovalı et al. (2010; 2012a) have characterized the seismic events with the help of the LDF process in Turkey. Küyük et al. (2011a) conducted earthquake and blast separation analysis in İstanbul using LDF, Quadratic Discrimination Function (QDF), Diaquadratic Discrimination Function (DDF) and Mahalabonis Discrimination Function (MDF) methods. Yılmaz et al. (2013) using the LDF methods have characterized earthquakes and quarry blasts in the Eastern Black Sea region of Turkey. Budakoğlu and Horasan (2018) distinguished earthquakes and explosions in Sakarya province using the LDF method. Yavuz et al. (2018) classified the seismic events in Armutlu by using LDF and QDF methods. Ceydilek and Horasan (2019) have distinguished seismic activities in and around Manisa using the LDF method. In addition to these methods, various ANNs algorithms are used to distinguish earthquakes and blasts from each other. Gitterman et al. (1998) tried to distinguish natural and artificial earthquakes in the Middle East Region from each other by using LDF and ANNs methods. Ursino et al. (2001) developed a direct method in an automated consulting classification to distinguish between earthquakes and blasts in the southeast of Sicily. Del Pezzo et al. (2003) developed a classification in Italy using a consulting learning algorithm based on multiple

neural network (MCN) structure. Küyük et al. (2009) tried to distinguish natural and artificially induced earthquakes in the İstanbul region using the reaction surface, multivariate regression and Learning Vector Quantization (LVQ) methods. Küyük et al. (2010; 2011b) tried to distinguish earthquakes and explosions from each other with the Self-Organizing Map (SOM) method in İstanbul. Yıldırım et al. (2011) studied the separation of natural and artificial earthquakes using Feedback ANNs (BPNNs), Matched Neural Fuzzy Logic Inference Systems (ANFIS) and Probabilistic Neural Networks (PNN) algorithms. Kekovalı et al. (2012b) made a segregation analysis with data mining application in Tuncbilek-Kutahya region. Kundu et al. (2012) used seismograms to distinguish between local earthquakes and chemical explosions recorded on the Gauribidanur Road in India, using an ANNs method known as the "Back Propagation Network", known as the Multilayer Artificial Neural Network (MLP). Küyük et al. (2012) used K-mean, Gaussian Mixing Model (GMM), LDF and Quadratic Discrimination Function (QDF) methods and ANNs algorithms to distinguish earthquakes and explosions with high accuracy in İstanbul. Hammer et al. (2013) classified seismic events, which they divided into three classes as earthquakes, blasts and rock falls, with the help of ANNs method according to the records in the Swiss Alps. Kortström et al. (2016) distinguished natural and artificial earthquakes in Finland using the Support Vector Machine (SVM) method. Mousavi et al. (2016) used a machine learning technique to investigate the relationship between the seismic properties and the location of the focal centers where the events belong to the signals recorded in the time, frequency and time-frequency domain in the United States. Kaftan et al. (2017) have calculated the monthly frequency of earthquakes in western Turkey by using multilayer neural network (MLP), Radial Basic Function ANNs (RBFYS), and compatible Neural Fuzzy Logic Inference Systems (ANFIS) methods. In addition, many researchers have studied using LDF and ANNs methods together or separately (Çetin et al., 2006; Gülbağ, 2006; Üstün, 2009a, b, c, Üstün and Yıldız, 2009; Küyük et al., 2009; Yıldırım et al., 2011; Çayakan, 2012, Yıldırım, 2013).

In this study, the distribution of seismic activities in and around Manisa and the location of the KULA station are shown in figure 1. GMT program was used for drawing the maps (Wessel and Smith, 1995). Most

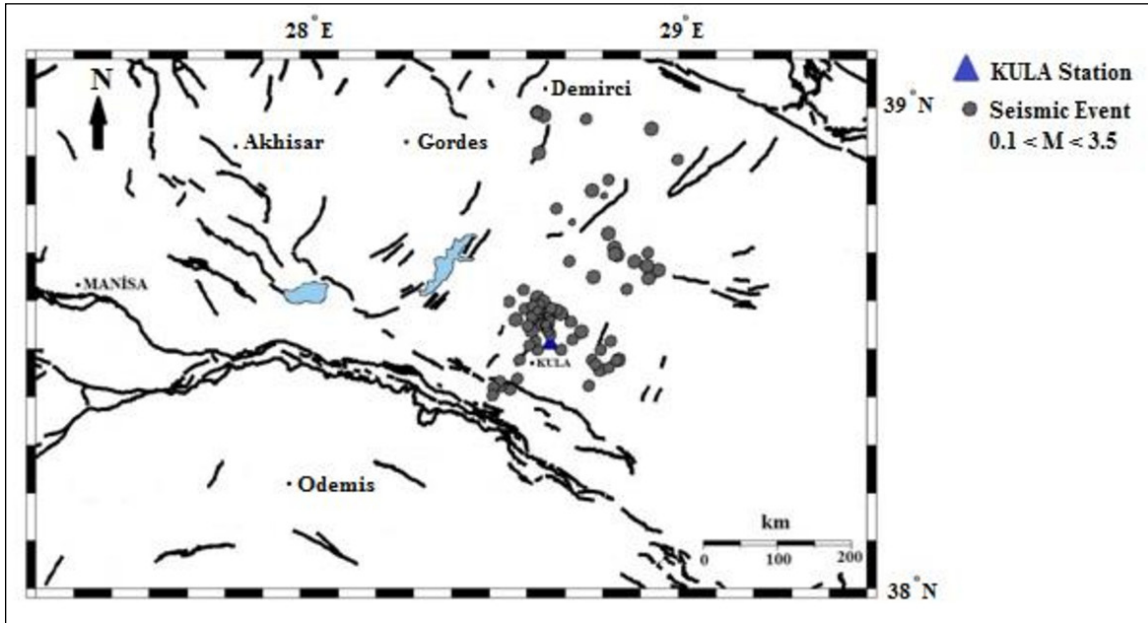


Figure 1- The distribution of seismic events with $M_L \leq 3.5$ that occurred between May 2009 and February 2014 in the study area and the location of the KULA station (KRDAE, BDTİM). The faults were taken from Şaroğlu et al. (1992) and Emre et al. (2013).

of the artificially sourced blasts recorded in the study area originate from the mines and quarries operated in the region to obtain mining and construction materials. The aim of this study is to distinguish the blasts in Kula (Manisa) and its surroundings from earthquakes using LDF and ANNs methods, using the numerical vertical component velocity seismograms recorded at the KULA station between May 2009 and February 2014. Thus, correct information can be used in seismicity studies. In addition, reliable data will be obtained in the creation of earthquake catalogs in earthquake research centers. Thus, contribution will be made to the preparation of catalogs containing natural seismic activity in the region. In this case, the amount of error will be significantly reduced in the determination of active faults, seismic risk studies and studies involving seismic activity in the region.

2. Data Acquisition

In this study, the numerical vertical component velocity seismograms of 77 seismic events with magnitude $M_L \leq 3.5$ recorded at the KULA station between May 2009 and February 2014 in the region between latitudes 38° - 39.30° N and longitudes 28° - 29.30° E were examined. The data were taken from Bogazici University Kandilli Observatory and Earthquake Research Institute (KRDAE,

BDTİM). The Manisa-Kula (KULA) station, which is broadband, was established on January 15, 2007 (Figure 1). Digital data were recorded at 50 samples per second.

When the distribution of the total number of seismic activities in the study area and only the number of earthquake activities according to the occurrence time is plotted, the histogram obtained is shown in figure 2.

While earthquakes and blasts are distinguished from each other, it is not sufficient to compare them only by day and time. Therefore, vertical component velocity seismogram and spectrum are used since these show significant differences in distinguishing quarry blast and earthquake data from each other. When the blast seismogram was examined, it was seen that the P-wave amplitude was higher than that of the earthquake. It is also observed that the direction of the first movement on the signal is upwards (Figure 3). The frequency contents of seismic events used in this study are shown in figure 4. Spectral corrugation is observed on the detonation spectrum when looking at figure 4. This is due to the delayed arrival of wave energy to the station during quarry blasts. Although the waveform and spectrum are used to visually distinguish earthquakes and explosions, the parameters obtained from them are compared in

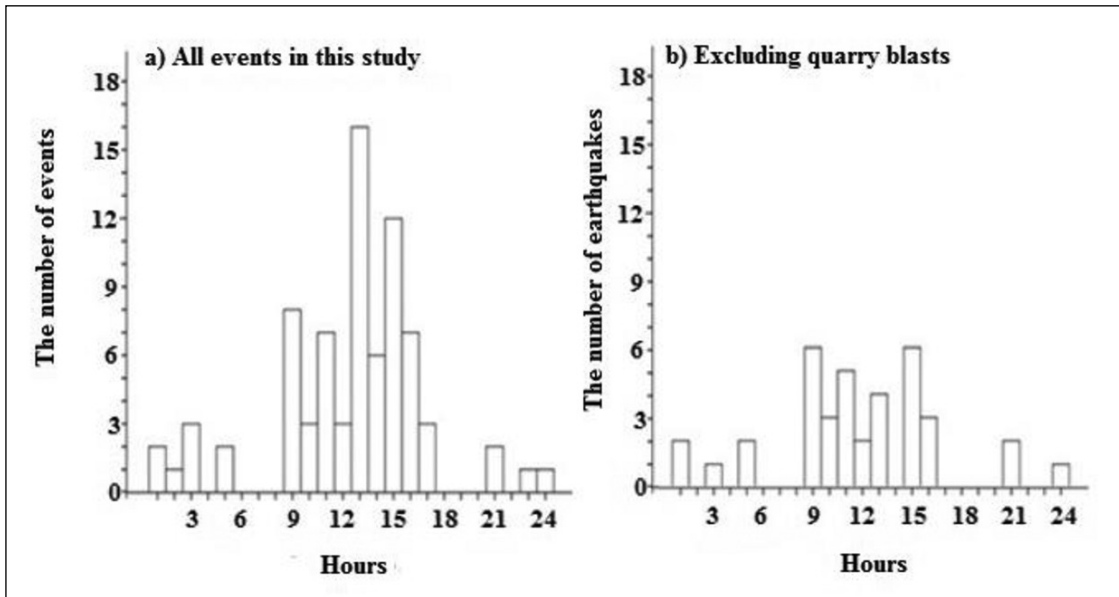


Figure 2- The distribution of the number of seismic activities (occurrences) in each hour (UTC) between 38-39.30°N and 28-29.30°E, May 2009-February 2014 in the study area. a) During the day, maximum activity is observed at 13:00 and a large increase in the number of events is observed between 13:00 and 15:00, b) Distribution of the number of earthquakes after the events determined as quarry blast as a result of this study were eliminated.

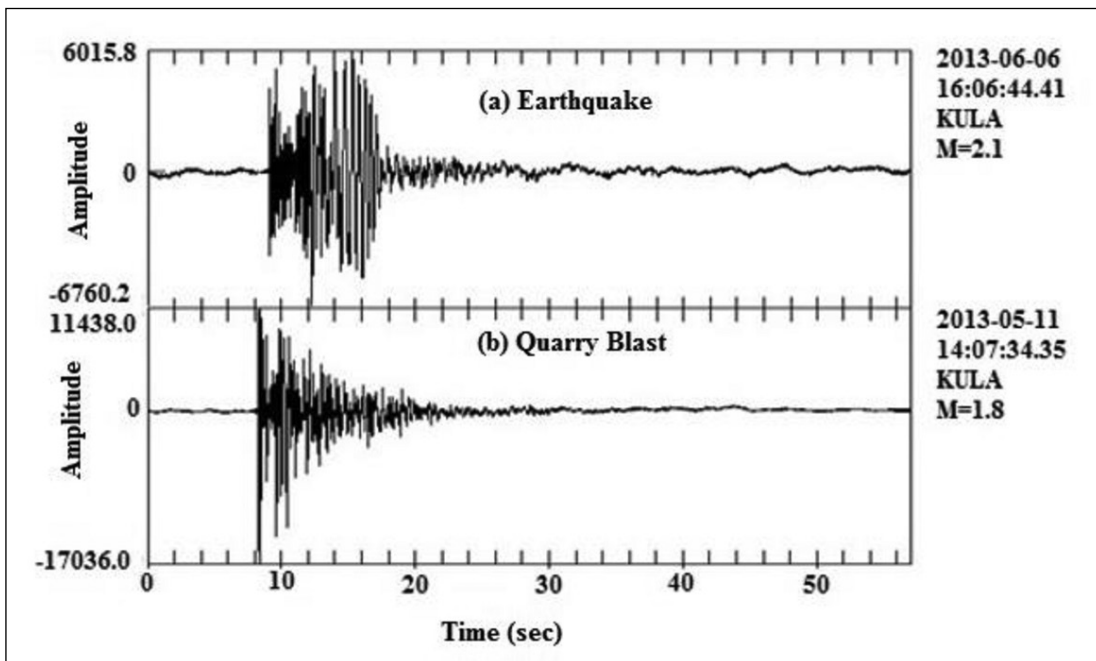


Figure 3- Vertical component velocity seismogram recorded at KULA station; (a) Earthquake, (b) Quarry Blast.

practice. Therefore, different parameter pairs will be calculated and the distribution between these parameter pairs will be examined.

In order to obtain the parameters, the ratio of the maximum S-wave amplitude to the maximum

P-wave amplitude of the vertical component velocity seismograms, the ratio of their complexities (Complexity-C) and the total signal duration of the waveform were calculated. These parameters are described below.

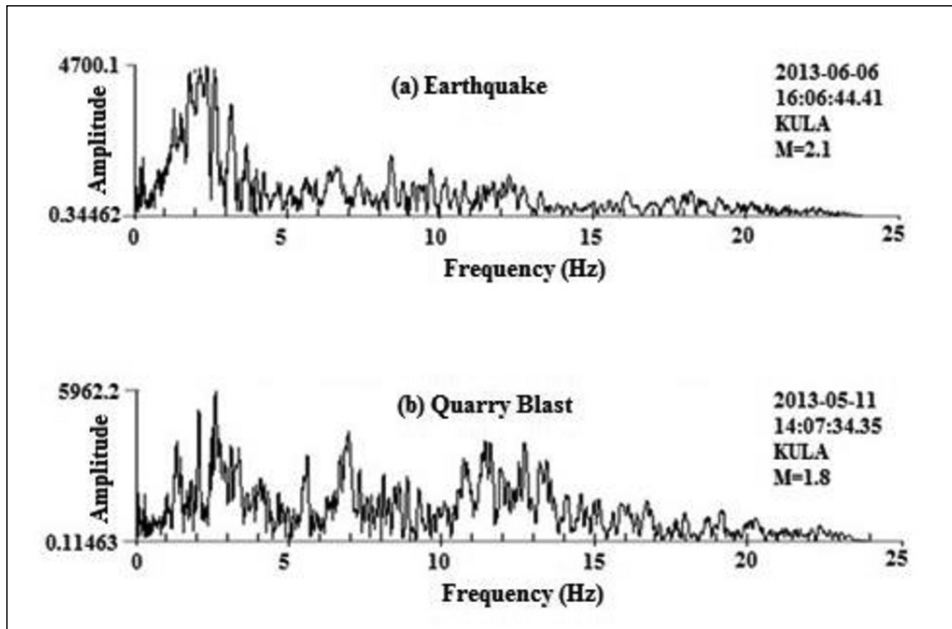


Figure 4- Normalized amplitude spectrum of the signal recorded at the KULA station; (a) Earthquake, (b) Quarry Blast.

2.1. Calculating the Ratio (C) of the Powers of the Two Time Windows Defined in the Seismogram

The ratios of the vertical component velocity seismograms for each seismic event, i.e. the complexity (C), are calculated according to the equation 1 below (Arai and Yosida, 2004).

$$C = \frac{\int_{t_1}^{t_2} S^2(t)dt}{\int_{t_0}^{t_1} S^2(t)dt} \quad (1)$$

where

- t_0 is expressed as arrival time of the P wave
- t_1 and t_2 are expressed as time window range.

In this study, t_1 and t_2 values are taken as 1 and 12 seconds for the KULA station, respectively. The 1-second time window is based on the P wave signal. The second time window is determined by considering the time difference $t_s - t_p$ of events at different distances used in the study.

2.2. Calculation of Amplitude Ratio (S / P Maximum Amplitude Ratio, Ratio)

After defining the maximum P-wave and maximum S-wave amplitudes from the vertical component velocity seismograms of earthquakes and blasts, the S / P maximum amplitude ratio (Ratio) for seismic events was calculated.

2.3. Defining Total Signal Duration (Duration)

The duration parameter is determined from the duration of the signal. After these parameters were calculated, normalization process as [-1, +1] was applied to the data set. The reason for this is to provide ease of establishing relationships between parameters. According to Patro and Sahu (2015), normalization process is shown in equation 2:

$$A^* = \left(\frac{A - \text{Maximum value of } A}{\text{Maximum value of } A - \text{Minimum value of } A} \right) * (E - D) + D \quad (2)$$

A*: Maximum-Minimum normalized data

[D, E]: Predefined border

A: Original data set

For [-1, +1]; D = -1 and E = +1

After the data set was normalized, LDF and ANNs methods were applied to distinguish earthquakes and explosions using the parameters described above.

3. Methods

3.1. Linear Discrimination Function (LDF) Method

LDF method is used to distinguish different data groups from each other (Fisher 1936). Linear

Discrimination Functions are generally shown in equation 3 in a simplified form:

$$F_{LDF} = a + b_1X_1 + b_2X_2 + \dots + b_mX_m \quad (3)$$

a: Constant number

b_1, \dots, b_m : Regression coefficients

X_1, \dots, X_m : normalized values of discrimination parameters.

Using the vertical component velocity seismograms of the KULA station in the study area, the ratio of the maximum S-wave amplitude to the maximum P-wave amplitude is plotted against the ratio (C) of the powers of the two time windows defined in the seismogram. In this graph (Figure 5a) earthquakes and explosions are

distinguished from each other by linear discrimination function. For this, Statistical Package Program of Social Sciences (SPSS, 2005) was used.

For the LDF method, the amplitude ratio versus logS and signal duration graphs are shown in figure 5b, c. The accuracy percentage results and diagnoses obtained by the LDF method for each parameter pair (Ratio-C, Ratio-logS and Ratio-Duration) of the data set belonging to KULA are shown in table 1.

3.2. Artificial Neural Networks (ANNs) Method

Seismic events in the region were also distinguished from each other by the method called Artificial Neural Networks (ANNs). According to Gülbağ (2006), the

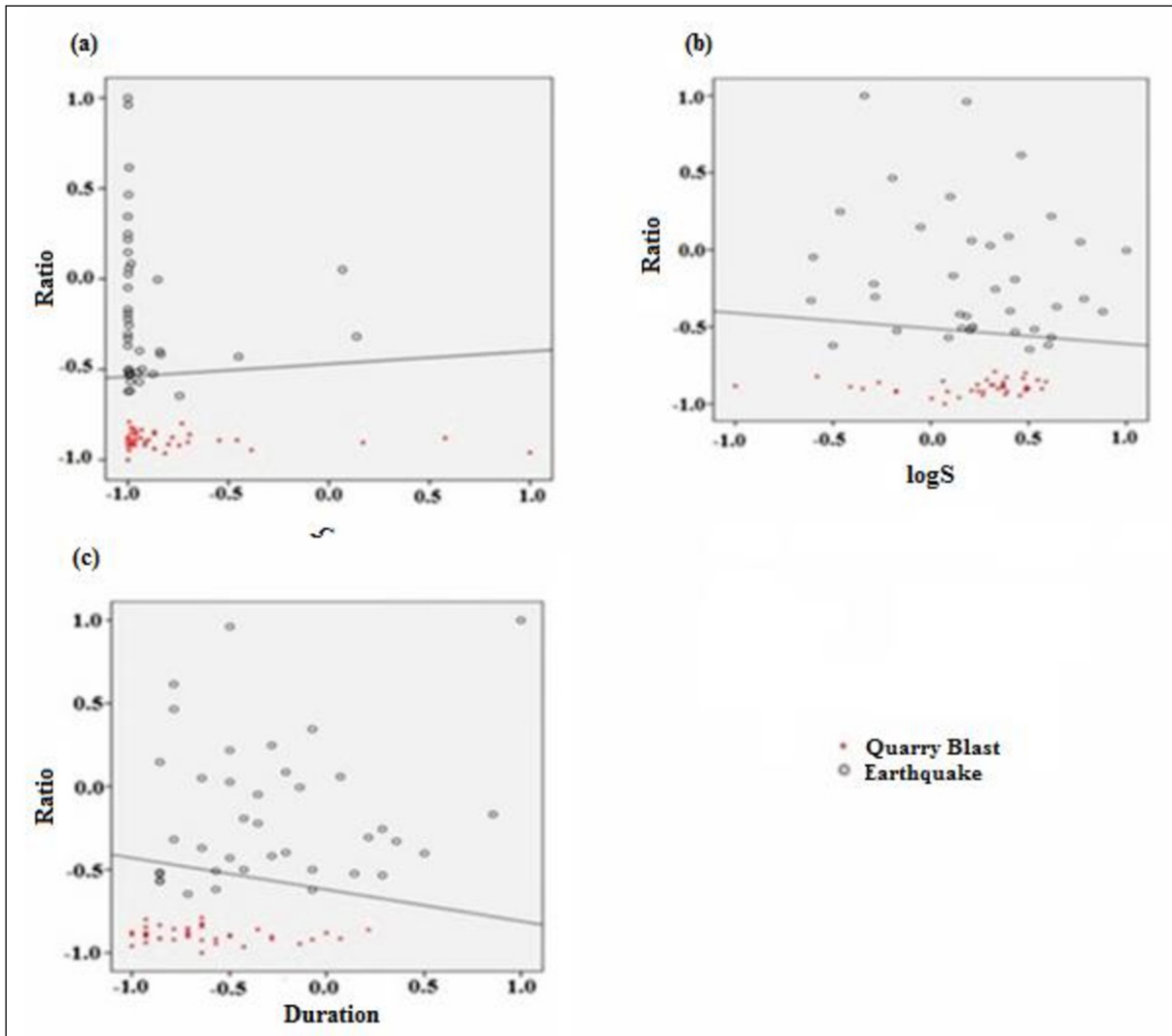


Figure 5- Percent accuracy values obtained by LDF method according to parameter pairs for KULA data. (a) 94% for Ratio-C parameter pair, (b) 93.5% for ratio-logS parameter pair and (c) 89.6% for Ratio-Duration parameter pair.

Table 1- Distinguishing seismic events recorded at Kula station by LDF method. Criteria: 1: The accuracy percentage obtained for the Ratio-C parameter pair is 94%; 2: The accuracy percentage obtained for the ratio-logS parameter pair is 93.5% and 3: The accuracy percentage obtained for the Ratio-Duration parameter pair is 89.6%.

Criteria		Classification	Predicted group		Total
			Quarry Blast (QB)	Earthquake (E)	
1	Total Number	Quarry Blast	39	0	39
		Earthquake	5	33	38
	%	Quarry Blast	100	0	100
		Earthquake	13.2	86.8	100
2	Total Number	Quarry Blast	39	0	39
		Earthquake	5	33	38
	%	Quarry Blast	100	0	100
		Earthquake	13.2	86.8	100
3	Total Number	Quarry Blast	39	0	39
		Earthquake	8	30	38
	%	Quarry Blast	100	0	100
		Earthquake	21.1	78.9	100

human brain is a complex system consisting of nerve cells called neurons and the connections between them. Neurons communicate with each other through these connections. ANNs learning algorithms are inspired by human nervous system architecture. According to Yıldırım (2013), after determining the problem, while deciding to train the network; "Unsupervised learning" with only inputs and "supervised learning" with input-output pairs are taken into account according to the type of learning. Choosing the learning algorithm that will train the artificial neural network is very important. There are different learning algorithms such as ANFIS (Compatible Neural Fuzzy Logic Inference Systems), LVQ (Learning Vector Quantization), BFNNs (Feedback ANNs), PNN (Probabilistic ANNs), BPNNs (Backpropagation - Feed Forward ANNs), MLP (Multi Layered ANNs) and RBFYSA (Radial Basic Function ANNs) (Çetin et al., 2006; Gülbağ, 2006; Küyük et al., 2009; Üstün, 2009a, b, c; Üstün and Yıldız, 2009; Yıldırım et al., 2011; Çayakan, 2012; Yıldırım, 2013; Kaftan et al., 2017).

3.2.1. Back Propagation - Feed Forward Anns (Bpnn) Learning Algorithm

The learning algorithm used in this study was selected as Back Propagation-Feed Forward Neural Networks. The reason for this is that it is a solution to our problem and it is a reliable learning algorithm because it is widely used (Çetin et al., 2006; Gülbağ, 2006; Küyük et al., 2009; Üstün, 2009a, b, c; Üstün and Yıldız, 2009; Yıldırım et al., 2011; Çayakan,

2012; Yıldırım, 2013; Kaftan et al., 2017). This algorithm got this name because it tries to reduce errors backwards, ie from output to input (Çetin et al., 2006). This network structure is simple and although it gives a lot of correct results, it is a slow learning algorithm (Çayakan, 2012). The weights according to the amount of error between the desired output and the actual value are arranged with this learning algorithm to obtain the most appropriate output values (Yıldırım, 2013). After deciding on the learning algorithm, the network topology, ie architecture, of the artificial neural network was created. In general, the elements of the network topology are shown as in figure 6 (Gülbağ, 2006).

After the learning algorithm is determined according to the type of the problem, a network structure in the form of input layer, hidden layer and output layer is created. In general, the elements of the network topology are defined as inputs, outputs, weights, sum function, activation (Transfer) function (Rumelhart et al., 1986). Entries are information entering the cell from other cells or external environments, and enter the cell over the weights on the connections. The weights (w) determine the effect of the relevant input on the cell (Figure 6).

In this study, the artificial neural network represents the feed forward artificial neural network according to its structure and the counseling learning according to the learning algorithm. In the artificial neural network model that we have determined

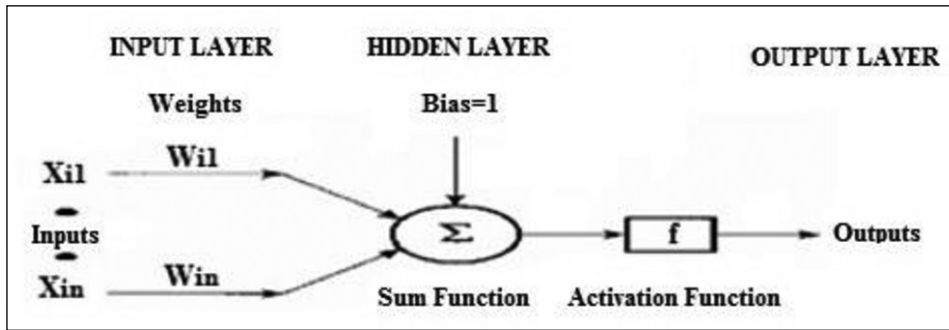


Figure 6 - Elements of network topology (Gülbağ, 2006).

according to our problem, in the learning algorithm applied to the network topology we have created, the artificial neural network is given both input values and output values that must be produced in response to this input, consulting learning has been applied according to the learning algorithm. In addition, the parameter pair to be tested was used as the input parameter to the system, and the diagnosis as the output parameter. These parameter pairs are, respectively, the ratio of the maximum S wave amplitude to the maximum P wave amplitude (Ratio) and the power ratio (C) (Figure 7a), the ratio of the maximum S wave amplitude to the maximum P wave amplitude (Ratio) and the logarithm of the maximum S wave amplitude ($\log S$) (Figure 7b) and the amplitude ratio (Ratio) of the maximum S wave to the maximum P wave and the total signal duration (Duration) of the waveform (Figure 7c).

3.2.2. Choosing the Number of Neurons (N_n)

While creating an artificial neural network topology, the choice of the number of neurons (N_n) is of great importance on the learning process (Gülbağ, 2006). The same researcher emphasized that the number of neurons is of great importance to achieve generalization. In general, a very small number of neurons normally causes less learning, ie poor learning, while an excessive number of neurons indicates that it can lead to over learning, or memorization. The problem of finding an optimal network architecture complicates the solution because each unique architecture has its own unique set of suitable parameters (Kermani et al., 2005). The choice of the number of neurons is very important in ANNs as it is one of the determining factors in distinguishing data groups. Using less than necessary number of neurons in the hidden layer results in less sensitive output than input data. Likewise, if more neurons are

used than necessary, difficulties arise in processing new types of data groups within the same network (Çetin et al., 2006). While creating the structure of the ANNs, the number of neurons (N_n) is decided by trial and error method (Yıldırım, 2013; Kaftan et al., 2017).

At the stage of determining the appropriate model, the number of neurons in a certain range, with a certain amount of increase is given to the algorithm, and then the artificial neural network model is selected with the highest percentage of accuracy (Gülbağ, 2006). In the literature, researchers have determined the number of neurons in increasing values with different number intervals. Gülbağ (2006) created ANNs models with the number of neurons increasing by 10 between 0 and 100. Küyük et al. (2009) compared the models with an increasing number of intermittent neurons increasing by 1 from 1 to 20 in their study and created an artificial neural network model with 5 neurons with the least error, that is, the best result. Yıldırım (2013) created ANNs topology with the number of neurons increasing by 2 between 0 and 22. Kaftan et al. (2017) created their own network network models by using the number of neurons increasing by 1 between 1 and 6.

In this study, before the application of the ANNs Method, the models with the number of neurons in increasing intervals of 5 from 1 to 25 were compared. Then, the number of neurons ($N_n = 10$ for Ratio-C, $N_n = 5$ for Ratio- $\log S$, $N_n = 5$ for Ratio-Duration) was determined for both parameter groups that were different from each other. An artificial neural network model has been created with the least error, that is, the number of neurons that give the best result. Training continued until the determination coefficient (R^2) approached 1. When the value of the determination coefficient (R^2) approaches 1, it actually means the

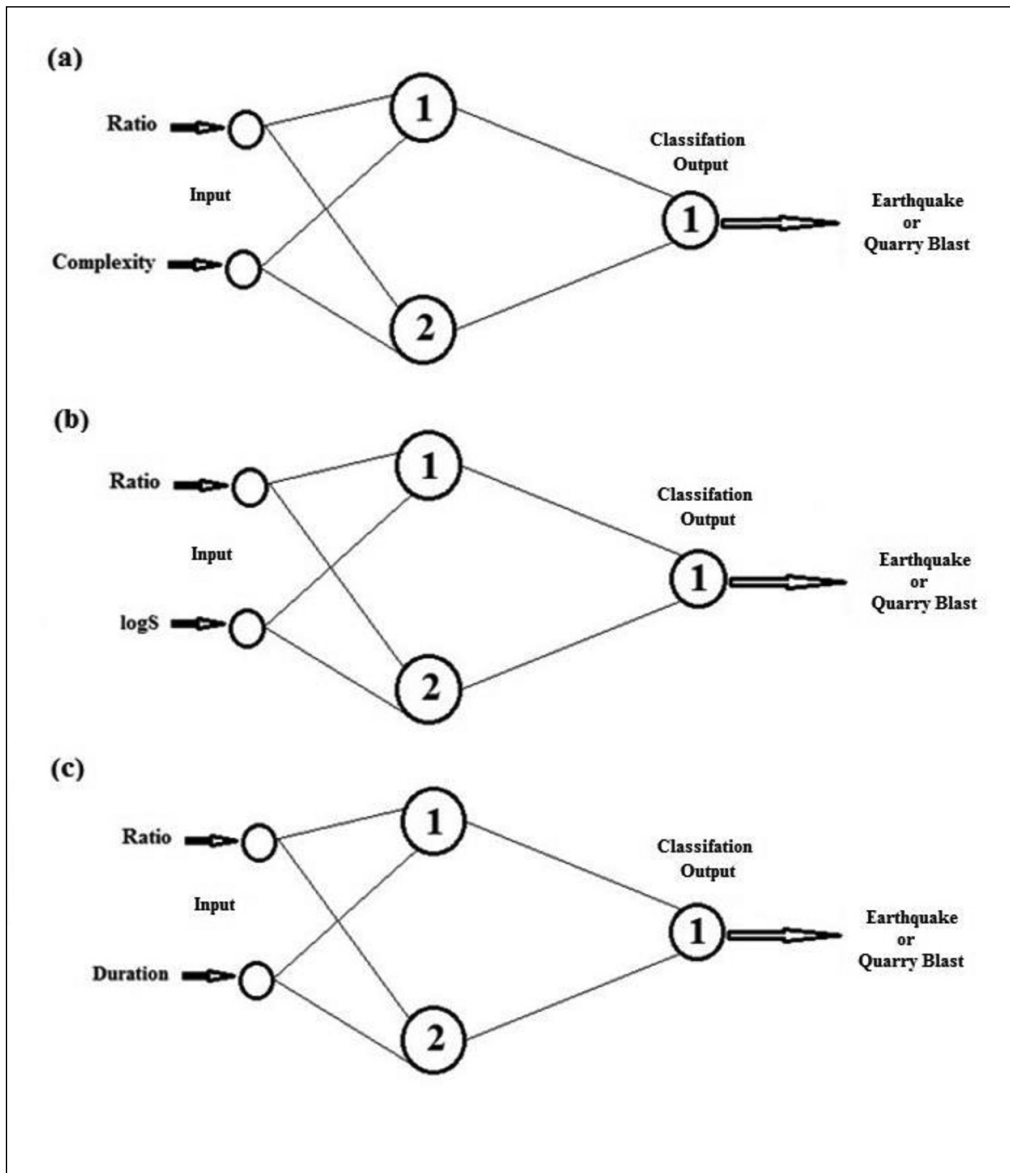


Figure 7- Artificial neural network structure for seismic events a) ratio versus C, b) ratio versus logS, c) ratio versus duration.

stopping criterion. At the same time, this means that the learning algorithm is successful for these parameters on the network structure created. Once the proper value has been obtained, the network has been tested.

Since it is necessary to decide on the number of neurons first, the number of neurons obtained in the following table (Table 2) is obtained by trial and error method. While creating an artificial neural network suitable for the problem in this study, the obtained

Table 2- The change of the total number of data and its relation with the Number of Neurons (Nn) for the parameter pairs belonging to the Manisa study area. Parameter pair for all data set belonging to KULA station Criteria: 1: Ratio-C, 2: Ratio-logS, 3: Ratio-Duration.

Criteria	ANNs (%) Nn:5	ANNs (%) Nn:10	ANNs (%) Nn:15	ANNs (%) Nn:20	ANNs (%) Nn:25
1	88	100	100	88	100
2	100	100	100	96	96
3	100	100	100	100	100

accuracy percentage values are shown in table 2 against the number of neurons determined for each parameter pair.

Since the number of neurons is decided according to the accuracy percentage values in the ANNs method, the number of neurons in the situation with the highest accuracy percentage value is selected. But if the accuracy percentage values are equal, the lowest value of the number of neurons is taken. This is because the artificial neural network model is desired to be less complex (Gülbağ, 2006). Therefore, Nn: 10 for the Ratio-C parameter pair, and Nn: 5 for Ratio-logS and Ratio-Duration parameter pairs were selected according to the ANNs method.

In addition, the training algorithm used in this study is Levenberg-Marquardt and the activation function is Tangent-Sigmoid activation function. Application of Levenberg-Marquardt ANNs learning has been explained in some studies (Hagan and Menhaj, 1994; Kermani et al., 2005). This algorithm (up to several hundred weights) has been shown to be the fastest method for advanced feed-forward ANNs learning. At the same time, the effective representation of the function in matrix form, as in the MATLAB programming language, offers an important solution in some studies (Charrier et al., 2007; Matlab, 2011).

With the help of MATLAB programming language "nntool", ANNs model with inputs, weights and activation function was developed and Levenberg-Marquardt was chosen as the training algorithm (Levenberg, 1944 and Marquardt, 1963) (Matlab, 2011) since this training algorithm has an important role in the functioning of this process. Kipli et al. (2012) also used the Levenberg-Marquardt training algorithm in their studies.

For the network architecture determined in this study, the hyperbolic tangent sigmoid activation function, also known as the tangent sigmoid activation function, is used. Tangent-Sigmoid, $\varphi(v)$, describes the neuron output with respect to the local induced v field. In fact, this activation function assumes a continuous function in the value range from -1 to +1. Therefore, the activation function expresses the positive function of the induced local area, as seen in equation 4.

$$\varphi(v) = \begin{cases} 1 & \text{if } v > 0 \\ 0 & \text{if } v = 0 \\ -1 & \text{if } v < 0 \end{cases} \quad (4)$$

This function is shown in combination as a sign function. For the corresponding form of the sigmoid function, the hyperbolic tangent sigmoid function was used in the form as shown below:

$$\varphi(v) = \tanh(v) \quad (5)$$

The hyperbolic tangent sigmoid activation function takes positive and negative values as indicated in equation 5 (Haykin, 2009).

Therefore, the hyperbolic tangent function, which was examined at the beginning, is used for values that provide input to all output layers except output layer. The hyperbolic tangent sigmoid activation function is defined as in equation 6.

$$\varphi(v) = \frac{2}{1+e^{(-2v)}} - 1 \quad (6)$$

In equation 6, $\varphi(v)$ is "Hyperbolic tangent sigmoid activation function". The change of the function is [-1 1] and this function varies according to the total input and the number of neurons. (Gradshteyn and Ryzhik, 2007).

3.2.3. Preparation of Data Set for ANNs Network Topology

After the number of neurons is determined, data sets of inputs and outputs are started to be arranged. After the normalization process, a new data set is created by randomly selecting a certain percentage of the data as training data and the rest as test data from the whole data set. Similarly, Kermani et al. (2005) randomly selected their data in their study. The reason for this is that the training data is trained with the learning algorithm used in ANNs and the training is completed when the determination coefficient (R^2) value approaches 1. The reason for continuing the ANNs process with test data is to provide the rule that "The designed artificial neural network has learned the learning algorithm with training data, so it can test its knowledge with test data". Then, the obtained results are compared with the test outputs and the accuracy percentage is calculated.

Different researchers prepared data sets using different percentage values to distinguish between training data and test data. Ursino et al. (2001) used 50% of the data set as training set and the other 50% as test data. Gülbağ (2006) created the ANNs data set as 84% training data and 16% test data in his study. Yıldırım et al. (2011) organized 25% of the data set as training and 75% as test data in their study, in accordance with their own problems. Kundu et al., (2012) allocated 51% of their data as training data and 49% as test data. In addition, Yıldırım (2013) divided 80% into training data and 20% as test data by selecting random data from the data set in his study. Kaftan et al. (2017) separated 85% of their data as training data and the remaining 15% as test data.

In this study, random data was selected from the whole data set belonging to the KULA station, and 70% of the data was divided into training data and 30% as test data. In this case, since all data is 77, training data is 53 and test data is 24.

In addition, reasonable results were obtained by applying the k-fold cross validation method (James et al., 2017) to the data. Thus, by obtaining reasonable results similar to the high accuracy percentages obtained by the ANNs method, the ANNs method was once again verified.

Each pair of parameters used in the LDF method is also used in the second method, the ANNs method, to distinguish earthquake and quarry blast data.

The determination coefficient (R^2) values corresponding to the number of neurons (Nn) values determined by ANNs method for ratio versus C, ratio versus logS and ratio versus duration values in Manisa are given in table 3. It is seen in this table that the R^2 values are different for each parameter pair. When R^2 values are close to 1, it can be said that the created artificial neural network structure is successfully created according to these parameter pairs. The R^2 values seen in table 3 are accepted as a stopping criterion for the feed-back learning algorithm that we use in this study. It shows that when the R^2 value approaches 1, the predicted artificial neural network structure has been successfully learned. The number of neurons (Nn) is designed to increase by 5 between 5 and 25 (Table 3).

R values alone are not sufficient to decide the number of neurons (Nn) representing the model, they are only a stopping criterion. Accuracy percentages of ANNs models corresponding to these neuron numbers selected with the help of table 3 are shown in table 4.

Accordingly, it was found that the accuracy percentage values obtained by the ANNs method were high and this method was also successful. In addition, the numbers of earthquakes and quarry blast in the training and test data of KULA data are shown in table 5.

For ANNs method, amplitude ratio versus complexity (C), logS and signal duration values are given in figure 8a, b, c.

Table 3- The change in the relationship between the coefficient of determination (R^2) and the number of neurons (Nn) for the parameter pairs belonging to the Manisa study area. Parameter pair for the data set of the Kula station Criteria: 1: Ratio-C, 2: Ratio-logS, 3: Ratio-Duration.

Criteria	Determination Coefficient				
	Nn:5	Nn:10	Nn:15	Nn:20	Nn:25
1	0.96	1	1	0.96	1
2	1	1	1	0.93	0.93
3	1	1	1	1	1

Table 4- The change of the number of incorrectly defined earthquakes and quarry blasts with the number of data in the training and test data set for the whole data set of the KULA station using the ANNs method, and the percentage of accuracy.

Criteria	Station	Total Number of Data	Number of Data in the Training Set	Number of Data in the Test Set	Misclassified Earthquake (ME)	Misclassified Quarry Blast (MQB)	ANNs (%)
1	KULA	77	53	24	0	0	100
2	KULA	77	53	24	0	0	100
3	KULA	77	53	24	0	0	100

Table 5- Number of training and test data modeled for the KULA region. The accuracy percentages obtained from the classification of the data set of the KULA station (Criteria 1: Ratio-C, 2: Ratio-logS, 3: Ratio-Duration) using the ANNs method are respectively 100%, 100% and 100%.

Criteria	Station	Total Number of Data	Training Data Set*			Test Data Set**		
			Number of Data in the Training Set	Earthquake (E)	Quarry Blast (QB)	Number of Data in the Test Set	Earthquake (E)	Quarry Blast (QB)
1	KULA	77	53	31	22	24	19	5
2	KULA	77	53	31	22	24	19	5
3	KULA	77	53	31	22	24	19	5

Training Data Set* = Training Set; Test Data Set ** = Test Set

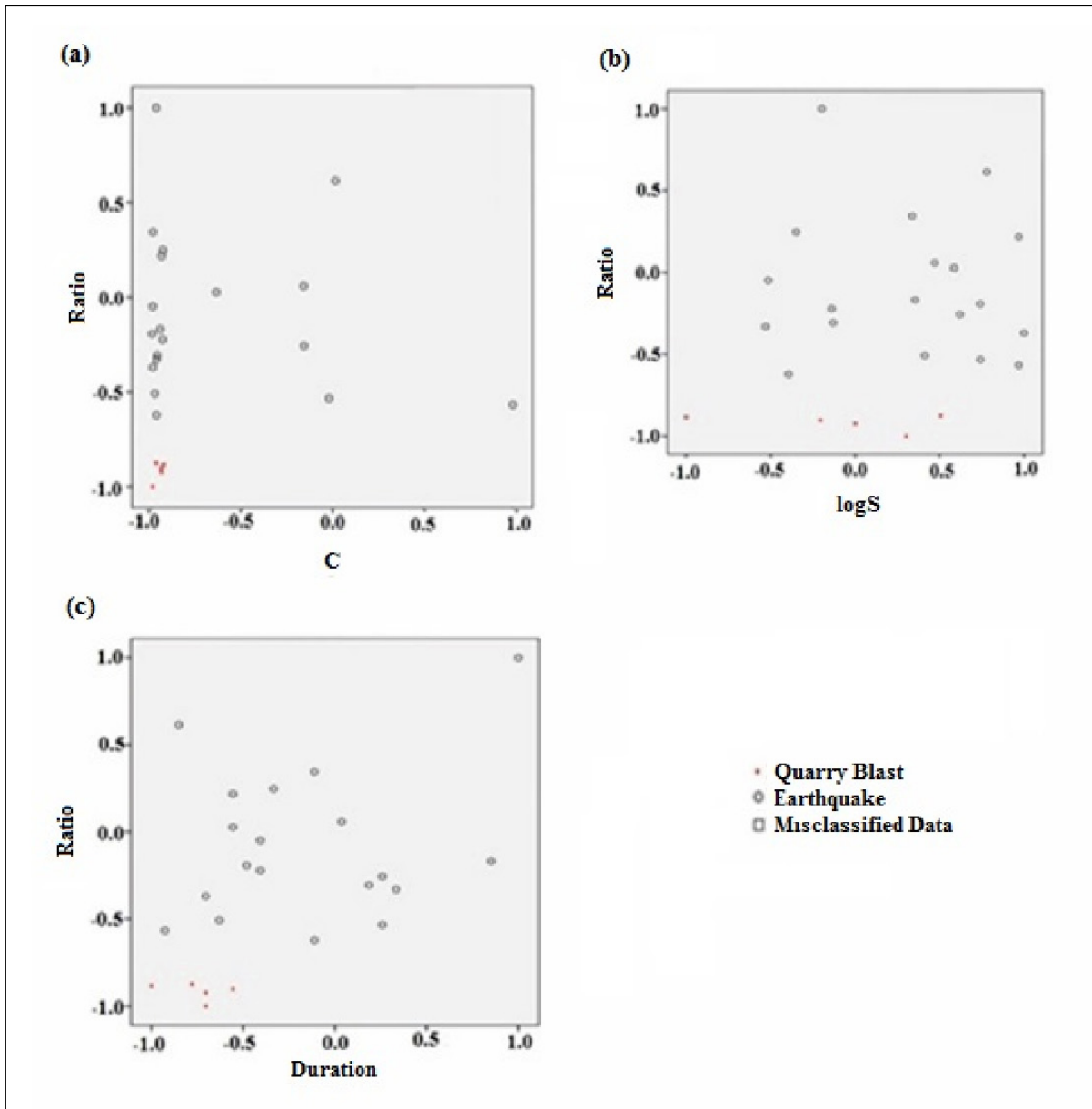


Figure 8- Accuracy percentage values obtained by ANNs method according to parameter pairs for KULA data. (a) 100% for ratio-C parameter pair; (b) 100% for ratio-logS parameter pair and (c) 100% for the Ratio-Duration parameter pair.

The accuracy percentage of the method was calculated by testing the data prepared with the help of MATLAB software (Matlab, 2011). ANNs method was applied for each parameter pair (C against Ratio, log S against Ratio and Duration against Ratio) and accuracy percentages were obtained for each. In addition, the number of neurons for Ratio versus C was taken as 10, for Ratio versus log S as 5, and for Ratio versus Duration, as 5. Accuracy percentages obtained from LDF and ANNs methods are given in table 6.

4. Results and Discussion

In this study, while LDF and ANNs methods were applied to the data in Manisa region for the first time, earthquakes and blasts were distinguished from each other. In order to distinguish earthquake and quarry blast events, 77 seismic events with $M_L \leq 3.5$ magnitude recorded at KULA station between May 2009 and June 2013 in the region between latitudes 38-39.30°N and longitudes 28-29.30°E were examined.

From the vertical component velocity seismograms recorded in the KULA station in the study area, parameters such as the ratio of the maximum S-wave amplitude to the maximum P-wave amplitude, the ratio of the strengths of the two time windows defined in the seismogram (C) and the signal duration (Duration) are determined, and their relationship with each other is examined by LDF and ANNs methods.

The results obtained by LDF and ANNs method for each parameter pair (Ratio-C, Ratio-logS and Ratio-Duration) of the data set belonging to KULA are given in table 6. In both methods, earthquakes and explosions were determined with high accuracy percentages.

As a result of the study, 39 (51%) of the 77 seismic events examined were determined as quarry blasts and 38 (49%) as earthquakes (Figure 9).

Table 6- Comparison of accuracy percentage values according to LDF and ANNs methods for the data set of KULA station (Criteria: 1. Ratio-C, 2. Ratio-logS, 3. Ratio-Duration).

Criteria	Method	Percentage of Accuracy (%)
1	LDF	94
	ANNs	100
2	LDF	93.5
	ANNs	100
3	LDF	89.6
	ANNs	100

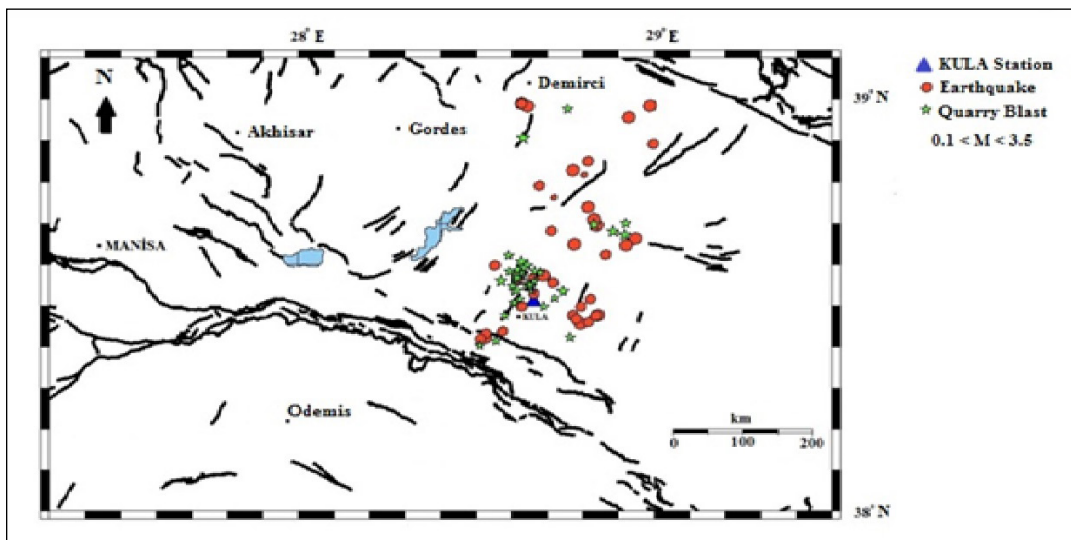


Figure 9- Earthquakes and blasts, $M_L \leq 3.5$, occurred in the study area between May 2009 and February 2014. The KULA station is marked with a blue triangle (KRDAE, BDTIM).

In this study, it was understood that the number of neurons is a very important criterion for ANNs. The reason for this is that the number of neurons directly affects the results in the creation of the artificial neural network topology. This shows that if the number of neurons is correctly decided during the preliminary study before the ANNs method is applied, the accuracy percentage value will be higher. In addition, when the ANNs method is applied, when the determination coefficient (R^2) value approaches 1 during training, the training is stopped and then, the test is started and information about the learning process is provided. In other words, the determination coefficient is a stopping criterion.

Comparing the differentiation accuracy percentages obtained by LDF and ANNs for different parameter pairs, it is seen that both methods are successful in distinguishing earthquakes and blasts from each other, but the ANNs method is more successful than the LDF method (Figure 5a, b, c, figure 7a, b, c; table 6).

In addition, when international and Turkish scientific studies are examined, it is seen that LDF and ANNs methods are frequently used to distinguish blasts from earthquakes in different study regions. Ceydilek and Horasan (2019) used the LDF method at four stations (AKHS, BLN, CAM and KTT) to distinguish earthquakes and explosions in the Manisa region. The accuracy percentages for the Ratio-logS parameter pair obtained from the events recorded by each of the AKHS, BLN, CAM and KTT stations are 94.4%, 95.8%, 90.0%, 93.2%, respectively. The accuracy percentages for the Ratio-Duration parameter pair obtained from the events recorded by the same stations are 91.2%, 89.6%, 91.4%, 88.6%, respectively. In this study, 94%, 93.5% and 89.6% accuracy values were obtained with the LDF method for Ratio-C, Ratio-logS and Ratio-Duration parameter pairs, respectively. It is seen that the results obtained from this study are compatible with the results obtained by Ceydilek and Horasan (2019) in Manisa region.

In addition, the LDF method is one of the most popular and successful methods used in earth sciences to distinguish between natural and artificial seismic events. Horasan et al. (2009) obtained the accuracy

percentage values with the Ratio-logS parameter pair for İstanbul-Gaziosmanpaşa, Çatalca, Gebze-Hereke, and İstanbul-Ömerli regions as 98.6%, 93.8%, 97.7% and 95.8%, respectively. Yılmaz et al. (2013) defined the accuracy percentage values as 96.3%, 89.3%, 100%, 100%, 96.5% and 100% for KTUT, ESPY, BAYT, PZAR, GUMT and BCA stations in Trabzon, respectively. Badawy et al. (2019) applied the LDF method to the Ratio versus logS values in Egypt, and the accuracy percentages for AYT, MYD and GLL stations were 91.7%, 83.7% and 83.2%, respectively. By applying the same method to Spectral Ratio values against C for the same study, Badawy et al. (2019) obtained the accuracy percentages as 95.7%, 98% and 98.4% for AYT, MYD and GLL stations, respectively. These values show that the method gives successful results. The accuracy percentages of the parameters may vary depending on the number of data, geological features and local ground effects.

ANNs method has also been used for about the last decade to distinguish natural and artificial seismic events from each other. Yıldırım et al. (2011) used three methods to distinguish natural and artificial seismic events in and around İstanbul. They achieved 99% accuracy with Back Propagation - Feed Forward ANNs (BPNNs), 97% accuracy with Probabilistic Artificial Neural Networks (PNN) and 96% accuracy with Fuzzy Logic Systems (ANFIS). In this study, the accuracy percentage values obtained by using the BPNNs learning algorithm with the ANNs method applied for the KULA station and its vicinity is 100% for each pair of parameters. In other words, accuracy percentage values close to each other were obtained. In this study, the BPNNs learning algorithm preferred in the ANNs method has been quite successful in distinguishing seismic events from each other.

In addition, the determination coefficient (R^2) values corresponding to the number of neurons (N_n), which are important in the ANNs method - 0.96 and 1 for the Ratio-C parameter pair, 0.93 and 1 for the Ratio-logS parameter pair, and 1 for the Ratio-Duration parameter pair - was obtained at different value ranges for all neuron count values ranging from 25 to 5 increments (Table 3). This situation indicates that the BPNNs learning algorithm used in the artificial neural network architecture created in this study is successful on these parameters.

In addition, if we compare the results obtained with LDF and ANNs methods with each other, 94% in LDF method and 100% in ANNs method for Ratio-C parameter pair; for the ratio-logS parameter pair, 93.5% in the LDF method and 100% in the ANNs method; for the Ratio-Duration parameter pair, 89.6% accuracy was obtained in the LDF method and 100% in the ANNs method.

In the LDF method, 39 of the 39 quarry blast events were determined as quarry blast in Table 1 for the Ratio-C parameter pair. Of the 38 events defined as earthquakes, 33 of them were earthquakes and 5 of them were quarry blasts. Thus, earthquakes and explosions were distinguished from each other with 94% accuracy with the LDF method. For the ratio-logS parameter pair, 39 of 39 blasts were determined as blasts with the LDF method. Of the 38 events defined as earthquakes, 33 were determined as earthquakes and 5 were quarry blasts (Table 1). The accuracy percentage in the LDF method for this parameter pair is 93.5%. For the Ratio-Duration parameter pair, the accuracy percentage value obtained by the LDF method is 89.6%. These accuracy percentage values show that the method is successful.

Accuracy percentage was evaluated by using only test data with ANNs method. The reason for this is to test the success of the learning algorithm used on the artificial neural network model. Accordingly, 19 of the 24 test data for each parameter pair were correctly identified as earthquakes and the remaining 5 as quarry blast. Thus, earthquakes and explosions were distinguished from each other with 100% accuracy by ANNs method. These results show that the ANNs method distinguishes earthquakes and explosions with high accuracy. Comparing the two methods with each other, both methods are very successful in distinguishing earthquakes and explosions from each other. In this application, it is seen that the ANNs method is more successful than the LDF method.

Studies to distinguish earthquakes and blasts from each other are important for seismicity studies in seismology. By correctly distinguishing earthquakes and blasts, it will contribute to the preparation of seismic catalogs with only earthquakes and therefore to more accurately determining active faults and seismic risk studies in the region. As in the relation proposed by Gutenberg and Richter (1949) given below,

$$\text{Log}N=a-bM \quad (7)$$

coefficients a and b can be found. In this relation, a and b are constant coefficients. While b -value is the slope of the line obtained by plotting the logarithm of the number corresponding to the magnitude, the coefficient a is where the line intersects the $\text{Log}N$ axis (Bayrak et al., 2013). With the help of these coefficients, the correct determination of the linear relationship between the numbers and magnitudes of earthquakes occurring in a certain area will provide correct results. In fact, by applying the linear regression method to calculate the Gutenberg-Richter (1949) relation for each seismic source zone in Kızılbüğa (2016) study, a and b parameters were obtained in the study area. Thus, by estimating the maximum acceleration values of earthquakes that may occur in that region, the earthquake hazard map of the region was obtained. Therefore, in the light of our study, parameters a and b , which will be determined correctly, will contribute to the preparation of earthquake hazard maps of a region.

Acknowledgements

During the preparation of this study, we would like to express our gratitude to the employees of Boğaziçi University Kandilli Observatory and Earthquake Research Institute Regional Earthquake-Tsunami Monitoring Center who shared data on the seismic events of the KULA station.

References

- Arai, N., Yosida, Y. 2004. Discrimination by short-period seismograms. International Institute of Seismology and Earthquake Engineering, Building Research Institute (IISEE), Lecture Note, Global Course, Tsukuba, Japan.
- Badawy, A., Gamal, M., Farid, W., Soliman, M.S. 2019. Decontamination of earthquake catalog from quarry blast events in northern Egypt. *Journal of Seismology* 23, 1357–1372.
- Baumgardt, D.R., Young, G.B. 1990. Regional seismic waveform discriminants and case-based event identification using regional arrays. *Bulletin Seismological Society of America* 80 (Part B), 1874–1892.
- Bayrak, Y., Bayrak, E., Yılmaz, Ş., Türker, T., Softa, M. 2013. En büyük olasılık yöntemi kullanılarak Batı Anadolu'nun farklı bölgelerinde aletsel dönem için deprem tehlike analizi. 2. Türkiye Deprem

- Mühendisliği ve Sismoloji Konferansı, 25-27 Eylül 2013 – MKÜ – Hatay, Türkiye, 1-7.
- Budakoğlu, E., Horasan, G. 2018. Classification of seismic events using linear discriminant function (LDF) in the Sakarya region. Turkey, *Acta Geophysica* 66, 895-906.
- Ceydilek N., Horasan G. 2019. Manisa ve Çevresinde Deprem ve Patlatma Verilerinin Ayırt Edilmesi, *Türk Deprem Araştırma Dergisi* 1(1), 26-47.
- Charrier, C., Lebru, G., Lezoray, O. 2007. Selection of features by a machine learning expert to design a color image quality metrics. 3rd Int. Workshop on Video Processing and Quality Metrics for Consumer Electronics (VPQM) 113-119, Scottsdale, Arizona.
- Çayakan, Ç. 2012. Estimation of partial saturation to be induced in liquefiable sands for mitigation using artificial neural network approach. Yüksek Lisans Tezi, İstanbul Teknik Üniversitesi Fen Bilimleri Enstitüsü İnşaat Mühendisliği EABD Deprem Mühendisliği Bilim Dalı, İstanbul, 117 s.
- Çetin, M., Uğur, A., Bayzan, Ş. 2006. İleri beslemeli yapay sinir ağlarında Backpropagation algoritmasının sezgisel yaklaşımı. IV. Bilgelik ve Akademik Bilişim 2006 Sempozyumu, 9-11 Şubat 2006, Denizli, Turkey.
- Del Pezzo, E. D., Esposito, A., Giudicepietro, F., Marinaro, M., Martini, M., Scarpetta, S. 2003. Discrimination of Earthquakes and Underwater Explosions Using Neural Networks. *Bulletin of the Seismological Society of America* 93, 1, pp. 215-223.
- Deniz, P. 2010. Deprem ve patlatma verilerinin birbirinden ayırt edilmesi. Yüksek Lisans Tezi, Sakarya Üniversitesi Fen Bilimleri Enstitüsü Jeofizik Mühendisliği EABD, Sakarya, 64 s.
- Dowla, F., Taylor, S. R., Anderson, R. W. 1990. Seismic discrimination with artificial neural networks: Preliminary results with regional spectral data. *Bulletin of the Seismological Society of America* 80 (5), 1346-1373.
- Emre, Ö., Duman, T.Y., Özalp, S., Elmacı, H., Olgun, S., Şaroğlu, S. 2013. Active Fault Map of Turkey with Explanatory Text. General Directorate of Mineral Research and Exploration, Special Publication Series 30 Ankara, Turkey.
- Fisher, R. A. 1936. The use of multiple measurements in taxonomic problems. *Annals of Human Genetics* 7 (2), 179-188.
- Gitterman, Y., Pinsky, V., Shapira, A. 1998. Spectral classification methods in monitoring small local events by the Israel seismic network. *Journal of Seismology* 2, 237-26.
- Gradshteyn, I.S., Ryzhik, I.M. 2007. Table of integrals, series, and products. Academic Press, Seventh Edition, pp. 28-35.
- Gutenberg, B., Richter, C. F. 1949. Seismicity of the earth and associated phenomenon, Princeton University Press, Princeton, New York.
- Gülbağ, A. 2006. Yapay sinir ağı ve bulanık mantık tabanlı algoritmalar ile uçucu organik bileşiklerin miktarsal tayini. Doktora Tezi, Sakarya Üniversitesi Fen Bilimleri Enstitüsü Elektrik-Elektronik Mühendisliği EABD, Sakarya 165 s.
- Hagan, M.T., Menhaj, M. 1994. Training feed-forward networks with the Marquardt algorithm. *IEEE Transactions on Neural Networks* 5(6): 989-99.
- Hammer, C., Ohrnberger, M., Fah, D. 2013. Classifying seismic waveforms from scratch: a case study in the alpine environment. *Geophys. J. Int. Seismology* 192: 425-439.
- Haykin, S. 2009. *Neural Networks and Learning Machines*. Third Edition, Pearson Prentice Hall Press, 14, ISBN: 9780131471399.
- Horasan, G., Boztepe-Güney, A., Küsmezer, A., Bekler, F., Ögütçü, Z. 2006. İstanbul ve civarındaki deprem ve patlatma verilerinin birbirinden ayırt edilmesi ve kataloglanması. Proje Sonuç Raporu, Proje No: 05T202, Boğaziçi Üniversitesi Araştırma Fonu, 45 s.
- Horasan, G., Boztepe-Güney, A., Küsmezer, A., Bekler, F., Ögütçü, Z., Musaoğlu, N. 2009. Contamination of seismicity catalogs by quarry blasts: An example from İstanbul and its vicinity, northwestern Turkey. *Journal of Asian Earth Sciences* 34, 90-99.
- James, G., Witten, D., Hastie, T., Tibshirani, R. 2017. An introduction to statistical learning with application in R. 7. Baskı, Springer Yayınları, sy. 801.
- Kaftan, I., Salk, M., Senol, Y. 2017. Processing of earthquake catalog data of Western Turkey with artificial neural networks and adaptive neuro-fuzzy inference system. *Arabian Geophysical Geosciences* 10:243.
- Kalafat, D. 2010. Türkiye'de Depremlerin Magnitüd-Frekans Uzaysal Dağılımı ve Deprem Kataloğundan Taş Ocağı - Maden Ocağı Patlatmalarının Ayıklanması. Aktif Tektonik Araştırma Grubu 14. Çalıştay Bildiri Özleri Kitabı 3-6 Kasım 2010, Adıyaman 27 p.
- Kartal, Ö. F. 2010. Trabzon ve civarındaki deprem ve patlatma verilerinin birbirinden ayırt edilmesi. Yüksek Lisans Tezi, Sakarya Üniversitesi Fen Bilimleri Enstitüsü Jeofizik Mühendisliği EABD, Sakarya 43 s.

- Kekovalı, K., Kalafat, D., Deniz, P., Kara, M., Yılmaz, M., Küsmezer, A., Altuncu, S., Çomoğlu, M., Kılıç, K. 2010. Detection of Potential Mining and Quarry Areas in Turkey Using Seismic Catalog, 19. Türkiye Uluslararası Jeofizik ve Sergisi, 23-26 Kasım 2010, Poster, Ankara, Turkey.
- Kekovalı, K., Kalafat, D., Deniz, P. 2012a. Spectral discrimination between mining blasts and natural earthquakes: Application to the vicinity of Tunçbilek mining area, Western Turkey. *International Journal of Physical Sciences* 7(35), 5339-5352.
- Kekovalı, K., Kalafat, D., Deniz, P., Kara, M., Köseoğlu, A., Yılmaz, M., Poyraz, S., Çomoğlu M. 2012b. Patlatma Deprem Ayırımına Yönelik Zaman-Frekans Ortamı Analizleri; Tunçbilek-Kütahya Sahası Veri Madenciliği Uygulaması. ATAG 16 Çalıştayı, 18-19 Ekim 2012, İstanbul, p. 29.
- Kermani, B.G., Schiffman, S.S., Nagle, H.G. 2005. Performance of the Levenberg–Marquardt neural network training method in electronic nose applications. *Science Direct, Sensors and Actuators B: Chemical* 110(1):13-22.
- Kızılbuğa, S. 2006. Isparta ilinin olasılıksal yöntem ile sismik tehlikesinin tahmini. Yüksek Lisans Tezi, Sakarya Üniversitesi Fen Bilimleri Enstitüsü Jeofizik Mühendisliği EABD, Sakarya 47 s.
- Kipli, K., Muhammad, M.H., Masra, S.M.W., Zamhari, N., Lias, K., Mat, D.A.A. 2012. Performance of Levenberg-Marquardt Backpropagation for full reference hybrid image quality metrics. *Proceedings of the International MultiConference of Engineers and the Computer Scientists IMECS2012*, 1, March 14-16, 2012, Hong Kong.
- Kortström, J., Uski, M., Tiira, T. 2016. Automatic classification of seismic events within a regional seismograph network. *Computers and Geosciences* 87:22-30.
- Kundu, A., Bhaduria, Y. S., Roy, F. 2012. Discrimination between earthquakes and chemical explosions using artificial neural networks, Scientific Information Resource Division, BHABHA Atomic Research Centre Technical Report, BARC/2012/E/004, Mumbai, India.
- Küyük, H. S., Yıldırım, E., Horasan, G., Doğan, E. 2009. Deprem ve taş ocağı patlatma verilerinin tepki yüzeyi, çok değişkenli regresyon ve öğrenmeli vektör nicemleme yöntemleri ile incelenmesi. *Uluslararası Sakarya Deprem Sempozyumu*, 1-3 Ekim 2009, Kocaeli 1-10.
- Küyük, H.S., Yıldırım, E. Doğan, E., Horasan, G. 2010. Self organizing Map Approach for discrimination of seismic event and quarry blasts in the vicinity of İstanbul. 14th European Conference on earthquake engineering, 30 August-3rd September 2010, Ohrid-Republic of Macedonia.
- Küyük, H.S., Yıldırım, E. Doğan, E., Horasan, G. 2011a. An unsupervised learning algorithm: application to the discrimination of seismic events and quarry blasts in the vicinity of İstanbul. *Natural Hazards of Earth System Sciences* 11, 93-100.
- Küyük, H.S., Yıldırım, E. Doğan, E., Horasan, G. 2011b. Clustering seismic activities using nonlinear discriminant analysis. *Sixth International Conference of Seismology and Earthquake Engineering*, 16-18 May 2011, Tehran-Iran.
- Küyük, H.S., Yıldırım, E. Doğan, E., Horasan, G. 2012. Application of k-means and Gaussian mixture model for classification of seismic activities in İstanbul. *Nonlinear Processes in Geophysics* 19, 411-419.
- Levenberg, K. 1944. A method for the solution of certain non-linear problems in least squares. *Quart Appl Math* 2:164-168.
- Marquardt, D.W. 1963. An Algorithm for Least-Squares Estimation of Nonlinear Parameters. *Journal of the Society for Industrial and Applied Mathematics* 11(2): 431-441.
- Matlab, 2011. Version 7.11.0 (R2011a), Natick, Massachusetts: The Math Works Inc.
- Mousavi, S.M., Horton, S.P., Langston, C.A., Samei, B. 2016. Seismic features and automatic discrimination of deep and shallow induced-microearthquakes using neural network and logistic regression. *Geophys. J. Int.* 207: 29–46.
- Öğütçü, Z., Horasan, G., Kalafat, D. 2010. Investigation of microseismic activity sources in Konya and its vicinity, central Turkey. *Natural Hazards* 58 (1), 497-509.
- Patro, K.S.G., Sahu, K.K. 2015. Normalization: A Preprocessing Stage, India (08/05/2019) arXiv:1503.06462.
- Rumelhart, D.E., Hinton, G.E., Williams, R.J. 1986. Learning internal representations by error propagation. In D. Rumelhart, D.L. and McClelland, J.L. eds, Vol 1, Chapter 8, Cambridge, MA: MIT Press.
- Spss, 2005. V.17.0 for Windows. SPSS (Statistical Package for the Social Sciences): Increments.
- Şaroğlu, F., Emre, Ö., Kuşçu, İ. 1992. Active fault map of Turkey. Publication of General Directorate of Miner. Res. Explor. Inst. Turkey, Ankara.
- Ursino, A., Langer, H., Scarfi, L., Grazia, G.D., Gresta, S. 2001. Discrimination of quarry blasts from

- tectonic earthquakes in the Iblean platform (Southeastern Sicily). *Annali di Geofisica* 44-4, 703-722.
- Üstün, O. 2009a. Genetik algoritma kullanılarak ileri beslemeli bir sinir ağında etkinlik fonksiyonlarının belirlenmesi. *Pamukkale Üniversitesi Mühendislik Bilimleri Dergisi* 15 (3), 395-403.
- Üstün, O. 2009b. Measurement and real-time modeling of inductance and flux linkage in switched reluctance motor., *IEEE Transactions on Magnetics* 45 (12), 5376-5382.
- Üstün, O. 2009c. A nonlinear full model of switched reluctance motor with artificial neural network. *Energy Conversion and Management* 50, 2413-2421.
- Üstün, O., Yıldız, İ. 2009. Geri-yayılmalı öğrenme algoritmasındaki öğrenme parametrelerinin genetik algoritma ile belirlenmesi. *Süleyman Demirel University International Technologic Science* 1(2), 61-73.
- Yavuz, E., Sertçelik, F., Livaoğlu, H., Woith, H. Lühr, B. G. 2018. Discrimination of quarry blasts from tectonic events in the Armutlu Peninsula, Turkey. *Journal of Seismology* 23 (1), 59-76.
- Yıldırım, E. 2013. Sismik dalgaların sönüm karakterinden zemin özelliklerinin belirlenerek sınıflandırılması. Doktora Tezi, Sakarya Üniversitesi Fen Bilimleri Enstitüsü Jeofizik Mühendisliği EABD, Sakarya, 176 s.
- Yıldırım, E., Gülbağ, A., Horasan, G., Doğan, E. 2011. Discrimination of quarry blasts and earthquakes in the vicinity of İstanbul using soft computing techniques. *Computers and Geosciences* 37, 1209-1217.
- Yılmaz, Ş., Bayrak, Y., Çınar, H. 2013. Discrimination of earthquakes and quarry blasts in the eastern Black Sea region of Turkey. *Journal of Seismology* 17 (2), pp. 721-734.
- Wessel, P., Smith, W.H.F. 1995. New version of the generic mapping tools (GMT) Version 3.0 released, *Transactions. American Geophysical Union* 76, 329.
- Wüster, J. 1993. Discrimination of chemical explosions and earthquakes in central Europe-a case study. *Bulletin of Seismological Society of America* 83, 1184-1212.



Bulletin of the Mineral Research and Exploration

<http://bulletin.mta.gov.tr>



Clay mineralogy and paleoclimatic properties of the Neogene Deposits in Sinanpaşa Basin (Afyon-Western Anatolia)

Elif AKISKA^{a*} and Zehra KARAKAŞ^b

^aAnkara University, Faculty of Engineering, Department of Geological Engineering, Ankara, Turkey

^bAnkara University, Faculty of Engineering, Department of Geological Engineering, Ankara, Turkey

Research Article

Keywords:

Neogene, Afyon,
Clay mineralization,
Paleoclimate, Smectite.

ABSTRACT

The Sinanpaşa basin, one of the Neogene basins formed in the extensional tectonic regime in Western Anatolia, is located on the eastern margin of Western Anatolia basins containing different types of evaporites, lignite, uranium and clay minerals. Miocene sequence was initiated with alluvial fan-fluvial units and followed by lacustrine sediments. River floodplains and lakeshore marshes locally contain economic coal levels. Since middle-late Miocene, the products of Afyon volcanism were deposited into a subaerial or a subaqueous environment alternating with lake sediments. Dominant clay minerals are illite and smectite within the sediments coexistence with the volcanics. These minerals were accompanied by chlorite, kaolinite, and zeolite in some samples. Feldspar, dolomite, thenardite, and gypsum are locally observed too. Sepiolite mineral enrichments are also noteworthy in shallow-coastal lacustrine environments where organic matter is abundant. Clay minerals are mostly detritic and developed due to the weathering of volcanoclastics and sedimentary rocks in temperate/humid climatic conditions. In particular, smectite and kaolinite minerals were formed in situ/ authigenic under subaqueous conditions due to the acidic/basic character of tuffs. As a result, different clay mineral types have been developed due to the mineralogical composition of source rocks, climatic factors (humid/semi-humid, arid), paleotopography, depositional environment and diagenetic factors.

Received Date: 18.12.2019

Accepted Date: 22.03.2020

1. Introduction

Extruding of Anatolian block to the west caused E-W directional compression, and then N-S directional extension in Western Anatolia (Şengör and Yılmaz, 1981; Koçyiğit, 1984; Robertson and Dixon, 1984; Şengör et al., 1985; Savaşçın and Güleç, 1990; Zanchi et al., 1993; Seyitoğlu et al., 1997; Yılmaz et al., 2000; Koçyiğit and Deveci, 2007; Ersoy et al., 2011; Prelevic et al., 2012). Due to the extensional tectonic regime, NW-SE, NE-SW and E-W directional Neogene graben basins have been formed in Western

Anatolia (Savaşçın et al., 1994; Bozkurt, 2003). Most of these Neogene graben basins are associated with significant economic deposits. Among these, lignite (eg Çanakkale-Çan, Muğla-Yatağan, Manisa-Soma, Kütahya-Tunçbilek, Seyitömer), evaporite (eg Balıkesir-Bigadiç, Sultançayırı, Bursa-Kestelek, Kütahya-Emet, Eskişehir-Kırka) and uranium (Manisa-Köprübaşı, Uşak-Fakılı, Aydın-Söke) deposits are the main ones. Miocene stratigraphy in all these basins was generally initiated with alluvial fan and fluvial deposits, and followed upward with

Citation Info: Akiska, E., Karakaş, Z. 2021. Clay Mineralogy and Paleoclimatic Properties of the Neogene Deposits in Sinanpaşa Basin (Afyon-Western Anatolia). Bulletin of the Mineral Research and Exploration 164, 93-117.
<https://doi.org/10.19111/bulletinofmre.707988>

*Corresponding author: Elif AKISKA, egunen@eng.ankara.edu.tr

Neogene lacustrine sediments (eg; Kaya, 1981; Helvacı and Alaca, 1991; Helvacı and Yağmurlu, 1995; Akal, 2003, 2008; Ersoy et al., 2008; Karaoğlu et al., 2010; Helvacı et al., 2017). In addition, these basins have been exposed to a strong volcanism under extensional tectonic conditions since late Cenozoic (Borsi et al., 1972; Keller and Villari, 1972; Ercan et al., 1978; Ercan, 1979; Başarı and Kun, 1982; Çevikbaş et al., 1988; Yılmaz, 1989, 1990; Savaşçın, 1990; Savaşçın and Güleç, 1990; Aydar and Bayhan, 1995; Floyd et al., 1998; Savaşçın and Oyman, 1998; Francalanci et al., 2000; Aldanmaz et al., 2000; Yılmaz et al., 2001; Akal, 2003, 2008; Çoban and Flower, 2007). The products of the volcanism were deposited in the Neogene lakes and occasionally alternated with lake deposits (Becker-Platen et al., 1977; Besang et al., 1977; Aydar and Bayhan, 1995; Aydar, 1998; Aydar et al., 2003; Akal, 2003, 2008; Prelevic et al., 2012; Akal et al., 2013, Prelevic et al., 2015). The Sinanpaşa (Afyon) basin, which is the subject of this article, is located on the eastern margin of the Western Anatolian graben system, and it is a typical example of

the deposition of volcanic and sedimentary sequences in Western Anatolia.

Sinanpaşa basin is adjacent to Western Anatolian basins that contain economic borate (Balıkesir-Bigadiç, Bursa-Kestelek, Kütahya-Emet, Eskişehir-Kırka), lignite (Çanakkale-Çan, Manisa-Soma, Kütahya-Seyitömer and Tunçbilek) and also uranium (Aydın-Söke, Manisa-Köprübaşı, Uşak-Fakılı) deposits. For this reason, the geological and economic importance of the Sinanpaşa basin increases. When the basin is evaluated in terms of industrial raw materials and clay-feldspar deposits, these occurrences are operated extensively in the Akharım region (southern part of the study area, Kuşçu and Yıldız, 2012; figure 1) and its surroundings (eg. İsehisar-Anayurt, Sandıklı-Kınık). Even though, the tectonic and magmatic evolution of the Sinanpaşa basin have been investigated so far, studies regarding the sedimentology and mineralogy of the Neogene lacustrine sediments have less studied in detail. There are only a few studies about Akharım clay deposits around Sandıklı, in the southern part of the

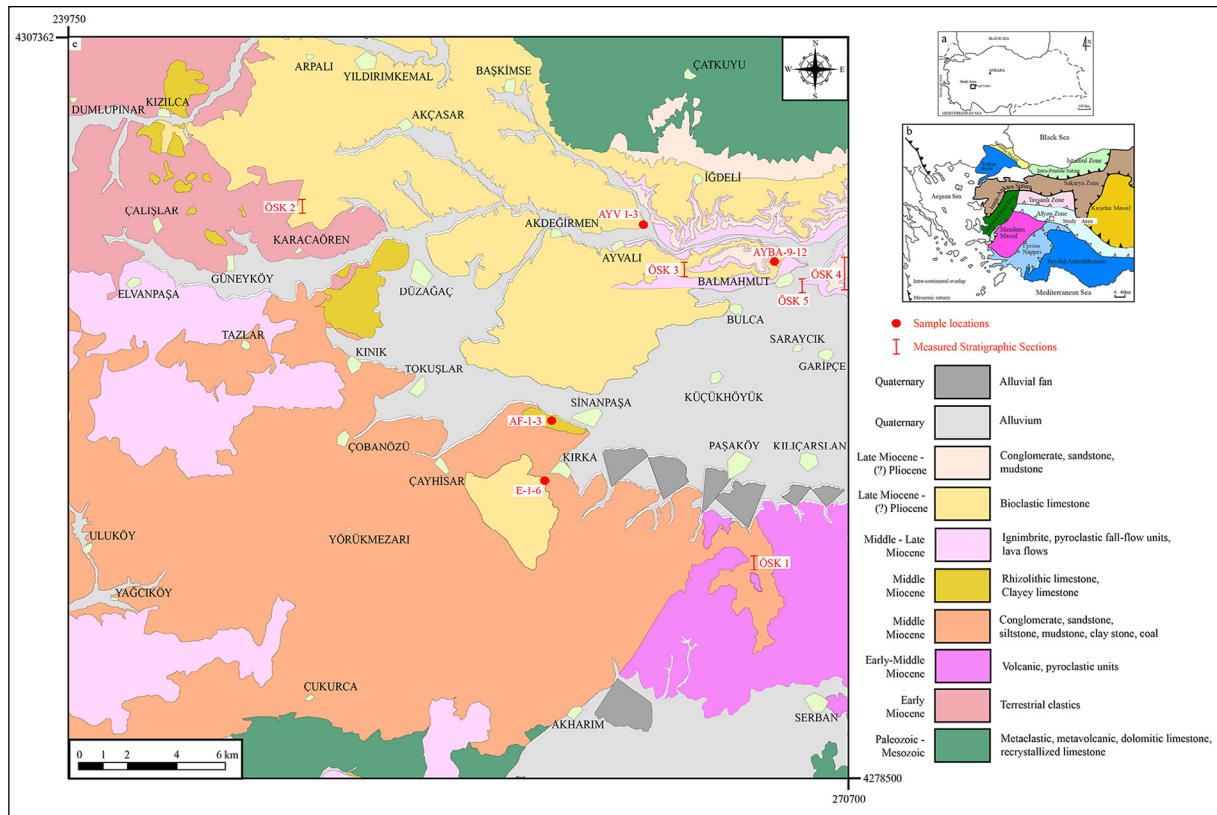


Figure 1- a) Location map of Sinanpaşa (Afyon) basin, b) generalized tectonic map of Western Anatolia and tectonic zones around Afyon Zone (simplified from Okay et al., 1996), c) geological map of Sinanpaşa basin (from Akıska and Varol (2020), who modified from Metin et al., 1987).

Sinanpaşa basin (Kuşçu and Yıldız, 2012). Therefore, this paper aims to investigate the mineralogical and petrographical properties of Neogene-aged lacustrine and volcanic/pyroclastic units accompanying the lacustrine sediments around Sinanpaşa village. In addition, it is aimed to determine the clay minerals and other accompanying mineral types deposited in different facies and also to determine their depositional environments, paleoclimate conditions and diagenesis properties.

2. Regional Geology

With the closure of the Neotethys Ocean, Anatolide-Tauride block was situated along the south of İzmir-Ankara suture zone. It was divided into four tectonic zones from north to south, such as Tavşanlı Zone, Afyon Zone, Menderes Massif and Lycian Nappes (Şengör and Yılmaz, 1981; Okay, 1984; Gönçüoğlu et al., 1996; Okay and Tüysüz, 1999; figure 1a, b). Among them, Afyon Zone rocks consist of Mesozoic units that unconformably overlie a Paleozoic basement. The studied Sinanpaşa Neogene basin rests unconformably on the Paleozoic and Mesozoic basement rocks around the central part of the Afyon zone (Figure 1c). The rocks, exposed in Afyon and its surroundings, were studied in three different groups. These are; (a) Pre-Neogene basement rocks (Afyon Zone), (b) Neogene sedimentary and volcanic rocks, and (c) Quaternary fluvial/alluvial deposits (Figure 2).

(a) *Basement rocks:* Afyon metamorphics are the predominant basement rocks of Afyon Zone. They (possibly during Cambrian and late Silurian) consist of mica schist, garnet mica schist, albite-chlorite and quartz schist, meta conglomerate, phyllite and marbles (Metin et al., 1987; figure 2). These rocks were unconformably overlain by the Middle-Late Devonian-late Permian Anatolian carbonate platform (Güvenç et al., 1994; Tolluoğlu et al., 1997). The carbonate platform consists of recrystallized limestones which have undergone low-grade metamorphism and contains clayey and sandy layers in places. According to the paleontological data, the age of the limestones was determined as Middle-Late Devonian, Carboniferous and Permian (Öztürk, 1981; Metin et al., 1987; Bektaş, 1996). Polygenic conglomerates consisting of metamorphic rock fragments overlie the Paleozoic rocks and were unconformably overlain by white, fossiliferous limestones of Triassic-Jurassic period (Güvenç et al., 1994; Bektaş, 1996; figure 2).

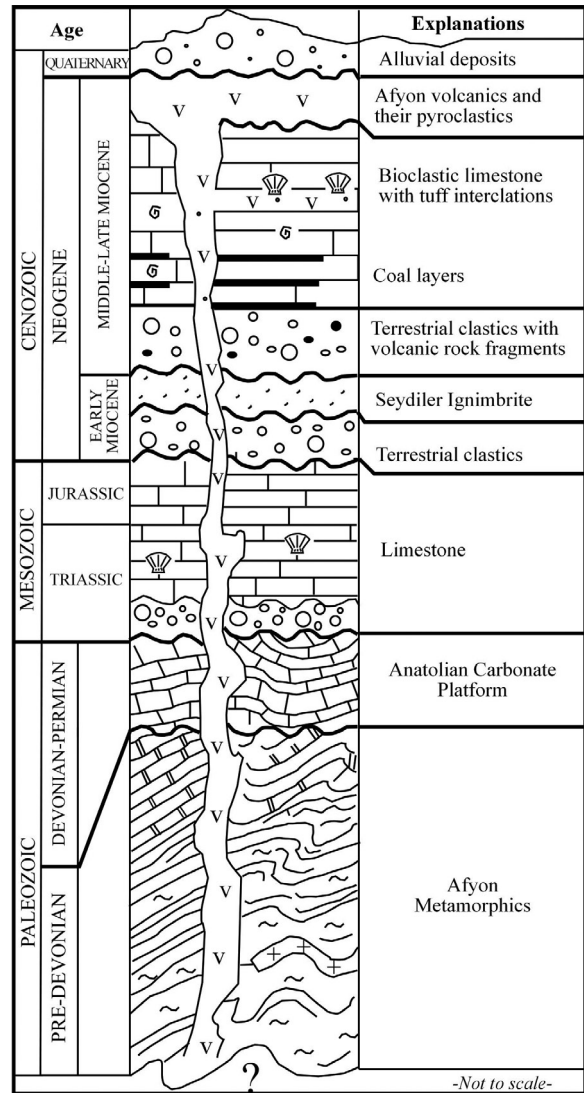


Figure 2- Generalized stratigraphic column of Sinanpaşa basin (simplified from Öztürk, 1981; Metin et al., 1987; Okay et al., 1996; Tolluoğlu et al., 1997).

(b) *Neogene rocks:* The basement rocks were unconformably overlain by Neogene rocks (Figure 1c). These rocks consist of a sedimentary sequence deposited in fluvial and lacustrine environments with locally economic coal layers and volcanic/pyroclastic products of Afyon volcanism (Becker-Platen et al., 1977; Besang et al., 1977; Çevikbaş et al., 1988; Metin et al., 1987; Aydar and Bayhan, 1995; Aydar et al., 2003; Akal, 2008; Akal et al., 2013; Prelevic et al., 2015). In the northern part of the basin, Neogene deposits were initiated with a polygenic conglomerate derived from the basement rocks and consist of sandstone, mudstone and claystone in the vicinity of Çalışlar-Karacaören villages. In the southern part of

the basin, around Kırka, the sequence was followed upward by a second conglomerate sequence with sandstone and mudstone deposition. This sequence contains pre-Neogene basement rock fragments and volcanic content due to its contact to early Miocene Seydiler ignimbrites (Yalçın, 1988). It was overlain by lacustrine sediments of middle Miocene. These sediments were characterized by coal-bearing mudstones situated along the Afyon-Sandıklı main road which is approximately 20 km southwest of Kırka village and by carbonates intercalated with coal levels in Kızılca village in the north and in Kırka village in the south. Meanwhile, Afyon volcanism was active during the middle-late Miocene period in the study area (Besang et al., 1977; Becker-Platen et al., 1977; Aydar and Bayhan, 1995; Akal, 2008; Prelevic et al., 2015) and the products of volcanism were either interstratified with lacustrine deposits or overly them (Aydar and Bayhan, 1995).

Afyon volcanics, exposed in the study area and its surroundings, were accepted as the products of Neogene volcanism (Keller, 1983). According to the radiometric determinations made on the lava and pyroclastics of volcanism, it was determined that Afyon volcanism, consisting of trachyandesite and trachitic lavas and their pyroclastic products (Aydar and Bayhan, 1995; Floyd et al., 1998; Akal and Helvacı, 1999; Aydar et al., 2003; Akal, 2003, 2008; Akal et al., 2013; Prelevic et al., 2015) was active between middle-late Miocene (8.5-14.5 Ma) (Besang et al., 1977; Becker-Platen et al., 1977). In the study area, while volcanic rocks were exposed around Elvanpaşa and Tazlar villages, toward the west of the basin, on the other hand, pyroclastic products were exposed around Balmahmut-İğdeli villages at the north of the basin (Figure 1c). At the end of the late Miocene, volcanism ended (Becker-Platen et al., 1977; Besang et al., 1977; Aydar and Bayhan, 1995; Akal, 2008; Prelevic et al., 2015) and the fluvial regime prevailed.

(c) *Quaternary units*: All Neogene units are unconformably overlain by Quaternary fluvial-alluvial deposits.

3. Material and Method

Petrographic studies have been carried out to determine the paleontological, compositional, textural

and diagenetic properties of Neogene limestones and conglomerates in the study area and to obtain detailed information about the depositional environments of them. Therefore, limestone and conglomerate samples were collected along the measured stratigraphic sections and also by both point to point method. Thin sections were prepared in Thin Section and Polishing Laboratory of Department of Geological Engineering in Ankara University and they were investigated in Leica DM/LSP model polarizing microscope. In addition, in cases where petrographic determinations are insufficient, micro-structure studies were carried out by the scanning electron microscope (SEM) to collect more detailed and healthy information especially about the morphology of the clay minerals. Energy Scattering Spectroscopy (EDX) analyses were performed for the chemical determinations. Analyses were made by Zeiss Evo MA 10 SEM model electron microscope and Bruker Nano XFLash 430M Energy Scattering X-ray (EDX) detector at Leoben University (Austria).

The mineralogical composition of the samples was examined with Philips PW 1830 model X-rays (XRD) diffractometer (Anode = CuK α 1.541871 Å, Filter = Ni, voltage = 40 kV, current = 30 mA, goniometer speed = 1 or 2°/min., paper speed= 2cm/min, 2 θ interval= 2 θ =2,5-70°) in the Mineralogy-Petrography Laboratories of the Mineral Research and Exploration General Directorate (MTA). Representative samples were prepared for clay-mineral analysis (size fraction <2 μ m) by separation of the clay fraction by sedimentation. Each sample mounted on glass were subjected to air-drying (N), ethylene-glycolating (EG) and heating (300 °C and 550 °C) procedures before the XRD studies. Diffractograms were evaluated using the American Society for Testing Material catalog (ASTM, 1972). Semi-quantitative estimates of both clay fraction and rock-forming minerals were calculated by an external standard method (Brindley, 1980; Yalçın and Bozkaya, 2002).

4. Lithology

4.1. Sedimentary units of middle Miocene

The sedimentological features of the middle Miocene units in the study area were examined in detail by Akıska and Varol (2020). Therefore, in this study, only the lithological properties of the studied units and their depositional systems will be discussed. Middle

Miocene sequence was initiated with conglomerate-sandstone sediments and continues with coal-bearing mudstones and carbonates (Figure 3). *Conglomerate-sandstone* deposits were well exposed around Kırka village at the southern part of Sinanpaşa town. These deposits were characterized by yellow-orange colored, medium-well rounded, poorly sorted, granule to block-sized clasts and cross-bedded, medium-coarse-grained sandstones. Clasts derived mainly from the basement rock fragments of Afyon metamorphics and rhyolitic lavas of Seydiler ignimbrites (early Miocene, figure 4a). The thickness of the sequence was about 100 meters. Cross stratifications observed within the sandstones, which are intercalated with the yellow-orange conglomerates and fine-grained sand matrix indicate normal stream flow units (Smith, 1986).

Coal-bearing mudstones were well exposed around 20 km southeast of Kırka village (ÖSK 1, figure 4b) at the south of the basin and also around the

coal mine around Karacaören village at the NW of the basin (ÖSK 2; figure 3b). Coal layers in both regions were alternated with gray colored mudstones and their total thickness is approximately up to 150-200 meters. The sequence was passed upward by sandstone-laminated mudstones at the southeast of the Kırka village (Figure 4c). Laminated mudstones containing a variety of fossilized plant roots are yellow-gray in color. The mudstones around Karacaören village were followed upward by the carbonate rocks of late Miocene (Figure 4d). According to the palynological analysis, the coals, in both regions, point to the late middle Miocene (Akıska, 2017). Characteristics such as limited propagation and rhythmic alternation reflect the features of typical marsh coals that developed during the first stages of the lake (Miall, 1977; McCabe, 1984).

Carbonate deposits of middle Miocene overlying the coal-bearing mudstones were represented by gray-

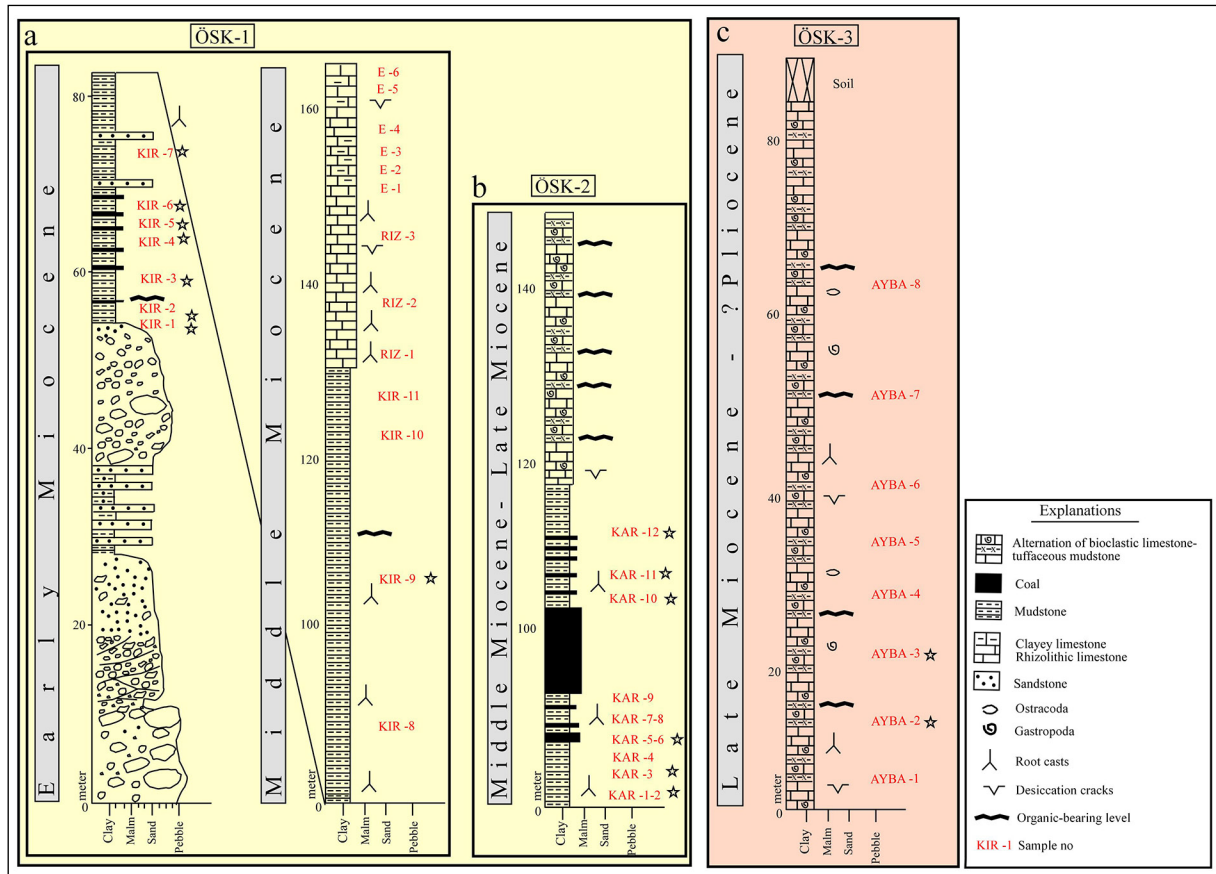


Figure 3- a) Measured stratigraphic section of middle Miocene sediments (ÖSK 1, Southeast of the Kırka village), b) measured stratigraphic section of middle Miocene sediments (ÖSK 2, Karacaören coal mine), c) measured stratigraphic section of late Miocene-?Pliocene deposits (ÖSK 3, Balmahmut village).

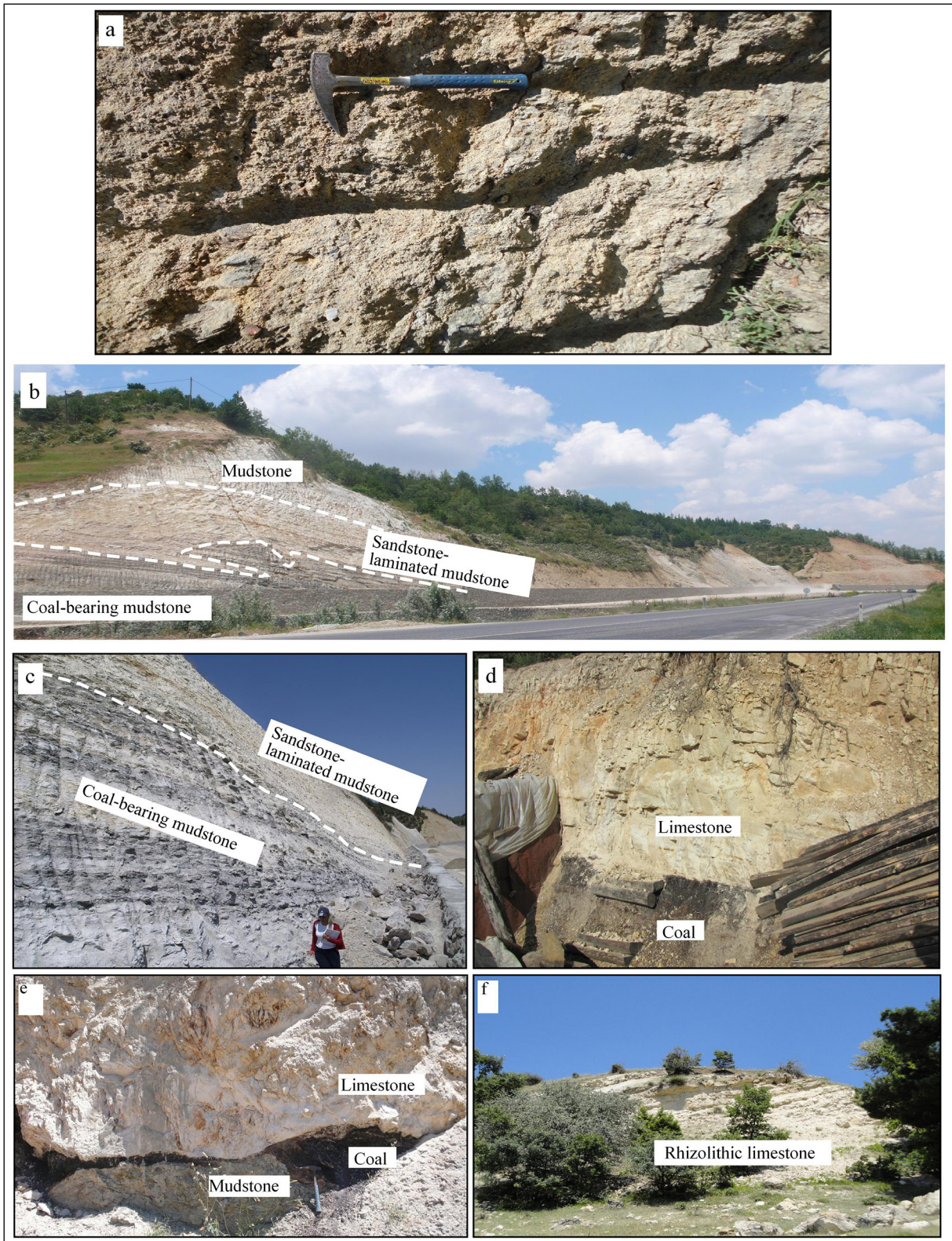


Figure 4- a) Volcanic gravels in poorly graded conglomerate, b) coal-bearing mudstone at the southeast of Kirka village, c) sandstone-laminated mudstone deposits overlying coal-bearing mudstones (Southeast of Kirka village), d) coal layers and overlying late Miocene carbonate deposits (Karacaören coal mine), e) mudstone underlying the coal layers and limestone overlying the coal layers (Karacaören coal mine), f) rhizoliths (Kirka village).

beige rhizolithic limestones and white-gray clayey limestones (Figure 4e). They were exposed around Kızılca village at the north of the basin and Kırka village at the south of the basin (Figure 4f).

4.2. Deposits of Late Miocene – (?) Pliocene

This period of time was represented by bioclastic limestones and tuffaceous organic-rich mudstones (ÖSK 3; figure 3c). *Bioclastic limestones* have widespread outcrops in both the northern (around Balmahmut and İğdeli villages) and southern parts of the basin (around Kırka village). This unit which has tabular and lenticular geometry, are composed of beige colored, parallel-bedded carbonate layers ranging in thickness from several centimeters to several meters (Figures 5a and 5b). According to the petrographic studies, iron and manganese plasterings, microcrystalline calcite patches and gastropod and

ostracod macro shells with a rate of approximately 50% are abundant (Figure 5c). The limestone have nodular appearances in the lower levels and alternates upward with tuffite-bearing organic rich mudstone layers (Figure 5a and 5b). These tuffs were the products of Afyon volcanism that was active during the middle-late Miocene period in the study area having a coexistence occurrence with the limestones and exhibiting an alternating deposition character with these sediments. The *organic-rich mudstones* are represented by parallel laminated, poorly-moderate lithified gray-dark gray mudstones with plant root fragments and gastropod shells. Lamina thickness is between 0.5-0.8 cm.

4.3. Pyroclastics of Middle-Late Miocene

Pyroclastics of Afyon volcanism well exposed in the vicinity of Balmahmut and İğdeli villages

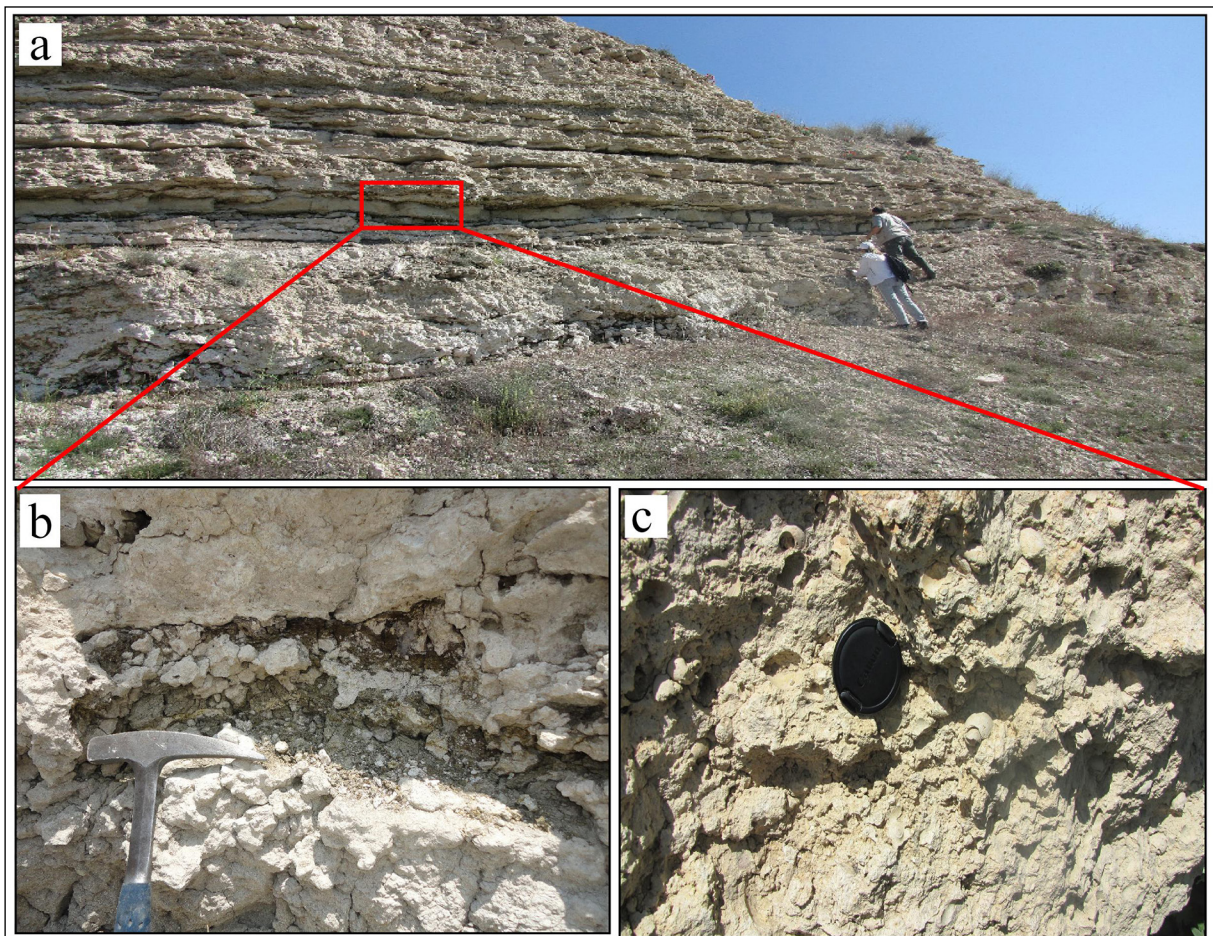


Figure 5- a) General view of alternation of tuffite bearing organic rich mudstone and bioclastic limestone, b) close up view of figure 5a center, c) close up view of macro gastropod and ostracod shells observed in limestones (Balmahmut village).

were classified as *ignimbrites*, *pyroclastic flows* and *porphyric lava flows* (Figure 6a and 6b). *Ignimbrites* consist of poorly sorted, angular and semi-rounded lithic blocks mostly having trachitic composition and pumice within them with the clast sizes of lapilli to block (Figure 7a). Fairy chimney structures were formed in places due to erosion where ignimbrites are non welded.

Two measured stratigraphic sections were taken around the vicinity of Balmahmut village where porphyric lava flows were well exposed (ÖSK 4, figure 6a and 7b; ÖSK 5; figure 6b and 7e). The lava flows were underlain and overlaid by pyroclastic flows in places.

In this area, ÖSK 4 commenced with bioclastic limestones and passes upward into poorly sized and reverse graded, lava and pyroclastic flows varying from ash size to block size, and tuff layers of cream-beige color (Figures 7c and 7d). On the other hand, ÖSK 5 is initiated with calich layers (Figure 7e and 7f) and followed up by thin-medium bedded tuffs and mollusk-bearing levels. Tuff-dominated deposition packages are terminated by coarse-grained pyroclastic units (Figure 7g). Pyroclastic flow deposits have lateral and vertical extent of 50 meters in both measured stratigraphic sections.

5. Petrographic Properties of Volcanic and Pyroclastic Rocks

Volcanic rocks exposed in the investigation area around the villages of Elvanpaşa and Tazlar. These rocks are macroscopically porphyritic aphanitic textured and mainly contain biotite and coarse-grained feldspar minerals. In addition, weathering structures such as the layers of a peeled onion are remarkable.

Based on the petrographic investigations of the volcanic rocks around Elvanpaşa village, they are called as trachyandesites and mainly composed of oligoclase, andesine + biotite ± volcanic glass ± opaque mineral ± hornblend (Figure 8a). These rocks have porphyritic texture with hypocrySTALLINE hipidiomorph groundmass and the matrix consists of microlites and volcanic glass. Furthermore, some of the mafic minerals are opacitized.

The trachyandesites around Tazlar village can be easily distinguished from other groups by their

trachytic texture. Vitrophyric, porphyritic, and hypocrySTALLINE hypidiomorph porphyritic textures are observed in thin sections. In trachyandesites including plagioclase + biotite ± volcanic glass ± opaque mineral ± hornblende, pilotaxitic and trachytic textures formed by microlite and volcanic glass are the characteristics of this rock group (Figures 8b and 8c).

Ignimbrites consist of 28% phenocryst and 72% groundmass. Ignimbrites with banded texture are composed of plagioclase + biotite + obsidian ± opaque mineral (Figure 8d). Plagioclases whose anorthite content is calculated by the Michel Levy method generally oligoclase-andesine (An_{25} - An_{46}) in composition, and they show polysynthetic twinning and a zoned structure. In subhedral and prismatic-formed plagioclase minerals, partial sericitization and rarely argillization are observed. Subhedral biotides generally have a porphyritic texture within the matrix. Light brown and red brown-colored biotites have quite typical basal cleavages and shows parallel extinction. In the sections, hydrobiotites are rarely observed while opacitizations are common. These opacitizations are formed especially in the rims of biotite minerals. There are splinter-shaped volcanic glass fragments, volcanic glass, and pumice pieces in the groundmass that connect the minerals in the rock and constitute the majority of the sections. The volcanic glass does not present a characteristic obsidian feature. Because this volcanic glass observed in ignimbrites is more like the volcanic glass splinters formed during the rock's cooling process. In addition, partial devitrification is also observed in the splinters.

The tuffs along ÖSK 4, where the *porphyric lava flows* were observed, are mainly composed of plagioclase + biotite + lithic component + pumice + splinter ± opaque mineral components (Figure 8e). The fact that there is no welding in the tuffs, where mainly vitrophyric texture is observed, is an important detail, and these tuffs are described as glassy tuff.

Plagioclase + biotite + lithic component + pumice + volcanic glass splinters ± opaque mineral components were observed in the beige-colored tuff samples located along ÖSK 5, where *porphyric lava flows* were seen. Basaltic andesite-type rock sections constitute the tuffs, which have lithic components (Figure 8f). The vesicles in the pumices that were observed in large amounts in the rock are generally circle-shaped.

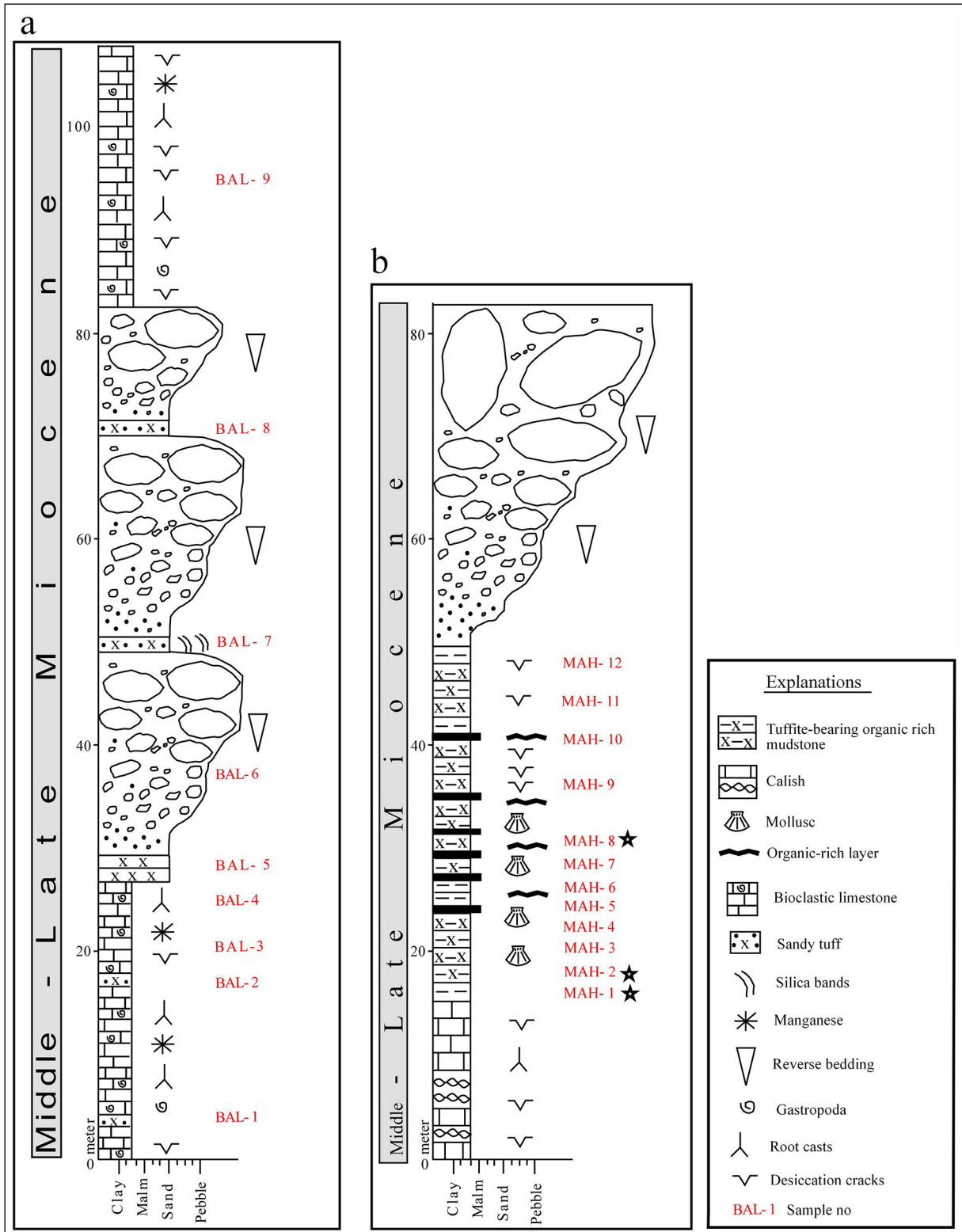


Figure 6- a) Measured Stratigraphic Section Line (ÖSK 4) with N35°E direction of pyroclastic units that exposed around the Balmahmut village. (ÖSK 4) and sample numbers for XRD analysis (middle-late Miocene), b) measured Stratigraphic Section (ÖSK 5) of pyroclastic units around the Balmahmut village and sample numbers for XRD analysis (middle-late Miocene).

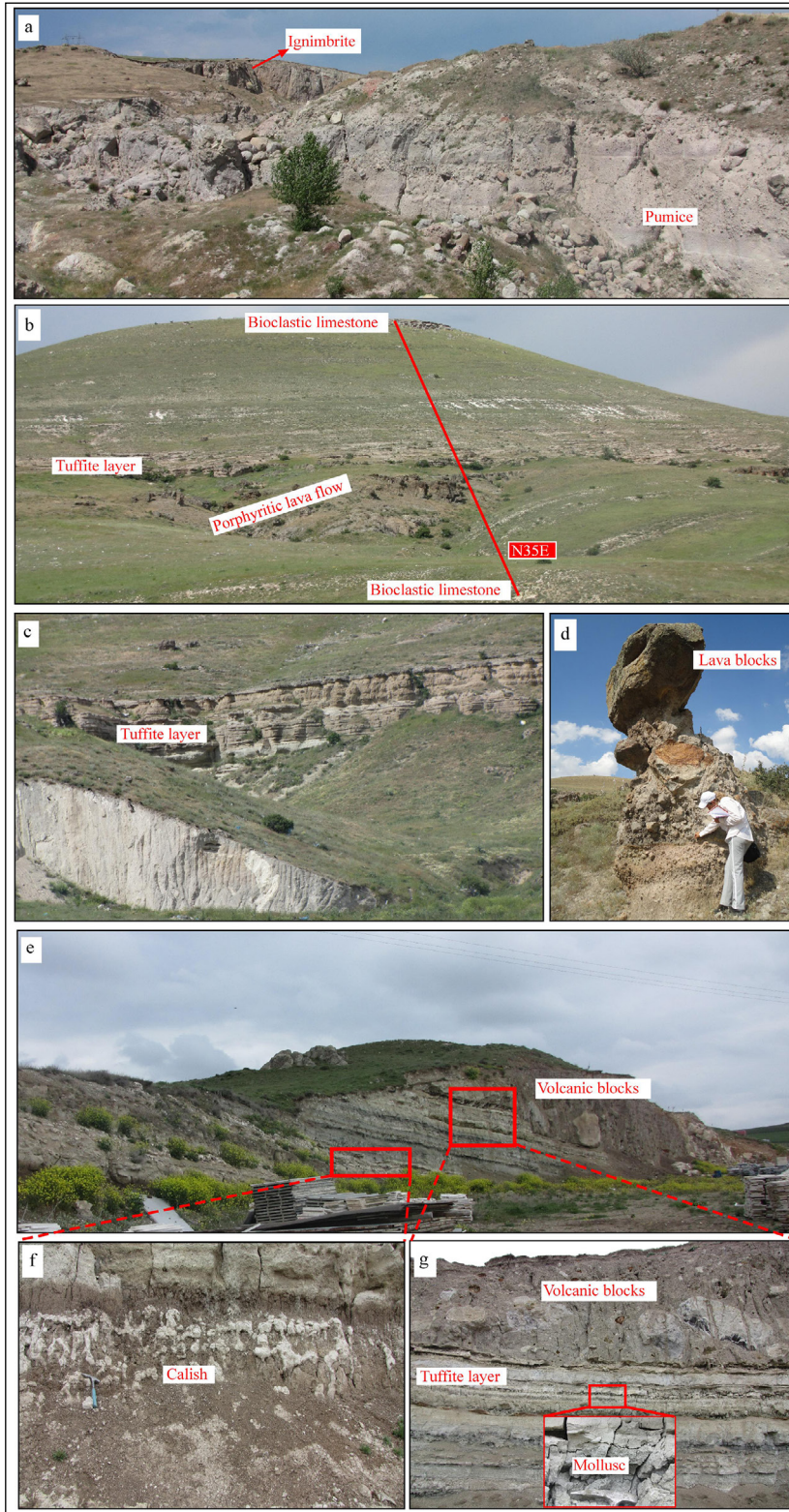


Figure 7- a) Lithic-rich ignimbrite (around the Balmahmut village, b) measured stratigraphic Section line with N35°E direction (ÖSK 4, Balmahmut village), c) close up view of tuffite layers, d) poorly graded lava flows varying from ash size to block size, e) general view of the pyroclastics around the Balmahmut village (ÖSK 5), f) close up view of caliche layers, g) mollusc-bearing thin to medium bedded tuffs and block-sized pyroclastics.

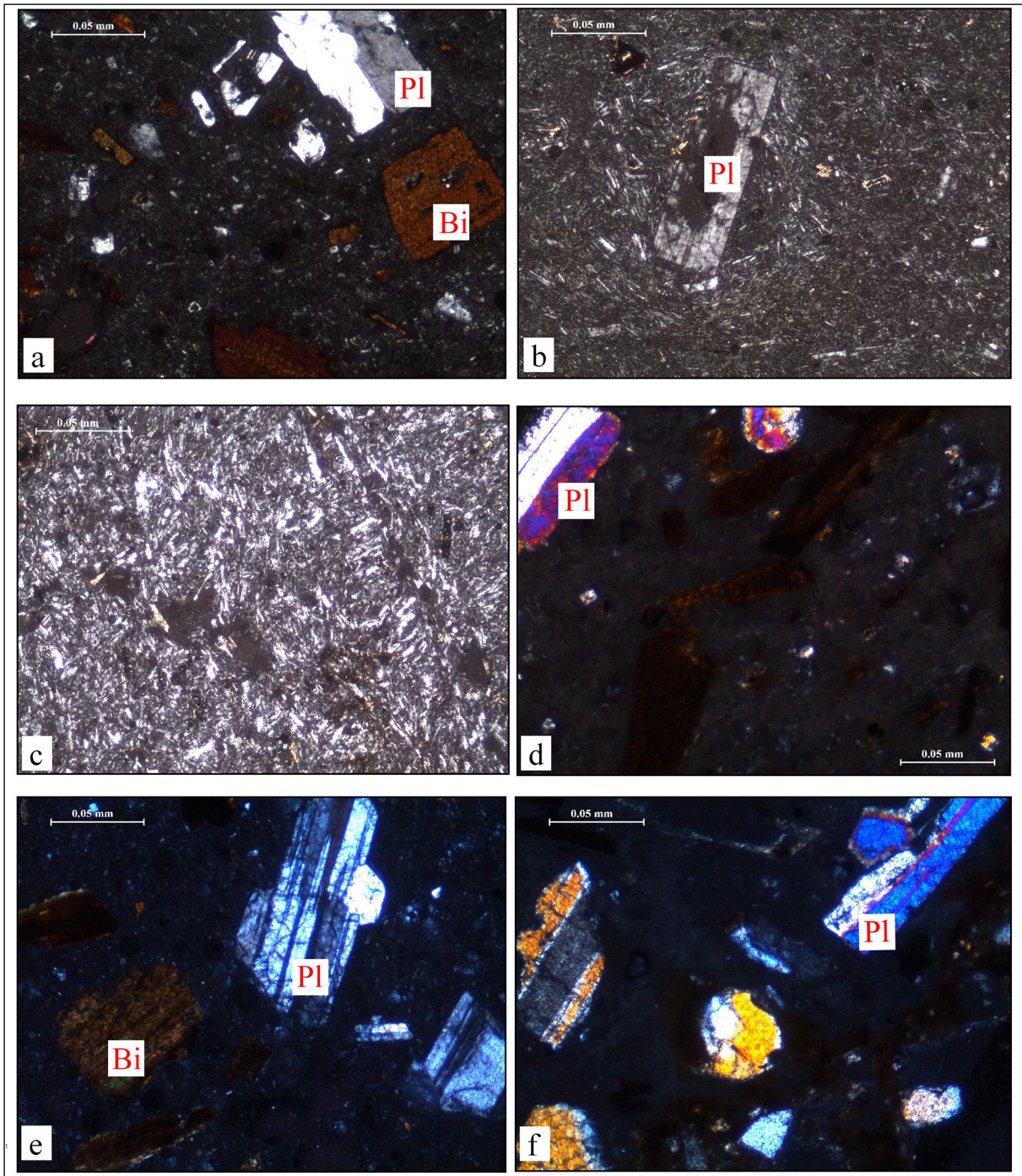


Figure 8- a) Microscopic image of trachyandesite around the Elvanpaşa village (Bt:biotite, Pl: plagioclase) (II. Nicol), b) pilotaxitic texture of the trachyandesite around the Tazlar village (II. Nicol), c) close up view of pilotaxitic texture, d) microscopic image of banded texture of ignimbrite (Çift nikol), e) microscopic image of glassy tuffs in ÖSK 4 (II. Nicol), f) microscopic image of lithic tuffs in ÖSK 5 (II. Nicol). Mineral abbreviations after Whitney and Evans (2010).

6. Mineralogical Properties of the Sinanpaşa Neogene Deposits

In order to determine the mineralogical compositions of mudstone, limestone, tuff and tuffite-bearing mudstone samples, The XRD results for the

bulk samples and clay fraction analyses are presented in tables 1, 2, and 3 respectively. The lithological units are classified as: (1) middle Miocene coal-bearing mudstones, (2) middle-late Miocene tuffs, and (3) late Miocene limestone and tuffite-bearing mudstones.

Table 1- XRD results of Middle Miocene sediments (Mineral abbreviations after Whitney and Evans, 2010).

Samp. No	Lithology	Bulk Rock									Clay Fraction				
		Qz	Cal	Pl	Gp	Dol	The	Crs	Py	Amp	Sme	Ilt	Chl	Kln	Sep
KIR-1	mudstone										az	+		+	
KIR-2	mudstone											+		+	
KIR-3	mudstone	+										+		+	+
KIR-4	mudstone	+										+		+	
KIR-5	mudstone	+										+	+	+	
KIR-6	mudstone	+								+		+	+		
KIR-7	mudstone	+			+							+		+	
KIR-8	mudstone											+		+	
KIR-9	mudstone				+							+		+	
KIR-10	mudstone											+		+	
KIR-11	mudstone											+		+	
KAR-1	mudstone	+	+									+			az
KAR-2	mudstone	+	+			+					+	+			az
KAR-3	mudstone	+	+			+	+					+	+	+	
KAR-4	mudstone	+	+								+				
KAR-5	mudstone	+	+	+		+						+	+		
KAR-6	mudstone	+		+							+	+		+	
KAR-7	mudstone	+		+	+					+	+	+		+	
KAR-8	mudstone	+	+		+	+	+				+	+	+		
KAR-9	mudstone	+		+	+	+		+	+		+	+	+	+	
KAR-10	mudstone	+	+								+	+	+	az	
KAR-11	mudstone		+	+	+						+	+	+	az	
KAR-12	mudstone	+	+								+	+	+	az	
RIZ-1	limestone	+	+									+			
RIZ-2	limestone	+	+									az			
RIZ-3	limestone	+	+									az			
E-1	limestone		+												
E-2	limestone	+	+									+			
E-3	limestone		+												
E-4	limestone		+												
E-5	limestone	+										+			
E-6	limestone	+										+			

(Qz: quartz, Cal: calcite, Pl: plagioclase, Dol: dolomite, The: thenardite, Crs: cristobalite, Py: pyrite, Amp: amphibole, Sme: smectite, Ilt: illite, Chl: chlorite, Kln: kaolinite, Sep: sepiolite). Abbreviations after Whitney and Evans (2010).

6.1. Mineralogical Properties of the Middle Miocene Deposits

The rock units of this time period and their characteristic clay mineral types are given below.

Coal-bearing mudstones: Except for the clay minerals, the rock-forming minerals such as quartz, calcite and plagioclase are determined as the result of XRD analysis of samples taken from coal-bearing mudstones exposed along the main Afyon-Sandıklı

road at the south of the basin and around Çalışlar-Karacaören villages at the north of the basin (Figure 9A). Quartz was determined by the reflection peaks of d(101) at 3.34 Å, d(100) at 4.25 Å, and d(112) at 1.817 Å. Calcite was characterized by the reflection peaks of d(104) at 3.02 Å, d(102) at 3.86 Å, and d(113) at 2.28 Å. Plagioclase was identified by the reflection peaks of d(040) at 3.18 Å, d(020) at 6.43 Å, and d(111) at 4.02 Å. In some samples, evaporite minerals such as dolomite, thenardite and gypsum have also

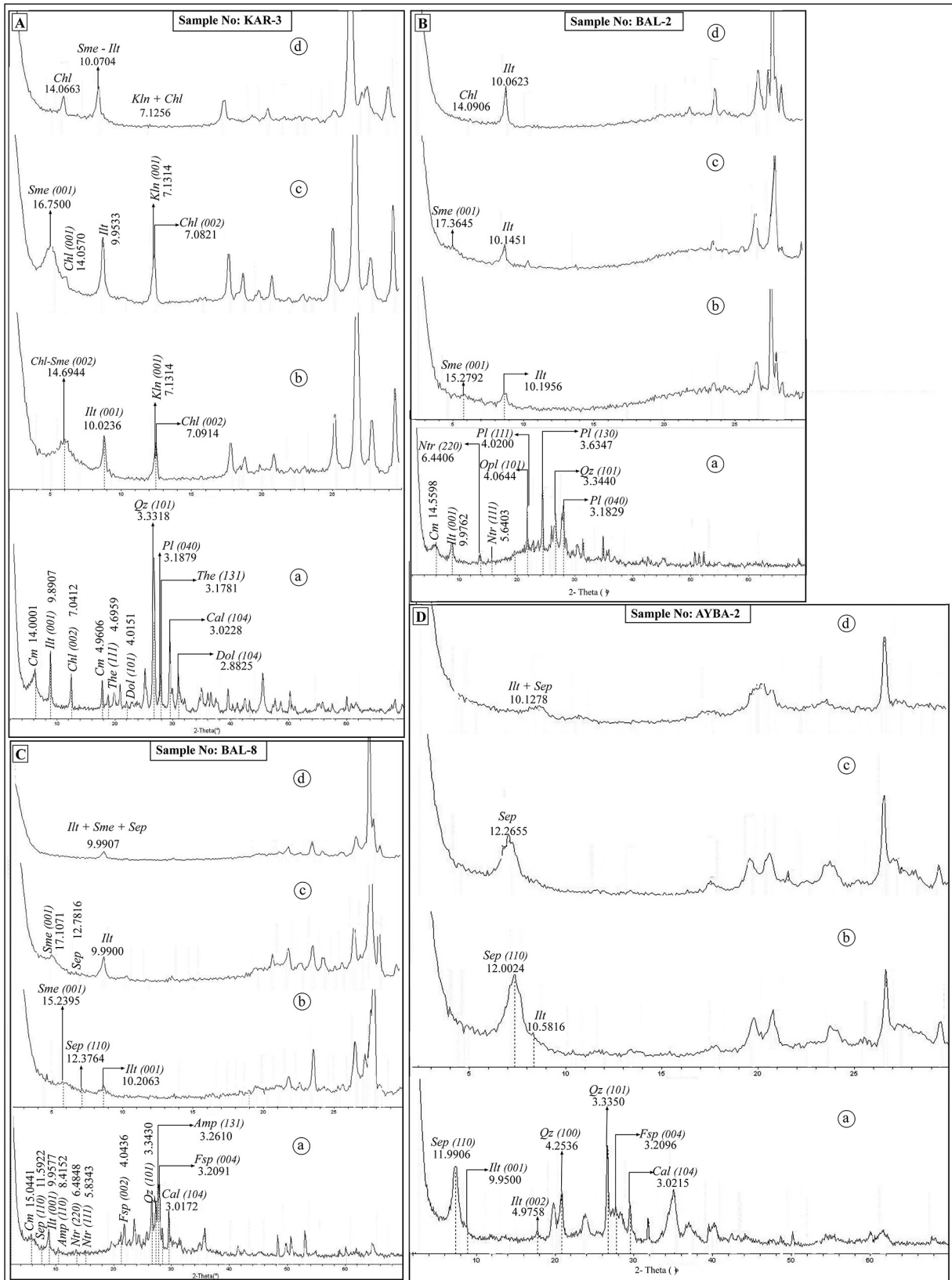


Figure 9- XRD diffractions of (A) KAR-3, (B) BAL-2, (C) BAL-8 and (D) AYBA-2 samples. Cm: clay, Sme: smectite, Kln: kaolinite, Sep: sepiolite, Chl: chlorite, Amp: amphibole, Dol: dolomite, Pl: plagioclase, Qz: quartz, Opl: opal-CT, Cal: calcite, The: thenardite, Ntr: natrolite (a = bulk rock, b = air-dried, c = ethylene glycol, d = heated at 550°C. (Mineral abbreviations after Whitney and Evans, 2010).

been identified (Table 1). Accordingly, dolomite was determined by the reflection peaks of d(104) at 2.89 Å, d(101) at 4.03 Å, and d(113) at 2.19 Å. Thenardite was identified by the reflection peaks of d(020) at 2.78 Å, d(111) at 4.69 Å, and d(131) at 3.18 Å. Gypsum, which was observed in small amounts, was distinguished by the reflection peaks of d(020) at 7.67 Å, d(141) at 3.06 Å, and d(200) at 2.86 Å. Illite is the dominant clay mineral in the clay fraction analysis of the same samples. In addition to illite, smectite, kaolinite and a small amounts of chlorite were also detected. Sepiolite is especially associated with the organic rich parts (Table 1). Illite is determined by the reflection peaks of d(001) at 10.1 Å, d(002) at ~5 Å, d(003) at 3.35 Å, and d(116) at 2.55 Å. In addition, d(001) reflection peaks at 10.1 Å of illite which were not affected by air-dried, ethylene-glycolating and heating method also helped to determine the illite (Figure 9A). On the other hand, the air-dried smectites show a peak at around 15 Å with d(001) reflection which expanded to around 17 Å with d(001) reflection after saturation with ethylene glycol. Peaks at 7.14 Å and 3.57 Å with d(001) and d(002) reflections represent kaolinite. Its 7.14 Å peak collapsed after heating at 550°C (Figure 9A).

Carbonate deposits: Calcite is the dominant mineral as rock forming mineral in the rhizoliths exposed around Kırka village at the south of the basin and Kızılcıca village at the north and in some silicified parts it is accompanied by quartz. These samples contain ~ 5% illite. The characteristic basal peaks of the illite show reflections at ~10.1 Å d(001), ~5 Å d(002), 3.35 Å d(003), and 2.55 Å d(116) (Table 1).

6.2. Mineralogical Properties of the Middle-Late Miocene Pyroclastic Rocks

These deposits were interbedded and/or intercalated with the giant sized granular volcanic materials especially around the Balmahmut and İğdeli villages at the north of the basin, as seen in figures 6a and 6b. Pyroclastic products of Afyon volcanism which was active since middle Miocene (Aydar and Bayhan, 1995) were exposed following siliciclastic precipitation of the alluvial/fluvial fan system and they were deposited contemporaneously with the lacustrine carbonate deposition. As a result of the mineralogical investigations on tuffs and tuffite-bearing organic rich mudstone samples (Table 2), except from clay

Table 2- XRD results of Middle-late Miocene pyroclastics (Mineral abbreviations after Whitney and Evans, 2010).

Samp. No	Lithology	Bulk Rock									Clay Fraction			
		Qz	Cal	Pl	Dol	Crs	Opl	Ntr	Amp	Sme	Ill	Chl	Kln	Sep
BAL-1	tuff. mudstone			+						+	+	az		
BAL-2	tuff. mudstone	+		+			+	+	+	+	+			
BAL-5	tuff. mudstone	+		+			+	+	+	+	+	az		
BAL-6	tuff. mudstone			+	+			+			+			
BAL-7	tuff. mudstone	+		+					+	+	+			
BAL-8	tuff. mudstone	+	+	+		+		+	+	az	+			az
MAH-1	tuff. mudstone	+	+	+						+	+		+	
MAH-2	tuff. mudstone						+			+	+			
MAH-3	tuff. mudstone		+	+						+	+			
MAH-4	tuff. mudstone			+						+	+	+	+	
MAH-5	tuff. mudstone		+							+	+			
MAH-6	tuff. mudstone		+					+		+	+			
MAH-7	tuff. mudstone						+			+	+		+	
MAH-8	tuff. mudstone		+							+		+		
MAH-9	tuff. mudstone		+	+									az	+
MAH-10	tuff. mudstone	+	+	+		+				+	+			+
MAH-11	tuff. mudstone	+	+	+		+				+		+	az	+
MAH-12	tuff. mudstone		+											+
MAH-13	tuff. mudstone		+						+	+	+	az		

(Q: quartz, Cal: calcite, Pl: plagioclase, Dol: dolomite, Crs: cristobalite, Opl: opal-CT, Ntr: natrolite, Amp: amphibole, Sme: smectite, Ill: illite, Chl: chlorite, Kln: kaolinite, Sep: sepiolite, tuff. Mudstone: tuffite bearing mudstone)

minerals, quartz, cristobalite, opal-CT, calcite, plagioclase, amphibole and zeolite (natrolite) have been determined (Figure 9B and 9C). Accordingly, the characteristic basal peaks of the cristobalite show reflection at 4.04 Å d(101), 2.84 Å d(102) and 2.49 Å d(200). Peaks at 8.40 Å d(110), 3.87 Å d(131) and 2.69 Å d(151) represent amphibole (Figure 9C). In addition, natrolite is characterized by the reflections at 6.55 Å d(220), 5.89 Å d(111) and 2.85 Å d(531). Smectite and illite are the dominant minerals in almost all the tuffite-bearing mudstone samples. Additionally, chlorite, kaolinite, sepiolite and a small amount of amorphous material were also determined in these samples (Table 2 and figure 9C).

6.3. Mineralogical Properties of the Late Miocene-Pliocene Deposits

According to the bulk-rock analyses of limestone and alternating tuffite-bearing mudstone samples, calcite and quartz are designated as the dominant minerals (Table 3). Apart from these minerals, illite, which was found in almost 60% of clay minerals, is determined in almost all samples, while

it is accompanied by smectite and small amounts of sepiolite in some samples (Table 3 and figure 9D).

7. Scanning Electron Microscope (SEM-EDX) Determinations

Clay-dominated samples were studied by SEM in order to determine the micromorphology, textural and diagenetic characteristics of the clay minerals and their relationships with non-clay minerals. Accordingly, illite was observed in fibrous morphology (Figure 10a, table 4). Consistent with the XRD results, it is observed that illite was accompanied by quartz in SEM analysis. Subhedral-anhedral crystals of quartz support the detritic origin. Euhedral calcite crystals with rhombohedral symmetry observed as cement in the intergranular spaces (Figure 10b). In addition, the euhedral gypsum crystals (with monoclinic symmetry) around illites occasionally indicate sulphur enrichments in the diagenetic environment (Figure 10c). This enrichment which is notable particularly in coal-bearing levels can be attributed to the activity of sulfate-reducing bacteria in the diagenetic environment (Castro et al., 1999). Chlorite

Table 3- XRD results of Late Miocene-Pliocene units (Mineral abbreviations after Whitney and Evans, 2010).

Samp. No	Lithology	Bulk Rock				Clay Fraction			
		Qz	Cal	Pl	Amp	Sme	Ilt	Chl	Sep
AYV-1	limestone		+						
AYV-2	limestone		+				+		
AYV-3	limestone		+				az		
BAL-3	limestone		+						
BAL-4	limestone		+						az
BAL-9	limestone		+						
AYBA-1	tuff. mudstone			+	+	+	+		
AYBA-2	tuff. mudstone	+		+	+		+		
AYBA-3	tuff. mudstone	+		+	+		+		+
AYBA-4	tuff. mudstone	+				+	+	+	
AYBA-5	tuff. mudstone	+	+			+	+		
AYBA-6	tuff. mudstone	+				+	+	+	
AYBA-7	tuff. mudstone	+	+			+	+		
AYBA-8	tuff. mudstone	+	+			+	+		
AYBA-9	limestone		+						az
AYBA-10	limestone		+						
AYBA-11	limestone		+						az
AYBA-12	limestone		+						

(Qz: quartz, Cal: calcite, Pl: plagioclase, Amp: amphibole, Sme: smectite, Ilt: illite, Chl: chlorite, Sep: sepiolite, tuff. Muudstone: tuffite bearing mudstone)

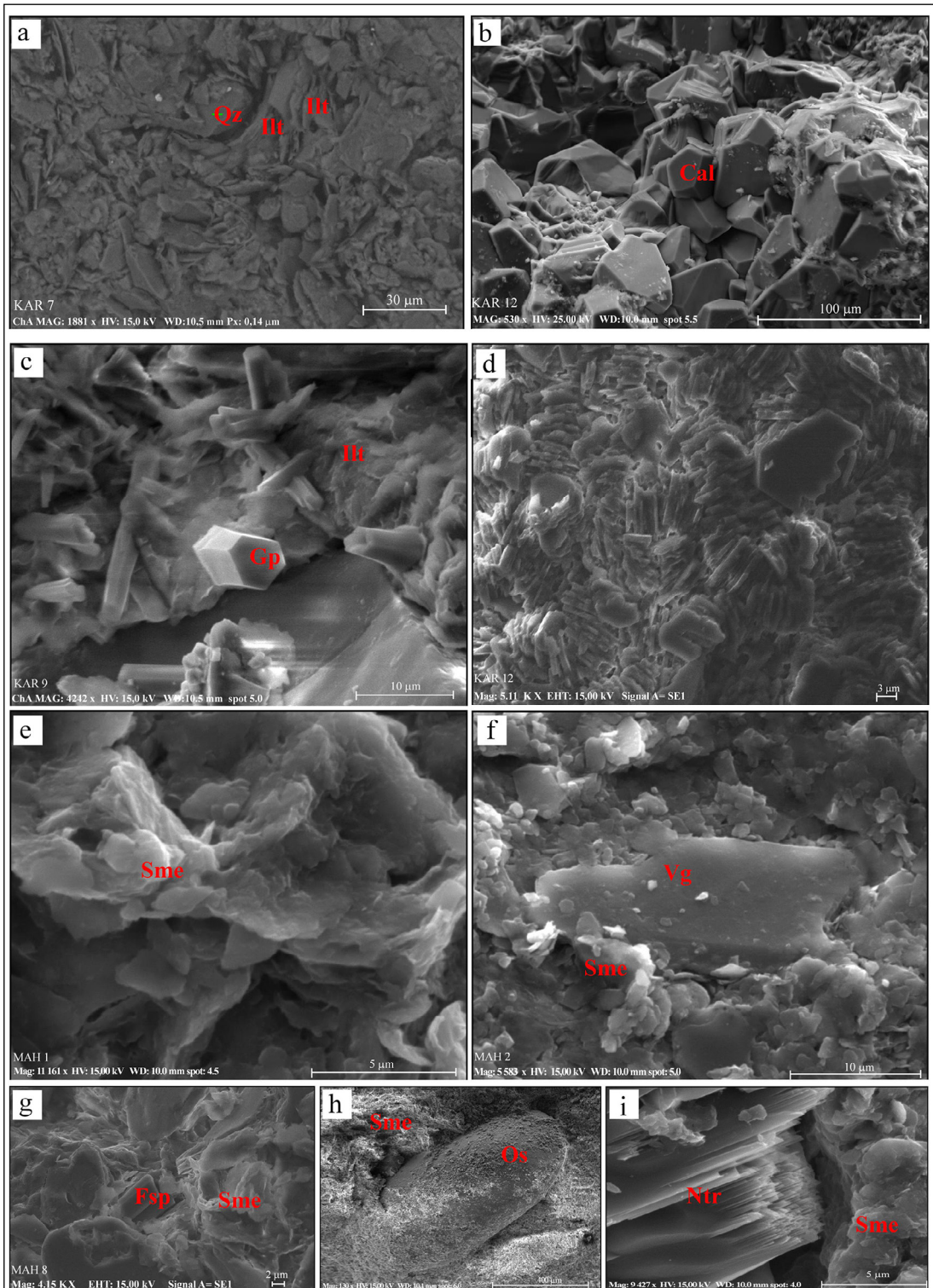


Figure 10- SEM images of a) fibrous illite (Ill) and accompanying quartz (Qz) minerals, b) idiomorphic calcite (Cal) with trigonal symmetry, c) idiomorphic gypsum crystals (Gp) with monoclinic symmetry between illite minerals (Ill), d) kaolinite, e) smectite mineral (Sme) with corn flakes and honeycomb texture, f) smectite mineral (Sme) developing on the edges and surfaces of fractured volcanic glasses (Vg), g) smectite mineral (Sme) on and around feldspar (Fsp), h) ostracod shell (Os) on plate-crystal of smectite, i) natrolite mineral (Ntr) and surrounding honeycomb textured smectite mineral (Sme). (Mineral abbreviations after Whitney and Evans, 2010).

Table 4- EDX analyses of illite, chlorite, kaolinite and plagioclase (wt.%).

Samp. No	SiO ₂	Al ₂ O ₃	FeO	MgO	K ₂ O	Na ₂ O	CaO	Total
KAR- 7*	53.1	33.98	1.83	1.83	9.73	-	-	99.98
KAR-3	41.78	26.26	10.99	20.96	-	-	-	99.99
KAR-12	46.92	43.68	1.94	-	7.34	-	-	99.88
BAL-2	68.71	19.82	-	-	-	11.00	0.47	100.00

*KAR-7: illite; KAR-3: chlorite; KAR-12: kaolinite; BAL-2: plagioclase.

is represented by thin stacks, pseudohexagonal and randomly oriented lath shaped plates with 5-10 μm crystal thickness. Chemical analyses by EDX determine the chlorite is iron rich (10.99%) (Table 4). The presence of pore-space filling chlorites with iron-rich composition indicates the diagenetic occurrence (Bartier et al., 1998). Kaolinite occurs as platy crystals with hexagonal shape, typically arranged in elongated stacks of books (Henning and Störr, 1986) (Figure 10d). The plates are 1-3 μm wide and generally occur as irregular forms. The EDX analysis of these plates shows similarities to kaolinite (Table 4). The concentration of kaolinite, especially in the coal-bearing levels, can be attributed to the autogenetic deposition of silicon and aluminum there (Koukouzas et al., 2009).

Smectite is observed as plate-shaped, honeycomb texture and in the form of wavy leaves (Figure 10e). Wavy morphology was described as cornflake texture by Keller (1978). Smectite leaves are developed on the surface of volcanic glass and/or in the fractures around

the glass particles (Figure 10f). In addition, in some samples, smectite is also developed by replacing the partially dissolved edges of plagioclases. According to EDX analysis, sodic feldspars with high Na content (Table 4) are observed as euhedral, prismatic, and rod-shaped (Figure 10g). Smectite fills the voids between the plagioclases and the glass particles. Therefore, smectite may act as a main cement in places. Samples having plate-shaped smectites, up to 1-4 μm in diameter, are mostly observed in tuffite-bearing mudstones which also contain ostracod shells (Figure 10h). The elemental composition of the plagioclase and volcanic glass that were partially replaced to smectite are composed of Si, Al, Fe, and Na. On the other hand, EDX analysis of pure smectite represents Mg, K, Na, and Fe, as well as Si and Al (Figure 11a). This mineralogical composition indicates that smectite is occurred as a result of partial dissolution of both volcanic glass and plagioclase. It also results from replacing these minerals, as well as occurring by authigenic precipitation in microfracture-fillings of the sediments (Fischer and Schmincke, 1984).

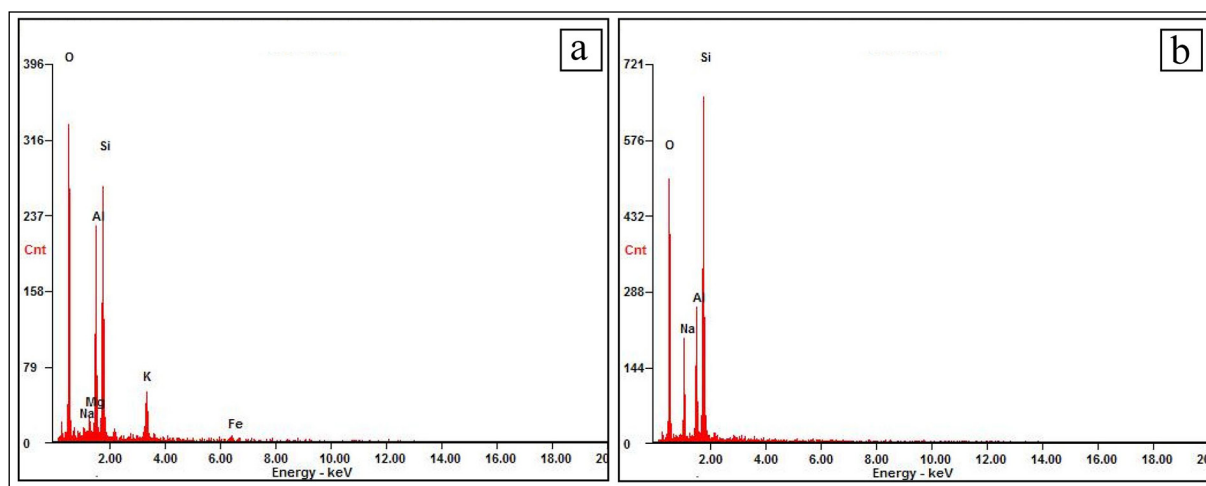


Figure 11- a) Energy Scattering Spectrometry (EDX) analyses of smectite, b) energy scattering spectrometry (EDX) analyses of natrolite minerals.

Zeolite-type minerals were also observed in SEM analysis (Figure 10i). EDX results were consistent with the element content of zeolite. Among them, natrolite, mainly accompanied by smectite, is characterized by strong Si, Al, and Na peaks (Figure 11b). Smectite has a honeycomb texture around the natrolite crystals. These mineralogical and micromorphological features indicate that the smectite and accompanying natrolite were formed as a result of the hydration of volcanic glasses and/or plagioclases (Karakaş and Kadir, 2000).

8. Discussion and Conclusions

One of the important parameters that control the formation of clay minerals in sedimentary sequences is the climatic factor. Clay mineral analysis, therefore, plays an important role in understanding ancient climate changes at different time periods (Singer and Galan, 1984; Moore and Reynolds, 1997; Thiry, 2000; Kemp et al., 2016). Similarly, the middle Miocene clay mineral diversity in the investigation area would have been influenced by climatic changes. The dominant illite-chlorite coexistence in the basin margin and marsh environments observed in the middle Miocene supports temperate and humid conditions (Weaver, 1989). Based on the palynological data, Yavuz-Işık et al. (2011) argued that almost subtropical climatic conditions were dominant in the early Miocene while temperate conditions prevailed towards the end of the middle Miocene in Western and Central Anatolia. Akkiraz et al. (2015), similarly, suggested the deposition of coal-bearing deposits in the Soma and Uşak-Güre (early-middle Miocene) basins occurred in humid and warm conditions. In addition, Kayseri and Akgün (2010) mentioned the existence of temperate climatic conditions indicate the Miocene Climatic Optimum during late Burdigalian-?Serravalian in northwestern Anatolia (Balıkesir-Gönen, Çanakkale-Çan) and during late Burdigalian-Langhian in southwestern Anatolia (Muğla-Milas). All these data are also consistent with the Miocene depositional systems of Sinanpaşa basin and their clay mineralogy. However, although evaporite minerals such as dolomite, gypsum, and thenardite are observed in the coal-bearing mudstones, these aridifications are thought to be periodic or controlled by limited changes in the diagenetic environment. For example, it is common for gypsum within the coal layers to be formed by sulfate-reducing bacteria (Castro et al., 1999). For this reason, their reflection on the

diagenesis environment together with the arid and semi-arid intermediate phases in the humid climatic belt should not be neglected (Sanz et al., 1994).

It is known that compressional and extensional tectonic movements in Western Anatolia caused the development of numerous basins restricted by normal faults during Cenozoic era (Dewey and Şengör, 1979; Şengör and Yılmaz, 1981; Koçyiğit, 1984; Robertson and Dixon, 1984; Şengör et al., 1985; Zanchi et al., 1993; Bozkurt, 2000; Koçyiğit et al., 2000; Seyitoğlu et al., 2004; Koçyiğit and Deveci, 2007; Ersoy et al., 2011). These basins were filled with sedimentary, volcanic, and volcanoclastic/pyroclastic units. Sinanpaşa basin, located at the eastern margin of the Western Anatolian graben system, is one of the much-debated basins with regard to the formation and development of Western Anatolia basins. It began to form as a NW-SE trending basin in the central part of the Akşehir-Simav Fault System during early Miocene (Koçyiğit and Deveci, 2007). The lithologic associations of the middle Miocene, middle-late Miocene and late Miocene-Pliocene periods overlying the Paleozoic and Mesozoic basement were distinguished from the bottom to the top as follows:

Middle Miocene period was commenced with fluvial deposits and followed upward by lacustrine sediments. The fluvial deposits represented by conglomerate and cross-bedded sandstone are well exposed at the south of the basin. On the other hand, lacustrine deposits have widespread outcrops around both southern and also north-northwestern part of the basin. Similar to the investigated area, some other Neogene freshwater lake deposits (e.g. Uşak-Güre, Manisa-Soma, Kütahya-Seyitömer) in Western Anatolia occasionally contain economic coal levels. On the basis of radiogenic, paleontological, and palynological data, many researches accepted that coal-occurrences in the neighboring basins are early Miocene (Uşak-Güre: Karaoğlu et al., 2010; Ersoy et al., 2011) and late early-middle Miocene (Soma: Akgün and Akyol, 1987, 1999; Kaya et al., 2007; Kayseri and Akgün, 2008; Seyitömer: Nakoman, 1968; Yavuz-Işık, 2007) in age. On the other hand, based on the palynological data in the investigated area, coal-bearing layers are late middle Miocene in age (Akiska, 2017; Akiska and Varol, 2020). The coal-bearing lacustrine deposits were followed upward by volcanics. Afyon volcanism was active

in the study area due to the extensional tectonic regime in Western Anatolia during the middle-late Miocene period (Keller and Villari, 1972; Besang et al., 1977; Aydar and Bayhan, 1995; Aydar, 1998; Akal et al., 2013; Prelevic et al., 2015). Materials from the volcanic activity occasionally filled the local lake areas (Aydar and Bayhan, 1995). During this time period, most common lacustrine deposits have widespread outcrops along the N-NE margin of the basin. The depositional sequence initiates with bioclastic limestone and alternates upward with lava flows and tuffite layers (Figure 1c). Volcanic activities became largely ineffective toward the end of late Miocene and ostracod and mollusk-bearing lacustrine deposits became clear. Limestones with abundant clastic (bioclast and pellet) and/or organic material contain widespread desiccation cracks. This indicates shallow local lake environments and also drying up conditions from time to time (Eugster and Kelts, 1983; Bustillo et al., 2002). In addition, laminated tuffite-bearing organic rich mudstones alternating with limestones indicate the water level fluctuations of the lake in certain climatic periods and changing to anoxic conditions (Sáez and Cabrera, 2002).

The mineralogical compositions of the lacustrine deposits have been greatly influenced by the climatic factors, mineralogy of volcanic material additives and diagenetic environment changes. According to the geological time processes, the association of calcite and quartz is dominant in the lacustrine mudstones of the middle Miocene and the limestone-clayey limestones overlying them (Table 1). These anhedral-subhedral quartz crystals indicate the detritic origin and are derived from non-volcanic basement rocks. The fact that the different degree of silicified volcanic glass observed at this level surrounded by illite also indicates the diagenetic origin. In a few mudstone samples (KAR 7-11), the association of calcite and quartz is accompanied by the feldspar mineral. The feldspars are detected as Na-rich plagioclases based on the petrographical and mineralogical studies. The limited propagation of mudstones and rhythmic alternation of coal layers in the lower and middle parts of this sequence reflect the features of typical marsh coals that developed at the basin margins before inundation of the lake (Miall, 1977; McCabe, 1984). Illite and chlorite were determined as the dominant clay minerals in these coal-bearing deposits. Except that, very rare smectite, kaolinite and

sepiolite type clay minerals are noteworthy in some samples. Illite represents the clay-size component of muscovite and is a marker of detritic origin along with the chlorite minerals (Ehrmann et al., 2005; Fagel, 2007). However, the areas where Fe-rich chlorite in the coal levels are seen as pore fillings, may also be genetically linked to diagenetic origin (Bartier et al., 1998). Kaolinite, on the other hand, may have formed by the in situ / authigenic deposition of silicon and aluminum elements dominant in these environments as a result of the chemical decomposition of feldspars (mostly sodic plagioclases) in high water-active environments (Koukouzas et al., 2009) and also can be transported detritically to this environment (Keller, 1978). Non-clay minerals such as quartz, feldspar, cristobalite, opal-CT, amphibole, and zeolite (natrolite) were detected in the middle-late Miocene pyroclastic deposits. Zeolite is thought to be formed as a result of alteration of volcanic ash or tuff in the water environment (Ataman, 1977; Grim and Güven, 1978; Yalçın, 1988; Bayhan and Yalçın, 1990). In particular, smectite with a honeycomb-shaped texture around and on the zeolite (natrolite) indicates these minerals are occurred by the hydration of volcanic glasses and/or plagioclases (Karakas and Kadir, 2000). In addition, the determination of chlorite-, kaolinite-, and sepiolite-type clay minerals accompanied by smectite in these levels may mark the result of the in-situ alteration of volcanic material in the lacustrine environment (Millot, 1964; Grim, 1968; Weaver, 1989). Therefore, the formation of smectite may have occurred by the alteration / dissolution of plagioclase and volcanic glass, and also it may occur by the transformation from amorphous to semi-amorphous structure in the alkaline conditions, and then to smectite (Karakas et al., 2007; Karakaya et al., 2007; Bayhan and Yalçın, 1990; Gürel and Kadir, 2006). Beside, smectite is observed on the microfracture fillings and in the dissolution voids of volcanic glasses. As a result of marginal replacing of volcanic glasses and feldspars by smectite and also due to partially/wholly dissolution of these minerals, smectite may authigenically form in the sediment voids (Millot, 1970; Furnes, 1975; Tucker, 1992; Christidis et al., 1995; Kadir and Karakas, 2000, 2002; Besbelli and Varol, 2002; Karakas et al., 2007). It is known that the association of smectite with volcano glass observed in volcano-sedimentary lacustrine basins and the presence of alkaline environment are important factors for sepiolite formation (Weaver and Beck, 1977; Starkey and Blackmon, 1979; Singer and

Galan, 1984; Velde, 1985). Sepiolite formation in the study area must have been controlled by the presence of volcano glass and feldspar minerals, which constitute the main component of volcanic units. In this period, due to the increase of fresh water discharge to the lake area, the drought phases that commenced following the enrichment of the lake water by the elements such as silica and magnesium transported from the volcanic and surrounding rocks, respectively should have provided suitable conditions for sepiolite formation (Weaver, 1984). In the phases following widespread smectite formation in the lake water fed by volcanic sources, the formation of zeolite (natrolite) minerals have occurred due to the enrichment of the lake water by Na, Al and K ions and the increase in pH (Gall and Hyde, 1989; Stamatakis, 1989; Hartley et al., 1991; Karakaş and Kadir, 2006). Therefore, zeolite minerals that accompany smectite minerals in the study area indicate arid or semi-arid climatic conditions (Mariner and Surdam, 1970; Gall and Hyde, 1989; Hartley et al., 1991; Renaut, 1993; Türkmenoğlu et al., 1995; Karakaş and Kadir, 2006). The smectite and kaolinite minerals in the study area must have been formed authigenically from the volcanic and pyroclastic units depending on the acidic and basic character of the environment (Chamley, 1989). As a result, the sedimentary sequence developing in the early Miocene-Pliocene range in Sinanpaşa Neogene basin and the mineralogical components that characterize them were shaped largely due to the changes in paleotopography, paleoclimate, volcanism, tectonism and diagenetic environment.

Acknowledgments

This manuscript consists of a part of the PhD thesis and the post-doctoral study of the first author. The authors are grateful to Baki E. Varol, who made a great contribution both during the field studies and in the formation of the manuscript. In addition, we would like to thank Cahit Helvacı, who made significant contributions during the field studies, and Erkan Aydar, who made valuable contributions in the classification of pyroclastic units. The authors also express their gratitude to Walter Prochaska, who shared both his valuable perspective and laboratory facilities (University of Leoben, SEM-EDX Lab.) during the first author's post-doctoral study. In addition, the authors would like to thank the reviewers (Hüseyin Yalçın and an anonymous reviewer) who

have contributed to the final version of the manuscript by sharing their valuable views. This study was supported by project no. 06B343006 of the Ankara University Scientific Research Project Office.

References

- Akal, C. 2003. Mineralogy and geochemistry of melilite leucitites, Balçıkhisar, Afyon, (Turkey). *Turkish Journal of Earth Sciences* 12, 215–239.
- Akal, C. 2008. K-richterite-olivine-phlogopite-diopside-sanidine lamproites from the Afyon volcanic province, Turkey. *Geological Magazine* 145, 4, 570-585.
- Akal, C., Helvacı, C. 1999. Mafic Microgranular Enclaves in the Kozak Granodiorite, Western Anatolia. *Turkish Journal of Earth Sciences* 8, 1-17.
- Akal, C., Helvacı, C., Prelević, D., Van den Bogaard, P. 2013. High-K volcanism in the Afyon Region, Western Turkey: from Si-oversaturated to undersaturated volcanism. *International Journal Earth Sciences* 102, 435-453.
- Akıska, E. 2017. Petrographic and palynological investigations of Sinanpaşa (Afyon) Miocene coals. *The Bulletin of Mineral Research and Exploration* 156, 151-166.
- Akıska, E., Varol, B. 2020. Alluvial-lacustrine sedimentation and volcanoclastic deposition in an intracontinental tectonic graben: paleoenvironmental evolution of the Neogene Sinanpaşa Basin, west-central Turkey. *Turkish Journal of Earth Sciences* 29, 295-324. Doi: 10.3906/yer-1907-28.
- Akgün, F., Akyol, E. 1987. Akhisar (Çıtak) çevresi kömürlerinin palinolojik incelemesi. *Türkiye Jeoloji Kurumu Bülteni* 30, 35-50.
- Akgün, F., Akyol, E., 1999. Palynostratigraphy of the coal-bearing Neogene deposits graben in Büyük Menderes Western Anatolia. *Geobios* 32, 3, 367-383.
- Akkiraz, M.S., Akgün, F., Utescher, T., Wilde, V., Bruch, A., Mosbrugger, V., Üçbaş-Durak, S.D. 2015. Erken-Orta Miyosen Yaşlı Kömürlü Tortuların Paleokolojisi: Uşak-Güre ve Soma Havzalarından Örnekler. *Türkiye Jeoloji Bülteni* 58, 3, 39-60.
- Aldanmaz, E., Pearce, J.A., Thirlwall, M.F., Mitchell, J.G. 2000. Petrogenetic evolution of late Cenozoic, post-collision volcanism in western Anatolia, Turkey. *Journal of Volcanology and Geothermal Research* 102, 67-95.

- ASTM. 1972. Inorganic index to the powder diffraction file. Joint committee on powder diffraction standards, Pennsylvania.
- Ataman, G. 1977. Batı Anadolu zeolit oluşumları. *Yerbilimleri* 3, 85-94.
- Aydar, E. 1998. Early Miocene to Quaternary evolution of volcanism and the basin formation in western Anatolia: a review. *Journal of Volcanology and Geothermal Research* 85, 69-82.
- Aydar, E., Bayhan, H. 1995. Le volcanisme alcalin d'Afyon, Anatolie de l'ouest orientale, Turquie: Approche volcanologique et petrologique. *Bulletin de Section Volcanologique, Societe Geologique de France* 36, 1-5.
- Aydar E., Bayhan H., Gourgaud A. 2003. The lamprophyres of Afyon stratovolcano, Western Anatolia, Turkey: description and genesis. *Comptes Rendus Geoscience* 335, 279-288.
- Bartier, D., Buatier, M., Lopez, M., Potdevin, J.L., Chamley, H., Arostegui, J. 1998. Lithological control on the occurrence of chlorite in the diagenetic Wealden complex of the Bilbao anticlinorium (Basco-Cantabrian Basin, Northern Spain). *Clay Minerals* 33, 317-332.
- Başarır, E., Kun, N. 1982. Afyon kalesi çevresindeki volkanik kayaların petrografik incelemesi, Karadeniz Teknik Üniversitesi *Yerbilimleri Dergisi* 2, 1-2, 87-96.
- Bayhan, E., Yalçın, H. 1990. Burdur Gölü çevresindeki Üst Kretase-Tersiyer yaşlı sedimanter istifin tüm kayaç ve kil mineralojisi, *Maden Tetkik Arama Dergisi* 111, 73-87.
- Becker-Platen, J.D., Benda, L., Steffens, P. 1977. Litho- und biostratigraphische deutung radiometrischer altersbestimmungen aus dem Jungtertiär der Türkei. *Geologisches Jahrbuch* 25, 139-167.
- Bektaş, F.Y. 1996, Afyon (Kızıldağı - Değirmendere - Işıklar) Yöresi Bölgesel Metamorfiklerinin Petrografik ve Yapısal incelenmesi. Yüksek Lisans Tezi, Hacettepe Üniversitesi Fen Bilimleri Enstitüsü, 104 s., Ankara (unpublished).
- Besang, C., Echart, F.J., Harre, W., Keruzer, H., Muller, P. 1977. Radiometrische altersbestimmungen an Neogenen erup-tigesteinen der Turkei. *Geologisches Jahrbuch* 25, 3-36.
- Besbelli, A., Varol, B. 2002. Tekke volkanitlerinde hidrotermal alterasyon ürünü kil mineralleşmeleri (Çubuk, Ankara KD). *Maden Tetkik Arama Dergisi* 125, 121-137.
- Borsi, J., Ferrara, G., Innocenti, F., Mazzuoli, R. 1972. Geochronology and petrology of recent volcanics in the eastern Aegean Sea (West Anatolia and Lesvos Iceland). *Bulletin of Volcanology* 36, 473-496.
- Bozkurt, E. 2000. Timing of extension on the Büyük Menderes Graben, western Turkey and its tectonic implications. Bozkurt, E., Winchester, J.A., Piper, J.D.A. (Ed.). *Tectonics and Magmatism in Turkey and the Surrounding Area. Geological Society of London. Special Publications* 173, 385-403.
- Bozkurt E. 2003. Origin of NE-trending basins in western Turkey. *Geodinamica Acta* 16, 61-81.
- Brindley, G.W. 1980. Quantitative X - ray mineral analysis of clays, In: *Crystal structures of clay minerals and their X - ray identification*. Brindley, G.W., Brown, G. (Ed.). Mineralogical Society, 125 - 195, London.
- Bustillo, M.A., Arribas, M.E., Bustillo, M. 2002. Dolomitization and silicification in low-energy lacustrine carbonates (Paleogene, Madrid Basin, Spain). *Sedimentary Geology* 151, 107-126.
- Castro, J.M., Wielinga, B.W., Gannon, J.E., Moore, J.N. 1999. Stimulation of Sulfate-Reducing Bacteria in Lake Water from a Former Open-Pit Mine Through Addition of Organic Wastes. *Water Environment Research* 71, 2, 218-223.
- Chamley, H. 1989. Clay formation through weathering. Chamley, H. (Ed.). *Clay Sedimentology*, Springer-Verlag, Berlin, 21-50.
- Christidis, G.E., Scott, P.W., Marcopoulo, T. 1995. Origin of the bentonite deposits of Eastern Milos, Aegean, Greece. Geological, mineralogical and geochemical evidence. *Clays and Clay Minerals* 43, 63-77.
- Çevikbaş, A., Ercan, T., Metin, S. 1988. Geology and Regional Distribution of Neogene Volcanics between Afyon Şuhut. *Journal of Pure and Applied Sciences* 21, 1-3, 479-499.
- Çoban, H., Flower, M.F.J. 2007. Late Pliocene lamproites from Bucak, Isparta (southwestern Turkey): Implications for mantle 'wedge' evolution during Africa-Anatolian plate. *Journal of Asian Earth Sciences* 29, 160-176.
- Dewey, J.F., Şengör, A.M.C. 1979. Aegean and surrounding regions: complex multiplate and continuum tectonics in a convergent zone. *Geological Society of America Bulletin* 90, 84-92.
- Ehrmann, W., Setti, M., Marinoni, L. 2005. Clay minerals in Cenozoic sediments off Cape Roberts (McMurdo Sound, Antarctica) reveal palaeoclimatic history. *Palaeogeography, Palaeoclimatology, Palaeoecology* 229, 187-211.

- Ercan, T. 1979. Batı Anadolu, Trakya ve Ege adalarındaki Senozoyik volkanizması. *Jeoloji Mühendisliği Dergisi* 9, 23-46.
- Ercan, T., Dinçel, A., Metin, S., Türkecan, A., Günay, E. 1978. Uşak yöresindeki Neojen havzalarının jeolojisi. *Türkiye Jeoloji Kurumu Bülteni* 21, 97-106.
- Ersoy, Y., Helvacı, C., Sözbilir, H., Erkul, F., Bozkurt, E. 2008. A geochemical approach to Neogene-Quaternary volcanic activity of western Anatolia: An example of episodic bimodal volcanism within the Selendi Basin, Turkey. *Chemical Geology* 255, 265-282.
- Ersoy, E.Y., Helvacı, C., Palmer, M.R. 2011. Stratigraphic, structural and geochemical features of the NE-SW trending Neogene volcano-sedimentary basins in western Anatolia: Implications for associations of supra-detachment and transtensional strike-slip basin formation in extensional tectonic setting. *Journal of Asian Earth Sciences* 41, 2, 159-183.
- Eugster, H.P., Kelts, K. 1983. Lacustrine chemical sediments. Goudie, A.S., Pye K. (Ed.). *Chemical Sediments and Geomorphology*. Academic Press, London, 321-368.
- Fagel, N. 2007. Clay minerals, deep circulation and climate. Proxies in Late Cenozoic. *Paleoceanography* 1, 139-184.
- Fischer, R.V., Schmincke, H.U. 1984. *Pyroclastic Rocks*. Springer-Verlag Berlin Heidelberg, 472.
- Floyd, P.A., Helvacı, C., Mittwede, S.K. 1998. Geochemical discrimination of volcanic rocks, associated with borate deposits: an exploration tool. *Journal of Geochemical Exploration* 60, 185-205.
- Francalanci, L., Innocenti, F., Manetti, P., Savaşçın, M.Y. 2000. Neogene alkaline volcanism of the Afyon-Isparta area, Turkey: petrogenesis and geodynamic implications. *Mineralogy and Petrology* 70, 285-312.
- Furnes, H. 1975. Experimental palagonization of basaltic glasses of varied composition. *Contributions to Mineralogy and Petrology* 50, 105-113.
- Gall, Q., Hyde, R. 1989. Alncime in lake and lakemargin sediments of the Carboniferous Rocky Brook Formation, Western Newfoundland, Canada. *Sedimentology* 36, 875-887.
- Göncüoğlu, M.C., Dirik, K., Kozlu, H. 1996. Geodynamic settings of alpine terranes in Turkey. *Annales Geologique de Pays Hellenique* 37, 123-137.
- Grim, R.E. 1968. *Clay mineralogy*: New York, McGraw Hill, 596.
- Grim, R.E., Güven, N. 1978. Bentonites: Geology, mineralogy, properties and uses. *Developments in Sedimentology* 24, Elsevier Science Publishing, 256.
- Gürel, A., Kadir, S. 2006. Geology, mineralogy and origin of clay minerals of the Pliocene fluviolacustrine deposits in the Cappadocian volcanic province, central Anatolia, Turkey. *Clays and Clay Minerals* 54, 5, 555-570.
- Güvenç, T., Demirel, İ.H., Tekinli, U.K. 1994. Lavrasya ve Gondvana arasında kalan Orta Doğunun Üst Paleozoyik paleocoğrafyası ve Paleozoyik stratigrafisi. *Türkiye 10. Petrol Kongre ve Sergisi*, 94-111.
- Hartley, A., Flint, S., Turner, P. 1991. Alncime: a characteristic authigenic phase of Andean alluvium, northern Chile. *Geological Journal* 26, 189-202.
- Helvacı, C., Alaca, O. 1991. Bigadiç borat yatakları ve çevresinin jeolojisi ve mineralojisi. *Maden Tetkik ve Arama Dergisi* 113, 61-92.
- Helvacı, C., Yağmurlu, F. 1995. Geological setting and economic potential of the lignite and evaporite-bearing Neogene basins of Western Anatolia, Turkey. *Israel Journal of Earth Sciences* 44, 91-105.
- Helvacı, C., Ersoy, E.Y., Billor, M.Z. 2017. Stratigraphy and Ar/Ar geochronology of the Miocene lignite-bearing Tunçbilek-Domaniç Basin, western Anatolia. *International Journal of Earth Sciences* 106, 1797-1814.
- Henning, K.H., Störr, M. 1986. Electron micrographs (TEM, SEM) of clays and clay minerals. *Bulletin de Minéralogie* 111, 350.
- Kadir, S., Karakaş, Z. 2000. Konya Miyosen yaşlı volkanik birimlerin mineralojik -petrografik ve jeokimyasal incelenmesi ile neofom kil mineral oluşumlarının irdelenmesi. *Bulletin of the Mineral Research and Exploration* 122, 95-106.
- Kadir, S., Karakaş, Z. 2002. Mineralogy, chemistry and origin of halloysite, kaolinite and smectite from Miocene ignimbrites, Konya, Turkey. *Neues Jahrbuch für Mineralogie Abhandlungen* 177, 113-132.
- Karakaş, Z., Kadir, S., 2000. Devitrification of Volcanic Glasses in Konya Volcanic Units, Turkey. *Turkish Journal of Earth Sciences* 9, 39-46.
- Karakaş, Z., Kadir, S. 2006. Occurrence and origin of alncime in a Neogene volcano-sedimentary lacustrine environment, Beypazarı-Çayırhan basin, Ankara, Turkey. *Neues Jahrbuch für Mineralogie Abhandlungen* 182, 3, 253-264.

- Karakaş, Z., Boyraz, S., Varol, B. 2007. Clay Mineralization of the Neogene Aged Volcanics of the Northeastern Sivrihisar (Mülk-Demirci). The Bulletin of Mineral Research and Exploration 134, 1-16.
- Karakaya, N., Karakaya, M. Ç., Faure, K. 2007. Doğu Karadeniz Bölgesi Kil Mineralleşmelerinin Oluşumu ve Kökeni, Selçuk Üniversitesi Mühendislik-Mimarlık Fakültesi Dergisi 23, 1-2.
- Karaoğlu, Ö., Helvacı, C., Ersoy, Y. 2010. Petrogenesis and $^{40}\text{Ar}/^{39}\text{Ar}$ geochronology of the volcanic rocks of the Uşak-Güre basin, western Türkiye. Lithos 3-4, 193-210.
- Kaya, O. 1981. Miocene reference section for the coastal parts of West Anatolia. Newsletters on Stratigraphy 10, 3, 164-191.
- Kaya, O., Ünay, E., Gökaş, F., Saraç, G., 2007. Early Miocene stratigraphy of Central West Anatolia, Turkey: implications for the tectonic evolution of the Eastern Aegean area. Geological Journal 42, 85-109.
- Kayseri, M.S., Akgün, F., 2008. Palynostratigraphic, palaeovegetational and palaeoclimatic investigations on the Miocene deposits in Central Anatolia (Çorum Region and Sivas Basin). Turkish Journal of Earth Sciences 17, 361-403.
- Kayseri M.S., Akgün, A. 2010. Türkiye’de Geç Burdigaliyen–Langiyen Periyodu ve Avrupa ile Paleortamsal ve Paleoklimsel Karşılaştırma: Muğla–Milas (Kultak) Geç Burdigaliyen–Langiyen Palinoflorası ve Paleoklimsel Özellikleri. Türkiye Jeoloji Bülteni 53, 1-44.
- Keller, J. 1983. Potassic lavas in the orogenic volcanism of the Mediterranean area. Journal of Volcanology and Geothermal Research Letters 18, 321-335.
- Keller, J., Villari, L. 1972. Rhyolitic ignimbrites in the region of Afyon (Central Anatolia). Bulletin of Volcanology 36, 4, 342-358.
- Keller, W.D. 1978. Classification of Kaolins exemplified by their textures in scan electron micrographs. Clays and Clay Minerals 26, 1-20.
- Kemp, S.J., Ellis, M.A., Mounteney, I., Kender, S. 2016. Palaeoclimatic implications of high-resolution clay mineral assemblages preceding and across the onset of the Palaeocene–Eocene Thermal Maximum, North Sea Basin. Clay Minerals 51, 793-813.
- Koçyiğit, A. 1984. Güneybatı Türkiye ve yakın dolaylarında levha içi yeni tektonik gelişim. Türkiye Jeoloji Kurumu Bülteni 27, 1-16.
- Koçyiğit, A., Deveci, Ş. 2007. A N–S-trending active extensional structure, the Şuhut (Afyon) graben: Commencement age of the extensional neotectonic period in the Isparta Angle, SW Turkey. Turkish Journal of Earth Sciences 16, 391-416.
- Koçyiğit A., Ünay, E., Saraç, G. 2000. Episodic graben formation and extensional neotectonic regime in west Central Anatolia and the Isparta Angle: a key study in the Akşehir -Afyon graben, Turkey. Geological Society of London. Special Publications 173, 405- 421.
- Koukouzas, N., Ward, C.R., Papanikolaou, D., Li, Z. 2009. Quantitative Evaluation of Minerals in Lignites and Intraseam Sediments from the Achlada Basin, Northern Greece. Energy and Fuels 23, 2169-2175.
- Kuşçu, M., Yıldız, A. 2012. Alanyurt (Afyonkarahisar) Killerinin Jeolojisi ve Mineralojisi. Süleyman Demirel Üniversitesi Fen Bilimleri Enstitüsü Dergisi 22, 3, 1232-1240.
- Mariner, R.H., Surdam, R.C. 1970. Alkalinity and formation of zeolites in saline alkaline lakes. Science 170, 977-979.
- McCabe, P.J. 1984. Depositional environments of coal and coal-bearing strata. Rahmani, R.A., Flores, R.M. (Ed.). Sedimentology of Coal and Coal-bearing Sequences. IAS Special Publications 7, 13-42.
- Metin, S., Genç, İ., Bulut, V. 1987. Afyon ve dolayının jeolojisi. Maden Tetkik ve Arama Genel Müdürlüğü Rapor No: 2113, Ankara (unpublished).
- Miall, A.D. 1977. A review of the braided river depositional environment. Earth Science Reviews 13, 1-62.
- Millot, G. 1964. Geologie des Argiles. Masson et Cie. 499, Paris.
- Millot, G. 1970. Geology of clays. (Translated by W.R Farrand and H. Paquet). Springer-Verlag, New York, 429.
- Moore, D.M., Reynolds, R.C. 1997. X-ray Diffraction and the Identification and Analysis of Clay Minerals (second edition), Oxford University Press, New York, 378.
- Nakoman, E. 1968. Contribution a l’etude de la microflore Tertiaire des lignites de Seyitömer (Turquie). Pollen et Spores 10, 521-556.
- Okay, A.I. 1984. Distribution and characteristics of the northwest Turkey blueschists, Robertson A.H.F., Dixon J.A. (Ed.). The geological evolution of the Eastern Mediterranean. Geological Society of London. Special Publications 17, 455-466.
- Okay, A.I., Satır, M., Maluski, H., Siyako, M., Monie, P., Metzger, R., Akyüz, S. 1996. Paleo- and Neo-

- Tethyan events in northwestern Turkey: Geologic and geochronologic constraints. Yin, A., Harrison, M. (Ed.). *Tectonic of Asia*. Cambridge University Press, 420-441.
- Okay, A., Tüysüz, O. 1999. Tethyan sutures of northern Turkey. Durand, B., Jolivet, L., Horvath, F., Seranne, M. (Ed.). *The Mediterranean basins: Tertiary extension within the Alpine orogen*. Geological Society of London. Special Publications 156, 475-515.
- Öztürk, A. 1981. Homa-akdağ (Denizli) yöresinin stratigrafisi. *Türkiye Jeoloji Kurumu Bülteni* 20, 2, 82-100.
- Prelevic, D., Akal, C., Foley, S. F., Romer, R.L., Stracke, A., Van Den Bogaard, P. 2012. Ultrapotassic Mafic Rocks as Geochemical Proxies for Post-collisional Dynamics of Orogenic Lithospheric Mantle: the Case of Southwestern Anatolia, Turkey. *Journal of Petrology* 53, 5, 1019-1055.
- Prelevic, D., Akal, C., Romer, R.L., Mertz-Kraus, R., Helvacı, C. 2015. Magmatic Response to Slab Tearing: Constraints from the Afyon Alkaline Volcanic Complex, Western Turkey. *Journal of Petrology* 56, 1-36.
- Renaut, R.W. 1993. Zeolitic diagenesis of Late Quaternary fluviolacustrine sediments and associated calcrete formation in the Lake Bogoria Basin, Kenya Rift Valley. *Sedimentology* 40, 271-301.
- Robertson, A.H.F., Dixon, J.E. 1984. Introduction: Aspects of the geological evolution of the eastern Mediterranean. Dixon, J.E., Robertson, A.H.F. (Ed.). *The evolution of the Eastern Mediterranean*. Geological Society of London. Special Publications 17, 1-74.
- Sáez, A., Cabrera, L. 2002. Sedimentological and palaeohydrological responses to tectonics and climate in a small, closed, lacustrine system: Oligocene As Pontes Basin (Spain). *Sedimentology* 49, 1073-1094.
- Sanz, M.E., Rodríguez-Aranda, J.P., Calvo, J.P., Ordóñez, S. 1994. Tertiary detrital gypsum in the Madrid Basin, Spain: Criteria for interpreting detrital gypsum in continental evaporitic sequences. Renault, R., Last, W.M. (Ed.). *Sedimentology and Geochemistry of Modern and Ancient Saline Lakes*. SEPM Special Publication 50, 217-228.
- Savaşçın, M.Y. 1990. Magmatic activities of Cenozoic compressional and extensional tectonic regimes in western Anatolia. *Proceedings of International Earth Sciences Congress on Aegean Regions 1-6 Ekim 1990, İzmir*, 420-434.
- Savaşçın, Y., Güleç, N. 1990. Neogene volcanism of Western Anatolia. Neogene volcanism of western Anatolia-Field excursion B3. *International Earth Sciences Congress on Aegean Regions 1-6 Ekim 1990, İzmir*, 78.
- Savaşçın, Y., Oyman, T. 1998. Tectono-Magmatic Evolution of Alkaline Volcanics at the Kırka-Afyon-Isparta Structural Trend, SW Turkey. *Turkish Journal of Earth Sciences* 7, 201-214.
- Savaşçın, M.Y., Birsoy, R., Dag, N., Nohutcu, E. 1994. Kırka-Afyon-Isparta structural trend and alkaline rock associations, Anatolia. *Bulletin of the Geological Society of Greece*, 30, 89-98.
- Seyitoğlu, G., Anderson, D., Nowell, G., Scott, B. 1997. The evolution from Miocene to Quaternary sodic magmatism in western Turkey: implications for enrichment processes in the lithospheric mantle. *Journal of Volcanology and Geothermal Research* 76, 127-147.
- Seyitoğlu, G., Işık, V., Çemen, İ. 2004. Complete Tertiary exhumation history of the Menderes massif, western Turkey: An alternative working hypothesis. *Terra Nova* 16, 358-363.
- Singer A., Galan E. 1984. Paligorskite-sepiolite. *Developments in Sedimentology* 37, Elsevier, Amsterdam, 473.
- Smith, G.A. 1986. Coarse-grained nonmarine volcanoclastic sediment: terminology and depositional process. *Bulletin of the Geological Society of America* 97, 759-772.
- Stamatakis, M.G. 1989. Authigenic silicates and silica polymorphs in the Miocene saline-alkaline deposits of the Karlovassi basin, Samos, Greece *Economic Geology* 84, 788-798.
- Starkey, H.C., Blackmon, P.D. 1979. Clay mineralogy of Pleistocene lake Tacopa, Inyo County, California: Geological Survey Professional Paper, United States, 1061, 34.
- Şengör, A.M.C., Yılmaz, Y. 1981. Tethyan evolution of Turkey: a plate tectonic approach. *Tectonophysics* 75, 181-241.
- Şengör, A.M.C., Görür, N., Şaroğlu, F. 1985. Strike-slip faulting and related basin formation in zones of tectonic escape: as a case study. Biddle K.T., Christie-Blick N. (Ed.). *Strike-slip faulting and basin formation*. Society for Sedimentary Geology SEPM Special Publication 37, 227-264.
- Thiry, M. 2000. Palaeoclimatic interpretation of clay minerals in marine deposits-an outlook from the continental origin. *Earth Science Reviews* 49, 201-221.

- Tolluoğlu, Ü., Erkan, Y., Sümer, Ö., Boyacı, M., Yavaş, F. 1997. Pre-Mesozoic metamorphic evolution of the Afyon metasedimentary group. *Geological Bulletin of Turkey* 40, 1, 1-14.
- Tucker, M.E. 1992. *Sedimentary Petrology*. Black-Well, Oxford, 260.
- Türkmenoğlu, A., Koçyiğit, A., Özalp, T. 1995. Kalecik-Hasayaz havzasındaki Tersiyer göl sedimanlarının jeolojisi ve kil mineralojisi. VII. Ulusal kil sempozyumu, 27-30 Eylül 1995, Ankara, 55-63.
- Velde, B. 1985. Clay Minerals, A physico-chemical exploration of their occurrence. *Developments in Sedimentology* 40, 427.
- Weaver, C.E. 1984. Origin and geologic implications of the palygorskite deposits of the S. E. United States. Singer, A., Galan, E. (Ed.). *Palygorskite-Sepiolite Occurrences, Genesis and Uses*. *Developments in Sedimentology* 37, Elsevier, 39-58.
- Weaver, C.E. 1989. Clays, Muds and Shales. *Developments in Sedimentology* 44, Elsevier, 819.
- Weaver, C.E., Beck, K.C. 1977. Miocene of the S.E. United States: A model for chemical sedimentation in a peri-marine environment. *Sedimentary Geology* 17, 1-236.
- Whitney, D.L., Evans, B.W. 2010. Abbreviations for names of rock-forming minerals. *American Mineralogist* 95, 185-187.
- Yalçın, H. 1988. Kırka (Eskişehir) yöresi volkanosedimanter oluşumlarının mineralojik-petrografik ve jeokimyasal incelenmesi. Doktora tezi, Hacettepe Üniversitesi Fen Bilimleri Enstitüsü, Ankara, 209 (unpublished).
- Yalçın, H., Bozkaya, Ö., 2002. Hekimhan (Malatya) çevresindeki Üst Kretase yaşlı volkaniklerin alterasyon mineralojisi ve jeokimyası: denizsuyu-kayaç etkileşimine bir örnek. *Cumhuriyet Üniversitesi Mühendislik Fakültesi Dergisi Seri A-Yerbilimleri* 19, 1, 81-98.
- Yavuz-Işık, N. 2007. Pollen analysis of coal-bearing Miocene sedimentary rocks from the Seyitömer Basin (Kütahya), Western Anatolia. *Geobios* 40, 701-708.
- Yavuz-Işık, N., Saraç, G., Ünay, E., Bruijn, H. 2011. Palynological Analysis of Neogene Mammal Sites of Turkey – Vegetational and Climatic Implications. *Bulletin of the Earth Sciences Application and Research Centre of Hacettepe University* 32, 2, 105-120.
- Yılmaz, Y. 1989. An approach to the origin of young volcanic rocks of Western Turkey. In: *Tectonic Evolution of the Tethyan Region*. Şengör, A.M.C. (Ed.). Kluwer Academic Publishers, 159-189.
- Yılmaz, Y. 1990. Comparison of young volcanic associations of western and eastern Anatolia formed under a compressional regime: a review. *Journal of Volcanology and Geothermal Research* 44, 69-77.
- Yılmaz, Y., Genç, C., Gürer, F., Bozcu, M., Yılmaz, K., Karacık, Z., Altunkaynak, Ş., Elmas, A. 2000. When did the western Anatolian grabens begin to develop? Bozkurt, E., Winchester, J.A., Piper, J.D.A (Ed.). *Tectonics and magmatism in Turkey and surrounding area*. Geological Society of London. Special Publications 173, 353-384.
- Yılmaz, Y., Genç, C., Karacık, Z., Altunkaynak, S. 2001. Two contrasting magmatic associations of NW Anatolia and their tectonic significance. *Journal of Geodynamics* 31, 243-271.
- Zanchi, A., Kissel, C., Tapırdamaz, C. 1993. Late Cenozoic and Quaternary brittle continental deformation in western Turkey. *Bulletin de la Société géologique de France* 164, 507-517.



Bulletin of the Mineral Research and Exploration

<http://bulletin.mta.gov.tr>



Upper Cretaceous-middle Eocene aged olistrostromal pelagic units in the Biga Peninsula (NW Anatolia); Balikkaya formation

Serdar AKGÜNDÜZ^{a*} and İzver ÖZKAR ÖNGEN^a

^a*Istanbul University-Cerrahpaşa, Faculty of Engineering, Department of Geological Engineering, Istanbul, Turkey*

Research Article

Keywords:

Balikkaya formation, Biga Peninsula, Pelagic foraminifera, Late Cretaceous-middle Eocene, Extensional tectonic regime.

ABSTRACT

Balikkaya formation consists of olistrostromal units with a burgundy coloured mudstone, siltstone and pelagic limestone matrix containing various sizes of Upper Jurassic-Lower Cretaceous limestone (Bilecik Limestone) blocks and Triassic Karakaya Complex blocks, which crop out in the west, south and southwest of Biga Town in Biga Peninsula (NW Anatolia). The matrix of Balikkaya formation, of which age and sedimentary environment are controversial, contains Late Cretaceous (Maastrichtian) *Abathomphalus mayaroensis* (Bolli), *Abathomphalus* sp., *Rosita fornicata* (Plummer), Globotruncanidae, early Paleocene (Danian) *Morozovella pseudobulloides* (Plummer), late Paleocene (Thanetian) *Morozovella velascoensis* (Bolli), early Eocene *Acarinina pentacamarata* (Subbotina), middle Eocene *Turborotalia frontosa* (Subbotina), *Turborotalia cerroazulensis* (Cole), *Orbulinoides beckmanni* (Saito), *Hantkenina* sp. pelagic foraminifera and Radiolaria fossils representing the deep marine environment. These paleontological, lithological and sedimentological data obtained from Balikkaya formation show that Balikkaya formation developed in a deep marine environment under tectonic control starting from Late Cretaceous and ending in early-middle Eocene. This pelagic unit indicates the presence of an extensional tectonic regime on the Biga Peninsula and the fault activity along the southeastern edge of the Thrace Basin in the Late Cretaceous-Middle Eocene time interval.

Received Date: 21.12.2019

Accepted Date: 10.04.2020

1. Introduction

The term olistostrom was first used by Flores (1955) to describe heterogeneous sedimentary deposits composed of blocks in a matrix fabric. Blocks in these chaotic units are called olistoliths. The blocky levels in the olistostromes can be found as interlayers with the normal stratified levels of a sedimentary sequence. Olistostromes are the geological masses that have a critical role in the study of old orogenic belts, subduction zones and multi-phase deformation events. Olistostromes, which provide excellent markers for

tectonic and climatic events, can be effectively used for basin analysis and modeling (Festa et al., 2016).

The area of investigation is located in Biga Peninsula (NW Anatolia), in the South-Southwest of Biga District. Biga Peninsula is the only area where Balikkaya formation consisting of late Mesozoic - early Cenozoic olistrostromal sedimentary units crops out (Figure 1-2). There is no study indicating the existence of a similar unit in the vicinity of Biga Peninsula. There are only a few studies on the age of Balikkaya formation, the environmental conditions in

Citation Info: Akgündüz, S., Özkaz Öngen, İ. 2021. Upper Cretaceous-Middle Eocene olistrostromal pelagic units in the Biga Peninsula (NW Anatolia); Balikkaya formation. Bulletin of the Mineral Research and Exploration 164, 119-145. <https://doi.org/10.19111/bulletinofmre.719876>

*Corresponding author: Serdar AKGÜNDÜZ, serdar.akgunduz@istanbul.edu.tr

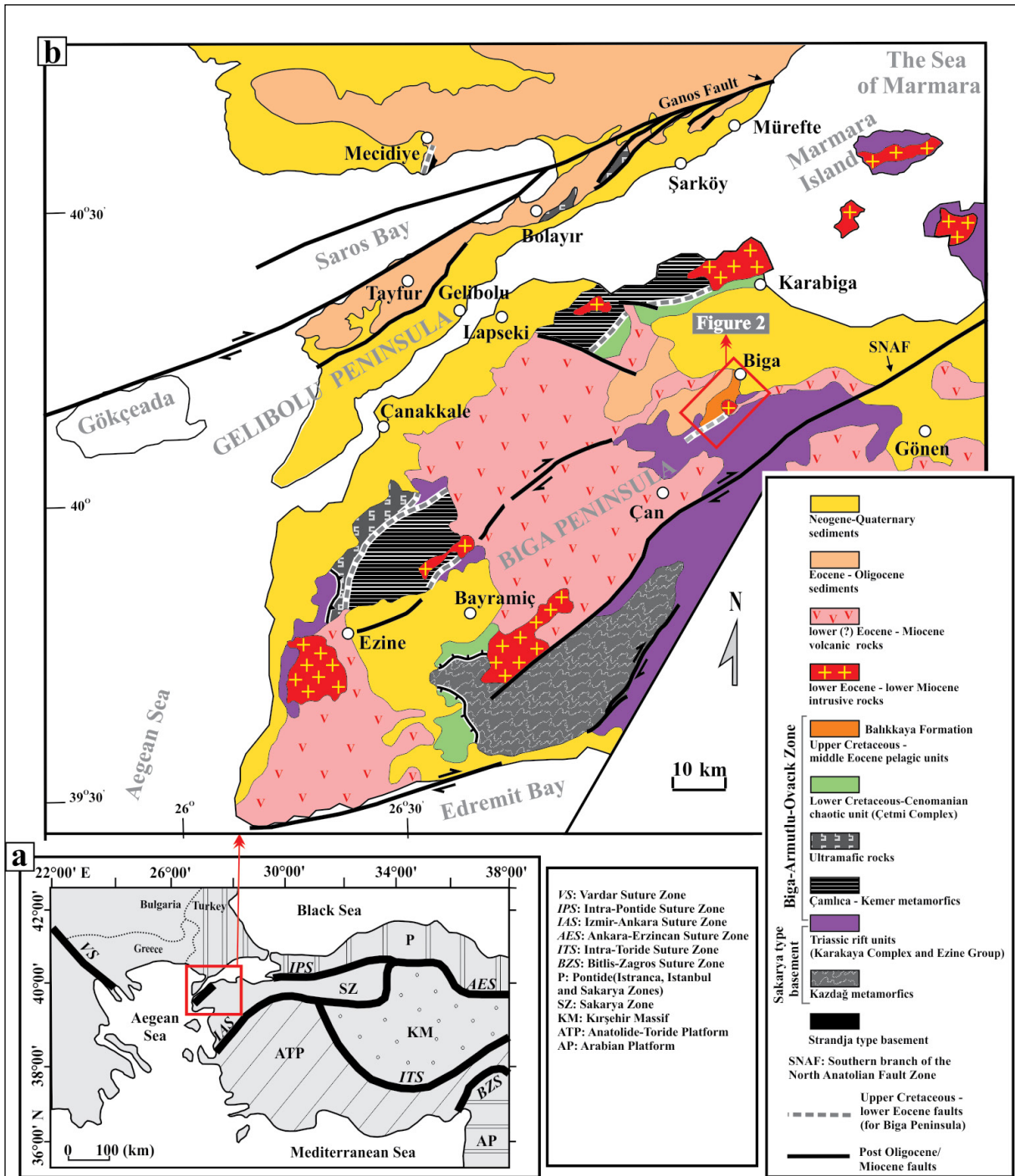


Figure 1- (a) Major tectonic units and suture zones of Turkey and its vicinity (Altunkaynak and Genç, 2007; Genç, 2004; Elmas, 2012; Karacık et al., 2008; Yılmaz et al., 2001) (b) generalized geological map in the Biga and Gelibolu Peninsulas (modified from Elmas, 2012 and Gürer et al., 2016).

which it developed and on its stratigraphy; these are limited to only two studies carried out by Yıkılmaz et al. (2002) and Atabey and Erdoğan (2003), and contain results that contradict each other. The formation was first named by Yıkılmaz et al. (2002) as Balıkkaya formation and presented as a Palaeocene-aged pelagic

unit. As for Atabey and Erdoğan (2003), they indicated that there is no such a unit that can be called as a formation in this region, and the blocked rifted units in this region that crop out only contains fossils pertaining to Late Cretaceous, and suggested that the existence of Balıkkaya formation is controversial. Although

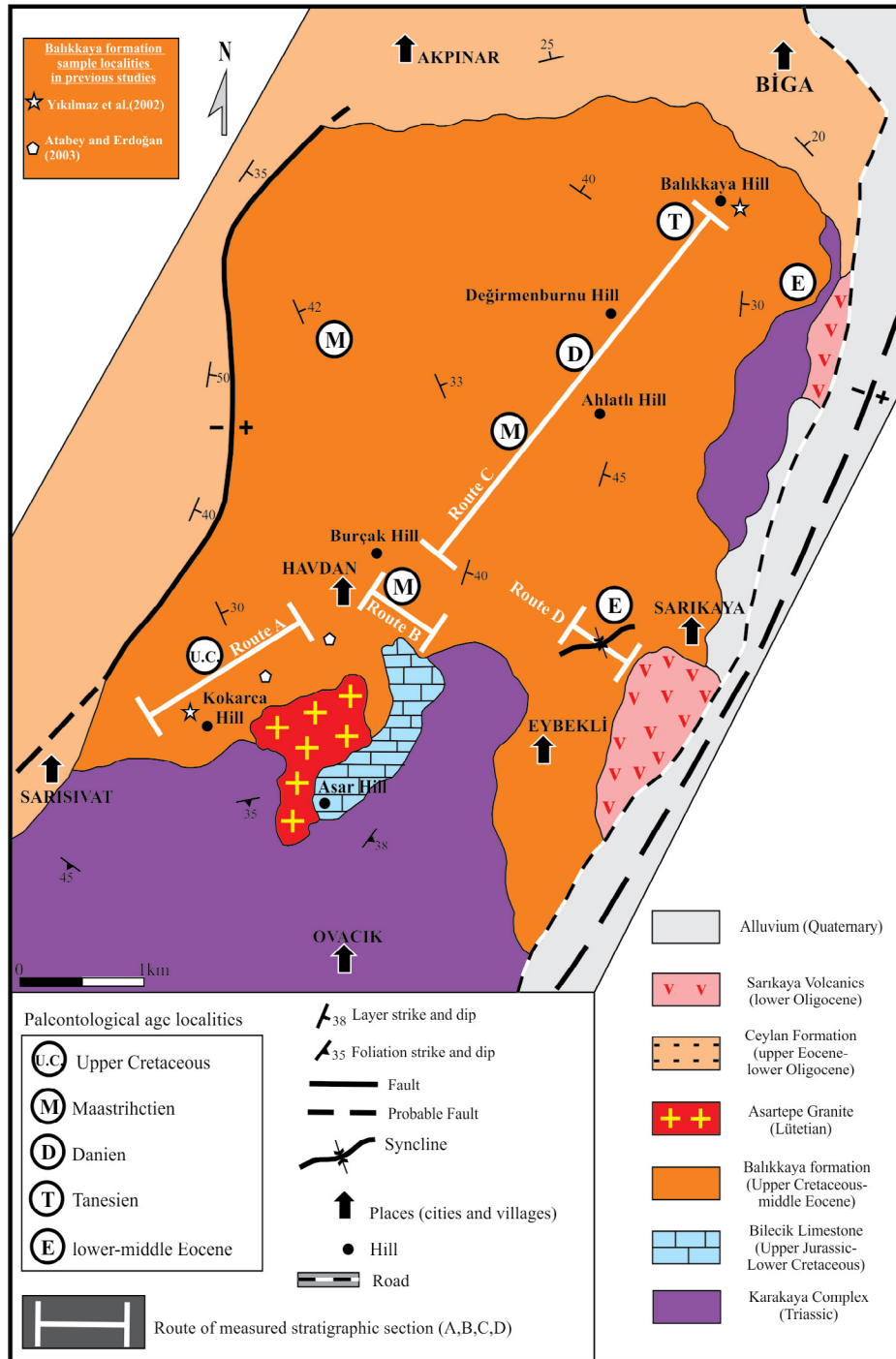


Figure 2- The geologic map of the Biga town and its surrounding area.

Yıkılmaz et al. (2002) indicate the unit is exposed in an area of 2km² and has a thickness over 100m, Atabey and Erdoğan (2003) suggest that there is not an outcrop as such for his formation. Besides, Atabey and Erdoğan (2003) have not provided a type locality and a type section for this unit. In this study, the name of Balikkaya formation is used for this olistostromal

unit that crops out in the South-Southwest of Biga district, in dedication to Balikkaya Hill where the unit is best exposed.

The Biga Peninsula, where the Balikkaya formation is exposed, is located on the junction of different continental fragments (Rhodope-Istranca

and Sakarya fragments) (Figure 1). Therefore, these olistostromal sediments are of critical importance to learn about the orogenic history of the region, the tectonic regime affecting the region and the expansion of the Thrace basin.

Within the scope of this study, for the purpose of clarifying the controversial age and sedimentary environment of Balıkkaya formation, the relationship between the surrounding units and contact was examined, measured stratigraphic sections were taken through four different routes (Figure 2), and new paleontological and stratigraphic data were obtained by collecting rock samples from matrix sections along the whole thickness in a way that they represent each section of Balıkkaya formation both laterally and vertically. The geological time interval and environmental conditions in which the unit developed were determined in the light of paleontological and stratigraphic data obtained from Balıkkaya formation.

2. Geology of Study Area

In Turkey, six main tectonic units are distinguished that are separated by different oceans (Figure 1a). These Istranca, İstanbul and Sakarya Zones, Anatolide-Tauride Platform and Arabian Platform (Şengör and Yılmaz, 1981; Şengör, 1982; Okay et al., 1994; Okay and Tüysüz, 1999). Istranca, İstanbul and Sakarya Zones that are located in the northern part of Turkey are collectively named as Pontides and are of Laurasia origin (Şengör and Yılmaz, 1981). Biga Peninsula are situated in the western most part of the Sakarya Zone, and limited from northwest with İstanbul, Rodop-Istranca zones and Thrace Basin along the Intra-Pontide Zone (Şengör and Yılmaz, 1981; Okay and Tüysüz, 1999; Bayrak et al., 2004; 2006). Pre-Cenozoic basic units in Biga Peninsula where the area of examination is located consist of Kazdağ Metamorphics, Karakaya Complex-Ezine Group, Çamlıca and Kemer metamorphics, Pre-Upper Cretaceous ophiolitic rocks (Denizgören Ophiolites), and Aptian-Cenomanian aged Çetmi Complex (Okay et al., 1991; Elmas, 2012) (Figure 1b).

Late Cretaceous-middle Eocene aged Balıkkaya formation that crops out in the South, Southwest and West of Biga town, sits on the Permo-Triassic aged Karakaya Complex at the bottom (Figure 1b, figure

2). On top, Balıkkaya formation is covered by late Eocene-early Oligocene Ceylan formation, early Oligocene Sarıkaya volcanics (Işıkeli volcanics; Aysal et al., 2011) and Quaternary deposits. Units pertaining to Balıkkaya formation in Asartepe locality in South-southwest of Biga (Figure 2) are cut by Lutetian aged Asartepe Granite (Akgündüz et al., 2012). Balıkkaya formation consists of olistostromal units with a burgundy coloured mudstone, siltstone and pelagic limestone matrix, which containing mainly Late Jurassic-Early Cretaceous aged limestone blocks and less amount belong to Karakaya Complex blocks (Figure 3).

3. Materials and Methods

Samples each weighing ca. 1 kg were collected for paleontological purposes. The samples were first crushed in a porcelain mortar, followed by washing in a sieve with mesh size of 63µ to remove its clay and mud. The samples were then treated with 10% HCl in porcelain vessels for 24 hours. This was followed by washing of the samples with pressurized water and then drying, in an oven set to 200°C. The dried samples were then sieved and size fraction below 500 µm were examined under binocular microscope. Fossils were handpicked, determined and photographed using Scanning Electron Microscope (FE-SEM) in İstanbul University-Cerrahpaşa Engineering Faculty Chemical Engineering Department, Process and Reactor Division Research Laboratory. The fossils were placed in their position on four measured stratigraphic sections, and temporal and spatial interpretations were made.

4. Paleontological Findings

Stratigraphic sections have been measured along four different routes (Figure 2, Route A, B, C, D) from the area where Balıkkaya formation crops out in order to determine the time lapse and environment in which the unit developed (Sarısivat-Havdan Section, figure 4; Havdan Section, figure 5; Burçak Hill-Balıkkaya Hill Section, figure 6; Sarıkaya Section, figure 7); and rock samples were collected from the matrix of Balıkkaya formation consisting of mudstone, shale, silt stone, sandstone and pelagic limestone lithologies during these section measurements, and then subjected to detailed paleontological examination.

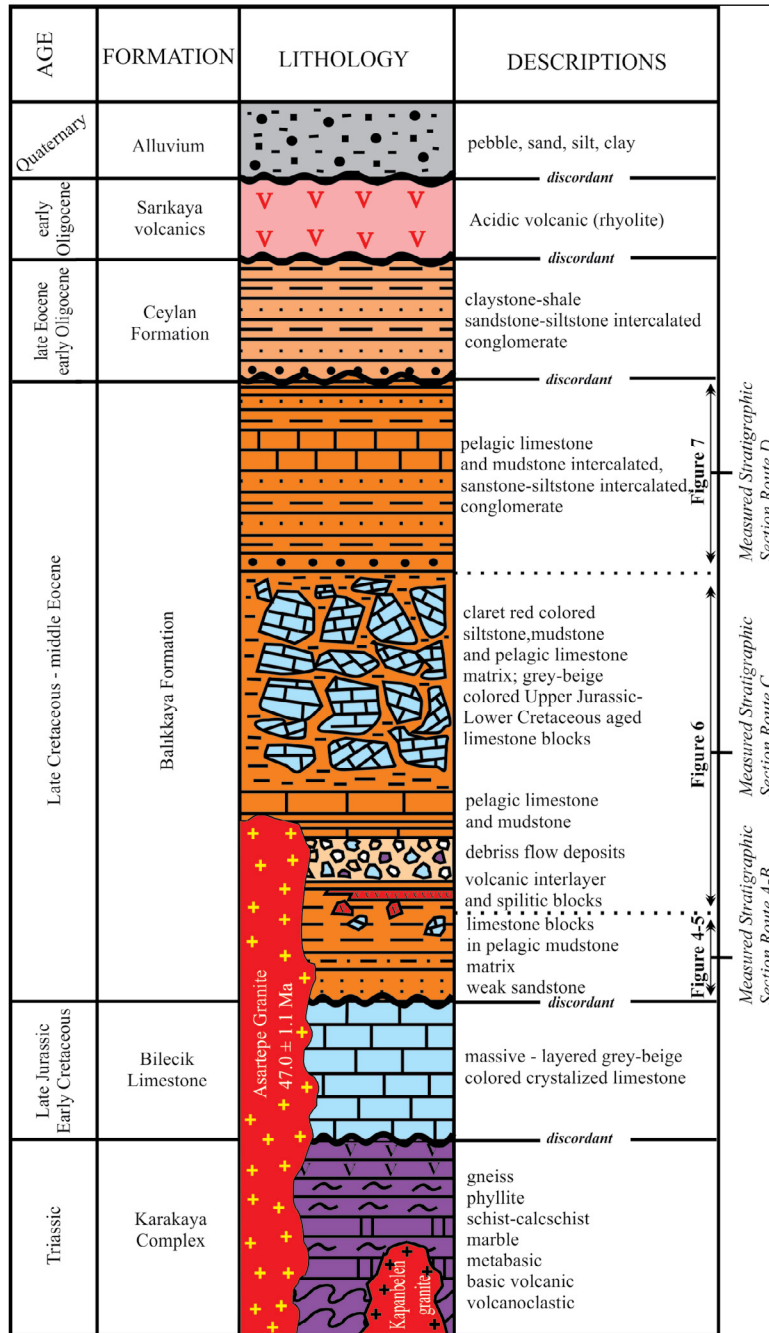


Figure 3- Generalized stratigraphic section of Biga Town and its surrounding area.

4.1. Measured Stratigraphic Sections

4.1.1. Sarisivat - Havdan Section (Route A)

This is the measured stratigraphic section taken from the route that extends from Southwest to Northeast from Sarisivat village located in the north-northwest of Asar hill in the southwest of Biga district to Havdan village in the North of Asar hill

(Figure 2, GPS coordinates: 40°11.090'N / 27°10.514'E - 40°11.817'N / 27°11.825'E). The total thickness of Sarisivat-Havdan section is 300 metres (Figure 4). Along the route from Sarisivat village to Havdan village (Route A), Balikkaya formation consists of burgundy and greenish mudstones – siltstones matrix (Figure 8a) containing Upper Jurassic-Lower Cretaceous limestone blocks and the layers are generally inclined towards the northeast. Along the

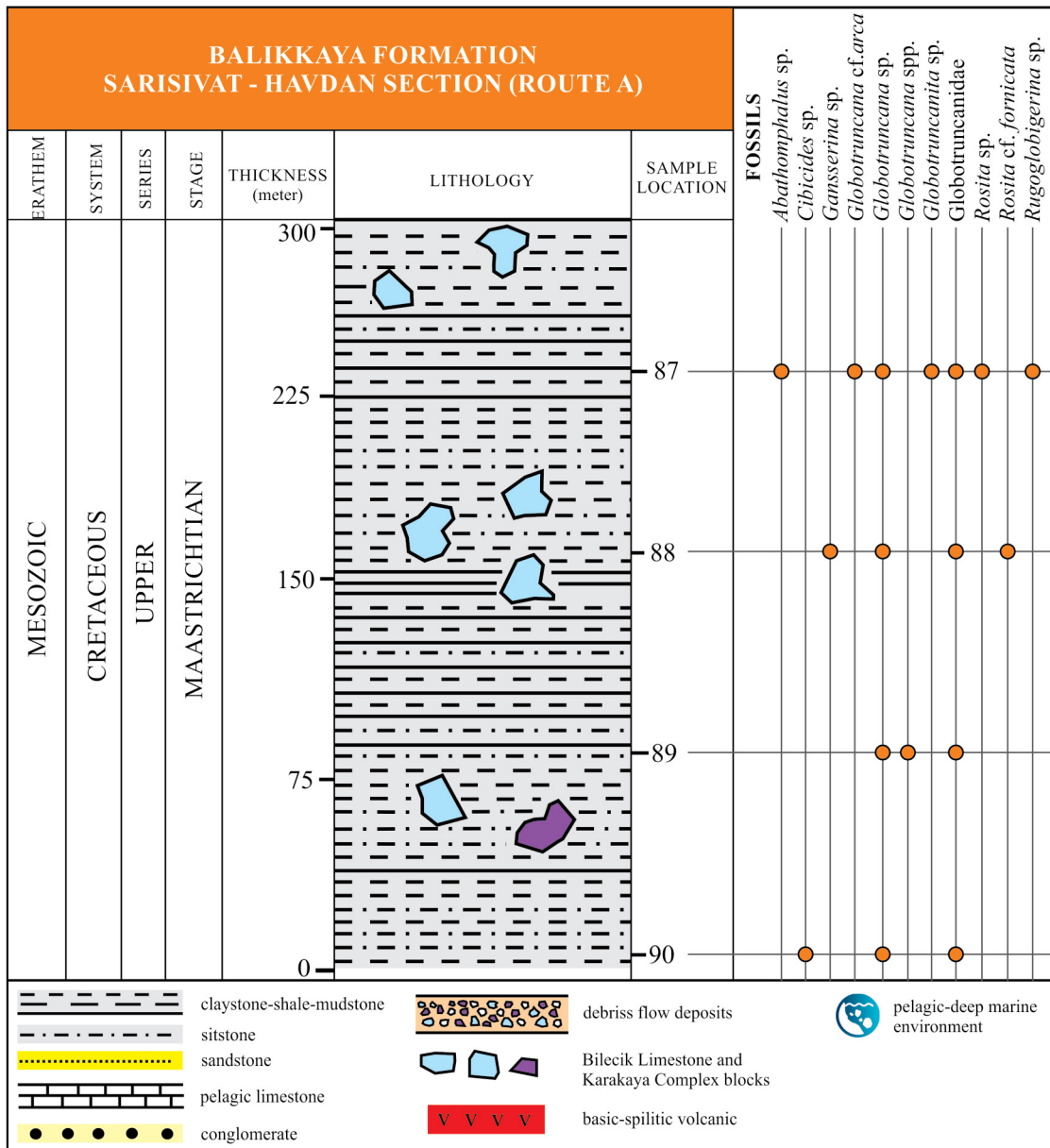


Figure 4- Sarisivat-Havdan measured stratigraphic section (Route A, see figure 2. GPS coordinates: 40°11.090'N / 27°10.514'E - 40°11.817'N / 27°11.825'E).

section, grain and rock samples from a total of 4 different levels were collected from Balikkaya formation matrix. Within this section, different planktonic foraminifera species were detected from *Abathomphalus* sp., *Gansserina* sp., *Globotruncana* cf. *arca* (Cushman), *Globotruncana* sp., *Globotruncanita* sp., *Rosita* cf. *fornicata* (Plummer), *Rosita* sp., *Rugoglobigerina* sp., *Cibicides* sp. and *Globotruncanidae* belonging to Late Cretaceous (Maastrichtian) (Figure 4, Plate I).

Yıkılmaz et al. (2002) indicated that the thin section of a micritic limestone taken from the southwest of

Havdan village contain *Planorotalites compressa* (Plummer), *Planorotalites* sp., *P. Morozovella* sp., *Globoconusa* sp., *Globotruncanita* cf. *stuarti* (d'Apparent), *Globotruncanita* sp., *Abathomphalus* sp., but stated that the *Globotruncana* species here could have probably been transported.

4.1.2. Havdan Section (Route B)

This is the measured stratigraphic section taken from the route that extends from Southeast to Northwest from the north-northeast of Asartepe

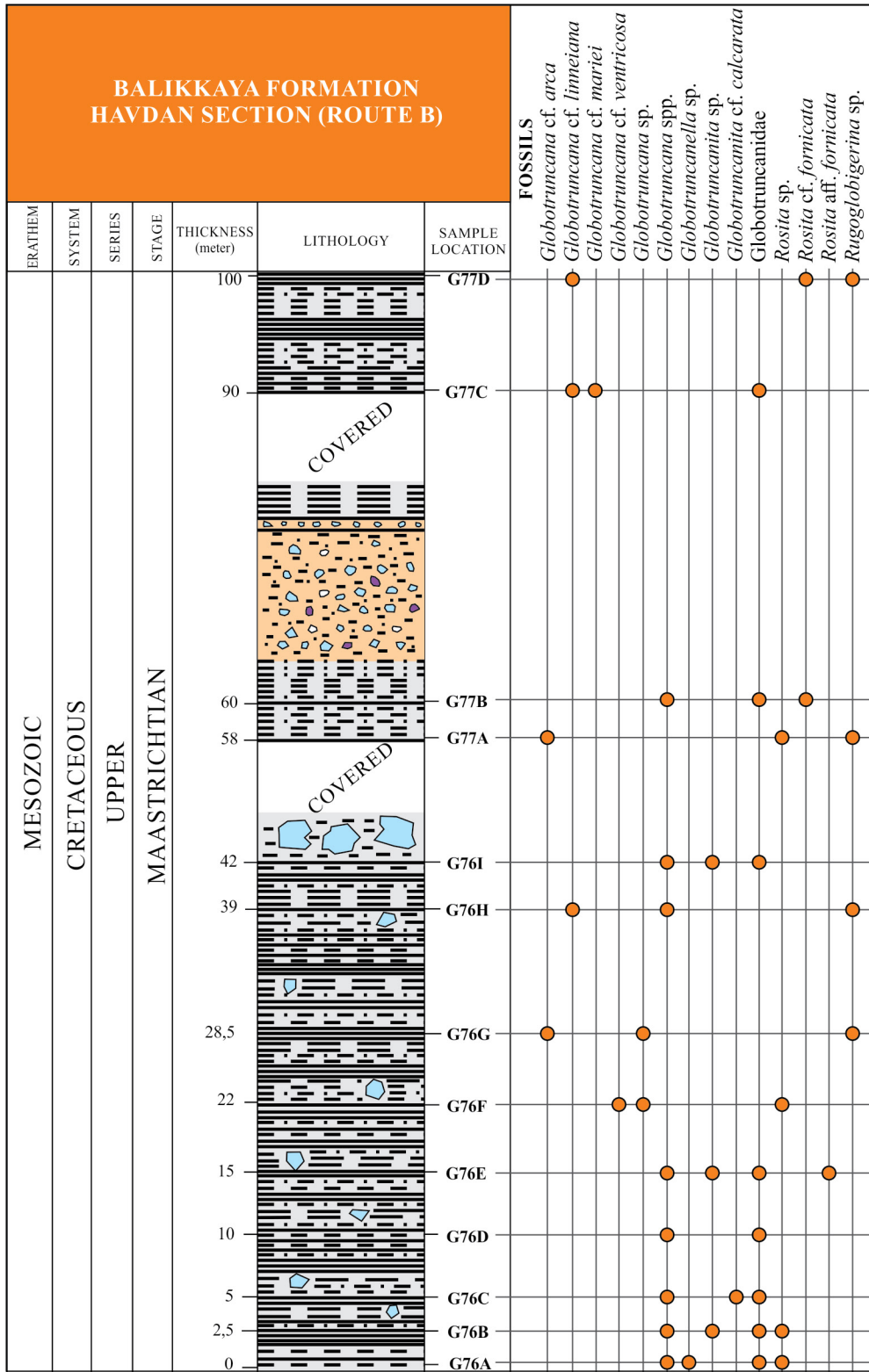


Figure 5- Havdan measured stratigraphic section (Route B, see figure 2. GPS coordinates: 40°11.564'N / 27°12.358'E - 40°11.851'N / 27°12.081'E).



Figure 8- Field photographs belonging to different stratigraphic levels of Balikkaya formation. (a) Pelagic mudstone matrix (North of Kokarca Hill). (b) conglomerate in pelagic matrix (Havdan village). (c) debris flow deposits, volcanic and pelagic mudstone levels (Ahlatlı Hill).

to Havdan village in the Southwest of Biga District (Figure 2, GPS coordinates: $40^{\circ}11.564'N$ / $27^{\circ}12.358'E$ - $40^{\circ}11.851'N$ / $27^{\circ}12.081'E$). The total thickness of Havdan section is 100 metres (Figure 5). In Havdan section, Balikkaya formation consists mainly of pink-purple coloured mudstone, siltstone, and partly, greenish-gray-coloured siltstones that contains Late Jurassic-Early Cretaceous aged limestone and gravels and blocks from Permo-Triassic aged Karakaya Complex, and rarely of gravelly levels (Figure 8b). The gravels in these gravelly levels consist of gray and burgundy coloured mudstones, gray siltstones, chert, and brown-beige-coloured

fine-grained sandstones. Along the section, grain and rock samples were taken from 13 different levels in Balikkaya formation matrix along the section. This section contains Late Cretaceous aged (Maastrichtian) *Globotruncana* cf. *arca* (Cushman), *Globotruncana* cf. *linneiana* (d'Orbigny), *Globotruncana* cf. *mariei* (Banner ve Blow), *Globotruncana* cf. *ventricosa* (White), *Globotruncana* sp., *Globotruncana* spp., *Globotruncanita* cf. *calcarata* (Cushman), *Globotruncanita* sp., *Globotruncanella* sp., *Rositac* cf. *fornicata* (Plummer), *Rosita* aff. *fornicata* (Plummer), *Rosita* sp. and *Rugoglobigerina* sp. planktonic foraminifera (Figure 5, Plate I).

Atabey and Erdoğan (2003) expressed that the red pelagic limestone samples they collected from the matrix of Balikkaya formation in the North of Sarısvat Village, and south and northeast of Havdan Village contain foraminifera with pelagic biofacies of the families *Globotruncana* gr. *linneiana* (d'Orbigny), *Globotruncana arca* (Cushman), *Globotruncanita stuartiformis* (Dalbiez) that are Maastrichtian aged, and *Globotruncanella citae* (Bolli), *Globotruncanella havanensis* (Voorwijk), *Abathomphalus* sp., *Rugoglobigerina rugosa* (Plummer) and Heterohelicidae that are late Maastrichtian aged.

4.1.3. Burçak Hill – Balikkaya Hill Section (Route C)

This is the measured stratigraphic section taken from the route that extends from southwest to northeast from Burçak Hill in the north-northwest of Havdan Village to Balikkaya Hill in the Southwest of Biga District (Figure 2, GPS coordinates: 40°11.990'N / 27°12.100'E - 40°13.454'N / 27°13.800'E). The section consists of grayish-beige coloured Jurassic-Cretaceous limestone blocks around Burçak Hill, and light yellowish-beige-coloured mudstones-siltstones and pink-purple coloured mudstones-pelagic limestone. There is a debris flow surface in the vicinity of Ahlatlı Hill (Figure 8c). The samples taken from burgundy coloured mudstones, siltstones and pelagic limestone between Burçak Hill and Ahlatlı Hill contain the Maastrichtian aged *Abathomphalus* sp., *Gansserina* cf. *gansseri* (Bolli), *Globorotalites* sp., *Globotruncana* cf. *aegyptiaca* (Nakkady), *Globotruncana* sp., *Globotruncana* spp., *Globotruncanella* cf. *havanensis* (Voorwijk), *Globotruncanella* sp., *Globotruncanita stuarti* (d'Apparent), *Globotruncanita* sp., Globotruncanidae, *Heterohelix* sp., Heterohelicidae, *Pseudotextularia* sp., *Rosita fornicata* (Plummer), *Rosita* sp., *Rugoglobigerina* sp., *Rugoglobigerina* spp. planktonic foraminifera and Radiolaria fossils (Figure 6, Plate I). Samples taken from pinkish-purple coloured pelagic mudstones, shales and limestone that crop out in the northeast of Ahlatlı hill and the southwest of Değirmenburnu hill contain early Paleocene (Danian) aged *Globigerina* sp., *Morozovella pseudobulloides* (Plummer), *Morozovella* cf. *bulloides* (Plummer), *Morozovella* sp. planktonic foraminifera and Radiolaria fossils (Figure 6, Plate II).

In Balikkaya hill locality, Balikkaya formation consists of a stratigraphic level that is abundant in

blocks. These Upper Jurassic-Lower Cretaceous limestone blocks are united among themselves, bluish grey-grayish beige in colour, grain supported, with variable sizes, rising up to 15-20 metres (Figure 9a-b). Towards the western slope of Balikkaya hill, the rate of matrix among the blocks increases. The matrix in the position of the binder of the blocks consists of pink-burgundy coloured mudstones-siltstones and limestone (Figure 9c). Burgundy coloured pelagic limestone taken from the vicinity of Balikkaya hill contains early Paleocene (Danian) aged *Globigerina* sp., *Morozovella pseudobulloides* (Plummer) planktonic foraminifera and Radiolaria (Figure 6, Plate II). Yıkılmaz et al. (2002) indicated that the fine sections of three micritic limestone samples taken from the vicinity of Balikkaya hill contain *Morozovella pseudobulloides* (Plummer), *M. uncinata* (Bolli), *M. cf. trinidadensis* (Bolli), *Morozovella* sp., *Planorotalites compressa* (Plummer), *Planorotalites* sp., *Globigerina triloculinoides* (Plummer), *Globigerina* sp., *Bolivina* sp. and Radiolaria that give the age of early Paleocene (Danian); again, a micritic limestone sample taken from the vicinity of Balikkaya hill contains *Morozovella velascoensis* (Bolli), *Planorotalites* sp. and Radiolaria that gives the age of late Paleocene (Thanetian).

4.1.4. Sarıkaya Section (Route D)

This is the measured stratigraphic section taken from the route that extends from Southeast to Northwest from Balikkaya formation, which crops out in a small area between the west-southwest of Sarıkaya Village and northeast of Eybekli Village (Figure 2, GPS coordinates: 40°11.641'N / 27°13.307'E - 40°11.658'N / 27°13.073'E). The total thickness of Sarıkaya Section is 54 metres (Figure 7) and the units in this area makes up a synclinal extending from northeast to southwest (Figure 2). In this section, Balikkaya formation consists of yellowish beige coloured - middle layered gravel, sandstone-siltstone sequence and burgundy coloured pelagic limestone and mudstones (Figure 9d). These units correspond to the highest levels of Balikkaya formation stratigraphically.

In Sarıkaya section, grain and rock samples were taken in three different points from burgundy coloured pelagic limestone and mudstones. Grain and rock samples taken contain *Acarinina* cf. *bullbrookii* (Bolli), *Acarinina pentacamarata* (Subbotina), *Acarinina* sp., *Bulumina* sp., *Clavulina* sp., *Cibicides*



Figure 9- Field photographs belonging to different stratigraphic levels of Balikkaya formation. (a-b) abundant and large blocky level (Balikkaya Hill). (c) Bilecik Limestone blocks in pelagic carbonate and mudstone matrix (SW of Balikkaya Hill). (d) Intercalated of pelagic limestone-mudstone and sandstone-conglomerate (West of Sankaya village).

sp., *Dentalina* sp., *Dorothia (Areneblumina)* sp., *Globigerina carcoselleensis* (Toumarkine ve Bolli), *Globigerinatheka* cf. *index* (Finlay), *Globigerinatheka* sp., *Hantkenina* sp., *Lagena* sp., *Morozovella* cf.

aragonensis (Nutta 2), *Morozovella* sp., *Orbulinoides beckmanni* (Saito), *Orbulinoides* cf. *beckmanni* (Saito), *Orbulinoides* sp., Osanguliridae, *Pseudohastigerina* sp., *Trochammina* sp., *Turborotalia boweri* (Bolli),

Turborotalia cf. boweri (Bolli), *Turborotalia frontosa* (Subbotina), *Turborotalia centralis* (Cushman ve Bermudez), *Turborotalia cf. cerrazulensis* (Cole), *Turborotalia cerroazulensis* (Cole), *Turborotalia* sp., *Uvigerina* sp. planktonic foraminifera and Radiolaria fossils from early-middle Eocene (Figure 7, Plate II, Plate III, Plate IV).

5. Discussions

Balıkkaya formation that crops out in the south, southwest and west of Biga town in northwest Anatolia mainly consists of Late Jurassic-Early Cretaceous aged limestone blocks of varying sizes and at a lower degree, units with a burgundy coloured mudstone, siltstone and pelagic limestone matrix, which contain blocks from Karakaya Complex. The formation was first named by Yıkılmaz et al. (2002) as Balıkkaya formation in dedication to the hill that is considered to best outcrop. However, Atabey and Erdoğan (2003) stated that the name of the hill was not Ballıkaya but Balıkkaya and for that reason they used Balıkkaya in parenthesis when they referred to the formation. Similarly, for the formation termed Ballıkaya by Yıkılmaz et al. (2002), the name Balıkkaya was preferred in this study.

Yıkılmaz et al. (2002) gave the age of Balıkkaya formation as Paleocene (Danian-Thantian) by the foraminifera in pelagic limestone (Table 1). They interpreted the *Globotruncana* forms in these foraminifera as transported from Upper Cretaceous. Atabey and Erdoğan (2003) indicated the age of the unit, of which existence they deem disputable, is late Maastrichtian by the *Globotruncana* forms obtained from burgundy coloured fine layered limestone, and did not encounter any fauna related to the Paleocene (Table 1). Yıkılmaz et al. (2002) gave the Paleocene age they obtained from the study they carried out in accordance with the fossils determined from 1 micritic limestone sample collected from the vicinity of Kokarca Hill and 3 micritic limestone samples from Balıkkaya Hill (Figure 2). In relation to the unit existence of which they find disputable, Atabey and Erdoğan (2003) indicated that the units in question are of Late Cretaceous age according to paleontological data they collected from the vicinity of Havdan and Sarısvat villages (Figure 2). However, Balıkkaya formation is not solely limited to these localities and have a wider expansion (Figure 2). Moreover, there is no detailed information about stratigraphic, sedimentological and environmental conditions of the

Balıkkaya formation in these studies (Yıkılmaz et al., 2002; Atabey and Erdoğan, 2003).

According to field observations in this study, Balıkkaya formation stratigraphically starts with a weak, yellowish-reddish sandstone level at the bottom (Figure 3). This weak sandstone level that does not contain any fossil was interpreted as Balıkkaya formation started to deposit in a terrestrial-shallow setting (Figure 10a). But the pelagic carbonates and mudstones overlying the terrestrial sandstones have been found to Late Cretaceous pelagic foraminifera. The starting age of Balıkkaya formation can be given as Late Cretaceous. The Upper Cretaceous time for the Biga Peninsula, where the Balıkkaya formation is exposed, is a geologically critical time. The northeast of the Vardar Ocean, which separates the Rhodope and Sakarya continents in Anatolia, closes in this period. Following the collision of the Rhodope and Sakarya continents, this suture zone acts as a strike-slip fault zone (Western Pontide Fault Zone) and begins to open the Thrace basin with the transtensional tectonic regime in the end of Late Cretaceous (Elmas, 2012). This transtensional tectonic regime was active during the Late Cretaceous-Paleocene period in the Northeastern Vardar Zone while it was active until the early-middle Eocene in the Armutlu-Ovacık zone to the east (Elmas, 2012). Balıkkaya formation developed under this transtensional tectonic regime and strike-slip fault system during the Late Cretaceous-middle Eocene (Figure 10a-d).

Blocky levels are more abundant in the Maastrichtian and Paleocene sections of this pelagic unit (Figure 6, figure 11). Furthermore, that the blocked levels within the Balıkkaya formation are mainly grain supported and poorly sized. This indicates the presence of the proximal source area and the sedimentation under the tectonic control in the pelagic environment (Figure 10b-c). However, blocky levels decrease at the upper levels of the sequence and a more regular sedimentation of pelagic limestone-mudstone and sandstone-conglomerate is observed (Figure 7, figure 11). This indicates that fault activity is not effective during the early-middle Eocene period in this region (Figure 10d).

6. Conclusion

Abathomphalus sp., *Abathomphalus mayaroensis* (Bolli), *Rosita fornicata* (Plummer) and different species of Globotruncanidae characterizing Upper

Table 1- Paleontological age data belonging to Balikkaya formation.

Age	Yıkılmaz et al. (2002)	Atabey and Erdoğan (2003)	This study	
early – middle Eocene			<p><i>Acarinina</i> cf. <i>bullbrookii</i> (Bolli) <i>Acarinina pentacamerata</i> (Subbotina) <i>Acarinina</i> sp. <i>Bathysiphon</i> cf. <i>eocenicus</i> (Cushman ve Hanna) <i>Bulumina</i> sp. <i>Clavulina</i> sp. <i>Cibicides</i> sp. <i>Coskinolina</i> sp. <i>Dentalina</i> <i>Dorethia (Areneblumina)</i> sp. <i>Globigerina carcoselleensis</i> (Toumarkine ve Bolli) <i>Globigerina linaperta</i> (Finlay) <i>Globigerina</i> cf. <i>senni</i> (Beckmann) <i>Globigerina</i> sp. <i>Globigerinatheka</i> cf. <i>index</i> (Finlay) <i>Globigerinatheka</i> spp. <i>Hantkenina</i> sp. <i>Marginulinopsis</i> sp. Miliolidae <i>Morozovella</i> cf. <i>aragonensis</i> (Nuttall) <i>Morozovella</i> cf. <i>crassata</i> (Cushman)</p>	<p><i>Morozovella</i> sp. <i>Orbulinoides beckmanni</i> (Saito) <i>Orbulinoides</i> sp. Osangularidae <i>Pseudohastigerina</i> sp. Radiolaria <i>Trochammina</i> sp. <i>Turborotalia</i> sp. <i>Turborotalia frontosa</i> (Subbotina) <i>Turborotalia cf. boweri</i> (Bolli) <i>Turborotalia centralis</i> (Cushman and Bermudez) <i>Turborotalia cerroazulensis</i> (Cole) <i>Turborotalia</i> spp. <i>Truncoroides</i> sp. <i>Uvigerina</i> sp. Verneullinidae <i>Verneullina</i> sp.</p>
Tanesian	<i>Morozovella velascoensis</i> (Bolli)			
Danian	<p><i>Bolivina</i> sp. <i>Globigerina</i> sp. <i>Globigerina triloculinoides</i> (Plummer) <i>Globoconusa</i> sp. <i>Morozovella</i> sp. <i>Morozovella pseudobulloides</i> (Plummer) <i>M. uncinata</i> (Bolli) <i>M. cf. trinidadensis</i> (Bolli) <i>Planorotalites compressa</i> (Plummer) Radiolaria</p>		<p><i>Morozovella pseudobulloides</i> (Plummer) <i>Morozovella</i> cf. <i>pseudobulloides</i> (Plummer) <i>Morozovella</i> sp. <i>Morozovella</i> spp. <i>Planorbulina</i> sp.</p>	
Late Cretaceous		<p><i>Abathomphalus</i> sp. <i>Globotruncana arca</i> (Cushman) <i>Globotruncana</i> gr. <i>linneiana</i> (d Orbigny) <i>Globotruncanella citae</i> (Bolli) <i>Globotruncanella havanensis</i> (Voorwijk) <i>Globotruncanita stuatiformis</i> (Dalbiez) Heterohelicidae <i>Rugoglobigerina rugosa</i> (Plummer)</p>	<p><i>Abathomphalus</i> sp. <i>Gansserina</i> cf. <i>gansseri</i> (Bolli) <i>Gansserina</i> sp. <i>Globorotalites</i> sp. <i>Globotruncana</i> cf. <i>aegyptiaca</i> (Nakkady) <i>Globotruncana</i> cf. <i>arca</i> (Cushman) <i>Globotruncana</i> cf. <i>bulloides</i> (Vogler) <i>Globotruncana</i> cf. <i>linneiana</i> (d Orbigny) <i>Globotruncana</i> cf. <i>mariei</i> (Banner and Blow) <i>Globotruncana</i> cf. <i>ventricosa</i> (White) <i>Globotruncana</i> sp. <i>Globotruncana</i> spp. <i>Globotruncanella</i> cf. <i>havanensis</i> (Voorwijk) <i>Globotruncanella</i> sp. <i>Globotruncanita</i> cf. <i>calcarata</i> (Cushman) <i>Globotruncanita stuarti</i> (d Lapparent)</p>	<p><i>Globotruncanita</i> sp. Globotruncanidae <i>Pseudotextularia</i> sp. Radiolaria <i>Rosita fornicata</i> (Plummer) <i>Rosita</i> cf. <i>fornicata</i> (Plummer) <i>Rosita</i> aff. <i>fornicata</i> (Plummer) <i>Rosita</i> cf. <i>plummerae</i> (Gandolfi) <i>Rosita</i> sp. <i>Rosita</i> spp. <i>Rugoglobigerina</i> sp. <i>Rugoglobigerina</i> spp. Heterohelix sp. <i>Lagena</i> sp. <i>Lenticulina</i> sp. Heterohelicidae <i>Anomalinoides</i> sp. <i>Cibicides</i> sp.</p>

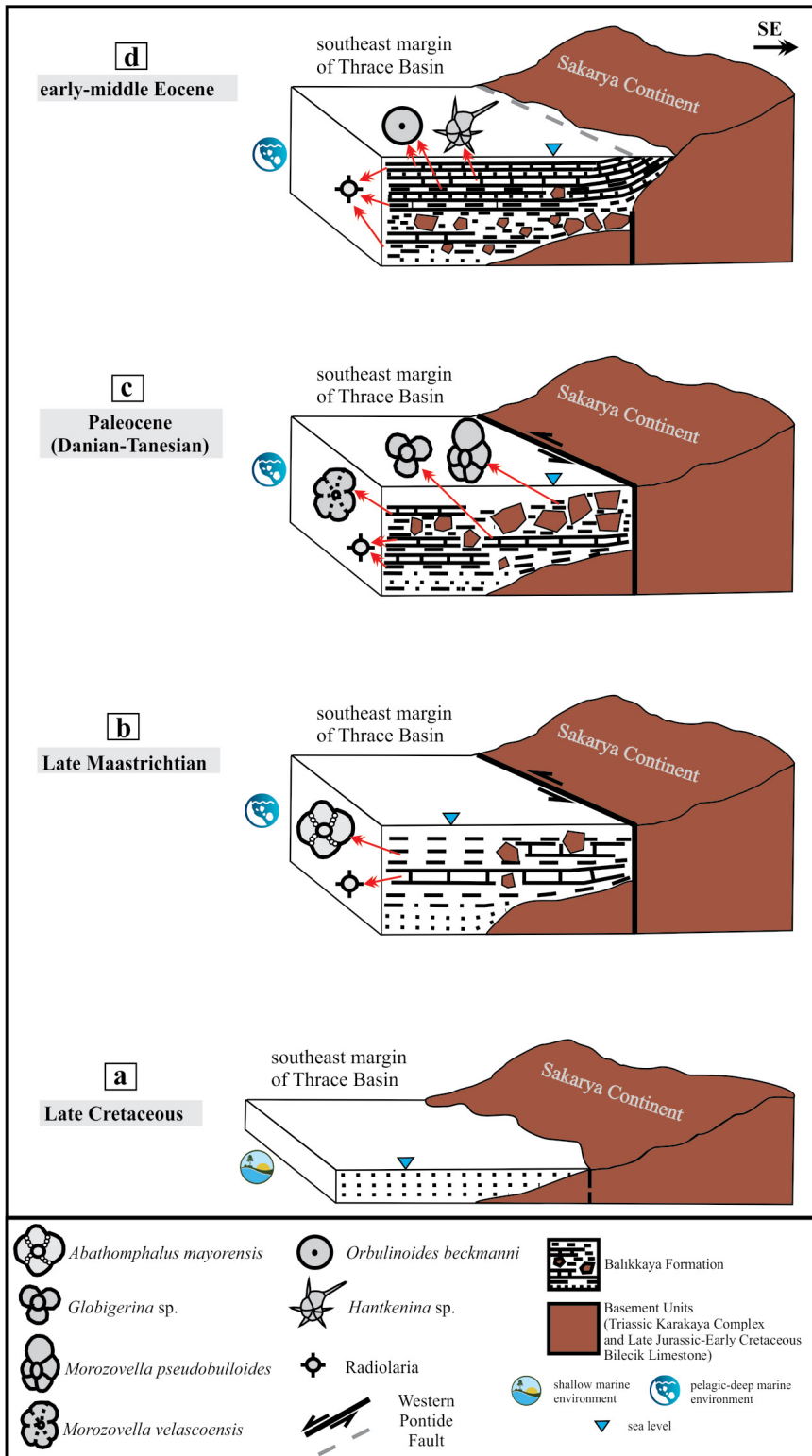


Figure 10- Paleoenvironment of Bahikkaya formation during the Late Cretaceous-middle Eocene interval.

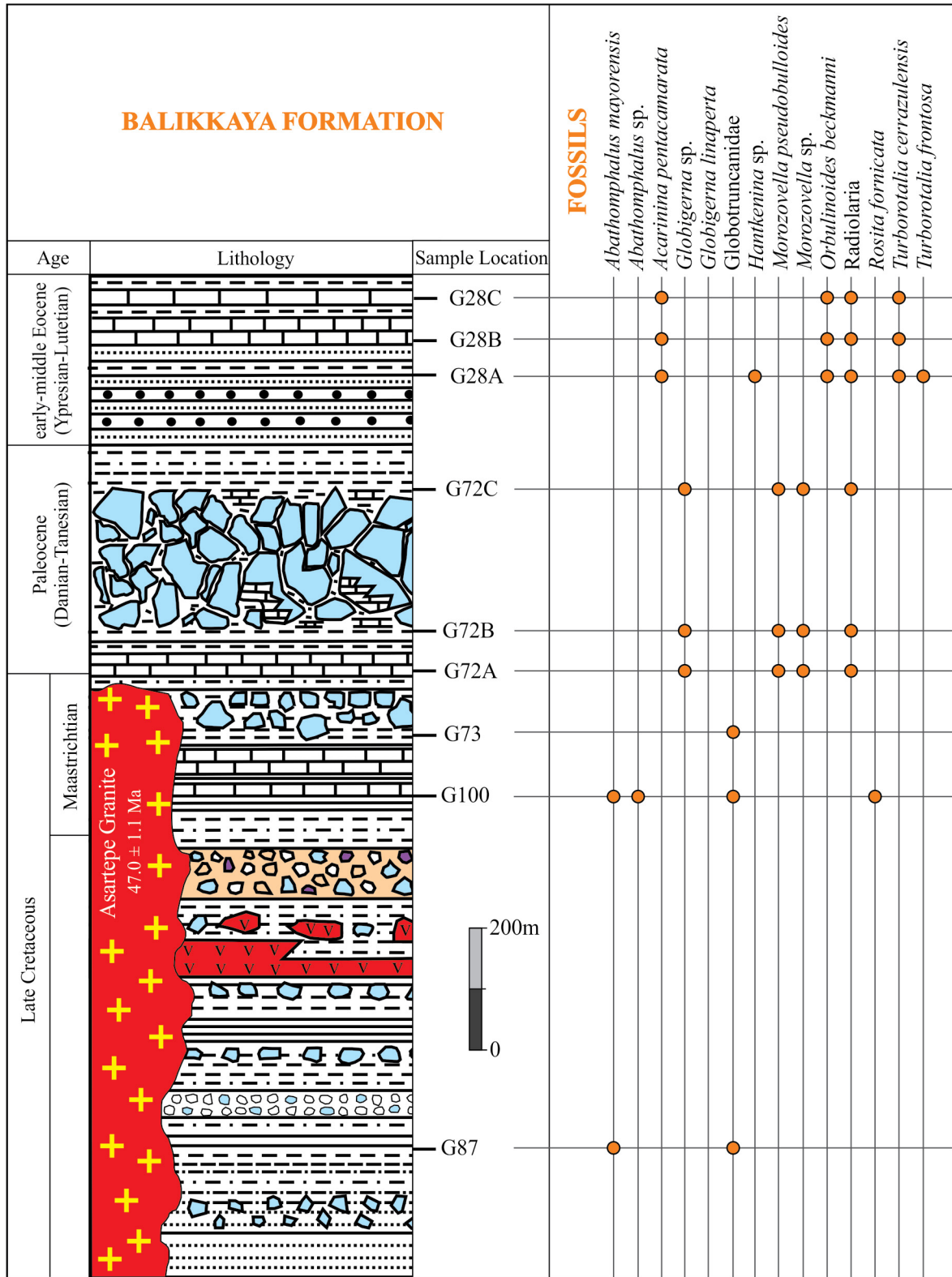


Figure 11- Vertical section and marker fossils of Balikkaya formation.

Cretaceous (Maastrichtian) were determined in the section close to the bottom of Balıkkaya formation; *Morozovella pseudobulloides* (Plummer) and different species of *Globigerina* symbolizing lower Paleocene (Danian) were determined in the upper sections of the formation that are abundant in blocks; and *Acarinina pentacamarata* (Subbotina) pointing to the lower Eocene, and *Orbulinoides beckmanni* (Saito), *Turborotalia cerroazulensis* (Cole), *Turborotalia frontosa* (Subbotina), *Turborotalia boweri* (Bolli), *Globigerina linaperta* (Finlay) and *Hantkenina sp.* pelagic foraminifera species that are the biozone fossils characterizing the middle Eocene were determined in the stratigraphically highest levels of the unit (Plate I-II-III-IV, Table 1). According to these paleontological data, the age of Balıkkaya formation is given is Late Cretaceous – middle Eocene. Furthermore, Radiolaria fossilssymbolizing deep marine environment were determined from the bottom to the top of Balıkkaya formation (from the Upper Cretaceous to middle Eocene).

As a result, according to paleontological and sedimentological data obtained, Balıkkaya formation age and environment of which is disputable, represents a deep marine environment under the control of tectonism that developed following a short terrestrial precipitation period and lasted from Late Cretaceous to middle Eocene. This pelagic unit indicates the presence of an extensional tectonic regime on the Biga Peninsula and the fault activity along the southeastern edge of the Thrace Basin during the LateCretaceous-middle Eocene time interval.

References

- Akgündüz, S., Duru, O., Elmas, M.A. 2012. KB Anadolu'da Eosen-Oligosen Çarpışma Sonrası Magmatizma: Asartepe Granitik ve Sarıkaya Volkanik Kayalarından Jeokimyasal ve Jeokronolojik Veriler, İstanbul Yerbilimleri Dergisi 25, 2, 119-143.
- Atabey, E., Erdoğan, K. 2003. Biga Yarımadasında varlığı tartışmalı pelajik bir Paleosen istifi: Balıkkaya (Balıkkaya) Formasyonu. Maden Tetkik ve Arama Dergisi 126, 43-47.
- Altunkaynak, Ş., Genç, Ş.C. 2007. Petrogenesis and time-progressive evolution of the Cenozoic continental volcanism in the Biga Peninsula, NW Anatolia (Turkey). Science Direct 102, 316-340.

- Aysal, N., Öngen, S., Keskin, M. 2011. Cenozoic volcano-stratigraphy and petrological evolution of post-collisional volcanic rocks in eastern Biga Peninsula, NW Anatolia, Turkey. In: International Multidisciplinary Scientific Geo Conference (SGEM-2011), 19–26.
- Bayrak, M., Gürer, A., Gürer, Ö.F. 2004. Electromagnetic imaging of the Thrace Basin and Intra-Pontide Subduction Zone, Northwestern Turkey. International Geology Review 46, 64–74, doi: 10.2747/0020-6814.46.1.64.
- Bayrak, M., Gürer, A., Gürer, Ö.F., İlkışık, O.M., Başokur, A.T. 2006. Mohr-circle-based rotational invariants of a magnetic data set from the Thrace region of Turkey. Turkish Journal of Earth Sciences 15, 95–110
- Elmas, A. 2012. Basement types of the Thrace Basin and new approach to the pre-Eocene tectonic evolution of the northeastern Aegean and Northwestern Anatolia: a review of data and concepts. Int J Earth Sci (Geol Rundsch) 101, 1895-1911.
- Festa, A., Ogata, K., Pini, G.A., Dilek, Y. 2016. Origin and Significance of Olistostromes in the Evolution of Orogenic Belts: A Global Synthesis. Gondwana Research 39, 180-203. DOI: 10.1016/j.gr.2016.08.002.
- Flores, G. 1955. Discussion, in Beneo, E., les resultats des etudes pour la recherche petrolifere en Sicile (Italie). 4 th. World. Petroleum Congress. Rome., Proct. Sect. I, 121-122.
- Genç, Ş.C., 2004. A Triassic large igneous province in the Pontides, northern Turkey: geochemical data for its tectonic settings. Journal of Asian Earth Sciences 22 (5), 503–516.
- Gürer, Ö.F., Sangu, E., Özbüran, M., Gürbüz, A., Gürer, A., Sınır, H. 2016. Plio-Quaternary kinematic development and paleostress pattern of theEdremit Basin, western Turkey. Tectonophysics 679, 199–210.
- Karacık, Z., Yılmaz, Y., Pearce, J.A., Ece, O.I. 2008. Petrochemistry of the south Marmara granitoids, northwest Anatolia, Turkey. International Journal of Earth Sciences 97, 1181–1200. doi:10.1007/s00531-007-0222-y.
- Şengör, A.M.C. 1982. Ege'nin neotektonik evrimini yöneten etkenler. Türkiye Jeoloji Kurultayı, Batı Anadolu'nun Geç Tektoniği ve Volkanizması Paneli, Ankara, 59-71.
- Şengör, A.M.C., Yılmaz, Y. 1981. Tethyan evolution of Turkey: a plate tectonic approach. Tectonophysics 75, 181–241.

- Okay, A.I., Tüysüz, O. 1999. Tethyan sutures of Northern Turkey. In: Durand, B., Jolivet, L., Horthváth, F., Séranne, M. (Eds.), *The Mediterranean Basin: Tertiary Extension within the Alpine Orogen*: Geological Society, London, Special Publication 156, vol. 156, 475–515.
- Okay, A. İ., Siyako, M., Bürkan, K. A. 1991. Geology ve Tectonic Evolution of the Biga Peninsula, Northwestern Turkey, İTÜ Bülteni 44, 191-256.
- Okay, A.I., Şengör, A.M.C., Görür, N. 1994. Kinematic history of the opening of the Black Sea and its effect on the surrounding regions. *Geology* 22, 267–270.
- Yıkılmaz, M.B., Okay, A.I., Özkar, I. 2002. A Pelagic Palaeocene Sequence in the Biga Peninsula Northwest Turkey. *Bulletin of the Mineral Research and Exploration* 123-124, 21-26.
- Yılmaz, Y., Genç, S.C., Karacık, Z., Altunkaynak, Ş. 2001. Two contrasting magmatic associations of NW Anatolia and their tectonic significance. *Journal of Geodynamics* 31, 243–271.

PLATES

Plate I. Fossil photos from Sarısvat-Havdan section (a, e), Havdan section (b) and Burçak Hill-Balıkkaya Hill section (c, d, f, g, h, i, j). Sample number; a: 90, b: G76F, c-d-f-g-h-i-j: G100, e:87.

a-b. *Globotruncana* sp., Late Cretaceous.

c. *Globotruncana stuarti* (de Lapparent), Maastrichtian.

d-e. *Abathomphalus* sp., Maastrichtian.

f. Heterohelicidae, Late Cretaceous.

g. *Rogoglobigerina* sp., Late Cretaceous.

h-i. Radiolaria.

i. *Abathomphalus mayaroensis* (Cole), Late Maastrichtian.

j. *Globorotalites* sp., Late Cretaceous.

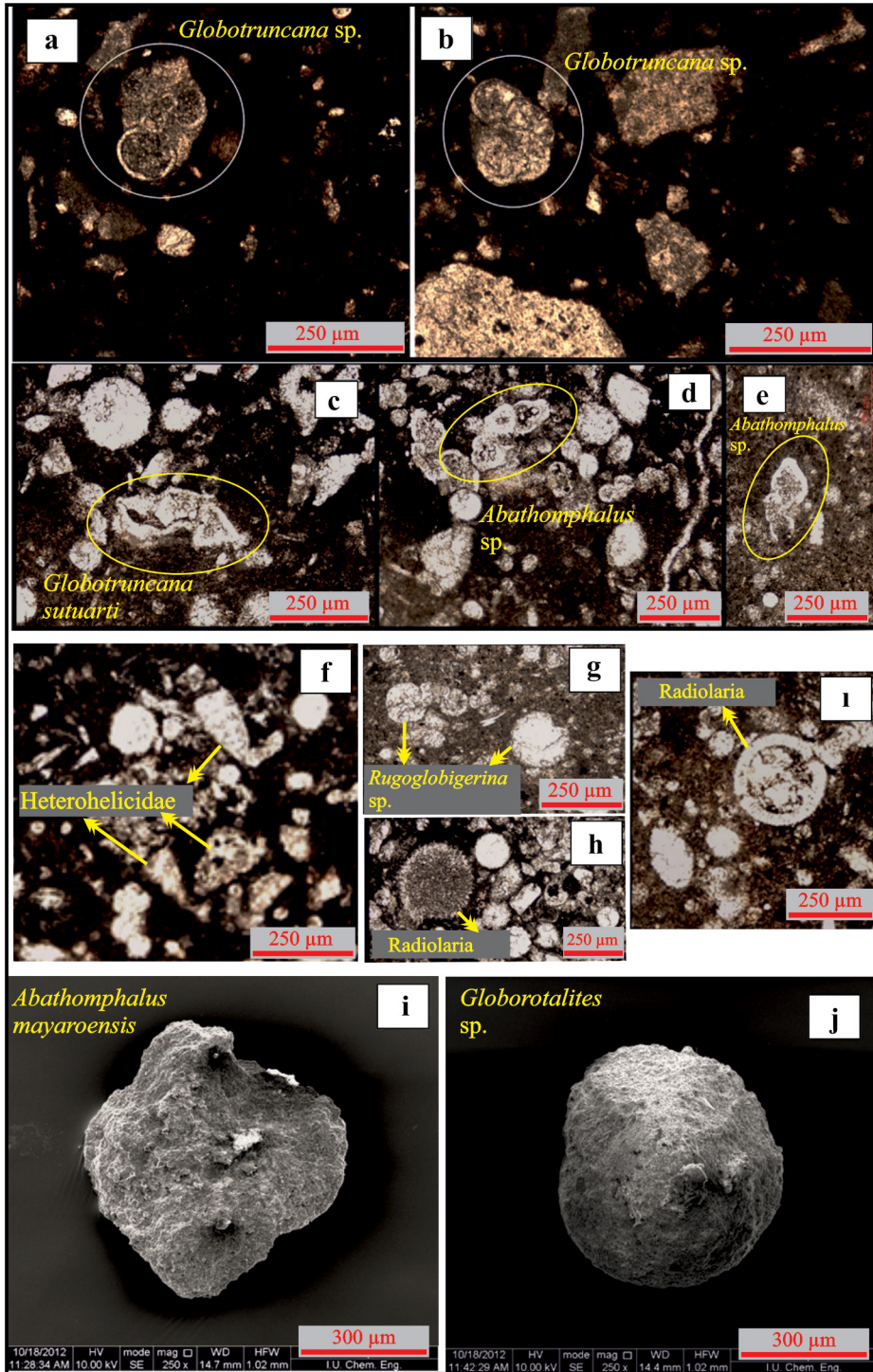


Plate II. Fossil photos from Burçak Hill-Balikkaya Hill section (a, b, c, d) and Sarıkaya section (e). Sample number; a: G72A, b-c-d: G72C, e: 28A.

a. *Globigerina* sp., Paleocene.

b-c. *Morozovella pseudobulloides* (Plummer), Danian.

d. *Globigerina* sp., Paleocene.

e. *Acarinina pentacamarata* (Subbotina), early Eocene.

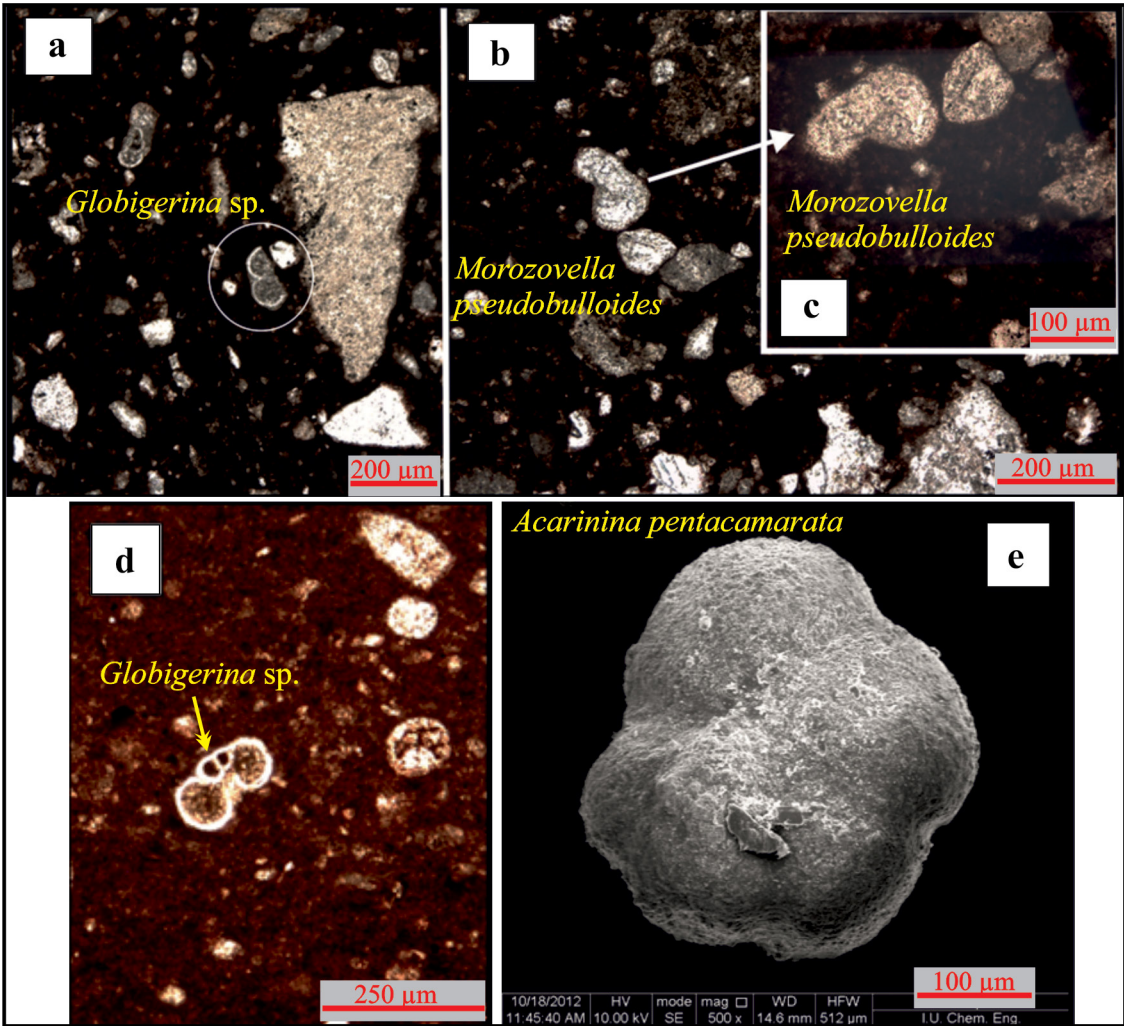


Plate III. Fossil photos from Sarıkaya section (a-f). Sample number; a-b: 28A, c-d: 28B, e-f: 28C.

a-b. *Hantkenina* sp., middle-upper Eocene.

c-d. *Turborotalia frontosa* (Subbotina), middle Eocene.

e. *Turborotalia cerroazulensis* (Cole), middle Eocene.

f. *Orbulinoides beckmanni* (Saito), middle Eocene.

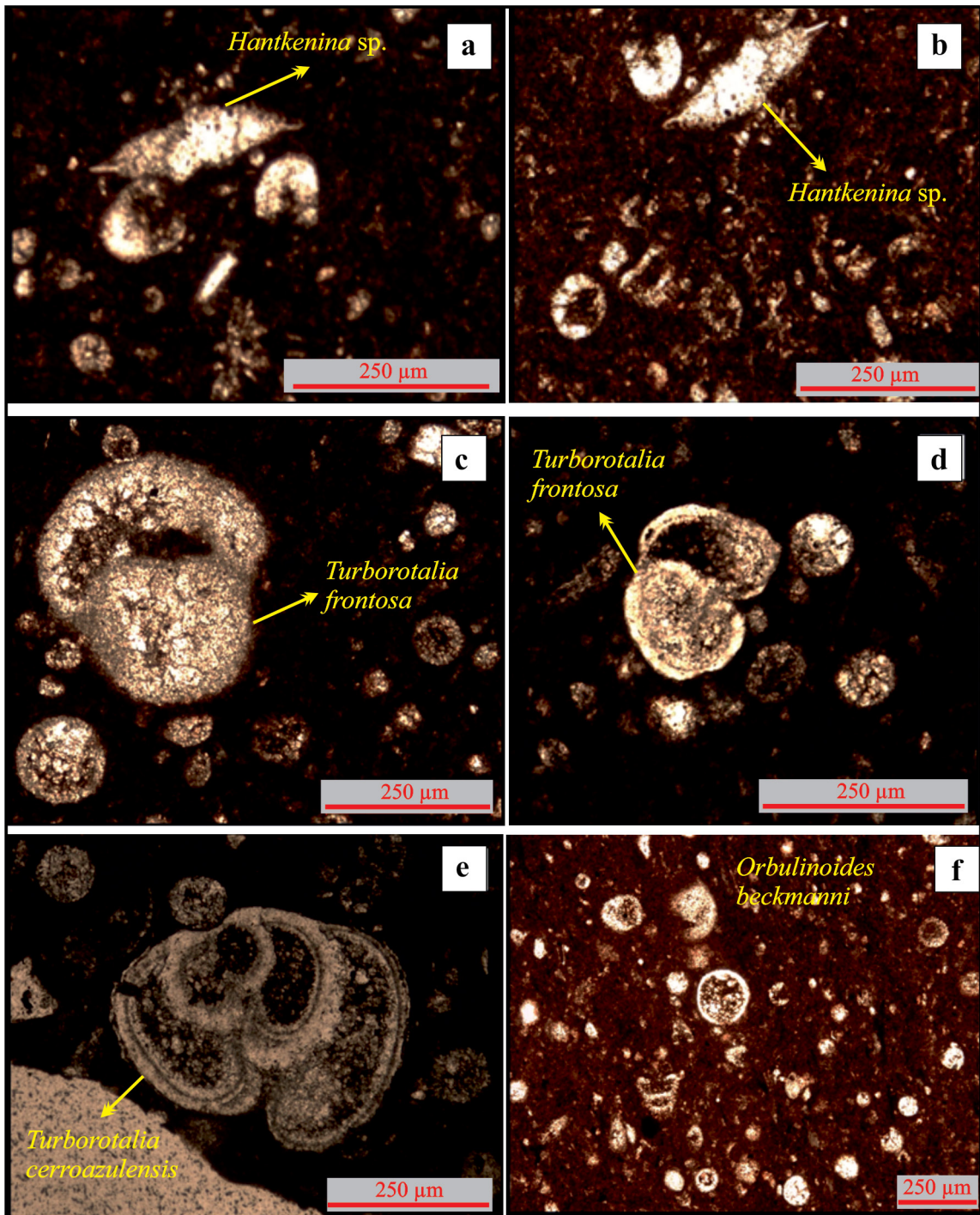
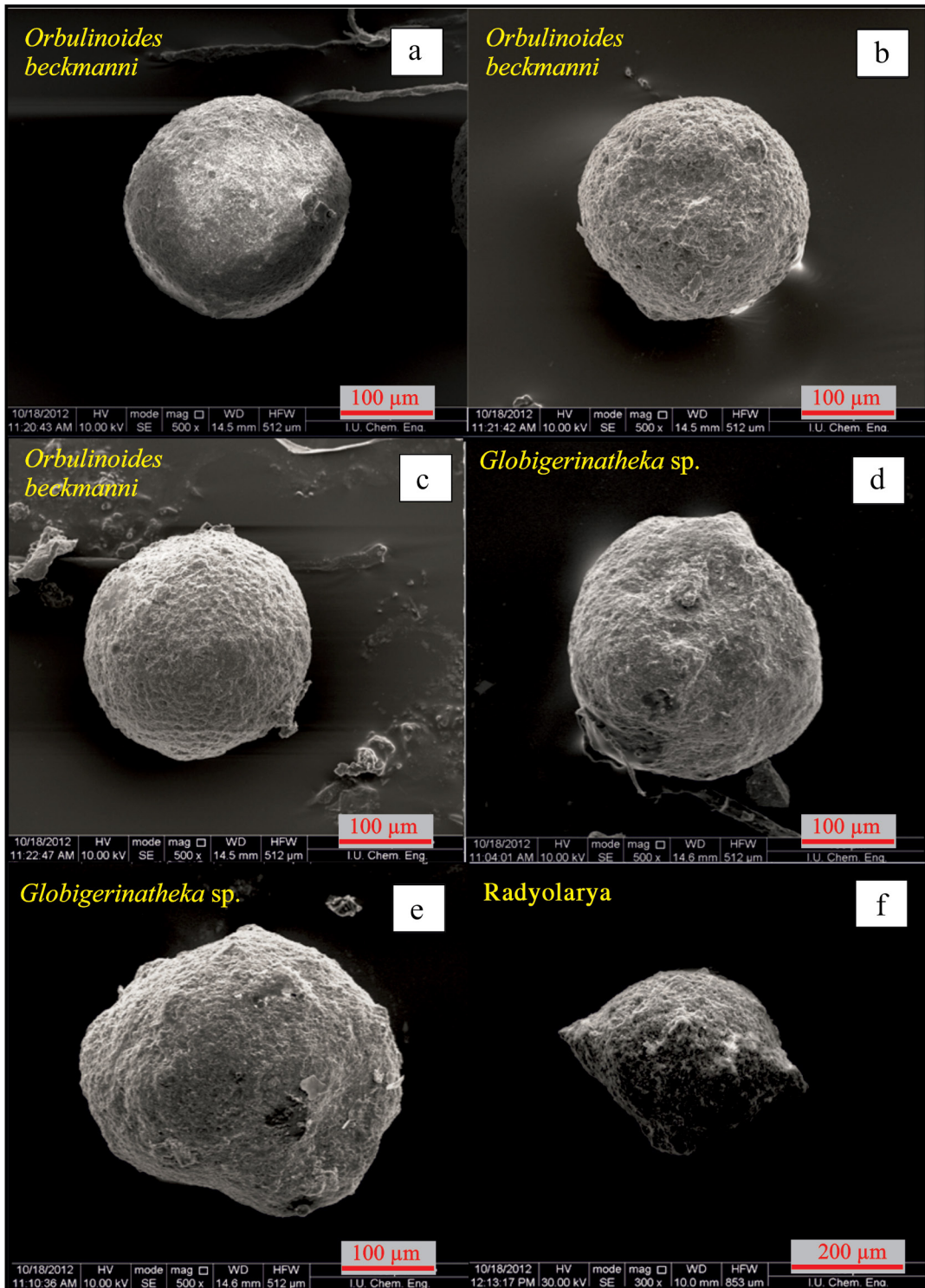


Plate IV. Fossil photos from Sarıkaya section (a-f). Sample number; a: 28A, b-d: 28B, c-e: 28C, f: 28C

a-b-c. *Orbulinoides beckmanni* (Saito), middle Eocene.

d-e. *Globigerinatheka* sp., middle Eocene.

f. Radiolaria





Bulletin of the Mineral Research and Exploration

<http://bulletin.mta.gov.tr>



Some criteria used in determining paleoshorelines, examples from Turkey and Rhodes Island

Okan TÜYSÜZ^{a*}

^a*Istanbul Technical University, Eurasia Institute of Earth Sciences, Maslak Campus, Sarıyer, Istanbul, Turkey*

Research Article

Keywords:

Paleoshoreline, Sea-levelchange, Rock boring organisms, Coastal morphology, Eocene and Quaternary coastal sediments.

ABSTRACT

Shorelines are important boundaries separating the erosional and the depositional areas. Determining the location of the shorelines in geological time and how it changes by the time is one of the major problems of geology. The most accurate estimate of the location of the shoreline, which is a dynamic structure, in the period when it was exist is very important in palaeogeographic studies. The determination of coastal changes by the time provides valuable information on active tectonic sand climate, and the relationships between these two. The most basic approach to determine the paleoshoreline is to estimate the geological events on the sea and land sides and thus to estimate the location of it indirectly. For this purpose, if the physical, chemical and biological conditions of the depositional environments from land to shore and from there to the basin and which land part and how fed this environment can be revealed, the location of the shoreline can be estimated. In contrast, some field observations provide direct and much more precise data for identifying the paleoshorelines. In this paper, it will be introduced how some rock-boring organisms, wave-cut feature sand coastal sediments can be used to estimate the paleoshorelines based on two examples of Quaternary sediments in Hatay and Rhodes Island along the Mediterranean coast and on some Eocene sediments in the vicinity of Çorum, Central Anatolia.

Received Date: 21.01.2020

Accepted Date: 28.03.2020

1. Introduction

Although determining a "moment of time" is often not possible for the past geological events, the shortest possible "time slice" is considered as the "moment of time" and the geological events that occurred in this period are interpreted as if they occurred at this moment. For example, while preparing a paleogeographic map for the Santonian period (85.8 to 83.5 million years ago), this period of 2.3 million years is considered as a single "moment of time". The shorter the "period of time" in question to be kept to the extent of possibilities, the greater the sensitivity of the study and the value of the interpretations. One of the oldest

and most reliable methods of determining time limits in geology is to reveal local or regional unconformities or discontinuities in deposition. The unconformity plane represents a wide period of time between the erosional and depositional periods. However, if the age and depositional conditions of the first sediments above the unconformity can be determined precisely, these data provide valuable information on both the location and the environmental characteristics of both the erosional and the new depositional periods.

A coast is shaped by interactive events occurring in the atmosphere, on the sea (or ocean), on the land and by their responses to these events (Davidson-

Citation Info: Tüysüz, O. 2021. Some criteria used in determining paleoshorelines, examples from Turkey and Rhodes Island. Bulletin of the Mineral Research and Exploration 164, 147-164.
<https://doi.org/10.19111/bulletinofmre.712862>

*Corresponding author: Okan TÜYSÜZ, tuyusz@gmail.com

Arnott, 2010; Absalonsen and Dean, 2011). The coasts are affected very quickly by climatic, tectonic and marine changes, the dynamics between them and even the biological activity, and they quickly change their shape as a response (McFadden et al., 2007). For this reason, when and where the paleo-shorelines were and how they changed by the time in terms of physical and chemical conditions provide valuable information about the regional conditions of that period. The main factors controlling a shoreline and causing its changes are; eustatic sea-level changes and climate; tectonic uplift and subsidence; relative erosion, transportation and precipitation rates; topography; wave activity; coastal geology; coastal fauna and flora, and weathering. In this respect, the determination of the locations and the ages of the paleo-shorelines provide valuable information about all these factors and their evolutions. This article will focus on some criteria for determination of paleo-shorelines and their evolution, with some examples from the Quaternary shores of Hatay and Rhodes Island in the Mediterranean, as well as an older example from Central Anatolia.

2. Some Criteria Used in Determining the Paleoshorelines

2.1. Bioerosion: Rock-boring and Sticky Organisms (Barrows, 1917)

A certain number of sea organisms live within the cavities they bore. Burrowing organisms live within the unconsolidated or partially consolidated sediments such as clay and sand depositing on the sea floor. The fossils of these organisms can be found at any level of a sedimentary sequence, and they provide information about the age and depositional conditions of that level if they can be dated by any method. In contrast to the burrowing ones, the rock-boring organisms live only within the indurated rocks, usually the carbonates or coral reefs that form the sea floor or shore. In other words, rock-boring organisms live on an older solid rock substratum at the beginning of a transgressive depositional period. These organisms live at the interface of the erosional surface and sediments depositing on this erosional surface. Therefore, the information provided by burrowing and rock-boring organisms are different. Since the rock-boring organisms live along the interface between an unconformity or non-depositional surface and the marine environment, they will provide information

about the age of the beginning of the deposition and the environmental conditions during the beginning of this depositional period. Perkins (1966) states that the fossils of these organisms, which have existed since Ordovician, and become widespread especially in Jurassic, Cretaceous and Tertiary, provide valuable information not only about unconformity surfaces but also non-depositional periods that developed as a result of uplifting-shallowing, and subsiding-deepening events in the stratigraphic record. On the other hand, since the rock-boring organisms live in shallow and clear waters facing the open sea, they also provide information about the characteristics of the depositional environment. Although fossils of sticky organisms, such as barnacles, are also useful, their preservation is less frequent compared to rock-boring organisms.

The bioerosion, which is a result of the mechanical and chemical functions of the rock-boring organisms, is an important part of marine deposition and benthic ecology, and is also one of the factors of long-term shaping of the shores. Rock-boring organisms are considered to be biological sea level markers indicating the paleo-shoreline (Barrows, 1917; Warme, 1975; Taylor and Wilson, 2003; Ricci et al., 2015; Smith and Ross., 2018). Although the rock-boring organisms generally prefer to live in carbonate rocks, Bolotov et al. (2018) found holes in Myanmar, which were bored by *Lignopholas fluminalis* on a siliceous foundation in freshwater environment. However, almost all rock-borers in marine environment bore into the carbonate rocks.

Rock-boring organisms form a large taxonomic group that includes bivalves, gastropods, annelids, sponges, sea urchins and others. Among these, the most common rock-borers seen in marine environments are the species belonging to Pholadidae and Mytilidae families (Photo 1). Since biological and paleontological classes of these organisms are outside the purpose of this article, all the rock-borers will hereinafter be referred to as "pholade" or "rock borer", regardless of the species and genus. More than 70 genera of the pholadidae family, also known as the angel wings, and more than 250 genera of the mytilidae family are among the most common ones.

In one of the valves of rock-borers, there are teeth used to grinding away the hole, which they live in. The organism enlarges the hole in the rock both by grinding

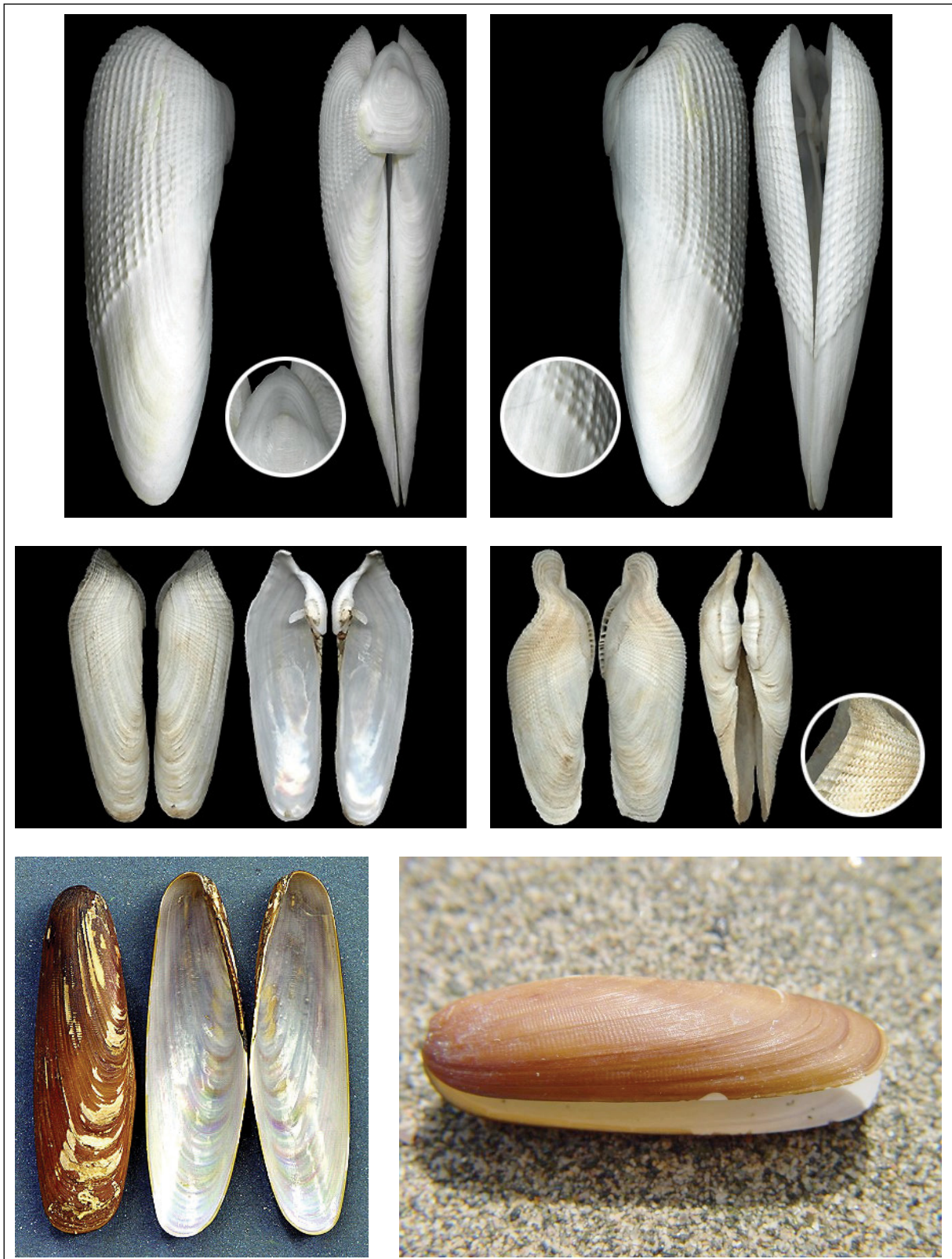


Photo 1- *Pholas* and *Litophaga* fossils: *Pholas orientalis* Gmelin at the top, *Pholas dactylus* Linnaeus in the middle, and *Litophaga* Linnaeus at the bottom. (http://www.idscaro.net/sci/01_coll/plates/bival/pl_pholadidae_1.htm, <http://www.apneamagazine.com/ibf/index.php?showtopic=80937>).

away and chemical decomposing. While some genera such as *Adula* and *Lithodomus* chemically decompose the rock and form a hole by emitting some kind of solvent, some other genera such as *Parapholas* open and expand the hole mechanically by using their shells. The organism expands and deepens the oval shape of the hole parallel to its growing, and stays there all along its life. Only the siphon, which is used to filter the water and take food throughout its lifetime remains outside. A rock-borer lives approximately 8 years and the other organisms occupy and fill this natural refuge after its death. The second owners of these holes can be sticky organisms, bryozoa and pelecypods such as, *Tapes*, *Cumingia*, *Kellia*, *Diplodonta*, *Entodesma* and *Mytilus*. If the sediments, which fill the hole, are not cemented in a short time, then the shell of the dead organism is broken, erodes and the hole becomes empty. The size of the rock-borers is usually around a few cm, but it even sizes up to 18 cm. The shells are usually white or pinkish in color.

Most of the rock boring organisms live on shores facing the open sea today. This is probably due to the abundance of plankton, high oxygen content in the water, and lack of silt size suspension material in the water. On the other hand, the rock-borers are not found very often at the edge of bays or lagoons protected against the waves, which are relatively poor in fresh plankton and low in oxygen and rich in suspension material. For this reason, the rock-borers provide information not only about the location of the shore but also its physical and biological conditions. On the other hand, any sudden change in marine conditions affects the organisms significantly, and in such changes, they all can leave the environment. However, the rock-boring organisms remain in the environment and provide valuable information as they are trapped in their bores.

Dating the fossils of rock-boring organisms provides sensitive data about the location and timing of evolution of a paleoshoreline. If the organism's shell is preserved in the bore, it can be dated by the methods such as ESR (Electro Spin Resonance) or AAR (Amino Acid Racemization). In cases when there are no or negligible methodological errors in dating, the place where the *in-situ* fossil exists can safely be interpreted as the paleoshoreline. In the case that there are fossils lived within the bore after the death of the original rock boring organism, this can

also be accepted as the reliable data considering the geological time, although it is relatively less reliable compare to the original one.

2.2. Marine Terraces

Marine terraces, which are one of important data sources in determining the paleoshores, are the coastal deposits preserved on shores that relatively raised due to tectonic or eustatic reasons. These deposits usually contain beach sands, beach stones or cliff debris. Although they consist of abundant fossils, most of these fossils are occasionally eroded and reworked from previous terrace deposits due to repeating relative sea level changes. For this reason, it is necessary to be careful in dating the terraces based on fossils, as the reworked fossils can be misleading. One method that can be used here is to make the age determinations on different fossils from the same stratigraphic level and use the youngest age found, if it can be determined, provided that it accepts a certain margin of error. The same applies for well cemented beach stones. Without *in-situ* fossils, it is necessary to be skeptical in aging of the terraces.

Marine terrace deposits have been often developed on an abrasion platform that marks the wave base. This platform is generally horizontal or gentle, and it is also inclined if affected by tectonic deformations. Although nature of terrace deposits vary depending on the coastal morphology, they generally develop by leaning on steep slopes on land side. Terrace deposits, which developed in a beach environment, can submerge or raise due to tectonic movements or eustatic sea level changes. The repetition of tectonic uplifting events causes the development of a step like morphology, the oldest terrace is at the top and the youngest terrace is at the bottom. If the age of each level can be determined, then the sea level changes and tectonic movements and their mutual effects can be determined (Keller and Pinter, 2002). However, it should be emphasized once again that the ages of marine terraces are often difficult to determine without *in-situ* fossils. Terraced older than Quaternary are rarely preserved due to erosion and become impossible to determine.

C^{14} method is widely used for dating Holocene marine terraces. In this method, the carbon-rich materials in coastal deposits can be used in addition

to fossil shells. The fact that the 35,000 years reliable age limit half-life of C^{14} isotope is the weakest aspect of this method. Although some other methods such as Th_{230}/U_{234} ratio can be used for dating in some cases, the clastic contamination or low uranium concentration in open systems reduce the reliability of this method. The marine terraces dated by paleomagnetism and OSL (Optic Stimulating Luminescence) methods are quite limited. However, the terrestrial cosmogenic nuclide methods, especially like Be^{10} and Al^{26} , have started to be used in recent years. In this way, the periods when marine terraces come to the surface and begin to be exposed to cosmic rays can be determined. On the other hand, the methods such as ESR and AAR have also been used for dating marine terraces. Although many methods have been used to date the marine terraces, it is also possible to encounter with the reworking problem apart from the error margins of each method as it is very difficult to find *in-situ* material in marine terraces, as mentioned above.

Marine terrace deposits are one of the most important data sources to determine the paleo-shores. However, difficulties in dating, destruction of their internal structures due to repeated erosions and depositions and being temporary structures due to their easily erodible nature can create problems to the use of this data source.

2.3. Wave Notches

Horizontal erosion that occur by chemical, physical and biological agents lead to the formation of wave notches located at an average sea level on relatively high-slope coasts. Wave notches (coastal notches or tidal notches) are morphological structures that result from the erosion of rocks along the shore with the strength to bear the upper load. Wave notches are generally considered as the indicators of paleo-shorelines (Pirazzoli et al., 1982a, b, 1989, 1991; Laborel et al., 1999; Kershaw and Guo, 2001; Evelpidou et al., 2011a, b, 2012a, b). The use of wave notches to determine the paleosea levels and paleo-shores possess significant difficulties due to their short living nature, high wave or tidal height in mid latitudes and tidal areas, and the differences in the resistance of rocks they erode. Detailed information about the development and classification of wave notches are given by Trenhaile (2015).

Wave notches are erosional structures located at the bottom of cliffs with depth and height ranging from centimeters to meters (Trenhaile, 2015). Wave notches are generally developed on shores that are composed of steep and resistant rocks, which are poor in terms of material carried from the shore and not affected by surficial weathering. Factors such as salt ratio of water, time and temperature differences between wetting and drying of rocks and biological erosion are also effective in the development of wave notch.

The wave notch located between the abrasion platform and paleocliff is an important element showing the maximum level transgression has reached, and therefore the paleo-shoreline. Therefore, the morphological factors are important, as well as terrace deposits, in determining the paleo-shoreline. The functions of the development and protection of the wave notches are given in figure 1.

The wave notches have extensively been used for the determination of eustatic sea level changes and tectonic movements in the Quaternary (Trenhaile 2015 and references here). In areas where the waves not very strong, such as the Mediterranean, and the areas with limited tidal events, the wave notches developed in resistive rocks such as limestones are considered as sensitive markers of the paleo sea level (Pirazzoli and Evelpidou, 2013). There are also some difficulties in using wave notches in tidal areas to determine the paleo sea level, because there are observed wave notches that developed at high tide level in some areas (Wentworth, 1939; Guilcher, 1953; Newell, 1956; Verstappen, 1960; Christiansen, 1963; Takenaga, 1968; Hills, 1971; Tricart, 1972; Trenhaile et al., 2015), below the average tide level in some areas (Schneider, 1976; Torunski, 1979) and at the average tide level in some other areas (Guilcher, 1958; Hodgkin, 1964; Fairbridge, 1968; Debrat, 1974; Trudgill, 1976; Bird et al., 1979; Woodroff et al., 1983; Tjia, 2013). In the Mediterranean, V- or U-shaped notch profile, which indicates the high wave and high tide levels, is encountered, and the apex of this shape is accepted as the average sea level (Pirazzoli and Evelpidou, 2013). Schneiderwind et al. (2017) investigated the development of wave notches in the Mediterranean environment and developed a numerical model for the development and classification of wave notches.

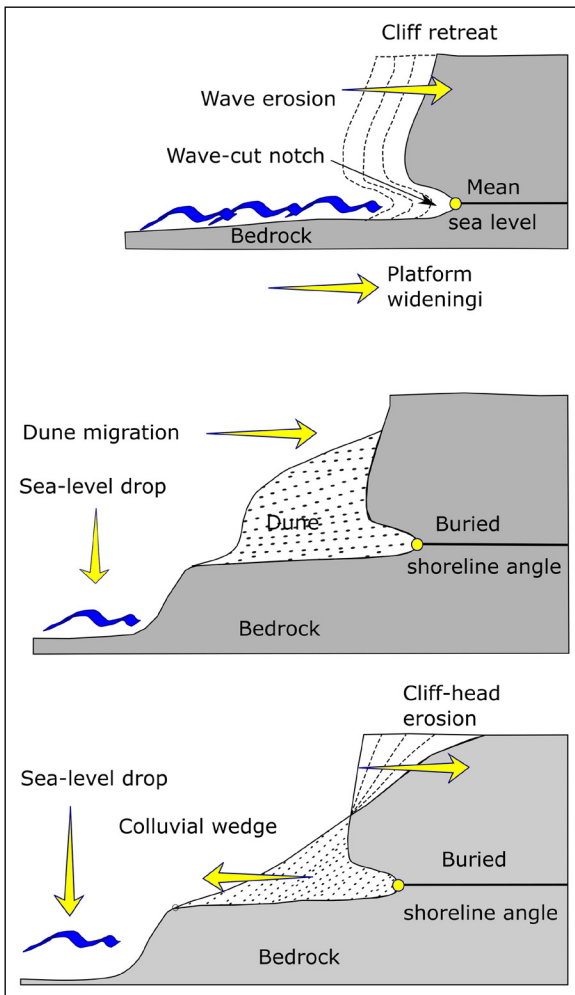


Figure 1- Processes associated with the generation of shoreline angles and their preservation. Wave-cut platforms result from the effects of wave erosion leading to cliff retreat during sea-level highstands. Wave erosion may generate a wave-cut tidal notch that marks the position of mean sea level. (Above) During sea-level lowstands, the shoreline angle may be covered by sediments transported along the beach, such as during the formation of dunes. (Middle) Shoreline angles may be covered by colluvium, or they may be eroded by the effects of fluvial incision. (Below) Geomorphic markers can be identified by using high resolution topography maps and numerical models (for example; TerraceM®, Jara-Muñoz et al. 2016) to determine the height of the marine terrace. (taken from Jara-Muñoz et al., 2016).

Although wave show the paleo-shorelines very precisely and the sea level changes in environments where tidal events are negligible and the height of the wave does not change much, it is very difficult to date them, especially for paleo-shorelines. On the other hand, some other reasons such as intense biological erosion, constant wetting and drying effect, salt

abrasion may also lead to the development of similar notches.

3. Examples from Turkey and Mediterranean

Three main criteria used in determining the paleoshorelines given above will be discussed with examples from Hatay, Rhodes Island and Çorum.

3.1. Marine Terraces Along the Shores of Samandağ, Hatay

Along the shore of Samandağ District of Hatay, SE Turkey, where the Asi River meets the Mediterranean, the indicators of paleoshorelines such as raised marine terraces and wave notches, standing elevations from the present sea level up to 180 m, are observed between Meydan village in the south and Çevlik village in the north (Figure 2). The properties of these structures have been investigated in detail and the age determinations have been made using different methods (Erol, 1963; Pirazzoli et al., 1991; Doğan et al., 2012; Tüysüz et al., 2012; Tarı et al., 2013, 2018; Florentin et al., 2014). The stratigraphy of marine terraces generally consists of a bottom section that changes depending on the nature of the basement on which the sediments deposited, and an upper section consisting mainly of cross-bedded loose sands and pebbles. In areas, which are fed by an ophiolitic source, these sands are green as they are rich in pyroxene and olivine.

The terraces developed on the relatively resistant late Miocene aged limestones are generally observed in south of the Asi River. Here, the deposition begins with large blocky and pebbly sediments that have a chaotic internal structure at the bottom, then grades into the crossbedded, well sorted loose beach sands. There are large limestone blocks perforated extensively by rock-borers within the chaotic lower part or within homogenous marine sands in the upper part (Photo 2).

Limestones, which are seen as blocks within sediments of terrace deposits, are surrounded by pebbles or sands. Some of the holes that are observed intensely on the blocks are empty while some of them are filled with sand. Shells of the original organism are rarely found in the holes, but usually the later settled gastropod or small and mostly broken bivalve shells are seen. The dimensions of limestone blocks generally range from a few 10 cm's to just over one meter. Most of the blocks are rounded and spherical in shape indicating that they were processed in high-

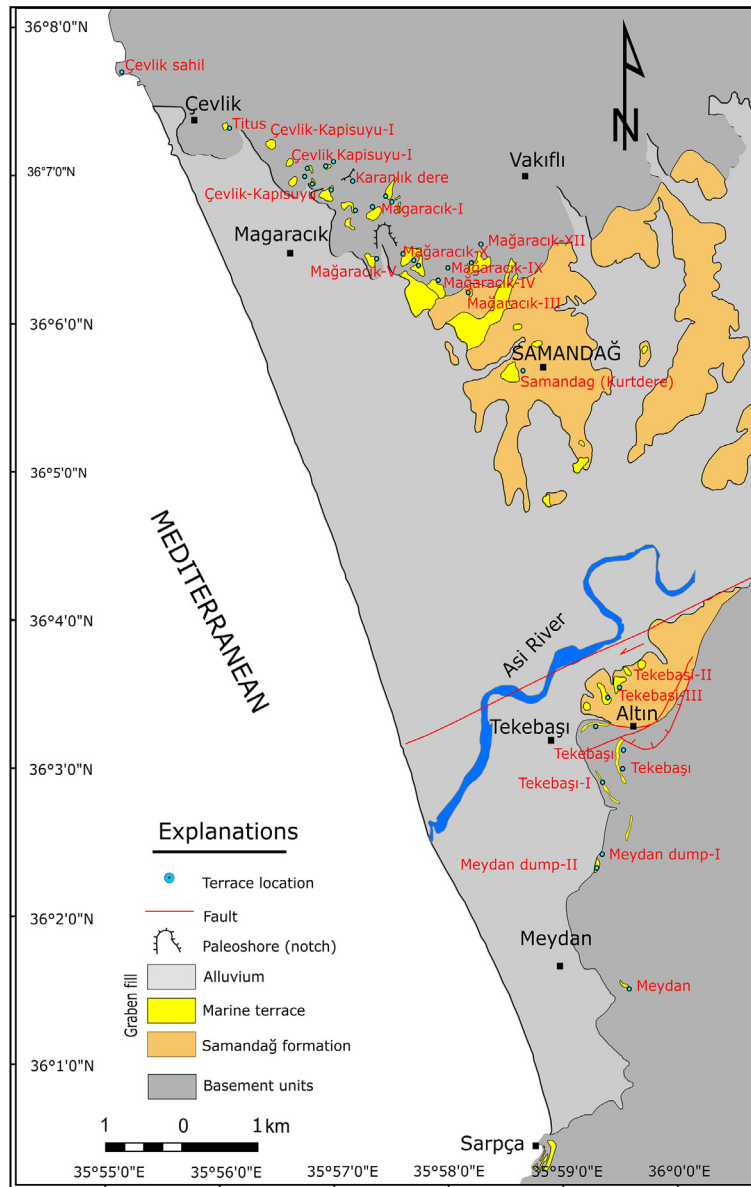


Figure 2- The map showing the distribution of sediments of the marine terraces observed in the north and south of the Asi River on the Samandağ coast (Tüysüz et al., 2012).

energy environment for a long time, and the presence of angular pebble and blocks between them was deposited in the same environment. In the light of these data, it was interpreted that the units in question were deposited in front of a cliff. These blocky unit deposited on a limestone substratum that were also dug by rock-borers and is overlain by very well sorted and cross-bedded beach sands at the top. This indicates that limestones in which these living organisms live on the coast have been rolled down from the cliff due to wave actions or gravity and some of them have been processed and rounded for a long time by the waves.

Hole sare commonly observed both in chaotic cliff front sediments and limestones located at the bottom of thick beach sands. Although most of them are empty or filled by gray-greenish colored, fine to medium sands rich in serpentinite or ultramafic rockclasts, some others have rarely preserved shells with rounded or oval sections. These structures are widely encountered both at the bottom and inside the terrace sediments standing at altitudes of 3 to 180 meters above the sea level, especially; around the Tekebaşı and Meydan villages and in their topographically higher parts. It is noteworthy that limestones are almost full of

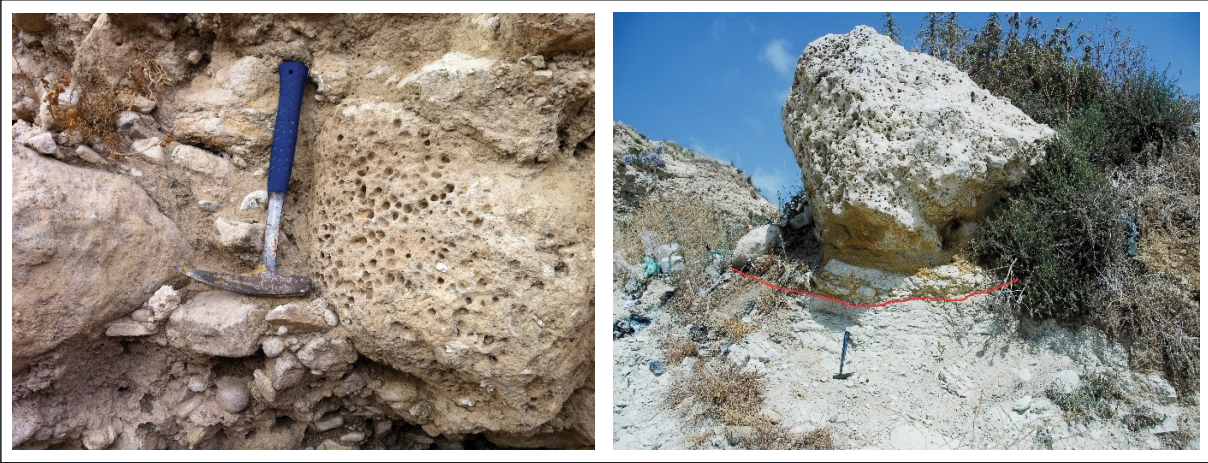


Photo 2- Limestone block containing pholade holes in the chaotic clastic unit at the bottom of marine terrace (left.) Presence of angular grains together with rounded blocks indicates a high-energy environment (cliff front) where clastics with different reworking degrees come together. Pholade holes in the big limestone block, which sits at the bottom of marine terrace (red line) deposits that deposited on the Pliocene claystones (right).

bores while there is not any bores inserpentines at the bottom of terrace sediments at 50 m elevation to the east of Meydan district (Photo 3). Tari et al. (2018) demonstrated that these terraces resting on different elevations were developed in different stages from bottom to top nearly between 8.3 and 214kyr (Figure 3).

Terraces in north of the Asi River, on the other hand, deposited on more easily erodible lithologies such as the Pliocene claystones and marls. Here, the terrace deposits generally consist of thick crossbedded medium to coarse grained loose sands. Chaotic deposits described in the south are not observed here, except for some large random blocks (Photo 2). This indicates that this part of the shore was an abrasion platform. However, it is possible to see the terrace

deposits on a horizontal and flat surface, raised to different levels around Mağaracık village (see Doğan et al., 2012; Tari et al., 2013 and 2018 for details of these terraces).

Terrace deposits rest on the Pliocene marls and claystones (Samandağ formation, Tari et al., 2013) in the east of Mağaracık village, basal elevation of which is 33.5 m. This outcrop is destroyed today by the farmers who replaced the highly permeable terrace sands with fertile agricultural soil. There are abundant *Litophagus* sp. fossils within bores in marls and claystones along very flat and planar unconformity plane. These fossils, which are 1-3 cm in diameter and 3-7 cm in length, are filled with hard clays so that their molds are largely preserved, however their shells



Photo 3- Pholade bores observed in lime stones around Meydan vilalge. Fossil shells (red arrow) are observed inthe bores filled with sand.

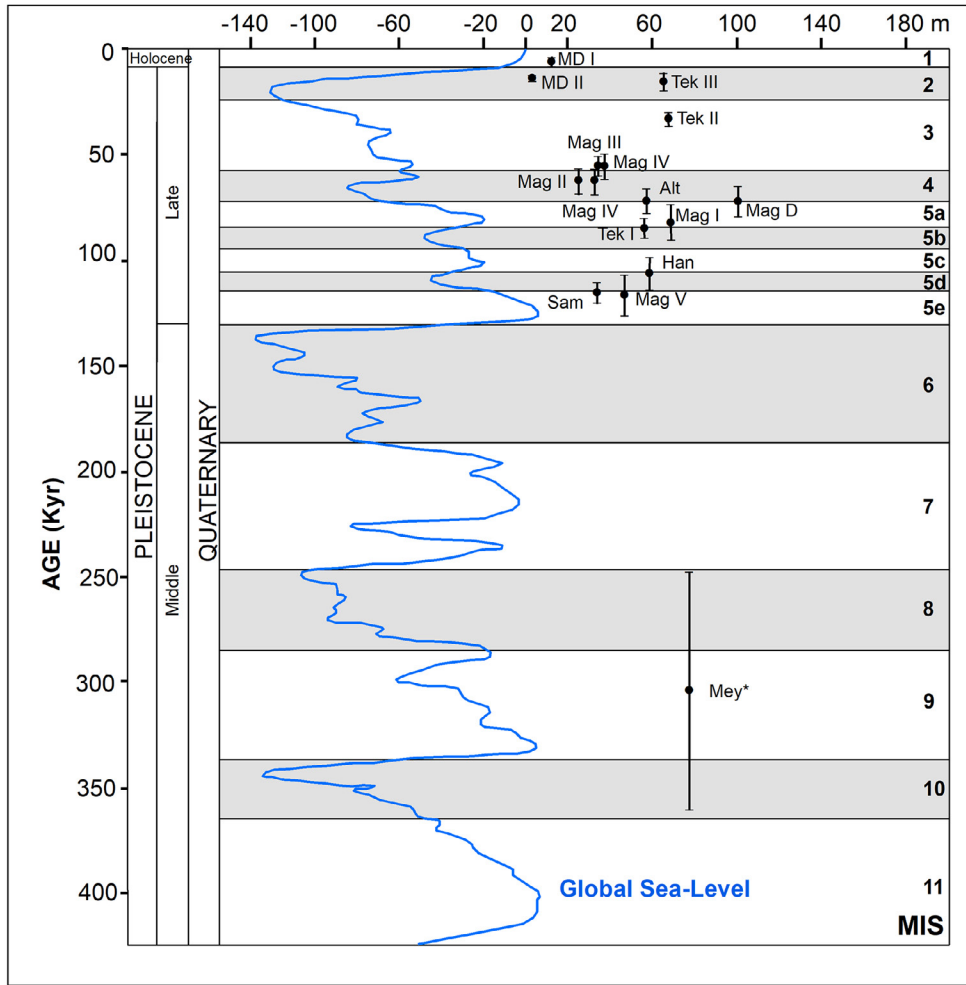


Figure 3- Correlation of the marine terraces on the shores of Samandağ, Hatay and the global sea level curve. Gray shaded areas indicate MIS (Marine Isotopic Stages) or the substages. Locations with measured marine terrace deposits: Mag- Mağaracık village, MagD Mağaracık village dump site, MD-Meydan village dump site, Tek- Tekebaşı village, Mey- Meydan village, Sam- Samandağ town, Alt- Altındistrict and Han- Hancağız district. The ages of terraces marked with * symbol may be younger than shown here as their age is not based on in-situ fossils (taken from Tari et al., 2018, it is recommended to refer to this article for details).

are usually weathered and chalked. In addition to the fossils, fine sands also fill the bores (Photo 4).

Mağaracık section has been interpreted as deposited on an abrasion plain and a bit far from the shore considering the flat geometry of the basal plane, the presence of boring organisms and homogeneous stratigraphy of the terrace sediments. Based on ESR age determinations on *Litophagus* shells, Tari et al. (2018) stated that this terrace, which began to deposit 63.2 ± 5.6 kyr, possibly in the late MIS 4 phase and tectonically uplifted to its present elevation, 33.5 m above present sea level.

Another important paleoshore markers on the Samandağ coast are the wave notches and abrasion platforms. Such structures are observed along the Çevlik-Mağaracık beach as well as on the steep limestone slopes of Keldağ, facing the Mediterranean (Photo 5). It is very difficult to date wave notches. If there is a *Vermes* or *Dendropoma* like fossil, which are coral or gastropod species living on the wave notch, and they are synchronous with the development of the notch, then the age determination can be made within previously mentioned limitations using methods such as U-Th, AAR or ESR. On the other hand, wave notches can be filled with marine sediments in some



Photo 4- In-situ *Litophagus* sp. fossils located at the bottom of the sands of the marine terraces in the Mağaracık terrace. White colored fossil shells are seen in the holes bored in the claystones (upper left). The claystone level is directly overlain by well sorted marine sands (upper right). *Lithophagus* sp fossils in their original position inside the bore (lower left), *Lithophagus* sp, fossils recovered from the holes (lower right).

cases (Photo 5). Although there are fossils suitable for the age determination within these sediments, it should be noted that they are more likely to be reworked due to high energy depositional environment.

The tilted abrasion platform located at the southern most edge of the Samandağ shore is one of the important morphological structure of paleoshorelines (Photo 5).

3.2. Terrace and Wave Notches on the Coasts of Rhodes Island

It is possible to see the traces of paleoshore along the beaches on Rhodes Island, as in most Aegean-Mediterranean islands. In particular, the coastline between Lindos and Faliraki along the southeast shores of the island offers beautiful examples of paleoshore traces in this respect. Howell et al. (2015) dated the traces of paleoshores on Rhodes Island carrying out AMS radiocarbon analyses of *Litophaga*

and coral fossils. They interpreted that these Holocene terraces were formed as a result of tectonic uplifting of the island due to a single big earthquake ($M > 7.7$) originated from the Hellenic subduction zone between the years of 2000-200 BC Cornée et al. (2006) studied the sedimentological and paleontological features of the late Pliocene-Middle Pleistocene deposits along these coasts and interpreted tectonic and climatic conditions during their deposition.

Although sedimentary and morphological traces of many paleoshores can be seen along the southwest coasts of Rhodes Island, one of best is seen on the southern slopes of the Prophitis Elias (Prophet Elijah) in south of Archangelos village and on the northern edge of Agathibeach. Prophitis Elias hill is formed by Triassic-Cretaceous limestones (Lekkas et al., 2007). Limestones are cut by normal faults trending approximately in N-S direction. Due to these faults, the Prophitis Elias Hill covers a graben and its shoulders (Figure 4).



Photo 5- Raised coastal traces at the Samandağ-Çevlik beach. The paleo wave notch that stands 1 m above the present sea level on the upper left. Coral and *Dendropoma* fossils, which have been grown on the raised wave notch on the upper right. Wave sediments that filled a raised wave notch in the lower left. There are gastropod fossils in these sediments. Raised wave cut platform (limestone) in the lower right.

Morphological elements in the form of a stepped terrace, which stands horizontally along the slopes of Prophitis Elias hill facing southward and eastward, draw attention (Figure 4). Cornée et al. (2006) assessed these flat areas, which developed on limestone, as abrasion platforms and 24 different levels of paleo coastal traces (abrasion platform) standing on the slopes of this 591 m high hill from the current sea level were determined. Cornée et al. (2006) stated that these terraces had burrows dug by the rock-boring organisms on limestones and that the Pliocene calcarenites were deposited on some of these rocks at higher levels. Although there is not any age data on all those 24 levels mentioned above, it is clear that these are related to sea level changes in the Mediterranean and tectonic uplifting on the Hellenic subduction zone between the Pliocene and recent.

The Agathi beach, located to the south of the Prophitis Elias hill, also offers beautiful examples of the recent coastal uplift. The bedrock on the northern

edge of the moon-shaped beach is again limestones. These limestones were perforated very intensely by the rock-boring organisms. Most of the bores are emptied, and some of them were eroded by waves and karstic dissolving. Nevertheless, it is observed that some bores, especially the ones overlain by the sedimentary cover, are preserved, filled with fine sands, and there are some fossils within them even if some are not fully preserved. These limestones with extensive bores of mollusks are overlain by beach sediments rich in fine sands and coarse clastics (Photo 6). In beach sediments, there are rounded, spherical shaped limestone pebbles and blocks that have been reworked for a long time due to the wave effect, and the bores are preserved even partially on large limestone blocks.

Sequences, similar to those of the Agathi beach are located at different levels along the entire coast between Rhodes and Lindos settlements on the southwest coast of Rhodes Island. In addition, there are also

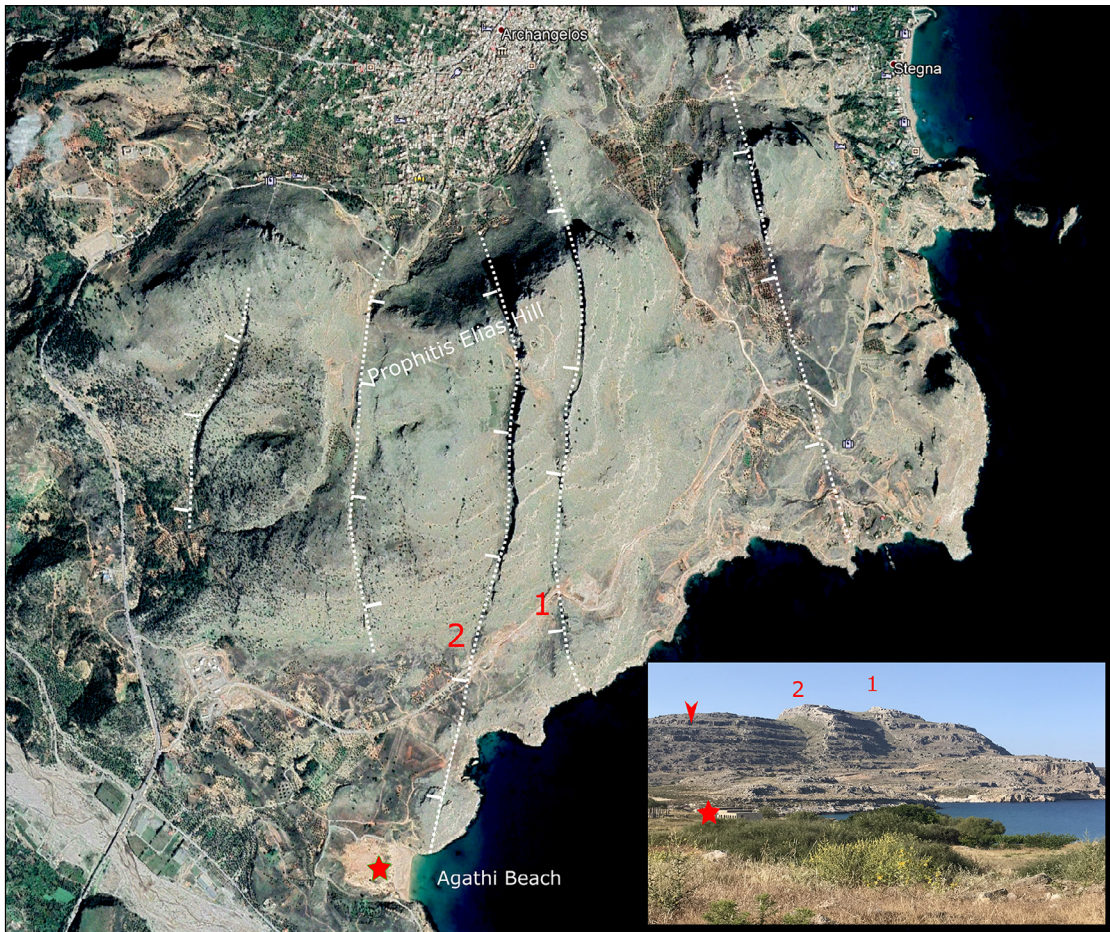


Figure 4- Satellite (Google Earth) image of the Prophitis Elias Hill. White dotted lines indicate the faults and white teeth on them indicate the slip direction. The levels, of which the only one is marked with a red arrow, show the paleo wave notches. View of Prophitis Elias hill from south in lower right: Red stars on the photo and map point the same place. Two steep slopes numbered as 1 and 2 on the photograph were created by the normal faults dipping west. These faults are shown with the same numbers on the map. Stair-like horizontal flats are wave notches and abrasion platforms that point to the paleoshorelines. Only one of them is marked with a red arrow.

well preserved wave notches and abrasion platforms along the entire coast in resistant rocks, especially in limestones (Pirazzoli et al., 1982b; Pirazzoli et al., 1989). The height of these wave notches above the current sea level reaches a height of 3.8 meters near the northeast end of the island, but decreases towards southwest. Kontogianni et al. (2002) also identified coastal notches that stand at heights of 4.2 and 5.2 m, higher than 3.8 m, but stated that they were developed during the pre-Holocene period. It is suggested to refer to Pirazzoli (1986, 1989), Kontogianni et al. (2002) and references herein on the age of these coastal notches and their relationship with active tectonic sea level change.

3.3. Bores of *Pholades* at the Base of Çorum Eocene Sediments

Some examples of physical and biological markers observed on shores of Hatay and Rhodes Island, though not limited with them, were given above. Could these functions their resulting markers, which are especially encountered in the Mediterranean Sea in the Pliocene-recent time interval also help us to understand the location and physical conditions of paleo-shores?

Tokat Massif¹ located in north of the Ankara-Erzincan suture belt in the Central Anatolia is a

¹ Although the term "massive" is used in literature for different purposes, it is used here in the sense of the region where metamorphic rocks are predominant



Photo 6- Pholadebores observed on the northern edge of the Agathi Beach in the upper left. A close-up view of them in the upper right. In the lower left, the marine terraces deposited on the limestones with pholade holes on the northern shore of the Agathi beach. Wave notches observed along the beach to the south of Lindos in the lower right.

region where the Permo-Triassic Karakaya Complex rocks (Bingöl et al., 1973), forming the basement of the Sakarya Unit (Okay and Tüysüz, 1999) crops out extensively. This group, which is divided into different formations around Çorum-Amasya (Tüysüz, 1996), consists of the intercalations of metapelites, metabasites and marble blocks within them. Sizes of these blocks range from a few meters to hundreds of meters. The Late Jurassic-Early Cretaceous aged neritic limestones (Bilecik limestone, Altınlı, 1973) unconformably overlie this basement. These limestones, which are oolitic in lower parts and micritic in upper parts, pass into the Early Cretaceous aged pelagic limestones in south (Soğukçam formation, Altınlı, 1973). The Upper Cretaceous ophiolites or chaotic rocks with ophiolitic blocks were imbricated with these units and thus a south-vergent fold and thrust belt was developed in the region (Tüysüz, 1996). It is accepted that this belt was developed due to continental collision of the Sakarya

Unit with the Kırşehir Continental Block. Following this collision, the Tokat Massif was uplifted and all Massif, except for the Çankırı Basin and the southern borders of the Massif, remained as an erosional area during the Paleocene (Tüysüz, 1993, 1996; Tüysüz and Dellaoğlu, 1992; Yılmaz et al., 1997).

Lutetian deposits of the Tokat Massif around Amasya and Çorum unconformably overlie the metamorphic rocks that form the Massif, the Jurassic-Cretaceous deposits overlying these metamorphites, the Upper Cretaceous ophiolitic units and the all contacts between these units imbricated together. In contrast to the folded and thrust structures of the units below the unconformity, the Lutetian deposits are quite thin and they are in the form of a flat cover, not affected from deformation. The characteristic of these units, which are obviously developed on a peneplain surface, changes towards the Ankara-Erzincan Ophiolitic Belt, which limits the Tokat Massif in south and west, and

the basins in front of this belt. They gradually pass into flyschoidal units and begin to consist of volcanic rocks. In addition to this lithological change, it is observed that Eocene sediments join the folded and thrust structure towards these areas. Based on these features, different Eocene units were distinguished in the region (Tüysüz, 1996). The Neogene units in the region are represented by terrigenous clastic and evaporites which unconformably overlie the older rocks.

The Eocene sedimentary rocks around Çorum and Amasya were named as the Dereağıl formation by Tüysüz (1996). The dominant lithologies of this formation are sandstones, siltstones and carbonaceous sandstones. The shallow marine limestones in this formation were named as the Ballı limestone member. The bottom of the Dereağıl formation usually consists of the red-yellowish, poorly cemented quartz-rich conglomerates and sandstones. These clastics at the lower part of the sequence pass upward into yellow, carbonate cemented, thin and irregularly layered sandstones with abundant nummulite fossils. Gastropods, brachiopods and echinoid fossils in addition to nummulites, and partly coalified plant

fragments are also observed in the rocks which cover the underlying units. In the north of Amasya, there are thick lignite seams in the middle Eocene deposits known as the Çeltek formation around Suluova. Atalay (2001) distinguished meandering river, lake, flood plain and marsh sediments in the Çeltek formation, which overlies the alluvial fan deposits at the bottom and conformably grades into shallow marine deposits at the top. This terrestrial sequence, which is peculiar to the Suluova-Merzifon area, is not observed in most parts of the Tokat Massif. The marine sediments located on the continental sequence in Suluova directly overlie the older units in most places.

The east of Çorum is one of the places where the basal parts of this transgressive marine sequence are best seen (Tüysüz ve Sakıncı, 1992). The Eocene sequence, around Palabıyık village to the south of Çorum-Amasya highway and in the west of area between Kuşsaray and Elvançelebi villages, unconformably overlies the Late Jurassic-Early Cretaceous aged Bilecik limestones and the Triassic schists (the Karakaya Complex) that thrust over these limestones (Figure 5). The sequence is usually represented by yellowish sands with carbonate cement

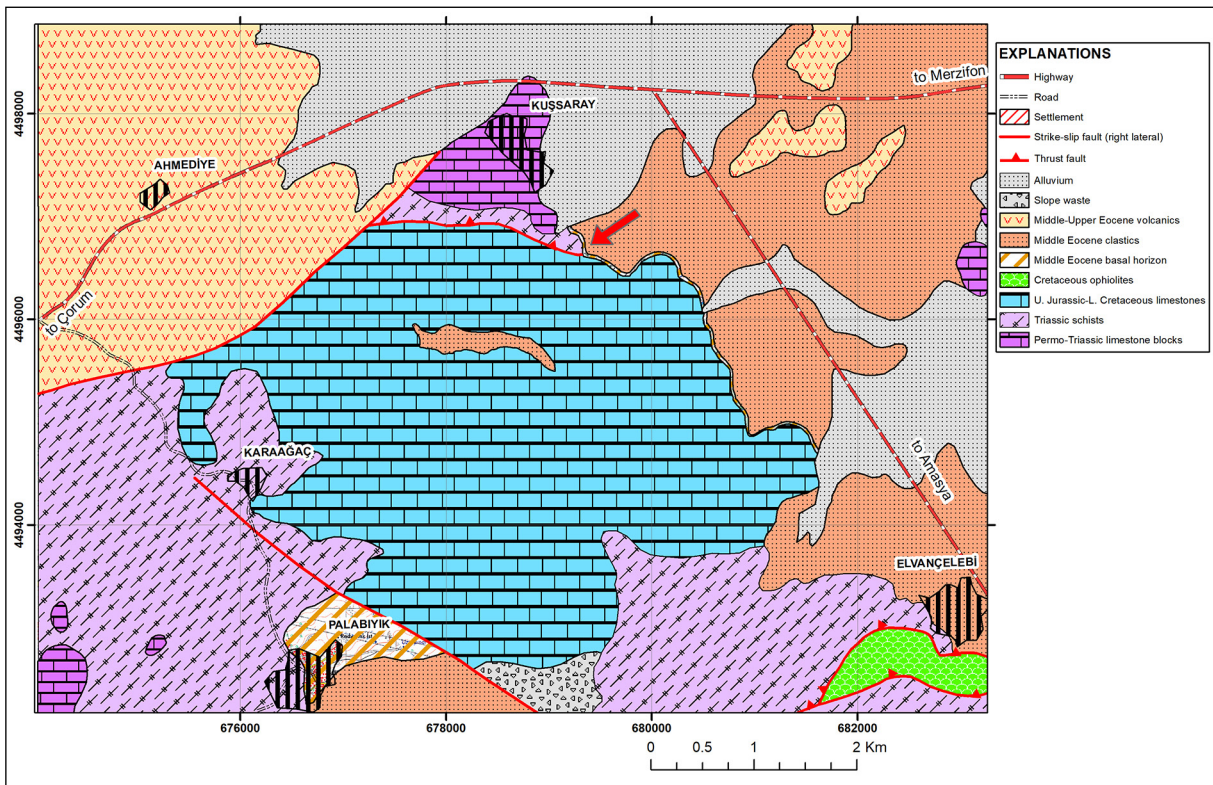


Figure 5- Geological map of Kuşsaray village and its vicinity located about 15 km NE of Çorum. Red arrow indicates the place where pholadebores are best seen at the base of Eocene sequence.

and is grades upward into volcanic rocks. Massive limestone intercalations and lenses are also exist within the sequence. The thickness of the formation is only a few meters in some places and may reach 150 meters in places protected from erosion.

There are abundant holes bored by rock-boring organisms on the Late Jurassic-Early Cretaceous aged Bilecik limestones, which are unconformably overlain by the Dereği formation around Kuşsaray and Palabıyık villages in the east of Çorum and the Dereği village in the north of Amasya. As these bores are quite common along the stream in south of the Palabıyık village, where the limestone is at the surface, this stream is called as the Deliklikayalar (rocks with holes) stream referring to those holes. *Lithodomus* sp. fossils have been found within these bores, which have not yet been completely eroded due to overlying Eocene deposits. They stand in a way that their valves would face downward in their cylindrical holes as bored perpendicular to the limestone surface (to the bottom of the unconformity plane). The long axes of the burrows are between 1-2 cm and 6-7 cm (Photo 7). They are filled with *Nummulites* sp. in addition to *Lithodomus* fossils and cemented with yellow sandy carbonates. The presence of *Lithodomus*

shells together with the nummulite fossils shows that *Nummulites* lived in the holes after the death of *Lithodomus*.

Similar structure is also observed in the north of Amasya, in the Ballı stream to the west of Dereği village and in the stream to the west of it, at the base of the Dereği formation (Photo 8). Here, the white-cream colored, hard, brittle, medium to thick-bedded oolitic or bioclastic textured Ballı limestone member directly overlies the Bilecik limestone, and the bores under this unconformity plane are noteworthy. On the other hand, there are coral fossils in growing stage in the outcrops to the northeast of Çorum, and they point out that the sedimentation continues in warm climatic conditions and shallow marine environment.



Photo 7- Pholade bore located in the Late Jurassic-Early Cretaceous limestone (JKb) filled with Eocene sandy limestone (Ted) in the section normal to the unconformity plane.



Photo 8- Holes opened by the rock-boring organisms during the Eocene period in the Late Jurassic-Early Cretaceous aged limestones and sandy limestones in the Delikli kayalar stream (upper) to the south of the Palabıyık village, Çorum and around Dereği village, Amasya (lower). In some holes, the shells have been preserved (lower), while some of them have been destroyed by karstic melting and erosion.

4. Results

In this study, the examples of some features that had formed along the coastal areas from Pliocene to recent are given from two different parts of the Mediterranean, Samandağ, Hatay and Rhodes Island. In addition, it was emphasized that these similar events that caused development of these features might occur also in paleo coastal sediments and provides information on locations of the shorelines in geological periods and on the characteristics of the depositional environments close to the coast.

One of the important markers of coastal line formed by limestones and facing to the open marine, is the rock-boring organisms. The fossils of these organisms can be used as the markers of paleo-shorelines as well as the unconformity planes. Considering that these organisms live on open and clean shores today, it can be said that their fossils reflect the same conditions for the past periods. Tracking of holes of the rock-boring organisms along the unconformity planes will allow precise determination of shorelines on site, which is an important element in determining the depositional and erosional areas. The structures such as wave notches and abrasion platforms, which are important elements of the coastal morphology, can also be identified within paleo sediments and can provide important information about paleocoastal forms.

References

- Absalonsen L., Dean, R. 2011. Characteristics of the Shoreline Change along Florida Sandy Beaches with an Example for Palm Beach County. *Journal of Coastal Research* 27/6A, 16-26.
- Altınlı, İ.E. 1973. BilecikJurasıği. Cumhuriyet'in 50. Yılı Yerbilimleri Kongresi, Tebliğler, 103-111.
- Atalay, Z. 2001. Amasya Yöresi'ndeki Linyitli Çeltek formasyonunun Stratigrafisi, Fasiyes ve Çökeltme Ortamı Özellikleri. *Türkiye Jeoloji Bülteni* 44/2, 1-22.
- Barrows, A.L. 1917. Geologic significance of fossil rock-boring animals. *Bulletin of the Geological Society of America* 28, 965-972.
- Bingöl, E., Akyürek, B., Korkmazer, B. 1973. Biga Yarımadası'nın jeolojisi ve Karakaya formasyonu'nun bazı özellikleri. Cumhuriyetin 50. Yılı Yerbilimleri Kongresi Bildiriler Kitabı, Maden Tetkik ve Arama Genel Müdürlüğü Yayınları 70-77.
- Bird, J.B., Richards, A., Wong, P.P. 1979. Coastal subsystems of Western Barbados, West Indies. *Geografiska Annaler Series A, Physical Geography* 61, 221–236.
- Bolotov I.N., Aksenova, O.V., Bakken, T., Glasby, C.J., Gufarov, M. Y., Kondakov, A. V., Konopleva, E., Lopes-Lima, M., Lyubas, A., Wang, Y., Bychkov, A.Y., Sokolova, A., Tanmuangpak, K., Tumpeesuwan, S., Vikhrev, I.V., Shyu, J.B.H., Win, T., Pokrovsky, O.S. 2018. Discovery of a silicate rock-boring organism and macro bioerosion in fresh water. *Nature Communications* 9:2882, 1-11.
- Christiansen, S. 1963. Morphology of some coral cliffs, Bismarck Archipelago. *Geografisk Tidsskrift-Danish Journal of Geography* 62, 1–23.
- Cornée, J.J., Moissette, P., Joannin, S., Suc, J.P., Quillévéré, F., Krijgsman, W., Hilgen, F., Koskeridou, E., Münch, P., Lécuyer, C., Desvignes, P. 2006. Tectonic and climatic controls on coastal sedimentation: The Late Pliocene–Middle Pleistocene of northeastern Rhodes, Greece. *Sedimentary Geology* 187, 159–181.
- Davidson-Arnott, R. 2010. *An Introduction to Coastal Processes and Geomorphology*. Cambridge University Press. The Edinburgh Building, Cambridge CB2 8RU, UK, 442.
- Debrat, J.M. 1974. Étude d'un karst calcaire littoral Méditerranéen: exemple du littoral de Nice à Menton. *Méditerranée* 17, 63–85.
- Doğan, U., Koçyiğit, A., Varol, B., Özer, İ., Molodkov, A., Zöhra, E. 2012. MIS 5a and MIS 3 relatively high sea-level stands on the Hatay-Samandağ coast, eastern Mediterranean, Turkey. *Quaternary International* 262, 65–79.
- Erol, O. 1963. Asi Nehri deltasının jeomorfolojisi ve dördüncü zaman deniz-akarsu sekileri: Die Geomorphologie des Orontes-Deltas und der anschließenden den pleistozänen Strand- und Flussterrassen, Provinz Hatay, Türkei (Geomorphology of the Asi River delta and Pleistocene marine and river terraces). *148 Dil ve Tarih Coğrafya Fakültesi Yayınları, Ankara, Türkiye*, 110.
- Evelpidou, N., Pirazzoli, P., Vassilopoulos, A., Tomasin, A. 2011a. Holocene submerged shorelines on Theologos area (Greece), *Z. Geomorphology* 55-1, 31–44.
- Evelpidou, N., Pirazzoli, P. A., Saliège, J.-F., Vassilopoulos, A. 2011b. Submerged notches and doline sediments as evidence for Holocene subsidence, *Continental Shelf Research* 31-12, 1273–1281.
- Evelpidou, N., Vassilopoulos, A., Pirazzoli P. A., 2012a. Submerged notches on the coast of Skyros Island (Greece) as evidence for Holocene subsidence, *Geomorphology* 141-142, 81–87.

- Evelpidou, N., Kampolis, I., Pirazzoli, P. A., Vassilopoulos, A. 2012*b*. Global sea-level rise and the disappearance of tidal notches. *Global and Planetetary Change* 92-93, 248–256.
- Fairbridge, R.W. 1968. Limestone coastal weathering. In: Fairbridge, R.W. (Ed.), *The Encyclopedia of Geomorphology*. Dowden, Hutchinson and Ross, Stroudsburg, 653–657.
- Florentin, J.A., Blackwell, B.A.B., Tüysüz, O., Tari, U., Genç, Ş.C., İmren, C., Mo, S., Huang, Y.E.W., Skinner, A.R., Blickstein, J.I.B., Skinner, A.R., Kim, M. 2014. Monitoring tectonic uplift and paleoenvironmental reconstruction for marine terraces near Mağaracık and Samandağ, Hatay Province, Turkey. *Radiation Protection Dosimetry* 159 (1/4), 220–232.
- Guilcher, A. 1953. Essais sur la zonation et la distribution des formes littorales de dissolution du calcaire. *Annales de Géographie* 62, 161–179.
- Guilcher, A. 1958. Coastal corrosion forms in limestones around the Bay of Biscay. *Scottish Geographical Magazine* 74, 137–149.
- Hills, E.S. 1971. A study of cliffy coastal profiles based on examples in Victoria, Australia. *Zeitschrift für Geomorphologie* 15, 137–180.
- Hodgkin, E.P. 1964. Rate of erosion of intertidal limestone. *Zeitschrift für Geomorphologie* 8, 385–392.
- Howell, A., Jackson, J., England, P., Higham, T., Synolakis, C. 2015. Late Holocene uplift of Rhodes, Greece: evidence for a large tsunamigenic earthquake and the implications for the tectonics of the eastern Hellenic Trench System. *Geophysical Journal International* 203, 459–474.
- <https://www.conchology.be>, date of acces: 25.03.2021
- Jara-Muñoz, J., Melnick, D., Strecker, M.R. 2016. TerraceM: A MATLAB® tool to analyze marine and lacustrine terraces using high-resolution topography. *Geosphere* 12- 1, 1–20.
- Keller, E.A., Pinter, N. 2002. *Active Tectonics, Earthquakes, Uplift and Landscape*. 2nd Edition, Prentice Hall, Upper Saddle River, 362.
- Kershaw, S., Guo, L. 2001. Marine notches in coastal cliffs: indicators of relative sea-level change, Perachora Peninsula, central Greece. *Marine Geology* 179, 213-228.
- Kontogianni, V.A., Tsoulos, N., Stiros, S.C. 2002. Coastal uplift, earthquakes and active faulting of Rhodes Island (Aegean Arc): modeling based on geodetic inversion. *Marine Geology* 186, 299-317.
- Laborel, J., Morhange, C., Collina-Girard, J., Laborel-Deguen, F. 1999. Littoral bioerosion, a tool for the study of sea level variations during the Holocene, *Bulletin of the Geological Society of Denmark* 45, 164-168.
- Lekkas, E., Danamos, G., Skourtsos, E. 2007. Implications for the correlation of the Hellenic nappes in SW of Aegean: The geological structure of the Archangelos Region, Rhodes Island. *Bulletin of the Geological Society of Greece, Proceedings of the 11. International Congress, Athens, May, 40, 1-12.*
- McFadden, L., Spencer, T., Nicholls, R.J. 2007. Broad-scale modelling of coastal wetlands: what is required? *Hydrobiologia* 577, 5-15.
- Newell, N.D., 1956. Geological reconnaissance of Raroia (KonTiki) Atoll, Tuamotu Archipelago. *Bulletin of the American Museum of Natural History* 109, 315-372.
- Okay, A. İ., Tüysüz, O. 1999. Tethyan sutures of northern Turkey. In: Durand, B. Jolivet, L. Horváth, F. and Séranne, M. (ed s), *The Mediterranean Basins: Tertiary Extension Within the Alpine Orogen*. Geological Society, London, Special Publications 156, 475-515.
- Perkins, B.F. 1966. Rock Boring Organisms as Markers of Stratigraphic breaks. *American Association of Petroleum Geologists Bulletin* 50(3), 631.
- Pirazzoli, P. 1986. Marine notches. In: van der Plassche, O. (Ed.), *Sea-level Research: A Manual for the Collection and Evaluation of Data*. GeoBooks, Norwich, 361-399.
- Pirazzoli, P.A. 1989. Recent sea-level changes in the North-Atlantic. In: Scott, D.B., Pirazzoli, P.A., Honig, C.A. (eds.) *Late Quaternary Sea-Level Correlation and Applications*, Kluwer, Dordrecht, NATO ASI Series C, 256, 153–167.
- Pirazzoli, P.A., Evelpidou, N. 2013. Tidal notches: A sea-level indicator of uncertain archival trustworthiness, *Palaeogeography Palaeoclimatology Palaeoecology* 369, 377-384.
- Pirazzoli, P. A., Laborel, J., Saliège, J. F., Erol, O., Kayan, İ., Person, A. 1991. Holocene raised shorelines on the Hatay coasts (Turkey): Palaeoecological and tectonic implications, *Marine Geology* 96(34), 2-95-311.
- Pirazzoli, P.A., Thommeret, J., Thommeret, Y., Laborel, J., Montaggioni, L.F. 1982*a*. Crustal block movements from Holocene shorelines: Crete and Antikythira (Greece). *Tectonophysics* 86, 27-43.
- Pirazzoli, P.A., Montaggioni, L., Thommeret, J., Thommeret, Y., Laborel, J. 1982*b*. Sur les lignes de rivage et la neo-tectonique à Rhodes (Grèce) à l'Holocène. *Institut Océanographique Monaco Annales* 58, 89-102.

- Pirazzoli, P.A., Montaggioni, L., Saliege, J., Segonzac, G., Thommeret, Y., Vergnaud-Grazzini, C., 1989. Crustal block movements from Holocene shorelines: Rhodes island (Greece). *Tectonophysics* 170, 89-114.
- Ricci, S., Perasso, C. S., Antonelli, F., Petriaggi, B. D. 2015. Marine bivalves colonizing Roman artefacts recovered in the Gulf of Pozzuoli and in the Blue Grotto in Capri (Naples, Italy): boring and nestling species. *International Biodeterioration and Biodegradation* 98, 89-100.
- Schneider, J. 1976. Biological and inorganic factors in the destruction of limestone coasts. *Contributions to Sedimentology* 6, 1-112.
- Schneiderwind, S., Boulton, S. J., Papanikolaou, I., Kázmér, M., Reicherter, K. 2017. Numerical modeling of tidal notch sequences on rocky coasts of the Mediterranean Basin. *Journal of Geophysical Research: Earth Surface* 122, 1154-1181.
- Smith, R. D., Ross, A. J. 2018. Ambergroundpholadid bivalve borings and inclusions in Burmese amber: implications for proximity of resin-producing forests to brackish waters, and the age of the amber. *Earth and Environmental Science Transactions of the Royal Society of Edinburgh* 107, 239-247.
- Takenaga, K. 1968. The classification of notch profiles and the origin of notches. *ChigakuZasshi (Journal of Geography, Hiroshima)* 77, 329-341.
- Tarı, U., Tüysüz, O., Genç, Ş.C., İmren, C., Blackwell, B.A.B., Lom, N., Tekeşin, Ö., Üsküplü, S., Erel, L., Altıok, S., Beyhan, M. 2013. Geology and morphology of the Antakya Graben between the Amik Triple Junction and the Cyprus Arc. *GeodinamicaActa* 26 (1/2), 27-55.
- Tarı, U., Tüysüz, O., Blackwell, B.A.B., Mahmud, Z., Florentin, J.A., Qi, J., Genç, Ş.C., Skinner, A. 2018. Sealevel change and tectonic uplift from dated marine terraces along the eastern Mediterranean coast, southeastern Turkey. *Palaeogeography, Palaeoclimatology, Palaeoecology* 511, 80-102.
- Taylor, P. D., Wilson, M. A. 2003. Palaeoecology and evolution of marine hard substrate communities. *Earth-Sciences Review* 62, 1-103.
- Tjia, H.D. 2013. Evidence of Holocene and historical changes of sea level in the Langkawi Islands. *Bulletin of Geological Society of Malaysia* 59, 67-72.
- Torunski, H. 1979. Biological erosion and its significance for the morphogenesis of limestone coasts and for nearshore sedimentation (northern Adriatic). *Senckenbergiana Maritima* 11, 193-265.
- Trenhaile, A.S. 2015. Coastal notches: Their morphology, formation, and function. *Earth-Science Reviews* 150 (2015) 285-304,
- Trenhaile, A.S., Porter, N.I., Prestanski, K. 2015. Shore platforms and cliff-notch transitions along the La Paz Peninsula, Southern Baja, Mexico. *Geologica Acta* 13, 167-180.
- Tricart, J. 1972. Landforms of the Humid Tropics: Forests and Savannas. Longman, London, 306.
- Trudgill, S.T. 1976. The marine erosion of limestones on Aldabra Atoll, Indian Ocean. *Zeitschriftfür Geomorphologie* 26, 164-200.
- Tüysüz, O. 1993. Karadeniz'den Orta Anadolu'ya bir Jeotravers: Kuzey Neo-Tetisin Tektonik evrimi. *Türkiye Petrol Jeologları Derneği Bülteni* 5/1, 1-33.
- Tüysüz, O. 1996. Amasya ve çevresinin jeolojisi. *Türkiye 11. Petrol Kongresi, Bildiriler, Jeoloji, Türkiye Petrol Jeologları Derneği/TMMOB Petrol Mühendisleri Odası/ TMMOB Jeofizik Mühendisleri Odası*, 32-48.
- Tüysüz, O., Dellaloğlu, A.A. 1992. Çankırı havzasının tektonik birlikleri ve jeolojik evrimi. *Türkiye 9. Petrol Kongresi, Bildiriler, Jeoloji*, 333-349.
- Tüysüz, O., Sakınç, M., 1992. Bozburun (Marmaris) ile Çorum'un büyük benzerlikleri nedir? *Cumhuriyet Bilim Teknik Sayı* 296, 6-7.
- Tüysüz, O., Genç, Ş.C., İmren, C., Tarı, U. 2012. Asi Nehri ve Samandağ Kıyılarındaki Nehir ve Deniz Taraçaları ile Bunların Güneydoğu Anadolu'nun Neotektoniğindeki Yeri. *TÜBİTAK 109Y128 Numaralı Proje Raporu*, 306. (<https://trdizin.gov.tr/publication/project/detail/TVRJek9USXk=>)
- Verstappen, H.Th. 1960. On the geomorphology of raised coral reefs and its tectonic significance. *Zeitschriftfür Geomorphologie* 4, 1-28.
- Warme, J. E. 1975. *The Study of Trace Fossils* (Ed Frey, R. W.) Springer, Berlin Heidelberg, 181-227.
- Wentworth, C.K. 1939. Marine bench-forming processes: II. Solution benching. *Journal of Geomorphology* 2, 3-25.
- Woodroffe, C.D., Stoddart, D.R., Harmon, R.S., Spencer, T. 1983. Coastal morphology and Late Quaternary history, Cayman Islands, West Indies. *Quaternary Research* 19, 64-84.
- Yılmaz, Y., Tüysüz, O., Yiğitbaş, E., Genç, Ş.C., Şengör, A.M.C. 1997. Geology and tectonic evolution of the Pontides. In: A. Robinson (Ed.), *Regional and Petroleum Geology of the Black Sea and Surrounding Region*. American Association of Petroleum Geologists Memoir 68, 183-226.



Bulletin of the Mineral Research and Exploration

<http://bulletin.mta.gov.tr>



Role of the Cretaceous normal faults on the formation of the Eocene (Pontide) fold-thrust belt structures in offshore Akcakoca-Amasra area, Western Black Sea basin, Turkey

Özgür TÜRKMEN^{a*} and İbrahim ÇEMEN^b

^aGeneral Directorate of Mineral Research and Exploration, Marine Researches Department, Ankara, Turkey

^bUniversity of Alabama, Department of Geology, Tuscaloosa, Al, 35406

Research Article

Keywords:

Western Black Sea,
Decollement, Tectonic
ramp, Pontide orogeny.

ABSTRACT

The Western Black Sea basin formed during the rifting of the Moesian Platform in Early Cretaceous. The closure of the Neotethys Ocean in the Middle Eocene resulted in the formation of the Pontide fold and thrust belt in northern Turkey. During this study, eight seismic reflection profiles were interpreted to determine the subsurface structural geometry and tectono-stratigraphic evolution of the offshore Akcakoca-Amasra area. The stratigraphy of the study area is determined based on a composite wireline well log of the Akcakoca-1 wildcat well, which was also used to construct a velocity model based on sonic data. We suggest that a major décollement surface was developed during the Eocene Pontide Orogeny. The décollement is located at the limestone clay-shale intraformational transition within the Late Cretaceous (Maastrichtian) - Paleocene Akveren Formation. Normal faults formed during the Cretaceous rifting in the region are located below the décollement surface. They provide tectonic ramps along the décollement surface and allow the décollement to develop ramp-flat thrust fault geometry. A well-developed duplex structure is also present along the seismic lines. The décollement surface serves as the floor thrust of the duplex structure. The roof thrust of the duplex is in the Pliocene Sarıkum formation, dominantly composed of claystone.

Received Date: 22.01.2020

Accepted Date: 07.08.2020

1. Introduction

The Black Sea basin (Figure 1) is composed of the Western and Eastern Black Sea basins. The Western Black Sea Basin formed as a result of rifting of the Moesian Platform in Aptian (Okay et al., 1994) (Figures 1 and 2). The Eastern Black Sea basin formed during the counterclockwise rotation of the Eastern Black Sea block around pole of rotation located north of Crimea (Görür and Tüysüz, 1997) in Santonian – Campanian (Figures 1 and 2). This rotation was coeval with the rifting in the Western Black Sea basin, and continued until Miocene (Okay et al., 1994) (Figures 2 and 3).

After the Aptian (Early Cretaceous) rifting, both Eastern and Western Black Sea basins experienced deep water depositions. In middle Eocene, the Istanbul and Sakarya blocks collided (e.g., Görür, 1988; Robinson et al., 1995; Yigitbaş et al., 1995; Stephenson et al., 2010) and formed the Pontide mountain range to the south of the Western and Eastern Black Sea basins. During Late Miocene, a major sea level fall occurred in the region which caused the two basins to become large shallow lakes and the interiors of the basins were filled with muds and basin floor clastics (Okay and Nikishin, 2015). The depth of water in the center of the basins was reduced to a few hundred meters.

Citation Info: Türkmen, Ö., Çemen, İ. 2021. Role of the Cretaceous normal faults on the formation of the Eocene (Pontide) fold-thrust belt structures in offshore Akcakoca-Amasra area, Western Black Sea basin, Turkey. Bulletin of the Mineral Research and Exploration 164, 165-182.

<https://doi.org/10.19111/bulletinofmre.777892>

*Corresponding author: Özgür TÜRKMEN, ozgur.turkmen@mta.gov.tr

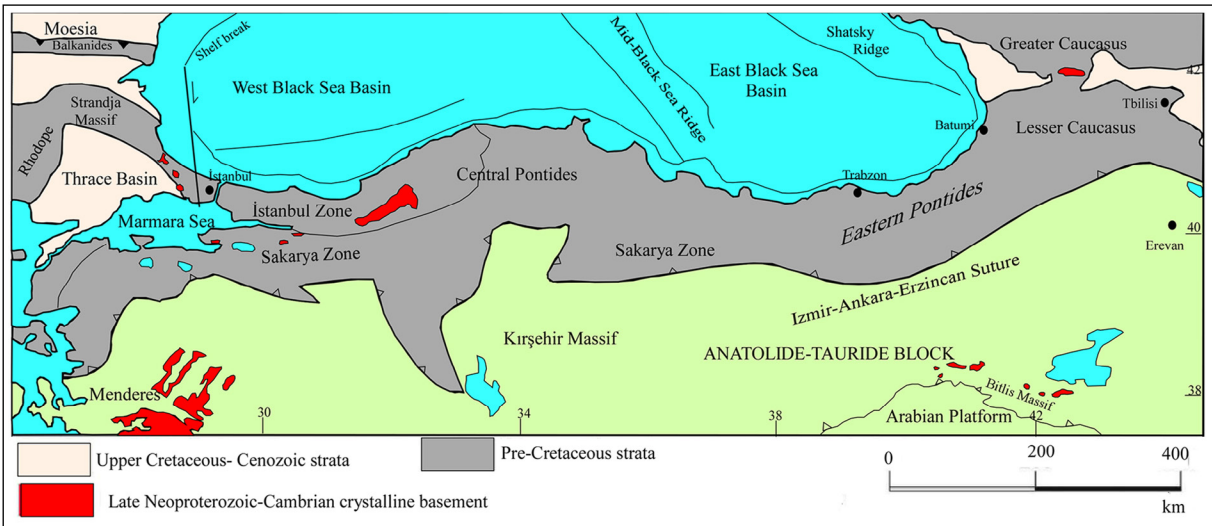


Figure 1- The main tectonic units in the Black Sea region (Modified from Okay and Nikishin, 2015).

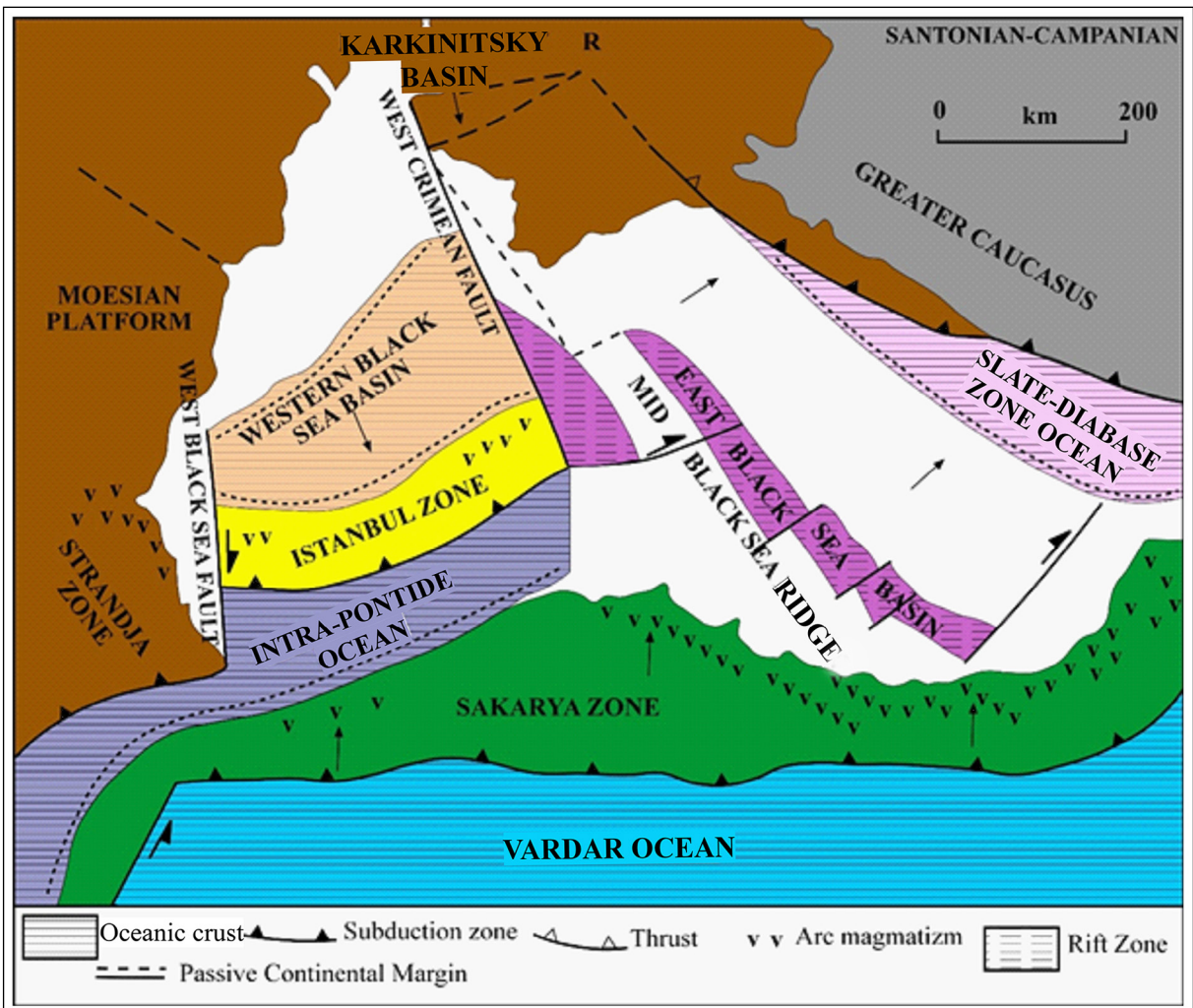


Figure 2- Diagram showing major tectonic elements of the Western and the Eastern Black Sea basins during the Santonian to Campanian (Cretaceous). R = rotation pole of the Eastern Black Sea block (Modified from Okay et al., 1994).

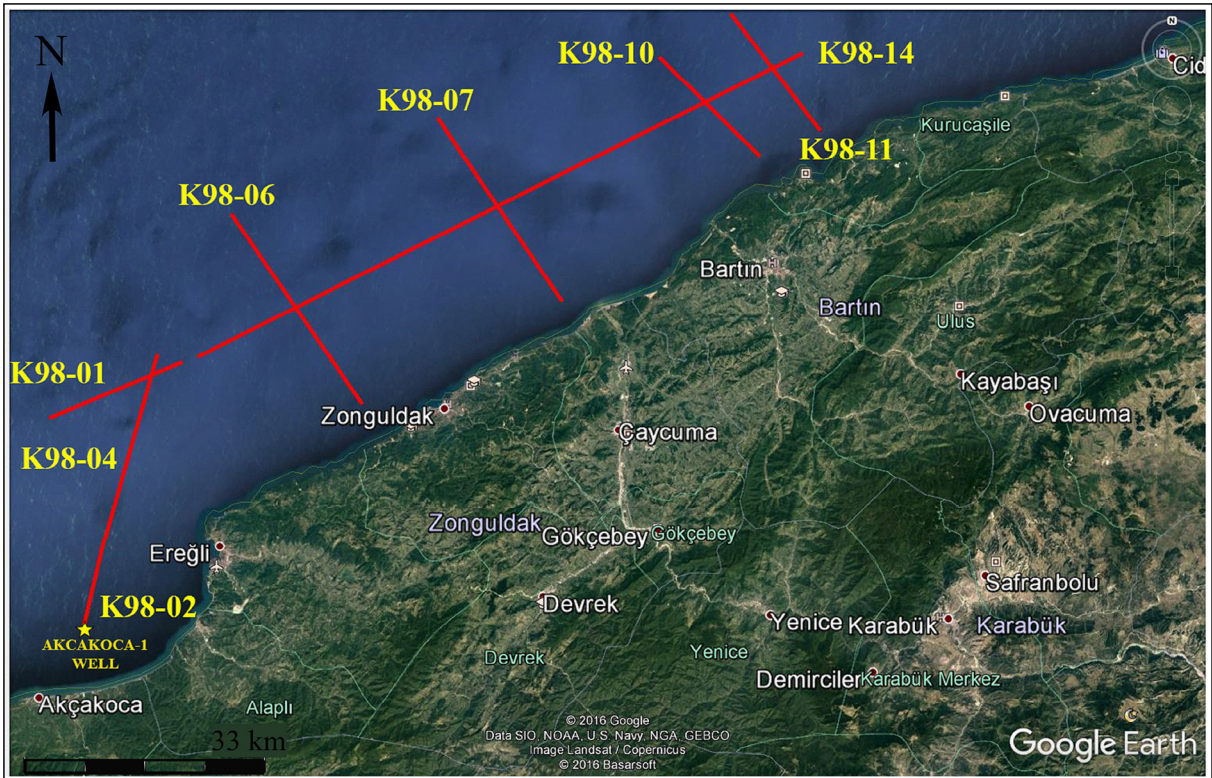


Figure 3- Location map of the offshore seismic lines of the study area.

This caused major incision of the basin margins and widespread deposition of fluvial strata over earlier shelf and even basinal areas (e.g., Robinson et al., 1995). The water level rose rapidly from the late Miocene to Pliocene due to a world-wide sea level rise and the two basins were coalesced again giving way to formation of the present day Black Sea basin (Figures 1 and 2). The general tectonic evolution of the Western Black Sea basin is relatively well understood (e.g., Şengör and Yılmaz, 1981; Okay et al., 1994; Nikishin et al., 2002). However, tectonostratigraphic evolution of the southern margin of the basin remains poorly understood because there is no published geological research based on interpretation of available seismic reflection profiles and well data.

The main purpose of this study is to determine the tectonostratigraphic evolution of the offshore Akçakoca-Amasra (NW Turkey-Black Sea) area (Figure 3) along the southern margin of the Western Black Sea basin based on interpretation of the four Southeast-Northwest (K98-06, K98-07, K98-10, K98-11), two Northeast-Southwest (K98-01, K98-14) and two approximately North-South (K98-02, K98-04) seismic reflection profiles (Figure 3), provided by the

Turkish General Directorate of Mineral Research and Exploration (MTA).

2. Geologic Overview

There are three main tectonostratigraphic units in the offshore Akçakoca-Amasra (NW Turkey-Black Sea) area (Figures 1 and 4) and its surrounding:

- (i) Early Devonian to Early Cretaceous pre-rift Paleozoic sedimentary units.
- (ii) Aptian to Eocene syn-rift Mesozoic sedimentary units.
- (iii) Eocene to present post-rift sedimentary units, deposited during the Pontide Orogeny.

The pre-rift Paleozoic sedimentary units include Istanbul Zone Paleozoic succession and Ordovician to Carboniferous non-metamorphosed sedimentary units (Figure 4) (Görür, 1997). They are not penetrated by the Akçakoca-1 well within the study area and cannot be identified in the available seismic reflection profiles. Therefore, the reader is referred to Tokay (1954 and 1955); Görür (1988); Görür and Tüysüz (1997); and Tüysüz (1999) for a thorough discussion

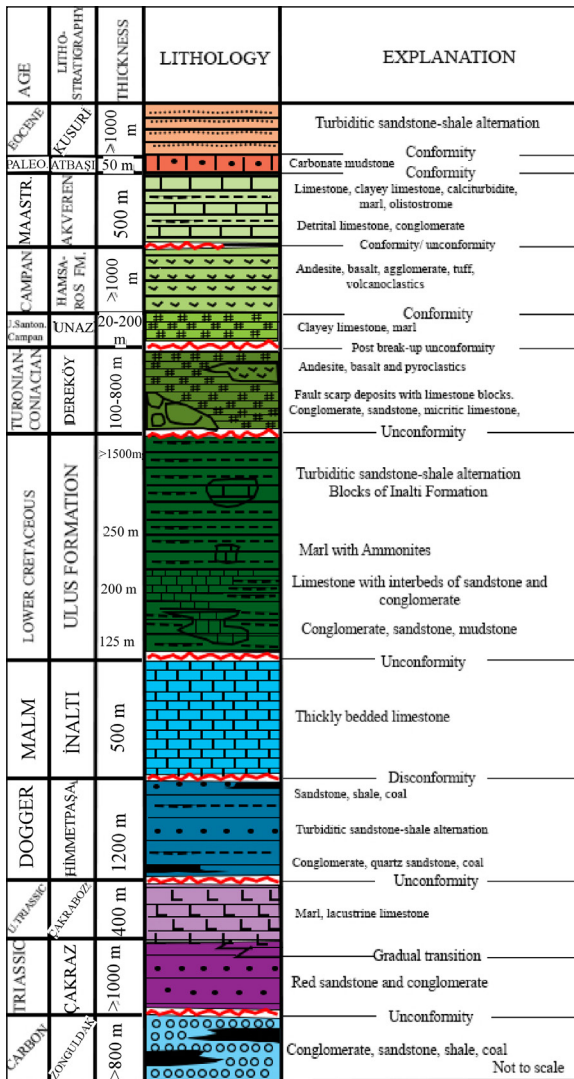


Figure 4- Generalized stratigraphic column of the southern margin of the Black Sea basin (Modified from Nabiev, A., 2007).

of pre-rift sedimentary units. The syn-rift and post-rift sedimentary units are penetrated by Akçakoca -1 well (Figures 3 and 7) and are discussed below.

The Aptian (Early Cretaceous) to Eocene syn-rift sedimentary succession unconformably overlies the pre-rift sedimentary units. The base of the syn-rift succession is the Ulus Formation composed of conglomerate, sandstone, mudstone, limestone and turbiditic rock units (Figure 4). The nannoplankton age determination indicates that the formation is Hauterivian to Late Aptian (Early Cretaceous) in age (Hippolyte et al., 2010). Therefore, the initiation age of rifting in the Black Sea basin is considered to be Early Cretaceous. The Ulus Formation is unconformably overlain by the Turonian-age Dereköy formation

(Figure 4), containing island arc magmatic rocks derived from the Western Pontides (Sunal and Tüysüz, 2002). The Dereköy formation contains voluminous volcanic rocks (Görür, 1997) and displays abrupt thickness and sedimentary environment changes attributed to normal faulting (Tüysüz and Yiğitbaşı, 1994; Tüysüz et al., 1995) in a back-arc rift setting. Syn-rift succession continued with the deposition of the Santonian Unaz Formation (Figure 4), composed of thin pelagic limestone. The Unaz Formation has a different contact relationship with the underlying units due to the horst-graben topography developed during the time of the Dereköy deposition. This suggests that erosional and deep marine depositional areas were closely juxtaposed before the deposition of the Unaz Formation. The dissected topography, developed during the deposition of the Dereköy formation, was covered by the pelagic carbonates of the Unaz Formation indicating regional subsidence in the Late Santonian-Campanian period (Tüysüz, 1999). The overlying Campanian Canbu formation (Figure 4) was deposited in an arc magmatism setting (Tüysüz, 1999). The Maastrichtian Akveren Formation records the end of arc-magmatism in the area and is composed of calciturbidites, olistostromes and pelagic mudstone and grades into Paleocene to the Eocene Kusuri Formation (Figure 4), which is primarily composed of pelagic mudstone and marl representing the beginning of the post-rift stage. The Pontide fold-thrust belt extends as a morphological entity from the Rhodope Mountains of Bulgaria in the west to the Caucasus Mountains in the east (Figure 1). It marks the post-rifting stage in the region and comprises three parts: Western, Central and Eastern Pontides (Figure 1). The northern boundary of the Pontides is covered by the Black Sea, in Northern Anatolia, Turkey. From Ankara westward, it splays into two branches; the northern branch is called as the Intra-Pontide suture, and the southern branch is called the İzmir-Ankara suture zone (Figures 1 and 4).

The Pontide fold-thrust belt (Figure 1) formed during the closure of the Neotethys Ocean in the region (Figure 5). The closure caused the tectonic style in the Western Black Sea area to change from extension to contraction in middle Eocene (Figure 5). The contraction dominated structural and sedimentological evolution of Western Black Sea basin from Eocene to recent (Robertson et al., 2012) (Figure 5).

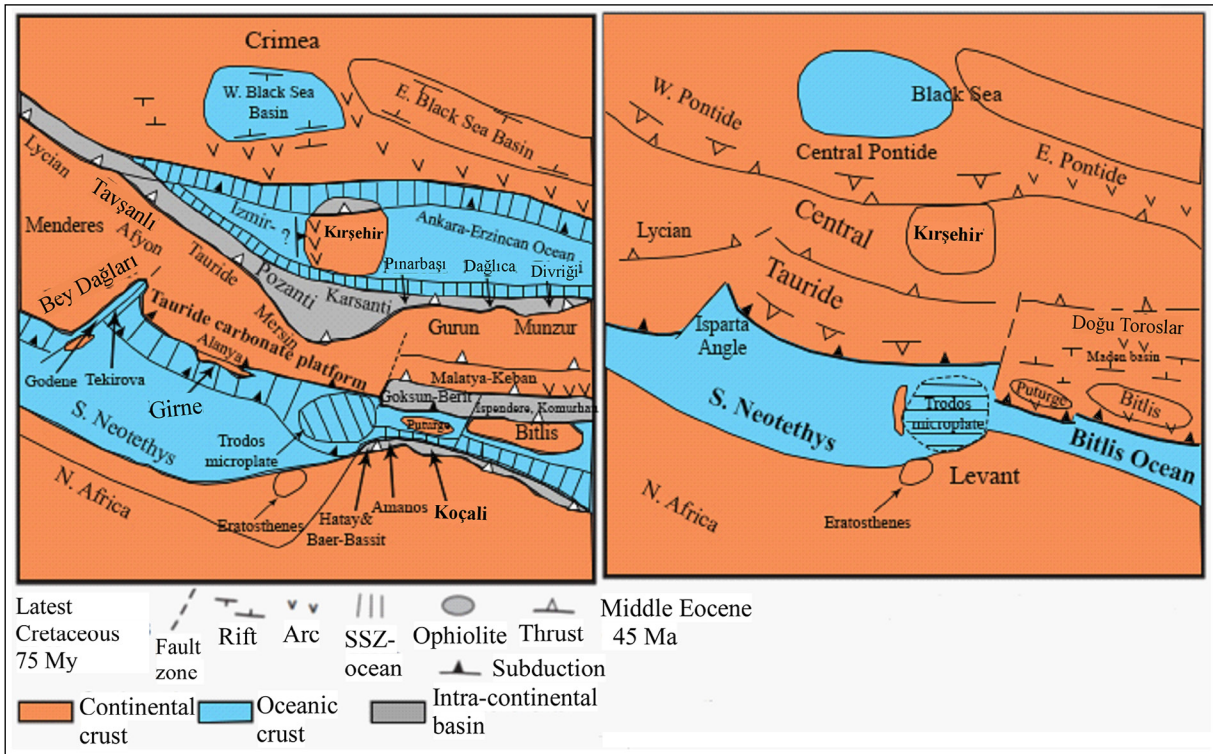


Figure 5- Closure of Neotethys Ocean and formation of Pontide Mountain belt from Late Cretaceous to Mid Eocene (Robertson et al., 2012)

3. Data and Methodology

The seismic reflection profiles used in this study were made available by the Turkish General Directorate of Mineral Research and Exploration (MTA). The data were acquired by R/V Sismik-1 vessel in 1998 by MTA. Although the first seismic process was applied in 1998, the whole data set was reprocessed by geophysicists in MTA Department of Marine Research using Promax software in 2015. The data set include eight 2D seismic reflection profiles with an 8-second TWT record length and a 50-m shot point interval between offshore Akçakoca and Amasra (Figure 3). The seismic data consist of five NW-SE trending seismic profiles: K98-06, K98-07, K98-10, K98-11, two NE-SW trending seismic profiles, K98-01, K98-14, and one almost N-S trending K98-02 and K98-04 seismic profile which connects to the longest seismic profile of the study area, K98-14 (Figure 3). The location of the seismic lines is arbitrary and the header data and location of geophones are not included in the seismic lines in order to protect the confidentiality of data.

Eight available seismic lines (Figure 3) were uploaded to Petrel software and their elevation

differences from the sea bottom were corrected by matching the top seismic reflections of each cross cutting seismic line (Figure 6). Structural interpretation of the seismic lines was carried out by Özgür Türkmen as part of his MS degree program at the University of Alabama under the supervision of İbrahim Çemen. The Akçakoca -1 wildcat well is located along the seismic profile, K98-02 (Figure 3). It was drilled in the study area by TPAO for exploration in 1976 and completed as a gas well. Its coordinates are: 41°12'36N and 31°07'36"E on the N-S trending seismic profile, K98-02. The well spotted at the Quaternary sea bottom sediments at -94.8 m and penetrated the Pliocene Sarıkum formation (587 m), the Eocene Kusuri Formation (1192 m), the Paleocene Atbaşı Formation (72 m) and the Upper Cretaceous Akveren Formation (318 m) before reaching the volcanic tuff units of Upper Cretaceous Hamsaros formation (14 m) at 2,270-m below the surface (Figure 7). The Akçakoca-1 database well data provided for this study consist of SP, gamma-ray, caliper, resistivity, density, neutron porosity and sonic logs. For the seismic to well tie, Akçakoca-1 Well was uploaded and correlated with K98-02 seismic line. The formation tops in the Akçakoca-1 Well were

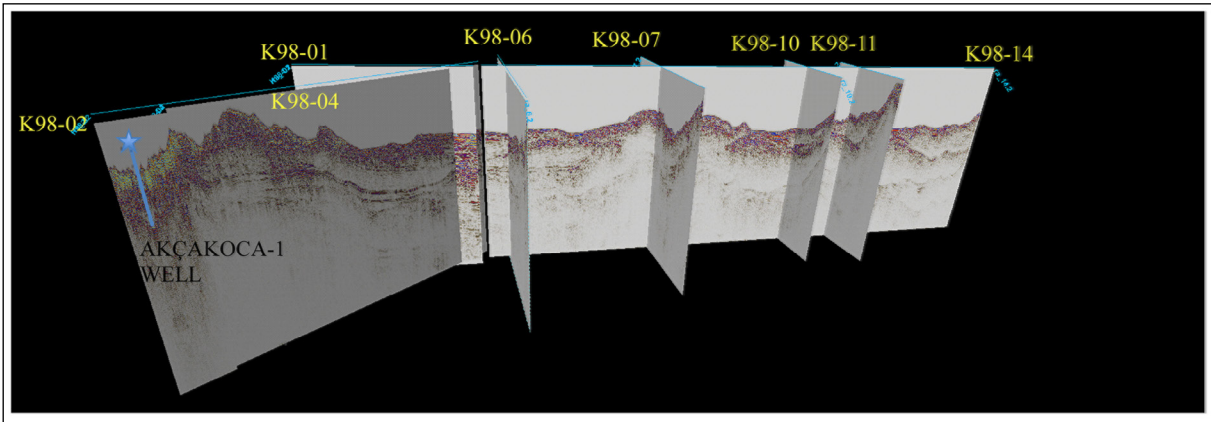


Figure 6- 3D view of the eight seismic lines from the Petrel project in the time domain.

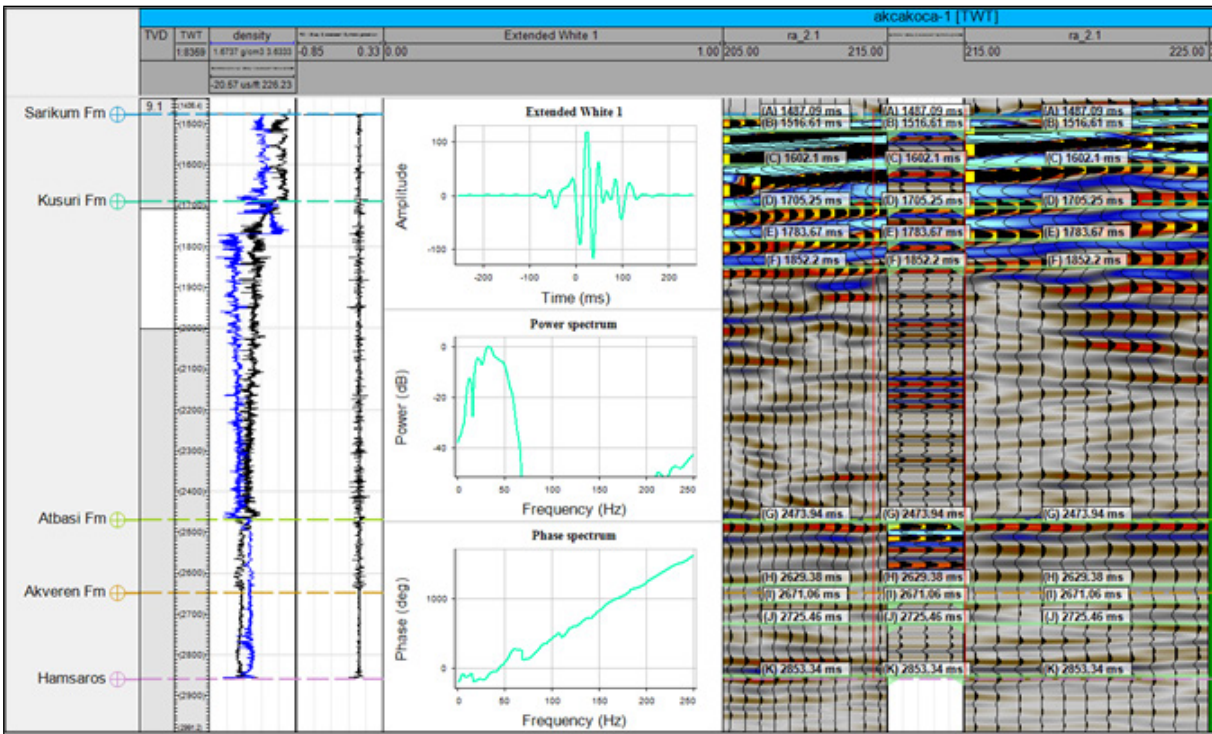


Figure 7- Synthetic seismogram generation using well log data from the Akçakoca-1 Well.

correlated to the seismic line, K98-02, by creating a synthetic seismogram (Figure7). The synthetic provided a seismic tie to determine formation tops and helped to determine structural geometry in the time domain. Although the original work, Türkmen, 2017, that this paper is based on is composed of eight seismic profiles, five of them will be discussed in order to explain the subsurface structural geology of the study area.

During this study, relative acoustic impedance is used as a seismic attribute to amplify the seismic

reflections in order to trace seismic horizons, where the resolution is very low. The process helped during the interpretation of 2-D seismic reflection profiles, and well to seismic tie. Based on the model by Bag et al., (2008), relative acoustic impedance of volume attributes tool in the fracture modeling section of Petrel software was applied to eight seismic profiles in the study area. As a result of the application of this seismic attribute, better seismic images are created for the study area.

4. Structural Interpretation of Seismic Reflection Profiles

4.1. Approximately N-S Trending Reflection Profile

4.1.1. K98-04 Seismic Line

Along the seismic profile K98-04 (Figures 3 and 6), the Cretaceous syn-rift normal faults on the southern side of the profile provide ramp geometry for the décollement surface that formed during the Eocene Pontide Orogeny. These normal faults cut the sedimentary succession up to the Upper Cretaceous Hamsaros formation (Figure 4) and do not disturb the formations younger than Hamsaros formation. This indicates that the normal faults were formed during the rifting in the Western Black Sea basin.

A well-developed decollement surface and a duplex structure are present along the seismic profile, K98-04. These contractional structures were formed during the Eocene Pontide Orogeny. The Decollement surface is located in the Upper Cretaceous Akveren Formation at the transition between clay and limestone, where limestone beds are displaying unified, horizontal reflections along the seismic reflection profiles while clay units are displaying more chaotic and mixed reflections due to their ductile nature of the clay units (Figure 8). The décollement surface serves as the floor thrust of the duplex structure. It penetrates towards the north by following the same clay unit in Akveren Formation, almost horizontally. The roof thrust of the duplex was developed in the Pliocene Sarikum formation, which is composed of claystone and splays up to the sea bottom (Figure 8).

The duplex structure between the roof thrust and the floor thrust along the seismic profile, K98-04, contains 13 horses with similar sizes (Figure 8). The horses penetrate through the Akveren Formation, and limestone units of the Paleocene Atbaşı Formation, sandstone, claystone, marl and shale intercalations of Eocene Kusuri Formation, and claystone units of Pliocene Sarikum formation.

4.2. Approximately NW-SE Trending Seismic Reflection Profiles

4.2.1. K98-06 Seismic Line

This seismic line is the westernmost of the NW-SE trending lines (Figure 3). Along this seismic line,

the décollement surface is in the Akveren Formation, same as K98-04 line. However, the roof thrust is not well developed (Figure 9). The lack of the roof thrust is probably due to the loss of the intensity in thrusting. Moreover, there are only 5 horses along the seismic section and the size of the horses is smaller than the ones in the western part of the study area. In some parts of the section, the décollement is elevated probably by the normal faults of the rifting stage; however, these faults cannot be observed clearly in the seismic section due to strong multiple effect and low resolution (Figure 9). The hanging wall strata in this section exhibit well developed folding, most likely due to the steep ramp geometry of the décollement surface southward towards the Black Sea shoreline (Figure 9).

4.2.2. K98-07 Seismic Line

While the base of this seismic line is dominated by the effects of multiples and bowties (Figure 10), the Hamsaros formation at the base and some parts of the décollement surface is questionably traced along the seismic line towards the offshore, after Common Depth Point (CDP) number 3456. This line has 5 horses (Figure 10). The roof thrust is not developed in this section similar to the seismic line K98-06 (Figure 9). However, the horse structures are bigger in size and less dense with respect to K98-06. The reason for the size and density differences of the two parallel sections is probably due to the steepness of the ramp geometry and the loss of intensity of thrusting towards the NW.

Along the section K98-06, the ramp geometry created by the normal faults of the rifting stage appear to be steeper than the ramp geometry along the line K98-07; therefore, the strata in the hanging wall of the thrust faults are folded less intensely than along the line K98-06 (Figure 10). The number of horses in this section is less than in the K98-04 seismic line, which is probably a result of decreases in the intensity of thrusting from the SW to NE.

Similar to other seismic lines, the décollement surface in the section is placed in the Akveren Formation (Figure 10), and the thrust faults are affecting all of the formations from the Akveren Formation up through to the Pliocene Sarikum formation. The Hamsaros formation top in this section

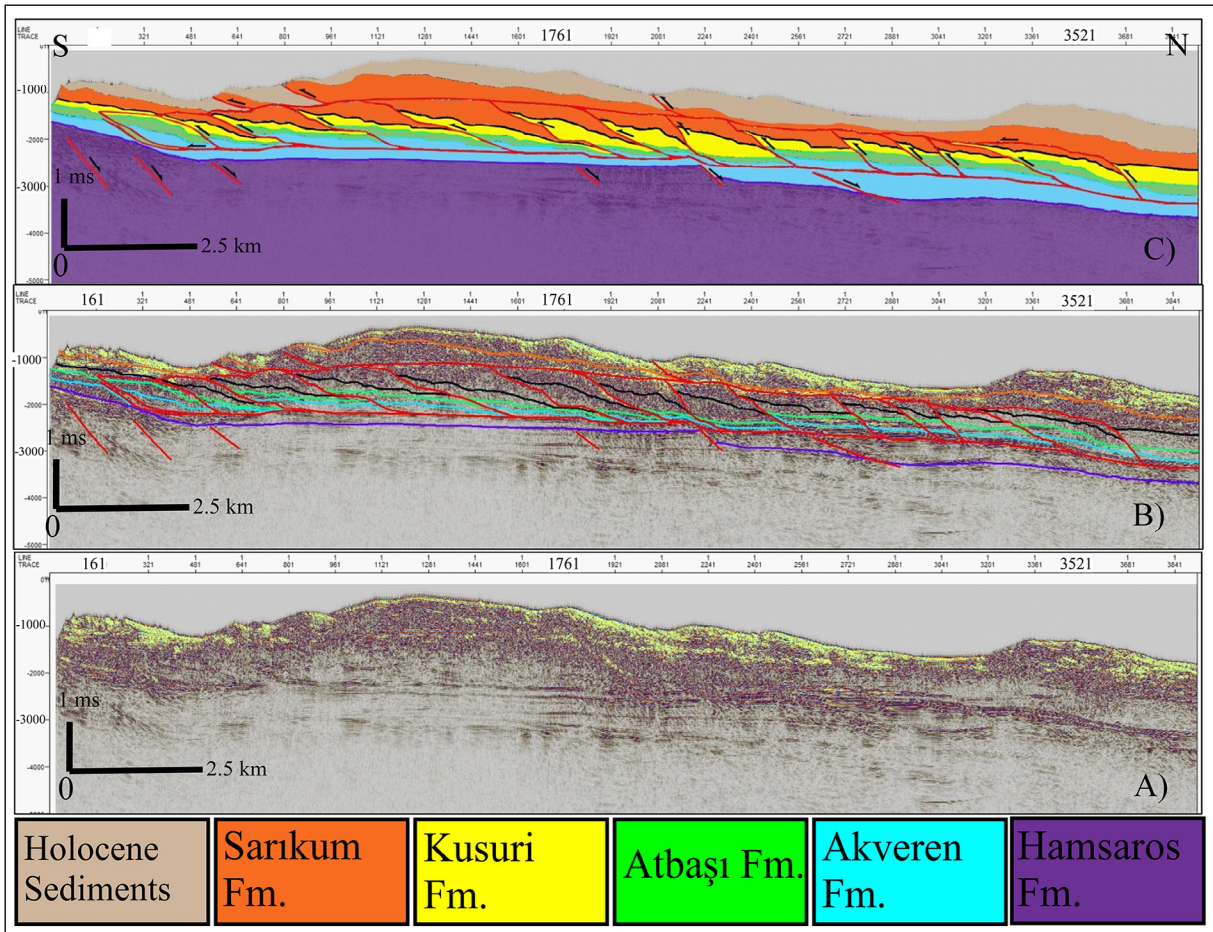


Figure 8- K98-04 seismic profile (between CDP numbers 0-3841): A) Uninterpreted; B) Interpreted and C) Line drawing. The profile shows well developed duplex structure developed between the floor within the Akveren Formation and the roof thrust within the Sarikum formation.

is determined based on the intersection with the K98-14 seismic line and is questionable due to the strong multiple effect (Figure 10).

4.3. Approximately NE-SW Trending Seismic Reflection Profiles

4.3.1. K98-01 Seismic Line

This seismic line is the southern continuation of the 100-km long K98-14 seismic line, which trends about N60°E is approximately parallel to the strike of the thrusting in the study area. Duplex structures and horses are observed in this section, similar to other sections that are approximately perpendicular to the strike (Figure 11). This is due to the change in the orientation of the strike of the thrust structure from NE-SW to almost N-S in the southeasternmost part of the study area.

Although the presence of some horses are highly questionable, we have interpreted eleven horses along this seismic section, A few splays and a well-developed roof thrust can be observed in the Pliocene Sarikum formation and décollement surface in the Upper Cretaceous Akveren Formation. The horse structures along this section are different from the other sections containing duplex structures; they are more elongated due to the oblique orientation of the section to the strike of thrusting in the study area (Figure 11). More horses are interpreted in this section than the sections towards the NE, probably because intensity of the thrusting was the strongest in the SW part of the study area (Figure 11).

Similar ramping of the décollement surface is observed along this section as well (Figure 11). However, due to the presence of strong multiple effect and bowties, the rifting stage normal faults,

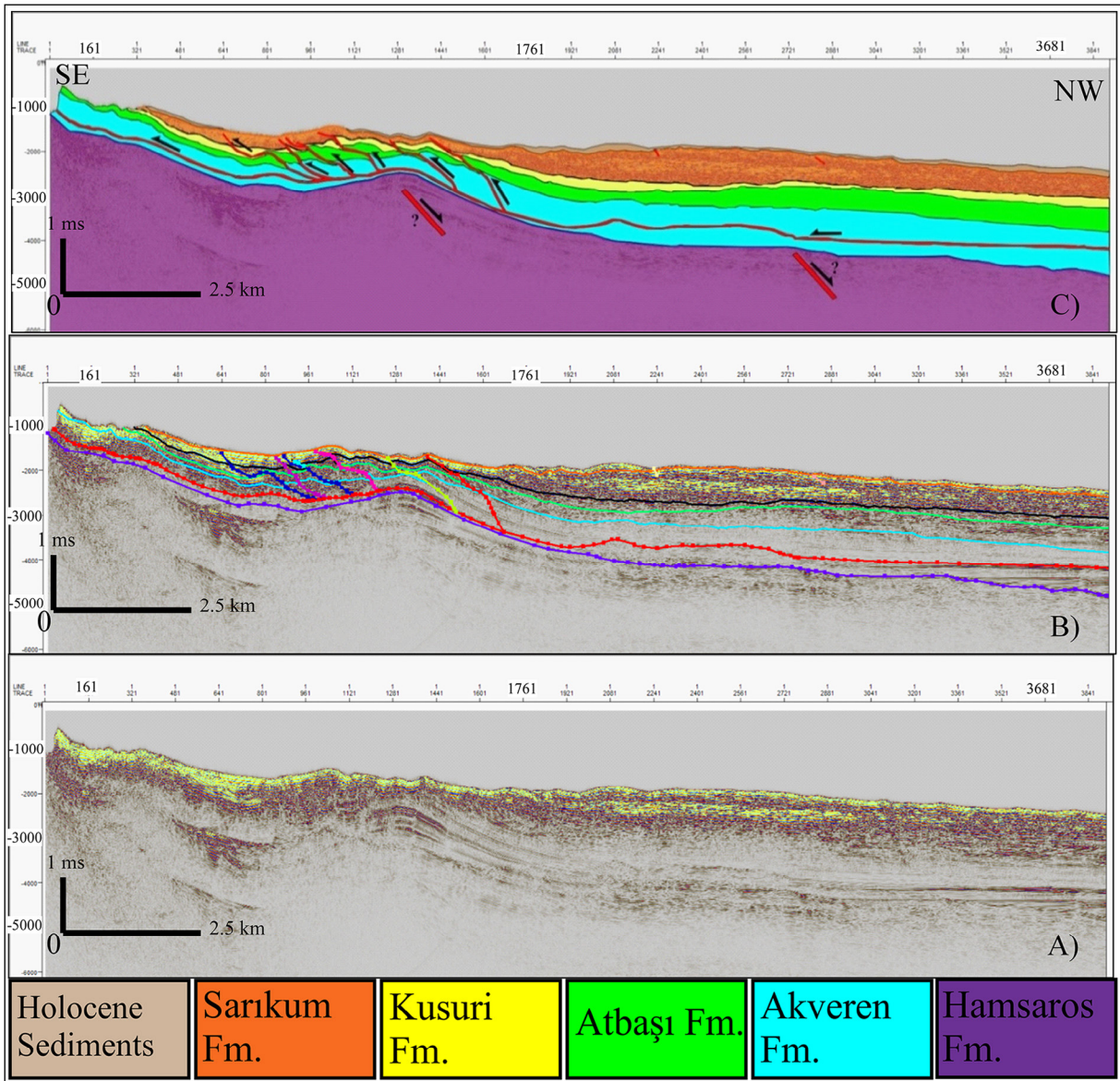


Figure 9- K98-06 (between CDP numbers 0-3841): A) Uninterpreted; B) Interpreted and C) Line drawing. Horses and décollement are well-observed. A normal fault is drawn below the décollement surface in the southeastern part of section where the décollement is elevated most likely due to a ramp along the décollement surface.

which are observed to produce ramp geometry of the décollement surface along other seismic sections (Figures 8, 9, 10), cannot be interpreted along the seismic line K98-01 (Figure 11). The normal faults strike almost parallel to the line of the section, and therefore they do not produce any diffraction along the seismic reflection profile. The K98-01 seismic section contains a Late Paleogene–Early Neogene angular unconformity towards the shoreline (Figure 11).

4.3.2. K98-14 Seismic Line

This seismic line also strike about N60°E and approximately 100 km long. Therefore it is divided into three parts between CDP numbers; a) 18856 and 14856 (Figure 12), b) 14856–10856, and c) 7656 to 5576. The entire line is approximately parallel to the strike of the Pontide thrusting in the study area and is almost perpendicular to the K98-06, K98-07, K98-10 and K98-11 seismic lines (Figure 3). The décollement surface can be traced along this seismic section in the Akveren Formation (Figures. 12, 13, 14 and 15).

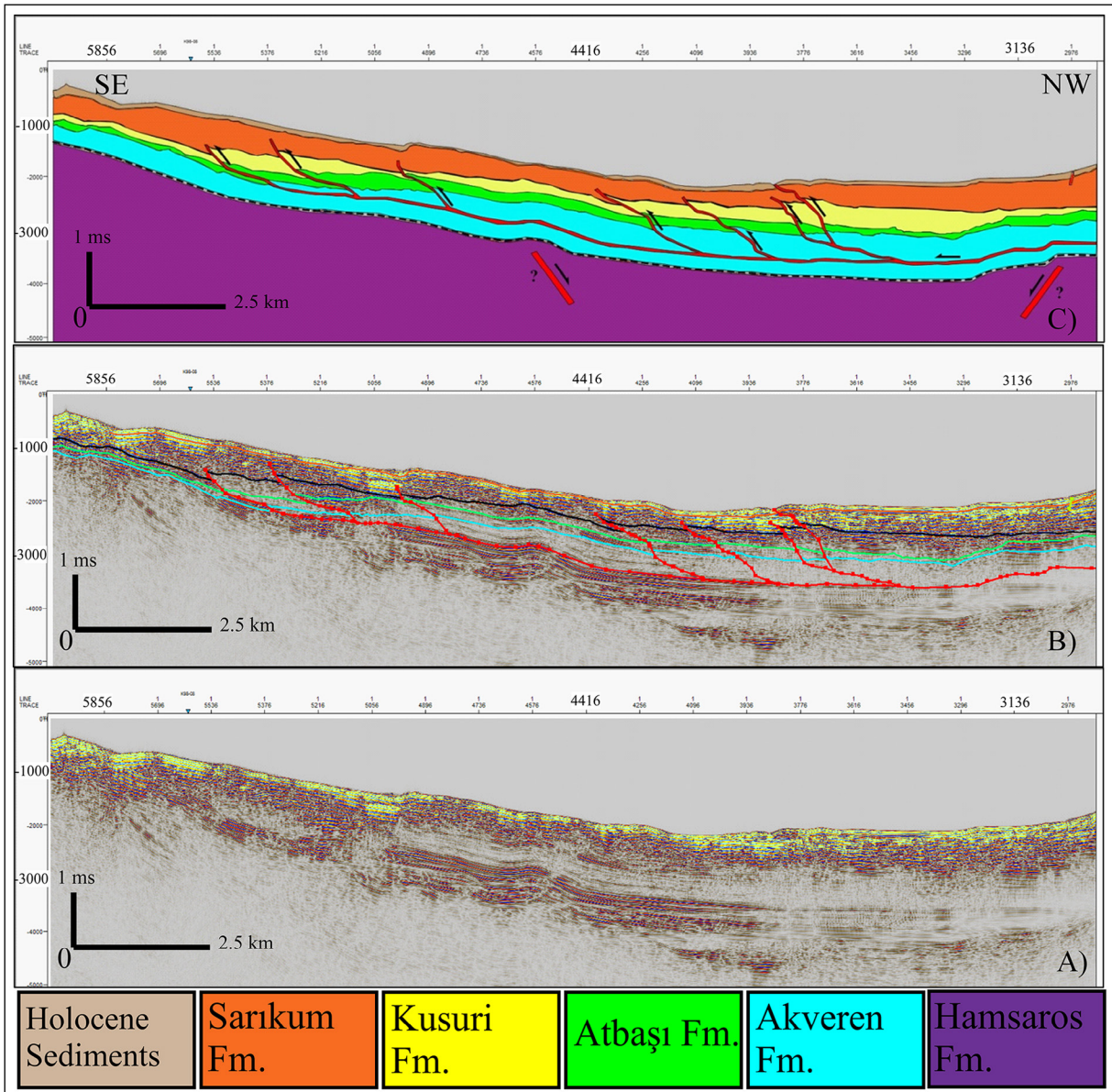


Figure 10- K98-07 (between CDP numbers 5856-2976): A) Uninterpreted, B) Interpreted and C) Line drawing. The décollement surface is present within the Akveren Formation. The section shows 5 horses within the duplex structure between the floor and roof thrusts. Normal faults, drawn below the décollement surface, are questionable because of the poor quality of the seismic line below the decollement surface.

Between CDP numbers 18856 and 14856 (Figure 12), there are some reverse faults, which cut through Sarikum, Kusuri and Atbaşı Formations; however, these faults are not connected to the main décollement surface. Towards CDP number 14856, the decollement surface all formation tops including Akveren and Hamsaros formations are elevated (Figure 12). This is interpreted as an effect of syn-rift stage extensional structures. However, these possible normal faults are not identified clearly due to the strong multiple effect

in this part of the seismic section around 5,000 ms close to CDP number 18856 and rising up to almost 4,000 ms around CDP number 14856 (Figure 12).

The part of the seismic line K98-14 between the CDP numbers 14856–10856 to the NE of the intersection with the line K98-07 and K98-14 seismic lines contains a normal fault with two antithetic faults. The antithetics are considered as part of the major landslide imaged in the study area (Figure 13). This

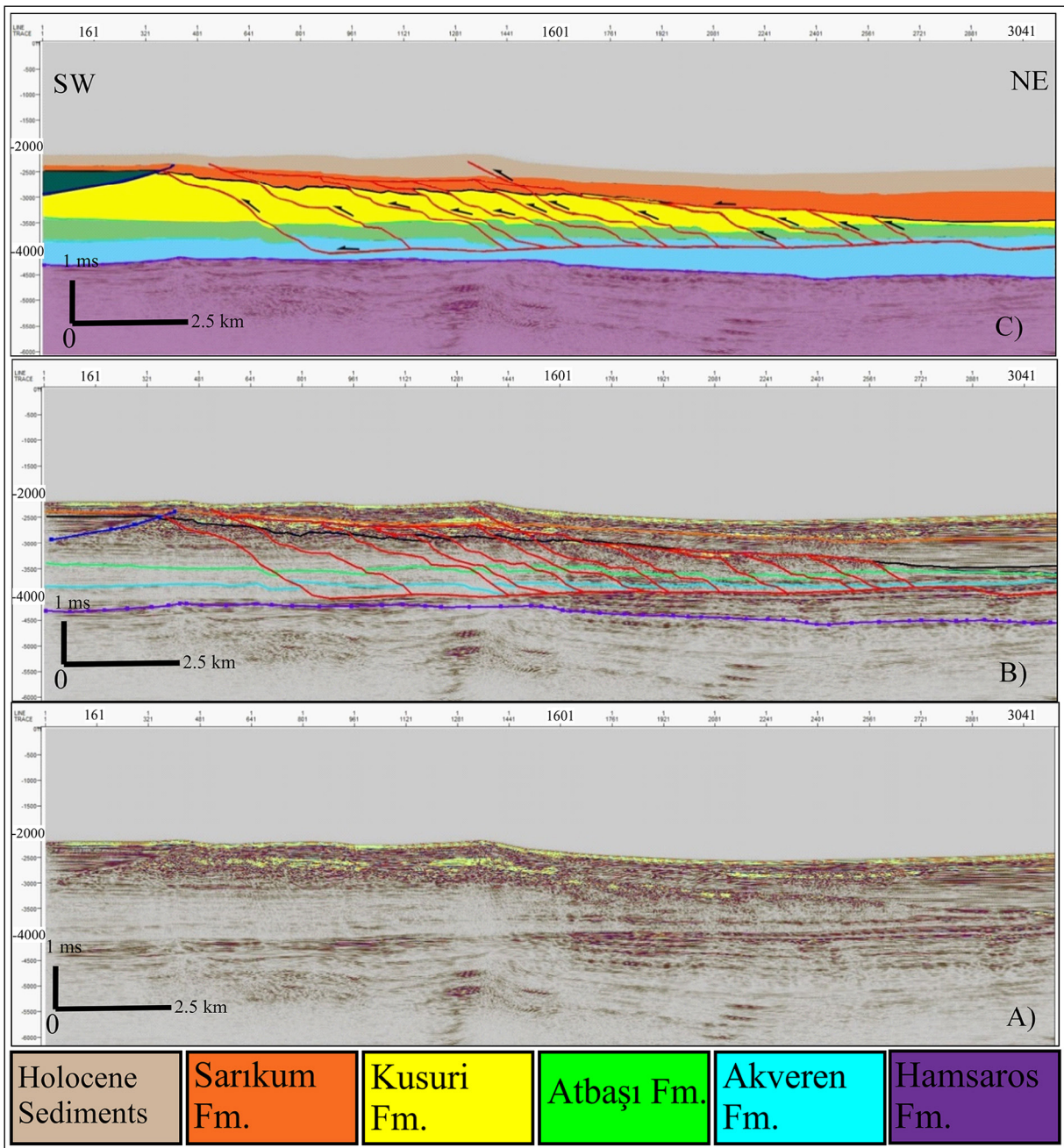


Figure 11- K98-01 (between CDP numbers 0-3041): A) Uninterpreted, B) Interpreted and C) Line drawing. Horses, roof thrust and décollement surfaces are well-observed. Rifting-stage normal faults strike almost parallel to the line of the section. Therefore, they did not produce any diffraction along the seismic reflection profile and cannot be detected below the décollement surface.

main normal fault may coincide with the décollement but was not interpreted in that way because the reflections at the base of this fault are continuous. No fault-like change in this seismic reflection line is observed in that part of the section (Figure 13). Between CDP numbers 11978 and 11498, there is a small basin possibly formed in Paleocene-Pliocene time interval. The basin is controlled by normal faults

(Figure 13). Towards CDP number 10856, normal faults create ramp geometry for a décollement surface along this part of the section (Figure 13). Between CDP numbers 10856 and 7656, the formations get thinner from NE to SW due to the elevated basement (Figure 14). Some of the normal faults cutting the base of the Hamsaros formation are observed in this part of the seismic section.

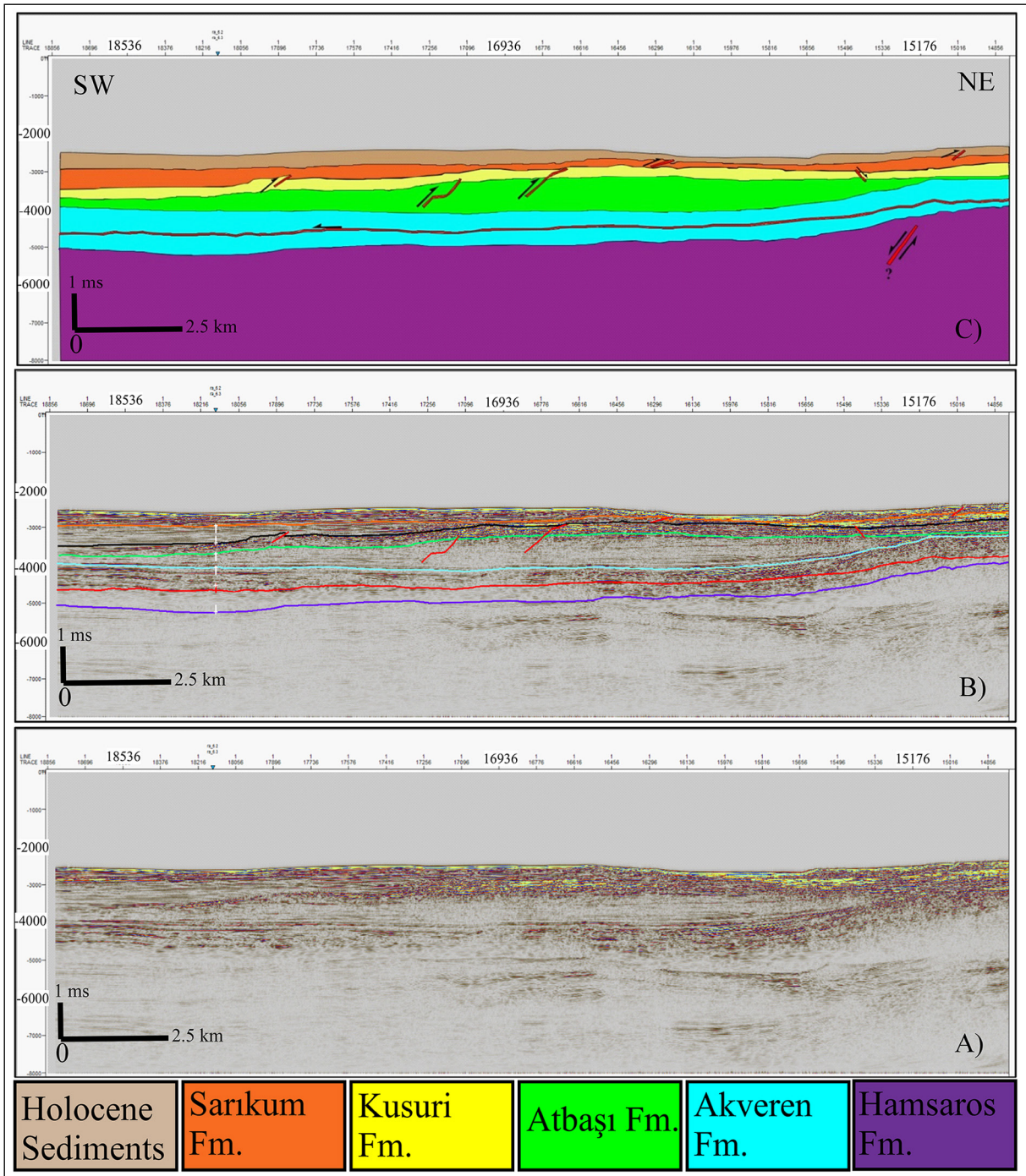


Figure 12- K98-14 (between CDP numbers 18856-14856): A) Uninterpreted, B) Interpreted and C) Line drawing. The decollement surface imaged along the seismic line perpendicular to the line K98-14 is also observed along this seismic line.

Between CDP numbers 7656 to 5576, the floor thrust is highly elevated and Eocene Kusuri and Paleocene Atbaşı Formations are exposed at the sea floor towards CDP number 5576 (Figure 15). However, there are small normal faults in Akveren and Atbaşı Formations between CDP numbers 6376

to 6056 (Figure 15), which can also be interpreted as possible small valleys. There is a normal fault in the middle of this part of K98-14 seismic line, which cuts from Akveren Formation along the seismic line (Figure 15).

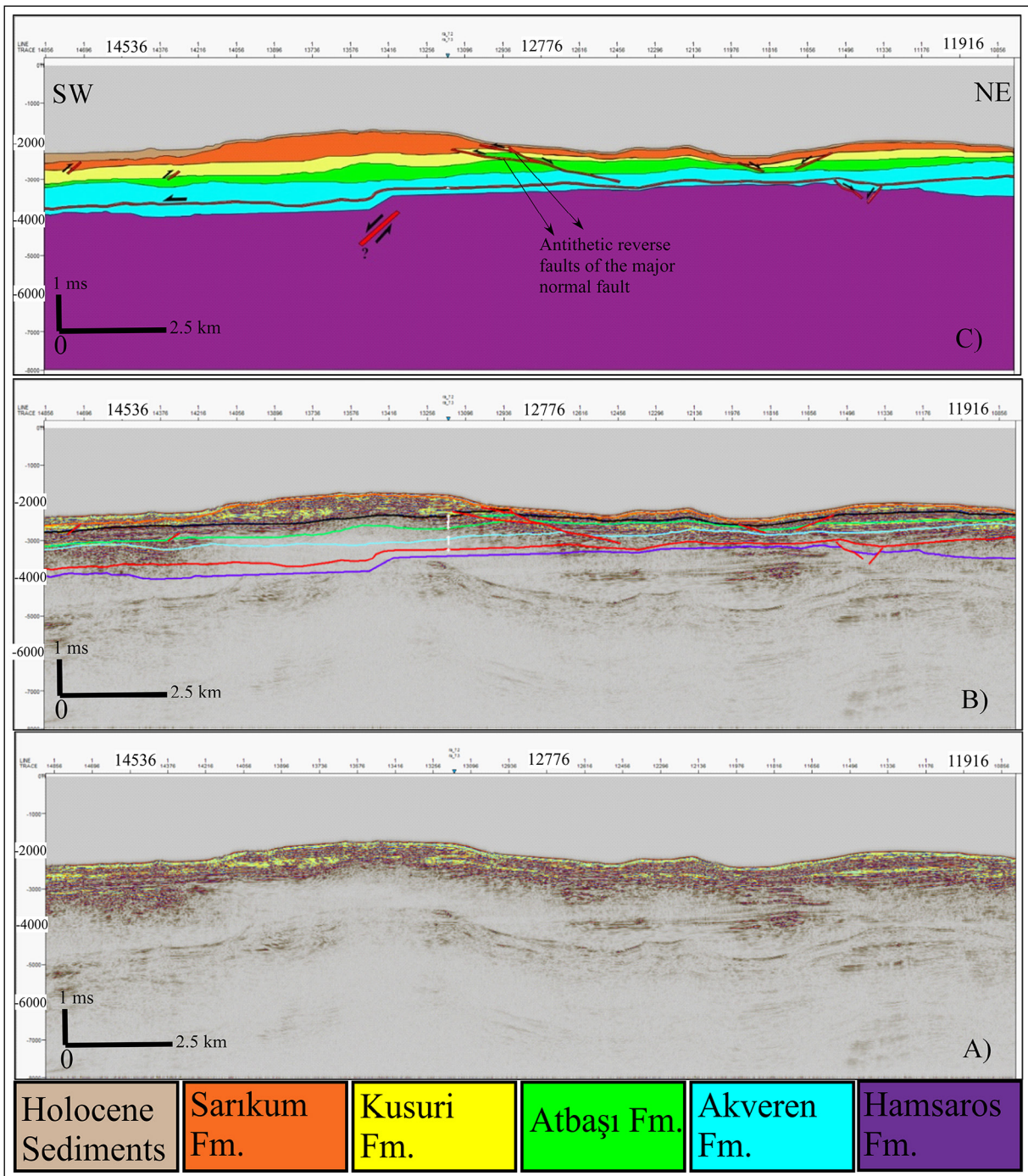


Figure 13- K98-14 (between CDP numbers 14856-10856): A) Uninterpreted, B) Interpreted and C) Line drawing. The decollement surface, southern boundary of the landslide and some of the syn-rift normal faults are well observed.

5. Summary and Conclusions

During this study area, structural interpretation of 8 available 2D reflection seismic profiles in Akçakoca-Amasra area was carried out to determine structural geometry of syn-rift extensional and post-

rift contractional structural features in the area. One of the seismic lines is used to tie the Akçakoca-1 well to the other seismic lines (Figure 3). The seismic profiles were acquired by MTA Marine Researches Department in 1998 for determining the landslides in shallow depth in the area, therefore, in the profiles,

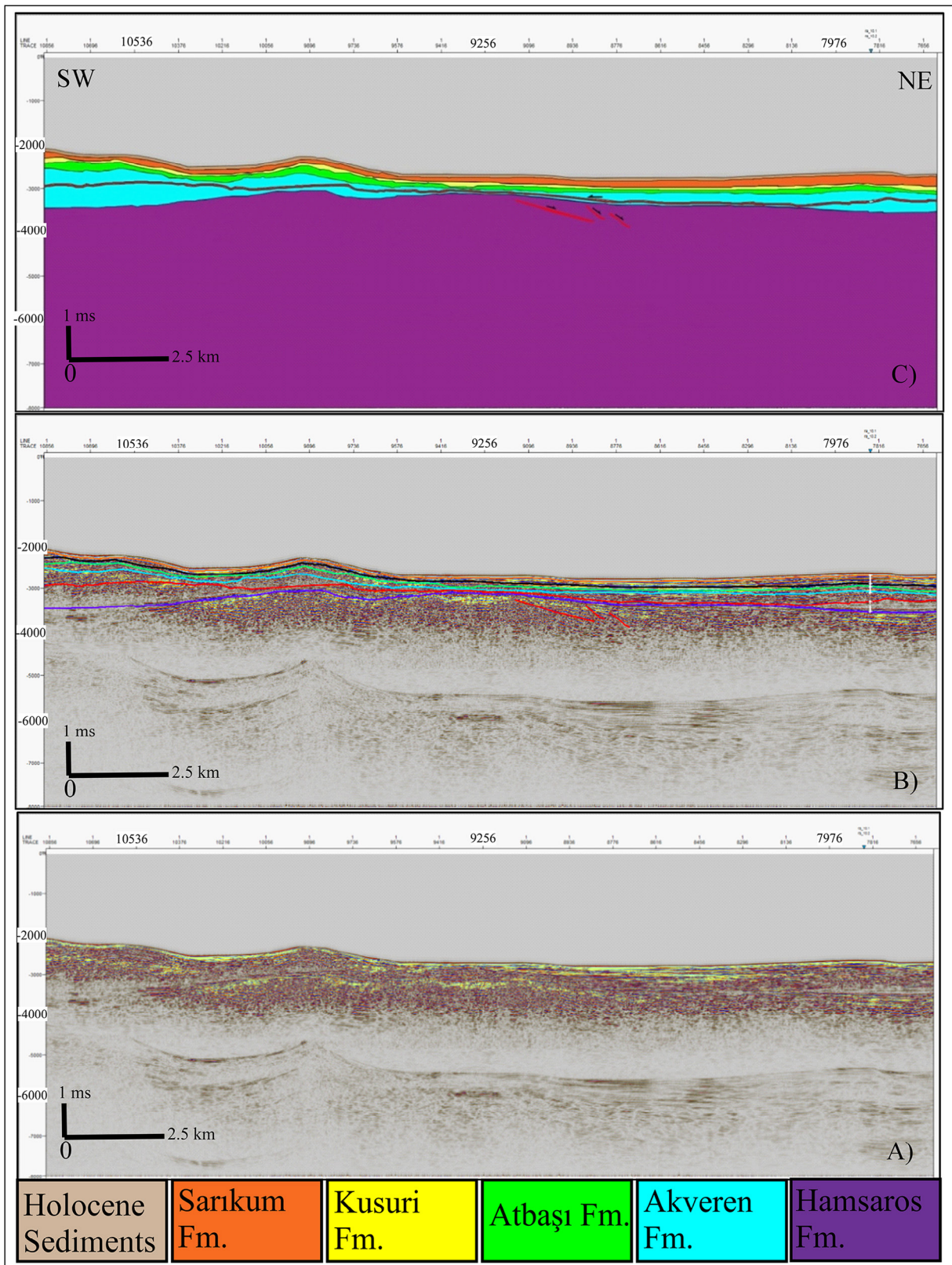


Figure 14- K98-14 (between CDP numbers 10856-7656): A) Uninterpreted, B) Interpreted and C) Line drawing. The decollement is using by the normal faults to ramp into a higher structural level.

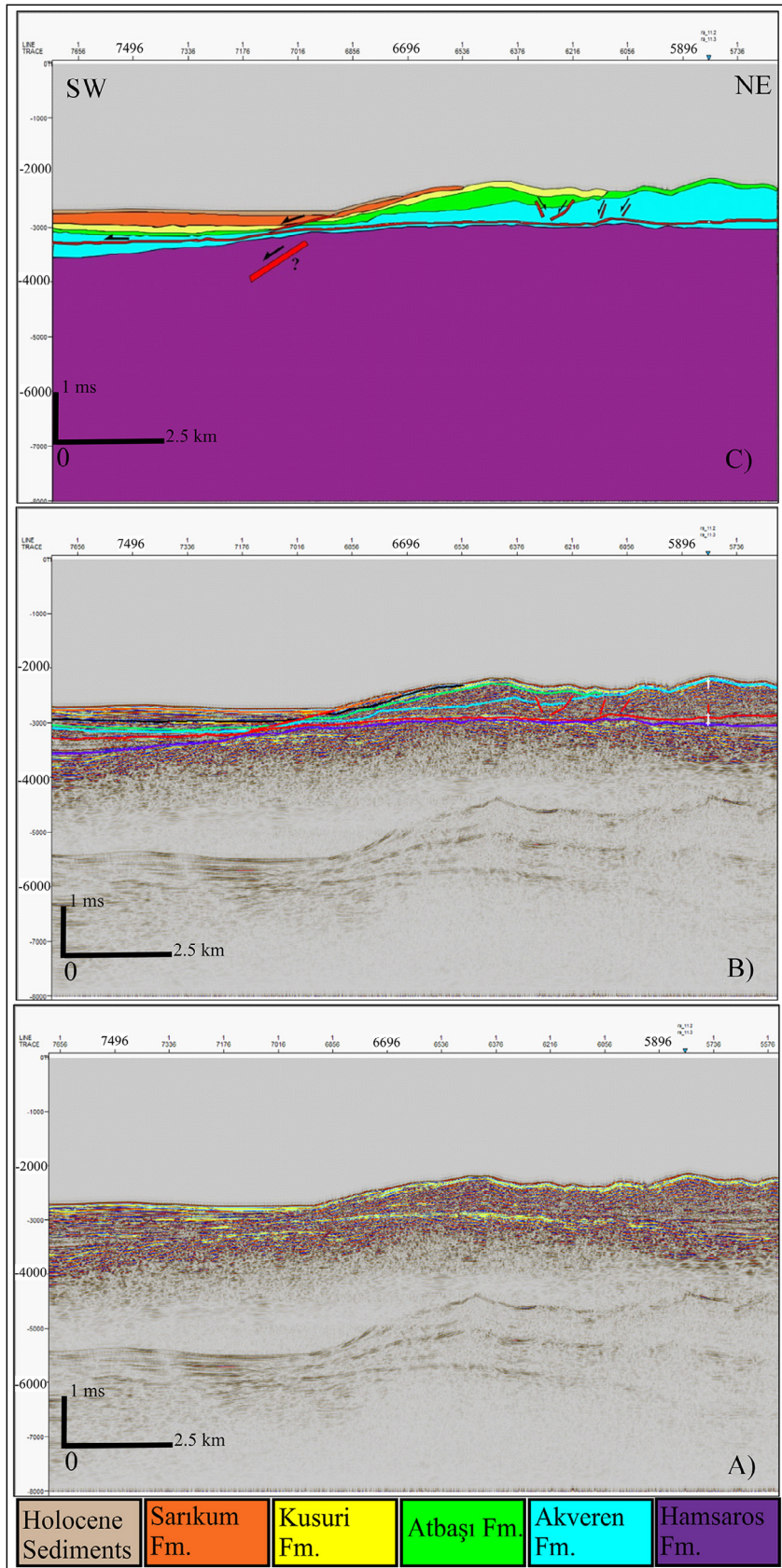


Figure 15- K98-14 (between CDP numbers 7656-5576): A) Uninterpreted, B) Interpreted and C) Line drawing. The decollement is well observed but the syn-rift normal faults are questionable.

below 3500-4000 ms, the basinal structures cannot be seen very clearly due to the strong multiple effect (Figures 8, 9, 10, 12 and 13).

The study area contains the sequence of syn-rift sediments widespread along to Mesozoic Alpine Western Black Sea basin in Northern Anatolia (e.g., Tüysüz, 1999; Okay and Nikishin, 2015). The base of syn-rift rock units is the Aptian Ulus Formation (Figure 4), composed of conglomerate, sandstone and mudstone at the bottom and grades upward into limestone interbedded with sandstone, conglomerate, and marl with ammonites and turbiditic sandstone-shale alternations. There are limestone blocks of the pre-rift İnaltı Formation within the Ulus Formation. The overlying Turonian-Coniacian Dereköy Formation is composed of fault scarp deposits with limestone blocks, conglomerate, sandstone and micritic limestone at the bottom, grading into andesite, basalt and pyroclastics (Figure 4). It is unconformably overlain by the Santonian-Campanian Unaz Formation, which is made out of clayey limestone and marl. The Unaz Formation is conformably overlain by the Campanian Hamsaros formation.

The Early Cretaceous syn-rift normal faults have been observed along most of the seismic lines (Figures 8, 9, 10, 11, 12, 13, 14, and 15). The normal faults die below the Maastrichtian-Paleocene Akveren Formation (Figure 4), which indicates that the formation was deposited after the back-arc rifting responsible for syn-rift sedimentation is ceased. The normal faults in the study area display well-developed horst-graben structures in the Western Black Sea basin during the syn-rift stage (Nikishin et al., 2012). Although there are bow-tie effects and low resolution under 3,500 ms in most seismic lines, some of these normal faults can be well delineated along the seismic line K98-04 (Figure 8). The seismic lines K98-01, K98-04, K98-06 and K98-07 (Figures 11, 8, 9, 10), which are almost

perpendicular to the strike of the Early Cretaceous rifting, also show well-developed normal faults below the Pontide contractional structures.

The study area contains a well-developed contractional duplex structure. The floor thrust of the duplex is the décollement horizon in the Maastrichtian (Late Cretaceous) Akveren Formation, at the intraformational boundary between claystone and limestone (Figures 8, 9, 10, 11, 12, 13, 14, and 15). The roof thrust of the duplex is observed only in seismic lines K98-01 and K98-04 (Figures 8, 11), in the Pliocene Sarıkum formation, which is mainly composed of claystone. The roof thrust is not observed along K98-06, K98-07, K98-10 and K98-11 profiles (Figures 9 and 10) most likely due to poor quality of the seismic lines and change in lithologies of the rock units involved in thrusting. The number of the horses that we were able to interpret along the seismic lines decreases from eleven along the K98-01 profile (Figure 11) in the southwestern part of the study area to three along the K98-11 profile in the northeastern part of the study area.

The décollement surface displays a well-developed ramp geometry, which leads the floor thrust to jump into higher structural levels (Figures 8, 9, 10, 11, 12, 13, 14, 15 and 16). Many seismic lines show the décollement making a ramp above the syn-rift normal faults to “jump” into the fine grained weak (ductile) sedimentary unit, higher in the sedimentary succession (Figures 8, 9, 10, 11, 12, 13, 14, 15 and 16). Thomas (1982) and Schedl and Wiltschko (1987) stated that these kinds of ramps, which are associated with the basement normal faults, are rooted at or near the corners of the footwall blocks. Figure 16A shows development of the ramp structure along the base of Decollement surface in Appalachian Mountains. Figure 16B shows the ramp structures developed along the Pontide décollement surface in the study area.

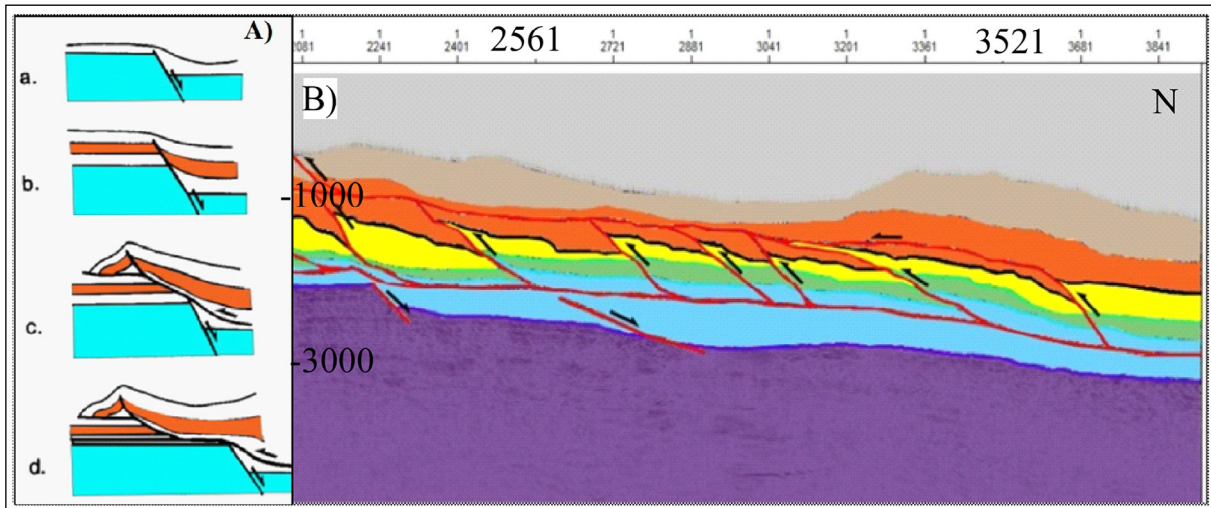


Figure 16- A) Schematic cross section showing the ramp geometry of the thrust faulting [Redrawn after Thomas (1982)]. B) One of the examples in the study area, K98-14 (between CDP numbers 14856-10856).

Acknowledgement

This study was carried out by interpreting the data collected by the R / V Seismic-1 research vessel of the MTA Marine Research Department and the data processed by the same department data processing team. We would like to thank to MTA Marine Research Department staff who contributed this study, especially fellow geophysicist Dr. Hakan Sarıtaş and B. Serkan Aydemir of the seismic data processing team, who processed this data set.

References

- Bag, S., Murthy, B. V. R. R. K., Anand, S. K. 2008. Seismic Attribute Analysis-A valuable tool for accurate Placement of Horizontal Drainhole: An Elucidation through a case study. 7th International Conference and Exposition on Petroleum Geophysics, 131-137
- Eyüboğlu, Y., Santosh, M., Bektaş, O., Ayhan, S. 2011. Arc magmatism as a window to plate kinematics and subduction polarity: Example from the eastern Pontides belt, NE Turkey. *Geoscience Frontiers*, 2(1), 49-56.
- Gomes, C. J. S., Ferreira, J. 2000. Geometry and kinematics of experimental antiformal stacks. *Anais da Academia Brasileira de Ciências*, 72(2), 195-217. doi:10.1590/S0001-37652000000200008
- Görür, N. 1988. Timing of opening of the Black Sea basin. *Tectonophysics* 147 (3e4), 247e262.
- Görür, N. 1997. Cretaceous syn- to postrift sedimentation on the southern continental margin of the Western Black Sea basin. In: Robinson, A. G. (Ed.), *Regional and petroleum geology of the Black Sea and surrounding region*. AAPG Memoir no. 68, 227-240.
- Görür, N., Tüysüz, O. 1997. Petroleum geology of southern continental margin of the Black Sea. In: A. Robinson (Ed.), *Regional and Petroleum geology of the Black Sea and Surrounding Region*. AAPG Memoir, 68, 241-254.
- Gwinn, V.E. 1970. Kinematic patterns and estimates of lateral shortening, Valley and Ridge and Great Valley Provinces, Central Appalachians, southcentral Pennsylvania, in Fisher, G. W., Pettijohn, F. J., Reed, J. C., Jr., and Weaver, K. N., eds., *Studies of Appalachian Geology: Central and southern*; New York, Interscience, p. 127-146.
- Hippolyte, J.C., Müller, C., Kaymakci, N., Sangu, E. 2010. Dating of the Black Sea Basin: new nannoplankton ages from its inverted margin in the Central Pontides (Turkey). *Geological Society, London, Special Publications*, 340, 113-36.
- Meijers, M.J.M., Kaymakci, N., van Hinsbergen, D.J.J., Langereis, C.G., Stephenson, R.A., Hippolyte, J. C. (2010), Late Cretaceous to Paleocene oroclinal bending in the central Pontides (Turkey), *Tectonics*, 29, TC4016, doi:10.1029/2009TC002620.
- Nabiev, A. 2007. Sedimentology and cyclostratigraphy of Turbeyani Marls and İnpiri Limestones: implications of possible source and reservoir rocks (NW Turkey). METU, M. Sc. Thesis.

- Nikishin, A.M., Ziegler, P.A., Abbott, D., Brunet, M. F., Cloetingh, S. 2002. Permo-Triassic intraplate magmatism and rifting in Eurasia: implications for mantle plumes and mantle dynamics. *Tectonophysics* 351, 3-39.
- Nikishin, A. M., Ziegler, P. A., Bolotov, S. N., Fokin, P. A. 2012. Late Paleozoic to Cenozoic evolution of the Black Sea-Southern Eastern Europe region: a view from the Russian platform. *Turkish J. Earth Sci.* 20, 571-634.
- Okay, A. I., Nikishin, A. M. 2015. Tectonic Evolution of the Southern Margin of Laurasia in the Black Sea Region. *International Geology Review* 57, 1051-1076.
- Okay, A. I., Şengör, A. M. C., Görür, N. 1994. Kinematic history of the opening of the Black Sea and its effect on the surrounding regions. *Geology* 22, 267-270.
- Robertson, A., Parlak, O., Ustaomer, T. 2012. Overview of the Palaeozoic-Neogene evolution of Neotethys in the Eastern Mediterranean region (southern Turkey, Cyprus, Syria) In : *Petroleum Geoscience* 18, 4, 381-404.
- Robinson, A., Giacomo S., Sierd C., John R. 1995. Stratigraphic evolution of the Black Sea: inferences from basin modelling. *Marine and Petroleum Geology* 12, 8.
- Schedl, A., Wiltschko, D. V. 1987. Possible effects of pre-existing basement topography on thrust fault ramping. *Journal of Structural Geology* 9, 1029-1037.
- Shillington, D.J., White, N., Minshull, T.A., Edwards, G. R.H., Jones, S. M., Edwards, R.A., Scott, C.L., 2008. Cenozoic evolution of the eastern Black Sea: a test of depth-dependent stretching models. *Earth Planet. Sci. Lett.* 265 (3e4), 360e378. <http://dx.doi.org/10.1016/j.epsl.2007.10.033>.
- Stephenson, R., Schellart, W. P. 2010. The Black Sea back-arc basin: insights to its origin from geodynamic models of modern analogues. In: Sosson, M., Kaymakci, N., Stephenson, R. A., Bergerat, F., Starostenko, V. (Eds.), *Sedimentary Basin Tectonics from the Black Sea and Caucasus to the Arabian Platform*, Geological Society, London, Special Publications, vol. 340. The Geological Society of London, 11-21.
- Sunal, G., Tüysüz, O. 2002. Palaeostress analysis of Tertiary postcollisional structures in the western Pontides, northern Turkey. *Geol. Mag.* 139, 343-359.
- Şengör, A.M.C., Yılmaz, Y. 1981. Tethyan evolution of Turkey: A plate tectonic approach. *Tectonophysics* 75, 3-4, 181-241.
- Thomas, W.A., 1974. Converging Clastic wedges in the Mississippian of Alabama. *Geologic Society of America Special paper*, 148, p. 187-207.
- Thomas, W.A. 1976. Evolution of Ouachita-Appalachian continental margin: *Journal of Geology* 84, 323-342.
- Thomas, W. A. 1982. Stratigraphy and structure of the Appalachian fold and thrust belt in Alabama, in Thomas, W. A., and Neathery, T. L., eds., *Appalachian Thrust Belt in Alabama: Tectonics and Sedimentation: 95th Annual Meeting Geological Society of America Guidebook for Field Trip 13*, 55-78.
- Tokay, M. 1954. Geology of the Bartın (Zonguldak) Region. *Bulletin of the Mineral Research and Exploration* 46 /47, 4663.
- Türkmen, O. 2017. Subsurface structural geology and tectonostratigraphy of the offshore Akçakoca-Amasra area, Western Black Sea Basin, Turkey, Unpublished M. S. Thesis, University of Alabama, Tuscaloosa, Alabama, 77.
- Tüysüz, O. 1999. Geology of the Cretaceous Sedimentary Basins of the Western Pontides. *Geological Journal* 34 (12), 75-93.
- Tüysüz, O., Yiğitbaş, E. 1994. The Karakaya Basin: A Palaeo-Tethyan marginal basin and its age of opening. *Acta Geol. Hungarica*, 37/3-4, 327-350.
- Tüysüz, O., Dellaloğlu, A. A., Terzioğlu, N. 1995. A magmatic belt within the Neo-Tethyan suture zone and its role in the tectonic evolution of Northern Turkey. *Tectonophysics* 243, 173-191.
- Vincent, S.J., Morton, A.C., Hyden, F., Fanning, M. (2013), Insights from petrography, mineralogy and U-Pb zircon geochronology into the provenance and reservoir potential of Cenozoic siliciclastic depositional systems supplying the northern margin of the Eastern Black Sea, *Mar. Pet. Geol.*, 45, 331-348, doi:10.1016/j.marpetgeo.2013.04.002
- Yiğitbaş E., Yılmaz Y., Şengör A. 1995. Transcurrent plate boundary along the Rhodop - Pontide fragment: Northwestern Turkey, *European Union of Geosciences Strasbourg, France*, 176-176.



Bulletin of the Mineral Research and Exploration

<http://bulletin.mta.gov.tr>



Systematics, biostratigraphy and paleoenvironmental investigation of early Ypresian *Alveolina* assemblages in the northern part of Isparta Angle (Keçiborlu, Isparta, SW Turkey)

Alper BOZKURT^{a*} and Muhittin GÖRMÜŞ^b

^aGeneral Directorate of Mineral Research and Exploration, Dept. of Geological Researches, Ankara, Turkey

^bAnkara University Faculty of Engineering, Department of Geological Engineering, Ankara, Turkey

Research Article

Keywords:

Alveolina, biostratigraphy, paleoenvironment, Eocene, Isparta.

ABSTRACT

Thanetian-early Ypresian (middle Ilerdian) limestones from the northern part of Isparta Angle (Keçiborlu, Isparta, SW Turkey) contain rich benthic foraminiferal assemblage. Ilerdian beds of the Büyükkırtepe formation are characterized by high diversity of the following *Alveolina* species: *Alveolina* (*Glomalveolina*) *karsica*, A. (G.) aff. *karsica*, A.(G.) *lepidula*, A.(G.) cf. *subtilis*, A. (*Alveolina*) *aragonensis*, A. (A.) *cemali*, A. (A.) *corbarica*, A. (A.) cf. *coudurensis*, A.(A.) *decipiens*, A.(A.) *dedolia*, A.(A.) *ellipsoidalis*, A.(A.) *erki*, A.(A.) *guidonis*, A.(A.) cf. *ilerdensis*, A.(A.) *montanarii*, A.(A.) *moussoulensis*, A.(A.) *pasticillata*, A.(A.) *pisella*, A.(A.) *rotundata kazancii*, A.(A.) *tremolina*, A.(A.) *varians*, and A.(A.) *vredenburgi*. In this study, 30 different *Alveolina* species including two new species and a new subspecies namely as A. (A.) *acari* n. sp., A. (A.) *ozbahcensis* n. sp., and A.(A.) *avsari fusunae* n. ssp. were identified for the first time. Besides, some probable new subspecies that were unnamed yet due to the insufficient number of individuals were also defined and proposed. Despite having close stratigraphic distributions with coeval assemblages described in different regions of Tethyan Province, *Alveolina* assemblages of the study area exhibit some stratigraphical range differences and present SBZ 3-SBZ 8 biozone intervals. The obtained data show that the study area was a lagoon to low energy shallow marine paleoenvironment with normal salinity in Thanetian – middle Ilerdian interval.

Received Date: 02.03.2020

Accepted Date: 17.05.2020

1. Introduction

Alveolinids are porcellaneous, planispirally coiled, involute larger benthic foraminifera, which frequently occur in the reef complexes and carbonates of restricted shelf environments throughout the Tethys (Hottinger, 1974). In the literature, it is seen that the highest species diversity of the alveolinid family, which range from Cretaceous to Recent, is in the genus *Alveolina* d'Orbigny. Numerous species of the genus *Alveolina* are index fossils representing of some

of the shallow benthic foraminiferal biozones (Serra-Kiel et al., 1998) in Paleogene throughout Tethys. Since the shallow benthic zones (SBZ) introduced by Serra-Kiel et al. (1998), the updated taxonomic and biostratigraphic data for alveolinids, occurring in these zones, have been presented by many researchers along the Tethyan Belt (White, 1992; Sirel, 2003; Özgen-Erdem et al., 2007; Vecchio et al., 2007; Sirel and Acar, 2008; Scheibner and Speijer, 2009; Drobne et al., 2011; Sirel et al., 2013; Fornaciari et al., 2019; Hadi et al., 2019; 2020).

Citation Info: Bozkurt, A., Görmüş, M. 2021. Systematics, biostratigraphy and paleoenvironmental investigation of early Ypresian *Alveolina* assemblages in the northern part of Isparta Angle (Keçiborlu, Isparta, SW Turkey). Bulletin of the Mineral Research and Exploration 164, 183-229.

<https://doi.org/10.19111/bulletinofmre.740944>

*Corresponding author: Alper BOZKURT, alper.bozkurt@mta.gov.tr

The study area is located in the Isparta Angle (Figure 1). This angle in the SW Turkey is one of the most significant regions in Turkey in terms of tectonic development and has been the subject to the regional and structural geology studies (Blumenthal, 1947; Gutnic et al., 1979; Koçyiğit, 1983; Poisson et al., 1984; Waldron, 1984; Yaçınkaya et al., 1986; Karaman, 1990; 1994; 2000; Görmüş and Özkul, 1995; Akıncı et al., 2003; Nemec et al., 2017). A chronological review of these studies has been given by Robertson et al. (2003) in detail. Paleontological

studies on the other hand are restricted by small number of thesis (e.g. Özkan, 1991; Köse-Yeşilot, 2000; Yüzgül, 2016) and articles (e.g. Sirel and Acar, 1982; Yıldız and Toker, 1991; Görmüş and Karaman, 1992; Görmüş and Nielsen, 2006; Sagular and Görmüş, 2006; Akkiraz et al., 2011; Bozkurt and Görmüş, 2019; Bozkurt et al., 2021). In the Isparta region where the study area is also located, there are no detailed studies on alveolinids especially regarding their biostratigraphy except for Sirel and Acar (1982), Bozkurt and Görmüş (2019) and Bozkurt et al. (2021).

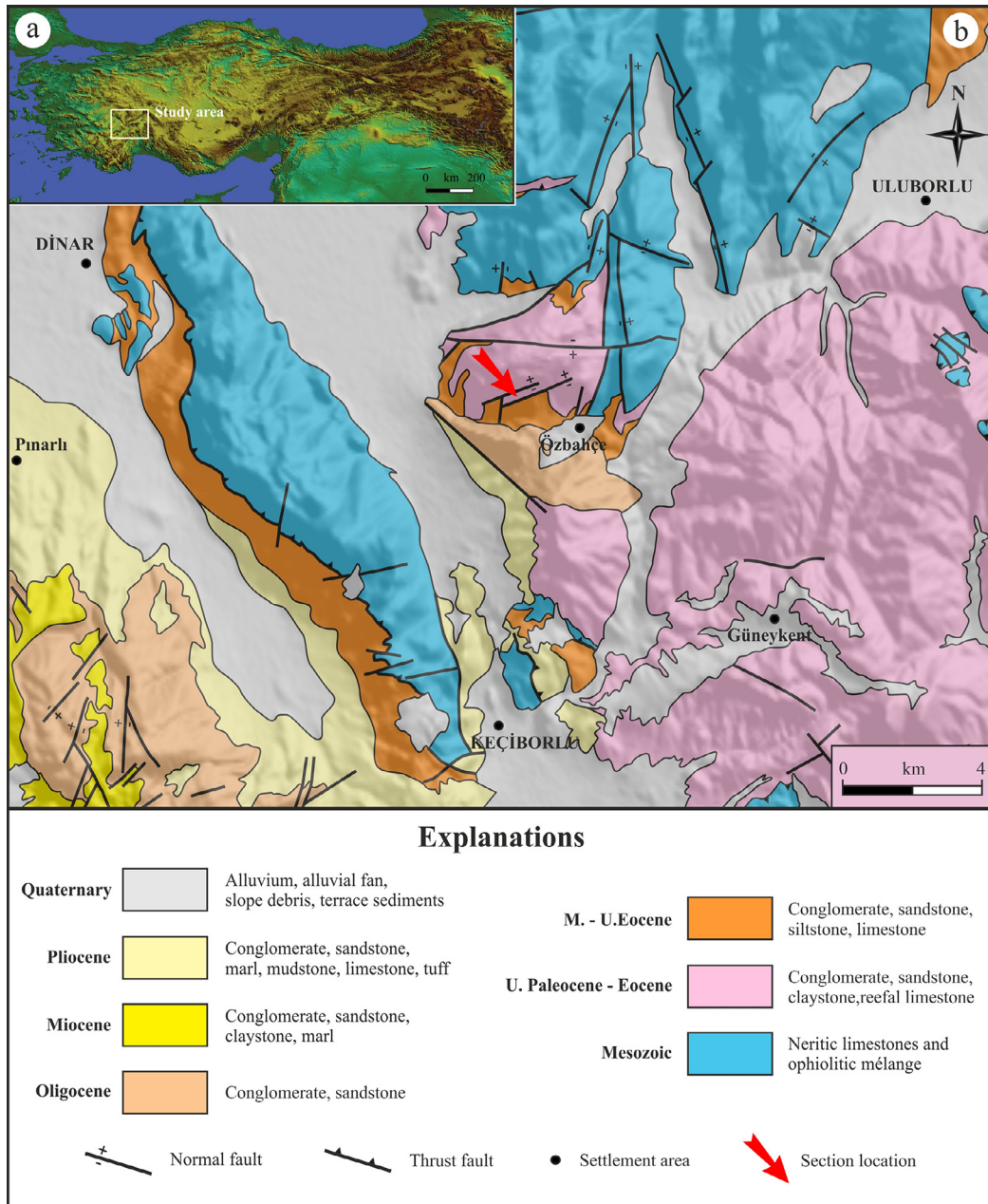


Figure 1- a) Location of study area on the 90 m resolution SRTM image of Turkey (Jarvis et al., 2008) and b) geological map (simplified from Balci, 2011 and Şenel, 1997).

In this study, alveolinid taxonomy and biostratigraphy of Thanetian-early Ypresian units outcropping in the north of the Özbahçe village (Keçiborlu, Isparta) on the 1/25.000 scale Afyon L24-c4 map sheet were studied. The determined assemblage was also compared with coeval assemblages described in different regions of the Tethyan Province. With the results obtained in this study, an abundant early Ypresian alveolinid assemblage was identified. New species and subspecies of the genus *Alveolina* were introduced from the assemblage of which systematic and biometric features were presented in detail. Considering the benthic foraminiferal assemblages of the study area and their characteristics, paleoenvironmental interpretations of the stratigraphic levels were discussed. In addition, the missing points in the paleogeographic development models of the region were tried to be enlightened with the obtained biostratigraphic data and the paleoenvironmental interpretations.

2. Material and Method

The studies were carried out in the Büyükkırtepe formation outcrops including rich alveolinids from the

north of Özbahçe village, north of Keçiborlu (Isparta) (Figure 1). It was difficult and impossible to get free alveolinid tests due to the formation lithology. The formation is composed of hard limestones. So all the oriented thin sections were prepared from hard rocks. Detailed descriptions of the preparation of oriented thin sections from hard rocks were given by Acar (2019a), and the similar methods were followed in this study. The ways to be followed in the preparation of thin sections of *Alveolina* species are presented in figure 2. In the preparation of the oriented thin sections, first of all, the hard rock sample taken from the field was cut along the number 1 and 2 horizontal and vertical planes in order to see the general orientation of the alveolinids in the rock (Figure 2a). Later, slabs were cut from the rocks sample in parallel with the surfaces where the axial and subaxial alveolinid sections were commonly observed as shown in the figure 2b, and individuals on the slabs were separated by cutting (individual locations are shown in figure 2b with red dashed lines). The chips containing clear and apparent individuals were selected for grinding. In cases where the coiling axis of the individual and the chip surface are parallel to the each other, the grinding process was made along the chip surface (Figure 2c). In the case

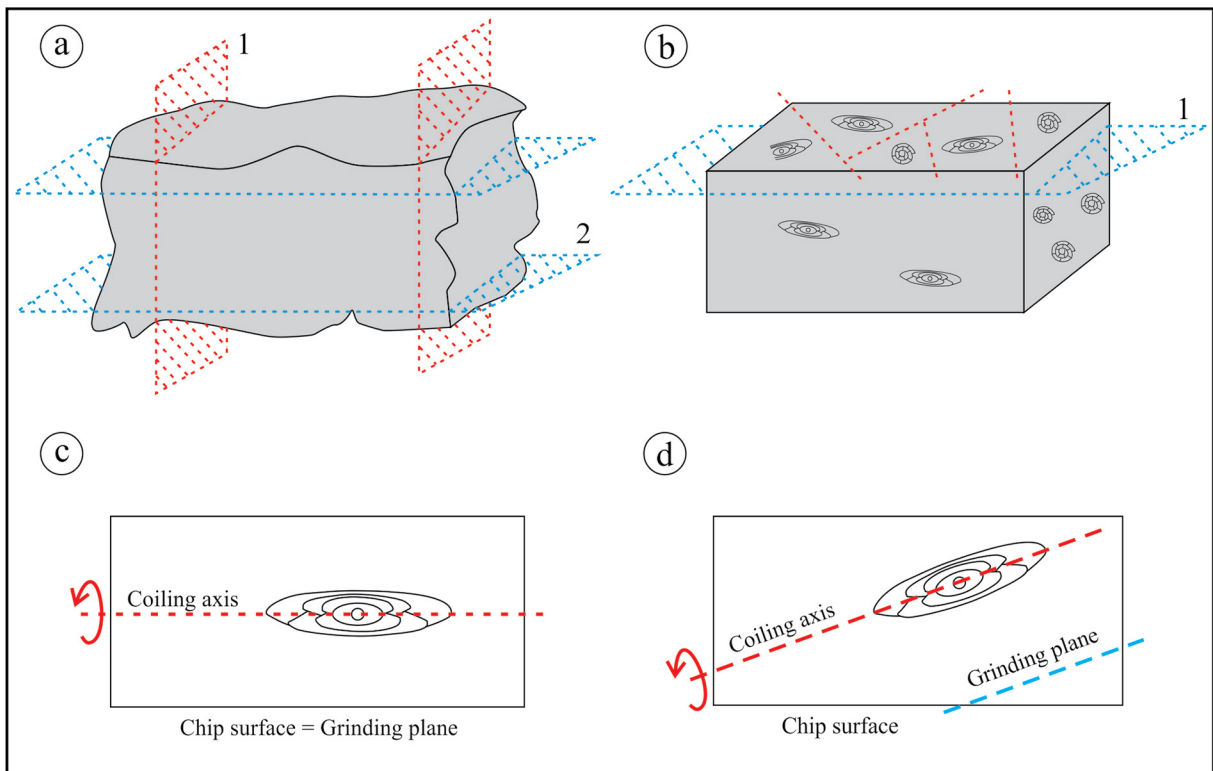


Figure 2- Schematic views showing the stages of oriented thin section preparation from the hard rock samples in the identification of *Alveolina* (see the text for process details, the figures are in hand sample size and not to scale).

of a certain angle being present between the coiling axis and chip surface, the grinding was performed by directing the chip to be parallel to the coiling axis (Figure 2d). The axial section plane obtained by completing the orientation was glued on the slide, the excess parts were grinded and thin section process was completed.

Total of 13 hard rock samples were taken from the Özbahçe measured stratigraphic section. Of these examples, a total of 232 thin sections, 201 of which were oriented, were prepared. Examinations of the foraminifers in thin sections were made under stereo microscope, and the microphotographs and biometric measurements were made in the laboratories of General Directorate of Mineral Research and Exploration (MTA) using the Leica MZ 16 A model research microscope in digital environment.

While preparing comparison graphics of biometric data for new species with other species, the values of the known species include only holotype and (if present) paratype data. The comparison graphics were prepared on the basis of number of whorls vs. index of elongation and the number of whorls vs. parameter C_n . The elongation index is the value, expressing a specific measure belonging to the test, obtained by dividing the axial diameter to the equatorial diameter in alveolinids (Hottinger, 1974; figure 3). White (1992) considered the greatest value of the axial thickening measured in the axial plane of alveolinid specimens as the Parameter C. From this point, the Parameter C_n was defined in this study in order to observe the changes of this parameter during all stages

of ontogeny and make comparison among the species, instead of regarding only the greatest value of the axial thickening. Here, the "n" refers to the order of the whorls after proloculus (Figure 3).

Thin sections used in this study are deposited in the General Directorate of Mineral Research and Exploration (MTA).

3. Stratigraphy

Pre-Cenozoic rocks outcropping in the study area and its close vicinity located in northern part of the Isparta Angle in the Taurus Belt are; the Mesozoic carbonates of the Lycian Nappes and of Anamas-Akseki Autochthonous, and the ophiolitic melange of the Marmaris Ophiolitic Nappe (Figure 1). Paleogene sediments overlying these basement rocks are widespread between Keçiborlu and Uluborlu, and they contain formations developed in different environments (Gutnic et al., 1979; Karaman et al., 1988; Görmüş and Özkul, 1995; Karaman, 2000; Nemeç et al., 2017). Upper Paleocene - Eocene sediments consist of calcarenites, neritic limestones and flyschoidal rock groups. This rock assemblage was called in different names in the literature, depending on their facies and lithological characteristics and on the basement rocks they cover, as Isparta Flysch (Gutnic et al., 1979), Koçtepe formation (Sarıöz, 1985), Kızılkırma formation (Karaman et al., 1988), Söbütepe formation (Yalçınkaya et al., 1986), Büyükkırtepe formation (Öztürk and Öztürk, 1989). The carbonate beds which are abundant in *Alveolina* in the study area and constitute the subject of this investigation, were

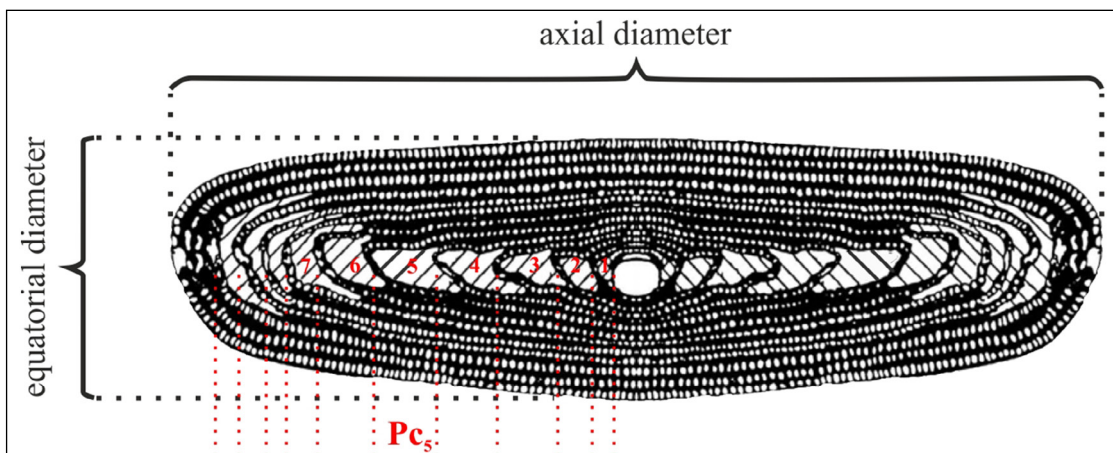


Figure 3- Illustration of axial and equatorial diameters used on determining the elongation index, and Parameter C_n (Pc_n is the axial thickening for the n^{th} whorl, where $n=5$) (modified from White, 1992).

named as the Büyükkırtepe formation (Öztürk and Öztürk, 1989) (Figure 4).

Büyükkırtepe formation was named after the Büyükkırtepe Hill, which is located in north of the Karabedir village at 15 kilometers north of the study area, in the study carried out by Öztürk and Öztürk (1989) around Balçıkhisar-Karadilli (Afyonkarahisar)-Dereköy (Isparta). The formation crops out in northern parts of the study area located on the southern slopes of Tekke Hill and the heights named as Tekke Hill and Çağıllımbaşı Hill in 1 / 25.000 scale L24-c4 sheet, including also the television transmitter (Figure 5). The formation, which begins with thick bedded and brecciated nummulitic limestones in the Büyükkır Hill (the type locality) at the bottom, continues with brecciated biosparites, passes into biomicrites in the upper levels and ends with clayey biomicrites (Öztürk and Öztürk, 1989). The unit, which is rarely observed as thin-bedded, consists of limestones with bedding thicknesses ranging generally from 20-30 cm to 1-2 m (Figure 4). Due to the fact that there is

a large amount of lichen on the limestone surface in some parts of the outcrops and their effect on the rock texture, they exhibit a massive, very thick-bedded appearance. It is generally in white or gray colored on weathered surfaces and light beige to white color on fresh surfaces. Thin to medium calcarenite interlayers containing abundant *Nummulites* fossils are yellowish gray in color. Limestones are occasionally saccaroid-textured and marble-like. Fault and joint systems are much developed and there are joint systems that cut the stratification in different directions (Figure 4). Pelagic deposits of the Büyükkırtepe formation, which are mostly represented by the platform carbonates, have been examined by some researchers as member (Öztürk and Öztürk, 1989: Kaklıktepe member). The Büyükkırtepe formation, which presents limited spread, has a thickness of 50-175 m (Öztürk and Öztürk, 1989).

Büyükkırtepe formation can be correlated with Tekke member of the Yukarıtırtar formation defined by Koçyiğit (1980) in north of the Hoyran Lake and

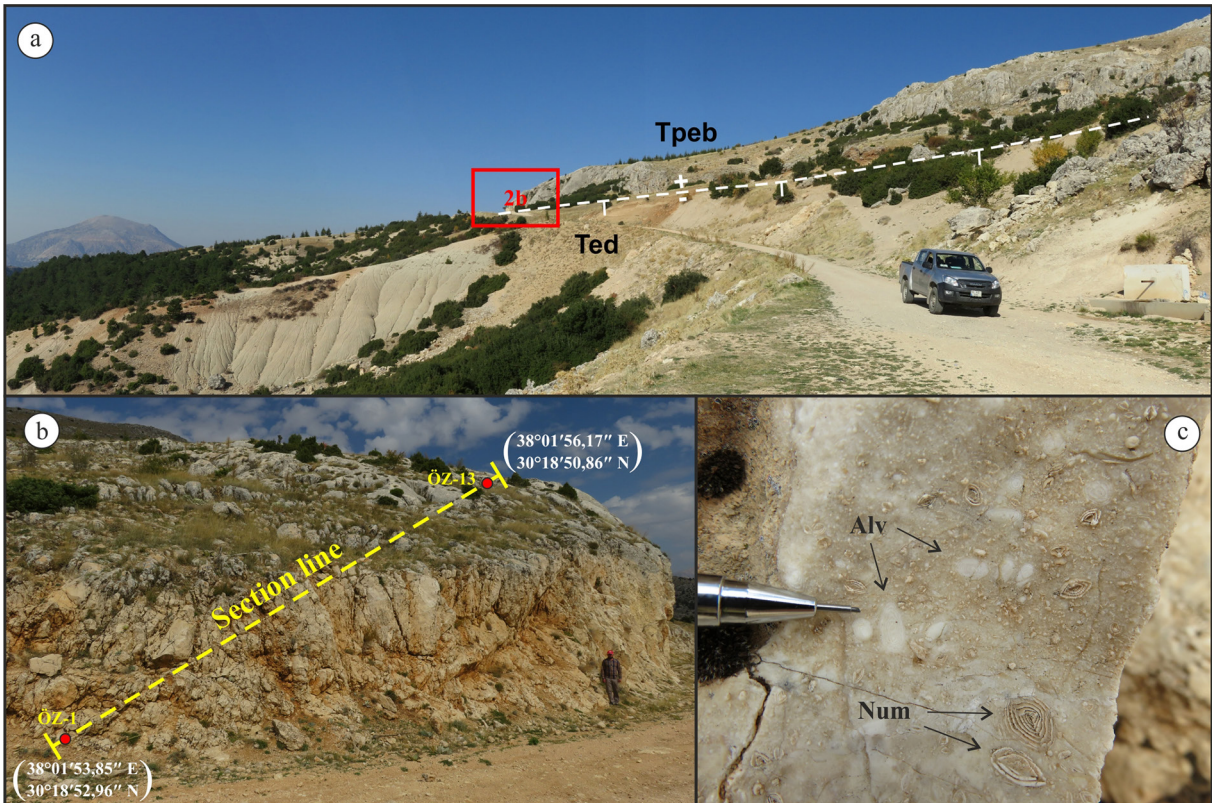


Figure 4- a) General view of the Büyükkırtepe formation (looking from SE to NW, Tpeb: Büyükkırtepe formation, Ted: middle-upper Eocene deposits). Outcrop of limestones in northwest of the Özbahçe village (Keçiborlu, Isparta), b) limestone outcrop from which the Özbahçe measured section was taken (looking from NW to SE) and c) their close up views (Alv: *Alveolina* sp., Num: *Nummulites* sp.).

neritic levels of the Kızılkırma formation defined by Karaman et al. (1988). Söbütepe formation, which was defined by Yalçinkaya et al. (1986) in a wide region including also the study area, is equivalent in age and lithology with the Büyükkırtepe formation. Büyükkırtepe formation can be assessed as the time-equivalent of basin interior deposits defined as the Koçtepe formation by Nemeç et al. (2017) (W. Nemeç, personal communication, 20th November 2019). The lithological and faunal characteristics of the unit indicate different environments ranging from lagoon to shelf environment.

Büyükkırtepe formation is laterally and vertically transitional with middle-upper Eocene flysch like sediments. These deposits of the Dereköy formation, which were defined by Koçyiğit (1980) from the Senirkent-Uluborlu region, have been revealed as being laterally and vertically transitional with upper Paleocene-Eocene deposits in the related literature (Koçyiğit, 1983; Öztürk and Öztürk, 1989; Görmüş and Özkul, 1995; Balcı, 2011). These deposits were named as the "Isparta Flysch" by Gutnic et al. (1979)

and as the "Kayıköy formation" by Karaman (1994, 2000) in Isparta region. The siliciclastics of the Dereköy formation, which is stratigraphically located above, moved downward with dip slip normal faults in the study area (Figure 5). It is seen that the faults are almost vertical.

The Oligocene consists of shelf deposits with molasse character including terrestrial intervals (Şenel, 1997). The Miocene, represented by shallow shelf deposits (Şenel, 1997) and the Pliocene, represented by lacustrine (Şenel, 1997) and fluvial (Öztürk and Öztürk, 1989), constitute the Neogene sediments in the vicinity of the study area. The youngest sediments in the region are Quaternary alluvium, alluvial fan, slope debris and terrace sediments.

4. Özbahçe Measured Stratigraphic Section

Özbahçe measured section was taken from approximately 2 km northwest of the Özbahçe village in 1/25000 scale Afyon L24-c4 sheet in north of Keçiborlu (Isparta) (Figure 1). The section was

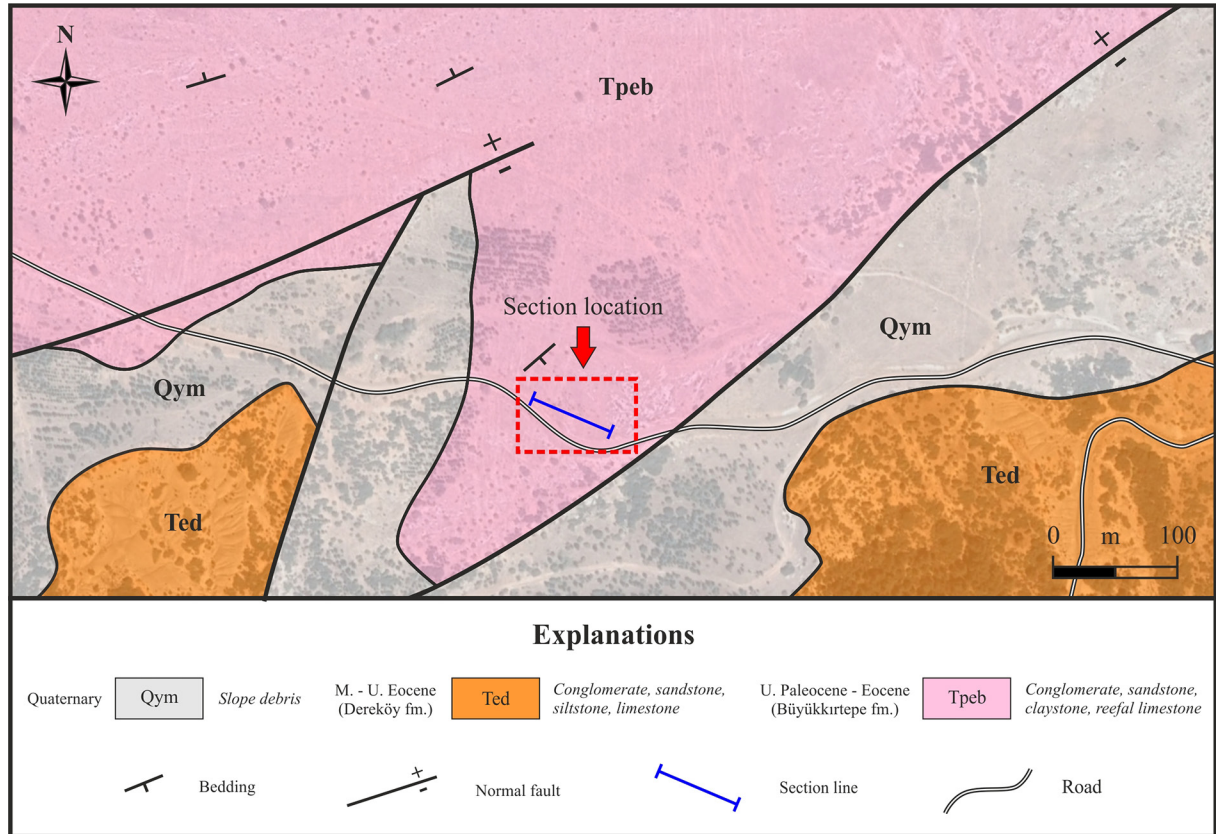


Figure 5- Geological map of the Özbahçe section and surroundings overlain on Google Earth image.

measured from 24.5 m thick part of the sequence between the coordinates of 38°01'53.85" E - 30°18'52.96" N and 38°01'56.17" E - 30°18'50.86" N, and the detailed studies were carried out on 13 limestone samples taken from the section.

It is observed that the Büyükkırtepe formation, which is frequently cut by normal faults, is also affected by reverse faults depending on tectonic development processes of the region. Likewise, the same stratigraphic levels were observed to be repeated within 24.5 m thickness in the section.

The foraminiferal assemblages of the sequence, which show a tectonostratigraphic structure in the study area, were evaluated by considering biostratigraphic principles. The distribution of foraminifers described throughout the section is given in figure 6. According to the evaluations made in this direction, the lower parts of the sequence (4.70 m) contain a foraminiferal assemblage of Thanetian age. Only one specimen of *Alveolina* (*Glomalveolina*) sp. was observed at this level, which is very poor in terms of *Alveolina* species. From these levels of the sequence, *Elazigina dienii*, *Idalina causae*, *I. sinjarica*, *Ranikothalia* sp., *Rotalia* sp., *Sistanites catali*, *S. cf. guvenci*, *S. iranicus*, *Sistanites* sp., *Socotraella?* sp. were also determined.

Lower Ilerdian levels, corresponding to a very low thickness (0.60 m) in the sequence, begin with the occurrence of *Alveolina* (*Alveolina*) *vredenburgi* and *A. (A.) varians*. Another species, *A. (G.) karsica*, which is another species representing early Ilerdian, appears for the first time at these levels. Besides, *A. (G.) aff. karsica*, *A. (G.) cf. subtilis*, *A. (A.) acari* n.sp., *A. (A.) cf. coudurensis*, *A. (A.) erki*, *A. (A.) moussoulensis*, *A. (A.) ozbahcensis* n.sp., *A. (A.) rugosa* ssp1 species were identified from these levels. This alveolinid assemblage is accompanied by such foraminifers as *Assilina* sp., *Discocyclina* sp., *Nummulites* sp., *Orbitolites* sp., *Ranikothalia* cf. *nuttalli*, *Ranikothalia* cf. *polatliensis*, *Rotalia* sp.

Middle Ilerdian, which represents the thickest part of the sequence (19,20 m), begins with the first appearance of *A. (A.) aragonensis*, *A. (A.) decipiens*, *A. (A.) dedolia*, *A. (A.) montanarii*. Apart from these, *A. (G.) karsica*, *A. (G.) lepidula*, *A. (A.) acari*, *A. (A.) avsari fusunaeae* n.ssp., *A. (A.) baldaccii* ssp1, *A. (A.) cemali*, *A. (A.) corbarica*, *A. (A.) cf. coudurensis*,

A. (A.) ellipsoidalis, *A. (A.) erki*, *A. (A.) guidonis*, *A. (A.) cf. ilterdenensis*, *A. (A.) montanarii* ssp1, *A. (A.) moussoulensis*, *A. (A.) muscatensis* ssp1, *A. (A.) ozbahcensis* n.sp., *A. (A.) pasticillata*, *A. (A.) pisella*, *A. (A.) rotundata kazancii*, *A. (A.) trempina*, *A. (A.) varians* were determined. This alveolinid assemblage is accompanied by foraminifers such as; *Assilina* sp., *Asterocyclina* sp., *Discocyclina* sp., *Elazigina* cf. *subsphaerica*, *Elazigina* sp., *Nummulites* sp., *Operculina* sp., *Opertorbitolites latimarginalis*, *Opertorbitolites* sp., *Orbitolites bellus*, *Orbitolites* cf. *complanatus*, *Orbitolites* cf. *megasphericus*, *Orbitolites* sp., *Ornatorotalia granum*, *Ranikothalia* cf. *nuttalli*, *Ranikothalia* sp., *Rotalia* sp., *Slovenites?* sp., *Sphaerogypsina* sp., gypsinid and stomatorbinid forms. *A. (A.) corbarica* and *A. (A.) trempina* species to appear as together in a sample taken from a section of 1,00 m corresponding to the top parts of the sequence, indicates that this level could probably be in the middle Ilerdian-upper Ilerdian transition.

5. Taxonomy of Alveolinids

In this section, the taxonomic criteria given by Hottinger (1960), Loeblich and Tappan (1987), Boudagher-Fadel (2008, 2018), Acar (2019b), Roskov et al. (2019) have been used. Taxa are presented in the alphabetical order. The ranges of species are given together with their corresponding shallow benthic zones (SBZ: Serra-Kiel et al., 1998). In this study, SBZ 3 and 4 zones, SBZ 5 and 6 zones, and SBZ 7 and 8 zones are presented by being merged due to coexistence of some index taxa representing these zones. The faunal assemblage accompanying each species is given in figure 6.

Phylum: Foraminifera D'ORBIGNY, 1826

Class: Tubothalamea PAWLOWSKI, HOLZMANN and TYSZKA, 2013

Order: Miliolida DELAGE AND HÉROUARD, 1896

Suborder: Miliolina DELAGE AND HÉROUARD, 1896

Superfamily: Alveolinoidea EHRENBERG, 1839

Family: Alveolinidae EHRENBERG, 1839

Genus: *Alveolina* D'ORBIGNY, 1826

Subgenus: (*Alveolina*) *Glomalveolina* HOTTINGER, 1960

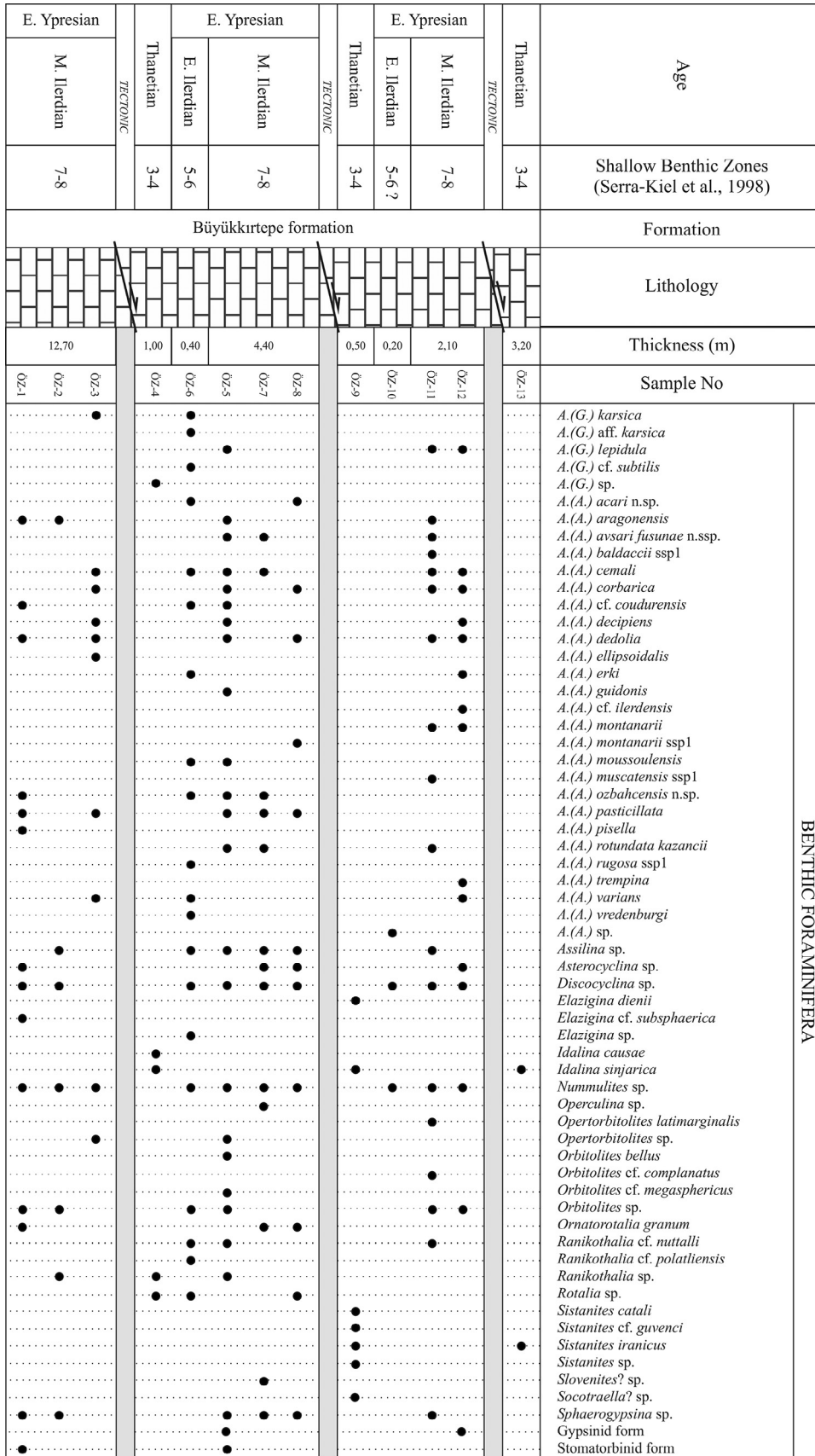


Figure 6- Foraminiferal distributions of the Özbahçe section.

Type species: *Alveolina dachelensis* SCHWAGER, 1883

***Alveolina (Glomalveolina) karsica* SİREL, 1998**

(Plate I, figure 4)

1998 *Alveolina (Glomalveolina) karsica* SİREL, pl.30, figs. 7-8; pl. 31, figs. 6, 7, 11.

2007 *Glomalveolina karsica* SİREL. ÖZGEN-ERDEM et al., p. 916, figs. 5b-c.

2008 *Glomalveolina karsica* (SİREL). SİREL and ACAR, pl.2, figs. 5-6, 8-9.

2008 *Glomalveolina karsica* SİREL. ÖZGEN-ERDEM, pl.I, fig. 8.

2019 *Alveolina (Glomalveolina) karsica* SİREL. BOZKURT and GÖRMÜŞ, pl.1, fig.5.

Material: 2 specimens representing the species were determined throughout the section (ÖZ-3, ÖZ-6).

Description: Test is small and subspherical. The axial and equatorial diameters are in the range of 0.54 - 0.67 mm and 0.44 - 0.61 mm, respectively. It has an elongation index of 1.10 - 1.23 and the proloculus is very small (0.02 mm). In two streptospiral cycles following the proloculus, there are undivided chambers in accordance with the characteristic feature of the subgenus *Glomalveolina*. In the following whorls, chambers are divided and consist of many spherical - subspherical chamberlets. Thickness of the basal layer and the chamber height increase gradually towards the outer whorls.

Range: *A. (G.) karsica* was found in the early - middle Ilerdian (SBZ 5-8) levels of the Özbahçe section. Sirel (1998) described this species in the Ilerdian of Kars region, and Özgen-Erdem et al. (2007) described it in the early Ilerdian of Eskişehir region. In addition, Özgen-Erdem (2008) described the same species in the middle Ilerdian of Kastamonu region.

***Alveolina (Glomalveolina) aff. karsica* SİREL, 1998**

(Plate I, figure 2)

1998 *Alveolina (Glomalveolina) aff. karsica* SİREL, pl.31, figs. 9, 10, 12.

2008 *Glomalveolina aff. karsica* (SİREL). SİREL and ACAR, pl.2, figs. 10-12.

Material: 1 specimen representing the species was identified throughout the section (ÖZ-6).

Description: In the obtained specimen, test is small and nautiloid. The axial and equatorial diameters are 0.76 mm and 0.86 mm, respectively. It has an elongation index of 0.88. It has 3-4 streptospiral cycles following the very small proloculus. In the following whorls, the coarse chamberlets are observed. The heights of spherical to subspherical chamberlets rapidly increase towards outer whorls. They are elongated in the outer whorls. The chamberlet height in the 6th whorl following the streptospiral cycles, reaches approximately twice the size of the first divided chamber.

Remarks: The specimen presents similar biometric and morphological features with *A. (G.) aff. karsica* described by Sirel (1998) and Sirel and Acar (2008), and it is distinguished from *A. (G.) karsica* by its large size, nautiloid shape, and the size and shape of the chamberlets.

Range: *A. (G.) aff. karsica* was found in the early Ilerdian (SBZ 5-6) levels of the Özbahçe section. This species was found at the same stratigraphic levels in Kars region (Sirel, 1998; Sirel and Acar, 2008).

***Alveolina (Glomalveolina) lepidula* (SCHWAGER), 1883**

(Plate I, figure 5)

1883 *Alveolina ellipsoidalis* SCHWAGER var. *lepidula* SCHWAGER, p.98, pl.25, figs. 3a-g.

1960 *Alveolina (Glomalveolina) lepidula* (SCHWAGER). HOTTINGER, pl.1, fig. 27.

2007 *Glomalveolina lepidula* (SCHWAGER). ÖZGEN-ERDEM et al., p. 916, fig. 5a.

2008 *Glomalveolina lepidula* SCHWAGER. ÖZGEN-ERDEM, pl.I, fig. 7.

2009 *Glomalveolina pilula / lepidula* SCHWAGER. SCHEIBNER AND SPEIJER, p. 210, fig. 11f.

2019 *Alveolina (Glomalveolina) lepidula* (SCHWAGER). BOZKURT and GÖRMÜŞ, pl.1, fig. 4.

Material: 4 specimens representing the species were identified throughout the section (ÖZ-5, ÖZ-11, ÖZ-12).

Description: Test is small and varies from spherical to oval. In oval forms, the poles are rounded. The axial and equatorial diameters are in the range of 1.00 - 1.32 mm and 0.75 - 1.24 mm, respectively. It has an elongation index of 1.06 - 1.33. The proloculus is very small (the largest diameter is 0.05mm). It has 3 streptospiral cycles following the proloculus. 4-5 whorls following those cycles constitute the adult stage. In this stage, cross-sections of the chamberlets are circular or tooth-shaped and their heights increase towards the outer whorls. Significant thickening in basal layer and loose coiling are observed in the last 2 or 3 whorls that constitute the senile stage. While the heights of the chamberlets increase further, their cross-sections change from circular to rectangular.

Range: *A. (G.) lepidula* was found in the middle Ilerdian (SBZ 7-8) levels of the Özbahçe section. The stratigraphic distribution of this species corresponds to the distribution given by Serra-Kiel et al. (1998). In addition, the presence of this species in the early - middle Cuisian (late Ypresian) in Niğde region was reported by Sirel and Acar (2008).

***Alveolina (Glomalveolina) cf. subtilis*
HOTTINGER, 1960**

(Plate I, figure 3)

Material: 1 specimen representing the species was identified throughout the section (ÖZ-6).

Description: Test is small, oval with pointed poles. Towards the ultimate whorls, this acuteness decreases. The axial and equatorial diameters are 1.06 mm and 0.68 mm, respectively. It has an elongation index of 1.56. Although the proloculus does not seem very clear in the only specimen obtained, it is probably very small. There are at least 2 or 3 streptospiral cycles after the proloculus. In the following 8 whorls, the heights of chamberlets progressively increase towards the outer whorls. Cross-section of chamberlets are circular throughout the ontogeny. Thickening of the basal layer in the axial direction is more than it is in the equatorial direction and increases gradually.

Remarks: The fact that this specimen, whose proloculus cannot be clearly observed, belongs to the microspheric generation, makes it much smaller in size than *A. (G.) subtilis* of which its holotype is megalospheric. This species, which is smaller in size

than *A. (G.) subtilis* in the present case, is considered different because of its smaller size than *A. (G.) subtilis*, was first described by Hottinger (1960).

Range: *A. (G.) cf. subtilis* was found in the early Ilerdian (SBZ 5-6) levels of the Özbahçe section. The stratigraphic distribution of this species is similar to the distribution given by Hottinger (1960) for *A. (G.) subtilis*.

Alveolina (Glomalveolina) sp.

(Plate I, figure 1)

Material: 1 specimen representing the species was identified throughout the section (ÖZ-4).

Description: Test is small, slightly nautiloid. For the single specimen obtained, the axial and equatorial diameters are 0.84 mm and 0.88 mm, respectively. The elongation index is 0.95. It is remarkable that the specimen whose juvenile stage cannot be seen clearly, has coarse chamberlets in 3-4 whorls of the adult stage. The basal layer is thick in the equatorial direction. The chamberlets are slightly depressed and subspherical.

Remarks: The biometric and morphological features observed in the single specimen obtained indicate that this species may belong to *A. (G.) primaeva* group (Hottinger, 1974). The foraminiferal assemblage that accompanies the specimen also supports this possibility.

Range: *A. (G.) sp.* was found in the Thanetian (SBZ 3-4) levels of the Özbahçe section.

Subgenus: *Alveolina* D'ORBIGNY, 1826

Type species: *Oryzaria bosicii* DEFRANCE in BRONN, 1825

Alveolina (Alveolina) acari n.sp.

(Plate II, figures 1-5)

Derivation of name: This species is dedicated to Dr. Şükrü Acar (MTA) who has made important contributions to the subject of Cenozoic benthic foraminifers, particularly the alveolinids.

Material: 8 specimens representing the species were identified throughout the section (ÖZ-6, ÖZ-8).

Holotype: Axial section of megalospheric specimen, illustrated by plate II, figure 1.

Type locality: Limestones outcropping approximately in 2 km NW of Özbahçe village, north of Keçiborlu (Isparta) (between the coordinates of 38°01'53,85" E - 30°18'52,96" N and 38°01'56,17" E - 30°18'50,86" N).

Type level: Büyükkırtepe formation, early - middle Ilerdian (SBZ 5-8). The section between 13,70 m and 18,50 m of the Özbahçe measured section.

Diagnosis: Small to medium megalospheric test is elongated and oval. The poles are rounded. In megalospheric specimens, the axial and equatorial diameters are in the range of 3.72 - 6.84 mm, and 1.58 - 3.64 mm, respectively. Total of 14 whorls of coiling is observed in a specimen with the axial diameter reaching 6,84 mm. The elongation index is between 1.76 and 2.35. The spherical proloculus is large and has a diameter of 0.24 to 0.38 mm. Following the proloculus, it has 2 or 3 tightly coiled whorls of juvenile stage. This is followed by 3 to 5 whorls, which suddenly thicken in the axial direction but not in the equatorial direction. No axial thickening is observed in the senile stage. In juvenile and adult stages, the chamberlets with circular cross-sections become rectangular and larger in the senile stage. In the first two stages, the chamberlet heights increase regularly. Thickness of the basal layer does not exceed half of the chamber height during ontogeny (except for one specimen). Microspheric specimens could not be obtained.

Differential diagnosis: This new species differs from the coeval *Alveolina* species by their size and type of coiling. The new species, showing similarities with *A. (A.) haymanaensis* in terms of Parameter C and morphology, is distinguished by its smaller size, higher elongation index and smaller proloculus (Figures 7a, d). It differs in that there is no thickening of basal layer in the equatorial direction and it is found in lower stratigraphic levels. It differs from *A. (A.) sakaryaensis* with its higher elongation index, smaller proloculus and that there is no thickening in the basal layer in the equatorial direction (Figure 7b). It is also different from the latter in terms of the course of Parameter C in juvenile and adult stages (Figure 7e). The new species, having similarities with *A. (A.)*

tumida in terms of the course of elongation indices throughout the ontogeny (Figure 7c), is different with the fact that it reaches the same whorl number in a larger test and has a larger proloculus. The axial thickening in *A. (A.) tumida* increases gradually until senile age and never reaches the exaggerated dimensions and remains constant in the last whorls (Figure 7f). The new species differs from *A. (A.) tumida* with its axial thickening progressing differently at different stages of ontogeny (Figure 7f).

Range: The new *A. (A.) acari* was found in the early - middle Ilerdian (SBZ 5-8) levels of the Özbahçe section.

***Alveolina (Alveolina) aragonensis* HOTTINGER, 1960**

(Plate I, figure 8)

- 1960 *Alveolina aragonensis* HOTTINGER, pl.6, figs. 5-8.
- 1978 *Fasciolites (Fasciolites) fornasinii* (CHECCHIA-RISPOLI). GAEMERS, pl.4, fig. 5.
- 2005 *Alveolina aragonensis* HOTTINGER. ÖZGEN-ERDEM et al., p. 413, fig. 10g.
- 2007 *Alveolina aragonensis* HOTTINGER. ÖZGEN-ERDEM et al., p. 917, fig. 6e.
- 2008 *Alveolina aragonensis* HOTTINGER. ÖZGEN-ERDEM, pl.II, fig. 2.
- 2008 *Alveolina aragonensis* HOTTINGER. SİREL and ACAR, pl.25, figs. 1-4.
- 2011 *Alveolina aragonensis* HOTTINGER. DROBNE et al., p.747, pl.1.

Material: 4 specimens representing the species were identified throughout the section (ÖZ-1, ÖZ-2, ÖZ-5, ÖZ-11).

Description: Small sized megalospheric test ranges from subspherical to oval. It is slightly depressed at the poles. In megalospheric specimens, the axial and equatorial diameters are in the range of 2.32 - 4.58 mm and 1.50 - 2.83 mm, respectively. The elongation index ranges from 1.20 to 1.62 and the diameter of the proloculus is in the range of 0.34 - 0.46 mm. The first 2 or 3 whorls following the proloculus are slightly tightly coiled. The next 3-4 whorls are loosely coiled,

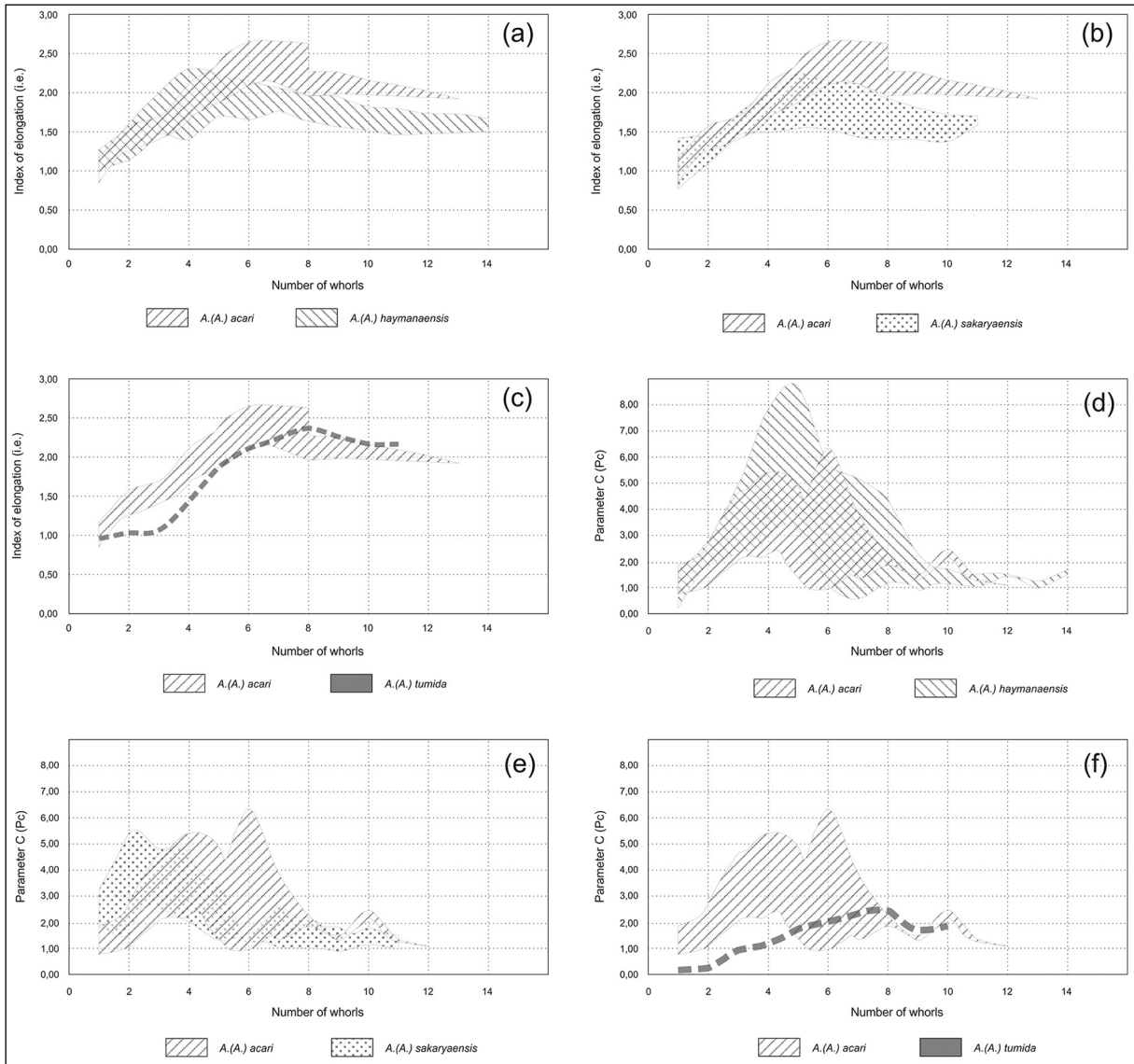


Figure 7- Number of whorls vs. elongation index comparison plots of *A. (A.) acari* n.sp. with a) *A. (A.) haymanaensis*, b) *A. (A.) sakaryaensis* and c) *A. (A.) tumida*; and the number of whorls vs Parameter C comparison plots of *A. (A.) acari* with d) *A. (A.) haymanaensis*, e) *A. (A.) sakaryaensis* f) *A. (A.) tumida*.

and the following 3-5 whorls become tightly coiled again. While the cross-sections of chamberlets change from circular to rectangular from inner to outer whorls, their heights also increase in the same direction. Microspheric specimens could not be obtained.

Range: *A. (A.) aragonensis* was found in the middle Ilerdian (SBZ 7-8) levels of the Özbahçe section corresponding to the distribution given by Hottinger (1960) and Serra-Kiel et al. (1998). On the other hand, Özgen-Erdem et al. (2007) reported that the distribution of this species in the Eskişehir region was from middle Ilerdian to late Ilerdian (SBZ 7-9).

***Alveolina (Alveolina) avsari* SİREL and ACAR
fusunae n.ssp.**

(Plate III, figures 6-7)

Derivation of name: This species is dedicated to valuable scientist Prof. Dr. Füsün Alkaya (Selçuk University) who contributed to the geology of Turkey with her studies on ammonites and the geologists she educated.

Material: 3 specimens representing the species were identified throughout the section (ÖZ-5, ÖZ-7, ÖZ-11).

Holotype: Axial section of megalospheric specimen illustrated by plate III, figure 6.

Type locality: Limestones outcropping approximately at 2 km northwest of the Özbahçe village, north of Keçiborlu (Isparta) (between the coordinates of 38°01'53,85" E - 30°18'52,96" N and 38°01'56,17" E - 30°18'50,86" N).

Type level: Büyükkırtepe formation, middle Ilerdian (SBZ 7-8). The sections of the Özbahçe measured section between 14,10 m and 18,50 m and between 19,20 m and 21,30 m.

Diagnosis: Small to medium sized megalospheric test is subspherical. In megalospheric specimens, the axial and equatorial diameters were measured as 2.58 - 3.44 mm, 2.25 - 2.96 mm, respectively. The elongation index is between 1.15 - 1.24 and the proloculus has a large diameter between 0.22 - 0.52 mm. There is no distinct juvenile stage following the proloculus. During 2 whorls after the first 2 whorls, weak flosculinization develops. Thickening of basal layer in the axial direction is more than that it is in the equatorial direction. Depending on this, the test is slightly elongated. Flosculinization is not observed during the next 3-5 whorls. The chamberlets are slightly depressed at the beginning. The chamberlets with circular cross-sections in the flosculinized stage are elongated in the last whorls and have a rectangular shape. Microspheric specimens could not be obtained.

Differential diagnosis: The new subspecies differ from *A. (A.) avsari* with its coarser inner structure and larger proloculus. While 9 whorls are observed in the test of *A. (A.) avsari* that has an axial diameter of 2,65 mm, the new subspecies have only 6 whorls at the same axial diameter. *A. (A.) avsari* never shows axial thickening throughout ontogeny, yet the new subspecies typically has axial thickening in 2 whorls following the juvenile stage.

Range: *A. (A.) avsari fusunae* n.ssp. was found in the middle Ilerdian (SBZ 7-8) levels of the Özbahçe section.

***Alveolina (Alveolina) baldaccii* CHECCHIA and RISPOLI ssp1**

(Plate I, figure 9)

Material: 1 specimen representing the species was identified throughout the section (ÖZ-11).

Diagnosis: Megalospheric test is small, subspherical to slightly oval. The axial and equatorial diameters of the single megalospheric specimen are 3.54 mm and 2.96 mm, respectively. The elongation index is 1.20. The diameter of the proloculus is 0.14 mm. The next 5 whorls after the flexostyle following the proloculus are tightly coiled. During these whorls that constitute the juvenile stage, the test is developed in oval shape. Following this, weak flosculinization is observed during 2-3 whorls. At this stage, the thickness of the basal layer reaches approximately 3 times of the height of the chamberlet. The next 8-9 whorls are loosely coiled and in this stage thickness of the basal layer and the chamberlet heights are almost. In juvenile stage, the spherical chamberlets are very small. While sizes of the chamberlets increase regularly in advanced stages of ontogeny, their cross-sections are rectangular in the senile stage.

Differential diagnosis: This potential new subspecies is distinguished from *A. (A.) baldaccii* with its weaker flosculinization, smaller chamberlets in the senile stage and accordingly, having more number of whorls in the same sized test.

Remarks: Acar (1995) described *A. (A.) dageri* as a new species, as he was probably not aware of existence of species *A. (A.) baldaccii*. Sirel and Acar (2008) acknowledged the same specimens as a subspecies of *A. (A.) blumenthali* considering their anatomical similarities. As *A. (A.) dageri* ACAR and *A. (A.) blumenthali dageri* SİREL and ACAR are anatomically and biometrically the same, they are junior synonyms of *A. (A.) baldaccii* and are invalid according to the rules of International Commission on Zoological Nomenclature (ICZN). Our specimen, which is most probably a new subspecies, is left to be named in future studies due to the insufficient number of individuals.

Range: *A. (A.) baldaccii* ssp1 was found in the middle Ilerdian (SBZ 7-8) levels of the Özbahçe section.

***Alveolina (Alveolina) cemali* SİREL and ACAR, 2008**

(Plate I figures 6-7)

1978 *Fasciolites (Fasciolites) fornasinii* (CHECCHIA-RISPOLI). GAEMERS, pl.4, fig. 6.

1995 *Alveolina (Alveolina) aff. pisella* DROBNE, n.sp., ACAR, pl.22, fig. 6.

2008 *Alveolina cemali* SİREL and ACAR, pl.20, figs. 1-8.

Material: 8 specimens representing the species were identified throughout the section (ÖZ-3, ÖZ-5, ÖZ-6, ÖZ-7, ÖZ-11, ÖZ-12).

Description: Test is small and spherical to subspherical. In megalospheric specimens, the axial and equatorial diameters were measured as 1.62 - 3.32 mm and 1.28 - 2.90 mm, respectively. It has an elongation index of 1.04 - 1.41. The diameter of the proloculus is in the range of 0.16 - 0.32 mm. 2 or 3 whorls following the proloculus form a slightly tightly coiled juvenile stage. While the dimensions of spherical chamberlets increase regularly towards the outer whorls, their shapes change from spherical to rectangular. In microspheric specimens, the axial and equatorial diameters are between 4.40 - 4.74 mm and 4.02 - 4.06 mm, respectively. It has an elongation index of 1.09 - 1.17. All other features are similar to megalospheric specimens and reflect the characteristics of the species.

Range: *A. (A.) cemali* was found in the early - middle Ilerdian (SBZ 5-8) levels of the Özbahçe section. The stratigraphic distribution of this species is given as the upper part of the early Ilerdian and the lower parts of the middle Ilerdian (SBZ 6-7) by Sirel and Acar (2008).

***Alveolina (Alveolina) corbarica* HOTTINGER, 1960**

(Plate IV, figures 4-5)

1960 *Alveolina corbarica* HOTTINGER, pl.2, figs. 20-24.

1995 *Alveolina (Alveolina) corbarica* HOTTINGER. ACAR, pl.18, figs. 1-4.

2005 *Alveolina corbarica* HOTTINGER. ÖZGEN-ERDEM et al., p. 413, fig. 10h.

2008 *Alveolina corbarica* HOTTINGER. ÖZGEN-ERDEM, pl.I, fig. 11.

2008 *Alveolina corbarica* HOTTINGER. SİREL and ACAR, pl.38, figs. 1-7.

Material: 5 specimens representing the species were identified throughout the section (ÖZ-3, ÖZ-5, ÖZ-8, ÖZ-11, ÖZ-12).

Description: Elongated, slightly fusiform shaped megalospheric test is small. In megalospheric specimens, the axial and equatorial diameters are in the range of 2.72 - 4.48 mm and 0.98 - 1.50 mm, respectively. It has an elongation index of 2.23 - 3.02 and the diameter of the proloculus is in the range of 0.36 - 0.38 mm. Its growth stages are indistinctly delimited. After the subspherical first whorl following the proloculus, a regular axial thickening develops. However, thickening in basal layer is not observed in the equatorial direction. The chamber connections at the poles may be truncated or slightly rounded. Chamberlets have circular cross-sections throughout ontogeny, and their sizes slightly increase from inner to outer whorls. Microspheric specimens could not be obtained.

Range: *A. (A.) corbarica* was found in the middle Ilerdian (SBZ 7-8) levels of the Özbahçe section. The range of species, which was given as the upper part of middle Ilerdian (SBZ 8) by Hottinger (1960) and Serra-Kiel et al. (1998), was found in the middle Ilerdian (SBZ 7-8) by Sirel and Acar (2008) in Ankara and Kayseri regions. This species was recorded in Tibet from SBZ 8 (BouDagher-Fadel et al, 2015).

***Alveolina (Alveolina) cf. coudurensis* HOTTINGER, 1960**

(Plate IV, figure 7)

Material: 3 specimens representing the species were identified throughout the section (ÖZ-1, ÖZ-5, ÖZ-6).

Description: Megalospheric test is elongated, subcylindrical and small sized. In megalospheric specimens, the axial and equatorial diameters are in the range of 2.30 - 4.32 mm and 0.76 - 1.24 mm, respectively. It has an elongation index of 2.72 - 3.48. In descriptions made on the subaxial sections of the megalospheric specimens, the boundaries of the proloculus could not be seen clearly. It is observed that the species, which do not have any tightly coiled juvenile stage after the proloculus, rapidly thickens in axial and equatorial directions. The thickening in axial direction is twice that it is in the equatorial direction. The chamber connections at the poles are rounded or truncated. Spherical chamberlets are depressed in stages where thickening in basal layer is present, and their size increase slightly from inner to outer whorls. Microspheric specimens could not be obtained.

Remarks: This species, which is similar to *A. (A.) coudurensis* in terms of coiling type and general morphology defined by Hottinger (1960), offers much smaller equatorial diameters in the same number of whorls though it reaches the similar axial diameter. Therefore, it has a higher elongation index compared to *A. (A.) coudurensis*. In addition, *A. (A.) coudurensis* occurs in younger levels than this species does in terms of the stratigraphic distribution (Hottinger, 1960).

Range: *A. (A.) cf. coudurensis* was found in the early - middle Ilerdian (SBZ 5-8) levels of the Özbahçe section. The stratigraphic distribution of *A. (A.) coudurensis* was given as late Ilerdian - early Cuisian by Hottinger (1960).

***Alveolina (Alveolina) decipiens* SCHWAGER, 1883**

(Plate I, figure 10)

1883 *Alveolina decipiens* SCHWAGER, p.98, pl.26 (3), fig. 1.

1960 *Alveolina decipiens* SCHWAGER. HOTTINGER, pl.8, figs. 1-4, 6, 8.

1977 *Alveolina (Alveolina) decipiens* SCHWAGER. DROBNE, p.35, text-fig. 17; pl.5, fig. 20.

1995 *Alveolina (Alveolina) decipiens* SCHWAGER. ACAR, pl.16, fig. 3.

2007 *Alveolina decipiens* SCHWAGER. ÖZGEN-ERDEM et al., p. 916, fig. 5a.

Material: 3 specimens representing the species were identified throughout the section (ÖZ-3, ÖZ-5, ÖZ-12).

Description: Megalospheric test is subcylindrical and small sized. The largest axial and equatorial diameters measured in megalospheric specimens are 2.84 mm and 1.46 mm, respectively. The elongation index is 1.95 and the diameter of the spherical proloculus is 0,20 mm. The species, having indistinctly delimited growth stages, 1 or 2 chambers following the proloculus are relatively tightly coiled. In the following chambers, thickening in basal layer develops in both axial and equatorial directions. The axial thickening is more than it is in the equatorial direction. At the poles, the chamber connections can occasionally be seen as depressed. The cross-sections of chamberlets are circular and could occasionally be seen as slightly flattened in the flosculinized stage.

Their dimensions gradually increase. Microspheric specimens could not be obtained.

Range: *A. (A.) decipiens* were found in the middle Ilerdian (SBZ 7-8) levels of the Özbahçe section corresponding to the distributions given by Hottinger (1960) and Serra-Kiel et al. (1998). *A. (A.) decipiens* was also identified in the late Ilerdian of Eskişehir by Özgen-Erdem et al. (2007).

***Alveolina (Alveolina) dedolia* DROBNE, 1977**

(Plate IV, figure 11)

1977 *Alveolina (Alveolina) dedolia* DROBNE, pl.5, figs. 9-11.

2007 *Alveolina dedolia* DROBNE. ÖZGEN-ERDEM et al., p. 917, figs. 5c-d.

Material: 8 specimens representing the species were identified throughout the section (ÖZ-1, ÖZ-3, ÖZ-5, ÖZ-8, ÖZ-11, ÖZ-12).

Description: Megalospheric test is spherical to subspherical and small sized. In megalospheric specimens, the axial and equatorial diameters range from 2.14 to 3.18 mm and 1.84 to 2.70 mm, respectively. The elongation index is between 1.02 - 1.34 and the diameter of the spherical proloculus ranges between 0,16 - 0,20 mm. The test poles are mostly rounded and rarely truncated. 3-4 whorls after the proloculus is tightly coiled. In these whorls, forming the juvenile stage, the chamberlets are quite small in size and have circular section. In the following whorls, the thickening in the basal layer develops both in axial and equatorial direction. The basal layer thickness is very close in both axial and equatorial directions. The chamberlets in this stage are spherical and sometimes tooth-shaped (downward oval) at the beginning; and rectangular in the last few whorls. Microspheric specimens could not be obtained.

Range: *A. (A.) dedolia* was found in the middle Ilerdian (SBZ 7-8) levels of the Özbahçe section. The stratigraphic distribution of this species was given as the lower part of the middle Ilerdian (*Alveolina moussoulensis* zone, SBZ 7) by Drobne (1977) and Serra-Kiel et al. (1998). On the other hand, Özgen-Erdem et al. (2007) described this species from the upper part of the early Ilerdian and lower part of middle Ilerdian (SBZ 6-7) in Eskişehir.

***Alveolina (Alveolina) ellipsoidalis* SCHWAGER, 1883**

(Plate IV, figure 10)

- 1883 *Alveolina ellipsoidalis* SCHWAGER, pl.25 (2), figs. 1-2.
- 1960 *Alveolina ellipsoidalis* SCHWAGER. HOTTINGER, pl.2, figs. 1-8.
- 1995 *Alveolina (Alveolina) ellipsoidalis* SCHWAGER. ACAR, pl.5, figs. 1-4; pl.6, figs. 1-2; pl.7, fig. 1.
- 2007 *Alveolina ellipsoidalis* SCHWAGER. ÖZGEN-ERDEM et al., p. 916, figs. 5e-f.
- 2007 *Alveolina ellipsoidalis* SCHWAGER. VECCHIO et al., p.29, pl.1, figs. 1-2.
- 2008 *Alveolina ellipsoidalis* SCHWAGER. SİREL and ACAR, pl.32, figs. 1-6; pl.33, figs. 1-3.

Material: 5 specimens representing the species were identified throughout the section (ÖZ-3).

Description: Megalospheric test is oval and small sized. In megalospheric specimens, the axial and equatorial diameters range from 2.42 to 4.26 mm and 1.66 to 3.34 mm, respectively. The elongation index ranges from 1.25 to 1.49 and the diameter of the spherical proloculus is between 0.10 - 0.32 mm. 3-4 whorls following the proloculus are tightly coiled. The test rapidly becomes oval after the first 1 to 2 whorls of spherical shaped. The poles can be acute or rounded. Chamberlets have circular cross-sections throughout all growth stages, and their sizes regularly increase. In the whorls following the juvenile stage, a slight axial thickening is observed. The absence of thickening in the equatorial direction in similar whorls leads the test to elongate in the axial direction. Microspheric specimens could not be obtained.

Range: *A. (A.) ellipsoidalis* was found in the middle Ilerdian (SBZ 7-8) levels of the Özbahçe section. Although this species was defined as index species for the upper part of the early Ilerdian (SBZ 6) by Serra-Kiel et al. (1998); it has been reported from a wider range. This species has been found in the early-middle Ilerdian levels by Özgen-Erdem (2008) in Kastamonu and Özgen-Erdem et al. (2007) in Eskişehir region, in the early-late Ilerdian levels by Acar (1995) and Sirel and Acar (2008) in Ankara, and in the middle Ilerdian

levels by Hadi et al. (2019) in the Elburz (Iran) region. *A.(A.) ellipsoidalis* appear at the top latest SBZ 6, Pb 5, in Tibet (BouDagher-Fadel et al, 2015).

***Alveolina (Alveolina) erki* ACAR, 1995**

(Plate III, figure 8)

- 1995 *Alveolina (Alveolina) erki* ACAR, pl.3, figs. 10-13.
- 2008 *Alveolina erki* ACAR. SİREL and ACAR, pl.36, figs. 1-3.
- 2008 *Alveolina erki* ACAR. ÖZGEN-ERDEM, pl.1, fig. 9.

Material: 2 specimens representing the species were identified throughout the section (ÖZ-6, ÖZ-12).

Description: Megalospheric test is oval and small. In megalospheric specimens, the axial and equatorial diameters were measured as 1.58 - 1.80 mm and 0.84 - 1.08 mm, respectively. The elongation index is between 1.67 and 1.88 and the diameter of the spherical proloculus is 0.30 mm. Following the proloculus, 1-2 whorls are tightly coiled. While a rapid axial thickening along the subsequent chambers are observed, no thickening is observed in the equatorial direction. The poles can be acute or rounded, and chamberlets are spherical and slightly increase in length towards the outer whorls. In some individuals, the sizes of chamberlets increase irregularly. Microspheric specimens could not be obtained.

Range: *A. (A.) erki* was found in the early-middle Ilerdian (SBZ 5-8) levels of the Özbahçe section. The stratigraphic distribution of this species was given as middle Ilerdian-early Cuisian by Acar (1995). In addition, this species was reported from the middle Ilerdian of Kastamonu region by Özgen-Erdem (2008), and from the earliest Ilerdian to late Ilerdian (SBZ 5 to 9) of Kayseri and Ankara regions by Sirel and Acar (2008).

***Alveolina (Alveolina) guidonis* DROBNE, 1977**

(Plate V, figure 4)

- 1977 *Alveolina (Alveolina) guidonis* DROBNE, pl.15, figs. 6-12.
- 2011 *Alveolina guidonis* DROBNE, DROBNE et al., p.747, pl.1.

Material: 2 specimens representing the species were identified throughout the section (ÖZ-5).

Description: Megalospheric test is oval and small sized. Based on two oblique axial sections obtained, axial and equatorial diameters of the megalospheric specimens vary between 2.80 - 3.18 mm and 1.44 - 1.86 mm, respectively. The elongation index varies between 1.71 - 1.94. The diameter of the subspherical prolocus is 0.36 - 0.52 mm. The size of divided chambers following the proloculus and chamberlets in these chambers increase regularly. There is no distinct juvenile stage. After the proloculus, a regular axial thickening is observed and this increase is regular. The poles are rounded. The chamberlets are spherical in the early stages, and in the following stages, they become upright oval with an increase in their heights towards outer whorls. Microspheric specimens could not be obtained.

Range: *A. (A.) guidonis* was found in the middle Ilerdian (SBZ 7-8) levels of the Özbahçe section corresponding to the stratigraphic distribution given by Drobne (1977). However, Serra-Kiel et al. (1998) suggest the upper part of the middle Ilerdian and late Ilerdian levels (SBZ 8-9) as the stratigraphic interval for this species. Also, the specimens that Hadi et al. (2019) identified as *A. (A.)* gr. *guidonis* are quite similar to the holotype of *A. (A.) guidonis* in terms of biometry and morphology, and were found in the middle Ilerdian (SBZ 8).

***Alveolina (Alveolina) cf. ilerdensis* HOTTINGER, 1960**

(Plate IV, figure 9)

Material: 1 specimen representing the species was identified throughout the section (ÖZ-12).

Description: Megalospheric test is elongated, oval and small sized. According to the descriptions made based on the almost axial section of only megalospheric specimen obtained, the axial and equatorial diameters are 2.36 mm and 1.18 mm, respectively. The elongation index is 2.00 and the diameter of the subspherical proloculus is approximately 0.16 mm. There are two tightly coiled whorls following the proloculus. Due to the axial thickening following these chambers, the test becomes oval in shape. The

poles are rounded. The whorls that axial thickening is observed, are loosely coiled in the equatorial direction. Chamberlets are spherical and very thin in all stages. Their dimensions slightly increase towards the outer whorls. Microspheric specimens could not be obtained.

Remarks: The obtained specimen presents morphological and biometric similarities with original species described by Hottinger (1960). The specimen, which may be a young form of *A. (A.) ilerdensis*, is described in this format as it was not well preserved.

Range: *A. (A.) cf. ilerdensis* was found in the middle Ilerdian (SBZ 7-8) levels of the Özbahçe section. The stratigraphic distribution of *A. (A.) ilerdensis* was given as the middle-late Ilerdian by Hottinger (1960) and Serra-Kiel et al. (1998).

***Alveolina (Alveolina) montanarii* DROBNE, 1977**

(Plate V, figures 3,5)

1977 *Alveolina (Alveolina) montanarii* DROBNE, p.29, text-figs. 12a-c; pl.4, figs. 19-24.

1995 *Alveolina (Alveolina) montanarii* DROBNE. ACAR, pl.14, figs. 4-7.

2008 *Alveolina montanarii* DROBNE. SİREL and ACAR, pl.5, figs. 1-3.

Material: 4 specimens representing the species were identified throughout the section (ÖZ-11, ÖZ-12).

Description: Megalospheric test is spherical to subspherical and small sized. In megalospheric specimens, the axial and equatorial diameters are 2.40 to 3.64 mm and 1.94 to 3.38 mm, respectively. The elongation index is between 1.08 to 1.31 and the diameter of spherical proloculus is between 0.12 to 0.16 mm. After the proloculus, 4 to 6 whorls are tightly coiled. During the following 1.5 to 2 whorls, flosculinization occurs. In this stage of *A. (A.) montanarii*, which exhibits heavy flosculinization, thickness of the basal layer reaches 6-7 times the height of the chamber. Although the basal layer thickness has significantly decreased after the flosculinized stage, it is still not tightly coiled. Generally, a slight increase in the dimensions of spherical chamberlets is observed towards the outer whorls. In the flosculinized stage,

the chamberlets are slightly depressed. In advanced specimens that have many whorls belonging to the senile stage, the chamberlets are elongated and become rectangular in the last whorls. Microspheric specimens could not be obtained.

Range: *A. (A.) montanarii* was found in the middle Ilerdian (SBZ 7-8) levels of the Özbahçe section. The stratigraphic distribution of this species was determined as middle Ilerdian by Drobne (1977) and as middle-late Ilerdian (SBZ 7-9) by Serra-Kiel et al. (1998).

***Alveolina (Alveolina) montanarii* DROBNE ssp1**

(Plate V, figure 2)

Material: 1 specimen representing the species was identified throughout the section (ÖZ-8).

Diagnosis: Test is small and subspherical. The axial and equatorial diameters of the only individual obtained are 1.78 mm and 1.50 mm, respectively. The elongation index is 1.19. The very small, spherical proloculus has a diameter of 0.04 mm. The first whorls of the specimen, whose embryonic stage cannot be clearly observed, seems to be arranged in milioline-way. Considering the dimensions of the proloculus and the appearance of the embryonic stage, our specimen may belong to the microspheric generation. Following the complex inner whorls, which probably arranged in milioline manner, 6 tightly coiled whorls containing divided chambers are observed. During the next two whorls after these, flosculinization occurs. In the flosculinized stage, thickness of the basal layer reaches 4-5 times the chamber height. There is no senile stage observed in the single specimen obtained. Size of the chamberlets with circular sections increase regularly. Chamberlets may occasionally appear as depressed in the flosculinized stage.

Differential diagnosis: The examined specimen reaches the same number of whorls in much smaller test as it has a chamber height lower than *A. (A.) montanarii*. Our specimen, which exhibit very close characteristics with *A. (A.) montanarii* in terms of morphological features and the development of growth stages, indicates that it might be a new subspecies due to occurring in the same stratigraphic levels with *A. (A.) montanarii*. It is left to be named in future studies due to the insufficient number of individuals.

Range: *A. (A.) montanarii* ssp1 was found in the middle Ilerdian (SBZ 7-8) levels of the Özbahçe section.

Alveolina (Alveolina) moussoulensis

HOTTINGER, 1960

(Plate V, figure 1)

1960 *Alveolina moussoulensis* HOTTINGER, pl.2, fig. 10-16.

1964 *Alveolina moussoulensis* HOTTINGER. DEVOTO, pl.II, fig. 3.

1977 *Alveolina moussoulensis* HOTTINGER. DROBNE, pl.1, figs. 4-8.

2008 *Alveolina moussoulensis* HOTTINGER. SİREL and ACAR, pl.28, fig. 1.

2019 *Alveolina moussoulensis* HOTTINGER. HADI et al., p. 145, fig. 4.7.

Material: 5 specimens representing the species were identified throughout the section (ÖZ-5, ÖZ-6).

Description: Megalospheric test is elongated oval and medium sized. In megalospheric specimens, the axial and equatorial diameters are 3.94 - 6.12 mm and 2.42 to 3.31 mm, respectively. The elongation index ranges from 1.34 to 1.89 and the diameter of the spherical proloculus varies from 0.14 to 0.32 mm. The test poles are usually rounded, sometimes acute. After the proloculus 2-3 whorls are tightly coiled and are in spherical pattern. Throughout the following 7 to 8 whorls, the axial thickening and accordingly, the oval test shape develops. No thickening in the basal layer is observed in the equatorial direction. There is no axial thickening in the last 4 to 5 whorls. At this stage, the poles sometimes depressed. Chamberlets have circular cross-sections in the inner whorls. Their size increases gradually towards the outer whorls and they become rectangular in shape. Microspheric specimens could not be obtained.

Range: *A. (A.) moussoulensis* was found in the early - middle Ilerdian (SBZ 5-8) levels of the Özbahçe section. The stratigraphic distribution of this species was given as middle Ilerdian (*A. moussoulensis* zone) by Hottinger (1960). Serra-Kiel et al. (1998) defined this species as index species for SBZ 7 in the middle Ilerdian. In Tibet, *A.(A.) moussoulensis* is recorded from SBZ 7 to SBZ 9 (BouDagher-Fadel et al., 2015).

***Alveolina (Alveolina) muscatensis* WHITE ssp1**

(Plate III, figure 5)

Material: 1 specimen representing the species was identified throughout the section (ÖZ-11).

Diagnosis: Small test is oval shaped. The axial and equatorial diameters of the single specimen obtained are 1.90 mm and 1.34 mm, respectively. The index of elongation is 1.42. The initial whorls of the specimen whose embryonic stage and the proloculus can not be clearly observed seem to be arranged in a milioline manner. In this regard, the specimen probably belongs to the microspheric generation. After the inner chambers (possibly not divided into chamberlets), tightly coiled 4-5 whorls that have divided chambers are observed. Throughout the 3 whorls following these whorls, there is a significant axial thickening, while a loose coiling is observed in equatorial direction. There is no senile stage in only specimen obtained. The sizes of the chamberlets, which are generally circular in cross-section, increase regularly towards the outer whorls. Chamberlets in the polar region of last few whorls are tooth-shaped (downward oval).

Differential diagnosis: The examined specimen differs from *A. (A.) muscatensis* by having a lower chamber height, thus reaching the same number of whorls in a smaller test. It offers similarities with *A. (A.) muscatensis* in terms of morphological features, elongation index and development of growth stages.

Remarks: Our specimen presents morphological and biometric similarities with *A. (A.) muscatensis* which is defined by White (1992) from the early Eocene of Oman. For this species, White (1992) stated that it would not be older than *A. dainellii* zone and refers to an age of Cuisian. The same species was defined by Özgen-Erdem et al. (2007) in Cuisian of the Eskişehir region and by Özcan et al. (2015) in the middle Ilerdian (SBZ 7-8) of Oman. Our specimen found in the middle Ilerdian of Özbahçe section probably points to a new subspecies considering the morphological similarities and biometric comparison with *A. (A.) muscatensis*. It is left to be named in future studies due to the insufficient number of individuals.

Range: *A. (A.) muscatensis* ssp1 was found in the middle Ilerdian (SBZ 7-8) levels of the Özbahçe section.

***Alveolina (Alveolina) ozbahcensis* n.sp.**

(Plate III, figures 1-4)

Derivation of name: Özbahçe is a village located in the north of Keçiborlu (Isparta).

Material: 9 specimens representing the species were identified throughout the section (ÖZ-5, ÖZ-6, ÖZ-7).

Holotype: Axial section of megalospheric specimen, illustrated by plate III, figure 1.

Type locality: Limestones outcropping at nearly 2 km northwest of the Özbahçe village in north of Keçiborlu (Isparta) (between the coordinates of 38°01'53,85" E - 30°18'52,96" N and 38°01'56,17" E - 30°18'50,86" N).

Type level: Büyükkırtepe formation, early - middle Ilerdian (SBZ 5-8). The section between 13,70 m and 18,50 m of the Özbahçe measured section.

Diagnosis: Small to medium megalospheric test is elongated and oval. The poles are rounded. In megalospheric specimens, the axial and equatorial diameters are in the range of 2.62 - 5.68 mm and 1.58 - 3.22 mm, respectively. An adult individual with a maximum axial diameter of 5.68 mm has 11 whorls. The elongation index is between 1.41 - 1.9 and the diameter of the spherical - subspherical proloculus varies between 0.22 - 0.48 mm. There are 2 or 3 spherical to subspherical whorls following the large proloculus of the species, which has no discernible juvenile stage. Subsequent whorls grow regularly in axial and equatorial directions. The basal layer gradually thickens in both directions. However, the thickening in the axial direction is larger than in the equatorial direction. Thickness of the basal layer reaches at maximum half of the chamber height in the equatorial direction, while reaching twice in axial direction. Chamberlets with circular cross-section become elongated in the last 1 or 2 whorls and have rectangular shape. Chamberlets are coarse throughout the ontogeny, and septa are very thin. Microspheric specimens could not be obtained.

Differential diagnosis: This new species shows similarities with *A. (A.) aragonensis* among coeval alveolinids and differs from the latter by its greater elongation index and indistinctly delimited juvenile stage. Unlike *A. (A.) aragonensis*, the growth steps in the new species are gradual (Figure 8a, d). The new

species, showing similar ontogenic development with *A. (A.) guidonis*, differs from this species by its size and Parameter C (Figure 8e). It reaches 1.5 times the size of test in the same whorl number. While test size for 11 whorls is 3 mm in *A. (A.) guidonis*, this value in the new species is 4.7 mm. The elongation indices also differ between the two species (Figure 8b). While the index of elongation is 1.7 to 2.0 for *A. (A.) guidonis*; it varies between 1.4 and 1.9 for new species. The new species which show similarities with *A. (A.) moussoulensis* in terms of elongation index and shape, is distinguished from the latter with the trend of chamberlet size throughout ontogeny, absence of discernable juvenile-adult-senile stages and course of Parameter C (Figure 8c, f).

Remarks: Although it shows similarities with *A. (A.) guidonis* in terms of development of growth stages and morphology, *A. (A.) ozbahcensis* n.sp. is found in relatively older stratigraphic levels. In this context, it could be inferred that these two species may belong to the same phylogenetic lineage.

Range: *A. (A.) ozbahcensis* n.sp. was found in the early - middle Ilerdian (SBZ 5-8) levels of the Özbahçe section.

***Alveolina (Alveolina) pasticillata* SCHWAGER,
1881**

(Plate IV, figure 6)

1883 *Alveolina (Flosculina) pasticillata* SCHWAGER, pl.26 (3), figs. 2a,b.

1960 *Alveolina pasticillata* SCHWAGER. HOTTINGER, pl.4, figs. 26-33.

1977 *Alveolina (Alveolina) pasticillata* SCHWAGER. DROBNE, pl.4, figs. 1-7.

1992 *Alveolina (Alveolina) pasticillata* SCHWAGER. WHITE, p. 57, pl.2, fig. 11.

2008 *Alveolina pasticillata* SCHWAGER. SIREL and ACAR, pl.5, figs. 4-5.

2011 *Alveolina pasticillata* SCHWAGER. DROBNE et al., p.747, pl.1.

Material: 5 specimens representing the species were identified throughout the section (ÖZ-5, ÖZ-7, ÖZ-8).

Description: In megalospheric specimens, test is spherical to subspherical and small sized. The axial

and equatorial diameters range from 1.92 to 3.68 mm and 1.62 to 3.40 mm, respectively. The elongation index is between 1.08 to 1.22 and the diameter of tiny proloculus is between 0.04 to 0.06 mm. Tightly coiled 4-5 whorls following the proloculus constitute juvenile stage and are in inflated lenticular-pattern. During the next 2 to 3 species, flosculinization occurs. In this stage, thickness of the basal layer increases towards the outer whorls and it reaches 8 times the chamberlet height in the thickest whorl. In the senile stage following the flosculinized stage, tightly coiled 4-5 whorls are observed. Chamberlets are spherical in the juvenile stage, while they are quite flattened in the flosculinized stage. In the senile stage, the chamberlet height increases and becomes slightly rectangular. Microspheric specimens could not be obtained.

Range: *A. (A.) pasticillata* was found in the middle Ilerdian (SBZ 7-8) levels of the Özbahçe section. Stratigraphic distribution of this species was given as early Ilerdian by Hottinger (1960). Serra-Kiel et al. (1998) defined SBZ 6 biozone by the biostratigraphic range of this species. Besides, Drobne et al. (2011) assigned the middle Ilerdian (SBZ 7-8) age for this species. Sirel and Acar (2008) also described this species from early?- middle Ilerdian of Bozcaada (Çanakkale). In Tibet, *A.(A.) pasticillata* is reported from top SBZ 6 to SBZ 7 (BouDagher-Fadel et al., 2015).

***Alveolina (Alveolina) pisella* DROBNE, 1977**

(Plate IV, figure 2)

1977 *Alveolina (Alveolina) pisella* DROBNE, p. 34, text-fig. 16; pl.5, figs. 17-19.

2007 *Alveolina pisella* DROBNE. ÖZGEN-ERDEM et al., p. 920, figs. 7a-c.

2011 *Alveolina pisella* DROBNE. DROBNE et al., p.747, pl.1.

Material: 1 specimen representing the species was identified throughout the section (ÖZ-1).

Description: Test is spherical and small sized. In the single megalospheric specimen obtained, the axial and equatorial diameters are 3.22 mm and 2.72 mm, respectively. The elongation index is 1.18 and the diameter of spherical proloculus was measured as 0.18 mm. The next 5 whorls following the proloculus form a tightly coiled juvenile stage. The subsequent 8 whorls are loosely coiled, but during these whorls thickness

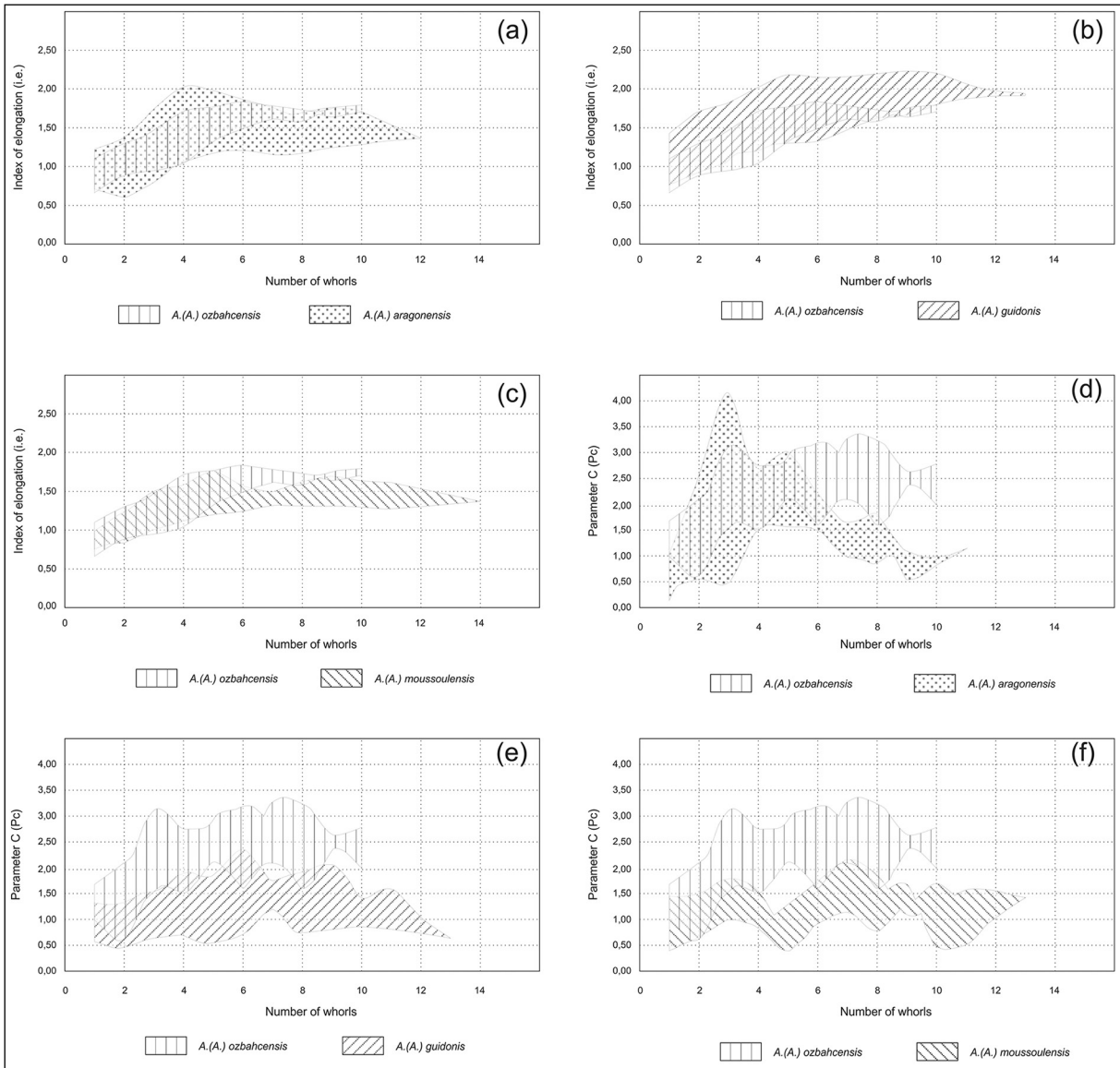


Figure 8- Number of whorls vs. elongation index comparison plots of *A. (A.) ozbahcensis* n.sp. with (a) *A. (A.) aragonensis*, (b) *A. (A.) guidonis*, (c) *A. (A.) moussoulensis*; the number of whorls vs Parameter C comparison plots of (d) *A. (A.) aragonensis*, (e) *A. (A.) guidonis*, (f) *A. (A.) moussoulensis*.

of the basal layer never reaches the chamber height. This species, which is characteristic with having delicate inner structure, chamberlets are small-sized and spherical throughout the juvenile stage. Sizes of the chamberlets slightly increase towards the outer whorls. In senile stage, they increase in size and become rectangular. A gradual increase in chamberlet size is also observed in this stage. Microspheric specimens could not be obtained.

Range: *A. (A.) pisella* was found in the middle Ilerdian (SBZ 7-8) levels of the Özbahçe section. The

stratigraphic distribution of this species was given as middle-late Ilerdian (SBZ 8-9) by Drobne (1977) and Serra-Kiel et al. (1998). Also, Özgen-Erdem et al. (2007) described this species in the upper Ilerdian of the Eskişehir region (SBZ 9).

***Alveolina (Alveolina) rotundata* HOTTINGER
kazancii SİREL and ACAR, 2008**

(Plate III, figure 10)

1995 *Alveolina (Alveolina) rotundata* HOTTINGER.
 ACAR, pl.22, figs. 2,3.

1995 *Alveolina (Alveolina) decipiens* SCHWAGER. ACAR, pl.16, fig. 4.

2008 *Alveolina rotundata kazancii* SİREL and ACAR, pl.34, figs. 1-3, 5, 7.

2016 *Alveolina rotundata kazancii* SİREL and ACAR. ÖZGEN-ERDEM et al., pl.1, figs. 8-10.

2019 *Alveolina (Alveolina) rotundata kazancii* SİREL and ACAR. BOZKURT and GÖRMÜŞ, pl.1, fig. 7.

Material: 3 specimens representing the species were identified throughout the section (ÖZ-5, ÖZ-7, ÖZ-11).

Description: Megalospheric test is elongated oval and small sized. The axial and equatorial diameters are between 2.35 and 3.44 mm and 1.19 and 1.91 mm, respectively. The elongation index ranges from 1.76 to 1.97 and the diameter of spherical proloculus was measured as 0.18 - 0.33 mm. The next 2-3 whorls following the proloculus are tightly coiled and in subspherical-pattern. During the following 4 whorls with loose coiling, test becomes elongated oval. In this stage, thickening in the axial direction is approximately 3 to 4 times of that in the equatorial direction. Both the basal layer thickness and chamberlet heights increase regularly from inner towards outer whorls. The chamberlets have circular cross-section in inner whorls, while in the loosely coiled outer whorls they are tooth-shaped (downward oval). Microspheric specimens could not be obtained.

Range: *A. (A.) rotundata kazancii* was found in the middle Ilerdian (SBZ 7-8) levels of the Özbahçe section. The stratigraphic distribution of this species is given as middle Ilerdian (SBZ 7-8) by Sirel and Acar (2008). Özgen-Erdem et al. (2016) also described this species in the middle Ilerdian of Kastamonu region.

***Alveolina (Alveolina) rugosa* HOTTINGER ssp1**

(Plate III, figure 9)

Material: 1 specimen representing the species was identified throughout the section (ÖZ-6).

Diagnosis: Test is small, fusiform-subcylindrical shaped. The axial and equatorial diameters of the only megalospheric individual are 4.40 mm and 1.02 mm, respectively. The elongation index is 4.31. The

proloculus is spherical and its diameter is 0.08 mm. Following the proloculus, 2-3 whorls are in lenticular pattern and tightly coiled. During these whorls, the chamberlets are very small. A remarkable axial thickening is observed during the next 5 whorls. In this stage, thickness of the basal layer in axial direction is about 10 times the thickness in the equatorial direction. Senile stage of the single specimen obtained contains only one whorl. At this stage, there is a distinct decrease in the axial thickening. Chamberlets have circular cross-sections throughout the ontogeny, and their size increases slightly towards the last whorl. While the poles of the test are sharp in the juvenile stage, they are subcylindrical in the last whorls.

Differential diagnosis: The examined specimen shows morphological similarities with *A. (A.) rugosa*. They are quite similar in terms of elongation indices and growth stages. This potential new subspecies differs from *A. (A.) rugosa* by having smaller dimensions and reaching the same number of whorls in a smaller test. In measurements taken from the paratype A form of *A. (A.) rugosa* (Hottinger, 1960: pl. 11, fig. 9), axial and equatorial diameters and proloculus diameter are 6.00 mm, 1.43 mm and 0.14 mm, respectively. However; the same values in this individual are 4.40 mm, 1.02 mm and 0.08 mm.

Remarks: Our specimen presents morphological similarities with *A. (A.) rugosa* defined by Hottinger (1960). For the age of *A. (A.) rugosa*, Cuisian was suggested by Hottinger (1960) and Serra-Kiel et al. (1998). Considering the morphological similarities and biometric comparison between our specimen obtained from Early Ilerdian and *A. (A.) rugosa*, it has been interpreted that this specimen could be a forerunner or subspecies of *A. (A.) rugosa*. Due to the insufficient number of individuals, it is left to be named in future studies.

Range: *A. (A.) rugosa* ssp1 was found in the early Ilerdian (SBZ 5-6) levels of the Özbahçe section.

***Alveolina (Alveolina) trempina* HOTTINGER, 1960**

(Plate IV, figure 8)

1960 *Alveolina trempina* HOTTINGER, pl.2, figs. 17-19.

2008 *Alveolina trempina* HOTTINGER. SİREL and ACAR, pl.39, figs. 1, 3.

non *Alveolina trempina* HOTTINGER. SİREL and ACAR, 2008, pl.39, fig. 2.

Material: 4 specimens representing the species were identified throughout the section (ÖZ-12).

Description: Megalospheric test is elongated oval, fusiform and medium sized. In megalospheric specimens, the axial and equatorial diameters are between 4,24 - 7,32 mm and 1,56 - 2,74 mm, respectively. The elongation index ranges from 2.67 to 2.72 and the diameter of the spherical proloculus is between 0,24 - 0,34 mm. Following the proloculus, 1-2 whorls are tightly coiled and in spherical pattern. Throughout the next 5 whorls, rapidly developing axial thickening is observed and this thickening regularly increases. The last 3-5 whorls, constituting senile stage, are tightly coiled in axial and equatorial directions. Thickness of the basal layer is 7 to 8 times greater than that of the equatorial region. While the coarse chamberlets have circular cross-sections in inner whorls, they become upright oval in the senile stage. The sizes of the chamberlets increase slowly towards the last whorls. The poles, which are acute or slightly rounded in adult stage, are subcylindrical in the senile stage. Microspheric specimens could not be obtained.

Range: *A. (A.) trempina* species was found in the middle Ilerdian (SBZ 7-8) levels of the Özbahçe section. The stratigraphic distribution of this species was given as the late Ilerdian (SBZ 9) by Hottinger (1960) and Serra-Kiel et al. (1998). In addition, Özgen-Erdem et al. (2007, 2008) described this species from the upper Ilerdian (SBZ 9) of Eskişehir and Kastamonu regions. In Tibet, this species is reported from SBZ 9. In this study, coexistence of *A. (A.) trempina* and *A. (A.) corbarica* has been interpreted that these levels might be a transition from the middle to late Ilerdian.

***Alveolina (Alveolina) varians* HOTTINGER, 1960**

(Plate IV, figure 3)

1960 *Alveolina varians* HOTTINGER, pl.8, figs. 9-12.

2007 *Alveolina varians* HOTTINGER. ÖZGEN-ERDEM et al., p.923, fig. 9f.

2008 *Alveolina varians* HOTTINGER. SİREL and ACAR, pl.24, figs. 7,8.

Material: 4 specimens representing the species were

identified throughout the section (ÖZ-3, ÖZ-6, ÖZ-12).

Description: Small sized megalospheric test is oval. In megalospheric specimens, axial and equatorial diameters are between 2.58 to 3.42 mm and 1.98 to 2.42 mm, respectively. The elongation index ranges from 1.27 to 1.53. The diameter of the spherical proloculus is between 0,12 to 0,18 mm. There are tightly coiled 4-5 whorls following the proloculus. During the next 6-7 whorls, coiling is regular and loose. Thickness of basal layer is approximate in axial and equatorial regions. The cross-sections of the delicate chamberlets are circular and slightly elongated in the outer whorls. The sizes of the chamberlets are quite small in tightly coiled inner whorls, and gradually increases towards the outer whorls. Microspheric specimens could not be obtained.

Remarks: *A. (A.) varians* specimens obtained from Keçiborlu samples lack of the senile stage in which thickness of the basal layer is excessively increased as seen in *A. (A.) varians* defined by Hottinger (1960).

Range: *A. (A.) varians* was found in the early - middle Ilerdian (SBZ 5-8) levels of the Özbahçe section. This species, which was defined in the early Ilerdian (*A. cucumiformis* zone) by Hottinger (1960), was described as the index species for SBZ 5 in early Ilerdian by Serra-Kiel et al. (1998). In addition, *A. (A.) varians* was identified in the middle Ilerdian of Eskişehir region by Özgen-Erdem et al. (2007) and of Ankara (Polatlı) region by Sirel and Acar (2008).

***Alveolina (Alveolina) vredenburgi* DAVIES and PINFOLD, 1937**

(Plate IV, figure 1)

1937 *Alveolina vredenburgi* DAVIES and PINFOLD, pl.5, fig. 25.

1960 *Alveolina cucumiformis* HOTTINGER, p.135, text-figs. 26, 29/1, 2, 71c, d, 72, 73.

1995 *Alveolina (Alveolina) cucumiformis* HOTTINGER. ACAR, pl.4, figs. 2-4.

2008 *Alveolina vredenburgi* DAVIES and PINFOLD. SİREL and ACAR, pl.31, figs. 1-3.

2009 *Alveolina vredenburgi* DAVIES and PINFOLD. SCHEIBNER AND SPEIJER, p. 209, fig. 10j.

Material: 1 specimen representing the species was identified throughout the section (ÖZ-6).

Description: Test is elongated oval and small sized. In the only megalospheric specimen obtained, axial and equatorial diameters are 4.06 mm and 1.64 mm, respectively. The elongation index is 2.48 and diameter of the spherical proloculus was measured as 0.12 mm. The next 2-3 whorls following the proloculus are tightly coiled. In this stage, test is in subspherical pattern. In the following whorls, a distinct elongation occurs in the axial direction and accordingly, the test becomes elongated oval. In this stage, thickness of the basal layer in axial direction is 5 times of that in equatorial direction. These 6 to 7 whorls constitute the adult stage. In the following senile stage, axial thickening decreases again. Cross-sections of chamberlets are circular and become upright oval in the outer whorls. Microspheric specimens could not be obtained.

Range: *A. (A.) vredenburgi* was found in the early Ilerdian (SBZ 5-6) levels of the Özbahçe section. This species, which was defined in the early Ilerdian (*A. cucumiformis* zone) by Hottinger (1960), was given as the index species of SBZ 5 in early Ilerdian by Serra-Kiel et al. (1998). In Tibet, this species is reported from SBZ 5 to earliest SBZ 6 (BouDagher-Fadel et al., 2015).

6. Biostratigraphic Findings and Discussion

In this study, the biostratigraphic data based on the *Alveolina* species representing mainly the early Ypresian (Ilerdian) period were presented. In determining the biozones, the studies of Hottinger (1960; 1974), Drobne (1977), Serra-Kiel et al. (1998), Özgen-Erdem et al. (2007), Sirel and Acar (2008) were based on; and Serra-Kiel et al. (1998) was followed in biozone identifications. Stratigraphic distributions and assemblages were presented in the taxonomy chapter and compared with the abovementioned studies. While giving the ranges, the equivalents of shallow benthic zones defined by Serra-Kiel et al. (1998) were specified. However, the SBZ 3 and 4 zones, SBZ 5 and 6 zones, and SBZ 7 and 8 zones were merged due to coexistence of some index species representing these zones (Figure 9).

Age	Thanetian	Early Ypresian	
		Ilerdian	
		Early	Middle
Serra-Kiel et al. (1998)	SBZ 3-4	SBZ 5-6	SBZ 7-8
Alveolinids			
<i>A. (G.) karsica</i>			
<i>A. (G.) aff. karsica</i>			
<i>A. (G.) lepidula</i>			
<i>A. (G.) cf. subtilis</i>			
<i>A. (G.) sp.</i>			
<i>A. (A.) acari</i> n.sp.			
<i>A. (A.) aragonensis</i>			
<i>A. (A.) avsari fusunae</i> n.ssp.			
<i>A. (A.) baldaccii</i> ssp1			
<i>A. (A.) cemali</i>			
<i>A. (A.) corbarica</i>			
<i>A. (A.) cf. coudurensis</i>			
<i>A. (A.) decipiens</i>			
<i>A. (A.) dedolia</i>			
<i>A. (A.) ellipsoidalis</i>			
<i>A. (A.) erki</i>			
<i>A. (A.) guidonis</i>			
<i>A. (A.) cf. ilerdensis</i>			
<i>A. (A.) montanarii</i>			
<i>A. (A.) montanarii</i> ssp1			
<i>A. (A.) moussoulensis</i>			
<i>A. (A.) muscatensis</i> ssp1			
<i>A. (A.) ozbahcensis</i> n.sp.			
<i>A. (A.) pasticillata</i>			
<i>A. (A.) pisella</i>			
<i>A. (A.) rotundata kazancii</i>			
<i>A. (A.) rugosa</i> ssp1			
<i>A. (A.) trempina</i>			
<i>A. (A.) varians</i>			
<i>A. (A.) vredenburgi</i>			

Figure 9- Stratigraphic distributions and biostratigraphic biozones of *Alveolina* species identified in the Özbahçe measured section.

6.1. SBZ3-SBZ4 (Thanetian)

In the study area that contains a fossil assemblage representing the Ilerdian period, age determination based on foraminiferal assemblages except *Alveolina*, shows that the bottom of the sequence is Thanetian (SBZ 3-4) aged. According to the definitions made by Serra-Kiel et al. (1998), considering the alveolinid groups, SBZ 3 and SBZ 4 biozones are defined by the biostratigraphic range of *Alveolina (Glomalveolina) primaeva* and *A. (G.) levis*, respectively. In these levels of the study area, only one specimen of *Alveolina (Glomalveolina) sp.*, belonging to the genus *Alveolina*, was identified. This species, accompanied by *Elazigina dienii*, *Idalina causae*, *I. Sinjarica*, *Ranikothalia sp.*, *Rotalia sp.*, *Sistanites catali*, *Sistanites cf. guvenci*, *Sistanites* was thought to belong to the *A. (G.) primaeva* group (Hottinger, 1974) by considering its morphological and biometric properties. The accompanying assemblage also proves

that the sequence begins with Thanetian. Thanetian levels were observed between the sections of 12,70 m to 13,70 m, 18,50 m to 19,00 m and 21,30 m to 24,50 m in the Özbahçe section.

6.2. SBZ5-SBZ6 (early Ilerdian)

The lower part of the early Ilerdian was defined as *Alveolina cucumiformis* zone by Hottinger (1960), and as SBZ 5 biozone by Serra-Kiel et al. (1998). When alveolinid groups are taken into consideration, the SBZ 5 biozone is defined by the biostratigraphic ranges of *Alveolina (Alveolina) vredenburgi*, *A. (A.) avellana avellana*, *A. (A.) aramaea aramaea* and *A. (A.) varians* (Serra-Kiel et al., 1998). In the study area, early Ilerdian was recognized by the first occurrences *Alveolina (Alveolina) vredenburgi* and *A. (A.) varians*, which are among the index taxa of this biozone. The upper part of the early Ilerdian was defined as the *Alveolina ellipsoidalis* zone by Hottinger (1960) and as SBZ 6 biozone by Serra-Kiel et al. (1998). This zone is defined by the biostratigraphic ranges of *Alveolina* species such as *A. (A.) ellipsoidalis*, *A. (A.) daniensis*, *A. (A.) pasticillata*, *A. (A.) solida* (Serra-Kiel et al., 1998). However, *A. (A.) ellipsoidalis* and *A. (A.) pasticillata* were not recognized in this interval in the study area. On the other hand, the current studies demonstrate that *A. (A.) ellipsoidalis* can be recognized in the whole the Ilerdian in different regions of Tethyan province (Özgen-Erdem et al., 2007; Özgen-Erdem, 2008, Sirel and Acar, 2008; Hadi et al., 2019; 2020). Similarly, the middle Ilerdian age is suggested for *A. (A.) pasticillata* (Sirel and Acar, 2008; Drobne et al., 2011). Indeed, these two species were not indicative for SBZ 5 biozone in the study area and observed at younger stratigraphic levels. The early Ilerdian fauna in the region consist of *Alveolina* species such as; *A. (G.) karsica*, *A. (G.) aff. karsica*, *A. (G.) cf. subtilis*, *A. (A.) acari* n.sp., *A. (A.) cemali*, *A. (A.) cf. coudurensis*, *A. (A.) erki*, *A. (A.) moussoulensis*, *A. (A.) ozbahcensis* n.sp., *A. (A.) rugosa* ssp1, and other larger bentic foraminifers such as; *Assilina* sp., *Discocyclina* sp., *Nummulites* sp., *Orbitolites* sp., *Ranikothalia* cf. *nutalli*, *Ranikothalia* cf. *polatliensis*, *Rotalia* sp., The first occurrence of *A. (A.) moussoulensis* defined in the lower parts of the middle Ilerdian (SBZ 7) for the Tethyan province, was determined as early Ilerdian in this region. The lower Ilerdian levels were observed between 13.70 m to 14.10 m and 19.00 m to 19.20 m in the Özbahçe section.

6.3. SBZ7-SBZ8 (middle Ilerdian)

The lower part of the middle Ilerdian was defined as *Alveolina moussoulensis* zone by Hottinger (1960), and as SBZ 7 biozone by Serra-Kiel et al. (1998); and the upper part was defined as *Alveolina corbarica* zone by Hottinger (1960) and as SBZ 8 biozone by Serra-Kiel et al. (1998). SBZ 7 is defined by the biostratigraphic distributions *Alveolina (Alveolina) moussoulensis*, *A. (A.) subpyreanica*, *A. (A.) dedolia*, *A. (A.) laxa*. SBZ 8 on the other hand is defined by the biostratigraphic distributions of *A. (A.) corbarica*, *A. (A.) recondita*, *A. (A.) brassica* (Serra-Kiel et al., 1998). As the species belonging to these two biozones coexist as mentioned earlier, these biozones were merged in this study. The middle Ilerdian in the study area starts with the first occurrences of *A. (A.) aragonensis*, *A. (A.) decipiens*, *A. (A.) dedolia*, *A. (A.) montanarii*. Unlike the other regions of Tethyan province, *A. (A.) corbarica*, *A. (A.) guidonis*, *A. (A.) pisella*, representing the younger levels, and *A. (A.) ellipsoidalis*, *A. (A.) pasticillata* and *A. (A.) varians* representing the older levels accompany these species. In addition to these species, the middle Ilerdian fauna of the region contains *Alveolina* species such as; *A. (G.) karsica*, *A. (G.) lepidula*, *A. (A.) acari*, *A. (A.) avsari fusunae* n.sp., *A. (A.) baldaccii* ssp1, *A. (A.) cemali*, *A. (A.) cf. coudurensis*, *A. (A.) erki*, *A. (A.) cf. ilterdensis*, *A. (A.) montanarii* ssp1, *A. (A.) moussoulensis*, *A. (A.) muscatensis* ssp1, *A. (A.) ozbahcensis* n.sp., *A. (A.) rotundata kazancii*, *A. (A.) trempina*, and other larger benthic foraminifers such as; *Assilina* sp., *Asterocyclina* sp., *Discocyclina*, *Elazigina* cf. *subsphaerica*, *Elazigina* sp., *Nummulites* sp., *Orbitolites bellus*, *Orbitolites* cf. *complanatus*, *Orbitolites* cf. *meGasphericus*, *Orbitolites* sp., *Opertorbitolites latimarginalis*, *Opertorbitolites* sp., *Operculina* sp., *Ornatorotalia granum*, *Ranikothalia* cf. *nutalli*, *Ranikothalia* sp., *Rotalia* sp., *Slovenites?* sp., *Sphaerogypsina* sp., gypsinid forms, and stomatorbinid forms. *A. (A.) trempina* defined as the index species of late Ilerdian (SBZ 9) by Hottinger (1960) and Serra-Kiel et al. (1998), was recognized in the middle Ilerdian in this region. The middle Ilerdian levels were observed between the levels of 0 m to 12.70 m, 14.10 m to 18.50 m, and 19.20 m to 21.30 m in the Özbahçe section.

7. Environmental Interpretation

The relationships between the test composition and the parameters of temperature, depth, salinity

etc. of the living environments can be constructed based on the samples of recent foraminifers, thus the paleoecological interpretations could be made (Hallock and Glenn, 1982; Reiss and Hottinger, 1984; Dong et al., 2018). The relative proportions of foraminifers with hyaline, porcellaneous and agglutinated tests can be used as environmental indicators (Jorissen et al., 2007). Debenay (2012) found that the proportion of hyaline species increased with increasing depth and mud content in the sediment. In studies conducted to determine the responses of recent benthic foraminifers to changes in temperature and salinity, it was observed that with increasing temperature, the assemblage shifted from hyaline rotaliids to porcellaneous miliolids (Dong et al., 2018).

Studies carried out on certain larger benthic foraminiferal groups, especially the alveolinids, nummulitids and amphisteginids, show that the test morphology changes depending on several parameters such as temperature, depth, light, hydrodynamic energy (Hottinger, 1960; 1997; Luterbacher, 1970; Hallock and Hansen, 1979; Hallock and Glenn, 1986; Murray, 1991; 2006; BouDagher-Fadel, 2008; 2018). It is known that the symbiont-bearing foraminifers with thin and flat tests can live at deeper environments than spherical, thick foraminifers (Hallock and Glenn, 1982).

In studies conducted particularly on alveolinids, the shape of test has been the primary parameter for paleoenvironmental interpretations. It has been determined that spherical alveolinids are mostly found in lagoon environments, however the elongated alveolinids are found in normal saline, restricted platform environments (Hottinger, 1960; Luterbacher, 1970). It was determined that alveolinids avoid generally the environments shallower than 5 m in the selection of habitat (Murray, 2006). Their recent relatives were reported to be abundant at depths between 25 and 35 m in the Maldives and the Gulf of Aqaba (Reiss and Hottinger, 1984). Hottinger (1977) stated that *Alveolina* species with higher elongation index live in relatively deeper environments. *Orbitolites* and *Opertorbitolites* from the soritid foraminifera also reflect the same environmental conditions as *Alveolina*. The coexistence of these genera shows low energy conditions in a shallow and protected marine environment (Hottinger, 1960; Luterbacher, 1970; Özgen-Erdem et al., 2016).

In the study area, the Thanetian period stands out with its low foraminiferal diversity. At these levels, foraminifer species with porcelain calcareous tests [*Idalina* spp., *Alveolina* (*Glomalveolina*) sp.] are dominantly seen, and they are accompanied by foraminifers with small amount of hyaline calcareous tests. Porcellaneous calcareous forms are typical forms of the low energy environments (Reiss and Hottinger, 1984) and indicate a high salinity (Murray, 2006).

The genus *Alveolina* is dominant in the early Ilerdian foraminiferal assemblage. It is accompanied by species belonging to the genera *Orbitolites* and *Opertorbitolites* and the hyaline calcareous groups (*Nummulites*, *Assilina*, *Discocyclina* etc.). It was reported that species belonging to groups of *Alveolina ellipsoidalis*, *Alveolina decipiens* and *Alveolina subpyreanica*, which are also common in the *Alveolina* assemblage in the study area, are mostly distributed in restricted platform environments with normal salinity (Hottinger, 1960). The elongated alveolinids such as *A. (A.) vredenburgi* are also found in the assemblage, which consist mostly of spherical alveolinids.

The middle Ilerdian beds of the Özbahçe section contains abundant *Alveolina* species, which is accompanied by the species of *Orbitolites*, *Opertorbitolites* and by the increasing amount of hyaline calcareous species. Although it has a similar foraminiferal assemblage to the early Ilerdian, there is a quantitative increase in the hyaline calcareous group (Bozkurt et al., 2021). The *Alveolina* assemblage contains both spherical and elongated shaped species.

It has been inferred from the foraminiferal assemblages and their features (e.g. test morphology, composition etc.) that the sequence located in the north of Keçiborlu was deposited in a lagoon environment with high salinity during the Thanetian, then the environment turned into a low energy shallow marine environment with normal salinity in the early Ilerdian. In addition to the similar foraminiferal assemblage in early Ilerdian, the increasing amount of the hyaline calcareous groups and generally discoidally shaped nummulitides indicates that the environment is relatively deepening.

8. Conclusions

In this study, alveolinid species were identified in detail from the measured section of the Büyükkırtepe

formation, which crops out in northern corner of the Isparta Angle, north of Keçiöorlu (Isparta).

It is seen that the foraminiferal assemblages include rich *Alveolina* species. Throughout the studied section, 30 different species/subspecies belonging to the genus *Alveolina* were recognized. Age of the lowest stratigraphic levels of the studied section that are poor in *Alveolina* was determined as Thanetian. In the lower Ilerdian beds, 9 known species and 2 new species of *Alveolina* were identified. 19 known species, 2 new species of *Alveolina* were described from the middle Ilerdian levels which has high diversity of *Alveolina* species. Considering other foraminiferal assemblages that accompany *Alveolina* species throughout the section, the age of cross section was determined as Thanetian - early Ypressian (middle Ilerdian).

A. (A.) acari n.sp., *A. (A.) ozbahçensis* n.sp. and *A. (A.) avsari fusunae* n.ssp. have been introduced for the first time. Possible new subspecies of *A. (A.) baldaccii*, *A. (A.) montanarii*, *A. (A.) muscatensis* and *A. (A.) rugosa* have been proposed, yet each has been named as spp1 in the related *Alveolina* species.

Stratigraphic distributions of some species such as *A. (A.) corbarica*, *A. (A.) ellipsoidalis*, *A. (A.) guidonis*, *A. (A.) moussoulensis*, *A. (A.) trempina*, *A. (A.) pasticillata*, *A. (A.) pisella* and *A. (A.) varians* show some differences comparing to their distributions known in the Tethyan province (Hottinger, 1960; Drobne, 1977; Serra-Kiel, 1998; Sirel and Acar, 2008). It has been also stated by some previous researchers that the benthic foraminiferal fauna on the Anatolian platform shows some differences with fauna in Western Mediterranean regions (Spain, Italy, France) (Özgen-Erdem et al., 2007; Sirel and Acar, 2008; Hadi et al., 2020).

Due to the fact that some key *Alveolina* species representing the shallow benthic zones (Serra-Kiel et al., 1998) coexist in the study area, the biozones corresponding to Thanetian (SBZ 3-4), early Ilerdian (SBZ 5-6) and middle Ilerdian (SBZ 7-8) were merged in this study.

Based on foraminiferal assemblages and their characteristics, it is seen that while the region was a lagoon with high salinity during the Thanetian period, it turned into a low energy shallow marine with normal salinity environment in the early and middle Ilerdian periods and relatively deepened in time.

Pre-Lutetian carbonate shelf sediments, which are missing in the regional paleogeographic models related to the formation of the Isparta Angle (e.g. Nemeç et al., 2017) but supporting these models, were identified in this study.

Acknowledgements

This article was prepared from a part of the first author's PhD thesis. In the sample collecting, facilities of the project no 2016-30-14-05 of Geological Researches Department of General Directorate of Mineral Research and Exploration (MTA) were benefited. We would like to thank Dr. Şükür Acar (MTA) for his supports to the laboratory studies and foraminiferal descriptions. Prof. Dr. Wojciech Nemeç (University of Bergen) made valuable contributions with his opinions on regional paleogeographic evaluations. We are thankful to Prof. Dr. Atike Nazik (Çukurova University), Prof. Dr. Marcelle BouDagher-Fadel (University College London) and the other two anonymous referees for their constructive criticism which improved the article.

References

- Acar, Ş. 1995. Türkiye'nin deęişik bölgelerinin Paleojen'inden bazı alveolin cinslerinin (*Alveolina* (*Alveolina*), *Alveolina* (*Glomalveolina*), *Borelis* ve *Praebullalveolina*) sistematik tanımları ve stratigrafik dağılımları. Doktora Tezi, Selçuk Üniversitesi, 166s., 38 Lev., Konya.
- Acar, Ş. 2019a. Burdur güneybatısı (Yarışlı Gölü güneyi, Batı Türkiye) Selandiyen yaşlı bentik foraminifer toplulukları ve bazı taksonomik revizyonlar. Maden Tetkik ve Arama Dergisi (2019) 158: 49-121.
- Acar, Ş. 2019b. *Alveolina* (*Glomalveolina*) Hottinger, 1960 ve *Alveolina* (*Alveolina*) d'Orbigny, 1826 altcinslerinin (Foraminiferida) tanımı, sistematığı ve revizyonu. Maden Tetkik ve Arama Dergisi (2019) 159, 91-99.
- Akıncı, Ö., Robertson, A., Poisson, A., Bozkurt, E. 2003. Preface: the Isparta Angle, SW Turkey – Its Role in the Evolution of Tethys in the Eastern Mediterranean Region. Geological Journal 38 (Spec. Issue 3–4), 191–193.
- Akkiraz, M.S., Akgün, F., Örcen, S. 2011. Stratigraphy and palaeoenvironment of the Lower-“middle” Oligocene units in the northern part of the Western Taurides (Incesu area, Isparta, Turkey). Journal of Asian Earth Science 40, 452-474.

- Balcı, V. 2011. 1:100.000 ölçekli Türkiye Jeoloji Haritaları Afyon L-24 paftası. Maden Tetkik ve Arama Genel Müdürlüğü, Ankara, No:162, 23s.
- Blumenthal, M. 1947. Seydişehir–Beyşehir hinterlandındaki Toros Dağlarının jeolojisi. Maden Tetkik ve Arama Enstitüsü Yayın Serisi, D2.
- Boudagher-Fadel, M.K. 2008. Evolution and Geological Significance of Larger Benthic Foraminifera, Developments in Paleontology and Stratigraphy 21, 1-540, Elsevier.
- BouDagher-Fadel, MK. 2018. Evolution and geological significance of larger Benthic Foraminifera. London: UCL Press. 704 p. Retrieved from <https://discovery.ucl.ac.uk/id/eprint/10047587/>
- BouDagher-Fadel, M. K., Price, G. D., Hu, X., Li, J. 2015. Late Cretaceous to early Paleogene foraminiferal biozones in the Tibetan Himalayas, and a pan-Tethyan foraminiferal correlation scheme. Stratigraphy 12 (1), 67-91.
- Bozkurt, A., Görmüş, M. 2019. Description Criteria for Eocene Alveolinids: Examples from Inner Western Anatolia. IOP Conf. Ser: Earth Environ. Sci. 362, 012019.
- Bozkurt, A., Görmüş, M., Türkmen-Bozkurt, B. 2021. Keçiborlu Kuzeyi (Isparta) Tanesiyen - Erken İpresiyen Alveolinidlerinin Biyoçeşitlilik İncelemesi ve Mikrofasiyeslere Dayalı Paleortamsal Yaklaşımlar. Uluslararası Katılımlı 73. Türkiye Jeoloji Kurultayı, Ankara, Türkiye (Baskıda).
- Bronn, H.G. 1825. System der urweltliche Pflanzthiere durch Diagnose, Analyse und Abbildung der Geschlechter erläutert: zum Gebrauche bey Vorlesungen über Petrefactenkunde und zur Erleichterung des Selbststudiums derselben. J.C.B. Mohr (Heidelberg). 1-59.
- D'Orbigny, A.D. 1826. Tableau méthodique de la classe des Cephalopodes. Annales des Sciences Naturelles 1, (7), 245-314, pl. 10-17, Paris.
- Davies, L.M., Pinfold, E.S. 1937. The Eocene Beds of the Punjab Salt Range. Memoirs of the Geological Survey of India, Palaeontologia Indica 24, 1-79.
- Debenay, J. P. 2012. A Guide to 1000 Foraminifera from Southwestern Pacific: New Caledonia. IRD éditions, Institut de recherche pour le développement, Marseille, Publications Scientifiques du Muséum, Muséum national d'Histoire naturelle, Paris 378.
- Delage, Y., Hérouard, E. 1896. Traité de Zoologie Concrète Vol. I. La Cellule et les Protozoaires, Paris: Schleicher Frères.
- Devoto, G. 1964. Zone ad Alveolinidae Nel Cretaceo e Paleocene Del Lazio Ed Abruzzo Centro-Meridionali. Geologica Romana III, 405-414.
- Dong, S., Lei, Y., Li, T., Jian, Z. 2018. Responses of benthic foraminifera to changes of temperature and salinity: Results from a laboratory culture experiment. Science China Earth Sciences 61, <https://doi.org/10.1007/s11430-017-9269-3>.
- Drobne, K. 1977. Alvéolines paléogènes de la Slovénie et de l'Istrie. Mémoires Suisses de Paléontologie 99, 9–174.
- Drobne, K., Čosović, V., Moro, A., Bucković, D. 2011. The role of the Palaeogene Adriatic Carbonate Platform in the spatial distribution of Alveolinids. Turkish Journal of Earth Sciences 20, 721–751.
- Ehrenberg, C. G. 1839. Über die Bildung der Kreidefelsen und des Kreidemergels durch unsichtbare organismen. Physikalische Abhandlungen der königlichen Akademie der Wissenschaften zu Berlin. 59-147.
- Fornaciari, B., Giusberti, L., Papazzoni, C.A. 2019. *Alveolina postalensis* n. sp. (Foraminifera, Alveolinidae) from the upper Ypresian of Monte Postale and Pesciara di Bolca (northern Italy). Bollettino della Società Paleontologica Italiana, 58 (2).
- Gaemers, P.A.M. 1978. Systematics of the Alveolinids of the Tremp Basin, South-Central Pyrenees, Spain. Leidse Geologische Mededelingen, Deel 51, Aflevering 1, 103-129.
- Görmüş, M., Karaman, E. 1992. Facies Changes and New Stratigraphical-Paleontological Data in the Cretaceous-Tertiary Boundary Around Söbüdağ (Çünür-Isparta). Çukurova Üniversitesi, Geosound 21, 43-57, Adana.
- Görmüş, M., Özkul, M. 1995. Gönen–Atabey (Isparta) ve Ağlasun (Burdur) arasındaki bölgenin stratigrafisi. Süleyman Demirel Üniversitesi Fen Bilimleri Enstitüsü Dergisi 1, 43–64.
- Görmüş, M., Nielsen, J.K. 2006. Borings in Larger Benthic Foraminifera From Turkey And Their Paleoenvironmental Significance. Journal of Foraminiferal Research 36 (2), 152-165.
- Gutnic, M., Monod, O., Poisson, A., Dumont, J.F. 1979. Géologie du Taurus occidentals (Turquie). Mémoires de la Société géologique de France 137, 1–112.
- Hadi, M., Vahidina, M., Abbasi, N. 2019. Ilerdian-Cuisian alveolinids from the western Alborz and eastern Iran zones: systematic and biostratigraphic implications. Journal of Foraminiferal Research 49, 141–162.

- Hadi, M., Özgen-Erdem, N., Sinanoğlu, D., Sarkar, S., Zareh, A. 2020. Distribution of *Alveolina* assemblages in the Ypresian (Ilerdian-Cuisian) successions from Iran and Turkey (central and western Tethys): biostratigraphic implications for regional correlation. *Micropaleontology* 66 (1), 51-74.
- Hallock, P., Hansen, H.J. 1979. Depth adaptation in *Amphistegina*: change in lamellar thickness: *Bulletin of the Geological Society of Denmark* 27, 99-104.
- Hallock, P., Glenn, E.C. 1982. Larger Foraminifera: A Tool for Paleoenvironmental Analysis of Cenozoic Carbonate Depositional Facies. *Palaios* 1 (1), 55-64.
- Hottinger, L. 1960. Recherches sur les Alveolines du Paleocene et de l'Eocene: *Abhandlungen der Schweizerischen Palaontologischen Gesellschaft* 75-76, 1-243.
- Hottinger, L. 1974. Alveolinids, Cretaceous-Tertiary Larger Foraminifera. *Esso Production Research-European Laboratories, Text and Plate Volumes* 70p., 106 plates, Basle.
- Hottinger, L. 1977. Distribution of larger Peneroplidae, Borelis and Nummulitidae in the Gulf of Elat, Red Sea: *Utrecht Micropaleontological Bulletins* 15, 35-109.
- Hottinger, L. 1997. Shallow benthic foraminiferal assemblages as signals for depth of their deposition and their limitations. *Bulletin de la Société géologique de France* 168 (4), 491-505.
- Jarvis, A., Reuter, H.I., Nelson, A., Guevara, E. 2008. Hole-filled SRTM for the Globe, Version 4. CGIAR-CSI SRTM 90m Database <http://srtm.csi.cgiar.org>
- Jorissen, F., Fontanier, C., Thomas, E. 2007. Paleocyanographical proxies based on deep-sea benthic foraminiferal assemblage characteristics. In: Hillaire-Marcel C, Vernal A de, eds. *Proxies in Late Cenozoic paleocyanography*. Amsterdam: Elsevier Science. 263-326.
- Karaman, M.E. 1990. Isparta güneyinin temel jeolojik özellikleri. *Türkiye Jeoloji Bülteni* C.33, 57-67.
- Karaman, M.E. 1994. Isparta-Burdur arasının jeolojisi ve tektonik özellikleri. *Türkiye Jeoloji Bülteni* 37 (2), 119-134.
- Karaman, M.E. 2000. Tectono-Stratigraphic Outline of the Burdur-Isparta Area (Western Taurides, Turkey). *Türkiye Jeoloji Bülteni* 43 (2), 71-81.
- Karaman, M.E., Meriç, E., Tansel, İ. 1988. Çünür (Isparta) dolaylarında Kretase-Tersiyer geçişi. *Akdeniz Üniversitesi Isparta Mühendislik Fakültesi Dergisi* 4, 80-100.
- Koçyiğit, A. 1980. Hoyran Gölü yöresinin (Afyon-Isparta) stratigrafik ve tektonik özellikleri. Doçentlik Tezi, Ankara Üniversitesi, Fen Fakültesi 172 s (unpublished).
- Koçyiğit, A. 1983. Hoyran Gölü (Isparta Büklümü) Dolayının Tektoniği. *Türkiye Jeoloji Kurumu Bülteni* 26, 1 -10.
- Köse-Yeşilot, S. 2000. Dinar-Isparta arasındaki eosan bentik foraminiferlerinin sistematik ve biyofabrik incelemesi. Yüksek Lisans Tezi, Süleyman Demirel Üniversitesi, Fen Bilimleri Enstitüsü 116 s.
- Loeblich, A.R., Tappan, H. 1987. Foraminiferal genera and their classification. Vol. 1, 1-970; 2. New York (Von Nostrand Reinhold).
- Luterbacher, H.P. 1970. Environmental distribution of early Tertiary microfossils, Tremp Basin, Northeastern Spain. *ESSO Production Research-European Laboratories*, 46p.
- Murray, J.W. 1991. Ecology and Palaeoecology of Benthic Foraminifera. *Routledge Taylor ve Francis Group*, ISBN13: 978-0-582-05122-5 (pbk)
- Murray, J.W. 2006. Ecology and Applications of Benthic Foraminifera. *Cambridge University Press*, ISBN-13: 978-0-511-33519-8.
- Nemec, W., Alçiçek, M.C., Özaksoy, V. 2017. Sedimentation in a foreland basin within synorogenic orocline: Palaeogene of the Isparta Bend, Taurides, SW Turkey. *Basin Research* 30: 650-670.
- Özcan, E., Abbasi, İ.A., Drobne, K., Govindan, A., Jovane, L., Boukhalfa, K. 2015. Early Eocene orthophragminids and alveolinids from the Jafnayn Formation, N Oman: significance of *Nemkovella* stockari Less ve Özcan, 2007 in Tethys. *Geodinamica Acta*, DOI: 10.1080/09853111.2015.1107437.
- Özgen-Erdem, N. 2008. Akçataş - Cebeci Yöresinin (KB Tosya – GD Kastamonu) Tanesiyen - İlerdiyen Bentik Foraminifer Biyostratigrafisi. *Maden Tetkik ve Arama Dergisi* 137, 67-77.
- Özgen Erdem, N., İnan, N., Akyazı, M., Tunoğlu C. 2005. Benthonic foraminiferal assemblages and microfacies analysis of Paleocene-Eocene carbonate rocks in the Kastamonu region, Northern Turkey. *Journal of Asian Earth Sciences* 25 (3), 403-417.
- Özgen-Erdem, N., Akyazı, M., Karabaşoğlu, A. 2007. Biostratigraphic interpretation and systematics of *Alveolina* assemblages from the Ilerdian-Cuisian limestones of Southern Eskişehir, Central Turkey. *Journal of Asian Earth Sciences* 29, 911-927.

- Özgen-Erdem, N., Canbolat, M.Y., Sinanoğlu, D. 2016. Araç Kuzeydoğusu (Kastamonu) Erken Eosen Sığ-Denizel Bentik Foraminifer Topluluğu ve Paleokolojik Yorum. Türkiye Jeoloji Bülteni 59 (3), 259-273.
- Özkan, T. 1991. Göлтаş-Senirce-Çünür (Isparta ili) dolayında Kretase-Tersiyer geçişi. Yüksek Lisans Tezi, İstanbul Üniversitesi, Fen Bilimleri Enstitüsü, 54 s.
- Öztürk, Z., Öztürk, E.M. 1989. Balçıkhisar - Karadilli (Afyon) - Dereköy (Isparta) dolayının jeolojisi. Maden Tetkik ve Arama Genel Müdürlüğü Rapor no:8946 (unpublished).
- Pawlowski, J., Holzmann, M., Tyszka, J. 2013. New supraordinal classification of Foraminifera: Molecules meet morphology. Marine Micropaleontology Volume 100, 1-10.
- Poisson, A., Orsay, A., Akay, E., Dumont, J.F., Uysal, S. 1984. The Isparta Angle: a Mesozoic palaeorift in the Western Taurides. In Geology of Taurus Belt, Tekeli O., Göncüoğlu M.C. (eds). Proceedings of International Symposium on the Geology of the Taurus Belt, Mineral Research and Exploration Institute (MTA) of Turkey Publication, 11–26.
- Reiss, Z., Hottinger, L. 1984. The Gulf of Aqaba, Ecological Micropaleontology. Ecological Studies vol. 50. Berlin: Springer-Verlag.
- Robertson, A.H.F., Poisson, A., Akıncı, Ö. 2003. Developments in research concerning Mesozoic–Tertiary Tethys and neotectonics in the Isparta Angle, SW Turkey. Geol. J. 38, 195–234.
- Roskov, Y., Ower, G., Orrell, T., Nicolson, D., Bailly, N., Kirk, P.M., Bourgoin, T., DeWalt, R.E., Decock, W., Nieukerken, E. van, Zarucchi, J., Penev, L. (eds.) 2019. Species 2000 ve ITIS Catalogue of Life, 2019 Annual Checklist. Dijital kaynak erişimi: www.catalogueoflife.org/annual-checklist/2019. Species 2000: Naturalis, Leiden, the Netherlands. ISSN 2405-884X.
- Sagular, E.K., Görmüş, M. 2006. New stratigraphical results and significance of reworking based on nannofossil, foraminiferal and sedimentological records in the Lower Tertiary sequence from the northern Isparta Angle, Eastern Mediterranean. Journal of Asian Earth Sciences 27, 78–98.
- Sariiz, K. 1985. Keçiborlu kükürt yataklarının oluşumu ve yörenin jeolojisi. Anadolu Üniv. yayın no: 91, Doktora Tezi.
- Scheibner, C. Speijer, R.P. 2009. Recalibration of the Tethyan shallow-benthic zonation across the Paleocene-Eocene boundary: the Egyptian record. Geologica Acta 7, (1-2), 195-214.
- Schwager, C. 1883. Die Foraminiferen aus den Eocaenablagerungen der lybischen Wüste und Aegyptens. Paleontographica (A), 30 (1), 79-154.
- Serra-Kiel, J., Hottinger, L., Caus, E., Drobne, K., Ferrandez, C., Jauhri, A.K., Less, G., Pavlovec, R., Pignatti, J., Samsó, J.M., Schaub, H., Sirel, E., Strougo, A., Tambareau, Y., Tosquella, J., Zakrevskaya, E. 1998. Larger foraminiferal biostratigraphy of the Tethyan Paleocene and Eocene. Bulletin Société Géologique France 169 (2), 281–299.
- Sirel, E. 1998. Foraminiferal description and biostratigraphy of the Paleocene-lower Eocene shallow-water limestones and discussions on the Cretaceous-Tertiary boundary in Turkey. General Directorate of the Mineral Research and Exploration, Monography series 2, 1-117, Pls. 68.
- Sirel, E. 2003. Foraminiferal description and biostratigraphy of the Bartonian, Priabonian and Oligocene shallow-water sediments of the southern and eastern Turkey. Revue de Paléobiologie, Genève, 22 (1), 269-339.
- Sirel, E., Acar, Ş. 1982. *Praebullalveolina*, a new foraminiferal genus from the Upper Eocene of the Afyon and Çanakkale region (west of Turkey). Eclogae geologicae Helvetiae 75 (3), 821-839.
- Sirel, E., Acar, Ş. 2008. Description and Biostratigraphy of the Thanetian-Bartonian Glomalveolinids and Alveolinids of Turkey. TMMOB Jeoloji Mühendisleri Odası Yayınları 103 (Chamber of Geological Engineers of Turkey, Publication 103), Scientific Synthesis of the Lifelong Achievement, Special 2, 108 p., 108 pls., Ankara.
- Sirel, E. Özgen-Erdem, N. Kangal, Ö. 2013. Systematics and biostratigraphy of Oligocene (Rupelian-Early Chattian) foraminifera from lagoonal-very shallow water limestone in the eastern Sivas Basin (Central Turkey). Geologia Croatica 66 (2), 83-109.
- Şenel, M. 1997. 1:100.000 ölçekli Türkiye Jeoloji Haritaları Isparta J-10 (M24) paftası. Maden Tetkik ve Arama Genel Müdürlüğü, Ankara, No:13.
- Vecchio, E., Barattolo, F., Hottinger, L. 2007. Alveolina horizons in the Trentinara Formation (Southern Apennines, Italy): stratigraphic and paleogeographic implications. Rivista Italiana di Paleontologia e Stratigrafia (Research In Paleontology and Stratigraphy) 113: 509–533.
- Waldron, J.W.F. 1984. Structural history of the Antalya Complex in the 'Isparta Angle', southwest Turkey. In: The Geological Evolution of the Eastern Mediterranean (Ed. by J.E. Dixon and A.H.F. Robertson), Geological Society of London, Special Publications 17, 273–286.

- White, M. R. 1992. On species identification in the foraminiferal genus *Alveolina* (Late Paleocene–Middle Eocene). *Journal of Foraminiferal Research* 22 (1), 52–70.
- Yalçinkaya, S., Ergin, A., Afşar, Ö.P., Taner, K. 1986. Batı Torosların Jeolojisi. Maden Tetkik ve Arama Genel Müdürlüğü Rapor no:7898 (unpublished).
- Yıldız, A., Toker, V. 1991. Çünür köyü yöresindeki (Isparta kuzeyi) Üst Kretase-Eosen yaşlı birimlerin planktik foraminiferler ile biyostratigrafik incelemesi. *Türkiye Jeoloji Kurumu Bülteni* 34 (2), 43-58.
- Yüzgöl, N.S. 2016. Gökçebağ (Burdur) ve Gölbaşı (Isparta) yöresindeki erken tersiyer denizel kayaç serilerinin nannoplankton stratigrafisi, Yüksek Lisans Tezi, Süleyman Demirel Üniversitesi, Fen Bilimleri Enstitüsü, 144 s.

PLATES

PLATE 1

- 1- *Alveolina (Glomalveolina)* sp., non-centered oblique section, (ÖZ-4-14).
- 2- *Alveolina (Glomalveolina)* aff. *karsica* SIREL, axial section, megalospheric? form, (ÖZ-6-12).
- 3- *Alveolina (Glomalveolina)* cf. *subtilis* HOTTINGER; axial section, (ÖZ-6-6).
- 4- *Alveolina (Glomalveolina)* *karsica* SIREL, axial section, megalospheric form, (ÖZ-3-2.1).
- 5- *Alveolina (Glomalveolina)* *lepidula* (SCHWAGER), axial section, megalospheric form, (ÖZ-5A-2.3).
- 6- *Alveolina (Alveolina)* *cemali* SIREL and ACAR, slightly oblique axial section, microspheric form, (ÖZ-5B-10-1).
- 7- *Alveolina (Alveolina)* *cemali* SIREL and ACAR, broken specimen, slightly oblique axial section, megalospheric form, (ÖZ-6-14-1).
- 8- *Alveolina (Alveolina)* *aragonensis* HOTTINGER, axial section, megalospheric form, (ÖZ-11-13).
- 9- *Alveolina (Alveolina)* *baldacci* CHECCHIA-RISPOLI ssp1., axial section, megalospheric form, (ÖZ-11-16).
- 10- *Alveolina (Alveolina)* *decipiens* SCHWAGER, axial section, megalospheric form, (ÖZ-5A-5-1).

PLATE 1

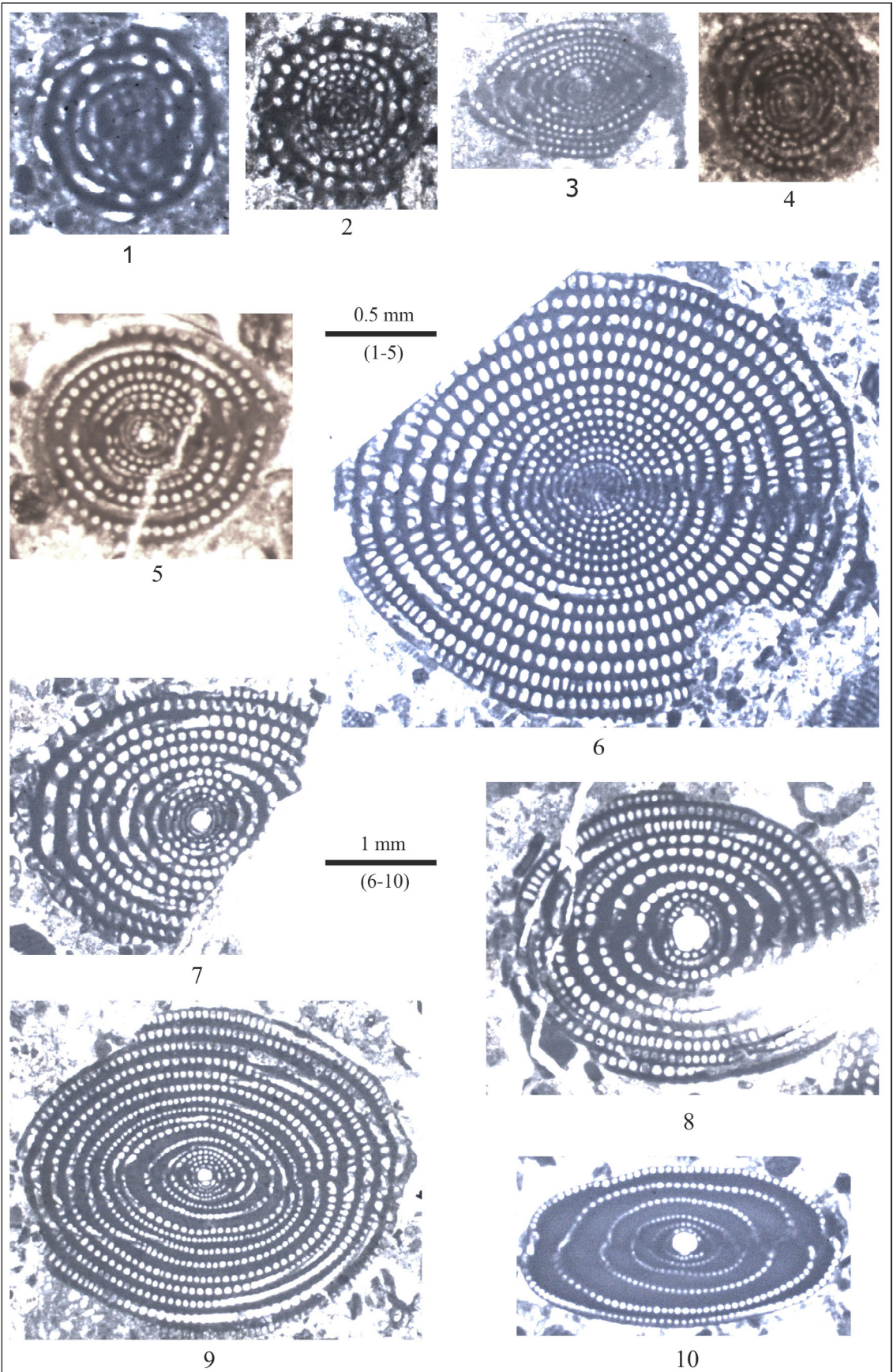


PLATE II

- 1- *Alveolina (Alveolina) acari* n.sp., holotype, broken axial section, megalospheric form, (ÖZ-6-10).
- 2- *Alveolina (Alveolina) acari* n.sp., axial section, megalospheric form, (ÖZ-6-21).
- 3- *Alveolina (Alveolina) acari* n.sp., slightly oblique axial section, megalospheric form, (ÖZ-6-19).
- 4- *Alveolina (Alveolina) acari* n.sp., axial section, megalospheric form, (ÖZ-8A-14).
- 5- *Alveolina (Alveolina) acari* n.sp., axial section, megalospheric form, (ÖZ-6-9).

PLATE II

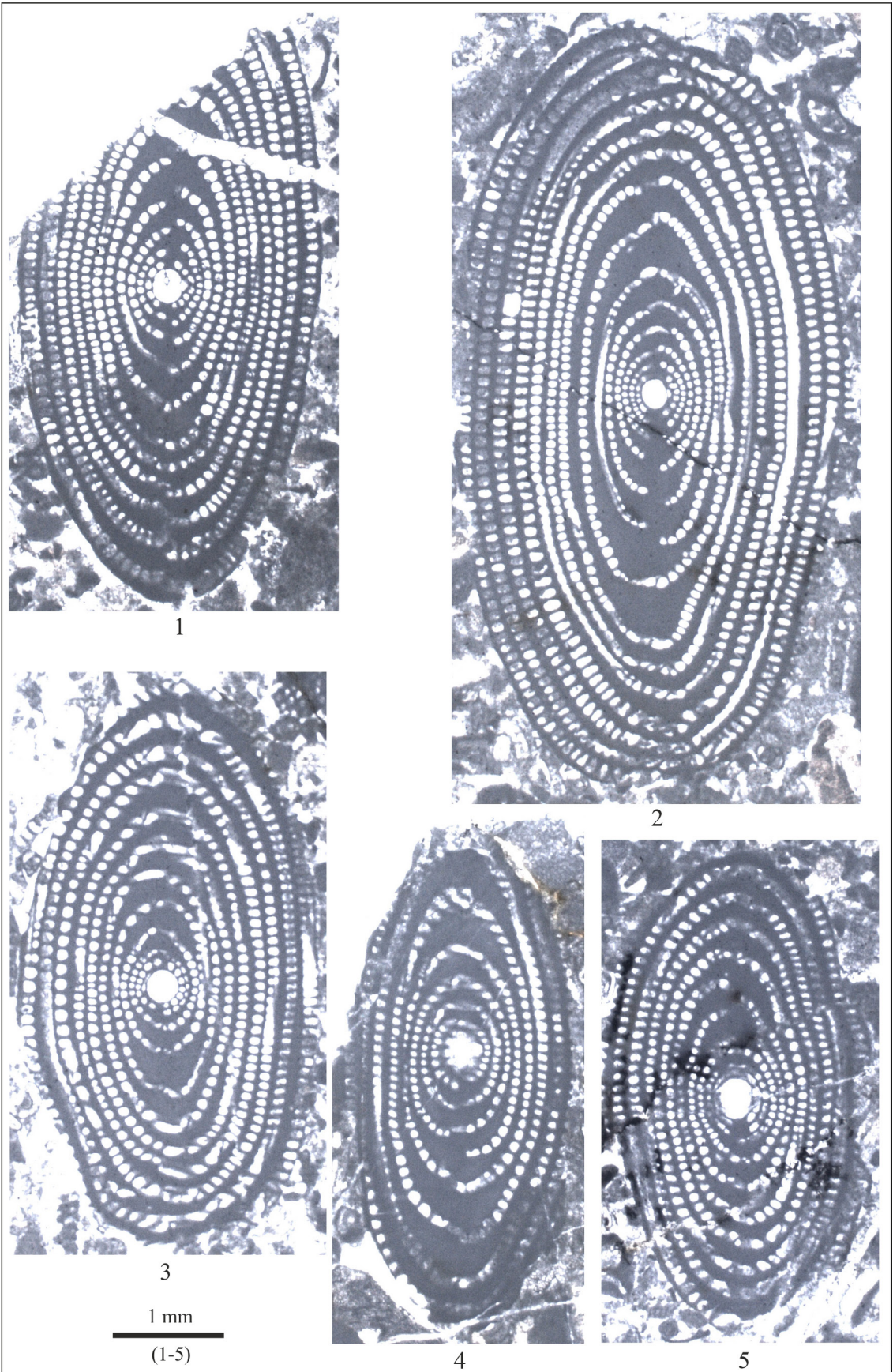


PLATE III

- 1- *Alveolina (Alveolina) ozbahcensis* n.sp., holotype, broken axial section, megalospheric form, (ÖZ-7-19).
- 2- *Alveolina (Alveolina) ozbahcensis* n.sp., slightly oblique axial section, megalospheric form, (ÖZ-5A-6).
- 3- *Alveolina (Alveolina) ozbahcensis* n.sp., slightly oblique axial section, megalospheric form, (ÖZ-6-15).
- 4- *Alveolina (Alveolina) ozbahcensis* n.sp., axial section, megalospheric form, (ÖZ-7-15).
- 5- *Alveolina (Alveolina) muscatensis* WHITE ssp1, axial section, microspheric? form, (ÖZ-7-19).
- 6- *Alveolina (Alveolina) avsari* SİREL and ACAR *fusunae* n.ssp., holotype, axial section, megalospheric form, (ÖZ-11-5-1).
- 7- *Alveolina (Alveolina) avsari* SİREL and ACAR *fusunae* n.ssp., broken axial section, megalospheric form, (ÖZ-7-17).
- 8- *Alveolina (Alveolina) erki* ACAR, slightly oblique axial section, megalospheric form, (ÖZ-11-4).
- 9- *Alveolina (Alveolina) rugosa* HOTTINGER ssp1, axial section, megalospheric form, (ÖZ-6-11).
- 10- *Alveolina (Alveolina) rotundata* HOTTINGER *kazancii* SİREL and ACAR, axial section, megalospheric form, (ÖZ-7-23).

PLATE III

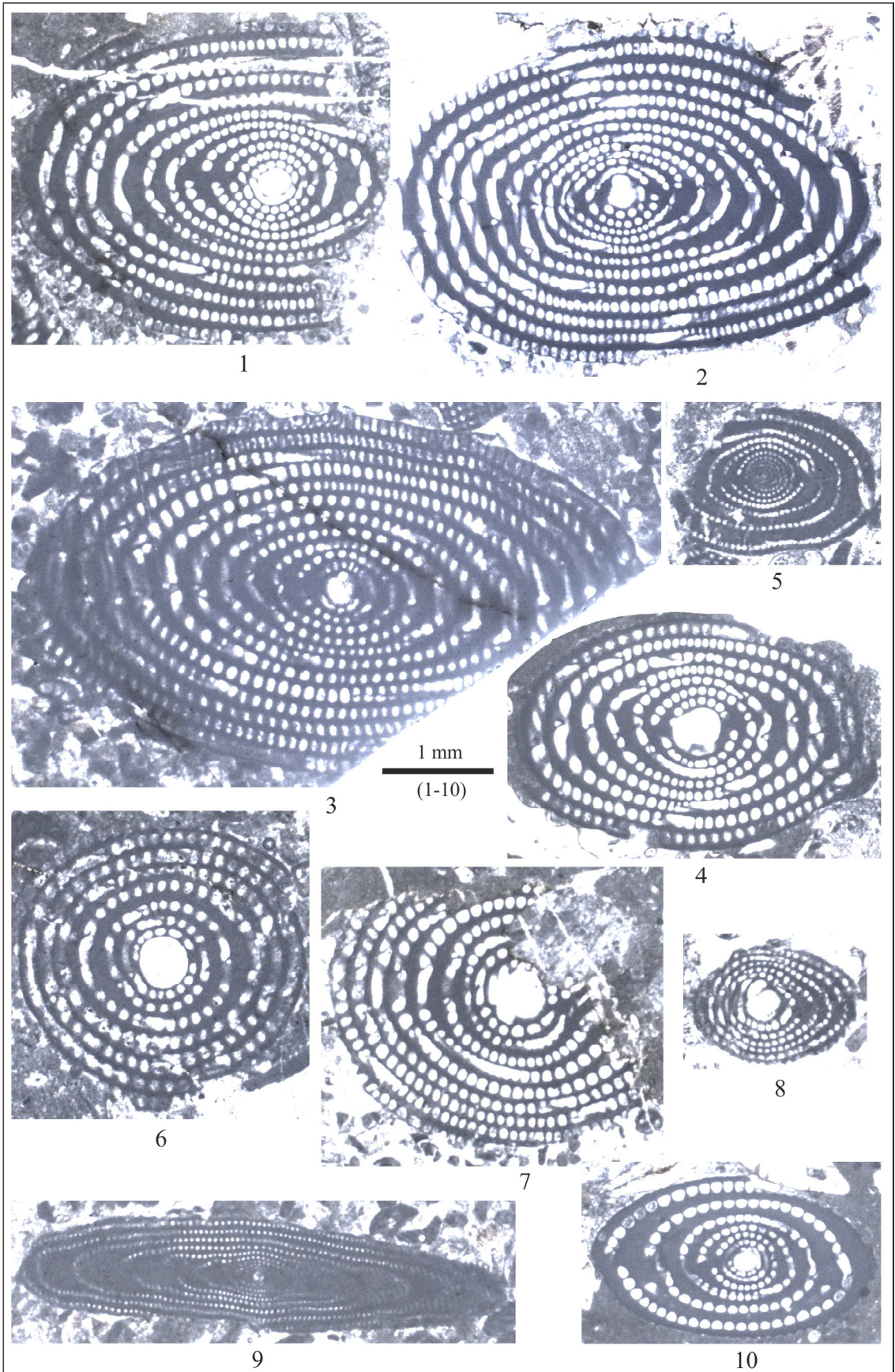


PLATE IV

- 1- *Alveolina (Alveolina) vredenburgi* DAVIES and PINFOLD, axial section, megalospheric form, (ÖZ-6-7-1).
- 2- *Alveolina (Alveolina) pisella* DROBNE, axial section, megalospheric form, (ÖZ-1-15-1).
- 3- *Alveolina (Alveolina) varians* HOTTINGER, axial section, megalospheric form, (ÖZ-3-7).
- 4- *Alveolina (Alveolina) corbarica* HOTTINGER, slightly oblique axial section, megalospheric form, (ÖZ-3-8).
- 5- *Alveolina (Alveolina) corbarica* HOTTINGER, axial section, megalospheric form, (ÖZ-11-6).
- 6- *Alveolina (Alveolina) pasticillata* (SCHWAGER), axial section, megalospheric form, (ÖZ-1-11).
- 7- *Alveolina (Alveolina) cf. coudurensis* HOTTINGER, subaxial section, megalospheric form, (ÖZ-5B-8).
- 8- *Alveolina (Alveolina) trempina* HOTTINGER, broken axial section, megalospheric form, (ÖZ-12-5).
- 9- *Alveolina (Alveolina) cf. ilerdensis* HOTTINGER, almost axial section, megalospheric form, (ÖZ-12-16).
- 10- *Alveolina (Alveolina) ellipsoidalis* SCHWAGER, axial section, megalospheric form, (ÖZ-3-5).
- 11- *Alveolina (Alveolina) dedolia* DROBNE, axial section, megalospheric form, (ÖZ-8A-4).

PLATE IV

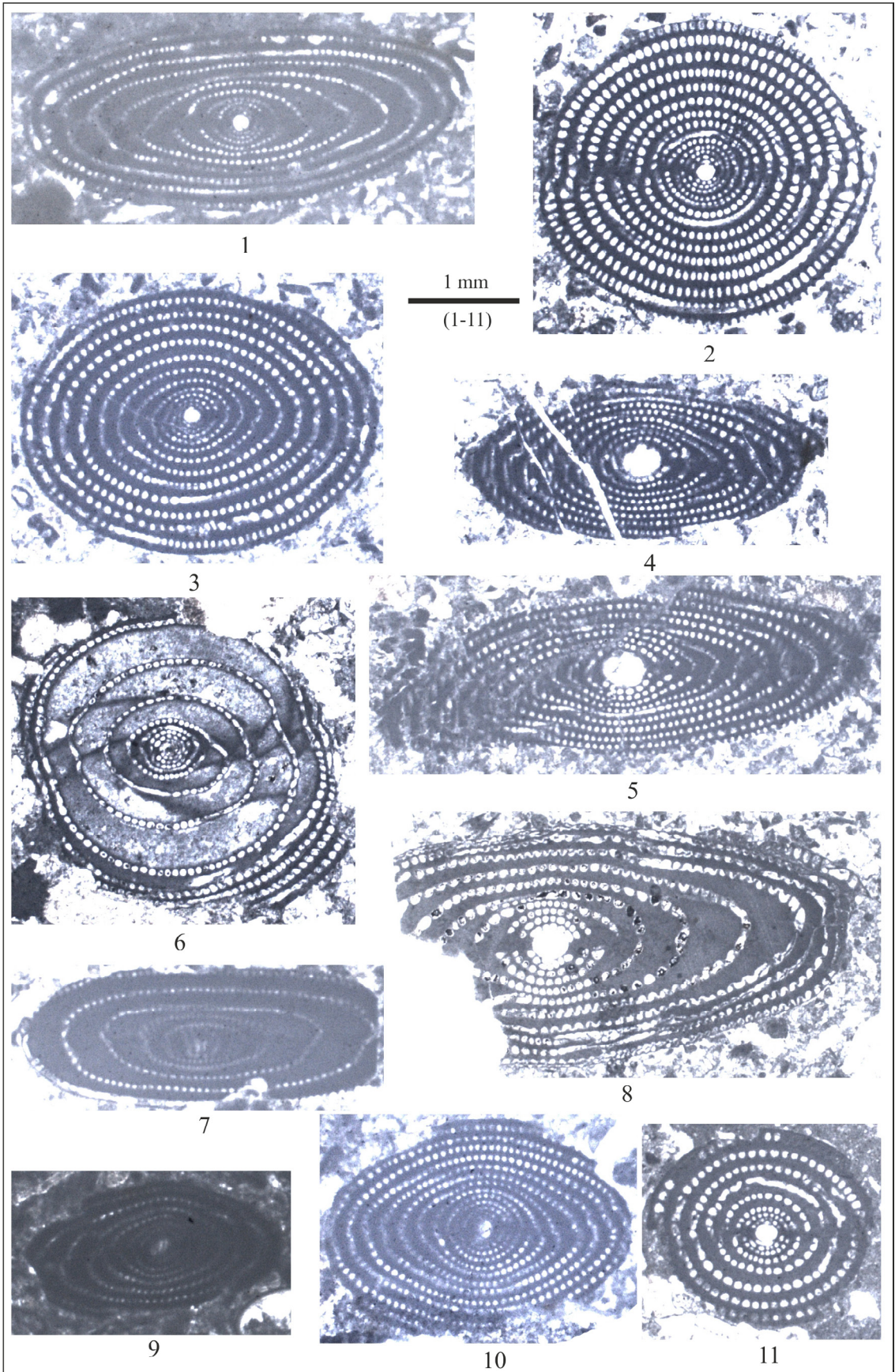


PLATE V

- 1- *Alveolina (Alveolina) moussoulensis* HOTTINGER, axial section, megalospheric form, (ÖZ-6-20).
- 2- *Alveolina (Alveolina) montanarii* DROBNE ssp1, axial section, microspheric? form, (ÖZ-8A-12).
- 3- *Alveolina (Alveolina) montanarii* DROBNE, axial section, megalospheric form, (ÖZ-12-3).
- 4- *Alveolina (Alveolina) guidonis* DROBNE, oblique axial section, megalospheric form, (ÖZ-5A-8).
- 5- *Alveolina (Alveolina) montanarii* DROBNE, slightly oblique axial section, megalospheric form, (ÖZ-11-20).
- 6- *Discocyclus* sp., axial section, megalospheric form, (ÖZ-11-9Dsc).
- 7- *Slovenites?* sp., vertical section, megalospheric form, (ÖZ-7-1-2).
- 8- *Ranikothalia* cf. *polatliensis* SIREL, axial section, microspheric? form, (ÖZ-6-2.6).
- 9- *Assilina* sp., axial section, microspheric form, (ÖZ-7-6Asl).
- 10- *Ranikothalia* cf. *nutalli* (DAVIES), axial section, megalospheric form, (ÖZ-5A-4).
- 11- *Nummulites* sp., broken axial section, microspheric form, (ÖZ-5B-14Num).

PLATE V

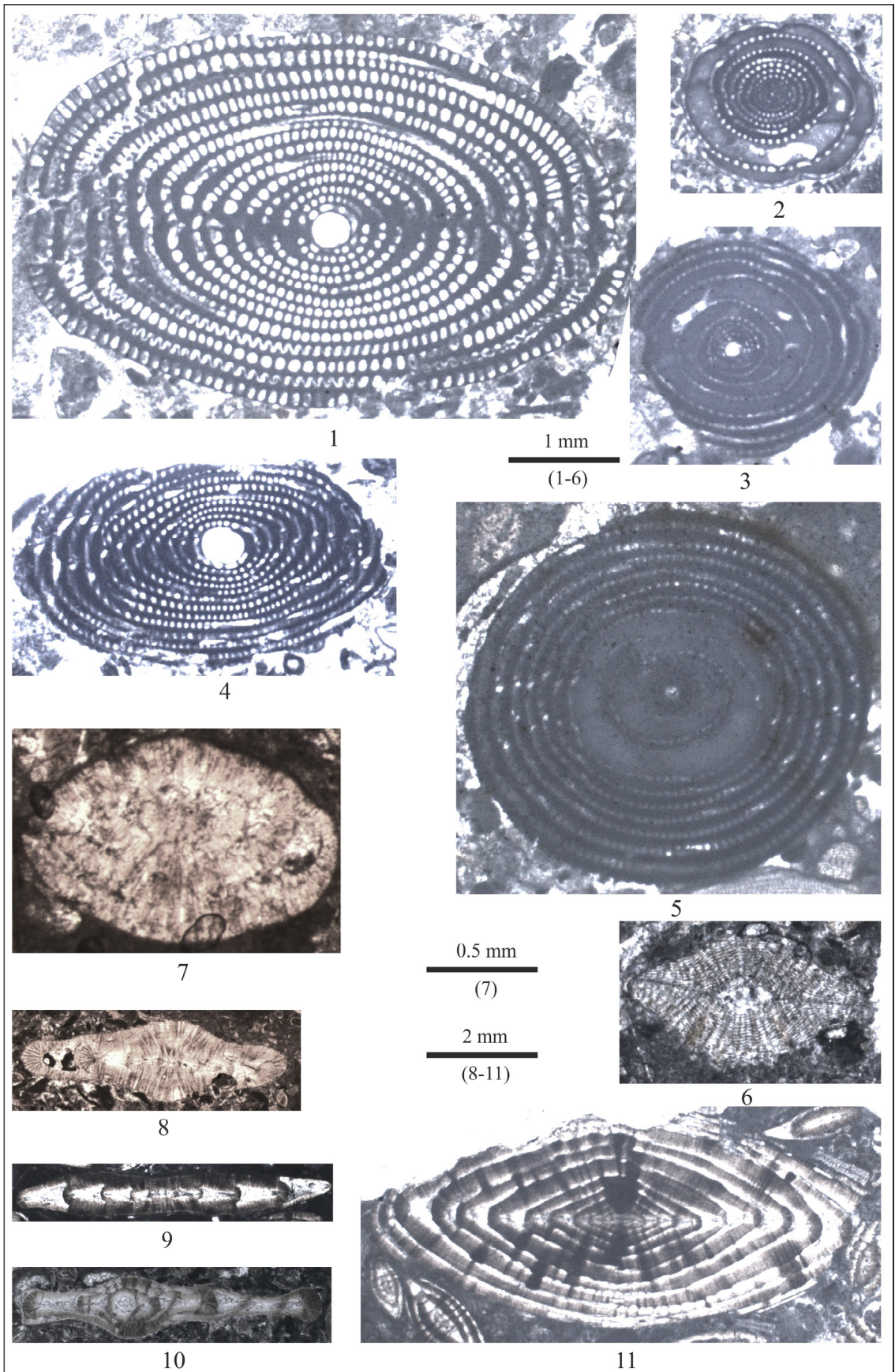


PLATE VI

- 1- *Orbitolites* cf. *complanatus* LAMARCK, non-centered oblique axial section, (ÖZ-11-11Orb).
- 2- *Orbitolites bellus* ZHANG, broken axial section, megalospheric form, (ÖZ-5B-1.3).
- 3- *Orbitolites* cf. *megasphericus* ZHANG, broken axial section, megalospheric form, (ÖZ-5A-1.2).
- 4- *Opertorbitolites latimarginalis* (LEHMANN), axial section, megalospheric form, (ÖZ-5B-1.3).
- 5- *Idalina causae* SIREL, section perpendicular to the apertural axis, megalospheric form, (ÖZ-4-8-2).
- 6- *Idalina sinjarica* GRIMSDALE, section parallel to the apertural axis, megalospheric form, (ÖZ-13-3).
- 7- *Idalina causae* SIREL, section perpendicular to the apertural axis, megalospheric form, (ÖZ-4-5).
- 8- *Idalina causae* SIREL, section perpendicular to the apertural axis, microspheric form, (ÖZ-4-7-1).
- 9- *Idalina causae* SIREL, section parallel to the apertural axis, microspheric form, (ÖZ-4-6).
- 10- *Operculina* sp., equatorial section, megalospheric form, (ÖZ-7-25Op).
- 11- *Ornatorotalia granum* BENEDETTI, DI CARLO and PIGNATTI, vertical section, (ÖZ-12-1.2).

PLATE VI

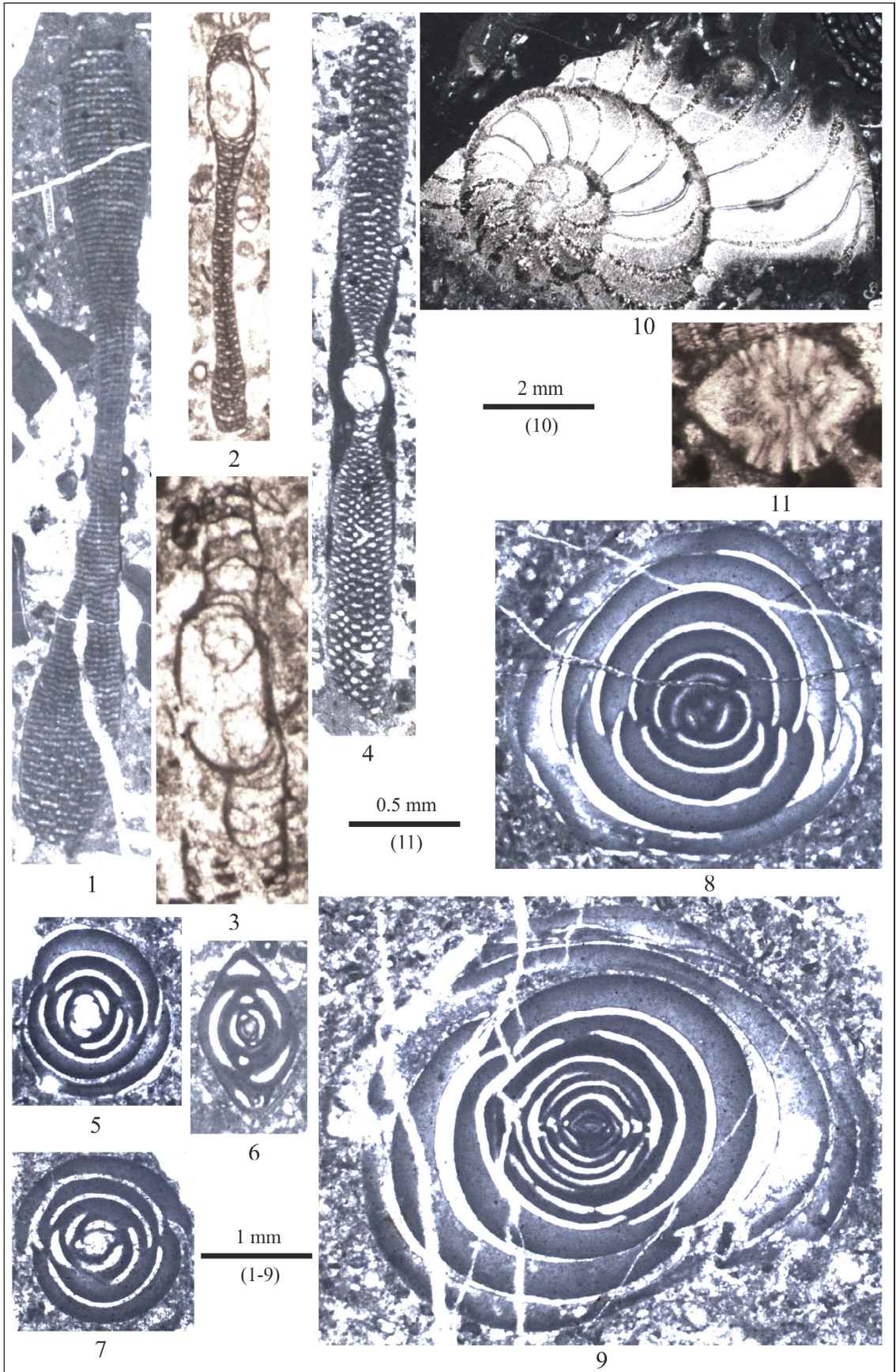
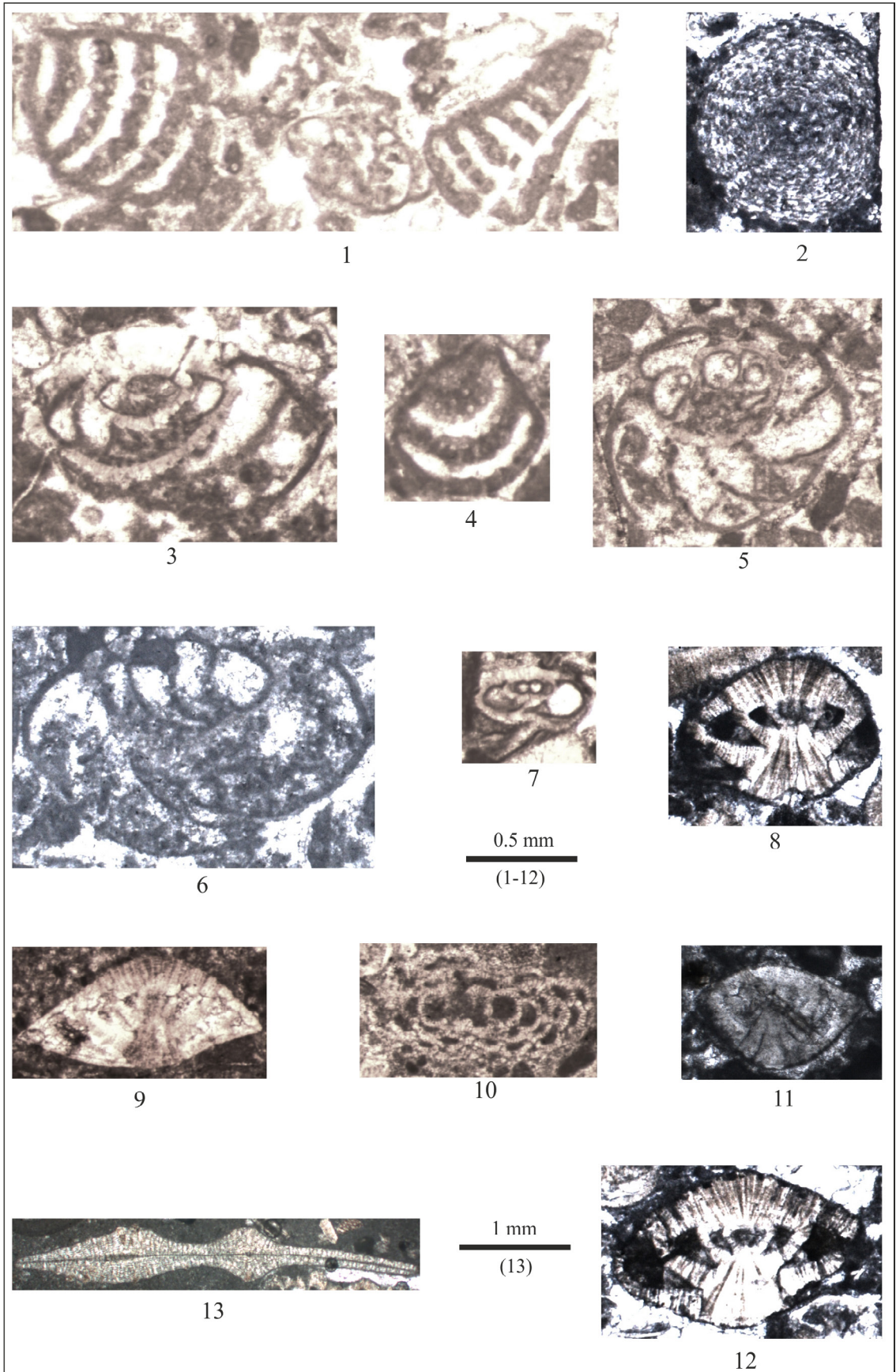


PLATE VII

- 1- *Socotraella?* sp., vertical sections (on the left and right), *Sistanites* sp. oblique section (in the middle), (ÖZ-9-1.4).
- 2- *Sphaerogypsina* sp., centered section, megalospheric form, (ÖZ-1-9).
- 3- *Sistanites catali* (ACAR), vertical section, megalospheric? form, (ÖZ-9-1-6).
- 4- *Socotraella?* sp., oblique basal section, (ÖZ-9-1-3).
- 5- *Sistanites iranicus* RAHAGHI, oblique section, megalospheric form, (ÖZ-9-2.1).
- 6- *Sistanites* cf. *guvenci* (ACAR), subvertical section, (ÖZ-9-3Sis).
- 7- Stomatorbinid form, vertical section, megalospheric form, (ÖZ-12-1.1).
- 8- *Elazigina* cf. *subsphaerica* (SIREL), vertical section, (ÖZ-1-5Rot).
- 9- *Rotalia* sp., vertical section, (ÖZ-4-2-1).
- 10- Gypsinid form, axial section, (ÖZ-12-1.1).
- 11- *Elazigina dieni* (HOTTINGER), vertical section, (ÖZ-9-4Rot).
- 12- *Elazigina* sp., vertical section, (ÖZ-5A-7).
- 13- *Asterocyclina* sp., axial section, (ÖZ-12-1.4).

PLATE VII





Bulletin of the Mineral Research and Exploration

<http://bulletin.mta.gov.tr>



Impact of solid waste on groundwater quality in selected dumpsites in Akwalbom State, Nigeria using resistivity and hydrochemical data

Abraham Christopher UDOH^{a*}, Augustine Ifeanyi CHINWUKO^b, Ajana Godwin ONWUEMESI^b, Emmanuel Kenechukwu ANAKWUBA^b, Augustine Oyonga OYONGA^c and Ayatu Ojonugwa USMAN^d

^aAkwa Ibom State University, Department of Geosciences, Mkpata Enin, Uyo, Nigeria

^bNnamdiAzikiwe University, Department of Applied Geophysics, Awka, Nigeria

^cUniversity of Calabar, Department of Geology, Calabar, Nigeria

^dAlex Ekwueme Federal University, Department of Physics/Geology/Geophysics, Ndufu-Alike Ikwo, Ebonyi State, Nigeria

Research Article

Keywords:

Schlumberger array, VES curve, Leachate, Transmissivity, Hydrogeological risk model.

ABSTRACT

This study examines the impact of solid waste on groundwater quality around three municipal dumpsites in Akwalbom State, Nigeria using resistivity and hydrochemical data. Thirty vertical electrical soundings and ten electrical resistivity tomography data were acquired across the area using Schlumberger array. The resistivity data which were analyzed with the aid of IPI2WIN software formed the input data for estimating and modeling leachate parameters. Twelve groundwater samples collected around the area were analyzed for physico-chemical parameters using Atomic Absorption Spectrometer (AAS). The leachate parameters computed from resistivity interpretation across the area show thickness (2 to 56 m); hydraulic conductivity (6.19 to 24.7 m/day); transmissivity (96.63 to 1351.18 m²/day) and erodibility (104.36 to 2948.94 m/day). The hydrochemical analyses reveal elevated values of Total Dissolved Solids, Cadmium and high electrical conductivity within the area. The leachate migration paths trend predominantly in NW-SE and NE-SW directions at Uyo and Oron, respectively. The hydrogeological risk models reveal that the static water level crisscrosses the leachate at 35 m in Oron, while Uyo area has 25 m gap between the leachate and the static water levels. The study concludes that Oron dumpsites really contaminated the groundwater quality and makes it unfit for the dwellers.

Received Date: 03.04.2020

Accepted Date: 12.06.2020

1. Introduction

Municipal solid waste (MSW) consists of refuse from homes, harmful solid waste from manufacturing, business and organizational firms such as hospitals, marketplaces, yard dissipate, along with avenue sweeping (Ogwueleka, 2009). Dahlin et al. (2010) established that the solid waste dumps consist of essential aspects of the soil hydrological composition along with a severe contamination risk to subsurface

and surface water. According to Christensen et al. (1992), the major local environmental problem of solid waste dump is the discharge of leachate into surrounding ground and surface waters. Indeed, the seepage that emanate from urban solid waste dumps is frequently linked with elevated ion concentrations with extremely low resistivity. In line with this, Frohlich et al. (2008) carried out an investigation on harmful effect of organic waste in parts of Western Rhode

Citation Info: Udoh, A. C., Chinwuko, A. I., Onwumesi, A. G., Anakwuba, E. K., Oyonga, A. O., Usman, A. O. 2021. Impact of solid waste on groundwater quality in selected dumpsites in Akwalbom State, Nigeria using resistivity and hydrochemical data. Bulletin of the Mineral Research and Exploration 164, 231-249.
<https://doi.org/10.19111/bulletinofmre.753240>

*Corresponding author: Abraham Christopher UDOH, abrahamudoh@aksu.edu.ng

Island of United State of America using electrical resistivity method. The scholars established that there were huge amount of harmful organic contaminants resulting from the dumpsite in the region and it has adversely contaminated the aquifers within the region.

Consequently, the use of waste dump for obvious reasons is not favorable because, it anticipates blowing garbage, foul odors, rodent infestations, increased truck traffic in the neighborhood as the trucks that bring the wastes drive in and out, hide-out for criminals and lowered property values. From an environmental and public health standpoint, probably, the most legitimate concerns about a waste dump are the potential to pollute the underlying groundwater with leaking liquid, called leachate. Contamination of any kind may be a signal that pollutants that are in fact hazardous to health and the environment are being transported from the dumpsites into groundwater reservoirs.

Generally, the management of refuse dumps in Nigeria is distinguished by ineffective collection scheme along with inappropriate dumping of refuse dumps or solid wastes. Due to influx of people in most of our cities in Nigeria including the study area, there are increases in disposal of solid wastes resulting from various consumer goods, which are mostly non-biodegradable materials. More so, both our surface and subsurface waters are not save from this ravaging environmental disasters because almost all companies discharge toxic chemicals in form of industrial wastes. Also, from our respective households, we do discharge raw sewage indiscriminately along with the sewage-truck which consistently dumped raw sewage into different water bodies around the environment, thereby polluting the water bodies within various states in Nigeria. However, a more severe case arises from the prevalent utilization of poisonous farming chemicals such as fertilizers in order to aid yield huge farm produces, but in turn causes groundwater pollution.

Akwalbom State faces major environmental challenges associated with poor waste management culminating in unregulated waste dumpsites in parts of the state especially at the study areas viz.: Uyo, IkotEkpene and Oron, which are located in the central, north-west and south-east parts of the State respectively (Figure 1). The dumpsites pose great risk to ground water quality as a result of leachate accumulation.

Although the layer parameters and geology of the area are essential in understanding the impact of leachate accumulation on groundwater, this information is not known, hence the need for this study. Furthermore, the study area which is predominantly underlain by mostly unconsolidated geological materials will surely pave way for infiltration and leaching of contaminants from the dumpsites into the groundwater body.

However, there is need to carry out a fast, reliable and non-invasive method of geophysical investigation in studying refuse dumps across the study area because investigations of contaminated sites are increasingly needed, both because of the pressure to reuse the land and increasingly stringent legislation to monitor contamination. Thus, the study aimed to determine the impact of solid waste on groundwater quality in selected dumpsites in AkwaIbom State using resistivity and hydrochemistry approach. The scope of this study includes the application of electrical resistivity techniques using vertical electrical sounding (VES) and tomography as well as hydrochemical methods to evaluate the physico-chemical properties of the groundwater. It also includes the interpretation of the rock layers encountered in the study area and evaluation of some layer parameters including the Dar Zarrouk parameters for establishment of major environmental challenges associated with waste generation and inadequate waste disposal and treatment within the study area.

1.1. Local Geology of the Study Area

Geologically, AkwaIbom State falls within two Sedimentary Basins of Nigeria: Anambra and Niger Delta Basins. Thus, the study area is overlain by three distinct lithostratigraphic units: Imo, Ameki and Benin Formations according to Mbipom et al., (1996); (Figure 1). The Imo Formation of Paleocene in age and it is underlying the Ameki Formation and it is mostly a mudrock layer comprising of dark grey to bluish grey shale, with intermittent intercalations of sandstone, ironstone, limestone and siltstone (Mbiopom et al., 1996; Nwajide, 2013). Ameki Formation is dated Eocene in age and it is the oldest geological material within the study area and Mbipom et al. (1996) established that the lithology comprises of loose false bedded, fine to medium sand, with few mudrock breaks. Also, overlying conformably on top of the Ameki Formation is the Benin Formation

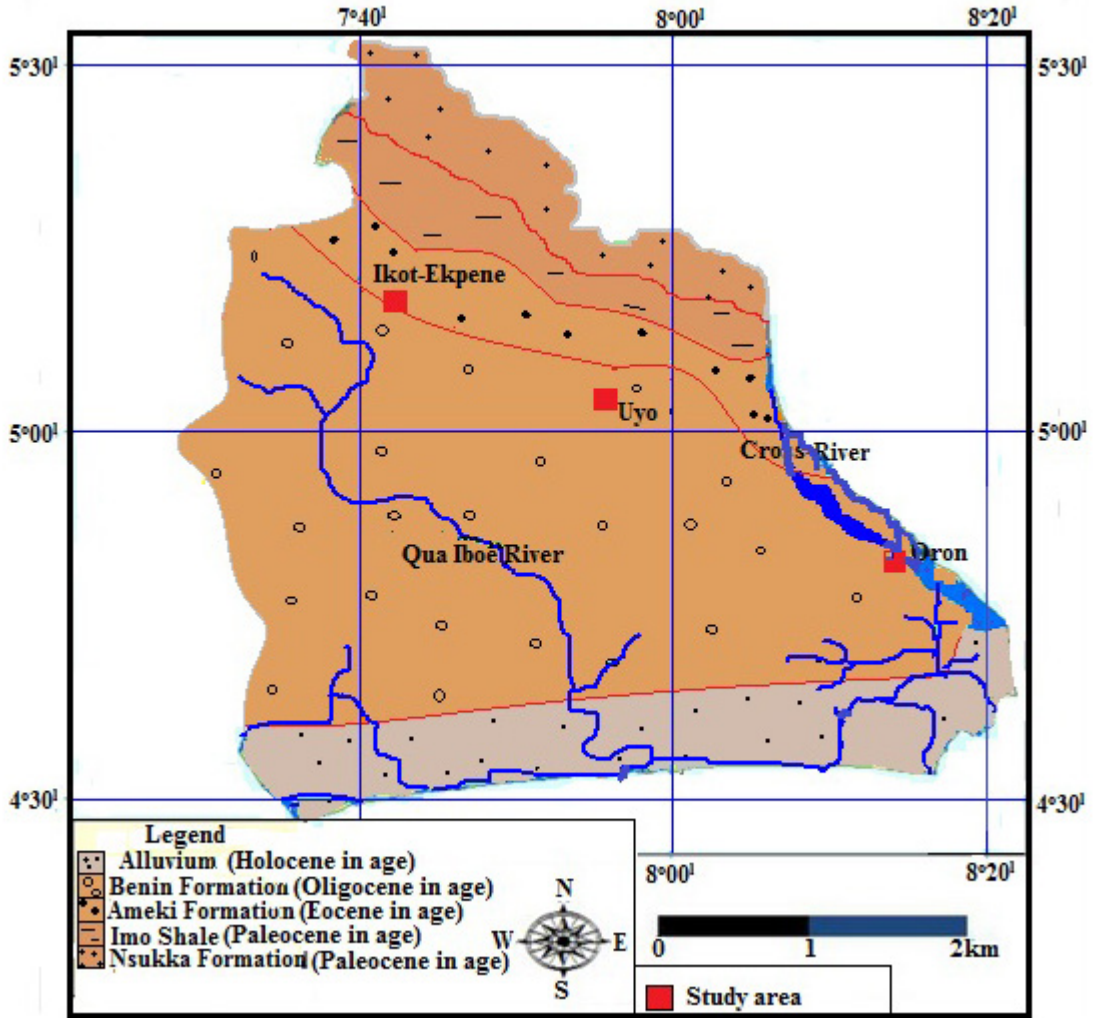


Figure 1- Geological map of Akwa Ibom State, Nigeria (Nigerian Geological Survey Agency, 2006).

of Oligocene in age which comprises of alternating sequences of gravels and sands of fine to medium/coarse grain sizes, and Quaternary alluvium (Ugbaja and Edet, 2004). In the view of Edet and Okereke (2002), the Benin Formation is to Recent in age and it is composed of continental materials such as sand (especially from flood plain), and alluvial deposits. It is good to note that the sand members of the Benin Formation are mature, coarse and poorly to moderately sorted with intercalations of silts and clays.

2. Methodology

The methodology involved the acquisition of thirty (30) vertical electrical soundings (VES) data along profile lines with survey stations placed at

equal intervals (30m) apart using Schlumberger configuration with current electrode spread ranged from 1 to 150 m across the study area (Figure 2). The coordinates of each station were taken using the global positioning system (GPS) equipment as shown in table 1a, b, c. A bi-logarithmic graph was used to plot current electrode spacing against the computed apparent resistivity values from the field data in order to generate various geoelectric attributes of layers penetrated such as resistivity and thickness of the layers. This technique has been functional in groundwater exploration by various investigators such as Heigold et al. (1979), Niwas and Singhal (1981), Olofsson et al. (2005), Onwuemesi and Egboka (2006), Nfor et al. (2007), Oseji and Ujuanbi (2009), Ezeh (2011), Okafor and Mamah (2012), Utom et

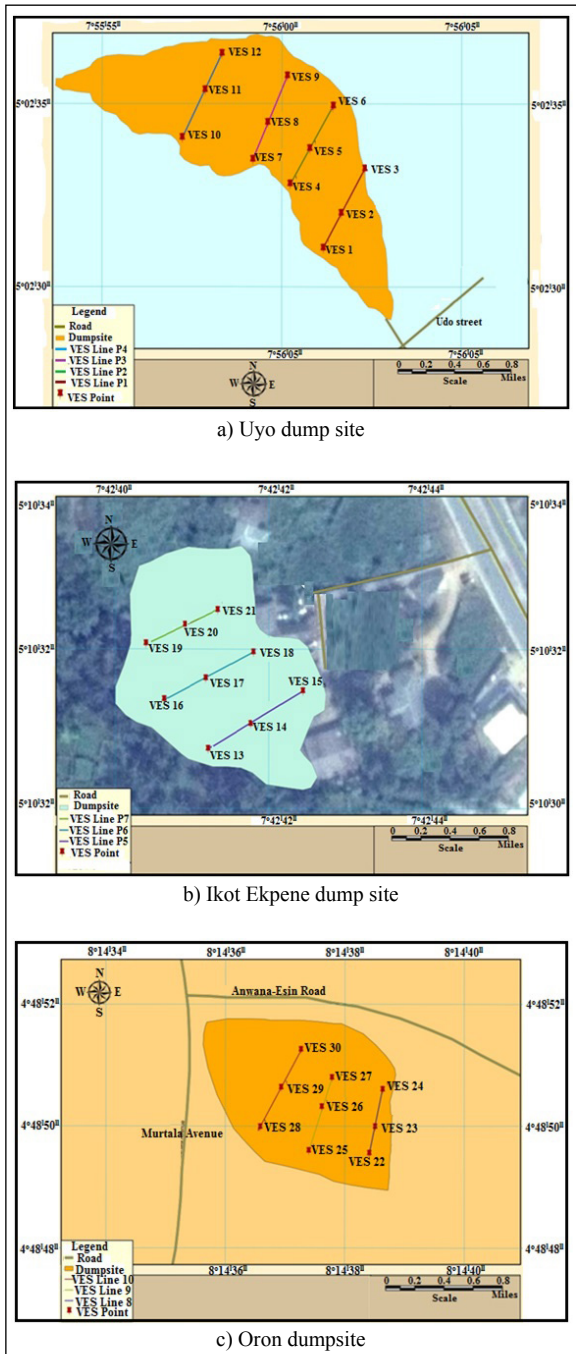


Figure 2- Map showing the geophysical VES points and geophysical VES profiles in the area.

al. (2012), Anakwuba et al. (2014), Chinwuko et al. (2015), Obiora et al. (2016), Amadi et al. (2017), Shaibu et al. (2018), Singh et al. (2018), Adeeko et al. (2019) and others.

According to Wunderlich et al. (2018), geoelectric data can be analyzed in a tomographic inversion process leading to images of the subsurface in terms of

Table 1- a) Coordinates of VES Stations at Uyo Dumpsite (VES line P1 – P4).

Label	Longitude (E)	Latitude (N)
P1VES1	7°56'1.303 ^{II}	5°2'31.051 ^{II}
P1VES2	7°56'1.812 ^{II}	5°2'32.025 ^{II}
P1VES3	7°56'2.457 ^{II}	5°2'33.135 ^{II}
P2VES4	7°56'0.398 ^{II}	5°2'32.773 ^{II}
P2VES5	7°56'1.043 ^{II}	5°2'33.628 ^{II}
P2VES6	7°56'1.518 ^{II}	5°2'34.857 ^{II}
P3VES7	7°55'59.325 ^{II}	5°2'33.454 ^{II}
P3VES8	7°55'59.885 ^{II}	5°2'34.462 ^{II}
P3VES9	7°56'0.291 ^{II}	5°2'35.708 ^{II}
P4VES10	7°55'57.861 ^{II}	5°2'36.303 ^{II}
P4VES11	7°55'58.369 ^{II}	5°2'35.708 ^{II}
P4VES12	7°55'59.014 ^{II}	5°2'36.048 ^{II}

Table 1- b) Coordinates of VES Stations at Ikot Ekpene Dumpsite (VES line P5 – P7).

Label	Longitude (E)	Latitude (N)
P5VES13	7°42'41.345 ^{II}	5°10'30.682 ^{II}
P5VES14	7°42'41.914 ^{II}	5°10'30.953 ^{II}
P5VES15	7°42'42.599 ^{II}	5°10'31.39 ^{II}
P6VES16	7°42'40.792 ^{II}	5°10'31.51 ^{II}
P6VES17	7°42'41.061 ^{II}	5°10'31.873 ^{II}
P6VES18	7°42'41.949 ^{II}	5°10'31.873 ^{II}
P7VES19	7°42'41.476 ^{II}	5°10'31.873 ^{II}
P7VES20	7°42'41.061 ^{II}	5°10'32.197 ^{II}
P7VES21	7°42'41.476 ^{II}	5°10'32.376 ^{II}

Table 1- c) Coordinates of VES Stations at Oron Dumpsite (VES line P8 – P10).

Label	Longitude (E)	Latitude (N)
P8VES22	7°56'1.303 ^{II}	5°2'31.051 ^{II}
P8VES23	7°56'1.812 ^{II}	5°2'32.025 ^{II}
P8VES24	7°56'2.457 ^{II}	5°2'33.135 ^{II}
P9VES25	7°56'0.398 ^{II}	5°2'32.773 ^{II}
P9VES26	7°56'1.043 ^{II}	5°2'33.628 ^{II}
P9VES27	7°56'1.518 ^{II}	5°2'34.857 ^{II}
P10VES28	7°55'59.325 ^{II}	5°2'33.454 ^{II}
P10VES29	7°55'59.885 ^{II}	5°2'34.462 ^{II}
P10VES30	7°56'0.291 ^{II}	5°2'35.708 ^{II}

resistivity (electric resistivity tomography). Therefore, electric resistivity tomography (ERT) usually results in different subsurface models that perfectly fit observed apparent resistivity values. In practice, four-point Multiple Vertical Electrical Sounding (MVES) such as the Schlumberger array run at constant stations interval along a profile is synonymous with Electrical Resistivity Tomography (ERT) and gives subsurface

layered resistivity images in two dimensions when modeled. The advantage of this survey type is that it allows the subsurface variation of resistivity values to be modeled both vertically and laterally, thus giving a clear resistivity image of the subsurface in 2D. The resistivity data was modeled using the computer resistivity iteration and inversion software called IPI2WIN, which is quite efficient in modeling resistivity data both by plotting apparent resistivity values against half-current electrode spacing ($AB/2$) and also generating pseudo and resistivity cross sections to give the resistivity image of the subsurface in resistivity profiling. Generally, the software has been used in many similar research works and has proven very effective for groundwater investigation and vulnerability studies. The VES results formed the input data for estimating and modelling leachate parameters. The maps of the leachate levels were generated such that, the migration conduits of the leachate could be delineated. Profiles of leachate level and elevation maps were correlated in order to model the groundwater risk factor associated with them.

The hydrochemical study involved laboratory analyses of the collected water samples according to world health organization (WHO) standard practice for physico-chemical and microbial properties. Twelve water samples were collected and the plastic containers used were rinsed three times with the sample to be collected. Duplicate samples were collected and labelled A and B. Sample A was stabilized using three drops of Hydrochloric acid to prevent the metals from adsorbing on the surface of the container. It was filtered with 0.45 mm filter paper and the sample was used for cation analysis. The Sample B which was not filtered because they were used for anion and microbial analyses. The samples were preserved using a plastic cooler with ice to maintain the temperature such that there would be no change in the constituent of the sample. The water was then taken to the laboratory of AkwaIbom State Water Company, Uyo Headquarters, within 24 hours for analyses. Cation analysis was done using Atomic Absorption Spectrometer (AAS), while the anions were analysed using the Ultraviolet (UV) Spectrophotometer. Some parameters were analysed using titrimetric method. Temperature, pH and turbidity were measured in the field in-situ using the portable pH meter, turbidity was measured using turbid meter, and temperature was measured using mercury-in-glass thermometer.

3. Result and Discussion

3.1. Geoelectrical Curves

The geoelectrical curves results generated for the selected profiles from figure 2 yielded some VES curves across the entire area as shown in Figure 3. The VES curves generated at Uyo and Oron areas are typically H and K-curves (Figure 3), which implies that the interpreted VES Curves are quite common in a sedimentary environment for multilayer structures of three or more layers. Uyo resistivity curves show typically H-curves which are quite common in a sedimentary environment for multilayer structures of three or more layers (Figure 3a) according to Anakwubaet al. (2014). At Ikot Ekpene, there are hybrid of K and H curves, A and K curves while one VES station has H-curve (Figure 3b). At Oron, it is predominantly K-curves, with one VES station having A-curve and hybrid KHK-curve (Figure 3c).

Consequently, the results of the VES interpretations in conjunction with the borehole data within the study area (Figure 4) show that Uyo is mainly of three (3) layers namely; top lateritic sand, leachate contaminated sand, and dry fine to medium-grained sand layers, except one Station that is up to five (5) layers of the same characterization with the former (Figure 4a, b). Ikot Ekpene and Oron are of three to four layers, except one Station at Oron, which is of five layers down to the depth of investigation. Figure 4a shows a VES correlation at Uyo which reveal that, the lithologicfacies are sandy lateritic overburden (19.80 – 232.00 ohm-m), leachate contaminated sand (4.06 – 20.00 ohm-m), dry fine to medium grained sand (11315 – 13654 ohm-m) and medium to coarse grained sand (1304.00 – 26542.00 ohm-m). Thin lateritic sand units which overlie the leachate contaminated sand units, signify that the study area is of unconfined region and there is possibility of leachate plume moving down the subsurface. More so, figure 4b shows that the VES correlation at Ikot Ekpene, the lithologicfacies are sandy lateritic overburden (64.60 – 3733.00 Ohm-m), medium to coarse-grained sand (126 – 24849 Ohm-m), fine to medium grained sand (58.30 – 94.90 Ohm-m). Thin lateritic sand units which overlie the medium to coarse-grained sand units, signify that the study area is more of unconfined region.

Furthermore, considering the VES correlation at Oron, the lithologicfacies are sandy lateritic overburden (103 – 167.00 Ohm-m), dry fine to medium

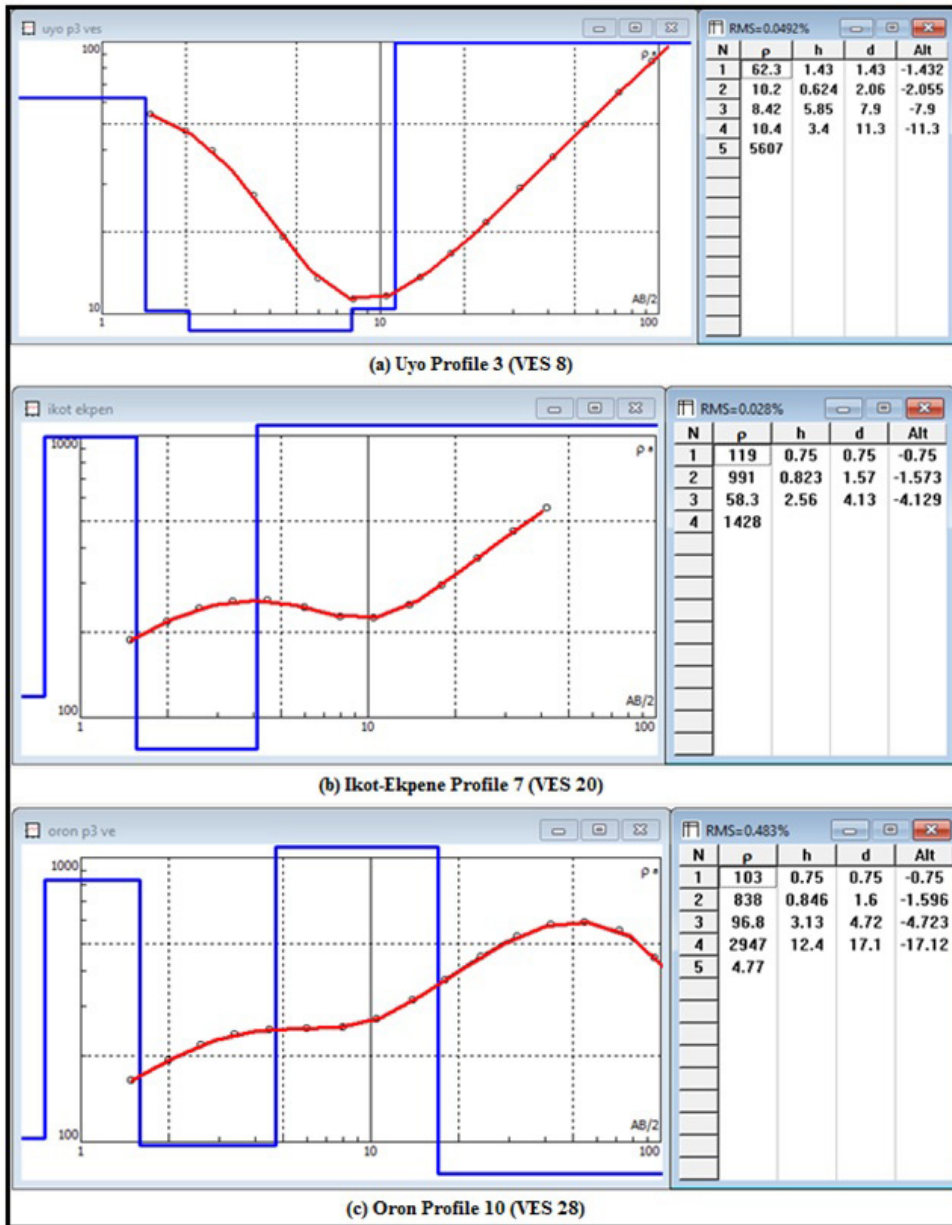


Figure 3- Some VES curves and calculated parameters for a) Uyo, b) Ikot Ekpene and c) Oron.

grained sand (838 – 2632 Ohm-m), medium to coarse grained sand (96.80 – 2947.00 Ohm-m) and leachate contaminated sand (4.77 – 19.00 Ohm-m). Thick sand units which overlie the leachate contaminated sand units, signifying that the study area is of unconfined region and there is possibility of flow of leachate plume down the subsurface.

Generally, these delineated layers exhibit some characteristics of the Benin Formation which this area is entirely made up of. The entire profile therefore shows sands of varying composition based on their

resistivity attributes. In line with this, Mbipom et al. (1996) established that the study area falls within the sedimentary area of Nigeria and is overlain by coastal plain sands of the Niger Delta sedimentary sequence known as the Benin Formation. It is good to note that the sand members of the Benin Formation are mature, coarse and poorly sorted with intercalations of silts and clays. Ugbaja and Edet (2004) also emphasized that the Benin Formation comprises of alternating sequences of gravels and sands of fine to medium/coarse grain sizes.

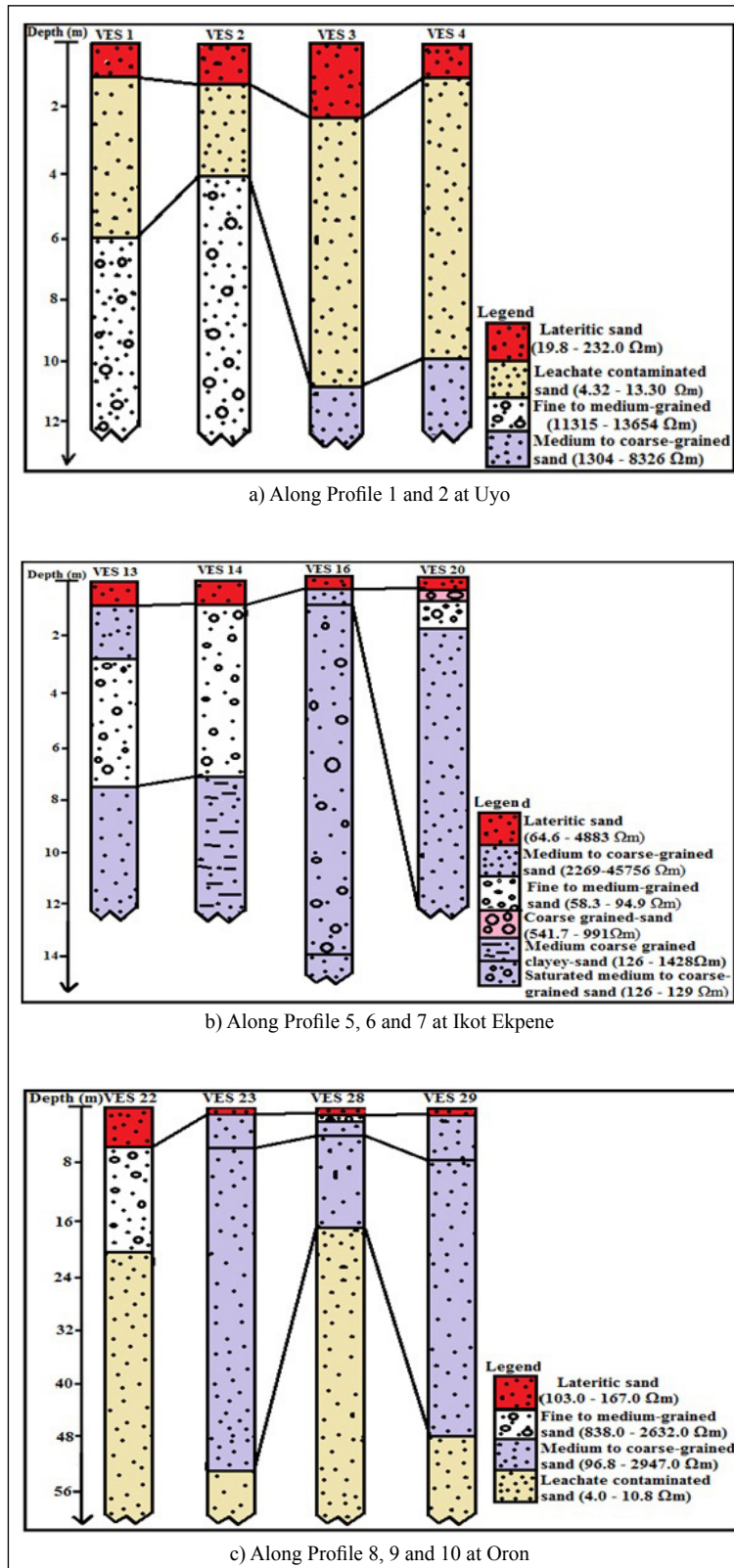


Figure 4- Electrical resistivity sections obtained by combining of VES results (from resistivity-depth parameters).

3.2. Geoelectrical Tomography

In practice, the interpretation of the pseudo cross-sections generated within the study area is based on colour codes depicting variation in apparent resistivity values of the subsurface as shown in figure 5. If this figure is examined, it can deduced that the black colour represents very low apparent resistivity values followed by the blue color code, whereas, the green colour code represents moderate apparent resistivity values followed by the yellow color code with higher apparent resistivity values. The highest resistivity values are represented by the red color code. These interpretations aligned with the already interpreted leachate-prone zones in figure 4. Figure 5 has abnormally low apparent resistivity values, which are designated as plumes of black and light blue colors associated with areas of vulnerability to contamination, while areas with green, yellow and red color codes represent areas of little or no vulnerability to contamination. The prominent trend evident in figure 5 is NE-SW direction across the study area.

In addition, the resistivity pseudo cross-sections of Uyo dumpsite shows three blocks representing VES 1, 2, 3, and each has three layers (Figure 5a). The range of low resistivity values (4.06 - 10.40 Ωm) of the second layers at Uyo dumpsite shows that the second layers are predominately leachate contaminated zones. The thickness of the leachate plumes within the Uyo dumpsite ranges between 4 to 8 meters in depth. The pseudo cross-section generated within Uyo dumpsite shows that the plume has migrated from VES 1 to a little beyond VES 2, which has a distance of more than 30m in the subsurface. Meanwhile, at Ikot Ekpene, the resistivity tomography is represented in figure 5b. The figure signifies that the resistivity values within Ikot Ekpene area range between 58.3 Ωm and above with the Ikot Ekpene dumpsite having no trace and/or very minimal impact of leachate plume. More so, at the Oron dumpsite, the resistivity tomography connotes leachate plume which is very prominent between VES 9 and VES 10 (Figure 5c). There are very low resistivity values of 4.28 – 10.8 Ωm in layer 3 which is interpreted as the leachate contaminated zone within the Oron dumpsite.

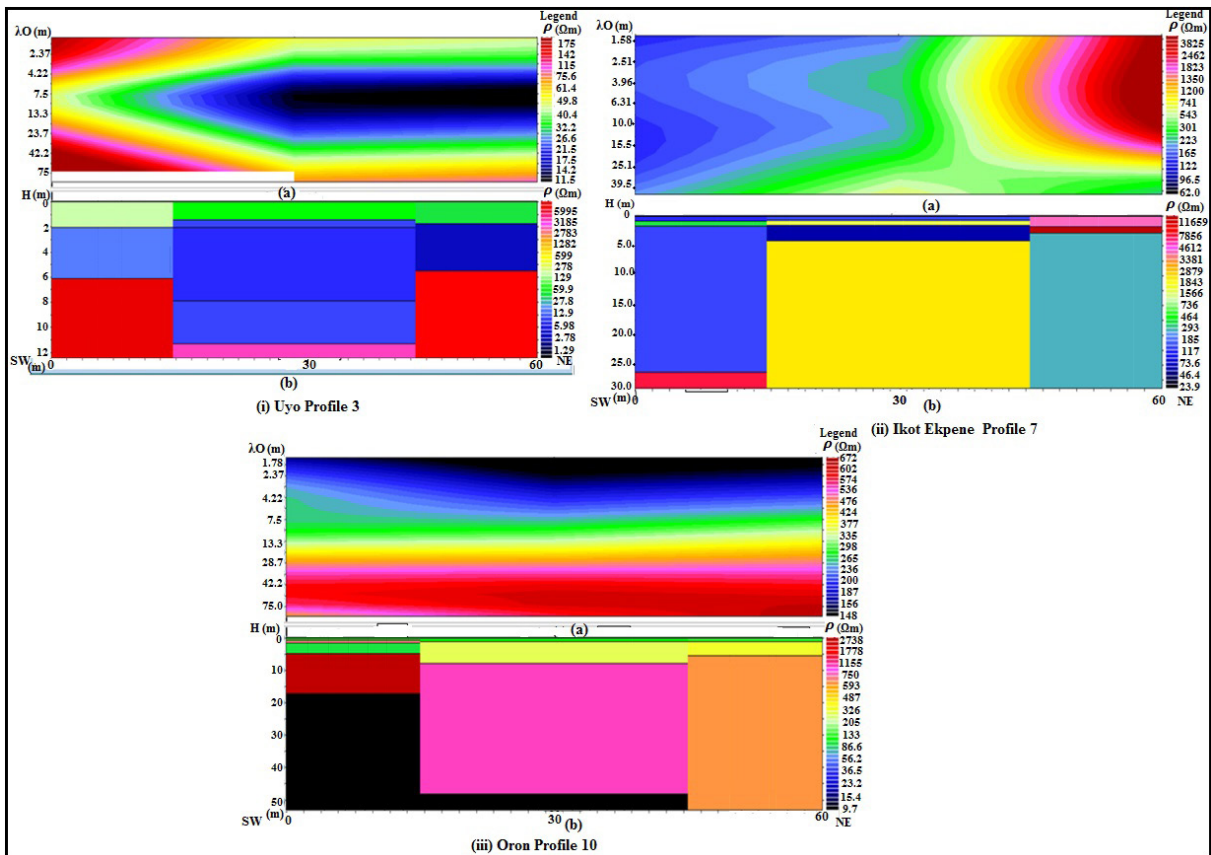


Figure 5- Some geoelectrical Tomography for a) Uyo, b) Ikot Ekpene and c) Oron.

3.3. Estimation of Leachate Parameters

In practice, Da-Zarrouk, Hydraulic Conductivity, and Transmissivity parameters are calculated and presented in table 2. Additionally, the hydraulic conductivity, transmissivity and erodibility distribution maps are shown in figures 6, 7 and 8. If this table is examined, the following deductions can be achieved;

3.3.1. Da-Zarrouk Parameters

The computed leachate Da-Zarrouk parameters result from the interpreted VES data (Table 2) show that, the values of various parameters range from low to high within the study area: for Uyo dumpsite, leachate resistivity varies from 4.06-20.00 Ωm; leachate thickness from 2.85-22.20 m; longitudinal conductance from 0.205-2.637 ohm-m. For Oron dumpsite, leachate resistivity varies from 4.26-19.00 Ωm; leachate thickness from 26.80-62.90 m; longitudinal conductance from 1.411-13.187 ohm-m.

3.3.2. Hydraulic Conductivity

Hydraulic conductivity of the leachate layer (K_l) can be defined as the ease with which any fluid such as

leachate or water will be able to travel through voids or cracks within the earth materials or layers. This parameter is dependent on three major factors namely; the intrinsic permeability of the rock unit, the degree of saturation within the rock unit and the density along with viscosity of the fluid such as the leachate. Mathematically, the hydraulic conductivity of the leachate layers (K_l) across the area was estimated using equation 1 generated by Heigoldet al. (1979);

$$K = 386.40R_{rw}^{-0.93283} \tag{1}$$

Where, K = Hydraulic conductivity; R_{rw} = Apparent resistivity of the layer.

At Uyo dumpsite area, the hydraulic conductivity of leachate unit (Table 2) ranges from 23.63 m/day to 104.56 m/day. The distribution map of hydraulic conductivity produced reveals that at the western part of the map (Figure 6a), there is relatively lower hydraulic conductivity of the leachate unit (23.63 – 65.00 m/day), while the pinkish colour at the eastern part corresponds to relatively higher hydraulic conductivity of the leachate unit (70 – 104.56 m/day). At Oron dumpsite (Figure 6b), the northeastern area possesses relatively lower hydraulic conductivity of

Table 2- Calculated leachate parameters for the study area.

Dumpsite/ Profile	VES Point	ρ_1 (Ωm)	h (m)	S (mhom)	T (m-Ohm)	C (mho)	κ_l (m/day)	τ_l (m ² /day)	κ_l (m/day)
UYO	1	11.4	4.95	0.434	56.430	0.088	39.914	197.574	399.209
P1	2	8.26	2.85	0.345	23.541	0.121	53.908	153.637	756.404
	3	13.3	8.32	0.626	110.656	0.075	34.568	287.606	283.822
	4	6.32	8.69	1.375	54.921	0.158	69.200	601.345	1206.177
	5	4.11	4.36	1.061	17.920	0.243	103.378	450.727	2871.435
P2	6	4.32	9.23	2.137	39.874	0.231	98.682	910.837	2509.543
	7	20	4.09	0.205	81.800	0.050	23.626	96.632	134.529
	8	9.67	3.29	0.340	31.814	0.103	46.537	153.108	523.124
P3	9	4.06	3.78	0.931	15.347	0.246	104.565	395.255	2948.936
	10	4.21	4.18	0.993	17.598	0.238	101.085	422.537	2241.645
	11	8.42	22.2	2.637	186.924	0.119	52.952	1175.523	474.803
P4	12	4.32	9.25	2.141	39.960	0.231	98.682	912.810	2503.604
	22	6.36	58.6	9.214	372.696	0.157	68.794	4031.307	865.329
ORON	23	19	26.8	1.411	509.200	0.053	24.784	664.220	104.355
P8	25	4.26	55.2	12.958	235.152	0.235	99.978	5518.792	1877.523
	28	4.77	62.9	13.187	300.033	0.210	89.969	5659.075	1508.921
P9	29	10.8	31.9	2.954	344.520	0.093	41.979	1339.119	310.953
	Average	8.45	18.86	3.115	143.434	0.156	67.800	1351.183	1265.901

Key symbols: ρ_1 = Leachate resistivity; h= Leachate thickness; S= Longitudinal conductance; T= Transverse resistance; C= conductivity; κ_l = Hydraulic conductivity of leachate; τ_l = Transmissivity of leachate; κ_l = Erodibility of leachate

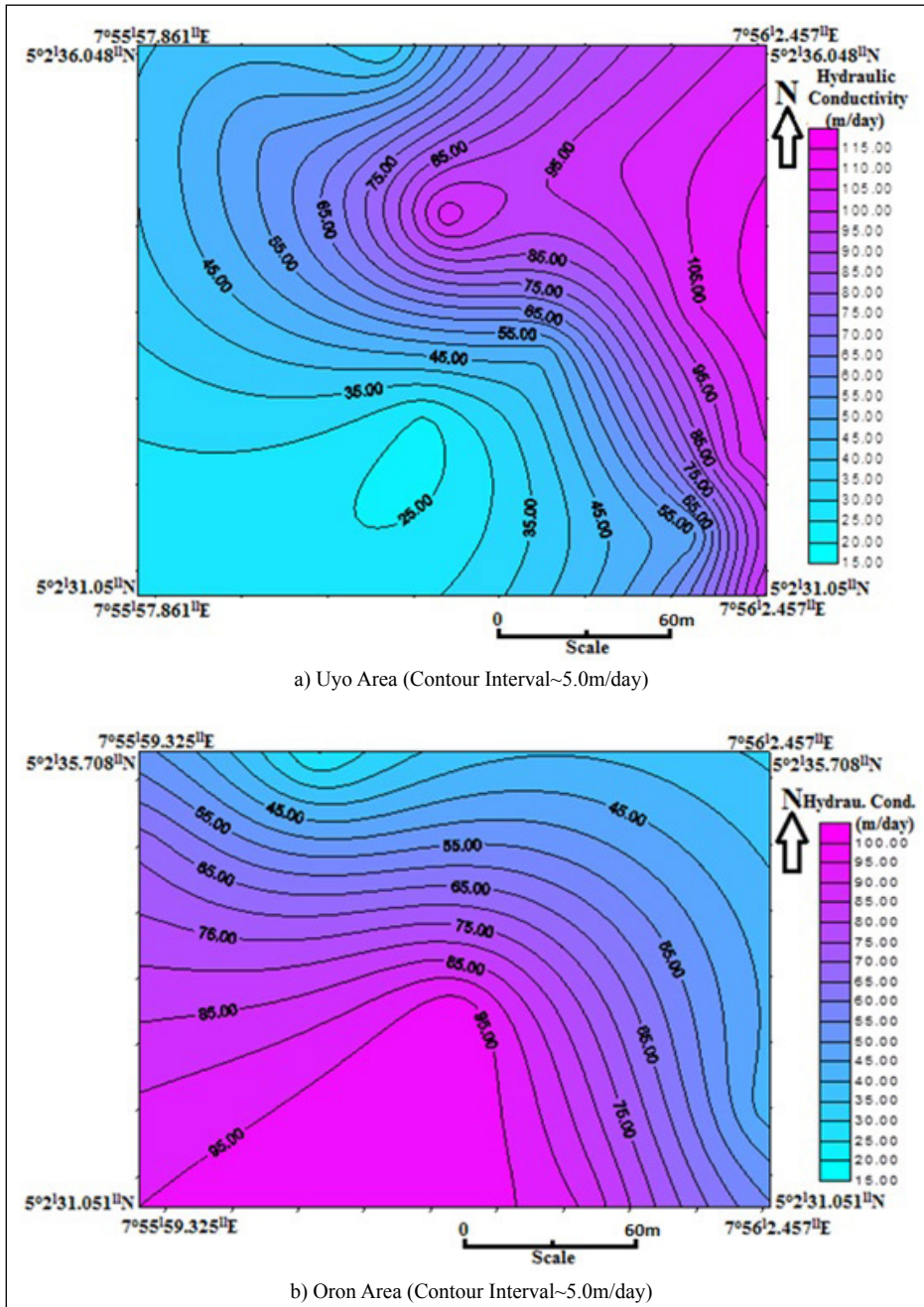


Figure 6-A distribution map showing hydraulic conductivity across a) Uyo and b)Oron areas.

the leachate unit (24.78 – 68.79 m/day), while the pinkish colour at the southwestern part corresponds to relatively higher hydraulic conductivity of the leachate unit (70 – 99.98 m/day). Generally, few of these values compared well with those obtained by Ekwe and Opara (2012) from interpreted VES data around Owerri and its environs, Southeastern Nigeria for leachate plume; which the hydraulic conductivity of the area.

3.3.3. Transmissivity

Transmissivity of leachate is the property which is directly related to hydraulic conductivity and it can be describe as the capacity of a specific fluid unit such leachate of a given thickness to transmit fluid. Mathematically, the transmissivity of the leachate layer (T_l) across the area was estimated using the equation 2 generated by Niwas and Singhal, 1981;

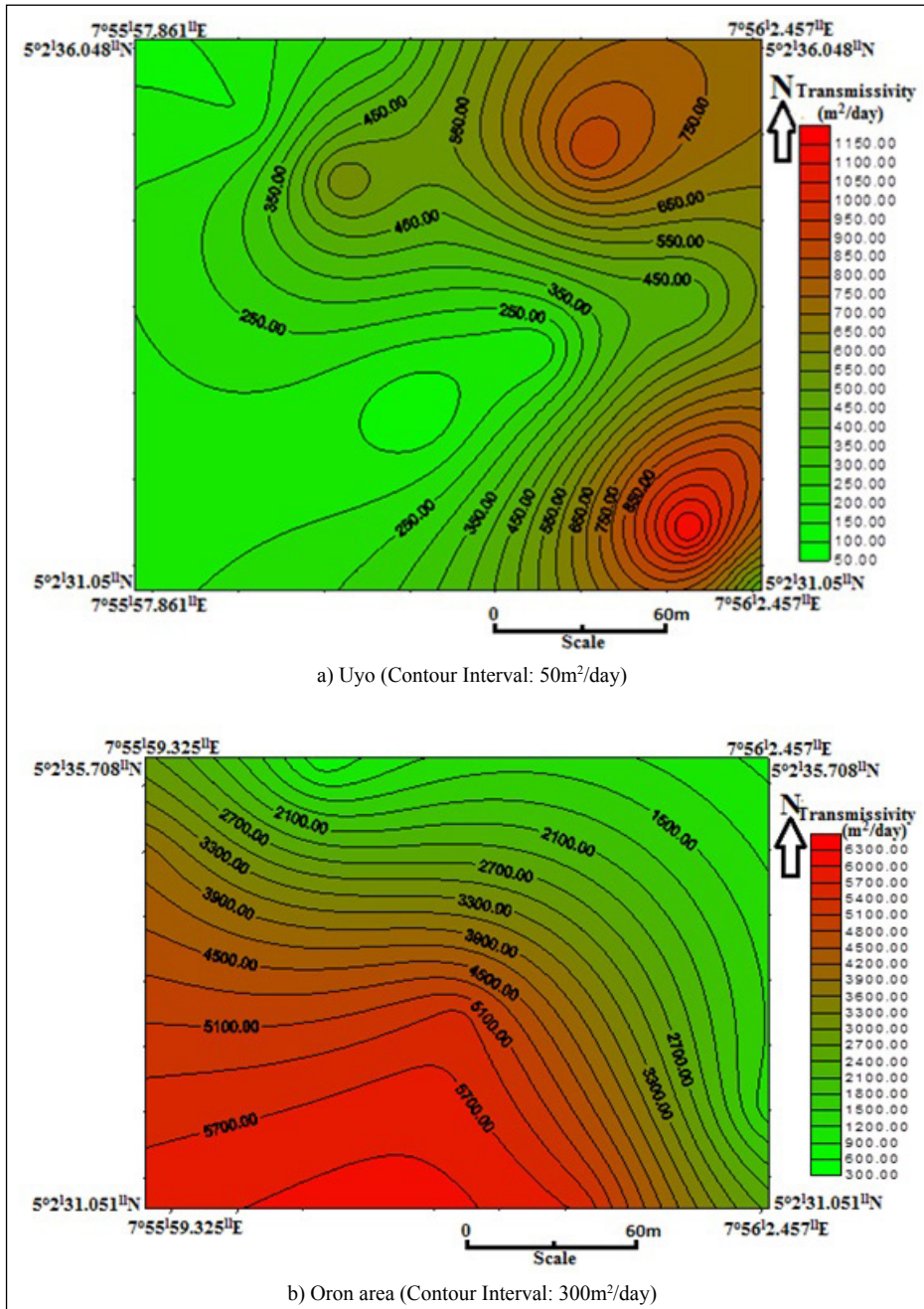


Figure 7- A distribution map showing transmissivity across a) Uyo and b) Oron areas.

$$T_L = K_L h_L \quad (2)$$

Where, K_L = Leachate transmissivity; K_L = Leachate hydraulic conductivity; h_L = Leachate thickness.

Consequently, the transmissivity of leachate calculated (T_L) from VES result ranges from 96. 63 to 1175.52 m²/day at Uyo (Table 2 and figure 7a), while

at Oron area, the transmissivity of leachate ranges from 664.22 to 5659.08 m²/day (Table 2 and figure 7b). Some of these values compared well with those obtained by Ekwe and Opara (2012) from interpreted VES data around Owerri and its environs, Southeastern Nigeria for leachate plume; which the transmissivity of the area was deduced to vary between 51.39 and 5659.08 m²/day. Figure 7 shows clearly the distribution

of transmissivity within the study area. Some of these values compared well with those obtained by Ekwe and Opara (2012) from interpreted VES data around Owerri and its environs, Southeastern Nigeria for leachate plume; with the range of transmissivity of the area obtained to be between 51.39 and 5659.08 m²/day.

3.3.4. Erodibility

Erodibility can be defined as the inherent yielding or non-resistance of earth materials such as soils and rocks to erosion. A high erodibility implies that the same amount of work exerted by the erosion processes leads to a larger removal of material. Hence, the erodibility of the overburden layers within the study area was calculated using the equation 3 according to Freeze and Cherry (1979);

$$K_z = \frac{b}{\left[\sum_{i=1}^m (b_i/K_i)\right]} \quad (3)$$

Where, K_L = erodibility or parallel flow within each lithologic layer; K_i = hydraulic conductivity of each individual layer of thickness; b_i = individual layer of thickness; b = Overall thickness of the sequence.

Subsequently, the obtained results show that the value of erodibility within the area is between 134.53 and 2948.94 m/day at Uyo area while that of Oron area ranges between 104.36 and 1877.52 m/day (Table 2). The leachate erodibility distribution maps were produced across the study area (Figure 8). At Uyo area (Figure 8a), two distinct zones were interpreted namely; a relatively high erodibility (1400 to 2948.94 m/day) and a relatively moderate erodibility (134.53 to 1206.18 m/day). More so, at Oron area (Figure 8b), two distinct zones were interpreted namely; a relatively high erodibility (900 to 1877.52 m/day) and a relatively moderate erodibility (104.36 to 865.33 m/day). Considering the average erodibility of the leachate units at Uyo area as 1404.44 m/day, and that of Oron area as 933.42 m/day, the study area can be classified as having a relatively high erodibility of the leachate units. This implies that the rate of removal of material within the area is considerably high due to the nature of geologic materials available.

3.4. Hydrogeochemical Characteristics

The hydrogeochemical analyses reveal that few water samples from boreholes surrounding the

dumpsites (Table 3) exhibit elevated Total Dissolved Solids (TDS), reduced pH and high electrical conductivity. Significantly, of the heavy metals, Cadmium is above the permissible limit (Samples DS3 and DS4). The dumpsite is encroaching albeit with minimal impact at the time of study. The acidic pH is a pointer to things that will happen that have not yet manifested. Both the acidic pH and high Cadmium are signs that things are getting wrong with the groundwater. There are a lot of anthropogenic influences adding Cadmium to the groundwater. The result of hydrogeochemical analyses also reveal that the pH values obtained (3.7-5.8) within the study area are not within the acceptable limits of 6.5-8.5 for human consumption. Indeed, Edet (2017) emphasized that this pH low values obtained in the study area can be as a result of humic acid generated from decaying plant. Also, the result of the analysis shows high amount of dissolve Oxygen in samples DS3 and DS4. This perhaps is due to high microbial activity within the environment as shown on table 3.

3.5. Elevation and Leachate Level Maps

The elevation maps of Uyo and Oron dumpsites (Figure 9) were produced for effective correlation with the leachate level maps. Nevertheless, the leachate levels across Uyo and Oron dumpsites were computed by subtracting depths to leachate layer from the surface elevations obtained during the data acquisition. At Uyo area (Figure 10a), the flow direction of the leachate plume is predominantly in NW-SE direction and hydrogeologically, it is the dominant groundwater flow direction in the area. Also, the thickness of the leachate level increases along this flow direction within this area. Subsequently, the flow direction of the leachate plume at Oron area (Figure 10b) is predominantly in NE-SW direction and hydrogeologically, it is the groundwater flow direction of the area. Hence, the thickness of the leachate level increases along this flow direction within this area. Also, cross sections G-G' at Uyo and H-H' at Oron were taken along the flow directions in order to unveil the sinks and peaks of the flow direction (Figure 11).

3.6. Hydrogeological Risk Implication Associated with Leachate Level

Different cross sections were taken at both the elevation map (Figure 9) and leachate level map

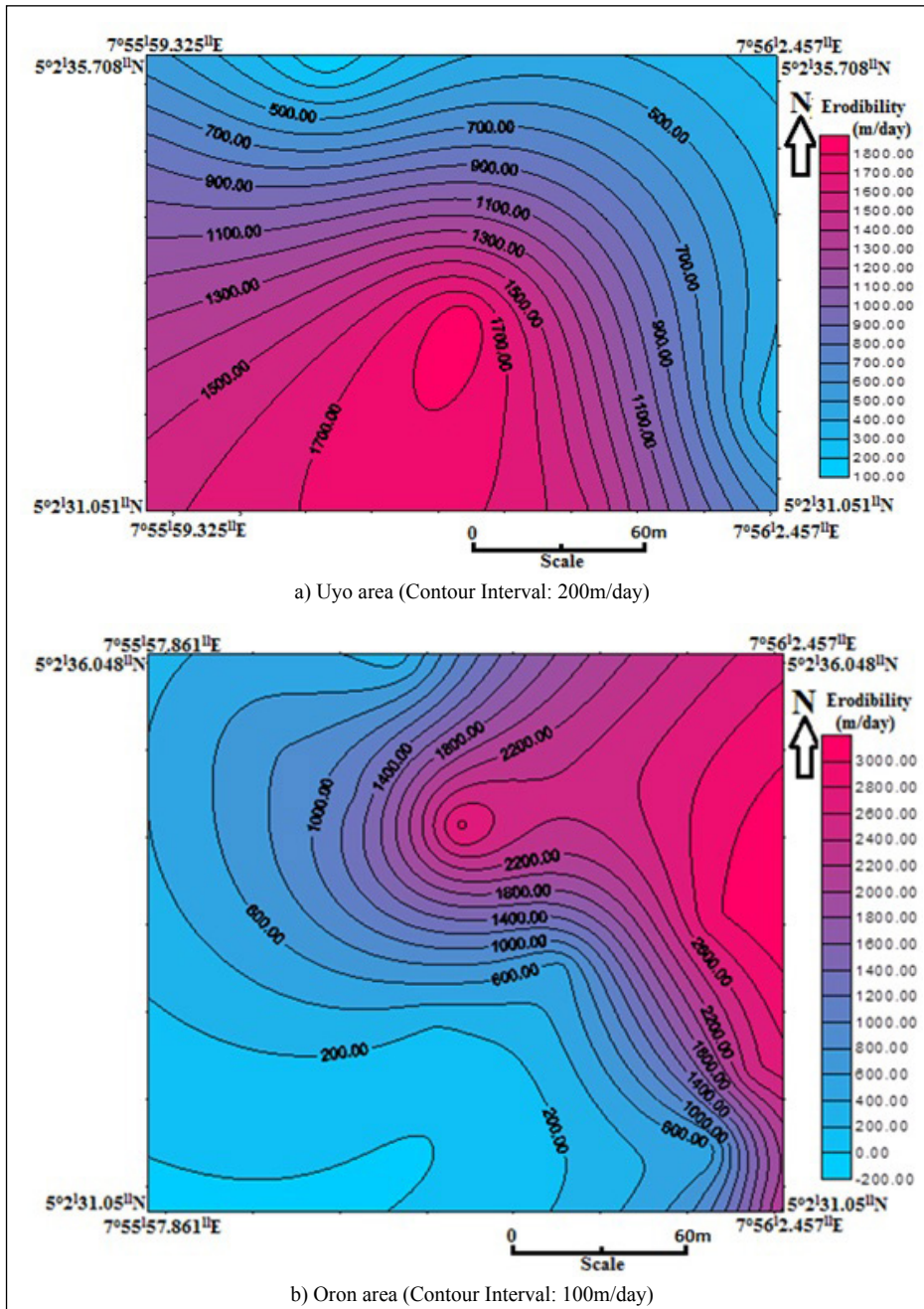


Figure 8- A distribution map showing erodibility across a) Uyo and b) Oron areas.

(Figure 10) at Uyo and Oron areas respectively. At Uyo, profiles running from A-A¹ at figure 8a and B-B¹ at figure 9a were superimposed in order to estimate the groundwater risk factor (Figure 12) obtainable in this area. We can deduce from figure 12a that there is close match between leachate level and topography, which implies that the topography controls the configuration of the leachate level (Figure 12a). Also, the gap

between the leachate level and the average static water level in Uyo area is 25 m since the depth of the sink leachate level and the static water level is 65 m and 38 m respectively (Figure 12a). This implies that the vertical movement of leachate (contaminate) will be slow thereby allowing physical (filtration), chemical and biochemical processes to remove contaminants before reaching the aquifer. Also, from the

Table 3- Results of hydrogeochemical analysis within the study area.

Parameters	66 Udo St (DS1)	H. Garden (DS2)	64 Udo St (DS3)	58 Udo St. (DS4)	68 Udo St. (DS5)	NSDWQ	W.H.O. (2017)
Appearance	Clear	Clear	Clear	Clear	Clear	Clear	
Colour (HU)	5	5	5	5		15	
Odour	Acceptable	Acceptable	Acceptable	Acceptable	Acceptable	Acceptable	
Temperature °c	27.7	31	29.4	29.2	22.7	Ambient	
pH	5	5.8	3.93	3.7	3.82	6.5-8.5	6.5-8.5
Turbidity (NTU)	1.03	20.1	0.5	0	1.17	5	
Iron (Fe ³⁺)mg/l	0.07	0.08	BD	0.16	0.25	0.3	0.3
Salinity %	0.9	1.3	0	0.1	0.1	0.5	
Electrical Conductivity µs/cm	1813	2059	40	131.4	231	1000	1000
Total Dissolved Solid mg/l	857	1242	16.4	79.3	110.1	500	1000
Residual Chlorine (d ₂) mg/l	----	-----	-----	-----	-----	0.2-0.25	
Manganese mg/l	0.08	0.08	0.035	0	BD	-	0.4
Nitrates (No ₃) mg/l	0.027	0.336	0.06	-0.02(BD)	0.4	50	50
Nitrite (No ₂) mg/l	0.018	0.018	0.006	0.001	0.013	0.2	3
Ammonia(NH ₃) mg/l	0.07	0.04	0	0	0	0	0.2
Phosphate (po ₁ ³) mg/l	0.033	0.001	0.025	0.043	0.006	3.5	
Suspended Solid mg/l	0.4	2.4	8	15	BD	10	
Total silica (SiO ₂) mg/l	-----	-----	0.029	0.002	0.035	17	
Sulphate (SO ₄) mg/l	11.2	11.2	5	3	5	1000	500
Total Hardness mg/l	72	34	36	46	32	500	
Calcium Hardness (Ca ²) mg/l	70	82	14	20	30	75	
Magnesium Hardness mg/l	2	BD	BD	BD	BD	0.2	
Acidity mg/l	0.8	0.48	0.04	0.64	0.08	4.5-8.2	
Total Alkalinity mg/l	13.2	15.6	4.8	4.88	24	100-200	
Chloride (Cl ⁻) mg/l	0.83	0.78	0.6	0.1	0	250	
Methyl Alkalinity mg/l	13.2	15.6	4.8		2.4	100-200	
Aluminum (Al ³⁺) mg/l	-----	-----	0.01	0.04	0	0.2	0.1-0.2
Selenium (Se) mg/l	-----	-----	0.101	0.04	0	-	0.01
Chromium (Cr)	0.002	0	0	0.01	0.01	0.05	0.05
Cadmium (Cd ²⁺) mg/l	0	0	1	1	0.004	0.003	0.003
Copper (Cu)mg/l	0.813	0.824	0.17	0.12	0.17	1	2.0
Cyanide (CN) mg/l	-----	-----	0.005	0	0.006	0.01	0.17
Lead (Pb ²⁺) mg/l	0.0007	0.0007	0.6	0	0.003	0.01	0.01
Arsenic (As) mg/l	-----	-----	0.03			0.01	0.01
Barium (Ba ²⁺) mg/l	-----	-----	7	7	BD	0.7	0.7
Dissolved Oxygen (O ₂) mg/l	0.77	0.78	43.4	10.8	1.2	1.0-5.0	

Key symbols: DS = Water sample from boreholes proximal to Dump Site; BD= Below Detection Limit

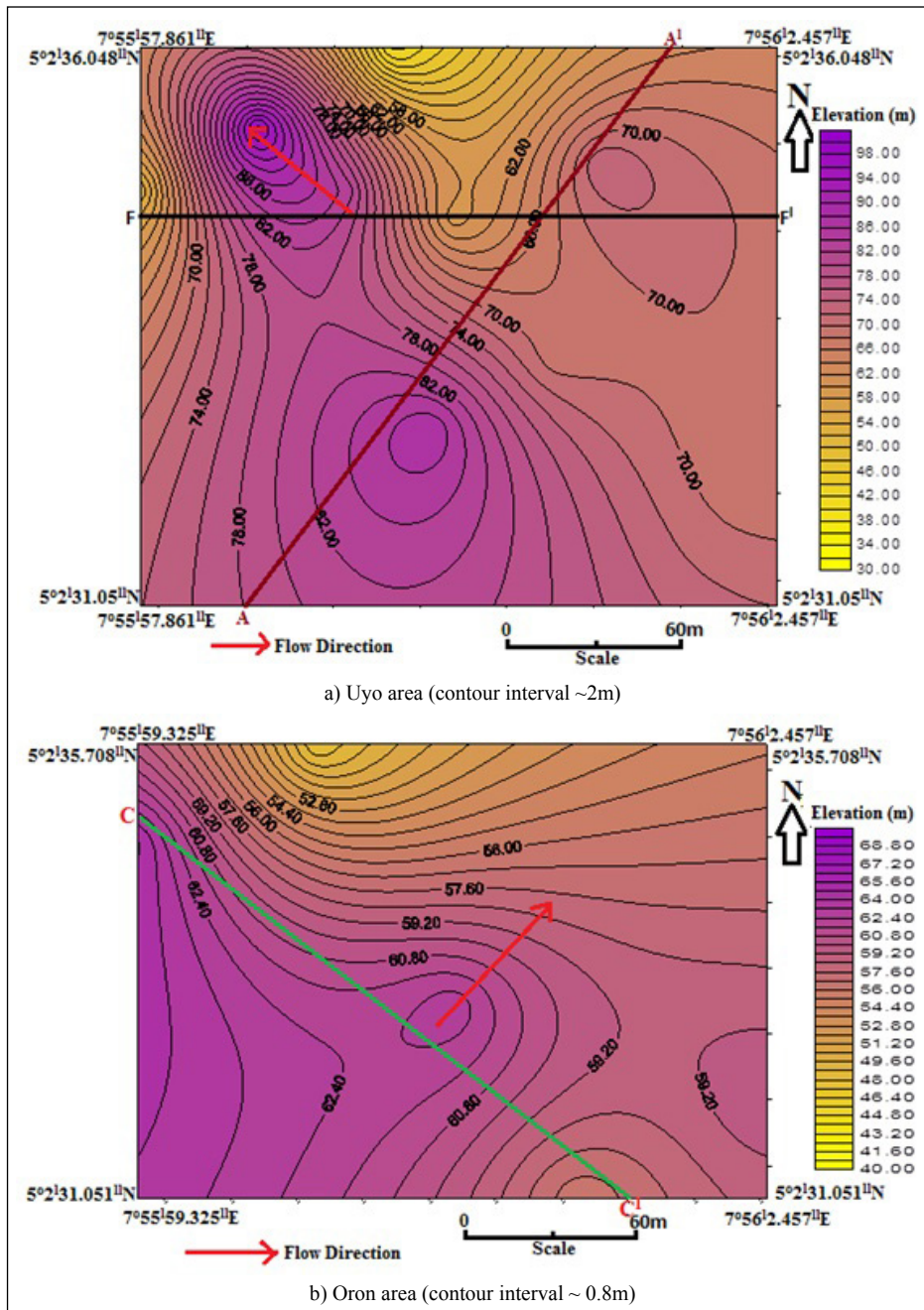


Figure 9- A distribution map showing elevation across a) Uyo and b) Oron areas.

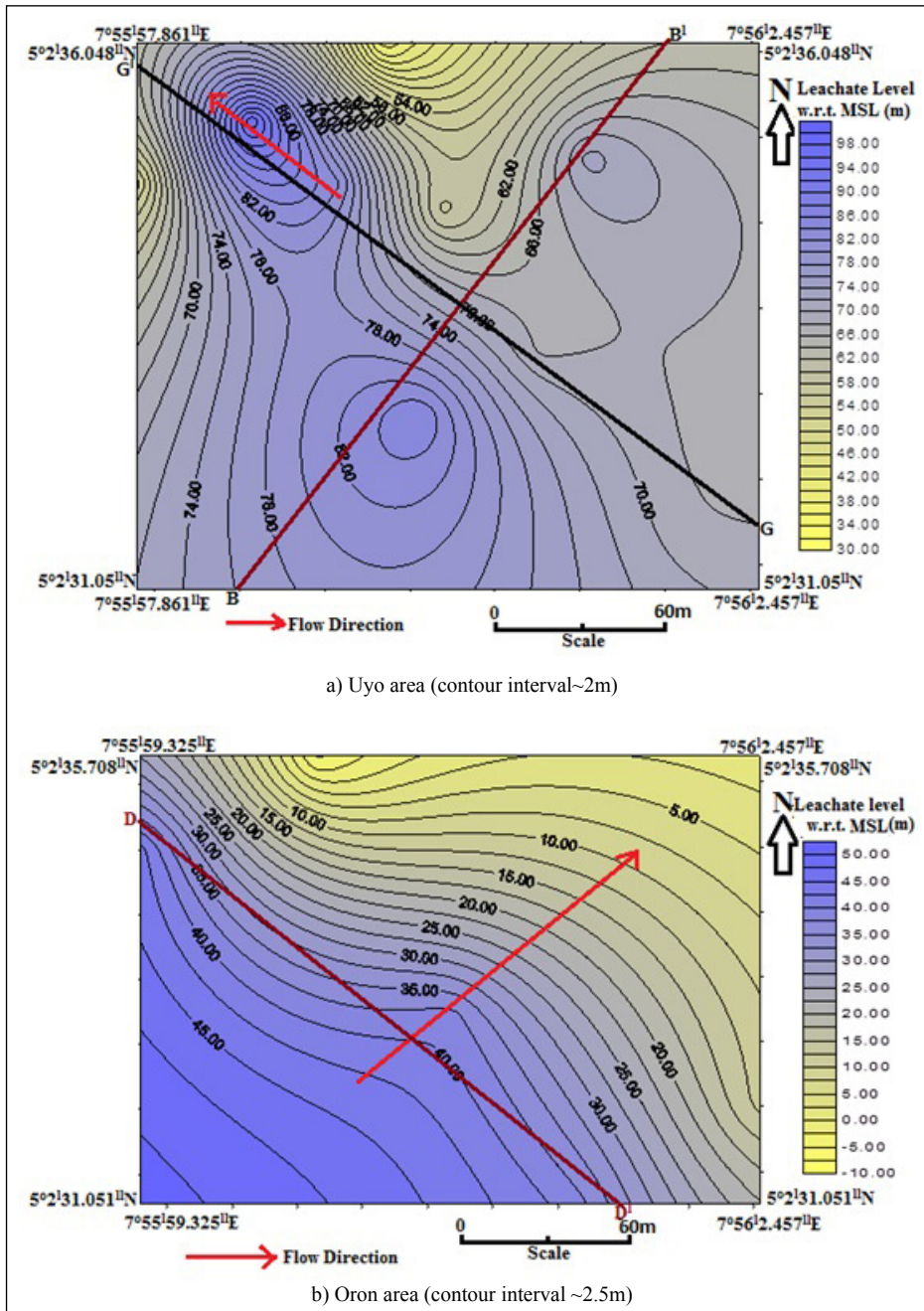


Figure 10- A distribution map showing leachate level across a) Uyo and b) Oron areas.

hydro chemical analysis, some of the indicator parameters at Uyo are very low and may not indicate much contamination from the dumpsite.

Furthermore, at Oron, profiles running from C-C' at figure 9b and D-D' at figure 10b were also superimposed in order to estimate the groundwater risk factor (Figure 12b) obtainable in this area. We can

infer from figure 12b that there is close match between leachate level and topography, which implies that the topography controls the configuration of the leachate level. More so, figure 12b shows an intersecting pattern such that the static water level crisscrosses the leachate level surface at 35 m. This implies that the sink of the leachate level is beyond the groundwater level which

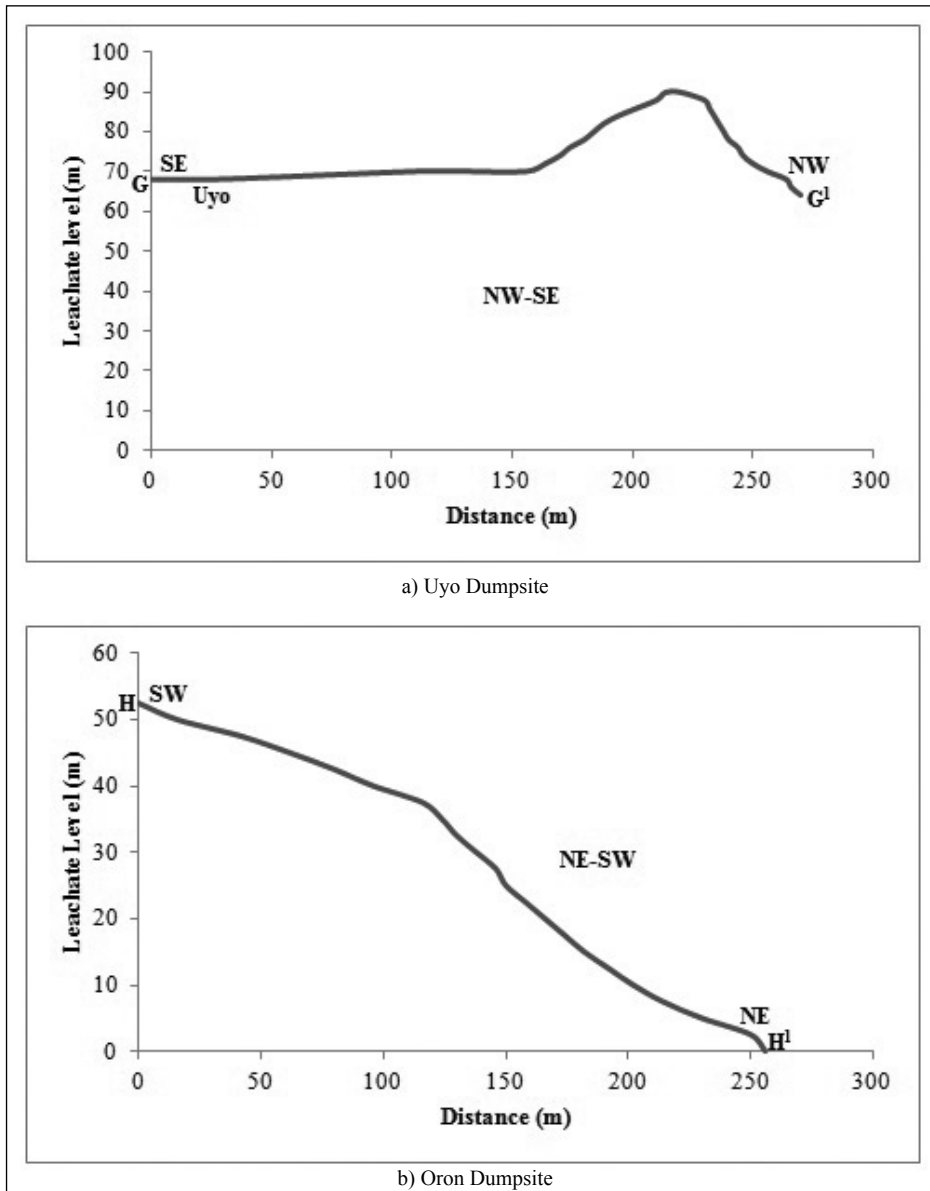


Figure 11- Cross- section showing the direction of leachate flow within across a) Uyo and b) Oron areas.

has contaminated the groundwater at in-situ already, as such; it is very risky for the users in this area. Also, some of the indicator parameters of hydrochemical analysis at Oron are considerably elevated and may indicate to a great extent contamination of groundwater quality within the dumpsite region in addition to it makes the groundwater unfit for the dwellers.

4. Conclusions

The computed results and models showed the capabilities of resistivity and hydrochemical methods in determining impact of solid waste on groundwater quality. The leachate from the Uyo dumpsite has insignificant effect on the groundwater quality compared to the Oron dumpsite, which really

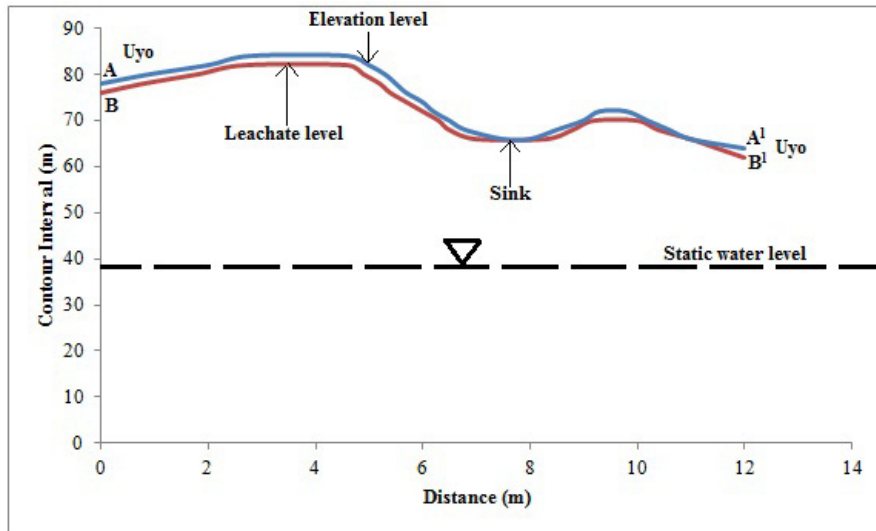


Figure 12- a) Risk model of leachate level within Uyo Dumpsite.

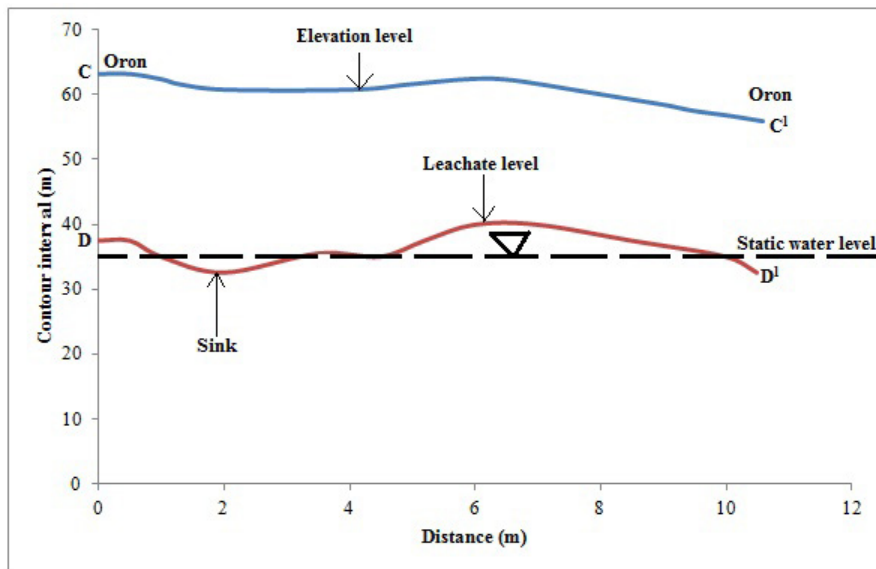


Figure 12- b) Risk model of leachate level within Oron Dumpsite.

contaminated the groundwater quality thereby making the groundwater unfit for the dwellers. The Ikot Ekpene dumpsite on the other hand is yet to affect the groundwater quality.

Acknowledgements

We acknowledged AkwaIbom State Ministry of Environment, the State Waste Management Board and Ikot Ekpene Club for their permission during the data acquisition of this present research.

References

- Adeeko, T.O., Samson, D.O., Umar, M. 2019. Geophysical Survey of Basement Complex Terrain Using Electrical Resistivity Method for Groundwater Potential. *World News of Natural Sciences (WNOFNS)* 23(1), 154-165.
- Amadi, S.C., Onwuemesi, A.G., Anakwuba, E.K., Chinwuko, A.I., Okeke, H.C. 2017. Estimation of Aquifer Hydraulic Characteristics from Surface Geo-Electrical Sounding of Affa And Environs Southeastern, Nigeria. *IOSR Journal of Applied Geology and Geophysics* 5(4), 14-25.
- Anakwuba, E.K., Nwokeabia, C.N., Chinwuko, A.I., Onyekwelu, C.U. 2014. Hydrogeophysical assessment of some parts

- of Anambra basin, Nigeria. *International Journal of Advanced Geosciences* 2(2), 72-81.
- Chinwuko, A.I., Anakwuba, E.K., Okeke, H.C., Usman, A.O., Owuasa, M.O., Okoye, I. F. 2015. Geo-electric Investigation for Groundwater Potential in Awka Anambra State, Nigeria. *International Journal of Science for Global Sustainability* 1 (1), 85-95.
- Christensen, T.H., Cossu, R., Stegmann, R. 1992. *Landfill of waste*. Elsevier Science publisher Ltd, England, 656p.
- Dahlin, T., Rosqvist, H., Leroux, V. 2010. Resistivity – IP mapping for landfill applications. *First Break* 28(8), 101-105.
- Edet, A.E. 2017. Hydrogeology and groundwater evaluation of a shallow coastal aquifer, southern Akwalbom State, Nigeria. *Springer Open* 7(5), 2397-2412.
- Edet, A.E., Okereke, C.S. 2002. Delineation of shallow groundwater aquifers in the Coastal plain sands of Calabar area (Southern Nigeria) using surface resistivity and hydrogeological data. *Journal of African Earth Sciences* 35(3), 433-443.
- Ekwe, A.C., Opara, A.I. 2012. Aquifer Transmissivity from Surface Geo-electrical Data: A Case Study of Owerri and Environs, Southeastern Nigeria. *Journal Geological Society of India* 80, 123-128.
- Ezeh, C.C. 2011. Geoelectrical studies for estimating aquifer hydraulic properties in Enugu State, Nigeria. *International Journal of the Physical Sciences* 6(14), 3319-3329.
- Freeze, R.A., Cherry J.A. 1975. *Groundwater*, Prentice-Hall, Englewood Cliffs, New Jersey, 604 pp.
- Frohlich, R.K., Barosh, P.J., Boving, T.B. 2008. Investigating changes of electrical characteristics of the saturated zone affected by hazardous organic waste. *Journal of Applied Geophysics* 64(1), 25-36.
- Heigold, P.C., Gilkeson, R.H., Cartwright, K., Reed, P.C. 1979. Aquifer transmissivity from surficial electrical methods. *Groundwater* 17(4), 338-345.
- Mbipom, E.M., Okwueze, E.E., Onwuegbuche, A.A. 1996. Estimation of transmissivity using VES data from the Mbaise area of Nigeria. *Nigerian Journal of Physics* 85, 28-32.
- Nfor, B. N., Olobaniyi, S. B., Ogala, J. E. 2007. Extent and distribution of groundwater resources in parts of Anambra state Southeastern, Nigeria. Department of geology, Delta State University Abraka, Delta State, Nigeria. *Journal of Applied Sciences and Environmental* 11(2), 215 – 221.
- Nigerian Geological Survey Agency, 2006, *Geological Map of Nigeria*, 1:2 million scale.
- Nigerian Standard for Drinking Water Quality. 2015. A Unit of Nigerian Industrial Standard (NIS)- Guidelines for drinking water uses, Abuja, Nigeria, 28p.
- Niwas, S., Singhal D.C. 1981. Aquifer transmissivity of porous media from Dar-Zarrouk parameters in porous media. *Journal of Hydrology* 82, 143-153.
- Nwajide, C. S. 2013. *Geology of Nigeria's Sedimentary Basins*. CSS Bookshop Limited, 347p.
- Obiora, D.N., Ibuot, J.C., George, N.J. 2016. Evaluation of aquifer potential, geoelectric and hydraulic parameters in Ezza North, Southeastern Nigeria, using geoelectric sounding. *Int. Journ Environ Sci Technol* 13, 435-444.
- Ogwueleka, T. 2009. Municipal solid waste characteristics and management in Nigeria. *Iran Journal of Environmental Health, Science and Engineering* 6(3), 173-180.
- Okafor, P., Mamah, L.I. 2012. Integration of geophysical techniques for groundwater potential investigation in Katsina-Ala, Benue State, Nigeria. *The Pacific Journal of Science and Technology* 13(2), 463-474.
- Olofsson, B., Jernberg, H., Rosenqvist, A. 2005. Tracing leachates of waste sites using geophysical and geochemical modelling. *Environmental Geology* 49(5), 720-732.
- Onwumesi, A.G., Egboka, B.C.E. 2006. 2-D Polynomial curve fitting techniques on watertable, and hydraulic gradients estimations in parts of Anambra basin, Southeastern Nigeria. *Natural and Applied Sci. Journal* 7(2), 6-13.
- Oseji, J.O., Ujuanbi, O. 2009. Hydrogeological investigation of groundwater potential in Emu Kingdom, Ndokwa land of Delta State, Nigeria. *International Journal of Physical Sciences* 4(5), 275-284.
- Shaibu, I., Udensi, E. E., Chinwuko, A.I., Usman, D. A., Adetona, A. A., Omale, M.E. 2018. Geophysical Investigation of Groundwater Potential in Millennium City Housing Estate Kaduna, Nigeria using Electrical Resistivity Method. *Kada Journal of Physics* 2(1), 14-22.
- Singh, A., Sharma, S.P., Akca, I., Baranwal, V.C. (2018). Fuzzy constrained Lp-norm inversion of direct current resistivity data. *Geophysics* 83(1), E11-E24.
- Ugbaja, A.N., Edet, A.E. 2004. Groundwater pollution near shallow waste dumps in Southern Calabar, South-eastern Nigeria. *Global Journal of Geological Sciences* 2(2), 199-206.
- Utom, A.U., Odoh, B. I., Okoro, A.U. 2012. Estimation of Aquifer Transmissivity Using Dar Zarrouk Parameters Derived from Surface Resistivity Measurements: A Case History from Parts of Enugu Town (Nigeria). *Journal of Water Resource and Protection* 4, 993-1000.
- Wunderlich, T., Fischer, P., Wilken, D., Hadler, H., Erkul, E., Mecking, R., Gunther, T., Heinzmann, M., Vott, A., Rabbel, W. 2018. Constraining electric resistivity tomography by direct push electric conductivity logs and vibracores: An exemplary study of the Fiume Morto silted riverbed (Ostia Antica, Western Italy). *Geophysics* 83(3), B87-B103.



Bulletin of the Mineral Research and Exploration

<http://bulletin.mta.gov.tr>



Optimization of leaching conditions for extraction of magnesium from a chromite beneficiation plant tailing predominantly containing lizardite

Hakan ÇİFTÇİ^{a*}, Bekir ARSLAN^a, Ayşegül BİLEN^b, Zeyni ARSOY^a and Bahri ERSOY^a

^aAfyon Kocatepe University, Department of Mining Engineering, Afyonkarahisar, Turkey

^bYıldız Technical University, Department of Metallurgy and Material Engineering, İstanbul, Turkey

Research Article

Keywords:

Leaching, Lizardite, Magnesium, Amorphous silicate, Chromite plant tailing.

ABSTRACT

In this study, leaching experiments were performed for extraction of magnesium from a chromite beneficiation plant tailing predominantly containing lizardite. The X-ray fluorescence (XRF) and X-ray diffraction (XRD) analyzes showed that the tailing sample contains 39.3wt.% MgO and consist of predominantly lizardite mineral. Hydrochloric acid (HCl) and sulphuric acid (H₂SO₄) were used as acids separately in leaching experiments. Acid concentration, leaching temperature, leaching time, and solid ratio were investigated as leaching parameters and optimized. Maximum magnesium extraction yield was determined to be nearly 98% for both acids under optimum leaching parameters which leaching temperature was 85°C, solid ratio was 20wt.%, leaching time was 120 minutes, and acid concentrations were 6 M for HCl and 4 M for H₂SO₄. In addition, it was determined that the leaching residue as a solid state was mainly composed of amorphous silicate according to the XRD analysis. Dissolution rate data were explained using Jander equation. Mg dissolution process found to be diffusion controlled.

Received Date: 09.04.2020

Accepted Date: 17.11.2020

1. Introduction

Serpentine minerals, phyllosilicates with a nominal composition of Mg₃Si₂O₅(OH)₄, contains approximately 40% MgO and are classified as lizardite, chrysotile, and antigorite according to their crystalline structures (Lacinska et al., 2016; Fedoročková et al., 2012). Some mineral beneficiation plant tailings contain high amount of these minerals. Serpentine can be evaluated in CO₂ capture and storage application (Wilson et al., 2006, 2009) or in the production of pure magnesium (Mg) metal, Mg compounds and amorphous silicate (SiO₂). Mg in serpentine structure can be easily taken into solution by acid leaching and then can be precipitated as

various Mg compounds. Mg is an important metal due to some of its characteristic features and used as alloy formation, medicinal products, sulfur removal in iron and steel production, fertilizers, refractory materials, synthesis of Grignard reagent, and fireproof (Raza et al., 2014). The leaching process of the serpentine also leaves amorphous silicate (SiO₂) as solid residue. Amorphous silicate can be used as a filler and additive in the production of some materials (plastics, rubbers, catalyst carriers, chemical sensors, adhesives, paper, paints, coatings, sealants, and insulating materials) and to improve the mechanical properties of some materials, such as film nanocomposites, and silicon carbide (Bałdyga et al., 2012; Kulikovskiy et al., 2008; Wang et al., 1997).

Citation Info: Çiftçi, H., Arslan, B., Bilen, A., Arsoy, Z., Ersoy, B. 2021. Optimization of leaching conditions for extraction of magnesium from a chromite beneficiation plant tailing predominantly containing lizardite. Bulletin of the Mineral Research and Exploration 164, 251-259.

<https://doi.org/10.19111/bulletinofmre.827630>

*Corresponding author: Hakan ÇİFTÇİ, hakanciftci86@gmail.com

Serpentines are also the most appealing minerals for the application of carbon dioxide (CO_2) capture and storage with mineralization (CCSM) which is promising technique that sequences CO_2 flue gas into stable magnesium carbonates (Daval et al., 2013; Sanna et al., 2013). CCSM application can be implemented in two ways. The first way involves the direct reaction of mineral and CO_2 gas at a given temperature and pressure. In the second method, firstly, the metal is leached from the mineral generally via acids and then reacted with CO_2 . In both methods, maximum efficiency depends on the structure of the mineral, parameters used in leaching and carbonation (temperature, solid ratio, particle size, chemical concentration, and pressure) (Bobicki et al., 2012; Nduagu et al., 2012; Sanna et al., 2012). CCSM can be seen as an advantageous method due to the easy production of raw material (Mg or Ca rich minerals) and the fact that the raw material has sufficient reserves.

There are many studies on Mg extraction from serpentine or other Mg rich minerals by acid leaching (Arce et al., 2017; Lacinska et al., 2016; Liu et al., 2010). According to the literature review, there was no study on investigating Mg extraction from chromite beneficiation plant tailings, however. This study focused on the optimization of leaching conditions to get maximum Mg extraction yield from a chromite beneficiation plant tailing predominantly containing lizardite for potential using for CCSM and in producing Mg compounds. Hydrochloric acid (HCl) and sulphuric acid (H_2SO_4) were used separately as two different acids. The effects of leaching temperature, solid ratio, acid concentration, and leaching time on the extraction yield of Mg were investigated separately and optimum leaching conditions were determined. Kinetic studies were also performed to explain leaching mechanism.

2. Materials and Methods

2.1. Materials

Starting sample (chromite beneficiation plant tailing) was collected from stockpile of chromite beneficiation plant of CVK/Ogelman Mining Co. located in Harmancık-Bursa/Turkey. In order to be homogeneous, the sample was collected from several different points by drilling technique. No pretreatment, such as crushing, grinding, or sieving, was carried out before the studies on the collected

sample. Hydrochloric acid (HCl, 35-37%) and sulphuric acid (H_2SO_4 , 95-97%) were purchased from Merck, Germany.

2.2. Characterization Techniques

Shimadzu XRD-6000 instrument with Cu-K α radiation (λ : 1.54184 Å) at 40 kV was used to determine the mineralogical composition of the starting sample and leaching residue. The samples were first dried at 100°C for 24 h, ground using a laboratory scaled ring mill, and then scanned with XRD. Morphology of the samples before and after the leaching was investigated using LEO 1430 VP scanning electron microscope (SEM). The chemical compositions of the samples were determined using a Rigaku ZSX Primus II XRF spectrometer (calibrated every 6 months) after the samples dried at 100°C for 24 h and ground using a laboratory scaled ring mill. Particle size distributions were determined by wet sieving using a series of retsch sieves (150-1,000 μm).

2.3. Leaching Experiments

Leaching experiments were performed using a laboratory scaled three necked glass reactor immersed in a thermo-controlled water bath (Figure 1). Mixing was performed using a mechanic mixer and a condenser was used to avoid loss of acid at high temperatures.



Figure 1- Glass reactor used in the leaching experiments.

The investigated leaching parameters and their used value ranges are given in the table 1.

Table 1- Investigated leaching parameters.

Acid concentration (M)	Leaching time (min)	Solid ratio (%)	Temp. (°C)
2	30	10	25
4	60	20	45
6	90	30	65
	120	40	85
	150		

The leaching experiments were performed using both diluted HCl and H₂SO₄ acids separately and started with the investigating the effect of acid concentration. After the acid concentration was optimized, the effects of the leaching time, solid ratio, and temperature were investigated and optimum values were determined. In a typical run, the starting sample (lizardite) was dried at 100°C for 24 h to remove physically adsorbed water first. A certain amount of dried material and 200 mL of diluted acid (HCl or H₂SO₄) were then put in glass reactor. The temperature was then increased to a certain degree and stirring was mechanically started at 800 rpm. At the end of the certain leaching time the stirring was stopped and solid/liquid separation was performed via vacuum filtration. Leaching residue was then washed with distilled water, dried at 100°C for 24 h, ground using ring mill, and then analyzed by XRF instrument to determine chemical composition. Mg extraction yield was determined according to XRF analysis data using equation 1.

$$\text{Yield, \%} = \frac{(F * f - R * r)}{F * f} * 100 \quad (1)$$

Where, F is the amount of fed (starting) material (g), f is the Mg content of fed (starting) material (wt.%), R is the amount of solid leaching residue (g), and r is the Mg content of solid leaching residue (wt.%).

3. Results and Discussion

3.1. Characterization of the Starting Sample

Chemical composition of the starting sample according to particle size distribution (Table 2) was obtained from XRF analysis. The data showed that the sample contain high percentage of SiO₂ and MgO (>74wt.%, in total) indicating the presence of serpentine minerals. The sample contains also small amount of iron oxides about 7.1wt.%. It was also concluded that the Mg, Si, and Fe contents showed homogeneous distribution according to particle size distribution (Table 2). This showed that a pre-beneficiation according to particle size is not necessary and the leaching experiments should be applied to the entire sample.

XRD pattern of the starting sample (Figure 2) revealed that the sample were constituted by predominantly serpentine mineral of lizardite-1T [Mg₃Si₂O₅(OH)₄] with small amounts of iron silicon (FeSi₂) and brucite [Mg(OH)₂].

Particle size distributions (Figure 3) revealed that the particles of the starting sample were distributed homogeneously between 100-1,000 μm scales. d_{10} , d_{50} , and d_{90} values which can be determined from the curve show cumulative amounts (10-50-90%) of particles that are smaller than a certain particle size in the sample. For example, d_{90} of the sample means that 90% of the sample consists of particles with a particle size less than 790 μm according to figure 3.

3.2. Leaching Experiments

Serpentine is a 1:1 hydrous magnesium iron phyllosilicate mineral consisting of tetrahedral silicate (SiO₂) and octahedral brucite (Mg(OH)₂) layers (Park and Fan, 2004). Leaching of serpentine minerals results in dissolution of the brucite layers

Table 2- Chemical composition of the starting sample according to particle size distribution.

Component	Content (wt.%)							
	Starting sample	-1,000+850 μm	-850+600 μm	-600+500 μm	-500+425 μm	-425+300 μm	-300+212 μm	-212 μm
MgO	39.30	39.27	39.17	39.30	39.55	39.67	39.64	39.38
SiO ₂	35.23	35.31	35.02	35.29	35.52	35.57	35.76	34.86
Fe ₂ O ₃	7.08	7.08	7.00	7.01	7.01	6.81	6.78	7.02
LOI	14.94	14.86	15.12	14.73	14.63	14.88	15.16	14.34

LOI: loss of ignition.

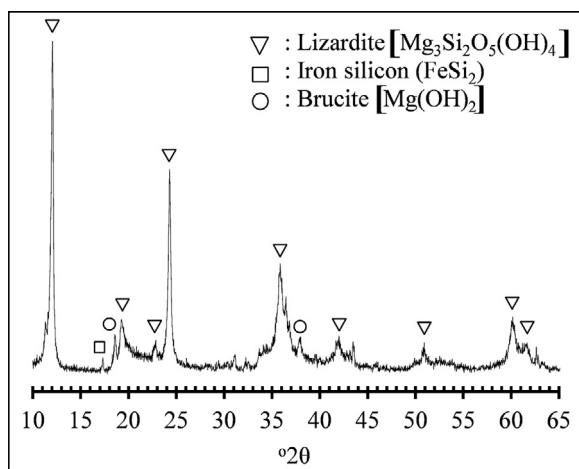


Figure 2- XRD pattern of the starting sample used in the experiments.

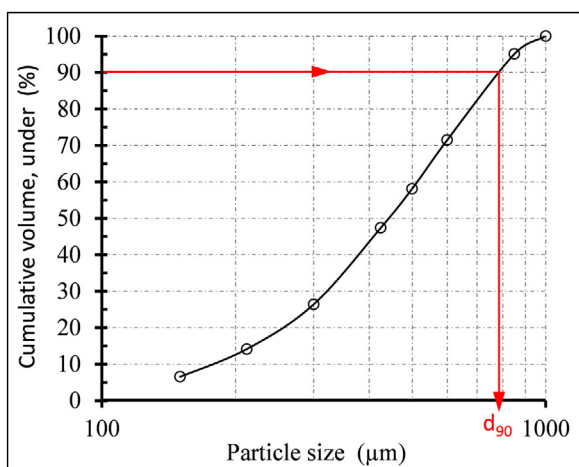


Figure 3- Cumulative particle size distribution of the starting sample.

and remaining amorphous silicate layers (Yoo et al., 2009). It is expected that brucite dissolution rate increases with the increasing of temperature, acid concentration, and time but decreases with increasing of solid ratio. Serpentine dissolution reaction in HCl and H_2SO_4 acids can be explained according to given equation 2.



While the effect of acid concentration experiments were performed (Figure 4a), leaching time, solid ratio, and leaching temperature were kept constant as 120 min, 20wt.%, and 85°C, respectively. Figure 4a revealed that acid concentration had critical effect on the Mg dissolution rate. Increasing of acid concentration from 2M to 4M resulted in increase of

Mg extraction yields from ~41% to ~75% and from ~75% to ~97% for HCl and H_2SO_4 acids, respectively. Mg extraction yield in H_2SO_4 acid was higher than HCl acid at the same concentrations up to 4M because H_2SO_4 contains twice as much H^+ ion. The dissolution of Mg in H_2SO_4 acid stabilized at 4M, while it increased up to 6M in HCl acid concentration. As a result, it was determined that the presence of 4M H_2SO_4 or 6M HCl acid in the dissolution media with other parameters kept constant was found to be sufficient to dissolve of the ≥ 98 wt.% Mg from lizardite mineral.

Acid concentration, solid ratio, and leaching temperature were kept constant as 4M H_2SO_4 , 6M HCl, 20wt.%, and 85°C, respectively, while the effect of leaching time experiments were performed. By increasing the leaching time up to 60 min, it was found that the dissolution of Mg increased rapidly, but then the dissolution rate slowed down slightly in the on going periods and stabilized at 120th min (Figure 4b). Slow progress after fast dissolution in the early stages of leaching was also reported by other studies (Lacinska et al., 2016; Yoo et al., 2009). Rapid dissolution rate in the first 60 min can be explained by the quick starting of the reaction by easy and quick encounter of hydronium (H_3O^+) ions with free $MgOH_2$ surfaces exposed by size reduction. After the rapid dissolution of free $MgOH_2$ surfaces, H_3O^+ ions advance the dissolution process more slowly by capillary diffusion between the layers. Optimum leaching time was determined as 120 min to obtain maximum Mg extraction (~98wt.%) at given parameters.

Figure 4c shows the effect of the solid ratio on the Mg extraction yield. The experiments were performed under changing solid ratios while acid concentration, leaching time, and leaching temperature were kept constant as 4M H_2SO_4 , 6M HCl, 120 min, and 85°C, respectively. It was clear from the chart that 20wt.% was the optimum solid ratio for the experiments. Increasing solid ratio to 30wt.% and 40wt.% was resulted in a high drop in Mg dissolution. When the solid ratio was kept at 10wt.% and 20wt.%, the dissolution yield was almost the same.

The effect of leaching temperature on the extraction yield of Mg from lizardite was investigated while acid concentration, leaching time, and solid ratio were kept constant as 4M H_2SO_4 , 6M HCl, 120 min, and 20wt.%, respectively. Figure 4d revealed that temperature has a significant effect on the dissolution of Mg and increase

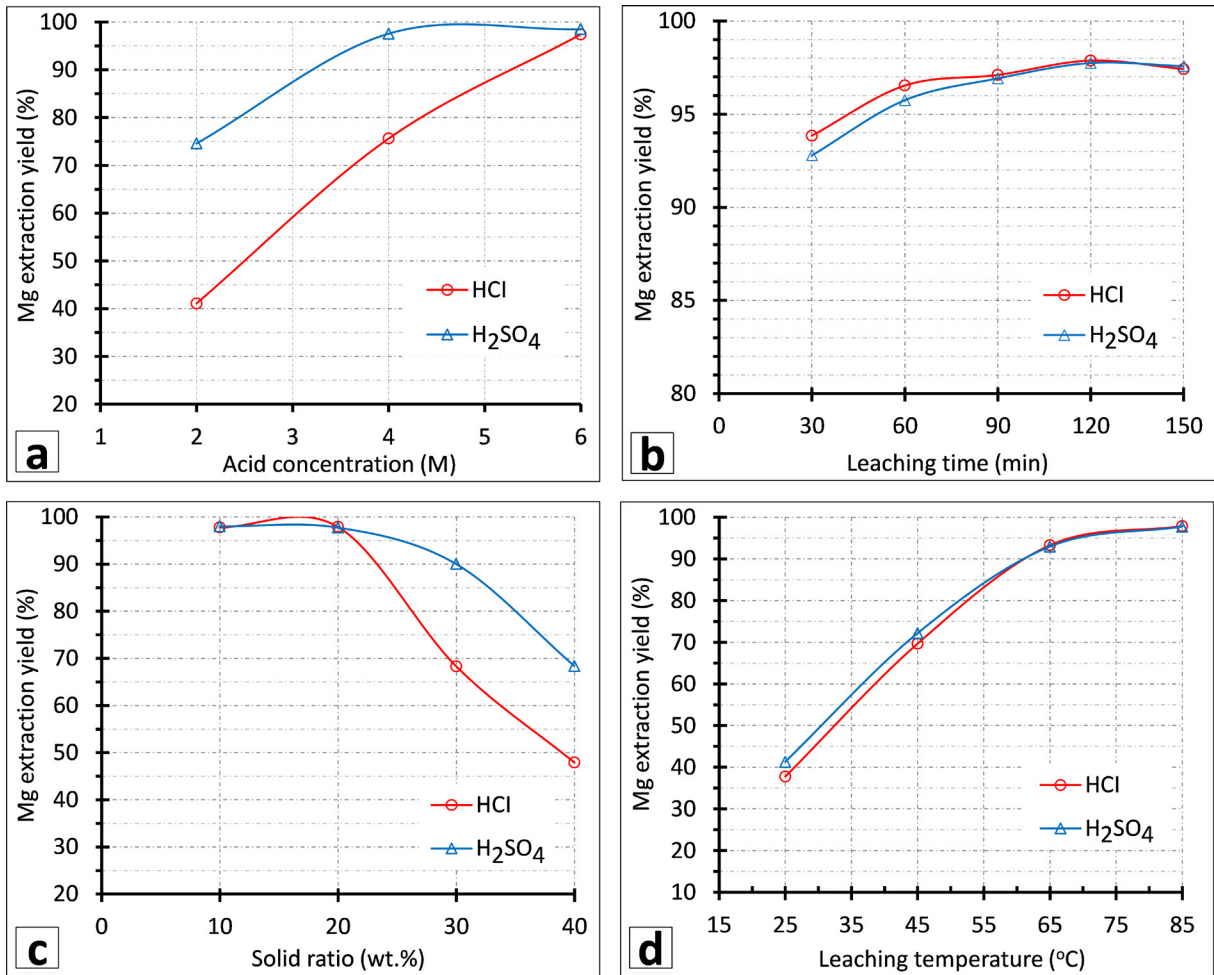


Figure 4- Mg extraction yields versus (a) acid concentration, (b) leaching time, (c) solid ratio, (d) leaching temperature.

in temperature resulted in increasing of dissolution rate highly which similar results were also reported in other studies (Sanna et al., 2013; Yoo et al., 2009; Teir et al., 2007). Increasing of the temperature from 25°C to 65°C caused a linear increase in Mg dissolution from ~40% to ~92%. This result can be related to the increased reactivity of the acids on the MgOH₂ layers with increasing temperature. The dissolution rate according to temperature was the same for both HCl and H₂SO₄ acids. Optimum leaching temperature was determined to be 85°C to obtain a Mg extraction yield of about 98wt.%.

As a result, optimum leaching conditions such as temperature, acid concentration, solid ratio, and leaching time were determined to be 85°C, 20wt.%, 6M HCl – 4M H₂SO₄, and 120 min, respectively. In leaching experiments carried out under optimum conditions, 50 g of starting material was used and as a result, 21.3 g of solid leach residue was obtained.

Accordingly, it was found that 28.7 g of solid was completely dissolved.

3.3. Characterization of Starting Sample and Leaching Residue

SEM micrographs (Figure 5a,b) and optic microscope photographs (Figure 5c) revealed that the starting sample generally consisted of light and dark green colored particles with rough surfaces, and have leaf-layer morphology with its angular edges. Figure 5d,e showed that leaching of the lizardite mineral left particles with porous morphology as a result of dissolution of MgOH₂ layers. Additionally, it was also found that the leaching residue particles were predominantly white colored and remained in large sizes (Figure 5f). Dissolution reaction did not affect the original particle size greatly but the residue particles were found to be much softer when tested with hand. This can be explained by the collapsing of

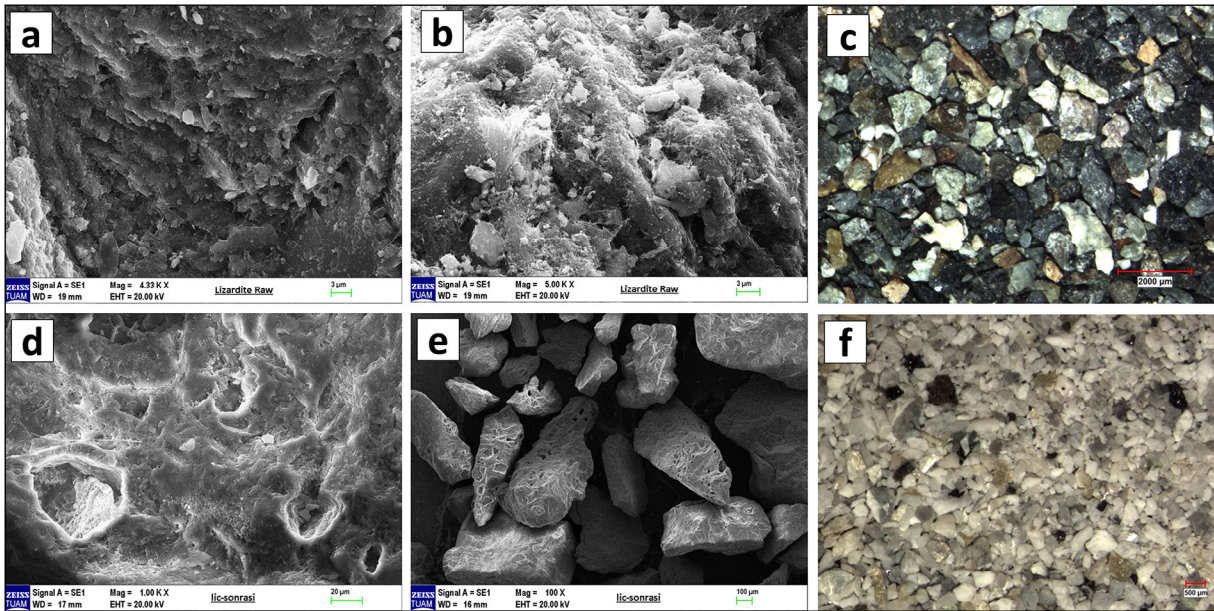


Figure 5- SEM and optic microscope photographs of the starting sample (a,b,c): before leaching, (d,e,f): after leaching.

thin silicate layers under minor pressure as a result of the dissolution of the $Mg(OH)_2$ layer in between.

The lizardite peaks based on the XRD pattern of the starting material in figure 2 were disappeared in the XRD pattern of the leaching residue material (Figure 6) as a result of complete disruption of the crystalline structure. Similar results were obtained by other studies (Arce et al., 2017; Sanna et al., 2013). Arce et al. 2017, investigated the acid leaching of the waste of asbestos fiber (sterile) production which contain serpentine minerals and as a result, the XRD patterns of leaching residue did not show the diffraction lines of brucite and clinochrysotile. Sanna et al., (2013), investigated

leaching conditions of serpentine using ammonium hydroxide solvent and as a result, the amorphous material was obtained at $140^\circ C$. XRD pattern of the leaching residue at optimum parameters (Figure 6) revealed that the residue was predominantly consist of amorphous silicate and small amounts of enstatite ($MgSiO_3$), antigorite [$Mg_3(Si_2O_5)(OH)_4$], sekaninaite [$(Fe^{2+}, Mg)_2Al_4Si_5O_{18}$], and Mg,Al,Cr,Fe oxide. Broad peak centered at $2\theta: 22,5$ represents high amounts of amorphous silicate (Fedoročková et al., 2016; Wang et al., 2006).

3.4. Leaching Kinetics and Mechanism

Leaching mechanism of Mg from lizardite was interpreted according to leaching experiments data and textural properties of lizardite. The textural structure of lizardite mineral (Figure 7d, Mevel, 2003) shows a layered 1:1 (tetrahedral Si layer : octahedral Mg layer) crystal structure. Leaching mechanism is defined by equation 3 if the reaction is chemically controlled and equation 4 if it is diffusion controlled. It is expected that the curve of the left side of that equation, which is the mechanism that determines the reaction rate, is very close to the linear, and the slope of the drawn curve is equal to the apparent rate constant (Levenspiel, 1972).

$$1 - (1 - X)^{1/3} = k \cdot t \quad (3)$$

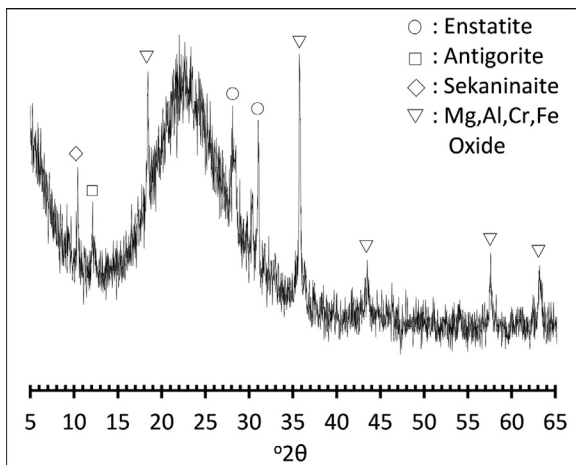


Figure 6- XRD pattern of the leaching residue.

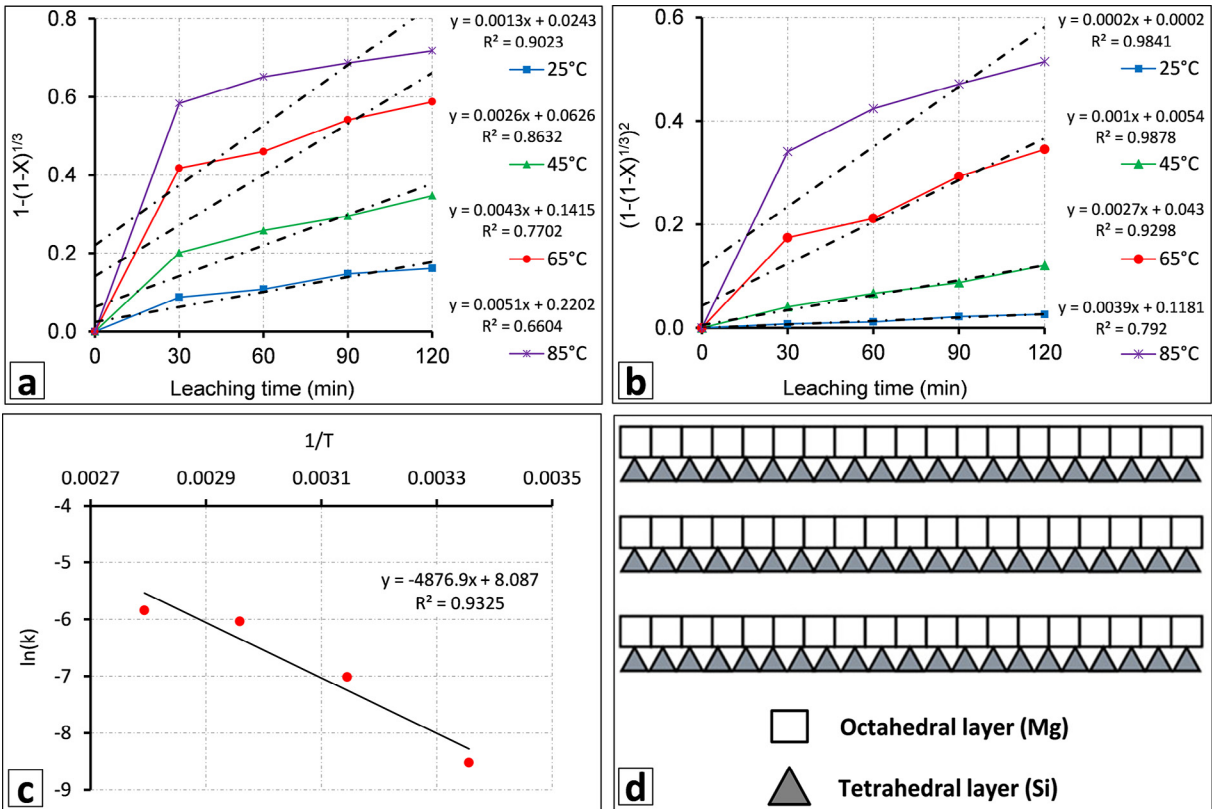


Figure 7- (a,b) Plot of the Mg dissolution results according to equation 3 and equation 4, respectively, (c) $\ln k$ - $1/T$ diagram, (d) crystal structure of the lizardite.

$$(1 - (1 - X)^{1/3})^2 = k \cdot t \quad (4)$$

Here, X: fraction of Mg dissolved (yield/100), k: apparent rate constant (min^{-1}), and t: reaction time (min).

The curves given in figure 7a and 7b were created by using the data obtained from the experiments of dissolution of Mg in H_2SO_4 acid in equations 3 and 4, respectively. When the curves are examined, the value of r^2 , which is the correlation coefficient, gave a closer result to 1 in the curves drawn if it was diffusion controlled (Figure 7b) for four temperature values. According to the data obtained, it can be said that the reaction is diffusion controlled. Mg extraction of lizardite starts with fast dissolution of free octahedral brucite (MgOH_2) surfaces exposed after crushing and grinding. Initial stage of dissolution cause to formation of pores on the surface and then continues with capillaries formation between the tetrahedral silicate layers. After that H_3O^+ ions advance the dissolution process more slowly by capillary diffusion. Obtained

results are in good agreement with Luce et al. (1972), who reported that the diffusion of ions in the mineral lattice itself or through a product layer is the speed control mechanism for the dissolution of magnesium silicates. Apostolidis and Distin (1978) have also reported same reasons for slowing dissolution of Mg from serpentine.

Rozalen and Huertas (2013) investigated the dissolution of chrysotile and reported that the dissolution is largely non-stoichiometric and the Mg layer dissolves ten times faster than silica. This can be attributed to the incongruent leaching process. Incongruent leaching may be a result of the precipitation of dissolved Si to the surface of the particles (Teir et al., 2007). The formation of a silica-rich layer can prevent the continuous leakage of Mg through the capillaries, which explains why the dissolution rate slows over time (Wang and Maroto-Valer, 2011). Dissolution rate of Mg from lizardite was also controlled by diffusion of Mg^{2+} , H_3O^+ , and SO_4^{2-} ions throughout the formed capillaries. According to these results, it can be said that the leaching process

of serpentine minerals is completed by dissolution of almost all of the octahedral Mg layers and a very small amount of the tetrahedral Si layers. At the end of the dissolution of the serpentine mineral, amorphous silicate remains as solid state while Mg is taken into the solution as a cation. Activation energy (EA) was calculated using the Arrhenius equation (Equation 5).

$$k = A \cdot \exp^{-E_A/R.T} \quad (5)$$

Here, k : apparent rate constant (min^{-1}), A : frequency factor, R : gas constant ($R = 8.314 \text{ J/molK}$) and T : reaction temperature (K).

When logarithm of both sides of equation 5 is taken and frequency factor A is accepted as 1, equation 6 is obtained. The slope of the curve given in the figure 7c gives $\ln k.T$ (-4,876.9) and activation energy can be calculated when this value is placed in equation 6.

$$\ln k = \frac{-E_A}{R.T} \quad (6)$$

Activation energy of the leaching experiment under optimum conditions was determined to be 40.55 kJ/mol.

4. Conclusions

XRF and XRD analysis revealed that the chromite plant tailing sample was predominantly consisted of Mg rich lizardite mineral. Mg and other elements in the sample were distributed homogenously according to particle size distribution. Dissolution of Mg from lizardite in HCl and H_2SO_4 acids using a glass reactor was investigated successfully. Optimum leaching conditions such as temperature, acid concentration, solid ratio, and leaching time were determined to be 85°C , 20wt. %, 6 M HCl – 4 M H_2SO_4 , and 120 min, respectively. Maximum Mg extraction yield for both two acids was determined to be nearly 98wt. %. The results showed that chromite tailings predominantly containing lizardite can be potentially used for CCSM and in producing Mg compounds. Leaching of lizardite left a solid residue mainly composed of amorphous silicate which can be used in various applications. Kinetic studies revealed that the dissolution of Mg from lizardite was found to follow Jander equation. Diffusion of Mg^{2+} , H_3O^+ , and SO_4^{2-} ions throughout the capillaries formed between tetrahedral silicate layers controlled the reaction speed rate.

References

- Apostolidis, C.I., Distin, P.A. 1978. The kinetics of the sulphuric acid leaching of nickel and magnesium from reduction roasted serpentine. *Hydrometallurgy* 3, 181-96.
- Arce, G.L.A.F., Neto, T.G.S., Ávila, I., Luna, C.M.R., Carvalho, J.A. 2017. Leaching optimization of mining wastes with lizardite and brucite contents for use in indirect mineral carbonation through the pH swing method. *Journal of Cleaner Production* 141, 1324-1336.
- Bałdyga, J., Jasińska, M., Jodko, K., Petelski, P. 2012. Precipitation of amorphous colloidal silica from aqueous solutions-Aggregation problem. *Chemical Engineering Science* 77, 207-216.
- Bobicki, E.R., Liu, Q., Xu, Z., Zeng, H. 2012. Carbon capture and storage using alkaline industrial wastes. *Progress in Energy and Combustion Science* 38, 302-20.
- Daval, D., Hellmann, R., Martinez, I., Gangloff, S., Guyot, F. 2013. Lizardite serpentine dissolution kinetics as a function of pH and temperature, including effects of elevated pCO_2 . *Chemical Geology* 351, 245-256.
- Fedoročková, A., Hreus, M., Raschman, P., Sučík, G. 2012. Dissolution of magnesium from calcined serpentinite in hydrochloric acid. *Minerals Engineering* 32, 1-4.
- Fedoročková, A., Raschman, P., Sučík, G., Ivánová D., Kavuličová, J. 2016. Utilization of chrysotile-type tailings for synthesis of high-grade silica by controlled precipitation. *Mineral Processing and Extractive Metallurgy Review* 37(5), 287-294.
- Kulikovskiy, V., Vorlíček, V., Boháč, P., Stranyánek, M., Čtvrtlík, R., Kurdyumov, A. 2008. Mechanical properties of amorphous and microcrystalline silicon films. *Thin Solid Films* 516(16), 5368-5375.
- Lacinska, A. M., Styles, M. T., Bateman, K., Wagner, D., Hall, M.R., Gowing, C., Brown, P. D. 2016. Acid-dissolution of antigorite, chrysotile and lizardite for ex situ carbon capture and storage by mineralization. *Chemical Geology* 437, 153-159.
- Levenspiel, O. 1972. *Chemical Reaction Engineering*. John Wiley and Sons, 2, 13-29.
- Liu, K., Chen, Q., Hu, H., Yin, Z. 2010. Characterization and leaching behaviour of lizardite in Yuanjiang laterite ore. *Applied Clay Science* 47, 311-316.
- Luce, R.W., Bartlett, R.W., Parks, G.A. 1972. Dissolution kinetics of magnesium silicates. *Geochimica et Cosmochimica Acta* 36, 35-50.

- Mevel, C. 2003. Serpentinization of abyssal peridotites at mid-ocean ridges. *Comptes Rendus Geoscience* 335(10-11), 825-852.
- Nduagu, E., Björklöf, T., Fagerlund, J., Wärnå, J., Geerlings, H., Zevenhoven, R. 2012. Production of magnesium hydroxide from magnesium silicate for the purpose of CO₂ mineralisation - Part 1: Application to Finnish serpentinite. *Minerals Engineering* 30, 75-86.
- Park, A.H.A., Fan, L.S. 2004. CO₂ mineral sequestration: physically activated dissolution of serpentine and pH swing process. *Chemical Engineering Science* 59(22-23), 5241-5247.
- Raza, N., Zafar, Z.I., Najam-ul-Haq, M. 2014. Utilization of formic acid solutions in leaching reaction kinetics of natural magnesite ores. *Hydrometallurgy* 149, 183-188.
- Rozalen, M., Huertas F. J. 2013. Comparative effect of chrysotile leaching in nitric, sulfuric and oxalic acids at room temperature. *Chemical Geology* 352, 134-142.
- Sanna, A., Dri, M., Hall, M.R., Maroto-Valer, M. 2012. Waste materials for carbon capture and storage by mineralisation (CCSM) - A UK perspective. *Applied Energy* 99, 545-554.
- Sanna, A., Wang, X., Lacinska, A., Styles, M., Paulson, T., Maroto-Valer, M.M. 2013. Enhancing Mg extraction from lizardite-rich serpentine for CO₂ mineral sequestration. *Minerals Engineering* 49, 135-144.
- Teir, S., Revitzer, H., Eloneva, S., Fogelholm, C.J., Zevenhoven, R. 2007. Dissolution of natural serpentinite in mineral and organic acids. *International Journal of Mineral Processing* 83, 36-46.
- Wang, Z., Yang, H., Wang, L., Zhao, M. 1997. Preparation of ultrafine SiO₂ with high surface area by the chemical precipitation method. *Materials Science and Engineering* 48, 211-214.
- Wang, L., Lu, A., Wang, C., Zheng, X., Zhao, D., Liu, R. 2006. Nano-fibriform production of silica from natural chrysotile. *Journal of Colloid and Interface Science* 295, 436-439.
- Wang, X., Maroto-Valer, M.M. 2011. Dissolution of serpentine using recyclable ammonium salts for CO₂ mineral carbonation. *Fuel* 90(3), 1229-1237.
- Wilson, S.A., Raudsepp, M., Dipple, G.M. 2006. Verifying and quantifying carbon fixation in minerals from serpentine-rich mine tailings using the Rietveld method with X-ray powder diffraction data. *American Mineralogist* 91, 1331-1341.
- Wilson, S.A., Dipple, G.M., Power, I.M., Thom, J.M., Anderson, R.G., Raudsepp, M., Gabites, J.E., Southam, G. 2009. Carbon dioxide fixation within mine wastes of ultramafic-hosted ore deposits: examples from the Clinton Creek and Cassiar Chrysotile, Canada. *Economic Geology* 104, 95-112.
- Yoo, K., Kim, B.S., Kim, M.S., Lee, J., Jeong, J. 2009. Dissolution of magnesium from serpentine mineral in sulfuric acid solution. *Materials Transactions* 50(5), 1225-1230.



Bulletin of the Mineral Research and Exploration

<http://bulletin.mta.gov.tr>



Geology of the Yeşilyurt gold deposit: an example of low-angle normal fault related mineralization, Eastern Anatolia-Turkey

Esra YILDIRIM^{a*}, Nail YILDIRIM^b, Cahit DÖNMEZ^c and Kurtuluş GÜNAY^d

^aFirat University, Department of Geological Engineering, Elazığ 23000, Turkey

^bIV. Regional Directorate of Mineral Research and Exploration, Malatya 44100, Turkey

^cGeneral Directorate of Mineral Research and Exploration, Ankara 06800, Turkey

^dMarmara Regional Directorate of Mineral Research and Exploration, Kocaeli, Turkey

Research Article

Keywords:

Yeşilyurt gold mineralization, Detachment fault/Low-angle normal fault, Fault gauge, Cataclasite, Breccia.

ABSTRACT

Yeşilyurt gold mineralization is located within the provincial borders of Malatya and Adıyaman in the East Anatolian Region. This mineralization is one of the gold deposits which correlated with low-angle normal/detachment fault. Low-angle normal fault associated with a tectonic setting which is potential extensional in Paleogene-Neogene (?) term. Marble-recrystallized limestone which belongs to the metamorphic core is the dominant rock (footwall) type in the bottom plate of the fault zone. There are deformed graphitic calc-schists (hanging wall) in the upper plate of the fault zone. The fault zone is characterized by fault gauge, cataclasite, and breccia. While the cataclasite, and breccia are the principal ore host, there is weaker mineralization in fault gauge. Alteration assemblages are: (1) silica replacements/veinlets and, (2) quartz-pyrite replacements / veinlets. High gold contents are closely related to silicification and quartz-pyrite alteration which damaged the primary textures. Small volume syn-tectonic magmatic rocks are simultaneous and typically monitored in the silicified areas which are border on the high-grade gold mineralization. Mineralization is a non-base metalliferous Au deposit that contains Au/Ag ~ 1.07, As (~0.27%), F (1.59%), and a trace amount of Sb. This deposit will lead to finding new gold deposits in Eastern Taurus Orogenic Belt.

Received Date: 29.07.2020

Accepted Date: 20.09.2020

1. Introduction

The mineralization area is located in the Eastern Taurus Orogenic Belt which is the part of the Alpine-Himalayan metallogenic belt, and covers the Malatya-Yeşilyurt and Adıyaman-Çelikhan region (Figure 1). This belt is one of the most important provinces in terms of mining regions. It contains different types of deposits such as; volcanogenic massive sulfide, epithermal, iron-oxide-Cu-Au (IOCG), skarn, and porphyry (Cu-Mo). Several academic studies and

mining activities have been mostly focused on IOCG deposits (Helvacı and Griffin, 1984; Yılmaz et al., 2003; Kuşcu et al., 2007, 2013; Çelebi, 2009), skarn deposits (Yılmaz et al., 1992; Yiğit, 2009; Kuşcu et al., 2010; Kalender, 2011; Hanelçi and Çelebi, 2013; Öztürk et al., 2019; Yıldırım et al., 2019), epithermal / porphyry deposits (Dumanlılar et al., 1999; Altman and Liskovich, 2011; İmer et al., 2012) and volcanogenic massive sulfide deposits (Şaşmaz et al., 1999; Akıncı, 2009; Yıldırım et al., 2012; Yıldırım, 2013; Yıldırım et al., 2016) because of their economic importance.

Citation Info: Yıldırım, E., Yıldırım, N., Dönmez, C., Günay, K. 2021. Geology of the Yeşilyurt gold deposit: an example of low-angle normal fault related mineralization, Eastern Anatolia-Turkey. Bulletin of the Mineral Research and Exploration 164, 261-279. <https://doi.org/10.19111/bulletinofmre.797729>

*Corresponding author: Esra YILDIRIM, eozyildirim@gmail.com

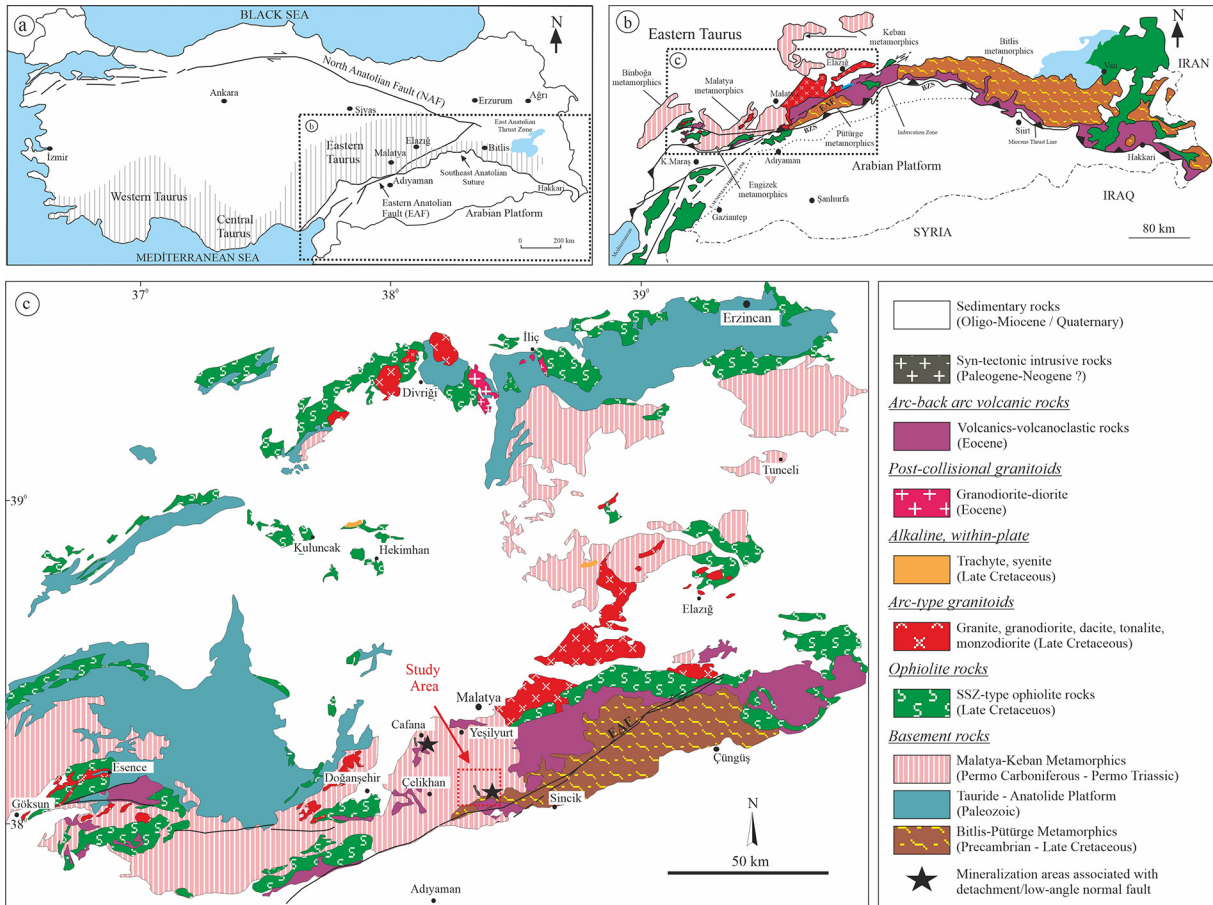


Figure 1- a) The location of the Taurus mountains and some of the main tectonic structures in Turkey, b) simplified geological map showing the main rock units of Eastern Taurus orogenic belt (MTA, 2002), c) mineralizations in the Eastern Taurus orogenic belt associated with large magmatic rock units (MTA, 2002; modified from Yıldırım et al., 2019)

In spite of these studies, low-angle normal fault/detachment fault systems and development of the ore deposits related to this system in the metamorphic core complexes, have not been reported before.

Although the mineralizations associated with low-angle normal fault or detachment fault have been mined since the 1860s, it has recently been defined as a different deposit type (Long, 1992). These deposits differ significantly from epithermal deposits with their characteristic mineral assemblages, alteration types, ore fluid types, and structural controls, and they are not well known. The model of this type of deposit has not yet been fully investigated and has so far been mostly described in West-Central Arizona, SE California, and the southern margins of Nevada (Long, 1992).

Detachment faults are regional-scale low angle (> 30) normal faults that cause significant regional extension as the footwall (sub-plate) moves upward,

generating displacements over tens of kilometers. Mineralization models associated with detachment faults include Fe and Cu oxide replacements, occasionally abundant sulfides in stockworks and veins, as well as barite and/or fluorite veins and Mn oxide veins (Spencer and Welty, 1986; Long, 1992). The fluid might be triggered by heat from either subplate rocks or syn-tectonic magmatic rocks ranging from micro-diorite to rhyolite (Reynolds and Lister, 1987; Long, 1992).

Yeşilyurt gold mineralization is one of the newly defined gold deposit group in the Eastern Taurus Orogenic Belt. Mineralization is located in the south of Malatya province and is 45 km away from the city (Figure 1b-c). Since this mineralization observed in the Eastern Taurus orogenic belt is important in terms of gold and fluorite, it has been the subject of some research studies (Revan and Genç, 2003; Şaşmaz et al., 2005; Altuncu, 2009). From previous studies, Şaşmaz et

al. (2005) have stated that fluorite-gold mineralizations might have occurred at low temperature, high fO_2 and hydrothermal conditions where there is no evidence of magmatic intrusion; Revan and Genç (2003) have claimed that it is strata-bound mineralization that is dependent on paleo-karstification processes and controlled by the dispersed Carboniferous-Permian discordance plane; Altuncu (2009) has argued that it is associated with a hydrothermal replacement type and a buried alkali magmatic mass. Previous studies contain some contradictory data. The types of structures in the metamorphic core complex could not be distinguished, and also the source of the hydrothermal solution is controversial.

The area was re-evaluated after prospecting and detailed exploration studies by MTA (General Directorate of Mineral Research and Exploration). In the field of gold mineralization in Yeşilyurt, the depth (0-115m) dimension of the mineralization was investigated for the first time with the drilling activities (mean depth 140 m; total core drilling 11,000 m) carried out by MTA, and 1,900,000 tons of gold resources with 1 g/ton of Au grade were estimated by using 0.4 g/ton cut-off grade over the field (Yıldırım et al., 2019). The mineralization has been interpreted as a deposit associated with a regional low-angle normal fault within the metamorphic complex.

This study aims to (I) describe and expand the typology of the gold deposit associated with the low-angle normal fault developed in the extensional environment and (II) propose a new regional metallogenic model by focusing on the existence of potential mineralization areas controlled by low-angle normal faulting. To achieve these goals, we tried to associate the results obtained from geology, structure, types of alteration, geochemistry, textural and mineralogical properties of gold mineralization to low-angle normal fault.

2. Geological Setting

2.1. Regional Geology

The geology and geodynamic evolution of the region should be well known to understand the mineralization and alterations associated with the low-angle normal fault within the metamorphic core complex in the study area located on the border of Malatya-Yeşilyurt and Adıyaman-Çelikhan.

Millions of years of complex geological movements have shaped the region called Turkey's Anatolia (Asia Minor). Turkey is a geologic part of the Alpine-Himalayan belt, also known as the Tethyan belt extending from the Atlantic Ocean to the Himalayas, apart from the small part of the country which is the continuation of the Arab platform located along the Syrian border. The Anatolian peninsula, which has an important place in the Alpine-Himalayan orogenic system, contains the remains of the Tethys (Paleo-Tethys and Neo-Tethys) oceanic basins between approximately E-W trending tectonic belts (Pontides, Anatolides, Taurides, and Margin Folds) (Şengör and Yılmaz, 1981; Ketin, 1983; Okay, 2008; Robertson et al., 2016a, b).

The mineralization area in the Eastern Taurids part of the Alp-Himalayan orogenic belt contains many important tectonostratigraphic/tectono-magmatic units (Figure 1b-c) and it has been affected by intensive fracturing, folding, thrusting, and nappe movements. The region includes Permo-Triassic metamorphic rocks, continental-arc, post-collision, intra-plate magmatites, back-arc basin products, and supra-subduction ophiolitic basement rocks (Figure 1c). These units are covered by Paleogene-Neogene (?) sedimentary, volcano-sedimentary, and volcanic rocks. The mineralization area is represented by Precambrian-Paleozoic Pütürge Metamorphics, Late Devonian-Late Cretaceous Bodrum nappe (Bedi and Yusufoglu, 2018), Devonian-Cretaceous Yahyalı nappe units (Bedi and Yusufoglu, 2018), and Early-middle Eocene Maden Group units (Figure 2).

Gold mineralizations that may create economic potential are within the metamorphic rocks of the metamorphic core complex (Figure 2). The metamorphic complex consists of marble, recrystallized limestone/dolomitic limestone, mica-schist, calc-schist, and these rocks metamorphosed under low temperature-low pressure conditions. These rocks largely outcrop in the south-southwest of Malatya province and have been identified as Permo-Carboniferous Malatya Metamorphics in previous studies. Some researchers (Asutay et al., 1986; Yılmaz et al., 1992) have considered Malatya Metamorphics as the equivalent of Keban Metamorphics and as their southerly extension (Figure 1c). According to the ages suggested by different researchers (Özgül, 1976; Kipman, 1981; Asutay et al., 1986), Keban Metamorphics are platform-type continental shelf sediments that

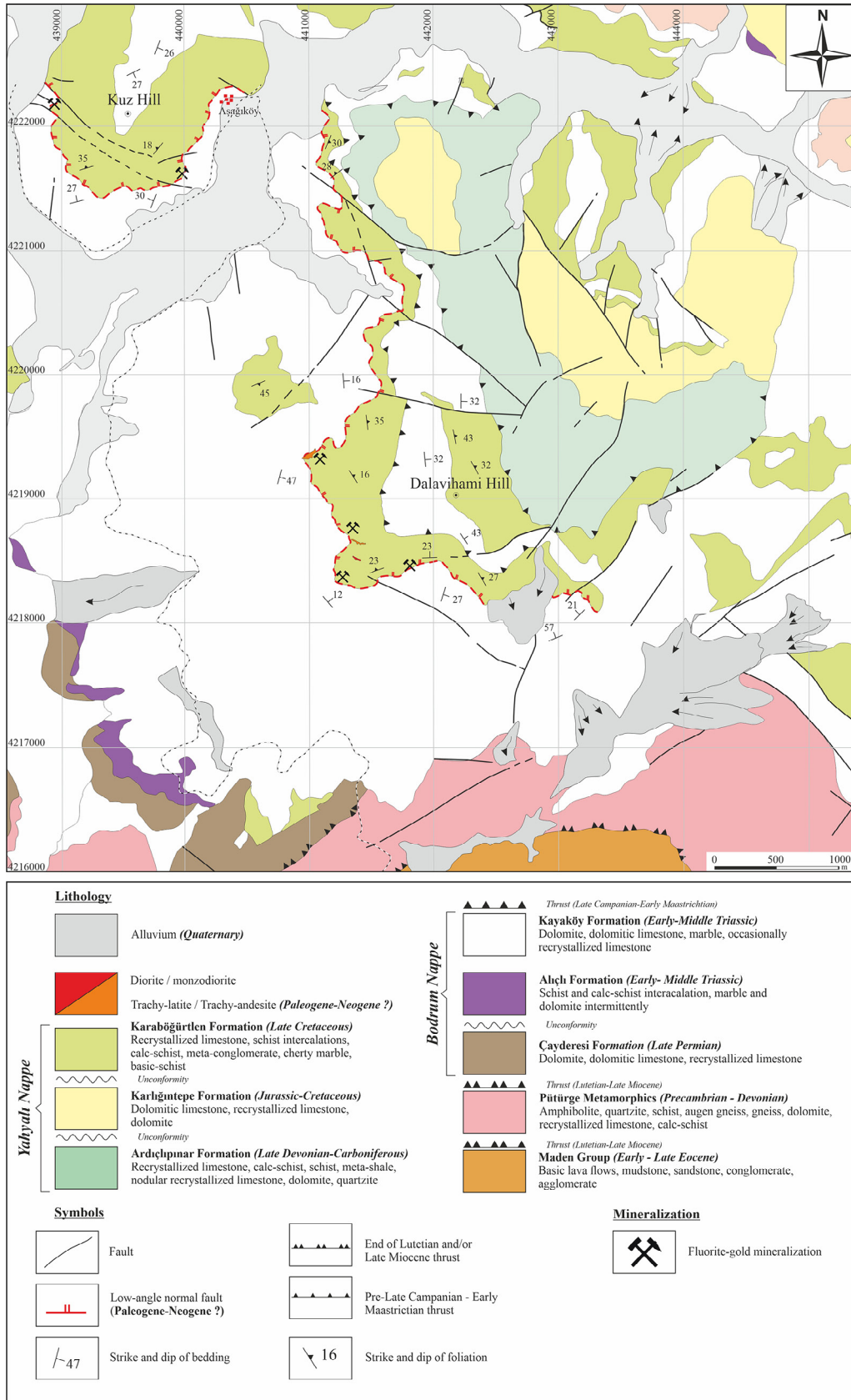


Figure 2- Geological map showing the mineralization in the study area and surroundings (modified from Bedi and Yusufoglu, 2018).

have undergone a deposition phase started during the Permo-Carboniferous and continued until the Triassic age.

2.2. Geology of the Mineralization Area

Yeşilyurt gold mineralization is observed as tabular bodies along the low-angle normal fault zone developed in Paleogene-Neogene, within the Late Triassic-Late Cretaceous metamorphic rocks. The slickenside of the fault zone is observed as a non-mineralized fault gauge. The hanging wall of the fault zone is a deformed graphite calc-schist of the metamorphic core complex and the footwall is composed of marble (Figures 3 and 4).

Precambrian-Paleozoic-Mesozoic and Cenozoic litho-stratigraphic units have been distinguished in the mineralization area and around. Structurally, from bottom to top and from south to north, respectively; the Late Devonian-Late Cretaceous Bodrum nappe tectonically overlies the Precambrian-Devonian aged Pütürge metamorphics nappe and the Maden Group consisting of volcanic and sedimentary rocks which

unconformably overlie the Precambrian-Devonian aged Pütürge metamorphic nappe (Figure 2). The metamorphic units of the Bodrum and Yahyalı nappe have been stated as lower lithological units (such as Kalecik marble, Düzağaç schists, Kerbelek limestone, Koltik formation, Pınarbaşı formation) within the Malatya metamorphics (Gözübol and Önal, 1986; Revan and Genç, 2003; Şaşmaz et al., 2005; Altuncu, 2009). Kayaköy and Karaböğürtlen formations of the Bodrum nappe were cut cross by Paleogene-Neogene igneous rocks as sills and dykes. Quaternary sediments composing of alluvium, alluvial fan, and talus are found at the top of the section in the region. The geological features of metamorphic and igneous rocks hosting the mineralization are given below.

2.2.1. Kayaköy Formation

This formation is observed as the footwall of the low-angle normal fault zone. Dolomite and dolomitic limestones containing recrystallized limestone/marble intercalations form the dominant lithology. Recrystallized limestone and marbles exposed to

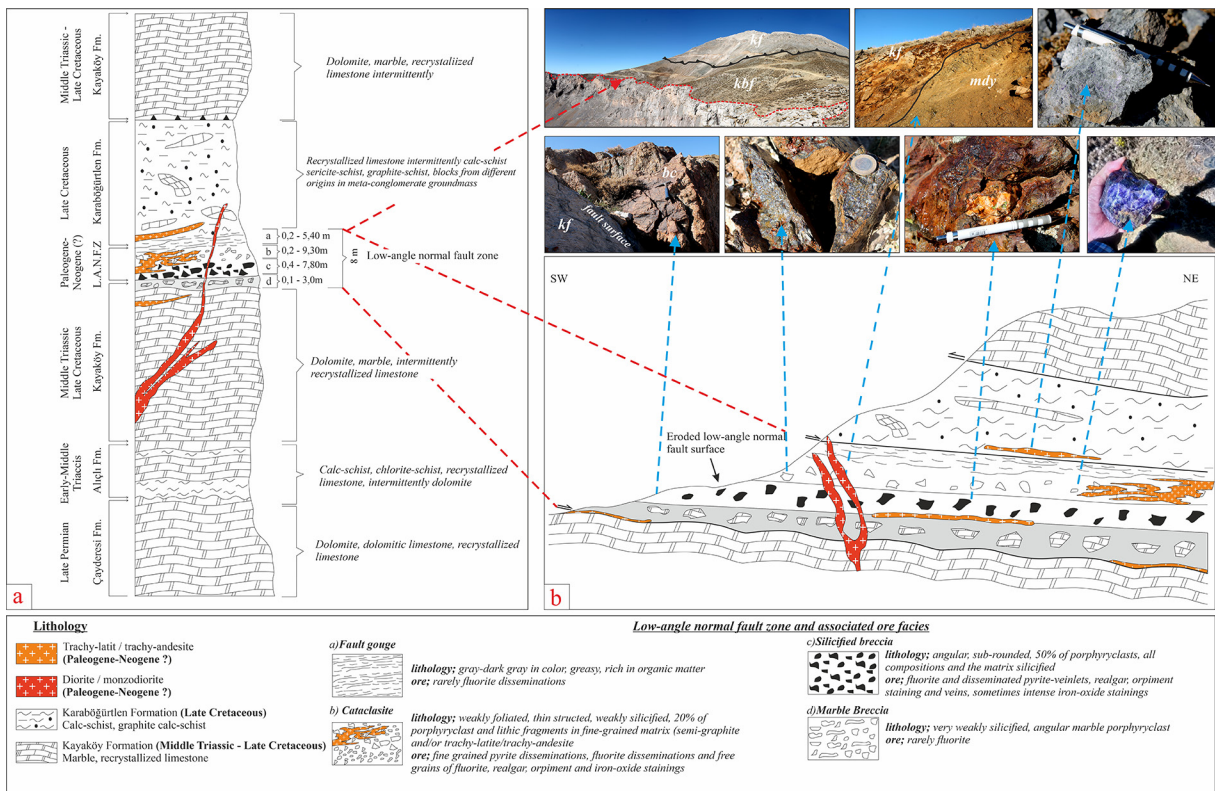


Figure 3- a) Generalized columnar section of the low angle fault zone and main rocks in Yeşilyurt gold mineralizations, b) NE-SW schematic cross-section (unscaled) of the ore sequence and low angle fault zone and associated ore facies (bş: breccia kf: Kayaköy formation, kbş: Karaböğürtlen formation, mdy: monzo-diorite).

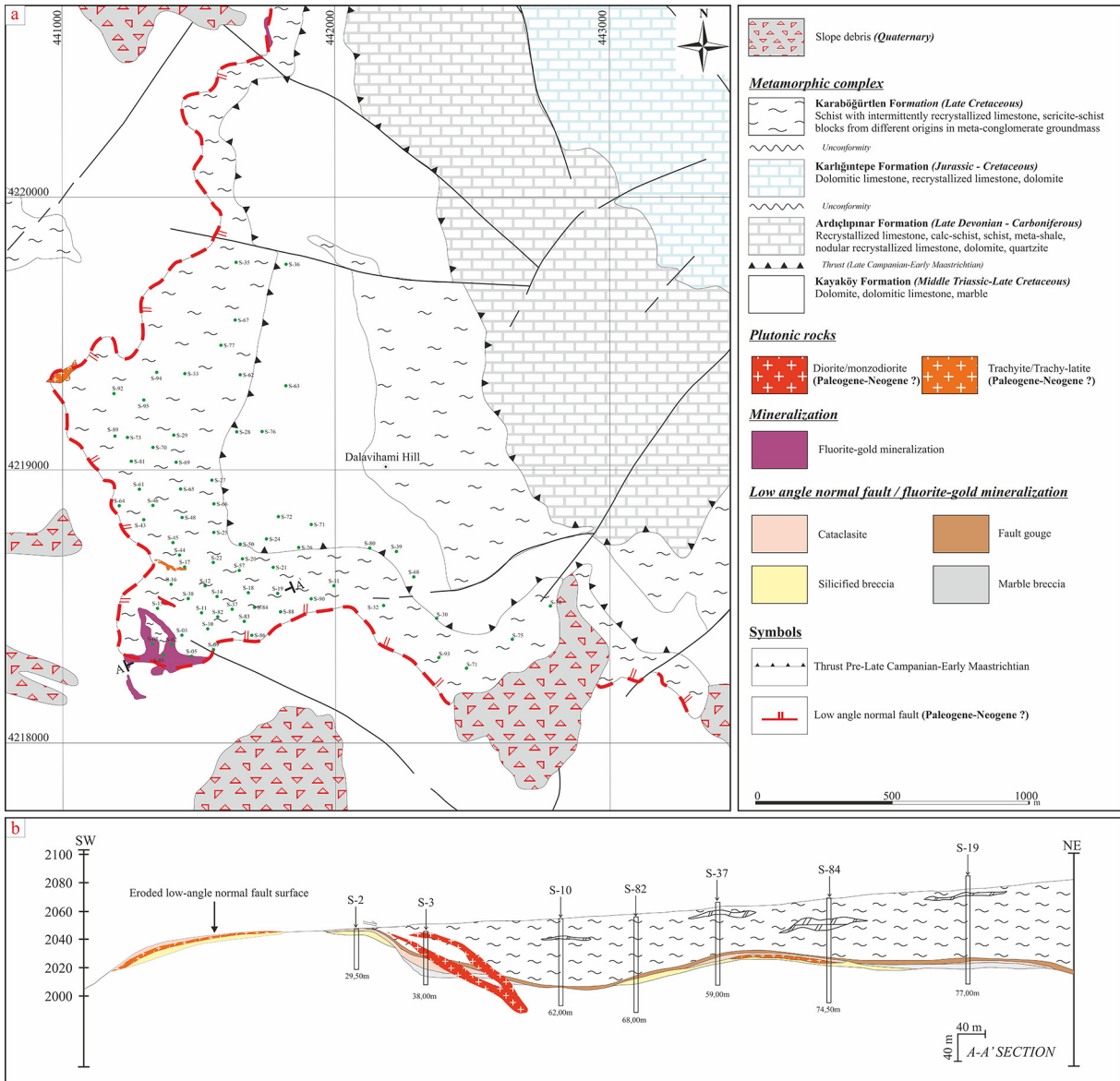


Figure 4- a) Detailed geological map of Yeşilyurt gold mineralization (modified from Bedi and Yusufoğlu, 2018), b) geological cross-section (drilling profiles showing vertical distribution of the ore zone; drilling well locations (from Yıldırım et al., 2019).

structural deformation and hydrothermal alteration host gold mineralization (Figure 3 and 4). The strikes and dips of the limestones appear to be approximately parallel to the low-angle normal fault zone (Figure 2).

2.2.2. Karaböğürtlen Formation

This formation is observed as a hanging wall of the low-angle normal fault zone, which consists of recrystallized limestone, dolomite, and graphite-calc-schists with cherty marble intercalations. In the study area, primarily overlies Middle Triassic-Late Cretaceous Kayaköy formation with an angular

unconformity and it is also possible to observe normal and reverse fault relationships with this unit (Figure 3 and 4). The strikes and dips of the limestones and the foliations in the schists appear to be consistent with the low-angle normal fault zone (Figure 2). Even though the foliations of the schists, which have been deformed, were distorted and rotated, they are generally parallel to the fault zone.

2.2.3. Paleogene-Neogene Magmatic Rocks

The magmatic rocks were determined for the first time in the study area and their surroundings are mostly

sills and dykes. The magmatic rocks are composed of sub-volcanic (trachy-latite/trachy-andesite) and intrusive (monzo-diorite, diorite) compositions with textures ranging from aphanitic to porphyry. While trachy-latite/trachy-andesite sills and dykes constitute the magmatic rock type related to mineralization, they mostly occur in ore zones, and generally as laminated flows in schist breccias (Figure 3 and 4). Magmatic rocks are common through in breccias and cataclasites (predominantly as a clast) between Late Triassic-Late Cretaceous Kayaköy and Karaböğürtlen formations along with the NW-SE striking and NE-dipping low-angle normal fault, however, there is no any evidence indicating a cross-cutting relationship with the fault gauge. They have been observed as clast and/or sills

up to several meters in thickness within breccia and cataclasites developed along the fault zone during drillings (Figure 3 and 4). Since the recrystallized limestones of the Kayaköy formation behave in basic composition, they have been able to form a weak (30-50 cm) baked zone through the contacts.

Trachy-latite/trachy-andesites are composed of feldspar, hornblende and biotite. Feldspar phenocrysts are distinguished from cataclasite and breccias by alterations such as carbonization, sericitization, and opacitization (Figure 5a) and the presence of biotite and hornblende (Figure 5a-c). The type of plagioclases could not be determined because the trachy-latite/trachy-andesite samples are heavily

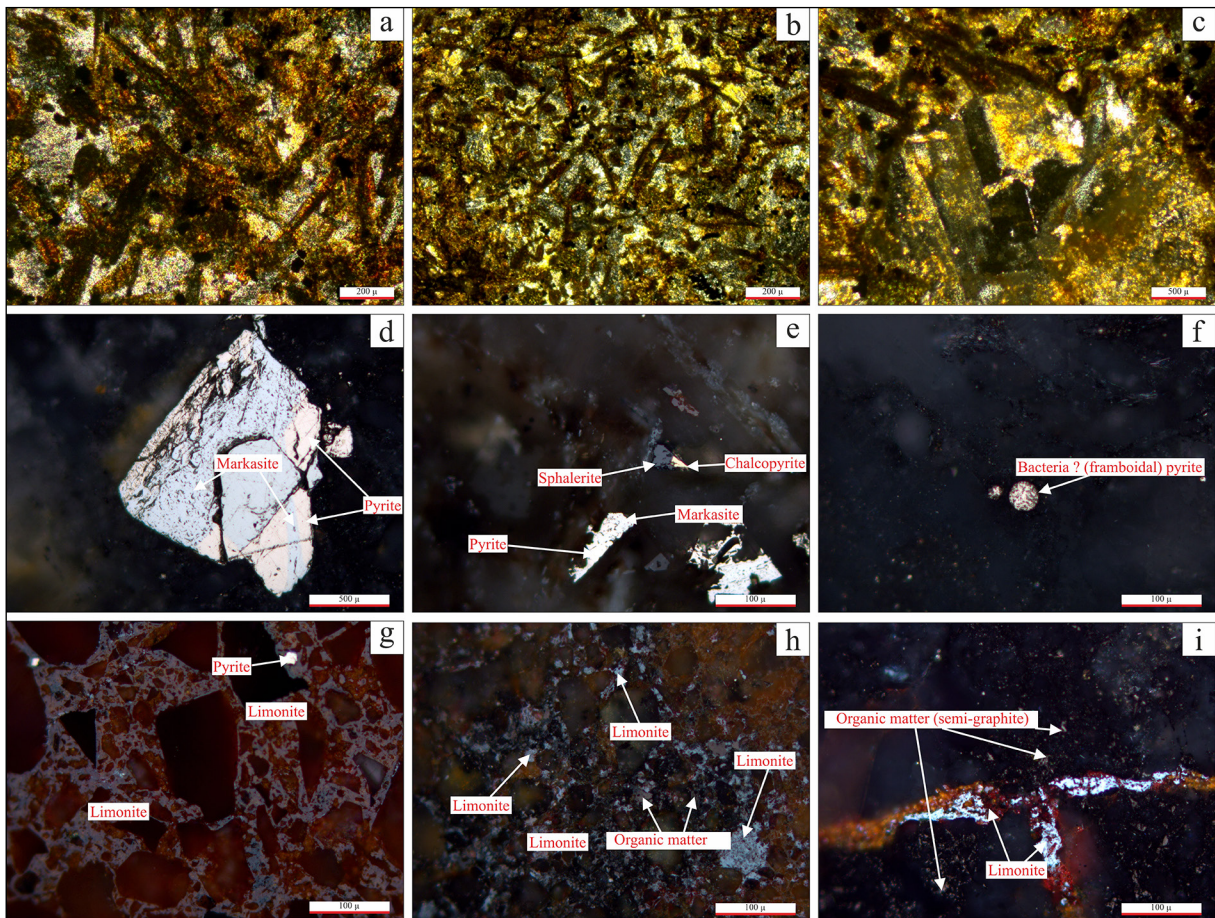


Figure 5- Mineralization views through low angle normal fault (detachment fault) zone in the Yeşilyurt gold mineralizations. a) non-mineralized fault gauge, b) quartz-fluorite in the form of free-space filling in the mineralized cataclasite zone and limonite in fracture fillings (transformation from pyrite), c) Laminated flows through schist breccias in trachy-latite contact, quartz-orpiment-fluorite in the form of space-filling, d) Iron-oxide staining through trachy-latite/organic matter matrix in cataclasites, e) contact between silicified breccia and trachy-latite and widespread iron-oxide staining, f) widespread silicification through breccias, g) the relationship between silicified breccia and trachy-latite, showing syn-genetic mineralization, h) non-mineralized marble breccia, i-j) widespread orpiment in the form of fracture filling and staining and widespread fluorite with open-space filling, k) cataclasite and l) trachy-latites cutting cross silicified breccias

altered. Plagioclases are located in the groundmass as small microlites (Figure 5b). Sericitization and carbonization are common. Hornblende minerals are generally subhedral or euhedral (Figure 5a-c). They are green-dark green, brown under plane-polarized light and they show pleochroism. Usually, prismatic crystals have cleavage in one direction and lozenge-shaped ones have distinct cleavage in two directions. Biotite minerals are generally in the form of opacified thin rod-like crystals and they are subhedral (Figure 5a-c). They appear in colors ranging from light brown to dark brown under plane-polarized light, and dark brown under cross-polarized light. While microlithic texture formed by mostly small crystals (Figure 5b) is observed in trachytes, microporphyratic texture in which sanidine phenocrystals are located in fine-grained groundmass is observed in some of the samples (Figure 5c). Based on the core samples obtained from the drillings, it has been observed that magmatic rocks are widely carbonated, sericitized, opacified, silicified and have disseminated in pyrite up to 2 % and they contain fluorite. The similar alteration of these rocks and mineralized areas and their presence in the mineralization area strongly reveal the direct genetic relationship of trachy-latite / trachy-andesites with the gold deposit. The composition, stratigraphic and structural positions and mineralization associations of the magmatites (Sağiroğlu, 1988; Kalender et al., 2009) defined in the Cafana Pb-Zn ore deposit (Figure 1c) located approximately 25 km northwest of the study area are similar to magmatic rocks in the Yeşilyurt gold mineralization area and they can be correlated. Although there is no available age data for these rocks, structural and stratigraphic positions and ore associations of those suggest that they may be of Paleogene-Neogene(?) age.

Diorite/monzodiorites are mostly in the form of dykes cutting-cross the Karaböğürtlen and Kayaköy formations (Figure 3 and 4). They include feldspar, plagioclase, amphibole, biotite, and opaque minerals and, also arenization is common. These rocks also cut-cross the low-angle normal fault plane (Figure 3 and 4b) and are younger than trachy-latites/trachy-andesites and are not thought to be associated with gold mineralization.

2.3. Structural Geology

The low-angle normal fault, between the Late Cretaceous-Late Triassic aged Kayaköy and

Karaböğürtlen formations of the Bodrum nappe, defined for the first time in the mineralization area has continuity for kilometers (> 10 km) and has a slope of about 10° (Figure 2, 3). In the previous studies, this fault has been interpreted and mapped either as unconformity (Revan and Genç, 2003; Bedi and Yusufoglu, 2018) or reverse fault (Şaşmaz et al., 2005; Altuncu, 2009). A recently defined low-angle normal fault is thought to be reactivated due to Paleogene-Neogene(?) extensional tectonism after the thrust faults previously developed within the metamorphic core complex (Figure 3b). In the mineralization area, syn-tectonic magmatic rocks (trachy-latite/trachy-andesite) have developed along the low-angle normal fault.

Mineralization has developed between the graphite-calc-schist forming the hanging wall and the marbles of the footwall of the low-angle normal fault. This fault zone is composed of three structural units: (1) fault gauge, (2) cataclasite, and (3) breccia zone. While cataclasite and breccia units are the main hosts of the ore, mineralization in the fault gauge is very weak (Figure 3a-b).

Fault gauge: This zone separates the graphitic calc-schists from the underlying marbles. The fault gauge thickens and thins along the plane, indicating a low-angle normal fault zone (Figure 3a). The gauge is averagely 2 meters thick and has probably formed during displacement along the fault, mostly by excessive reduction of grain size of the overlying graphitic-calc-schists and much less underlying marble breccias. Cataclasite, trachy-latite/trachy-andesite, and breccia levels are present in the lower parts of the fault gauge (Figure 3a-b). The fault gauge is rich in organic matter (semi-graphite) and greasy, gray-dark gray. It rarely contains fluorite.

Cataclasite: It is the zone where mineralization is intensely observed and has an average thickness of 2.50 m (Figure 3a). Cataclasites are observed as weakly-foliated, thin structured, greasy and they contain porphyroclasts (calc-schist, quartz, and very little marble) and lytic fragments ranging from <1 mm to 10 mm in size within the fine-grained matrix (rich in organic matter) having generally similar compositions (Figure 3a-b). The lineation along porphyroclasts is notable. The matrix contains very fine-grained quartz, carbonate, and fluorite, and has sometimes iron-

oxide staining. While the grain size and abundance decrease towards the fault gauge, they increase towards the underlying breccia zone. Deformation is more dominant than brittle behavior. Cataclasites are generally mineralized because they present suitable environments for fluid flow and contain fine-grained pyrite disseminations and sequences, fluorite dissemination and veinlets, and also realgar-orpiment (Figure 3b). Silicification is more common in the levels close to the underlying breccia zone.

Breccia: The silicified breccia zone underlying the cataclasites represents the lower part of the fault and is approximately 2.50 m in thickness (Figure 3a). While the upper part is rich in fine-grained matrix and schist fragments, it consists of angular, sub-rounded marble fragments towards lower parts. Brittleness is more dominant than deformation. It is the zone where the mineralization is most intensely observed together with the cataclasites. The breccia levels close to cataclasites have been intensively silicified and affected by hydrothermal alteration. The silicified breccia zone contains fluorite, disseminated pyrite, pyrite veinlets, and realgar, orpiment veinlets (Figure 3b). Some levels intensely contain Fe-oxide (limonite).

Slightly silicified marble breccias (averagely 1.00 m) are present in areas close to the marble contact of the Kayaköy formation (footwall) (Figure 3a-b).

3. Mineralization

Mineralizations in the study area and around are observed in three different locations; west of Kuz Hill, south of Kuz Hill, and Dalavihami Hill (Figure 2). Mineralizations are intermittently observed along the NW-SE direction on the low-angle normal fault zone of approximately 11 km length (Figure 2). West of Kuz Hill and Dalavihami Hill are the outcrops where mineralizations are best observed. The Dalavihami Hill mineralizations observed along the fault plane at approximately 2 km length and 0.20-22 m thickness constitute the subject of this study (Figure 4a). The hanging wall of the low-angle normal fault is occasionally eroded at the intersections and the ore can be traced directly on the marbles (Figure 4b). Drilling activities have shown that mineralizations are approximately 1.5 km in the N-S direction, 1 km in the E-W direction, and averagely 4 m in thickness (Yıldırım et al., 2019; figure 4a-b).

The mineralizations are associated with the low-angle normal fault which is between the Mid Late Triassic-Late Cretaceous aged Kayaköy formation and the Late Cretaceous Karaböğürtlen formation of the Bodrum nappe (Figure 4a-b) and they have not been affected by metamorphism.

The ore facies consists of breccia and cataclasite, and the mineralizations are mostly limited with silicified breccia and overlying cataclasites (Figure 4b). The predominant alteration is intense silicification and pyrite alteration. While pyrites are generally in the form of clusters and dissemination, they can also be observed as thin bands in cataclasites. Breccia grain size increases from the cataclasites to the marble breccias below. The thicknesses of cataclasites (0.20-9.30 m) and breccias (0.40-7.80 m) are approximately the same (Figure 3a and 4b). Trachy-latites/trachy-andesites are approximately 2 m in thickness and generally have a close spatial relationship with the mineralizations (Figure 3 and 4b). The sub-volcanic rocks are common in the cataclasites and breccia zone and are rarely observed as sills through the schists forming the hanging wall (Figure 3b). Sills are generally poorly mineralized.

Ore microscopy studies have shown that sulfide concentrations predominantly consist of pyrite, chalcopyrite, and sphalerite in descending order. Pyrites are very fine-grained, subhedral, anhedral, and cataclastic (Figure 5d, e). Trace amounts of bacteria (fromboidal) are observed in pyrite (Figure 5f). Pyrites show transformation into limonite (Figure 5g-i) and marcasite (Figure 5d, e) along with the fractures and cracks. Pyrite inclusions in limonites indicate transformation from pyrite. Au, observed along the fractures as little bubbles and discrete particles within the pyrite grains. Trace amounts of chalcopyrite and sphalerite are anhedral, fine-grained, and interlocked within the gangue minerals (Figure 5e). Organic matters are observed between gangue minerals and fractures under a microscope. They are mostly clustered within limonites (Figure 5h, i). It has been determined that organic matter is semi-graphite.

Gold mineralization is associated with silicification and pyrite. The predominant sulfide mineral is pyrite containing a trace amount of chalcopyrite and sphalerite. Transformation to limonite and a small amount of hematite are observed in pyrites. Gold

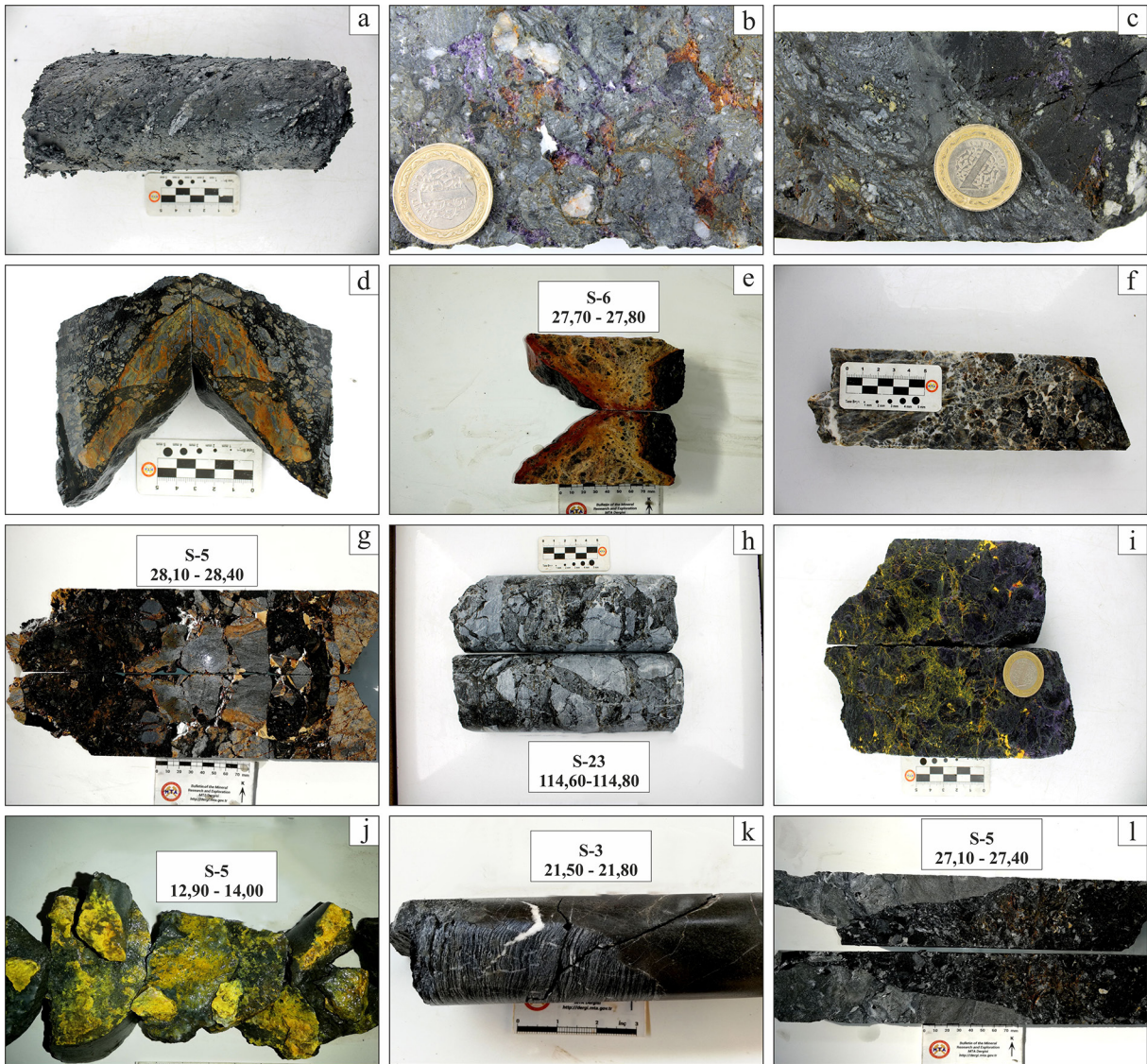


Figure 6- a) Euhedral, biaxially sliced hornblende crystals and opacitized biotites in trachy-latite/trachy-andesite, b) microlitic texture, c) sanidine phenocrystal showing carlsbad twinning, observed in microporphyric textured trachytes, d) euhedral pyrite showing transformation to marcasite, e) pyrite and trace amounts of anhedral sphalerite and chalcopyrite, f) pyrite in the form of bacteria (framboidal), g) widespread limonitization in silicified breccia zone, h) non-mineralized, i-j) florite staining and organic matter (semi graphite) between crack and gague minerals and at the grain boundaries, k) cataclastics and l) tarchy-latite cutting silicified.

might be transported as bisulfite complexes. Fluorite is mostly in thin quartz-fluorite veinlets and the form of space-filling (Figure 6b, i). Besides, realgar and orpiment occurrences are mostly observed as staining in the fracture zones of trachy-latite/trachy-andesites (Figure 6i, j) and sometimes in cataclastite and breccia.

3.1. Hydrothermal Alteration

Alterations defined in the mineralization area are; (I) silica replacements/veinlets and (II) quartz-pyrite replacements/veinlets.

Cataclastites with intense organic matter, containing fluorite, pyrite matrix, and mostly schist-quartz fragments just below the fault gauge (Figure 6a) and are poorly silicified (Figure 6b-c). Limonitization/hematitization (transformation from pyrite) is common through some of the levels (Figure 6d).

The most common alteration is silica replacement, which is often associated with high-grade gold mineralization. Silicification is mostly in breccias and is cut-cross by limonite vein/veinlets (Figure 6f). Silicified parts are sometimes overlain by limonite

(Figure 6e). Thin quartz veins cutting the silicification irregularly are observed. Silica replacement/veinlets are observed as matrix replacement within the breccia and partial absorption is observed in the breccia fragments (Figure 6g). The colour of silica ranges from dark-gray to light-gray. Dark-gray parts contain <1-2 % fine-grained disseminated pyrite. Very high gold grades are in the dark-gray silicified parts with iron-oxide staining. This zone passes into the less silicified and organic matter-rich cataclasite zone at the top and the non-mineralized marble breccia at the bottom (Figure 6h).

Quartz-pyrite alteration usually occurs in the breccia zone as a gray-green matrix replacement and quartz veins often cut-cross the altered matrix. Pyrites are usually localized in veins and are less common. Quartz-pyrite alteration transitions dark-gray silicification towards upper levels and marble breccia towards lower levels. This alteration can be distinguished from trachy-latite/trachy-andesites by the absence of feldspar phenocrystals. Apart from the silica replacement, it is the second important type of alteration for gold mineralization.

Hydrothermal alterations and associated minerals can be observed both laterally and vertically. While the most intense silicification is in the breccias of the fault zone, it is much less in the cataclasites. The fault gauge is not silicified.

4. Analytical Techniques

Chemical analyses of thirty seven rock samples collected from the mine area including drill cores, made in MTA (General Directorate of Mineral Research and Exploration) laboratories. Drill cores with ore were sampled at onemeter intervals. The sampling procedure was completed according to standards recommended by international organizations like Crirco (Committee for Mineral Reserves International Reporting Standards) and JORC (Joint Ore Reserve Committee, Australia). The most characteristic samples were chosen from the data set and are presented as a table 1 in the article. Four fault gauge samples, ten cataclasite samples, eight trachy-latite/trachy-andesite samples, ten silicified breccia samples and five marble breccia samples were selected for whole rock analyses using lithium metaborate/tetraborate fusion ICP for SiO₂, Al₂O₃, TiO₂, Fe₂O₃(T), K₂O, Na₂O, CaO, MgO, MnO and P₂O₅.

5. Geochemistry

In the field of mineralization, the analysis of the samples obtained from the drillings carried out by MTA for exploration and reserve studies have revealed high Au values, but base metal concentrations are insignificant (Figure 7). Both detailed geological studies and drilling studies have indicated new data in the field of mineralization and have revealed the economic importance of gold mineralization in buried areas. The chemistry of the ore, host rocks (Table 1) and even drill core samples have contributed to identify and classify the mineralization.

The element concentrations of the low-angle normal fault zone containing the gold mineralization are high in silicified breccias, cataclasites, and trachy-latites, but much lower in fault gauge and marble breccias (Figure 7; table 1). The concentrations of the main units are: Fault gauge 21-31 ppm Cu, 27-76 ppm Zn, <1 ppm Ag, 25-125 ppb Au, 239-1199 ppm As, 5-19 ppm Sb, %<0.01-0.11 F; cataclasite 11-28 ppm Cu, 41-495 ppm Zn, <1-15.5 ppm Ag, 790-3500 ppb Au, 899-5976 ppm As, 25-171 ppm Sb, %1.6-11,0.50 F; silicified breccia 11-23 ppm Cu, 12-185 ppm Zn, <1-3.4 ppm Ag, 850-6300 ppb Au, 105-3996 ppm As, 6-103 ppm Sb, %<0.01-0.8 F; trachy-latite/trachy-andesite 11-28 ppm Cu, 7-264 ppm Zn, <1-21 ppm Ag, 1000-4800 ppb Au, 895-11577 ppm As, 23-293 ppm Sb, %<0.01-0.5 F; marble breccia <3-7 ppm Cu, 21-470 ppm Zn, <1 ppm Ag, 110-210 ppb Au, 100-431 ppm As, <5-12 ppm Sb, %<0.01 F.

6. Discussion and Results

Yeşilyurt gold mineralization has developed as part of the silicification and quartz-pyrite alteration hosted by the low-angle normal fault zone. Mineralization is polymetallic, which is related to gold deposits associated with silver, arsenic, and fluorite as well. A simple genetic model of mineralization can be developed by discussing the origin of the fault zone and the origin of the subsequent hydrothermal system. This genetic model may give an idea about the mineralization associated with the extensional environment in the Eastern Taurus.

6.1. Origin of the Fault Gauge

The main structural elements in the mineralization area are the low-angle normal fault as well as the

Table 1- Compositional data of the samples from low-angle normal fault zone, Yeşilyurt gold mineralization.

	Sample	Au (ppb)	Ag (ppm)	As	Bi	Co	Cu	Mo	Ni	Pb	Sb	V	Zn	F (%)	Au/Ag (ppm)
Fault Gauge	S-11-21	25	<1	279	<5	7	31	<5	28	9	5	5	76	<0.01	0.03
	S-14-20	125	<1	1023	<5	7	28	<5	73	8	7	5	27	<0.01	0.13
	S-16-07	60	<1	239	<5	<5	21	<5	133	9	5	5	48	<0.01	0.06
	S-16-09	55	<1	1199	<5	9	26	<5	199	14	19	<5	60	0.11	0.06
Cataclasite	S-17-03	3500	15.5	2370	<5	<5	20	69	54	95	134	53	151	5.71	0.23
	S-94-22	3200	6.5	2657	<5	8	28	31	78	27	32	60	495	2.09	0.49
	S-17-04	2205	8.8	1672	<5	5	26	58	300	94	67	47	132	4.81	0.25
	S-17-02	2200	6.8	1878	<5	8	22	18	56	28	75	33	125	2.80	0.32
	S-08-08	1560	<1	3379	<5	<5	21	14	96	25	104	55	297	1.80	1.56
	S-08-07	1080	2.1	2695	<5	6	18	14	46	19	64	37	70	1.60	0.51
	S-08-06	1040	2.2	5976	<5	8	18	22	129	35	171	44	186	1.88	0.47
	S-02-02	985	<1	1198	<5	<5	16	17	244	49	39	56	52	11.50	0.99
	S-02-01	905	<1	1922	<5	<5	11	19	177	51	41	49	44	4.50	0.91
	S-02-03	790	<1	899	<5	<5	12	34	41	46	25	38	41	4.60	0.79
Trachy-laitite/trachy-andesite	S-46-29	4800	21.0	2143	<5	<5	12	95	26	12	293	35	22	0.01	0.23
	S-46-28	3700	9.9	11577	<5	<5	15	38	23	14	225	36	33	0.01	0.37
	S-46-31	3100	16.7	8797	<5	5	17	42	41	21	60	89	264	0.20	0.19
	S-46-30	2900	17.7	895	<5	<5	13	50	32	13	62	50	7	0.01	0.16
	S-80-54	1700	6.1	2522	<5	11	28	12	79	20	38	13	84	0.20	0.28
	S-20-41	1400	<1	1707	<5	<5	20	31	25	15	41	28	164	0.01	1.40
	S-46-32	1350	7.7	5143	<5	<5	11	15	23	12	23	45	148	0.50	0.18
	S-20-42	1000	<1	964	<5	<5	20	21	31	19	27	19	112	0.40	1.00
Silicified breccia	S-37-13	6300	1.5	998	<5	<5	23	11	9	5	24	14	28	0.01	4.20
	S-37-14	6100	<1	2093	<5	<5	11	15	8	5	65	52	38	0.01	6.10
	S-14-24	3300	1.1	1423	5	5	22	12	365	13	53	32	140	<0.01	3.00
	S-05-19	2390	3.4	2478	6	17	21	7	233	22	53	11	33	0.01	0.70
	S-44/1-07	2050	2.3	1556	<5	5	23	31	56	90	103	71	88	0.01	0.89
	S-83-11	2015	1.0	3996	<5	6	15	11	26	<5	20	31	185	0.80	2.02
	S-44/1-06	1835	1.8	951	<5	5	22	26	21	81	31	52	12	0.60	1.02
	S-05-18	1140	3.0	1628	<5	10	15	16	469	31	27	14	37	0.01	0.38
	S-05-21	955	2.3	1167	<5	17	21	5	228	11	26	11	28	0.03	0.42
	S-90/1-10	850	<1	105	<5	<5	11	18	17	8	6	16	167	0.50	0.85
Marble breccia	S-57-36	210	<1	184	<5	<5	7	18	5	5	12	19	141	<0.01	0.21
	S-73-35	170	<1	431	<5	<5	3	6	19	20	5	23	276	<0.01	0.17
	S-22-18	130	<1	167	<5	<5	4	7	7	7	10	31	470	<0.01	0.13
	S-29/1-36	110	<1	423	<5	<5	<3	<5	5	<5	<5	12	21	<0.01	0.11
	S-57-35	110	<1	100	<5	<5	<3	<5	<5	<5	6	9	81	<0.01	0.11

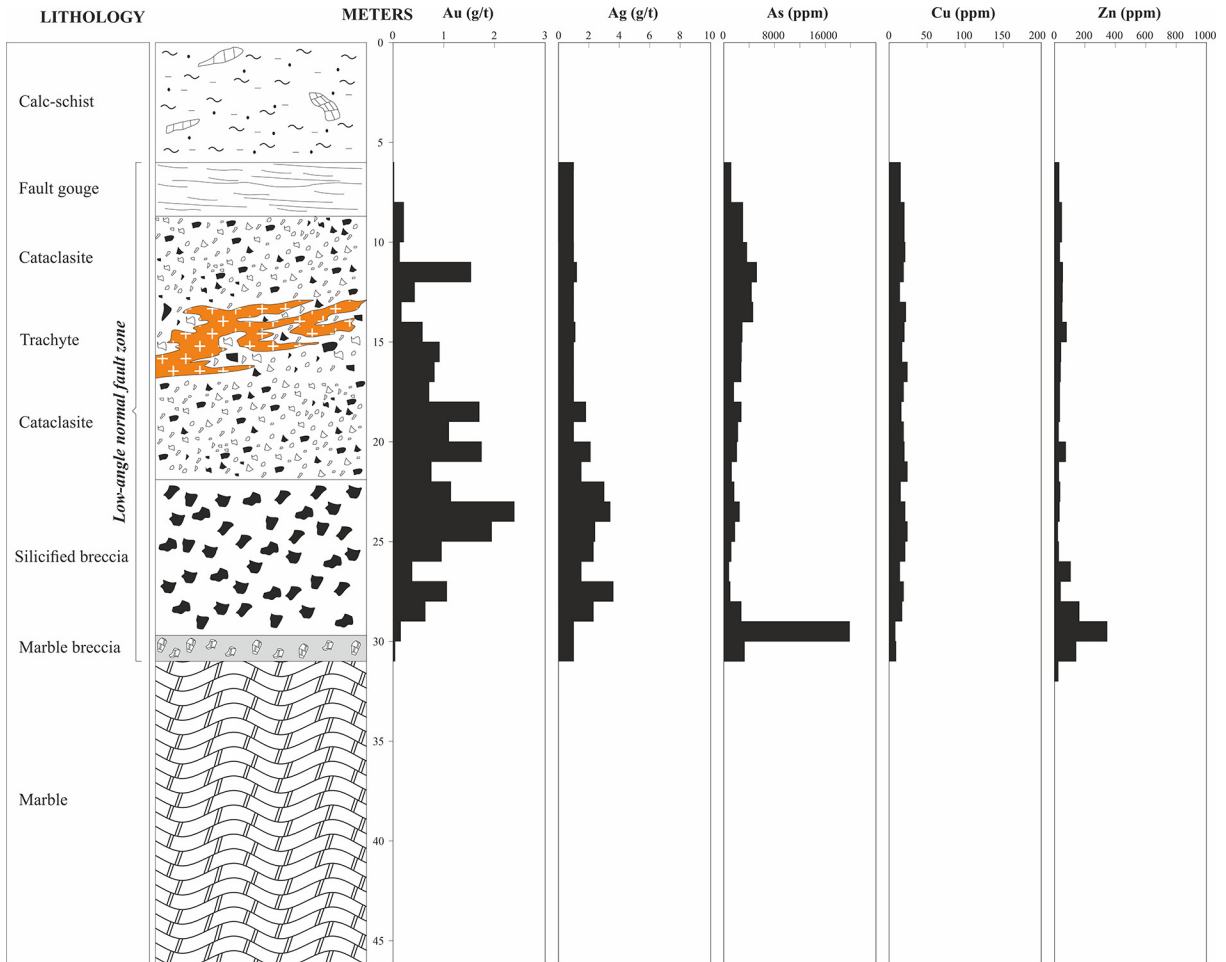


Figure 7- Graphical log of the S-5 drilling shown in figure 4. Gold, silver, arsenic, copper, and zinc contents of the low-angle normal fault zone and main lithological units are shown (Sample intervals of 1 meter; modified from Yıldırım et al., 2019).

reverse and strike-slip faults. The region is located in a tectonically active environment. It is known that the compressive tectonic regime has been active especially during the Late Cretaceous-Paleogene-Neogene (?) period (Şengör and Yılmaz, 1981). The low-angle normal fault must have developed in the Paleogene-Neogene (?) period, with the active role of an extensional tectonic environment. During this period, it is thought that thrust faults within the metamorphic core complex have reactivated as normal faults. Paleogene-Neogene (?) extensional tectonics is associated with back-arc extension and/or subduction rollback. During this period, small-volume of felsic magmas (trachy-latite/trachy-andesite) have settled in shallow crust levels along the low-angle normal fault.

The suggestions about detachment like faulting on Yeşilyurt gold mineralization are based on local and regional observations. The most important arguments;

(I) existence of fault gauge, (II) asymmetric folding on cataclasites and relatively silicified breccias just below fault gauge, and (III) evidence showing that the faulting is partially coincident with the emplacement of the trachy-latite/trachy-andesite intrusions.

The fault gauge zone always separates the hanging wall schists from the footwall marbles. The fault presents a braided structure due to surface erosion. The fault gauge along these inter-sections have moved away from the environment after this erosion, which has made mineralization reveal. Asymmetrical folds have been observed in the cataclasites and breccias underlying the fault gauge. The down-dipping parts of the folds are slightly steeper and increase the possibility of normal faulting and displacement. Also, high-grade extensional shear textures and low-grade fault gauge and breccias support this situation as well.

The emplacement of Paleogene-Neogene (?) sub-volcanic sills and dykes appears to be simultaneous with low-angle faulting. Local and regional geological evidence suggest that the fault zone in the mineralization area indicates an origin of detachment faulting within extensional tectonism during the Paleogene-Neogene (?) period.

Mineralization is observed within the zones which have been heavily silicified and brecciated at the same time of faulting. Also, alterations and mineralizations overlying the cataclastic textures indicate that post-faulting processes in the ore deposit have been also effective. However, there is also evidence for post-mineralization faulting. Deformed pyrites can be an example of this.

6.2. Geochemical Characteristics of Mineralization Associated with Low-Angle Normal Fault

Element (Au, Ag, Pb, Zn, Sb, Mo, F, As) distributions were studied to understand the relationship between low-angle normal fault and mineralization. Correlation coefficients between minor elements and enrichment coefficients were calculated (Table 2). The mineralization factors reflect a strong positive correlation of gold against silver, antimony, and molybdenum (0.48, 0.50, 0.51; table 2, 8a-c), while weaker positive correlation against arsenic (0.34; figure 8d). A relatively negative correlation of gold against Zn and Cu (-0.08, 0.15; figure 8e, f) was

observed. The Gold/Silver ratio is between 0.16 and 6.1 (Table 1).

Fluorites are observed in the mineralization area within the fault zone and gold concentrations in these zones are relatively higher. Fluor values are in the range of 0.01-11.5% (Table 1; average 1.59%), and they are considered to be economically insignificant. However, they might be recovered as a by-product. The source of high arsenic values in the ore zone (Table 1; mean 0.27%) are realgar and orpiment.

Geochemical data may have the following consequences:

I. Low-angle normal fault zone provides permeable fluid channel which is necessary for precipitation of minerals from hydrothermal fluids. Organic materials, creates suitable reduced setting for precipitating of sulfides. Therefore, high concentrations of Au and As may be associated with faulting processes. Most of the possible gold mineralizations in the region must be in the detachment fault zone.

II. Au and Ag have a weak positive correlation with other elements such as F, Mo, Sb. This may indicate that it is part of polymetallic mineralization and may suggest the element assemblage of deposits to be discovered in the area.

III. The higher concentrations of Au, Ag, and As in the center of the low-angle normal fault zone and

Table 2- Correlation coefficients between analyzed elements.

	Au	Ag	As	Bi	Co	Cu	Mo	Ni	Pb	Sb	V	Zn	F
Au	1.00	0.49	0.34	0.07	-0.09	0.15	0.49	-0.08	0.07	0.51	0.40	-0.08	-0.03
Ag		1.00	0.42	-0.02	-0.08	0.02	0.83	-0.11	0.18	0.62	0.43	-0.01	0.04
As			1.00	0.02	-0.01	0.06	0.26	-0.06	0.00	0.55	0.45	0.12	-0.03
Bi				1.00	0.59	0.08	-0.13	0.21	-0.02	0.00	-0.18	-0.12	-0.09
Co					1.00	0.34	-0.29	0.43	-0.12	-0.09	-0.37	-0.15	-0.16
Cu						1.00	0.02	0.29	0.27	0.04	-0.01	-0.08	0.06
Mo							1.00	-0.09	0.45	0.72	0.51	-0.03	0.23
Ni								1.00	0.24	-0.05	-0.09	-0.16	0.25
Pb									1.00	0.22	0.53	-0.04	0.55
Sb										1.00	0.37	-0.10	0.07
V											1.00	0.32	0.39
Zn												1.00	0.001
F													1.00

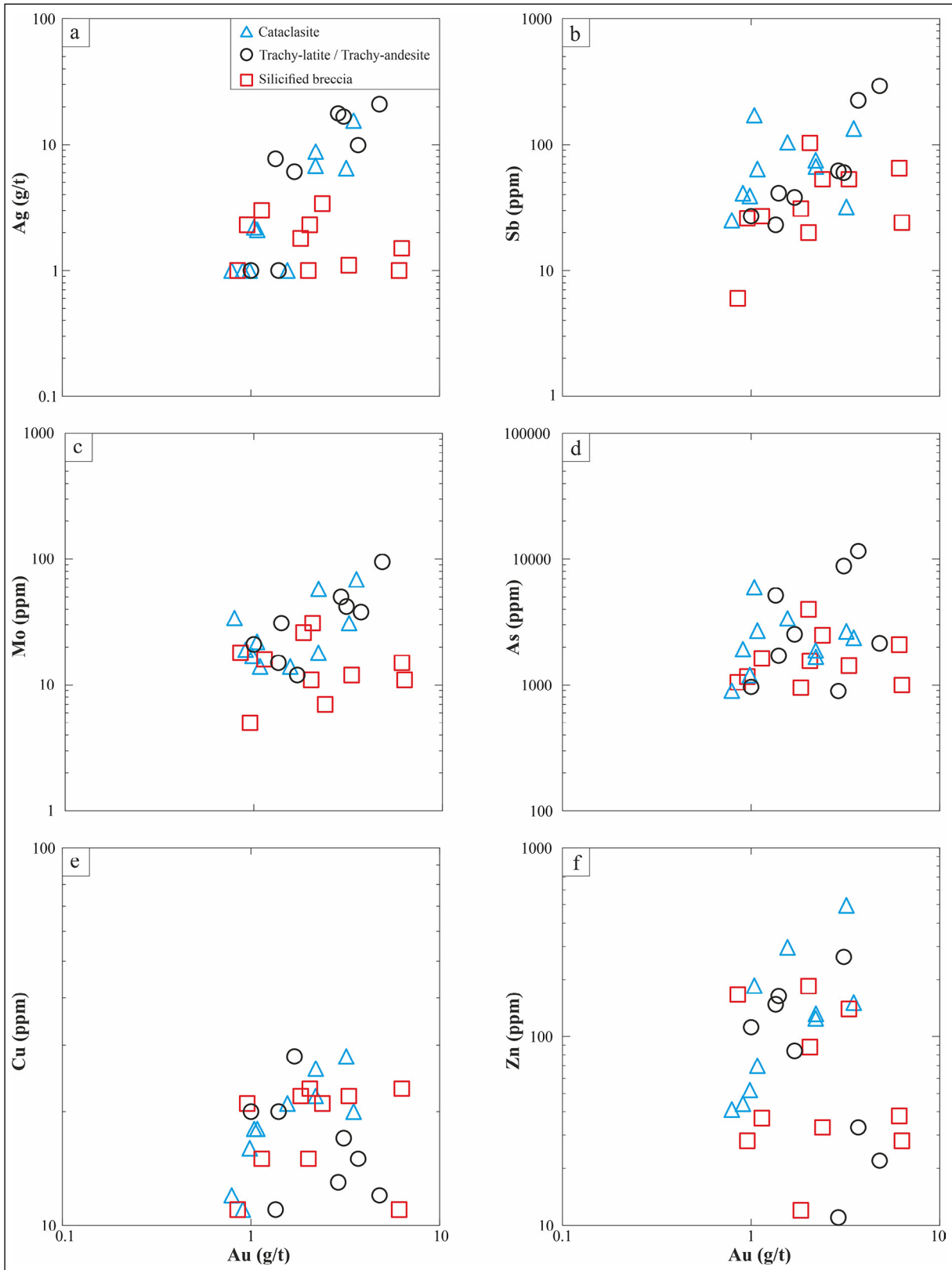


Figure 8- Binary variation diagrams against gold versus a) Ag, b) Sb, c) Mo, d) As, e) Cu and f) Zn. Compositional distributions of cataclasite (blue triangle), trachy-latite/trachy-andesite (empty circle), and silicified breccia (red square) of Yeşilyurt mineralizations.

lower towards the edges of the fault zone may indicate higher permeability and/or organic material. When geochemical data are combined with detailed geology, it gives the idea that this area is important in terms of Au, Ag, and As mineralizations. Therefore, the researches over the region should be continued.

6.3. Mineralization Genesis and Genetic Model

The origin of the fluids causing Yeşilyurt gold mineralization is currently not well understood. Trachy-latite/trachy-andesites exposed to intense sericite and carbonate alteration are directly associated with the ore and there is no age data. The spatial relationship of these rocks with the ore and the association of gold, fluorite, realgar, orpiment, and sulfide suggest that they have a genetic relationship with Paleogene-Neogene (?) magmatism.

Metal-containing fluids should have precipitated sulfides in a relatively low-temperature/low-pressure environment along the low angle fault zone (cataclasite and breccia) in the Yeşilyurt mineralization area. The erosion of the low angle fault zone caused erosion of the hanging wall itself as well. This situation has made the mineralization exhumed to be discovered.

The presence of brecciated, folded, and undisturbed quartz veins on the surface indicates faulting is a part of syn-mineralization. The presence of pyrite, fluorite, realgar, and orpiment together with breccia and cataclasites also suggest syn-mineralization.

Yeşilyurt gold mineralization is located along an unusual regional detachment/low-angle normal fault and it is the first gold deposit associated with a low-angle normal fault identified in the eastern Taurus orogenic belt. This mineralization will lead to the discovery of a new gold deposit belt along the Eastern Taurus orogenic belt.

6.4. Gold Deposits Associated with Detachment Faults

Different types of mineralization observed in low-angle detachment faults associated with metamorphic core complexes have mostly been described in the southwestern USA. Most of the studies have been in the Arizona Geology Survey. These deposits include Piacho (Drobeck et al., 1986; Liebler, 1988), Bullard Peak (Roddy et al., 1988), southwestern Arizona;

Cyclopic (Myers and Smith, 1986), northwestern Arizona; Riverside Pass (Wilkinson et al., 1988), Whipple-Buckskin-Rawhide (Spencer and Welty, 1986), Mesquite (Manske et al., 1988) southeastern California; San Luis (Benson and Jones 1996), Colorado. Apart from these deposits, Kokanee Range (Beaudoin et al., 1991) British Columbia; Luolin-Henan (Dai and Haiyang, 2005), China; Ada Tepe (Marchev et al., 2004), Bulgaria; Ernesto-Lavrinha (Puritch et al., 2016) and Brazilian deposits are examples of this mineralization type.

Such beds are divided into two categories by Eng et al., (1995) as base metalliferous (Whipple-Buckskin-Rawhide and Kokanee) and base-metal-poor (Piacho, Riverside Pass, Ada Tepe, and San Luis) deposits. Base-metal-poor deposits can be interpreted as detachment fault-controlled low-sulfidation gold mineralization. Mineralizations are in the form of massive, tabular ore bodies within the fault zone and they are open-space ore filling type in listric faults (Zappettini et al., 2017). Ores are observed in the areas showing intense silicification and brecciation taken place simultaneously with the detachment fault.

Quartz and fewer calcite minerals are the main gangue minerals in Yeşilyurt gold mineralization which has many common features with base-metal-poor gold deposits such as the presence of gold as tabular ore body in shallow-dipping detachment fault, quartz-pyrite and silica replacements and veinlets, limonite-hematite (transformation from pyrite) developed as supergene and also low base metal and low Au/Ag (average 1.07) content. On the other hand, the characteristics of the mineralization reveal some notable differences with the presence of common fluorite, realgar-orpiment (high As content), semi-graphite, and bacterial pyrite despite the lack of copper, specular hematite, and adularia, compared to the base-metal poor mineralizations associated with detachment faults. Besides, the lack of adularia which indicates the epithermal mineralization with low sulfidation and boiling of neutral pH solution, is an important factor that separates this deposit from epithermal system. In addition to these, syn-tectonic magmatic rocks defined along the detachment fault in the mineralization area have a genetic relationship with the ore and these syn-tectonic magmatic rocks have also been described in different areas around the world (Reynolds and Lister, 1987).

Yeşilyurt gold mineralization with its distinctive structures and differences is the first gold deposit associated with a low-angle normal fault in the region and country. Besides, the correlation between base metalliferous deposits associated with the low-angle normal fault and the stratigraphical and structural position and mineralization assemblage of the Cafana (Görgü)-Malatya Pb-Zn mineralization located in the north of the studied area can bring a new perspective to mineral exploration in the region.

Acknowledgments

This study was carried out as a part of MTA project titled “Maden Karmaşığı Polimetallik Maden Aramaları (2018/2020-32-13-01-1)”, affiliated to the General Directorate of Mineral Research and Exploration, Department of Mineral Research and Exploration. We would like to thank Geological Engineer (MSc.) Mahmut Eroğlu and Geological Engineer Turan Bengin who contributed to the field studies, Geological Engineers Tahsin Aksoy and Füsün Niğdeli (Feasibility Department), who estimated the reserve of the mineralization, and the Geological Engineer Yunus Sönmez for the revision of the figures in the article. Last but not least, we would like to thank all the MTA team. We also thank Ali Sholeh for his constructive criticism and suggestions.

References

- Akıncı, O.T. 2009. Ophiolite-hosted copper and gold deposits of southeastern Turkey: formation and relationship with seafloor hydrothermal processes. *Turkish Journal of Earth Sciences* 18, 475–509.
- Altman, K., Liskovich, M. 2011. Çöpler Sulfide Expansion Project prefeasibility study, Erzincan province, Turkey: Canadian National Instrument 43-101 Technical Report 176.
- Altuncu, S. 2009. Türkiye Fluorit Yataklarının Karşılaştırmalı İncelenmesi. Doktora Tezi, İstanbul Üniversitesi, Fen Bilimleri Enstitüsü, 147 (unpublished).
- Asutay, H. J., Turan, M., Poyraz, N., Orhan, H., Tari, E., Yazgan, E. 1986. Doğu Toroslar Keban-Baskil (Elazığ) Dolaylarının Jeolojisi. Maden Tetkik ve Arama Genel Müdürlüğü, Rapor No: 8007, Ankara (unpublished).
- Beaudoin, G., Taylor, B.E., Sangster, D.F. 1991. Silver-lead-zinc veins, metamorphic core complexes, and hydraulic regimes during crustal extension. *Geology* 19, 1217–1220.
- Bedi, Y., Yusufoglu, H. 2018. 1/100.000 scale Turkish Geological Maps, Malatya-L40 Quadrangle, No: 261, Publication of General Directorate of Mineral Research and Exploration 89. (in Turkish with English Abstract).
- Benson, R. G., Jones, D.M. 1996. Geology of the San Luis gold deposit, Costilla County, Colorado; an example of low-angle normal fault and rift-related mineralization in the Sangre De Cristo Range of Colorado. Special Publication - Colorado School of Mines
- Çelebi, H. 2009. Türkiye apatitli manyetit yatakları: jeolojisi, jeokimyası ve ekonomik potansiyeli. *İstanbul Yerbilimleri Dergisi* 22, 1, 67-83.
- Dai, T.G., Haiyang Z. 2005. The relationship between detachment faults and mineralization in Luolin district, Henan, China Mineral Deposit Research: Meeting the Global Challenge 909-911
- Drobeck, P.A., Hillemeier, J.L., Frost, E.G., Liebler, G.S. 1986. The Picacho Mine: a gold mineralized detachment in southeastern California. In: Beatty, B. and Wilkinson, P.A.K. (eds): *Frontiers in geology and ore deposits of Arizona and the Southwest*. Arizona Geological Society Digest. XVI, Tucson, 187–221.
- Dumanlılar, H.D., Aydal, D., Dumanlılar, O. 1999. Geology, mineralogy and geochemistry of sulfide mineralization in the İspendere region (Malatya). *Bulletin of the Mineral Research and Exploration* 121, 225–250.
- Eng, T., Boden D.R., Reischman, M.R., Biggs, J.O. 1995. Geology and mineralization of the Bullfrog Mine and vicinity, Nye County, Nevada. In: Coyner, A.R. and Fahey, P.L. (eds.): *Geology and ore deposits of the American Cordillera*. Symposium Proceedings, Geological Society of Nevada, Reno/Sparks, Nevada. 1, 353–400.
- Gözübol, A.M., Önal, M. 1986. Çat Barajı İsale tünelinin mühendislik jeolojisi ve kaya mekanik inceleme ve Malatya-Çelikhan alanının jeolojisi. TÜBİTAK, TB AG-647, Ankara.
- Hanelçi, Ş., Çelebi H. 2013. Geology and petrology of igneous rocks of the Zeryandere Lagerstaettendistriktes Keban, Elazığ Province, Turkey. *Journal of Geology Sciences* 41/42 (5-6), 301-315.
- Helvacı, C., Griffin, W.L. 1984. Rb-Sr geochronology of the Bitlis massif, Avnik (Bingöl) area, SE Turkey. In: Dixon, J.E. and Robertson, A.H.F. (eds). *Geological Evolution of the Eastern Mediterranean*. Special Publication of the Geological Society of London 17, 403-413.

- İmer, A., Richards, J.P., Creaser, R.A. 2012. Age and tectonomagmatic setting of the Eocene Çöpler-Kabatas, magmatic complex and porphyryepithermal Au deposit, East Central Anatolia, Turkey. *Mineralium Deposita* 48, 557–583
- Kalender, L. 2011. Oxygen, carbon and sulfur isotope studies in the Keban Pb-Zn deposits, eastern Turkey: an approach on the origin of hydrothermal fluids. *Journal of African Earth Sciences* 59 (4-5), 341–348.
- Kalender, L., Kırat, G., Bölücek, C., Sağıroğlu, A. 2009. Görgü (Malatya-Türkiye) Pb-Zn Cevherleşmelerinin Eski İmalat Pasalarının Jeokimyası, 62. Jeoloji Kurultayı, Ankara.
- Ketin, İ. 1983. Türkiye Jeolojisine Genel Bir Bakış: İTÜ Kütüphanesi, Sayı 1259, 595
- Kipman, E. 1981. Keban'ın jeolojisi ve Keban şaryajı İstanbul Üniversitesi Yerbilimleri Dergisi 1(1-2), 75-81.
- Kuşcu, İ., Yılmaz, E., Demirela, G. 2007. Iron oxide-copper-gold deposits in Turkish Tethyan collage: Society for Geology Applied to Mineral Deposits (SGA), roceedings of the 9th Biennial SGA Meeting, Dublin, 853–857.
- Kuşcu, İ., Gencalioglu-Kuşcu, G., Tosdal, R.M., Ullrich, T., Friedman, R., 2010. Magmatism in the Southeastern Anatolian orogenic belt: transition from arc to postcollisional setting in an evolving orogen. Geological Society, London, Special Publications 340, 437–460.
- Kuşcu, İ., Tosdal R.M., Gencalioglu Kuşcu, G., Friedman, R., Ullrich, T.D. 2013. Late Cretaceous to Middle Eocene magmatism and metallogeny of a portion of the Southeastern Anatolian orogenic belt, East-Central Turkey. *Economic Geology* 108 (4), 641-666
- Liebler, G.S. 1988. Geology and gold mineralization at the Picacho mine, Imperial County, California. In: Schafer, R.W., Cooper, J.J., Vikre, P.G. (eds): Bulk mineable precious metal deposits of the Western United States, Symposium Proceedings, Geological Society of, Reno/Sparks, Nevada. Part IV, Gold-silver deposits associated with detachment faults, 453–504.
- Long, K.R. 1992. Preliminary descriptive deposit model for detachment-fault-related mineralization. In: Bliss, J. (Ed.), *Developments in Mineral Deposit Modeling*. U.S. Geological Survey Bulletin 2004, 52-56.
- Manske, S.L., Matlack, W.F., Springett, M.W., Strakele, A.E., Jr, Watowich, S.N., Yeomans, B., Yeomans, E. 1988. Geology of the Mesquite deposit, Imperial County, California. *Mining Engineering* 40, 439-444.
- Marchev, P., Raicheva, R., Downes, H., Vaselli, O., Massimo, C., Moritz, R. 2004. Compositional diversity of Eocene-Oligocene basaltic magmatism in the Eastern Rhodopes, SE Bulgaria: implications for its genesis and geological setting. *Tectonophysics* 393, 301–328
- MTA, 2002. 1:500.000 scale geology map of Turkey. General Directorate of Mineral Research and Exploration (Turkey), Ankara, Turkey.
- Myers, I.A., Smith, E.I. 1986. Control of gold mineralization at the Cyclopic mine, Gold Basin district, Mohave county, Arizona. *Economic Geology* 81, 1553-1557.
- Okay, A.I. 2008. Geology of Turkey: A Synopsis. *Anschnitt* 21, 19-42.
- Özgül, N. 1976. Toroslar'da bazı temel jeoloji özellikleri. *TJK Bülteni* 19, 65-78
- Öztürk, H., Haniçli, N., Altuncu, S., Kasapçı, C. 2019. Rare Earth Element (REE) resources of Turkey: an overview of their formation types. *Bulletin of the Mineral Research and Exploration* 159, 127–141.
- Puritch, E., Bradfield, A., Routledge, R., Sutcliffe, R., Burga, D., Barry, J., Cornejo, F., Batelochi, M., Lister, D. 2016. Technical Report and updated Resource Estimate on the EPP Project. Mato Grosso, Brazil. Aura Minerals Inc. NI 43-101 & 43 - 101F1 Technical Report.
- Revan, M.K., Genç, Y. 2003. Malatya-Yeşilyurt altınlı fluorit cevherleşmesi: Toroslarda paleokarst tipi bir yatak. *Jeoloji Mühendisliği Dergisi* 27/2, 76-93.
- Reynolds, S.J., Lister, G.S. 1987. Structural aspects of fluid-rock interactions in detachment zones. *Geology* 15, 362-366.
- Robertson, A.H.F., Boulton, S.J., Taslı, K., İnan, N., Yıldırım, N., Yıldız, A., Parlak, O. 2016a. Late Cretaceous-Miocene sedimentary development of the Arabian continental margin in SE Turkey (Adıyaman Region): implications for regional palaeogeography and the closure history of Southern Neotethys. *Journal Asian Earth Science* 115, 571-616
- Robertson, A.H.F., Parlak, O., Yıldırım, N., Dumitrica, P., Taslı, K. 2016b. Late Triassic rifting and Jurassic–Cretaceous passive margin development of the Southern Neotethys: evidence from the Adıyaman area, SE Turkey. *International Journal of Earth Sciences* 105, 167–201
- Roddy, M.S., Reynolds, S.J., Smith, B.M., Ruiz, J. 1988. K-metasomatism and detachment-related

- mineralization, Harcuvar Mountains, Geological Society of America Bulletin 100 (10), 1627-1639.
- Sağiroğlu, A. 1988. Cafana (Görgü) Malatya karbonatlı Zn-Pb yatakları. Cumhuriyet Üniversitesi Mühendislik Fakültesi Dergisi Seri A, 5(1), 3-13.
- Spencer, J.E., Welty, F.W. 1986. Possible controls of base- and precious-metal mineralization associated with Tertiary detachment faults in the lower Colorado River through, Arizona and California. *Geology* 14, 195-198.
- Şaşmaz, A., Önal, A., Önal, M. 1999. Çelikhan (Adıyaman) fluorit cevherleşmeleri ve bunların NTE jeokimyası. I. Batı Anadolu Hammadde Kaynakları Sempozyum Bildirileri, 378-387
- Şaşmaz, A., Önal, A., Sağiroğlu, A., Önal, M., Akgül, B. 2005. Origin and nature of the mineralizing fluids of thrust zone fluorites in Çelikhan (Adıyaman, eastern Turkey): a geochemical approach. *Geochem J* 39, 131-139
- Şengör, A.M.C., Yılmaz, Y. 1981. Tethyan evolution of Turkey: A plate tectonic approach. *Tectonophysics* 75, 181 - 241.
- Wilkinson, W.H., Wendt, C.J., Dennis, M.D. 1988. Gold mineralization along Riverside Mountains Detachment Fault, Riverside County, California. Bulk mineable precious metal deposits of the Western United States, Symposium Proceedings, Part IV, Goldsilver deposits associated with detachment faults Nevada, 487-504.
- Yıldırım, E., Yıldırım, N., Dönmez, C., Koh, S., Günay, K. 2019. Mineralogy, rare earth elements geochemistry and genesis of the Keban-West Euphrates (Cu-Mo)-Pb-Zn skarn deposit (Eastern Taurus metallogenetic belt, E Turkey) *Ore Geology Reviews* 114 103102.
- Yıldırım, N. 2013. Havza-kuşak madenciliği kapsamında keşfedilen "GD Anadolu Kıbrıs Tipi VMS Metalojenik Kuşağı": Koçali Karmaşığı, Adıyaman Bölgesi, Türkiye. Maden Tetkik ve Arama Genel Müdürlüğü Doğal Kaynaklar ve Ekonomi Bülteni 14, 47-55.
- Yıldırım, N., İlhan, S., Yıldırım, E., Dönmez, C. 2012. The geology, geochemistry and genetical features of the Ormanbaşı Hill (Sincik, Adıyaman) copper mineralization. *Bulletin of the Mineral research and exploration* 144, 75-104.
- Yıldırım, N., Dönmez, C., Kang, J., Lee, I., Pirajno, F., Yıldırım, E., Günay, K., Seo, J.H., Farquhar, J., Chang, S.W. 2016. A magnetite-rich Cyprus-type VMS deposit in Ortaklar: A unique VMS style in the Tethyan metallogenetic belt, Gaziantep, Turkey. *Ore Geology Reviews* 79, 425-442.
- Yıldırım, N., Eroğlu, M., Aksoy, T., Niğdeli, F. 2019. Malatya-Yeşilyurt-Şerefhan yöresindeki AR: 201100417 (ER: 3102513) no'lu IV. Grup ruhsat sahasına ait (Au) madeninin buluculuk talebine esas kaynak tahmin raporu. Maden Tetkik ve Arama Genel Müdürlüğü (unpublished).
- Yılmaz, Y., Yiğitbaş, E., Yıldırım, M., Genç, Ş.C. 1992. Güneydoğu Anadolu metamorfik masiflerinin kökeni. Türkiye 9. Petrol Kongresi Bildirileri 296-306.
- Yılmaz, E., Kuşcu, İ., Demirela, G. 2003. Divriği A-B kafa cevherleşmeleri: Alterasyon zonları ve zonlanma süreçleri: *Bulletin of the Geological Society of Turkey*, 46, 17-34.
- Yiğit, Ö. 2009. Mineral Deposits of Turkey in Relation to Tethyan Metallogeny: Implication for Future Mineral Exploration. *Economic Geology* 104, 19-51.
- Zappettini, E.O., Rubinstein, N., Crosta, S., Segal, S.J. 2017. Intracontinental rift-related deposits: A review of key models. *Ore Geology Reviews* 89, 594-608.

Bulletin of the Mineral Research and Exploration Notes to the Authors

1. Aims of Publication

- To announce and share researches in all fields of geoscientific studies in Turkey with geoscientists worldwide.
- To announce scientific researches and practices on geoscientific surveys carried out by the General Directorate of Mineral Research and Exploration (MTA) to the public.
- To use the journal as an effective media for international publication exchange by keeping the journal in high quality, scope and format.
- To contribute to the development of Turkish language as a scientific language.

2. Scope

At least one of the following qualifications is required for publishing the papers in the Bulletin of Mineral Research and Exploration.

2.1. Research Articles

2.1.1. *Original Scientific Researches*

- These articles cover and contribute to the main subjects of the earth sciences, the original scientific researches and its results related to all aspects of disciplines in geoscience like exploration and evaluation of the underground sources and environmental problems, and
- The studies, which apply new aspects and methods for the solution of problems about the earth sciences and researches, which apply new aspects and methods for the solution of the problems, in the engineering sciences carried out in MTA.

2.1.2. *Review Articles*

These papers include comprehensive scholarly review articles that summarize and critically assess previous geoscientific researches with a new perspective and reveal a new approach.

2.2. Discussion/Reply

- This type of article is intended for the discussion of papers that have already been published in the latest issue of the Bulletin. The discussion/reply type articles, which criticize all or a part of a recently published article, are published in the following

first issue if it is submitted within six months after the publication of the Bulletin.

- The discussions are sent to the corresponding author of the original paper to get their reply before publication. The discussions about the paper with two or more authors are sent only to the corresponding author.
- If the review article is not published within the prescribed period then it is published alone. Later sent replies are not published. Re-criticising of the replies is not allowed.
- The authors should obey the rules of scientific ethics and discussions in their discussion/reply papers. The papers in this category should not exceed four printed pages of the journal including figures and tables etc. The format of the papers should be compatible with the “Spelling Rules” of the Bulletin.

2.3. Short Notes

- The short notes part of the Bulletin covers short, brief and concisely written research reports for papers including the data obtained from ongoing and/or completed scientific researches and practices related to geoscience and new and/or preliminary factual findings from Turkey and worldwide.
- The short notes will follow a streamlined schedule and will normally be published in the following first or second issue shortly after submission of the paper to the Bulletin.
- This type of articles should not exceed four printed pages of the journal including figures, tables and an abstract.

3. Submission and Reviewing of Manuscripts

- Manuscript to be submitted for publishing in the Journal must be written clearly and concisely in Turkish and/or English and prepared in the Bulletin of Mineral Research and Exploration style guidelines. All submissions should be made online at the <http://dergi.mta.gov.tr> website.
- The manuscript submitted for reviews must not have been published partially or completely previously in another journal.

- The rejected manuscripts are not returned back to author(s) whereas a letter of statement indicating the reason of rejection is sent to the corresponding author.
- Submitted manuscripts must follow the Bulletin style and format guidelines. Otherwise, the manuscript which does not follow the journals' style and format guidelines, is given back to corresponding author without any reviewing.
- Every manuscript which passes initial Editorial treatise is reviewed by at least two independent reviewers selected by the Editors. Reviewers' reports are carefully considered by the Editors and associated editors.
- The manuscript that need to be corrected with the advices of reviewer(s) is sent back to corresponding author(s) to assess and make the required corrections suggested by reviewer(s) and editors. The authors should prepare a letter of well-reasoned statement explaining which corrections are considered or not.
- If there are any suggestions given by editors and referees that are not accepted and corrected by the author, then it should be sent to the Editor's Office with corrected copies of the report explaining the reason for not accepting these suggestions and corrections.
- Figures and tabless should be 1/3 of the main text.
- To be published in the Bulletin of Mineral Research and Exploration, the printed length of the manuscript should not exceed 30 printed pages of the journal including an abstract, figures and tables. The publication of longer manuscripts will be evaluated by Editorial Board if it can be published or not.
- The authors must do the reviewer's corrections and proposals in 60 days and must upload to the system.
- At the printing stage after the last control, the first print of the manuscript are sent to the author/ authors in pdf version and asked from the author/ authors to make the press control.

4. Publication Language and Periods

- The Bulletin of Mineral Research and Exploration is published at least twice a year and each issue is published both in Turkish and English. Thus, the manuscripts are accepted in Turkish or English.

The spelling and punctuation guidelines of Turkish Language Institution are preferred for the Turkish issue. However, the technical terms related to geology are used in accordance with the decision of the Editorial Board.

5. Spelling Draft

Manuscripts should be written in word format in A4 (29,7 x 21 cm) size and double-spaced with font size Times New Roman 10-point, margins of 25 mm at the sides, top and bottom of each page.

The formulas requiring the use of special characters and symbols must be submitted by the symbols part of the Microsoft Office Word Program on computer.

Initial letters of the words in sub-titles must be capital. The first degree titles in the manuscript must be numbered and left-aligned, 10 point bold Times New Roman must be used. The second degree titles must be numbered and left-aligned, they must be written with 10 point normal Times New Roman. The third degree titles must be numbered and left-aligned, they must be written with 10 point italic Times New Roman. The fourth degree titles must be left-aligned without having any number; 10 point italic Times New Roman must be used. The text must continue placing a colon after the title without paragraph returns (See: Sample article: <http://bulletin.mta.gov.tr>).

One line spacing must be left after paragraphs within text.

Paragraphs must begin with 0,5 mm indent.

The manuscript must include the below sections respectively;

- o Title Page
- o The Name and Surname of the author and * sign (Adress, e-mail adres must be given at the bottom of the page)
- o Abstract
- o Key Words
- o Introduction
- o Body
- o Discussion
- o Conclusion
- o Acknowledgements
- o References

5.1. Title Page

The title must be short, specific and informative and written with small letters font size Times New Roman 12-point bold. The title mustn't contain the subjects insufficiently processed in the article.

5.2. Author(S)'S Name, Addresses and Email Address

- The name and surname of the author/authors must be written without affiliations. Name must be written in small letters, the surname must be written in capital letters.
- At the affiliation (work adres) written after the name and the surname of the author/authors only the name of the company must be written, the author's job mustn't be written.
- Information about the addresses must be given at the next line as 10-point and italic.
- ORCID number should be taken from www.orcid.org and placed below the address.
- At the articles with two or more than two authors, the numbers must be written above the surnames of the authors, the informations about their adresses must be given at the next line by leaving one space line. Also, at this part the corresponding author must be indicated by the (*) symbol and the telephone, FAX and e-mail address of the corresponding author must be given.
- Abbreviations must not be made while writing the name of the uthor and the affiliation adres. Adresses must be given in Turkish in the Turkish version, in English in the English version.
- At the end of the article the name of the corresponding author and contact informations must be added.

5.3. Abstract

- The abstract must be understandable before having a look at the text.
- The abstract should state briefly the overall purpose of the research, the aim of the article, its contributions to the known theories, new data, principle results and major conclusions.
- Tha abstract must contain short and brief sentences.
- Addressing other sections and illustrations of the text or other writings must be avoided.

- The information, which have not been mentioned in the text, must not be in the abstract.
- The article must be written as one paragraph, preferably. Please provide an abstract which doesn't exceed 200 words.
- The abstract must be written with 10-point, normal Times New Roman in single-spaced lines.
- "Abstract" must not be given for the writings that will be located in "Short Notes" section.
- The English abstract must be under the title of "Abstract".

5.4. Key Words

Immediately after the abstract, please provide up to 5 key words and with each words seperated by comma. These key words will be used for indexing purposes.

5.5. Introduction

- The introduction section should state the objectives of the work, research methods, location of the study area and provide an adequate and brief background by avoiding a detailed literature survey.
- Non-standard or uncommon classifications or abbreviations should be avoided. But if essential, then they must be defined at their first mention and used consistently thereafter. Seperate paragraphs could be organized for each of the subjects at the introduction part. If it is necessary, the subtitle can be given for each of them (for example method, material, terminology etc.).
- When pre-information is needed for facilitating the understanding of the text, this section can also be used (for example, statistical data, bringing out the formulas, experiment or application methods, and others).

5.6. Body

- In this chapter, there must be data, findings and opinions that are intended to convey to the reader about the subject. The body section forms the main part of the article.
- The data used in other sections such as "Abstract", "Discussions", and "Results" are caused by this section.
- While processing the subject, the care must be taken not to go beyond the objective highlighted in the "Introduction" section. The knowledge, which

do not contribute to the realization of the purpose of the article or are useless for conclusion, must not be included.

- All data used and the opinions put forward in this section must prove the findings obtained from the studies or they must be based on a reference by citation.
- The guidance and methods to be followed in processing subjects vary according to the characteristics of the subjects mentioned. Various topic titles can be used in this section as many as necessary.

5.7. Discussions

- Discussion of the data and findings that are objectively transferred in the Main Text section of the article should be done in this section. This must be written as a separate section from the results section.

5.8. Conclusions

- The main conclusion of the study provided by data and findings of the research should be stated concisely and concretely in this section.
- The subjects that are not mentioned sufficiently and/or unprocessed in the body section must not be included in this section.
- The conclusions can be given in the form of substances in order to emphasize the results of the research and to make the expression understandable.

5.9. Acknowledgements

- In this section, the significant contributions made in the realization of investigation that form the topic of the paper is specified. While specifying contributions, the attitude diverted the original purpose of this section away is not recommended. Acknowledgements must be made according to the following examples.
- This study was carried out within scope ofproject.
- I/we would like to thank to for contributing to the development of this article with his/her critiques.
- Academic and/or authoritorial affiliations are written for the contributions made because of requirement of ordinary task.

- For example:
- “Prof. Dr. İ. Enver Altınlı has led the studies”.
- “The opinions and warnings of Dr. Tandoğan Engin are considered in determining the chemistry of chrome minerals.”
- The contributions made out of the requirement of ordinary task:
- For example:
- “I would like to thank to Professor Dr. Melih Tokay who gives the opportunity to benefit from unpublished field notes”; “I would like to thank to the preliminary-Plan Chief Engineer Ethem Göğçer, State Hydraulic Work, 5th Zone”. Academic and / or task-occupational titles are indicated for such contributions.
- The contributions, which are made because of requirement of ordinary task but do not necessitate responsibility of the contributor mustn't be specified.
- For example:
- Sentences such as “I would like to thank to our General Manager, Head of Department or Mr. / Mrs. Presidentwho has provided me the opportunity to research” must not be used.

5.10. References

- All references cited in the text are to be present in the reference list.
- The authors must be sure about the accuracy of the references. Publication names must be written in full.
- Reference list must be written in Times New Roman, 9-point type face.
- The reference list must be alphabetized by the last names of the first author of each work.
- If an author's more than one work is mentioned, ranking must be made with respect to publication year from old to new.
- In the case that an author's more than one work in the same year is cited, lower-case alphabet letters must be used right after publication year (for example; Saklar, 2011a, b).
- If the same author has a publication with more than one co-author, firstly the ones having single author

are ranked in chronological order, then the ones having multiple authors are ranked in chronological order.

- In the following examples, the information related to works cited is regulated in accordance with different document/work types, considering punctuation marks as well.
- If the document (periodic) is located in a periodical publication (if an article), the information about the document must be given in the following order: surnames of the author/authors, initial letters of author's/ authors' first names. Year of publication. Name of the document. Name of the publication where the document is published, volume and/ or the issue number, numbers of the first and last pages of the document.

For example:

Gürsoy, M. 2017. Munzur Dağları Alt Miyosen çökelleri mollusk topluluğu ve paleoekolojisi (Doğu Anadolu, Türkiye). Maden Tetkik ve Arama Dergisi 155, 75-99.

Pamir, H.N. 1953. Türkiye'de kurulacak bir hidrojeoloji enstitüsü hakkında rapor. Türkiye Jeoloji Bülteni 4, 1, 63-68.

Robertson, A.H.F. 2002. Overview of the genesis and emplacement of Mesozoic ophiolites in the Eastern Mediterranean Tethyan region. Lithos 65, 1-67.

- If more than one document by the same authors is cited, firstly the ones having single name must be placed in chronological order, then the ones having two names must be listed in accordance with chronological order and second author's surname, finally the ones having multiple names must be listed in accordance with chronological order and third author's surname.
- If the document is a book, these are specified respectively: surnames of the author/authors, initial letters of author's/authors' first names. Year of publication. Name of the book (initial letters are capital). Name of the organization which has published the book, name of the publication where the document is published, volume and/ or the issue number, total pages of the book.

For example

Einsele, G. 1992. Sedimentary Basins. Springer-Verlag, p 628.

Meriç, E. 1983. Foraminiferler. Maden Tetkik ve Arama Genel Müdürlüğü Eğitim Serisi 23, 280p.

- If the document is published in a book containing the writings of various authors, the usual sequence is followed for the documents in a periodic publication. Then the editor's surname and initial letters of their name/names are written. "Ed." which is an abbreviation of the editor word is written in parentheses. Name of the book containing the document (initial letters are capital). Name of the organization which has published the book. Place of publication, volume number (issue number, if any) of the publication where the document is published, numbers of the first and last page of the document.

For example:

Göncüoğlu, M.C., Turhan, N., Şentürk, K., Özcan, A., Uysal, Ş., Yalınız, K. 2000. A geotraverse across northwestern Turkey. Bozkurt, E., Winchester, J.A., Piper, J.D.A. (Ed.). Tectonics and Magmatism in Turkey and the Surrounding Area. Geological Society of London Special Publication 173, 139-162.

Anderson, L. 1967. Latest information from seismic observations. Gaskell, T.F. (Ed.). The Earth's Mantle. Academic Press. London, 335-420.

- If name of a book where various authors' writings have been collected is specified, those must be indicated respectively: book's editor/editors' surname/surnames, and initial letters of their name/names. "Ed." which is an abbreviation of the editor word must be written in parentheses. Year of Publication. Name of the book (initial letters are capital). Name of the organization which has published the book, total pages of the book.

For example:

Gaskell, T.F. (Ed.) 1967. The Earth's Mantle. Academic Press, 520p.

- If the document is an abstract published in a Proceedings Book of a scientific activity such as conference/symposium/workshop ...etc. , information about the document must be given in the following order: surnames of the author/authors, initial letters of author's/authors' first names. Year of publication. Title of the abstract. Name, date and place of the meeting where the Proceedings Book

is published, numbers of the first and last pages of the abstract in the Proceedings Book.

For example:

Öztunalı, Ö., Yenişol, M. 1980. Yunak (Konya) yöresi kayaçlarının petrojenezi. Türkiye Jeoloji Kurumu 34. Bilim Teknik Kurultayı, 1980, Ankara, 36

Yılmaz, Y. 2001. Some striking features of the Anatolian geology. 4. International Turkish Geology Symposiums 24-28 September 2001, London, 13-14.

- If the document is one of the unpublished documents as report, lecture notes, and so on., information about the document must be given by writing the word “unpublished” in parentheses to the end of information about the document after it is specified in accordance with usual order which is implemented for a document included in a periodic publication.

For example:

Akyol, E. 1978. Palinoloji ders notları. EÜ Fen Fakültesi Yerbilimleri Bölümü, 45 p., İzmir (unpublished).

Özdemir, C. Biçen, C. 1971. Erzincan ili, İliç ilçesi ve civarı demir etütleri raporu. General Directorate of Mineral Research and Exploration Report No: 4461, 21 p. Ankara (unpublished).

- The followings must be specified for the notes of unpublished courses, seminars, and so on: name of the document and course organizer. Place of the meeting. Name of the book, corresponding page numbers.

For example:

Walker, G. R. Mutti, E. 1973. Turbidite facies and facies associations. Pacific Section Society for Sedimentary Geology Short Course. Anaheim. Turbidites and Deep Water Sedimentation, 119-157.

- If the document is a thesis, the following are written: surname of the author, initial letter of the author's first name. Year of Publication. Name of the thesis. Thesis type, the university where it is given, the total number of pages, the city and “unpublished” word in parentheses.

For example:

Seymen, İ. 1982. Kaman dolayında Kırşehir Masifi'nin jeolojisi. Doçentlik Tezi, İTÜ Maden Fakültesi, 145 s. İstanbul (unpublished).

- Anonymous works must be regulated according to publishing organization.

For example:

MTA. 1964. 1/500.000 ölçekli Türkiye Jeoloji Haritası, İstanbul Paftası. Maden Tetkik ve Arama Genel Müdürlüğü, Ankara.

- The date, after the name of the author, is not given for on-printing documents; “in press” and / or “on review” words in parenthesis must be written. The name of the article and the source of publication must be specified, volume and page number must not be given.

For example:

○ Ishihara, S. The granitoid and mineralization. Economic Geology 75th Anniversary (in press).

- Organization name, web address, date of access on web address must be indicated for the information downloaded from the Internet. Turkish sources must be given directly in Turkish and they must be written with Turkish characters.

For example:

○ ERD (Earthquake Research Department of Turkey). <http://www.afad.gov.tr>. March 3, 2013.

- While specifying work cited, the original language must be used; translation of the title of the article must not be done.

6. Illustrations

- All drawings, photographs, plates and tables of the article are called “illustration”.

• Illustrations must be used when using of them is inevitable or they facilitate the understanding of the subject.

• While selecting and arranging the illustrations' form and dimensions, page size and layout of the *Bulletin* must be considered, unnecessary loss of space must be prevented as much as possible.

• The pictures must have high quality, high resolution suitable for printing.

• The number of illustrations must be proportional to the size of the text.

- All illustrations must be sent as separate files independent from the text.
- While describing illustrations in the text, abbreviations must be avoided and descriptions must be numbered in the order they are mentioned in the text.
- Photographs and plates must be given as computer files containing EPS, TIFF, or JPEG files in 600 dpi and higher resolutions (1200 dpi is preferred) so that all details can be seen in the stage of examination of writing.

6.1. Figures

- Drawings and photos (except for the plates in the text) will be evaluated together as “Figure” and they must be numbered in the order they are mentioned in the text.
- The figures published in the Bulletin of Mineral Research and Exploration must be prepared in computer considering the dimensions of single-column width 7.4 m or double-column width 15.8 cm. Figure area together with the writing at the bottom should not exceed 15.8x21 in maximum.
- Unnecessasry details must not be given in figures or care must be taken not to use much space for information transfer.
- Figures must be arranged in such a way to be printed in black/white or colored.
- The figure explanations being justified in two margins must be as follows:

Figure 1- Sandıklı İlçesinin (Afyon); a) güneybatısının jeolojik haritası, b) İnceleme alanının genel dikme kesiti (Seymen 1981), c) Türkiye'nin önemli neotektonik yapıları (Koçyiğit 1994'den değiştirilerek).

Figure 1- a) Sandıklı ilçesinin güneybatısının jeolojik haritası, b) İnceleme alanının genel dikme kesiti (Seymen, 1981), c) Türkiye'nin önemli neotektonik yapıları (Koçyiğit 1994'den değiştirilerek).

- Drawings must be made by well-known computer programs painstakingly, neatly and cleanly.
- Using fine lines, which can disappear when figures shrinks, must be avoided. Symbols or letters used in all drawings must be in Times New Roman and not less than 2 mm in size when shrink.

- All standardized icons used in the drawings must be explained preferably in the drawing or with figure caption if they are too long.
- Linear scale must be used for all drawings. Author's name, figure description, figure number must not be included into the drawing.
- Photos must be in quality and quantity that will reflect the objectives of the subject.

6.2. Plates

- Plates must be used when needed a combination of more than one photo and the publication on a special quality paper.
- Plate sizes must be equal to the size of available magazine pagespace.
- Figure numbers and linear scale must be written under each of the shapes located on the Plate.
- The original plates must be added to the final copy which will be submitted if the article is accepted.
- Figures and plates must be independently numbered. Figures must be numbered with Latin numerals and plates with Roman numerals (e.g., Figure1, Plate I).
- There must be no description text on Figures.

6.3. Tables

- All tables must be prepared preferably in word format in Times New Roman fonts.
- Tables together with table top writing must not exceed 15x8 cm in size.
- The table explanations being justified in two margins must be as follows:

Table 1- Hydrogeochemical analysis results of geothermal waters in the study area.

7. Nomenclature and Abbreviations

- Non-standard and uncommon nomenclature abbreviations should be avoided in the text. But if essential, they must be described as below: In cases where unusual nomenclatures and unstandardized abbreviations are considered to be compulsory, the followed way and method must be described.
- Full stop must not be placed between the initials of words for standardized abbreviations (MER, SHW, etc.).
- Geographical directions must be abbreviated in English language as follows: N, S, E, W, NE ...etc.

- The first time used abbreviations in the text are presented in parenthesis, the parenthesis is not used for subsequent uses.
- The metric system must be used as units of measurement.
- Figure, plate, and table names in the article must not be abbreviated. For example, “as shown in generalized stratigraphic cross-section of the region (Figure 1.....”

7.1. Stratigraphic Terminology

Description of Stratigraphic units must be done according to rules of International Stratigraphic Guide (<https://stratigraphy.org/guide/>)” and “Turkey Stratigraphy Committee” (https://www.mta.gov.tr/v3.0/sayfalar/birimler/belgeler/Stratigrafi_adlama_kurallari.pdf). In addition, should be paid to attention to the use of Chronostratigraphy (lower, middle, upper, etc) and Geochronology (early, middle, late etc.) of the units, which have been updated by the “International Stratigraphy Committee” and accepted to be used in Turkish/English (<https://stratigraphy.org/chart>). “Approved/official and unapproved/unofficial” rules must be followed in naming and using all stratigraphic units.

7.2. Paleontologic Terminology

Fossil names in phrases must be stated according to the following examples:

- For the use of authentic fossil names;

e.g. Limestone with *Nummulites*

- When the authentic fossil name is not used;
- e.g. nummulitic Limestone
- Other examples of use;

e.g. The type and species of *Alveolina* / *Alveolina* type and species

- Taxonomic ranks must be made according to the following examples:
- The names of the fossils should be stated according to the rules given below:
 - For the first use of the fossil names, the type, species (cf., aff. ve gr.) and the author names must be fully indicated;

Alveolina aragonensis Hottinger, 1960, not reference

Alveolina cf. *aragonensis* Hottinger, 1960, not reference

Alveolina aff. *aragonensis* Hottinger, 1960, not reference

Alveolina gr. *aragonensis* Hottinger, 1960 not reference

- When a species (cf., aff. ve gr.) is mentioned for the second time in the text;

A. aragonensis

A. cf. aragonensis

A. aff. aragonensis

A. gr. aragonensis, not reference

- It is accepted as citation if stated as *Alveolina aragonensis* Hottinger (1960). Cited Hottinger (1960), stated in the Reference section.

Plate / Plate, In the descriptions of the figures / figures: Plate / Plate, In the descriptions of the figures / figures: Genus / Subgenus or Type / Subtype text should be written in bold and Italic, surname / surnames and year should be written normally.

Ordo: Foraminiferida Eichwald, 1830 Super family: Alveolinacea Ehrenberg, 1939	Not reference, Not stated in the Reference section
Family: Alveolinidae Ehrenberg, 1839	
Type genus: <i>Borelis</i> de Montfort, 1808	
Type species: <i>Borelis melenoides</i> de Montfort, 1808= <i>Nautilus melo</i> Fitchel and Moll, 1798	
<i>Borelis vonderschmitti</i> (Schweighauser, 1951) (Plate, Figure, Figure in Text)	Schweighauser, 1951 not reference
1951 <i>Neoalveolina vonderschmitti</i> Schweighauser, page 468, figure 1-4	Cited Schweighauser (1951), stated in the Reference section.
1974 <i>Borelis vonderschmitti</i> (Schweighauser), Hottinger, page, 67, plate 98, figure 1.7	Cited Hottinger (1974), stated in the Reference section.

Parahaymanella hakyemezae Acar, 2019;

Pseudohottingerina burdurensis Acar, 2019.

- The statement of plates and figures (especially for the articles of paleontology):

a. for the statement of species mentioned in the body text; *Borelis vonderschmitti* (Schweighauser, 1951)

(Plate, Figure, Figure in the body text).

b. When cited for other articles;

1951 *Neovalveolina vonderschmitti* Schweighauser, page 468, figure 1-4, figure in body text.

1974 *Borelis vonderschmitti* (Schweighauser), Hottinger, page 67, plate 98, figure 1-7.

c. For the citation in the text

(Schweighauser, 1951, page, plate, figure, figure in the body text)

(Hottinger, 1974, page, plate 97, figure 67, plate 98, figure 1-7, figure in the body text).

8. Citations

All the citations in the body text must be indicated by the last name of the author(s) and the year of publication, respectively. The citations in the text must be given in following formats.

- For publications written by single author:
 - It is known that fold axial plain of Devonian and Carboniferous aged units around Istanbul is NS oriented (Ketin, 1953, 1956; Altınlı, 1999).
 - Altınlı (1972, 1976) defined the general characteristics of Bilecik sandstone
- For publications written by two authors:
 - The upper parts of the unit contain Ilerdian fossils (Sirel and Gündüz, 1976; Keskin and Turhan, 1987, 1989).

- For publications written by three or more authors:

According to Caner et al. (1975) Alıcı formation reflects the fluvial conditions.

The unit disappears wedging out in the East direction (Tokay et al., 1984).

- If reference is not directly obtained but can be found in another reference, cross-reference should be given as follows:
 - It is known that Lebling has mentioned the existence of Lias around Çakraz (Lebling, 1932: from Charles, 1933).

9. Reprints

The author(s) will receive 2 two hard copies of the related issues.

10. Copyright and Conditions of Publication

- It is a condition of publication that work submitted for publication must be original, previously unpublished in whole or in part.
- It is a condition of publication that the authors who send their publications to the Bulletin of Mineral Research and Exploration hereby accept the conditions of publication of the Bulletin in advance.
- All copyright of the accepted manuscripts belong to MTA. The author or corresponding author on behalf of all authors (for papers with multiple authors) must sign and give the agreement under the terms indicated by the Regulations of Executive Publication Committee. Upon acceptance of an article, MTA can pay royalty to the authors upon their request according to the terms under the “Regulations of Executive Publication Committee” and the “Regulations of Royalty Payment of Public Office and Institutions”

All the information and forms about the Bulletin of Mineral Research and Explorations can be obtained from <http://bulletin.mta.gov.tr>